WOODHEAD PUBLISHING SERIES IN ELECTRONIC AND OPTICAL MATERIALS

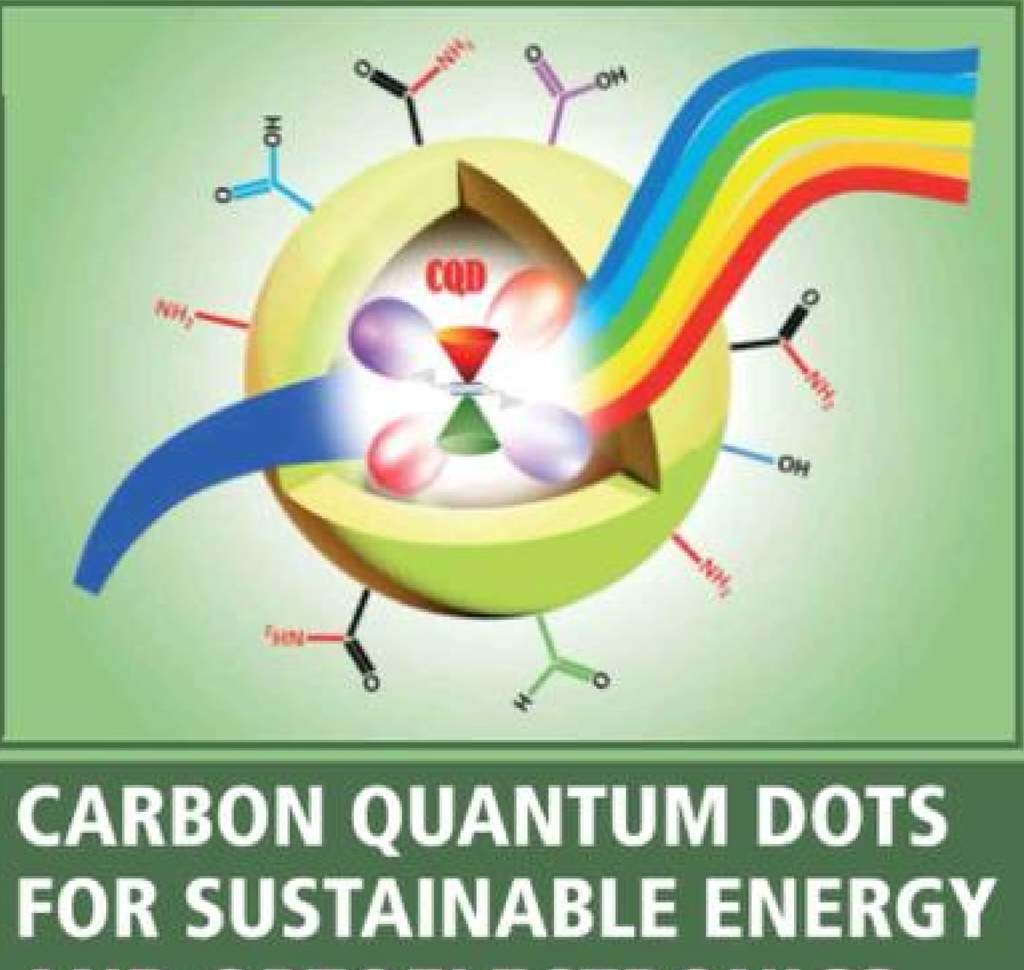
O
NH2
O
OH
OH
O
CQD
NH2
O
NH2
OH
NH2
H2N
O
H
O

CARBON QUANTUM DOTS FOR SUSTAINABLE ENERGY AND OPTOELECTRONICS

Edited by
SUDIP KUMAR BATABYAL
BASUDEV PRADHAN
KALLOL MOHANTA
RAMA RANJAN BHATTACHARJEE
AMIT BANERJEE

ELSEVIER

Carbon Quantum Dots for Sustainable Energy and Optoelectronics

Woodhead Publishing Series in Electronic and Optical Materials

Carbon Quantum Dots for Sustainable Energy and Optoelectronics

Edited by

Sudip Kumar Batabyal

Basudev Pradhan

Kallol Mohanta

Rama Ranjan Bhattacharjee

Amit Banerjee

ELSEVIER
WOODHEAD PUBLISHING
An imprint of Elsevier

Woodhead Publishing is an imprint of Elsevier
50 Hampshire Street, 5th Floor, Cambridge, MA 02139, United States
The Boulevard, Langford Lane, Kidlington, OX5 1GB, United Kingdom

Copyright © 2023 Elsevier Ltd. All rights reserved.

No part of this publication may be reproduced or transmitted in any form or by any means, electronic or mechanical, including photocopying, recording, or any information storage and retrieval system, without permission in writing from the publisher. Details on how to seek permission, further information about the Publisher's permissions policies and our arrangements with organizations such as the Copyright Clearance Center and the Copyright Licensing Agency, can be found at our website: www.elsevier.com/permissions.

This book and the individual contributions contained in it are protected under copyright by the Publisher (other than as may be noted herein).

Notices

Knowledge and best practice in this field are constantly changing. As new research and experience broaden our understanding, changes in research methods, professional practices, or medical treatment may become necessary.

Practitioners and researchers must always rely on their own experience and knowledge in evaluating and using any information, methods, compounds, or experiments described herein. In using such information or methods they should be mindful of their own safety and the safety of others, including parties for whom they have a professional responsibility.

To the fullest extent of the law, neither the Publisher nor the authors, contributors, or editors, assume any liability for any injury and/or damage to persons or property as a matter of products liability, negligence or otherwise, or from any use or operation of any methods, products, instructions, or ideas contained in the material herein.

ISBN: 978-0-323-90895-5 (print)

ISBN: 978-0-323-90896-2 (online)

For information on all Woodhead Publishing publications
visit our website at https://www.elsevier.com/books-and-journals

Publisher: Matthew Deans
Acquisitions Editor: Kayla Dos Santos
Editorial Project Manager: Sara Greco
Production Project Manager: Anitha Sivaraj
Cover Designer: Miles Hitchen

Typeset by MPS Limited, Chennai, India

ELSEVIER
Book Aid International
Working together
to grow libraries in
developing countries
www.elsevier.com • www.bookaid.org

List of contributors

Azrina Abd Aziz Faculty of Civil Engineering Technology, Universiti Malaysia Pahang, Kuantan, Pahang, Malaysia

Christabel Adjah-Tetteh Institute for Materials Research and Innovation, University of Louisiana at Lafayette, Lafayette, LA, United States; Department of Chemical Engineering, University of Louisiana at Lafayette, Lafayette, LA, United States

Daksh Agarwal Department of Materials Science and Engineering, University of Pennsylvania, Philadelphia, PA, United States; Lam Research Corporation, Fremont, CA, United States

Erin U. Antia Institute for Materials Research and Innovation, University of Louisiana at Lafayette, Lafayette, LA, United States; Department of Chemical Engineering, University of Louisiana at Lafayette, Lafayette, LA, United States

Aditya Banerjee Amity Institute of Applied Science, Amity University, Noida, Uttar Pradesh, India

Amit Banerjee Physics Department, Bidhan Chandra College, Asansol, West Bengal, India

Suranjana Banerjee Department of Electronics, Dum Dum Motijheel College, Dum Dum, Kolkata, West Bengal, India

Sudip K. Batabyal Department of Sciences, Amrita School of Engineering Coimbatore, Amrita Vishwa Vidyapeetham, Coimbatore, Tamil Nadu, India; Amrita Centre for Industrial Research and Innovation (ACIRI), Amrita School of Engineering Coimbatore, Amrita Vishwa Vidyapeetham, Coimbatore, Tamil Nadu, India

Lopamudra Bhattacharjee PSG Institute of Advanced Studies, Coimbatore, Tamil Nadu, India

Rama Ranjan Bhattacharjee Department of Chemistry, Sister Nivedita University, Kolkata, West Bengal, India

Jaydeep Bhattacharya NanoBiotechnology Lab, School of Biotechnology, Jawaharlal Nehru University, New Delhi, Delhi, India

Ashkan Momeni Bidzard Department of Basic Sciences, Abadan Faculty of Petroleum Engineering, Petroleum University of Technology, Abadan, Iran

S. Charis Caroline Department of Sciences, Amrita School of Engineering Coimbatore, Amrita Vishwa Vidyapeetham, Coimbatore, Tamil Nadu, India

Arup Chakraborty Department of Chemistry, Institute of Nanotechnology and Advanced Materials, Bar-Ilan University, Ramat Gan, Israel

Barsha Chakraborty Bionanotechnology Lab, Department of Chemistry, Indian Institute of Science Education and Research Bhopal, Bhopal, Madhya Pradesh, India

Oendrila Chatterjee Bionanotechnology Lab, Department of Chemistry, Indian Institute of Science Education and Research Bhopal, Bhopal, Madhya Pradesh, India

Soumyo Chatterjee School of Physical Sciences (SPS), Indian Association for the Cultivation of Science (IACS), Jadavpur, Kolkata, West Bengal, India

Nikhil Dole Department of Electrical and Computer Engineering, University of Houston, Houston, TX, United States

Tanoy Dutta Bionanotechnology Lab, Department of Chemistry, Indian Institute of Science Education and Research Bhopal, Bhopal, Madhya Pradesh, India

Manas Ranjan Gartia Department of Mechanical and Industrial Engineering, Louisiana State University, Baton Rouge, LA, United States

Morteza Sasani Ghamsari Photonics and Quantum Technologies Research School, Nuclear Science and Technology Research Institute, Tehran, Iran

Bharat Kumar Gupta Department of Physics, Deen Dayal Upadhyay Gorakhpur University, Gorakhpur, Uttar Pradesh, India

Apurba Lal Koner Bionanotechnology Lab, Department of Chemistry, Indian Institute of Science Education and Research Bhopal, Bhopal, Madhya Pradesh, India

Nikhil Kumar Department of Physics, Deen Dayal Upadhyay Gorakhpur University, Gorakhpur, Uttar Pradesh, India

Prashant Kumar Department of Energy Engineering, Central University of Jharkhand, Ranchi, Jharkhand, India

Sandeep Kumar Department of Energy Engineering, Central University of Jharkhand, Ranchi, Jharkhand, India

Akanksha Kumari Amity Institute of Integrative Science and Health, Amity University Gurgaon, Panchgaon, Haryana, India

Kah Hon Leong Department of Environmental Engineering, Faculty of Engineering and Green Technology, Universiti Tunku Abdul Rahman, Jalan Universiti, Kampar, Perak, Malaysia

Ashwathi A. Madhavan NanoBiotechnology Lab, School of Biotechnology, Jawaharlal Nehru University, New Delhi, Delhi, India

Arup Mahapatra Department of Energy Engineering, Central University of Jharkhand, Ranchi, Jharkhand, India; Centre of Excellence (CoE) in Green and Efficient Energy Technology (GEET), Central University of Jharkhand, Ranchi, Jharkhand, India

Tanmoy Majumder Department of Physics, National Institute of Technology, Agartala, Tripura, India; Department of Electronics and Communication Engineering, Tripura Institute of Technology, Agartala, Tripura, India

Sourav Mitra Institute for Functional Intelligent Materials, National University of Singapore, Singapore, Singapore

Kallol Mohanta PSG Institute of Advanced Studies, Coimbatore, Tamil Nadu, India; Nanotech Research Innovation and Incubation Centre (NRIIC), PSG Institute of Advanced Studies (PSG IAS), Peelamedu, Coimbatore, Tamil Nadu, India

Suvra Prakash Mondal Department of Physics, National Institute of Technology, Agartala, Tripura, India

Minhaj Uddin Monir Department of Petroleum and Mining Engineering, Jashore University of Science and Technology, Jashore, Bangladesh

Ranjita Ghosh Moulick Amity Institute of Integrative Science and Health, Amity University Gurgaon, Panchgaon, Haryana, India

Supratik Mukhopadhyay Department of Environmental Sciences, Louisiana State University, Baton Rouge, LA, United States

Pardhasaradhi Nandigana CSIR–EMF Division, Central Electrochemical Research Institute, Karaikudi, Tamil Nadu, India; Academy of Scientific & Innovative Research (AcSIR), Ghaziabad, Uttar Pradesh, India

Nagapradeep Nidamanuri Department of Chemistry, Middle East Technological University, Ankara, Turkey

Umi Rabiatul Ramzilah P. Remli Faculty of Civil Engineering Technology, Universiti Malaysia Pahang, Kuantan, Pahang, Malaysia

Subhendu K. Panda CSIR–EMF Division, Central Electrochemical Research Institute, Karaikudi, Tamil Nadu, India; Academy of Scientific & Innovative Research (AcSIR), Ghaziabad, Uttar Pradesh, India

Basudev Pradhan Department of Energy Engineering, Central University of Jharkhand, Ranchi, Jharkhand, India; Centre of Excellence (CoE) in Green and Efficient Energy Technology (GEET), Central University of Jharkhand, Ranchi, Jharkhand, India

Ankita Saha Amity School of Applied Sciences, Amity University, Kolkata, West Bengal, India

Sushant P. Sahu Department of Chemistry, University of Louisiana at Lafayette, Lafayette, LA, United States

Lan Ching Sim Department of Chemical Engineering, Lee Kong Chian Faculty of Engineering and Science, Universiti Tunku Abdul Rahman, Kajang, Selangor, Malaysia

Ryan Simon Department of Chemistry, University of Louisiana at Lafayette, Lafayette, LA, United States

Vidyadhar Singh Department of Physics, Jai Prakash University, Chapra, Bihar, India

Sumit K. Sonkar Department of Chemistry, Malaviya National Institute of Technology, Jaipur, Rajasthan, India

P. Sriram CSIR–EMF Division, Central Electrochemical Research Institute, Karaikudi, Tamil Nadu, India; Academy of Scientific & Innovative Research (AcSIR), Ghaziabad, Uttar Pradesh, India

M. Shiva Subramani Nanotech Research Innovation and Incubation Centre (NRIIC), PSG Institute of Advanced Studies (PSG IAS), Peelamedu, Coimbatore, Tamil Nadu, India

Sujatha D. CSIR–EMF Division, Central Electrochemical Research Institute, Karaikudi, Tamil Nadu, India; Academy of Scientific & Innovative Research (AcSIR), Ghaziabad, Uttar Pradesh, India

Tam Tran Institute for Materials Research and Innovation, University of Louisiana at Lafayette, Lafayette, LA, United States; Department of Chemical Engineering, University of Louisiana at Lafayette, Lafayette, LA, United States

Ravi P.N. Tripathi Department of Physics, Jai Prakash University, Chapra, Bihar, India

Yu Wang Department of Chemistry, University of Louisiana at Lafayette, Lafayette, LA, United States; Institute for Materials Research and Innovation, University of Louisiana at Lafayette, Lafayette, LA, United States

Yudong Wang Institute for Materials Research and Innovation, University of Louisiana at Lafayette, Lafayette, LA, United States; Department of Chemical Engineering, University of Louisiana at Lafayette, Lafayette, LA, United States

Guanguang Xia Institute for Materials Research and Innovation, University of Louisiana at Lafayette, Lafayette, LA, United States; Department of Chemical Engineering, University of Louisiana at Lafayette, Lafayette, LA, United States

Xiao-Dong Zhou Institute for Materials Research and Innovation, University of Louisiana at Lafayette, Lafayette, LA, United States; Department of Chemical Engineering, University of Louisiana at Lafayette, Lafayette, LA, United States

Contents

List of contributors xiii

Preface xix

1 Photophysical properties of carbon quantum dots **1**

Tanoy Dutta, Oendrila Chatterjee, Barsha Chakraborty and Apurba Lal Koner

1.1 Introduction 1

1.2 Optical absorption properties of carbon quantum dots 2

1.3 Factors influencing the photoluminescence properties of carbon quantum dots 4

1.3.1 Quantum confinement effect 4

1.3.2 Doping nonmetallic heteroatoms 5

1.3.3 Local heterogeneity originated from heteroatom-mediated surface defects 8

1.3.4 Influence of edge states 8

1.3.5 Red edge effect 9

1.3.6 Surface defect states 11

1.3.7 Aggregation-induced emission in carbon quantum dots 12

1.3.8 Förster resonance energy transfer 20

1.3.9 Photoinduced electron transfer 22

1.3.10 Electroluminescence of carbon dots 23

1.4 Conclusions and future aspect 25

References 26

2 The physical and chemical properties of carbon dots via computational modeling **29**

Arup Chakraborty

2.1 Introduction 29

2.2 Different carbon dots 29

2.3 Computational methods applied to study the properties of carbon dots 31

2.4 Theoretical studies of different properties of carbon quantum dots 32

2.4.1 Electronic structure 32

2.4.2 Optical properties 33

2.4.3 Electrocatalytic properties 35

2.4.4 Transport properties 36

2.4.5 Kondo effect in carbon quantum dots 36

2.5 Summary and outlook 37
References 38

3 **Synthesis of carbon quantum dots** **39**
Ankita Saha, Lopamudra Bhattacharjee and Rama Ranjan Bhattacharjee
3.1 Introduction 39
  3.1.1 Carbon quantum dots 39
3.2 Basic techniques for carbon quantum dot preparation 42
  3.2.1 Top-down approach 42
  3.2.2 Bottom-up approach 48
3.3 Conclusion 52
References 52
Further reading 53

4 **Characterization and physical properties of carbon quantum dots** **55**
Sujatha D., Pardhasaradhi Nandigana, P. Sriram and Subhendu K. Panda
4.1 Introduction 55
  4.1.1 Carbon quantum dots 56
  4.1.2 Structure of carbon quantum dots 59
  4.1.3 Types 60
4.2 Physical properties 62
  4.2.1 Physiochemical properties (catalytic) 64
  4.2.2 Optical properties 66
  4.2.3 Photoinduced electron transfer 72
  4.2.4 Biological properties 72
4.3 Characterization 73
  4.3.1 Structural characterization 73
  4.3.2 Photophysical analysis 80
  4.3.3 Stability of carbon quantum dots 85
4.4 Conclusions 85
References 86

5 **Surface engineering of carbon quantum dots** **91**
Ankita Saha, Lopamudra Bhattacharjee and Rama Ranjan Bhattacharjee
5.1 Introduction 91
  5.1.1 Carbon nanotube versus carbon quantum dots 91
  5.1.2 Fundamentals of surface engineering in carbogenic allotropes 93
5.2 Methodology 93
  5.2.1 Hydrothermal carbonization 93
  5.2.2 Microwave-assisted pyrolysis 96
  5.2.3 Sol−gel reaction 99
  5.2.4 Condensation reaction 100
  5.2.5 Oxidation−polymerization reaction 101
5.3 Conclusion 102
References 102

6 Photodetector applications of carbon and graphene quantum dots 105
Suvra Prakash Mondal and Tanmoy Majumder
6.1 Introduction 105
6.2 Synthesis of carbon quantum dots and graphene quantum dots 106
  6.2.1 Top-down synthesis process 106
  6.2.2 Bottom-up synthesis process 107
6.3 Optical absorption, emission, and electrical properties 108
6.4 Optoelectronics applications of carbon quantum dots and graphene quantum dots 112
6.5 Photodetector applications of carbon quantum dots and graphene quantum dots 113
  6.5.1 FET-based photodetectors using carbon quantum dots and graphene quantum dots 114
  6.5.2 Carbon quantum dots or graphene quantum dots-sensitized nanomaterial-based photodetectors 120
  6.5.3 Polymer nanocomposite-based photodetectors 125
6.6 Conclusions 128
References 128

7 Photovoltaic application of carbon quantum dots 135
Prashant Kumar, Arup Mahapatra, Sandeep Kumar and Basudev Pradhan
7.1 Introduction 135
7.2 Carbon quantum dots in dye-sensitized solar cells 136
  7.2.1 Carbon quantum dots as sensitizer 137
  7.2.2 Carbon quantum dots as counter electrode 142
7.3 Carbon quantum dots in organic solar cells 144
7.4 Carbon quantum dots in solid-state solar cells 148
7.5 Carbon quantum dots in perovskite solar cells 150
7.6 Carbon quantum dots in all-weather solar cells 154
7.7 Summary and perspective 154
Acknowledgments 155
References 155

8 Light-emitting diode application of carbon quantum dots 159
Morteza Sasani Ghamsari and Ashkan Momeni Bidzard
8.1 Introduction 159
8.2 Synthesis methods of functionalized carbon quantum dots 159
  8.2.1 Electrochemical synthesis 160
  8.2.2 Arc discharge 160
  8.2.3 Pulsed laser ablation/passivation technique 161
  8.2.4 Microwave-assisted synthesis 161
  8.2.5 Hydrothermal and solvothermal synthesis 163
8.3 Optical properties of carbon quantum dots 163
  8.3.1 Optical absorption 164

8.3.2 Photoluminescence emissions from ultraviolet to near-infrared regions 164
8.3.3 Electroluminescence 168
8.4 Carbon quantum dots device applications 169
8.4.1 Light-emitting diodes 169
8.4.2 Optical gain and lasing 174
8.5 Summary 175
References 176

9 Nanoelectronic applications of carbon quantum dots 183
M. Shiva Subramani, Soumyo Chatterjee and Kallol Mohanta
9.1 General introduction 183
9.2 Memory devices 185
9.2.1 Classifications of memory devices 185
9.2.2 Random access memory 187
9.3 Transistors 193
9.3.1 Basics of transistor 193
9.3.2 Carbon quantum dots used in transistor applications 194
9.4 Sensors 197
9.5 Carbon quantum dot laser 200
Reference 200

10 Carbon quantum dot-based nanosensors 205
Ankita Saha, Lopamudra Bhattacharjee and Rama Ranjan Bhattacharjee
10.1 Introduction to nanosensors 205
10.2 Chemical sensing 206
10.2.1 Fluorescence-based chemical sensing 206
10.2.2 Chemical sensors: nanoparticles as superior components 208
10.2.3 CQDs: fluorescent sensor material 208
10.2.4 pH sensor 212
10.2.5 Effect of solvent: sensing dielectric of surrounding medium 216
10.2.6 Doped CQDs in sensors: metal ion detection 216
10.2.7 Gas sensing with conducting carbon dots 218
10.2.8 A VOC sensor based on CQDs 221
10.3 Conclusion 223
References 223

11 Carbon dots: biomedical applications 225
Ashwathi A. Madhavan, Ranjita Ghosh Moulick and Jaydeep Bhattacharya
11.1 Carbon dots: structure and functionalization 225
11.2 Biosynthesis of carbon dots 226
11.3 Bioimaging applications of carbon dots 226
11.3.1 Carbon dots: optical properties 227

11.4 Biomedical applications of carbon dots 227
  11.4.1 Drug delivery 227
  11.4.2 Crossing blood-brain barrier 229
  11.4.3 Gene delivery 230
11.5 Biosensing applications using carbon dots 230
11.6 Future scope and challenges 232
References 233

12 Bioimaging applications of carbon quantum dots 239
Akanksha Kumari, Jaydeep Bhattacharya and Ranjita Ghosh Moulick
12.1 Introduction 239
12.2 Development of various bioimaging modalities 240
12.3 Requirement of imaging agents 241
12.4 Nanomaterials as imaging agents 242
12.5 Carbon quantum dots 243
12.6 Synthesis and modifications in carbon quantum dots 244
  12.6.1 Chemical ablation 244
  12.6.2 Electrochemical method 244
  12.6.3 Laser ablation 244
  12.6.4 Arc Discharge method 245
  12.6.5 Hydrothermal method 245
  12.6.6 Microwave irradiation 245
  12.6.7 Pyrolysis method 245
12.7 Surface activation 245
  12.7.1 Surface passivation 246
  12.7.2 Surface functionalization 246
  12.7.3 Doping 247
12.8 Properties of carbon quantum dots 247
  12.8.1 Fluorescence 247
  12.8.2 Quantum yield 248
12.9 cDot in bioimaging 248
  12.9.1 In vitro imaging 250
  12.9.2 In vivo imaging 251
  12.9.3 Single-molecule imaging 251
12.10 Conclusion 254
References 254

13 Photocatalytic applications of carbon quantum dots for wastewater treatment 263
Umi Rabiatul Ramzilah P. Remli, Azrina Abd Aziz, Lan Ching Sim, Minhaj Uddin Monir and Kah Hon Leong
13.1 Overview on advanced oxidation process and photocatalysis 263
13.2 Mechanism of photocatalysis 266
13.3 Photocatalysts material 268
13.4 Binary metal oxides 268

13.5 Metal sulfides 270
13.6 Fundamentals of carbon quantum dots 271
13.7 Roles of carbon quantum dots in photocatalysis 274
  13.7.1 Broaden the optical absorption range of photocatalyst 274
  13.7.2 Improved charge separation and electron transfer 276
  13.7.3 Allocate additional surface for adsorption and reaction 277
13.8 Synthesis route of carbon quantum dots 277
  13.8.1 Top-down method 277
  13.8.2 Bottom-up method 278
13.9 Hydrothermal treatment of carbon quantum dots 278
13.10 Watermelon rinds potential as carbon precursor 283
13.11 Application of carbon quantum dots in photocatalysis 283
  13.11.1 Application of carbon quantum dots-based composite in water purification 283
References 285

14 Current prospects of carbon-based nanodots in photocatalytic CO_2 conversion 295
Sushant P. Sahu, Christabel Adjah-Tetteh, Nagapradeep Nidamanuri, Sumit K. Sonkar, Erin U. Antia, Tam Tran, Guanguang Xia, Yudong Wang, Ryan Simon, Manas Ranjan Gartia, Supratik Mukhopadhyay, Yu Wang and Xiao-Dong Zhou
14.1 Introduction 295
14.2 Synthetic approaches and optical properties of carbon quantum dots 299
  14.2.1 Carbon dots and graphene quantum dots: an overview 299
14.3 Carbon-based quantum dots in CO_2 photoconversion 310
  14.3.1 Photocatalytic CO_2 reduction 310
  14.3.2 Photophysical characteristics and CO_2 photoconversion with carbon-based catalysts 314
14.4 Concluding remarks 326
Acknowledgments 334
References 334

15 Carbon quantum dots and its composites for electrochemical energy storage applications 341
S. Charis Caroline and Sudip K. Batabyal
15.1 Introduction 341
15.2 Fundamentals of supercapacitors and batteries 342
  15.2.1 Fundamentals of supercapacitors 342
  15.2.2 Fundamentals of batteries 345
15.3 Desired properties of carbon quantum dots for charge storage applications 349
  15.3.1 Structural properties 349
  15.3.2 Electrical properties 350
  15.3.3 Optical properties 350

15.4 Carbon quantum dots for supercapacitors 351
  15.4.1 Carbon quantum dots—inorganic hybrid for supercapacitors 353
  15.4.2 Carbon quantum dots—organic hybrid supercapacitors 355
  15.4.3 Graphene quantum dots 360
15.5 Carbon quantum dots for batteries 361
  15.5.1 Carbon quantum dots in lithium-ion and sodium-ion batteries 362
  15.5.2 Carbon quantum dots in potassium-ion batteries 364
  15.5.3 Carbon quantum dots in lithium-sulfur batteries 364
  15.5.4 Carbon quantum dots in zinc-ion batteries 365
References 366

16 Magnetic and nanophotonics applications of carbon quantum dots 377
Ravi P.N. Tripathi, Vidyadhar Singh, Bharat Kumar Gupta and Nikhil Kumar
16.1 Introduction 377
16.2 Applications 378
  16.2.1 Magnetic applications 378
  16.2.2 Nanophotonic applications and single-photon emission 382
16.3 Summary and future perspectives 390
Acknowledgments 392
References 392

17 Carbon quantum dots: An overview and potential applications in terahertz domain 397
Suranjana Banerjee
17.1 Introduction 397
17.2 Characteristic lengths 400
17.3 Quantum dot 402
  17.3.1 Density of states of electrons in quantum dots 403
17.4 Fabrication techniques of quantum dots 404
  17.4.1 Quantum dots based on II−VI compound semiconductors 405
  17.4.2 Self-assembled quantum dots 406
17.5 Optical properties of quantum dots 407
  17.5.1 Optical properties of indirect gap nanocrystal 409
17.6 Applications of carbon quantum dot in the biomedical field 410
  17.6.1 Optical imaging 410
  17.6.2 Photoacoustic imaging 413
  17.6.3 Drug delivery 413
  17.6.4 Crossing blood−brain barrier 413
  17.6.5 Gene delivery 414
17.7 Carbon nanostructures in terahertz domain 414
  17.7.1 Terahertz time-domain spectroscopy for generation of coherent radiation 414

17.7.2 Time-resolved spectroscopy and terahertz conductivity in carbon nanostructures 416
17.8 Conclusion and future prospect 416
References 417

18 Nanocarbon-based single-electron transistors as electrometer 423
Sourav Mitra
18.1 Theory 423
18.1.1 Introduction to single-electron transistor 423
18.1.2 Origin of coulomb blockade oscillation 423
18.2 Application: single-electron transistor as an electrometer 426
18.2.1 Measuring inverse compressibility 426
18.2.2 Experimental realization of a single-electron transistor electrometer: comparing aluminum single-electron transistor to carbon nanotube single-electron transistor 429
18.3 Reviewing published work 434
18.3.1 Application of Al-based single-electron transistor 434
18.3.2 Application of carbon nanotube-based single-electron transistor 442
18.4 Conclusion 452
References 453

19 Nanodiamonds for advanced photonic and biomedical applications 455
Daksh Agarwal, Nikhil Dole, Aditya Banerjee and Amit Banerjee
19.1 Introduction to nanodiamond photonics 455
19.1.1 Optical emission from diamond 455
19.1.2 ND photonic applications 457
19.2 NDs for biomedical applications 459
19.2.1 Cancer therapy applications 459
19.2.2 Biomedical imaging applications 462
19.3 Conclusions 466
Acknowledgments 467
References 467

20 Future perspectives of carbon quantum dots 473
Amit Banerjee, Sudip K. Batabyal, Basudev Pradhan, Kallol Mohanta and Rama Ranjan Bhattacharjee
20.1 Introduction 473
20.2 Future perspectives of CQDs 474
20.2.1 Luminescent doped/co-doped CQDs for optical sensing 474
20.3 Conclusion 477
Acknowledgments 477
References 478

Index 481

Preface

In congruence with all progress made by human society, the thrust on natural resources has escalated incessantly, which has had a detrimental impact on the health of ecosystems and the well-being of people. Hence, striking a balance between progressive industrialization led economic development and consumption of natural resources is the only way forward for the sustainability of the evolution of society. Sustainable development is defined by the United Nations as the development of present society keeping in view the generations to come. As natural resources are limited, they should be used judiciously and optimally to ensure that there is enough left for future generations as well, without affecting the present quality of life. A sustainable society must thrive to be socially responsible, technologically accessible, and economically feasible keeping in view environmental protection and dynamic equilibrium between human and natural ecosystems. The main pillars of sustainable development are energy, water, and health care. The United Nations has declared them as the goals in the United Nations Sustainable Development Goals SDG7 and SDG6 to ensure access to affordable, clean, reliable, sustainable, and modern energy and to ensure availability and sustainability of clean water and sanitation to all without affecting the environment. Scientific community should focus their research toward attaining these goals. Nanotechnology, a recently developed innovative technology dealing with the science and technology in a nano dimension, is established as a promising tool for achieving these goals. Nanotechnology has the potential to fulfill the overwhelming demand for energy and basic commodities and advancing technology without affecting our environment, climate, and natural resources. The global sustainability challenges our world faces today can be solved by nanotechnology as an environmentally acceptable technique. The main components of nanotechnology in the battle are the nanomaterials and quantum dots. Quantum dots, few nanometers in size, are particles where quantum mechanics are predominant, with the associated quantum mechanical waves confined in nano-dimensions and generating size-dependent discrete energy levels. Generally, in a quantum dot, the energy gap between the conduction band and the valence band or the gap between the HOMO and LUMO is dependent on the particle size. The electronic waves associated with the free electrons on the particles are confined within the boundary of the particle (dimension of the particle) and the energy associated with them is quantized according to the size of the particle. So, the optical and electronic properties of the quantum dots differ largely from their bulk counterparts. The quantum dots have the properties lying somewhere between the bulk and the atom/molecules, and they vary with size and shape. Now the carbon quantum dots (CQDs) have emerged as a game changer among different quantum dots and other allotropes of nanocarbon because of simple and sustainable fabrication methods involved. There are different types of allotropes of nanocarbon such as carbon nanotube, buckminsterfullerene, graphene and nanodiamond used in nano-engineering facilitating sustainable development. Carbon, the group 14 member of the periodic table, has a very interesting electronic structure and multiple valance and coordination numbers. Because of different oxidation numbers and catenation properties of carbon, there exist a large variety of allotropes with orbital hybridization along with the structure, governing their properties. Among the nanocarbon allotropes, CQDs are attracting a good deal of research interest because of their ease of synthesis and versatile applications. The CQDs can be synthesized from carbon-containing materials, mainly biomaterials, by a simple chemical reduction process. The simple technique for surface passivation and functionalization adds to the host of characteristics of CQDs for applications in different fields for sustainable development.

This book solely focuses on the different aspects of CQDs facilitating sustainable development of our society. First, this book discusses the structure−property relationship of CQDs in optical domains in detail. As the photophysical properties of CQDs are the most interesting and studied ones, we focused on understanding the photophysical properties and their origin. This book also discusses the theoretical modeling of the CQDs from a basic to an advanced level. The synthesis of CQDs is more beneficial compared to other nanomaterials, especially carbon nanomaterials like CNT and graphene, as it does not require sophisticated instrumentation and technology. A facile and cost-effective synthesis method for CQDs makes them very popular among researchers. The third chapter of the book delivers the details of the synthesis method of CQDs. Following the synthesis, the physical properties and different characterization techniques of CQDs are covered. As the properties of the CQDs are predominantly controlled by the surface states of the CQDs, this book pays special attention to the surface functionalization of CQDs in the next chapter. Most of the fabrication methods of CQDs are sustainable ones, but if we want to highlight the role of CQDs in sustainable development, it is mainly derived from the different application aspects of the CQDs. We focus on the application of CQDs in energy harvesting, energy storage, and wastewater treatment to biosensing in other chapters. Biomedical applications of CQDs ranging from bioimaging to theranostics are covered in subsequent chapters. The magnetic applications of CQDs and composites of CQDs are also discussed. Finally, the CQD-based optical and electronic nanodevices are discussed with a special focus on terahertz applications and single electron transistor applications. Another form of carbon nanoparticle, nano-diamond, is explored for photonic and biomedical applications. The book concludes with a summary of recent advancements and future prospects of CQDs for sustainable applications.

Sudip Kumar Batabyal
Basudev Pradhan
Kallol Mohanta
Rama Ranjan Bhattacharjee
Amit Banerjee

Photophysical properties of carbon quantum dots

1

Tanoy Dutta, Oendrila Chatterjee*, Barsha Chakraborty* and Apurba Lal Koner*
Bionanotechnology Lab, Department of Chemistry, Indian Institute of Science Education and Research Bhopal, Bhopal, Madhya Pradesh, India

1.1 Introduction

Luminescent nanomaterials have gained significant attention due to their tunable optical properties, stability, and suitable surface passivation for various applications such as optoelectronic application, sensing, drug delivery, photocatalysis, and biological imaging. As emerging luminescent nanomaterials, carbon-based nanomaterials have received overwhelming attention in multiple disciplines. Carbon dots is a generic term used for a variety of nanosized carbonaceous materials which include graphene quantum dots (GQDs), carbon nanodots, carbon quantum dots (CQDs), and carbonized polymer dots. CQDs with a size smaller than 10 nm have attracted much of our attention due to their unique advantageous properties such as ease of synthesis, high photostability, good solution dispersibility, low toxicity with chemical inertness, and most importantly tunable luminescence properties. Due to these aforementioned properties, CQDs have been extensively used in light-emitting devices, biosensing, and bioimaging applications. Since the first discovery of luminescent CQDs from single-walled carbon nanotubes back in 2004, mainly two major types of synthetic approaches are adopted. In the top-down method, using laser ablation and arc discharge methods, larger carbonaceous materials are converted into small nanosized structures with a size smaller than 10 nm. However, in the bottom-up approach, small organic molecule precursors are used to get CQDs using various chemical synthesis methods such as chemical oxidation, ultrasound synthesis, microwave-assisted synthesis, and hydrothermal synthesis. The bottom-up approach is preferred over the top-down due to the easy tuning of the reaction parameters to achieve a desirable size distribution and optical properties. The quality of CQDs emission can be tuned using a choice of precursor, concentration, reaction time, surface functionality, and the rate of formation of the CQDs (Fig. 1.1).

Generally, the synthesized CQDs possess a spherical to nearly spherical shape with a diameter less than 10 nm with a graphitic core, and the surface is decorated with various functional groups such as carboxyl, hydroxyl, amide, epoxide, and carbonyl. The luminescence properties of CQDs are illusive as they show excitation

---

* Contributed equally to this work.

Carbon Quantum Dots for Sustainable Energy and Optoelectronics. DOI: https://doi.org/10.1016/B978-0-323-90895-5.00015-1
© 2023 Elsevier Ltd. All rights reserved.

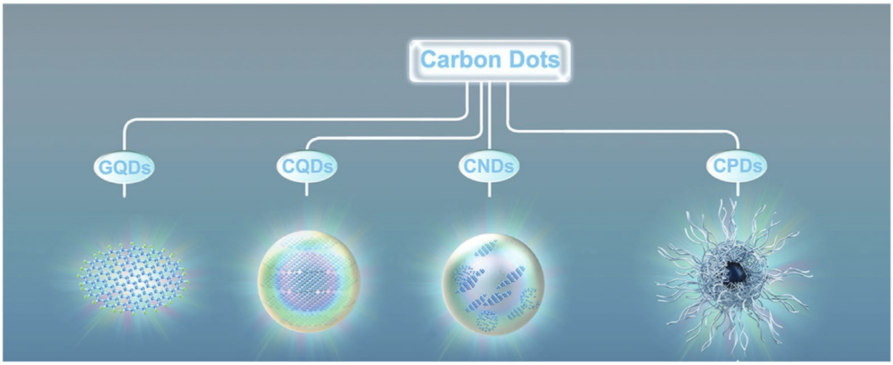

Figure 1.1 Classes of quantum dots (QDs), including graphene quantum dots (GQDs), carbon quantum dots (CQDs), carbon nanodots (CNDs), and carbonized polymer dots (CPDs) [1].
Source: From Copyright 2019 Wiley.

wavelength-dependent photoluminescence (PL) properties, photoinduced electron transfer, surface defects, localized trap states, and electrochemical properties. Although a great deal of investigation has been carried out to understand the photophysical properties, the mechanism of PL still remains a matter of discussion. In this chapter, we plan to provide an in-depth and current understanding of the origin of the photophysical properties of CQDs.

1.2 Optical absorption properties of carbon quantum dots

The optical absorption of carbon dots lies primarily in the UV region which occasionally tails the visible and even near infrared (NIR) region. Fig. 1.2 illustrates the absorption spectrum of CQDs as a function of electronic transitions of both the core and shell of CQDs. The shell refers to the functional groups embellished on the core. The short wavelength bands below 300 nm (Fig. 1.2, Band I) correlate to the π-π^* transition of aromatic sp^2 carbons, while the tail in the region of 300–400 nm (Fig. 1.2, Band II) arises from the n-π^* transition of the carbonyl bond. These aforementioned transitions pertain to the core of CQDs. Absorption bands beyond 400 nm (Fig. 1.2, Band III–V) are endemic to surface state transitions involving electron lone pairs. Note that the n-π^* transition of the core is often overlapped with the broad absorption bands of the surface state. It is worth mentioning that the absorption band at 300 nm ensues either from π-π^* or n-π^* charge transfer transitions or interlayer charge transfer with a predominance of π-π^* character. Moreover, additional factors, such as structural fluctuations, surrounding environment, protonation-deprotonation, and excitonic coupling, can only weakly alter the absorption spectra. When graphitic nitrogen is added to the existent sp^2 lattice, the

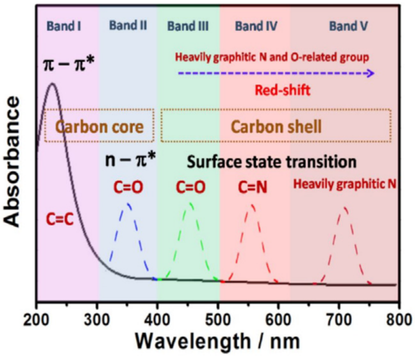

Figure 1.2 Schematic representation of the UV−visible spectrum and different possible electron transitions of CQDs over the range of wavelengths [2]. *CQDs*, Carbon quantum dots.

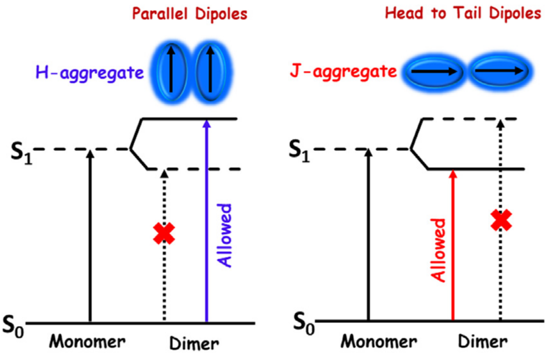

Figure 1.3 Schematic representation to elucidate Kasha's molecular exciton theory about H- and J-aggregates.

absorption spectrum is bathochromically shifted from visible (420 nm) (Fig. 1.2, Band III) to the NIR region (Fig. 1.2, Band V). Such remarkable red shift in absorption spectrum occurs on account of lowering of the HOMO-LUMO energy gap, owing to the insertion of excess electrons into the unoccupied π^* orbital. It should also be noted that upon decorating the surface of CQDs with oxygen-containing functional groups such as hydroxyl, carboxyl, and epoxy, the HOMO-LUMO energy gap is also attenuated, giving rise to a red-shifted absorption spectrum.

However, under the influence of aggregation, shifts in the absorption peak position can be observed implying $\pi-\pi$ stacking. In certain cases, shifts in the peak position are also accompanied by the evolution of a new intense band at a longer wavelength. Following Kasha's molecular exciton theory, these $\pi-\pi$ stacking phenomena are classified as H- and J-aggregation (Fig. 1.3), depending on whether the transition to the higher or lower excitonic state is allowed by electric dipole approximation.

1.3 Factors influencing the photoluminescence properties of carbon quantum dots

1.3.1 Quantum confinement effect

The quantum confinement effect (QCE) or size effect is a well-known phenomenon for carbon dots that occurs when carbon dots are smaller in size than their exciton Bohr radius. The QCE involves the change of valence band and conduction band from the continuous energy level to the discrete energy level. This bandgap increases with the decrease of the size of the three-dimensional nanomaterials which can cause the bandgap transition in the range of 430−650 nm and also enhance the fluorescent quantum yield. It has also been speculated that the QCE due to the inhomogeneous size distributions of carbon dots could play a role in the excitation wavelength-dependent emission. The dependence of emission spectra on the size distribution of carbon dots has been studied by various research groups.

Lee et al. have observed that different-sized CQDs showed different emission colors [3]. The visual images of these CQDs of four typical size distributions when irradiated under white light (left, daylight lamp) and UV lamp (right, 365 nm) have been shown in Fig. 1.4A. As the sizes of CQDs increase, it produces bright blue, green, yellow, and red emission respectively as shown in corresponding PL spectra (Fig. 1.4B). The in-depth study explained that the discrepancy of the emission properties was closely related to the CQD sizes (Fig. 1.4C). The smaller CQDs (1.2 nm) emitted in the UV region around 350 nm, medium-sized CQDs (1.5−3 nm) gave visible light emission (400−700 nm), and larger-sized CQDs (3.8 nm) showed NIR emission at around 800 nm. The theoretical calculations (Fig. 1.4D) showed that the HOMO-LUMO gap is dependent on the size of the graphene fragment. As the size of the fragment increases, the gap gradually decreases, and the gap energy in the visible spectral range was obtained from graphene fragments with a diameter of 14−22 Å, which agrees well with the visible light emission of CQDs with diameters of less than 3 nm. These results support the emission of CQDs that arises from the quantum-sized graphite structure instead of the carbon−oxygen surface.

At present to gain an idea about the remarkable QCE, the concept of embedding isolated sp^2 clusters in the sp^3 carbon matrix has been generally accepted [4]. This phenomenon is well explained by Qu et al. who have found that N-atom doped GQD (N-GQD) shows unique optoelectronic properties. The N-GQD with an N/C atomic ratio of c. 4.3% gave a sharp blue emission compared to the N-free counterparts of similar size (2−5 nm) which are green emissive (see the top part of Fig. 1.5). Based on the previous studies, they suggested that the strong electron-withdrawing ability of the N-atom in the N-GQDs could contribute to the blue-shifted emission and the excitation-dependent PL emission. In this study, the concept of radiative recombination of electron−hole pairs localized in the sp^2 clusters leads to excitation wavelength-dependent emission has been accepted. On that account, a specific wavelength of light exclusively excits sp^2 clusters having specific sizes, irrespective of other components, and dives into the size-independent emission (Fig. 1.5) [5].

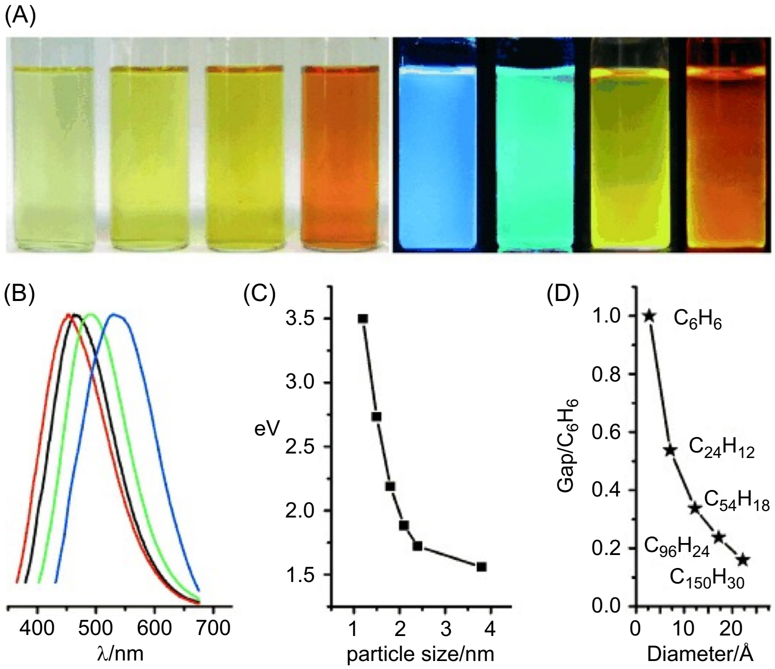

Figure 1.4 (A) Images of CQDs in daylight (left) and 365 nm UV light (right). (B) PL spectra of the blue-, green-, yellow-, and red-emissive CQDs represented by the red, black, green, and blue lines. (C) Relationship between their sizes and PL properties. (D) Graph showing the HOMO-LUMO gap depends on the sizes of graphene fragments. *PL*, Photoluminescence; *CQDs*, carbon quantum dots.
Source: Reprinted with permission from H.T. Li, X.D. He, Z.H. Kang, H. Huang, Y. Liu, J. L. Liu, et al., Water-soluble fluorescent carbon quantum dots and photocatalyst design, Angewandte Chemie International Edition 49(26) (2010) 4430−4434. Copyright 2010 Wiley Online Library.

1.3.2 Doping nonmetallic heteroatoms

The elemental composition of CQDs is typically carbon, oxygen, and hydrogen. However, in recent times, the tuning of CQDs' optical properties upon incorporation of other heteroatoms has gained significant attention. The doping of heteroatom in the CQDs can be classified as nonmetal (B, N, F, P, S, etc.) and metal/metal-oxides-based (Fe, Ag, Zn, Mn, and others). Such doping of CQDs core with heteroatoms is primarily responsible for tuning the bandgap and the state of hybridizations to achieve desirable and unexpected emissions. Metals and metal-oxide-doped CQDs have found application in photocatalytic applications and typically have a reservation for their applications in the area of biology. A facile and robust synthesis of nonmetal-doped CQDs has been achieved easily due to comparable

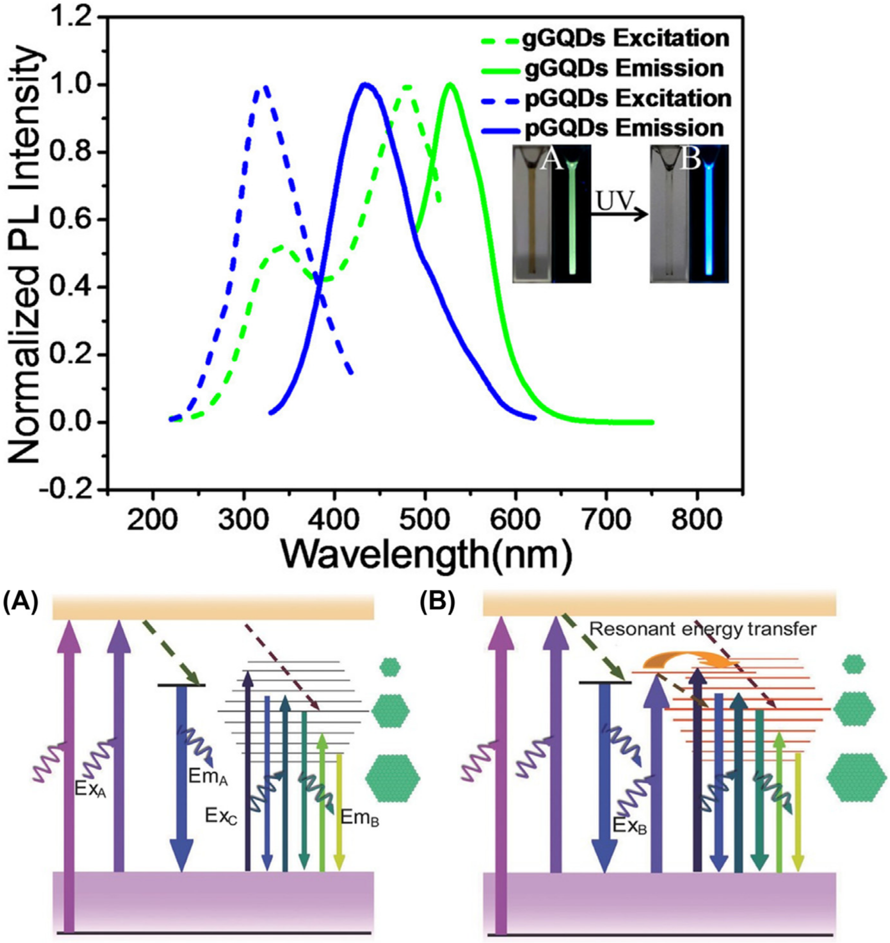

Figure 1.5 (Top) Normalized PL spectra of the gGQDs ($\lambda_{ex} = 480$ nm) and the pGQDs ($\lambda_{ex} = 320$ nm). Inset shows the photograph of the (A) gGQD and (B) pGQDs in aqueous solutions captured in visible light and 365 nm light. (Bottom) Representation of the PL emission mechanism showing the two parts of the emission, defect state (left side) and the size effect-driven localized energy levels (right side). (A) The blue emission is predominant for the rGOs (the wide arrow), (B) the enhanced PL of functionalized rGOs [5]. *PL*, Photoluminescence.

Source: Reprinted with permission. Copyright 2013 Wiley Online Library.

atomic size and multivalency. In this chapter, we are focusing mainly on how nitrogen can modulate CQDs' optical properties. Other heteroatom-doped CQDs can have interesting optical properties which can be tuned by doping percentage [6].

Nitrogen doping is the most popularly adopted strategy to improve CQDs properties. The optical absorption and emission of N-doped CQDs are generally red-shifted. Permatasari et al. have demonstrated pyrrolic-N-rich CQDs with an absorption maxima of 650 nm using urea as a nitrogen source. The nitrogen atom injects electrons into the CQD core and modulates the internal electronic environment [7]. N-containing pyridinic, pyrrolic, and graphitic groups can be embedded easily in the carbon core and the electronic transition will be more likely from the ground state to the lower singlet state with improved emission properties. N-doped CQDs show excitation wavelength-dependent emission properties and the quantum efficiency of emission is enhanced with the increase of the doping percentage (see Fig. 1.6A and B; i.e., amount of nitrogen source used during the synthesis) [9,10].

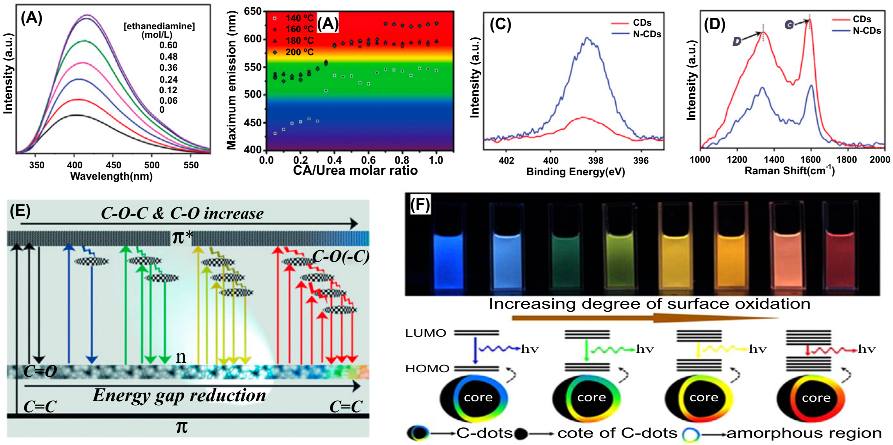

Figure 1.6 (A) The nitrogen precursor effect (ethylenediamine) on the PL of CQDs; (B) excitation wavelength-dependent emission maxima (CA, citric acid); (C) modulation of binding energy upon N-doping; (D) effect on Raman signal due to changes in sp^2 hybridized sites upon N-doping; (E) schematic representation of emission of CQDs modulated via different or related surface groups. (F) CQD's surface or core can be co-doped with nitrogen-containing functional groups such as amino, pyridinic, hydrazine, or graphitic N-atom apart from an oxygen-containing functional group [8]. *PL*, Photoluminescence; *CQDs*, carbon quantum dots.

Source: (A, C, and D) Reprinted with permission from Y. Liu, L. Jiang, B. Li, X. Fan, W. Wang, P. Liu, et al., Nitrogen doped carbon dots: mechanism investigation and their application for label free CA125 analysis. Journal of Materials Chemistry B 7(19) (2019) 3053–3058. Royal Society of Chemistry 2019. (B and E) Reprinted with permission from X. Miao, D. Qu, D. Yang, B. Nie, Y. Zhao, H. Fan, et al., Synthesis of carbon dots with multiple color emission by controlled graphitization and surface functionalization. Advanced Materials 30(1) (2018) 1704740, respectively, Copyright 2018 (B) and 2015 (F, top part) Wiley Online Library. (F) Bottom panel, Reprinted with permission from H. Ding, S.-B. Yu, J.-S. Wei, H.-M. Xiong, Full-color light-emitting carbon dots with a surface-state-controlled luminescence mechanism, ACS Nano 10(1) (2016) 484–491. Copyright 2016 American Chemical Society.

The N doping induces the formation of more sp^2 hybridized sites as confirmed by Raman spectroscopic investigation, leading to reduced band gap energy which eventually improves emission property (Fig. 1.6C and D) [9].

The CQD surface can also be decorated with nitrogen- and oxygen-containing functional groups. These groups also serve as continuous defect states and, therefore, tune the surface state-related emission properties. Structurally, the core of CQDs is usually accompanied by many imperfect sp^2 islands. Those sites act as exciton-capturing energy traps that give rise to surface defect state-related PL. Such surface defect dynamics of CQDs are quite complex and mainly responsible for their multicolor emissions (Fig. 1.6E). An increase in surface oxidation results in defects state and multiple low-lying emissive states that are ultimately responsible for providing multicolor emissions [8,11] (Fig. 1.6E).

1.3.3 Local heterogeneity originated from heteroatom-mediated surface defects

Structurally, the core of CQDs is composed of sp^2 conjugated frameworks and in the process of synthesis, the core of CQDs usually gets accompanied by a huge number of imperfect sp^2 domains. Such imperfectness in the core and associated surface defect states containing various oxygen- and nitrogen-containing functional groups are one of the major causes for such interesting optical properties of CQDs. These surface defect states are responsible to trap electrons or holes for excitons and do not allow excitation recombination. According to literature reports, surface defects of CQDs are highly convoluted as these are closely associated with both sp^2 and sp^3 hybridized carbon atoms and other functional groups containing a heteroatom. Most of the reported CQDs contain an abundant amount of oxygen-containing functional groups such as epoxide, hydroxyl, carbonyl, carboxyl, and sulfoxides. These surface functional groups connected to the carbon backbone not only impart sufficient polarity and charges to CQDs but also create diverse surface defects and low-lying energy levels responsible for tunable luminescence properties. Oxygen-containing functional groups induce significant local distortion and result in creating new energy levels between $n-\pi^*$ gaps which consequently produce a wide range of excitation energy and excitation wavelength-dependent emissive property. The bandgap of oxygen-containing CQDs is reduced with the increasing number of the oxygen atom and as a result of such oxidation, a significant red shift is observed. This was simply verified with pH-dependant luminescence properties.

1.3.4 Influence of edge states

One of the important phenomena about one-dimensional graphite ribbons is typically shaped edges in terms of energy band are responsible for the difference in the electronic state with respect to the bulk graphite. There is a well-known theoretical model regarding the chemical composition of the edges of graphene sheet which

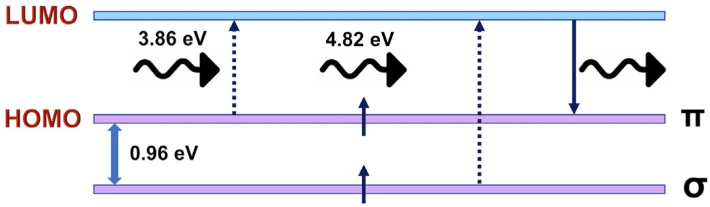

Figure 1.7 Typical electronic transitions of triple carbenes at zigzag sites were observed in the optical spectra.

states that there are two types of free edge states that exist: one is carbene type free zigzag sites and the other one is free armchair sites which are carbyne. It is also postulated in this model that the carbene type structures have triplet ground states while the carbyne types have singlet ground states. These carbene centers were stabilized at zigzag edges as a consequence of the localization of itinerant π electron through $\sigma-\pi$ coupling.

Based on these phenomena, scientists found that electronic structure of carbon dots is also influenced by these typically shaped edges, especially by the zigzag edge states. Consequently, the PL properties of GQD [12] or carbon dots are affected by the free zigzag sites and this is also reported in a study by Wu et al. They proposed a PL mechanism that is based on the emissive free zigzag states by a scheme that is mentioned below. As depicted in Fig. 1.7, the ground state of carbene has two electronic configurations: singlet and triplet. The singlet state is described by σ^2 where the two nonbonding were paired in σ orbital and the π orbital remains vacant while the triplet state is designated as $\sigma^1\pi^1$ as both are singly occupied. The energy difference (dE) between σ and π orbitals is an important factor in deciding the ground state multiplicity of carbene. For a triplet ground state, dE should be below 1.5 eV as predicted by Hoffman. As zigzag edges are enriched by the triplet carbenes, the two electronic transitions of 320 nm (3.86 eV) and 257 nm (4.82 eV) are obtained in the PL spectra considered as a transition from σ and π orbitals that is HOMO to LUMO orbitals. The assignment of these two transitions is further verified by the calculated dE which is 0.96 eV satisfying the cutoff range for triplet carbene (<1.5 eV). Since the two transitions are directly associated with the observed blue fluorescence, the irradiation decay of activated electrons from LUMO to the HOMO results in this blue emission [12].

1.3.5 Red edge effect

Generally, the emission spectra are independent of the excitation energy source due to the duration of the process involved. According to Kasha's rule, fluorescence is independent of the excitation energy as all excited electrons are independent of initial excitation photon energy. Therefore, these excited electrons will come back to the band edge before fluorescence occurs. A study by Wu and co-workers demonstrated that the "giant red edge effect" which breaks Kasha's rule is the reason for

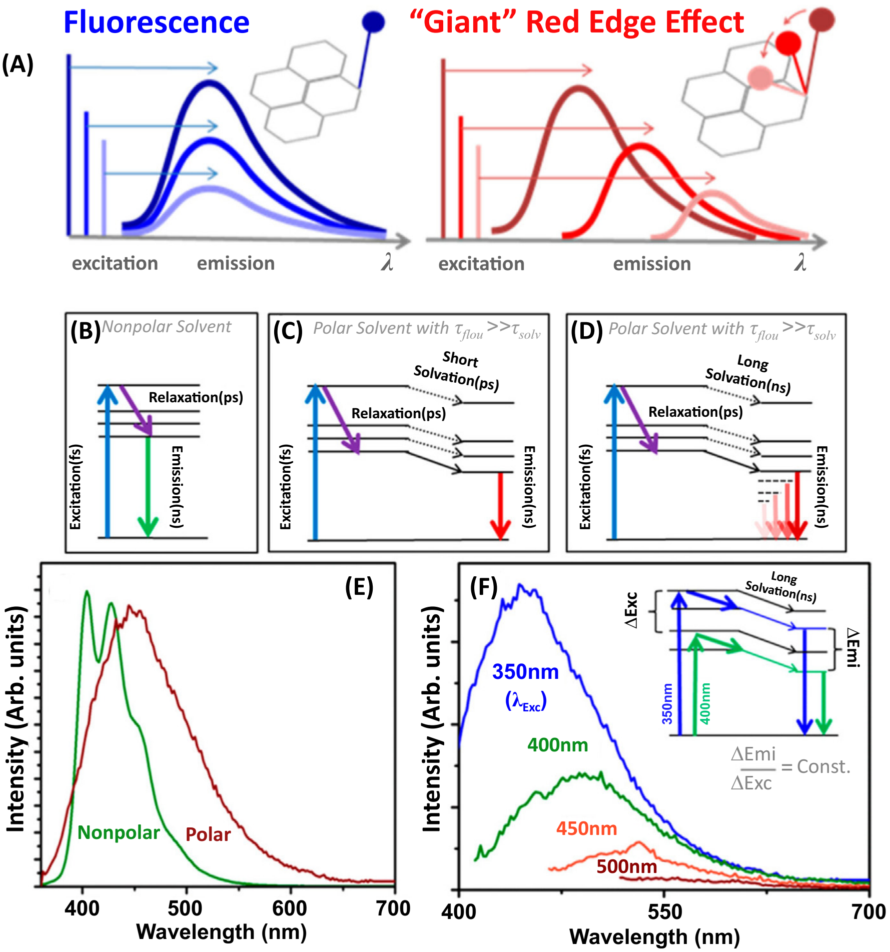

Figure 1.8 (A) Schematic representation of the 'giant' red edge effect. (B) In nonpolar solvents, the fluorescence PL occurs through the excitation (fs), thermal relaxation of the carriers (ps), and emission (ns). (C) While in polar solvents, the excited-state energy is lowered to result in a red-shifted emission due to solvent relaxation. (D) The same timescale of the solvent interactions and fluorescence lifetime leads to the time-dependent emission and thereby the red edge effect. (E) The PL of GO is excitation wavelength-independent in nonpolar solvents whereas the spectrum is red-shifted and broadened in polar solvents. (F) Excitation wavelength-dependent fluorescence of the GO in an aqueous medium. *PL*, Photoluminescence.

Source: Reprinted with permission. S.K. Cushing, M. Li, F.Q. Huang, and N.Q. Wu, Origin of strong excitation wavelength dependent fluorescence of graphene oxide, ACS Nano 8(1) (2014) 1002–1013. Copyright American Chemical Society 2014.

strong excitation-dependent emission in graphene oxide (GO) (Fig. 1.8A). They found that in nonpolar solvent, GO showed a narrow emission peak which does not depend on the excitation wavelength (Fig. 1.8B). Whereas in a polar solvent, the spectra of GO are broadened and dependent on excitation polar solvent as is shown in Fig. 1.8C–E. In polar solvent, the fluorophore interacts with the environment leading to an additional process that is solvation in the fluorescence process.

There is a disruption of the equilibrium between the fluorophore and solvent dipole when the excitation energy is applied. The excited fluorophore is further stabilized by adjacent solvent molecules as these solvent molecules can rotate to align with the excited fluorophore resulting in the reduction of interaction energy. For common polar organic solvents, the solvation time is around 10 ps (Fig. 1.8B), whereas the lifetime of organic molecules in a polar solvent is in nanoseconds timescale (Fig. 1.8B and C). Thus, before the fluorescence process, solvation occurs and due to this solvent relaxation, there is a solvatochromic red shift in the fluorescence maxima (Fig. 1.8F). When the solvation process is not an order of magnitude faster than the lifetime of the fluorophore then it can emit concurrently to the excited-state energy being reduced, resulting in time-dependent emission energy. This phenomenon is known as “the red edge effect” where emission wavelength is dependent on the excitation wavelength. As it is shown in Fig. 1.8F, when the excitation wavelength is changed from 350 to 500 nm, the emission maxima of GO is red-shifted from 440 to 580 due to this red edge effect [13].

1.3.6 Surface defect states

Another well-known reason for excitation wavelength-dependent emission is that CQDs are enriched with surface defect states. The surface defect relates to an edge zone or a spherical cell that is different from the carbon core region or the body. Three major reasons can cause surface defects in carbon dots: (1) the presence of oxygen-containing functional groups such as $-COOH$, $-OH$, and $C-O-C$ in the spheroidal regions of CQDs; (2) the sheets of carbon dots also contain sp^2 and sp^3 hybridized carbon atoms; (3) the small-sized dangling bonds at the surface. The fluorescence of carbon dots might be generated from the surface defect states that become emissive upon stabilization as a result of surface passivation as shown in Fig. 1.9A [14]. This defect state also can serve as a capture center for exciton and hence can be attributed to the PL emission by radiation relaxation from the excited-state to the ground state. When the CQDs are excited by photons of specific energy and whose wavelength matches the optical band gap, they will undergo transition and assemble in the nearby surface defect states. Thereafter these photons come back to the ground state to give emission of various wavelengths in the visible region (Fig. 1.9B). The red edge excitation shift (REES) phenomenon is also influenced by the surface defects; with the increment of the degree of surface oxidation, there is an enhancement in the surface trap states and emission sites. As a result, there is a red shift in the emission maxima upon shifting the excitation wavelength (Fig. 1.9C).

It was discussed earlier that CQDs with various oxygen-containing functional groups suffer from multiple surface defects. Hu et al. observed that upon changing the reagent and synthesis condition in the preparation of CQDs, the fluorescence emission wavelengths are tunable in the visible region from 400–700 nm. They predicted that sp^2 carbon that contains surface epoxides or hydroxyls can cause

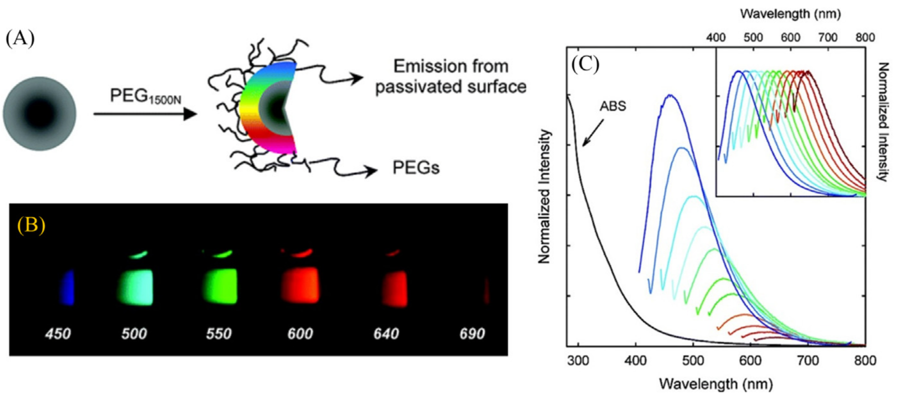

Figure 1.9 (A) Schematic representation of surface-passivated carbon dots with polyethylene glycol (PEG). (B) The aqueous solution of the PEG1500N-attached carbon dots excited at 400 nm and photographed through band-pass filters of different wavelengths as indicated. (C) The absorption and luminescence spectra of PPEI-EI carbon dots in an aqueous solution excited at 400 nm with 20 nm gap (inset: normalization spectra of excitation wavelength-dependent emission) [14].

Source: Reprinted with permission. Copyright 2006 American Chemical Society.

local distortion and then generate different energy levels. These new energy levels could be located in between n—π* gaps and thus different types of radiative recombination occur, resulting in a wide range of excitation energies and excitation wavelength-dependent emission [8].

1.3.7 Aggregation-induced emission in carbon quantum dots

Carbon-based materials spanning from traditional industrial carbon (e.g., activated carbon, carbon black) to new carbon nanomaterials such as graphene, carbon nanotubes, and carbon dots have attracted increasing attention in the fields of chemistry, materials, and other interdisciplinary areas. Over the years, carbon dots have emerged as appealing nanomaterials primarily on account of their diverse physicochemical properties and encouraging attributes such as unique optical properties, eco-friendliness, cost-effectiveness, and sufficient biocompatibility.

Aggregation-induced emission (AIE) was a term coined by Tang and co-workers in 2001, based on silole derivatives. This phenomenon is dramatically opposite to the notorious aggregation caused quenching (ACQ) that renders luminophores “nonemissive” in the aggregated state. Luminophores with disk- or rod-like shapes experience intense intermolecular π—π stacking interactions. The excited states of such aggregates often relax back to the ground state via nonradiative channels, resulting in emission quenching of these luminophores. The structure of the luminophore and its packing determines whether ACQ or AIE predominates in a particular system. A typical example of an ACQ-phore is perylene: when dissolved in a good solvent, such as tetrahydrofuran (THF), the dilute solution of perylene shows strong luminescence. However, upon gradual addition of a poor solvent, such as water, its emission weakens due to severe aggregate formation. On the other hand, tetraphenylethene (TPE) is an example of AIEgen. The central olefinic stator of the TPE molecule is surrounded by four peripheral phenyl rings. The rotations caused by these phenyl rings against the olefinic stator nonradiatively dissipate the exciton energy making it nonemissive in dilute solution. However, in the aggregated state, the emission is induced by the synergistic effect of restriction of intramolecular motion and inefficient intermolecular $\pi-\pi$ stacking. Hence, the nonradiative emission is hampered due to this restricted intramolecular rotation and a radiative pathway causes the enhanced emission. Thus, in the case of the flexibly structured molecules, the intramolecular motion facilitates a greater nonradiative decay. Nevertheless, upon aggregation, the scenario changes and the nonradiative decay rate is decreased.

In 2013, Gao et al. reported that CQDs exhibit AIE properties, wherein adenosine-5-triphosphate (ATP) induces the aggregation of CQDs prepared from C_{60}. Since this very first report, AIE in CQDs has attracted attention from the scientific community due to their intriguing properties such as the solvent polarity and pH sensitivity, large Stokes shift, better photostability, and improved biocompatibility. These can be proved to be useful for a wide range of future applications.

Let us now look into the plausible routes of AIE in CQDs. In general, the aggregation of CQDs is significantly influenced by solvent polarity, material concentration, and the presence of external metal ions and molecules (Fig. 1.10).

1.3.7.1 Effect of solvent polarity

The polarity of the dispersion medium greatly impacts the aggregation of CQDs, and consequently their absorption and emission properties. Liu et al. showed that

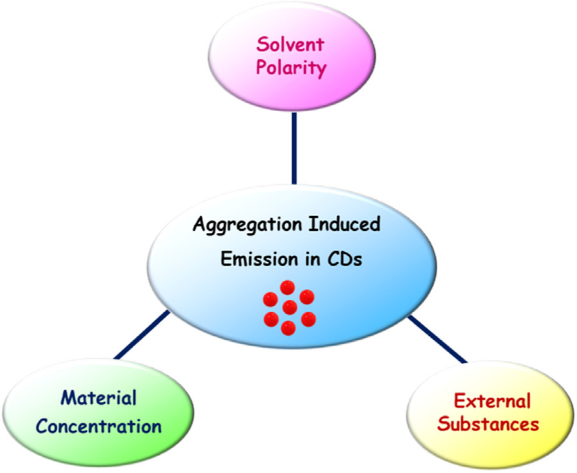

Figure 1.10 Schematic representation describing the factors responsible for aggregation-induced emission of CQDs. *CQDs*, Carbon quantum dots.

the dispersion of CQDs prepared from tartaric acid into THF led to its strong aggregation [2]. These CQDs displayed the characteristic excitation-dependent emission (Fig. 1.11A) and aggregation-induced enhanced emission (AIEE) properties were observed at 455 nm upon exciting at 350 nm. The AIEE properties arose on account of the rotational hindering of the surface groups of these CQDs. Here, the results demonstrated that the aggregate formation was influenced by the permittivity of the solvent and the PL intensity remained unaltered in case of permittivity lower than THF. With an increase in the concentration of THF from 6.7% to 20%, a continuous bathochromic shift (Fig. 1.11C) of the absorption spectra was observed. The recorded PL spectra showed a small hypsochromic shift as the concentration of THF was increased (Fig. 1.11B). With the onset of aggregation, lifetime was decreased from 1.85 ns in an aqueous solution to 1.21 ns in 80% THF. The quantum yield (QY), which is a measure of PL efficiency, was increased from 7.16% in an aqueous solution to 42.65% [15].

Yang et al. prepared hydrophobic CQDs (H-CQDs) via one-pot solvothermal treatment demonstrating a blue dispersed emission and red AIE. The UV−visible absorption spectra reveal that upon injection of water, the absorbance at 360 nm continuously decreases while a red-shifted band at 559 nm appears (Fig. 1.12a) and consistently increases. This spectral red shift indicates that H-CQDs indeed form J-aggregates owing to their enhanced $\pi-\pi$ stacking. When fully dispersed as a homogeneous solution, H-CQDs show blue fluorescence. However, upon the addition of water, hydrophobic interactions lead to the formation of H-CQD clusters and consequently red aggregation-induced emission (Fig. 1.12B and C) [16].

Choudhury et al. combined hydrophobically tailored naphthalene diimide (NDI)-based fluorescent organic nanoparticles (FONPs) with surface-functionalized CQDs in order to construct FONP−CQD nanoconjugates exhibiting enhanced AIE. The NDI derivative formed organic nanoparticles in the THF−water mixture and exhibited aggregation-induced orange emission (Fig. 1.13A). When the water percentage was increased, the emission intensity attenuated because of the poor dispersibility of NDI−FONPs (Fig. 1.13B). The poor emission intensity of the NDI−FONPs was remarkably enhanced upon the addition of surface-functionalized CQDs of varying

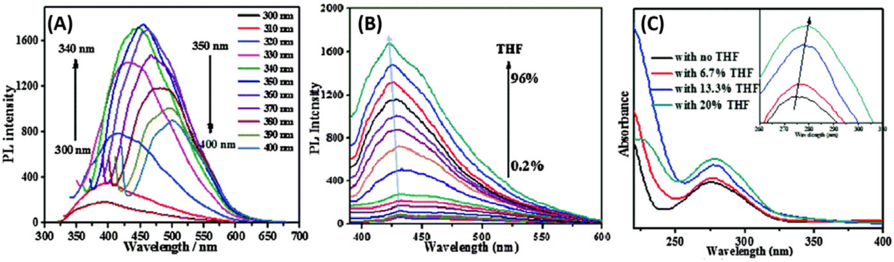

Figure 1.11 (A) Excitation-dependent emission of CQDs. (B) Emission spectra of CQDs with increasing THF, displaying enhanced emission. (C) Absorption spectra of CQDs with increasing THF, showing a bathochromic shift [15]. *CQDs*, Carbon quantum dots.
Source: Reprinted with permission. Copyright 2009 Royal Society of Chemistry.

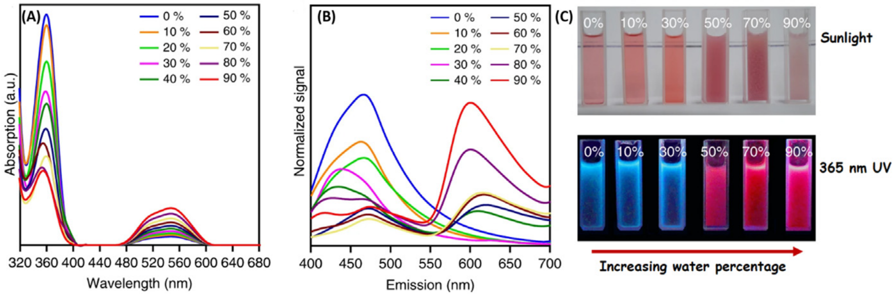

Figure 1.12 Changes in the CQDs. (A) Absorption, (B) emission properties upon aggregation. (C) Photograph of the CQDs solution with varying water fraction under sunlight (top) and 365 nm UV irradiation (bottom) [16]. *CQDs*, Carbon quantum dots.

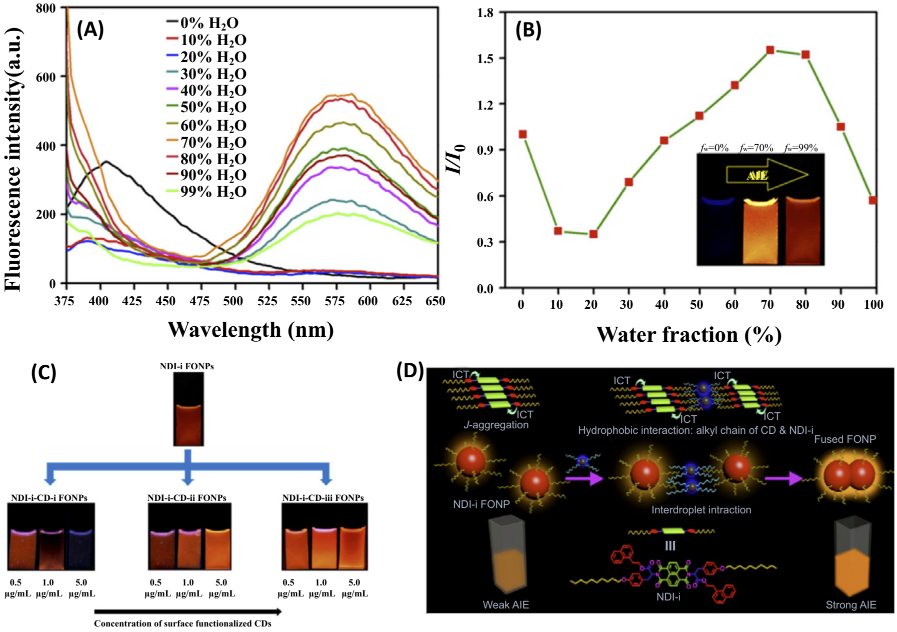

Figure 1.13 (A) Emission spectra of the NDI derivative in different THF–water solvent percentages. (B) Graph shows the change in relative emission intensity against the varying THF–water mixture. (C) Picture shows the emission color and intensity change of NDI–FONPs as the concentration of CQDs are increased. (D) Schematic representation of the enhancement of AIE of NDI–FONPs in presence of CQDs [17].
Source: Reprinted with permission. Copyright 2019 American Chemical Society.

alkyl chain lengths (Fig. 1.13C). With increasing chain length on the CQD surface, inter-chain hydrophobic interactions were facilitated between the FONPs and surface-functionalized CQDs. In the FONP–CQD nanoconjugates, the extent of intramolecular charge transfer (ICT) between the donor (naphthyl group) and acceptor (NDI core) residues became more efficient to show enhanced AIE (Fig. 1.13D) [17]. They thus resorted to the concept of CQDs-induced microstructural modulation and emission enhancement of FONPs which circumvented the fluorescence quenching property of CQDs.

Wang et al. prepared glutathione-conjugated CQDs (GSH-CQDs) that exhibited characteristic excitation-dependent emission. After the addition of volumetric fractions of ethanol to the as-synthesized GSH-CQDs, aggregates were formed. Furthermore, the PL intensity centered at 500 nm continuously increased with an increasing fraction of ethanol, on being excited at 420 nm (Fig. 1.14A–C). This enhancement in PL intensity accredited this phenomenon as aggregation-induced enhanced emission. In the aggregates, intramolecular motions were restricted which blocked the nonradiative decay and opened up radiative decay. Their strategy reestablished the previous literature reports that CQDs protected with GSH showed AIEE, on account of being an important scaffold to stabilize nanomaterials [18].

Gude et al. synthesized CQDs from sucrose and demonstrated that the CQDs are composed of aggregated single chromophoric hydroxymethylfurfural (HMF) derivatives. HMF can easily form aggregates through noncovalent interactions such as dipole–dipole, π–π stacking, and van der Waals interaction. There is a terminal polar aldehyde group present in the HMF derivative oriented in an antiparallel fashion and thus can be expected to form short-range order in the condensed phase. These carbon dots exhibited excitation independent emission (Fig. 1.15A) and single exponential PL decay (Fig. 1.15B) on account of the formation of the HMF derivative (Fig. 1.15C) [19].

1.3.7.2 Effect of material concentration

AIE can also be affected by the concentration of CQD solution. To cite an example, in 2019 Chen group prepared citric acid-based CQDs that can efficiently transform from ACQ to AIE. It was found that as the concentration of the prepared CQDs solution was increased from 0.2 to 1000 mg/mL, the initial emission peak at

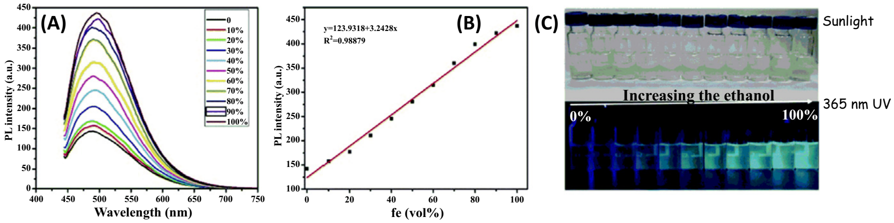

Figure 1.14 (A) PL spectra of GSH-CQDs in varying ethanol–water mixtures. (B) Plot of PL intensity of GSH-CQDs vs ethanol–water volume fraction. (C) Photograph of the CQDs solution with varying water fraction under sunlight (top) and 365 nm UV radiation (bottom) [18]. *PL*, Photoluminescence; *CQDs*, carbon quantum dots.
Source: Reprinted with permission. Copyright 2016 Royal Society of Chemistry.

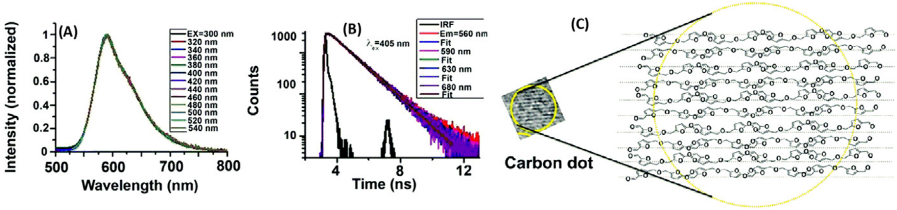

Figure 1.15 (A) Emission and (B) PL decay curves of the CQDs. (C) Probable aggregation pattern of the HMF derivatives in the CQDs [19]. *PL*, Photoluminescence; *CQDs*, carbon quantum dots.
Source: Reprinted with permission. Copyright 2016 Royal Society of Chemistry.

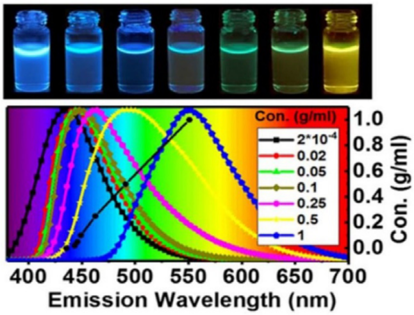

Figure 1.16 Digital photographs of the CQD solution with increasing concentration (top) and the corresponding emission spectra (bottom). *CQDs*, Carbon quantum dots.
Source: Reprinted with permission. Copyright 2019 American Chemical Society.

435 nm (attributed to monodispersed CQDs) was replaced by new emission peaks at a longer wavelength and were red-shifted to 550 nm (attributed to aggregates), which intensified gradually [20] (Fig. 1.16). The gradual weakening of the band at 450 nm is attributed to ACQ, while the gradual strengthening of the band at 550 nm is ascribed to AIE.

The authors have mentioned a possible route for ACQ to AIE transformation. They have suggested that with increasing concentration, monodispersed CQDs grow into aggregates. The remaining blue emissive dispersed CQDs can easily transmit their energy to the yellow emissive aggregates of CQDs. The CQD aggregates can easily reabsorb the blue light emitted by the dispersed CQDs and hence their yellow emission is enhanced with increasing concentration of CQDs (Fig. 1.17) [20].

In 2020, the Zheng group prepared CQDs via the pyrolysis of citric acid and thiourea. As the concentration of CQDs increases from 0.002 to 1.0 mg/mL, the absorption spectra gradually broaden accompanying a red shift of the absorption peaks (Fig. 1.18). With the increase in the concentration of the CQDs, the emission maxima are red-shifted from 461 to 615 nm registering a red shift of 154 nm. At

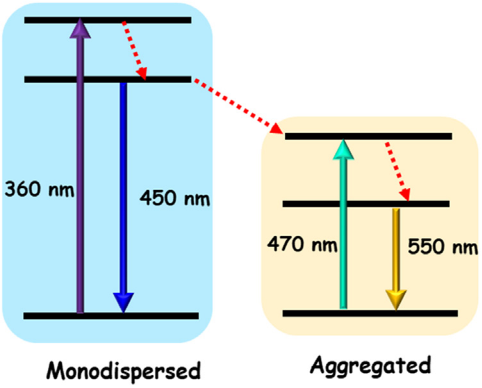

Figure 1.17 Schematic representation of the energy transfer process occurring upon aggregation.

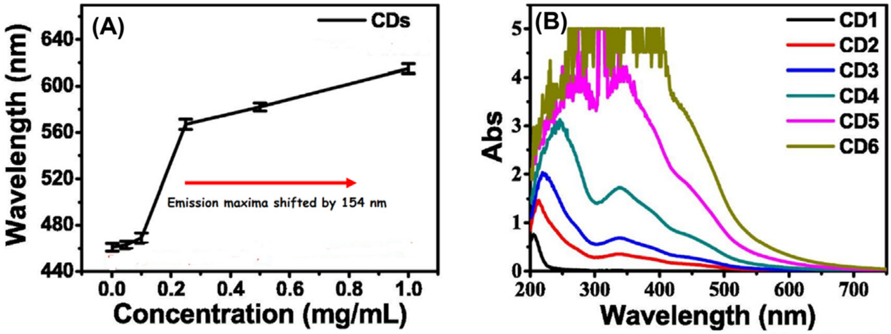

Figure 1.18 (A) The plot of emission maxima versus concentration of CQDs. (B) Absorption spectra of the CQDs with varying concentrations [21]. *CQDs*, Carbon quantum dots.

Source: Reprinted with permission. Copyright 2020 Elsevier.

high concentration, the uniform dispersion of CQDs become unstable owing to the exceedingly short distance among the CQDs along with their high surface energy. Thus, in order to remain stable in the solution, the CQDs tend to aggregate (Fig. 1.19) [21].

Apart from the effect of solvent polarity and material concentration, the aggregation of CQDs can also be tuned via the introduction of external entities, such as a metal ion or molecule. The following section will thus elucidate the role of such external substances in modulating the aggregation of CQDs.

1.3.7.3 Effect of added metal ions

Huang et al. in 2019 demonstrated the copper ion-induced aggregation of CQDs. For this purpose, they prepared CQDs from *o*-phenylenediamine (OPD) which

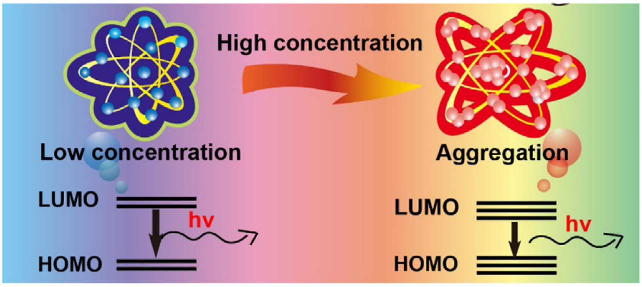

Figure 1.19 Schematic illustration of the concentration-dependent luminescence mechanism. *Source*: Reprinted with permission. Copyright 2020 Elsevier.

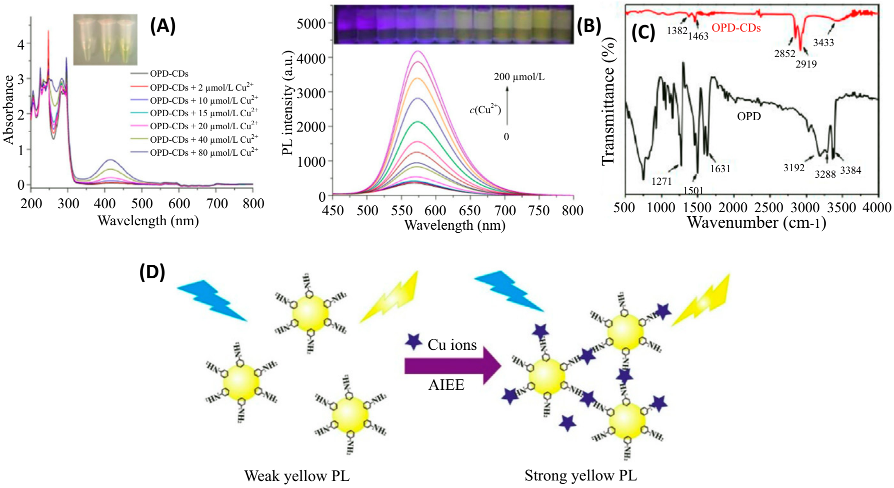

Figure 1.20 Aggregation of OPD-CQDs in presence of Cu^{2+} monitored in (A) absorption, (B) emission, (C) FT-IR spectra of the OPD-CQDs and the raw CQDs. (D) Illustration of the Cu^{2+}-induced AIEE property of OPD-CQDs [22]. *CQDs*, Carbon quantum dots.
Source: Reprinted with permission. Copyright 2019 Elsevier.

showed a weak yellow emission, validated by the appearance of an emission band at 568 nm upon excitation at 420 nm. Interestingly, this weak yellow emission was greatly enhanced in the presence of copper ion, thus procreating a Cu^{2+}-induced aggregation of OPD-CQDs. To explain the observed intensity enhancement, the authors carried out a series of experiments that included UV—visible absorption spectra, scattering spectra, and Fourier transform infrared (FT-IR) spectra. The band at 410 nm in the absorption spectra of OPD-CQDs was undoubtedly increased with Cu^{2+} ion addition into the OPD-CQDs solution, reiterating the fact that Cu^{2+} might coordinate with the OPD-CQDs, forming Cu^{2+}—(OPD-CQD) complexes (Fig. 1.20A). The PL spectrum was similarly enhanced upon Cu^{2+} addition on account of an increase in the n-π^* transition efficiency (Fig. 1.20B). The broadening

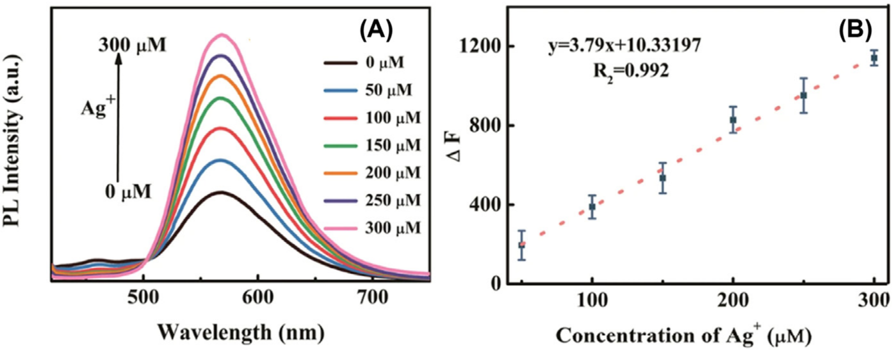

Figure 1.21 (A) Aggregation features of the N-CQDs in presence of Ag^+ monitored in emission. (B) PL intensity ratio of the N-CQDs with increasing concentration of Ag^+ [23]. *PL*, Photoluminescence; *CQDs*, carbon quantum dots.

of the bands in the IR spectra also bespeaks the increased n-π^* transition efficiency due to the interaction between Cu^{2+} and amino groups of the CQDs (Fig. 1.20C). Thus, in this work, aggregation of CQDs occurred via complexation with Cu^{2+}. Aggregation of CQDs restricted intramolecular vibration and thereby the nonradiative decay channels, leading to AIEE (Fig. 1.20D) [22].

Guo et al. in 2019 demonstrated the effect of the addition of Ag^+ into nitrogen-doped carbon dots (N-CQDs). The N-CQDs were prepared from OPD by hydrothermal method. The initial yellow emission of these CQDs at 566 nm could be enhanced in the presence of Ag^+, without any change in the peak position (Fig. 1.21). In an effort to unravel the mechanism for this emission enhancement, the authors calculated the zeta potential values before and after the addition of Ag^+. They found that on the addition of Ag^+ into the CQDs, the Zeta potential decreased from -34.0 to -27.8 mV. This downward trend in surface charge implies that the interparticle interaction gradually diminishes. Thus, the decrease of mutual repulsion leads to AIEE [23].

1.3.8 Förster resonance energy transfer

Fluorescence resonance energy transfer or Förster resonance energy transfer (FRET) is a highly sensitive technique in bulk fluorescence spectroscopy and microscopy as well as single-molecule systems. It is widely utilized in the ratiometric analysis, biosensors development, optical imaging, and biomedical applications. FRET involves the nonradiative energy transfer between a fluorescent donor and acceptor by means of intermolecular long-range dipole–dipole coupling. However, they have to fulfill the criteria of being in close physical proximity of 10–100 Å. Another common example of this technique can be found in biophysics and molecular biology. The quantitative analysis of molecular dynamics, monitoring of protein–protein interactions, protein–DNA interactions, and protein conformational changes are the major applications to be mentioned.

In this context, carbon dots have been potential candidates to account for a FRET system. It is due to their broad excitation as well as emission ranges that make them eligible for both donors as well as acceptors. The CQD-based FRET systems provide a significant advancement in overcoming the drawbacks such as spectral crosstalk, photobleaching, and direct acceptor excitation. The CQD-based FRET systems also come up with improved sensitivity for both single and multifunctional usage.

The first report of a metal ion selective FRET system consisting of carbon dots came out in 2012. The report demonstrates the energy transfer from the donor—amine-functionalized carbon dots to the acceptor—noncovalently functionalized grapheme with 18-crown-6 [24]. The crown ether has a high affinity for the K^+ ions and hence the energy transfer is inhibited in presence of K^+ ions. The carbon dot-based FRET system can also be employed as a potential tool for real-time monitoring of drug delivery [25]. The system is independent of any fluorescent tag while the carbon dots act as energy donors and drug carriers. Doxorubicin, the acceptor moiety, was adsorbed onto the carbon dot surface via electrostatic interaction bringing the donor and acceptor to closer proximity. However, the FRET signal can efficiently monitor the release of doxorubicin from the carbon dot surface as depicted in Fig. 1.22. This report is the first direct and sensitive FRET-based carbon dots drug delivery system. Fig. 1.23 illustrates another example of this system to distinguish between the native DNA and the damaged DNA [26]. The FRET pair consists of the donor carbon dots complexed with DNA and acceptor ethidium bromide (EtBr), a well-known DNA intercalator. Due to the FRET, the carbon dots emitted weakly and a brighter EtBr signal could be recorded.

The scenario changed upon gradual UV exposure to the DNA and the emission of EtBr was quenched. The FRET mechanism is proved to be useful for the

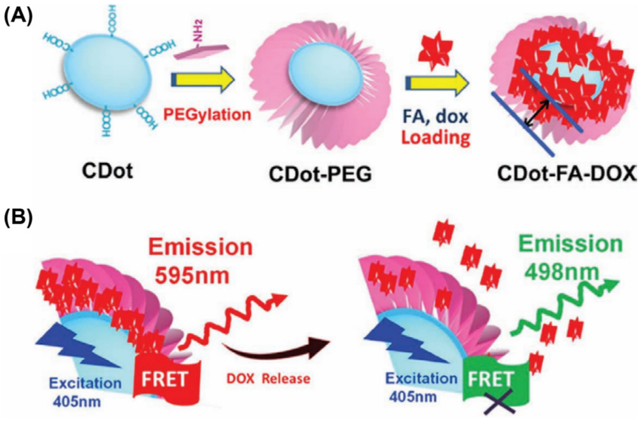

Figure 1.22 (A) The scheme shows the surface coupling chemistry for FRET-CQD-DDS, (B) a plausible mechanism of the FRET-CQD-DDS suitable for drug delivery applications. The PL of CQDs is recovered once the DOX is released from the surface [25]. *PL*, Photoluminescence; *CQDs*, carbon quantum dots.
Source: Reprinted with permission. Copyright 2013 Wiley.

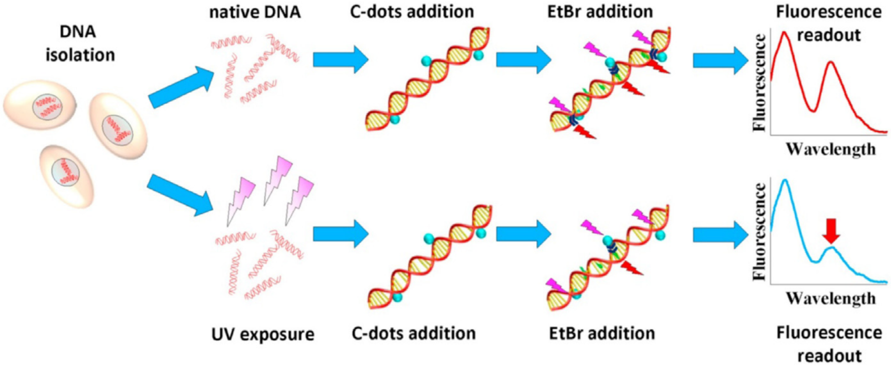

Figure 1.23 Schematic representation of the damaged DNA detection mechanism by the CQD-EtBr based FRET pair. The emission signal of EtBr at 612 nm decreases with the increased UV irradiation time to damage the DNA [26]. *CQDs*, Carbon quantum dots. *Source*: Reprinted with permission. Copyright 2017 Elsevier.

detection of vitamin B_{12} where CQDs act as donors and vitamin B_{12} is the acceptor [27]. Another example shows how the real-time ratiometric monitoring of anticancer prodrug activation in living cells was made possible using a CQD-based FRET system. The energy transfer occurs from CQDs to the prodrug cisplatin (IV) [28].

Such FRET systems have also been applied for the development of efficient and sensitive nanoprobes to detect metal ions. In these cases, the acceptor unit is the metal ion itself complexed with fluorescent molecules. The detection of Al^{3+} ions in aqueous solutions was demonstrated in a designed FRET-based nanoprobe CQD−rhodamine−Al^{3+} [29]. Similarly, nanoprobes have also $Cu^{2+}$and Zn^{2+} metal ions have also been developed for their detection. To detect Fe^{3+} ions, CQDs were employed as an energy acceptor. In this case, the energy transfer occurs between the donor tryptophan unit and the acceptor CQDs, and this system could be used as a sensitive probe for Fe^{3+} detection.

A recent example shows the mechanism of micro-RNA sensing based on a FRET system. The FRET occurs between CQDs and carboxyfluorescein-labeled DNA, and the CQD fluorescence is quenched. This nanoprobe can be a potential marker for the early detection of breast cancer. The finding of Zhang et al. highlights a FRET system based on polymerized dopamine (PDA) and CQDs for bioimaging [30]. The FRET effect occurs between the CQDs and PDA units resulting in efficient and tunable emission. In addition, the bioimaging and cytotoxicity of the system were also explored assuring good biocompatibility and strong prospects for biotechnological applications.

1.3.9 Photoinduced electron transfer

Photoinduced electron transfer (PET) from a donor (D) to an acceptor (A) results in the formation of a charge-separated state. For an intramolecular PET process, the donor and acceptor are part of the same molecule or moiety while they belong to

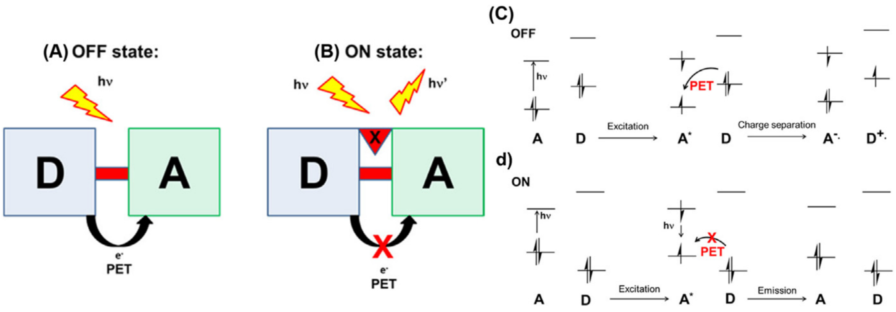

Figure 1.24 (A and B) Schematic representation of the mechanism of a PET system consisting of D and A, (B) the energy levels depicts the FMO energies of the OFF (C) and ON (D) states of the D-A system [31]. *PET*, Photoinduced electron transfer.
Source: Reprinted with permission. Copyright 2016 American Chemical Society.

different molecules for an intermolecular PET process (Fig. 1.24a-d). Both these intramolecular and intermolecular PET processes are responsible for the decrease of PL quantum yield and lifetime.

The Rehm–Weller equation is used to estimate the change in Gibb's free energy between an electron donor and an electron acceptor.

$$\Delta G_{ET} = E_{D/D^+} - E_{A/A^-} - E_S - C$$

where, $E_{D/D+}$ and $E_{A/A-}$ denote the oxidation potential of the donor and acceptor, respectively. E_S is the excited-state energy of the donor, and C is a Coulombic term that considers donor-acceptor interaction.

The electron-donating as well as accepting properties of CQDs make them a suitable candidate for the PET process. The photoexcited CQDs are useful for the photoreduction of Ag^+ to Ag involving 450 nm visible wavelength. In the same report, the strong electron acceptance properties of CQDs were also explored where a well-known electron donor N,N-diethylaniline resulted in the luminescence quenching of CQDs. Interestingly, the quenching efficiency is also solvent polarity dependent as the Stern–Volmer quenching constant is much higher in methanol compared to chloroform. The wide range of applications of the PET process involving CQDs includes PL quenching by metal ions and their sensing, quenching with nitroxide radical and sensing of antioxidants, electron transfer from CQDs to chloroplasts which can be useful for promoting photosynthesis to fasten the conversion of light energy to the electrical energy.

1.3.10 Electroluminescence of carbon dots

Electroluminescence, originally discovered in 1936 by Destriau, is a process by which photons are generated when the excess electron–hole pairs are created by an electric current caused by an externally applied bias. It does not involve the generation of heat. Among several others, light-emitting diodes (LED) are the most common, and lighting application of electroluminescence. The remarkable growth of nanotechnology in the optoelectronic sector has eventually led to the development of cost and energy-efficient devices, mostly based on their electroluminescence properties. The electroluminescence properties of carbon dots can be harnessed in developing QD-based electroluminescent LEDs.

The carbon dots-based LED fabrication process can be divided into two general strategies. One is the widely used method of using the phosphorescence of carbon dots on a GaN-based blue or UV LED chip. This method generates both multicolor and white LEDs. Even though marketized, the method is dependent on the quality of the LED chips themselves, and the potential PL properties are not utilized. Now, the second strategy involves the development of the devices consisting of a carbon dot emissive layer sandwiched between an organic hole transport layer (HTL) and an organic or inorganic electron transport layer (ETL) fabricated by a solution-based process (Fig. 1.25). The carbon dot emissive layer is mainly made of pure CQDs or CQDs/polymers host-guest complexes.

The electrodes and part of transport layer materials are processed by thermal evaporation, while the CQD-based active emission layers and some organic conjugate buffer layer materials are processed by solution processing. Hence, the solubility of CQDs in solvents is of significant importance in constructing LED devices. The holes and electrons are first transfused into the ETL and HTL followed by the recombination at the active emissive layer that ultimately triggers the light emission. Now, simply utilizing the tuneable emission wavelength of carbon dots, multicolor LEDs can be developed.

The report of the first electroluminescent device using CQDs tends back to 2011 [33]. 1-hexadecylamine passivated CQDs were used as the active emissive layer. Poly(3,4-ethylenedioxythiophene):poly(styrenesulfonate) and 1,3,5-tris(N-phenylbenzimidazol-2-yl) benzene (TPBI) are the materials used for HTL and ETL, respectively. The highlight of this system is the increase of the anode work function of ITO coupled with a simultaneous decrease in its surface roughness. To have a deeper understanding of the light-emitting mechanism of such a system, a simple

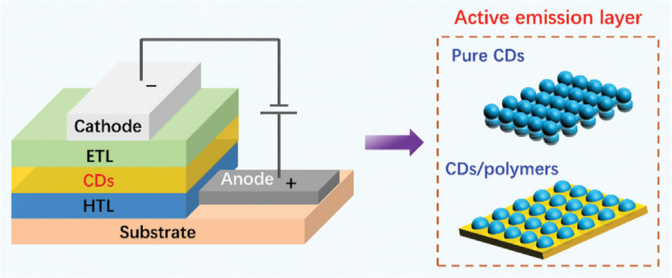

Figure 1.25 Representation of a CQD-based electroluminescent LED structure [32]. *CQDs*, Carbon quantum dots; *LED*, light-emitting diodes.
Source: Copyright 2021 Wiley.

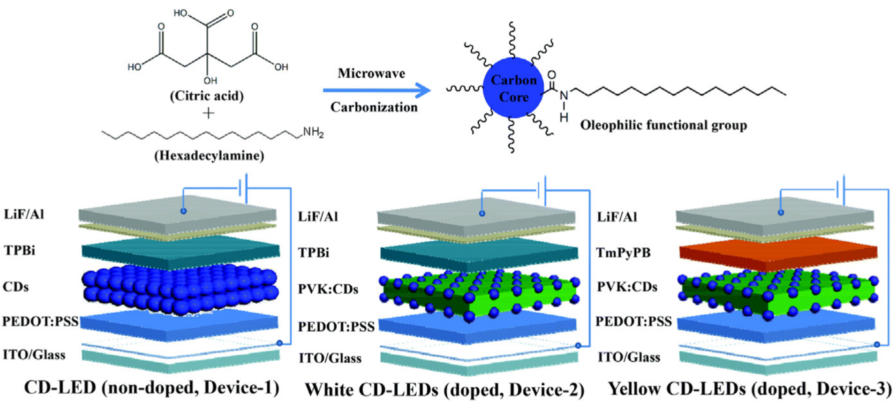
(Citric acid)
+
(Hexadecylamine)
Microwave
Carbonization
Carbon Core
Oleophilic functional group
LiF/Al
TPBi
CDs
PEDOT:PSS
ITO/Glass
CD-LED (non-doped, Device-1)
LiF/Al
TPBi
PVK:CDs
PEDOT:PSS
ITO/Glass
White CD-LEDs (doped, Device-2)
LiF/Al
TmPyPB
PVK:CDs
PEDOT:PSS
ITO/Glass
Yellow CD-LEDs (doped, Device-3)

Figure 1.26 Illustration of the structures of the CQD-LED and doped CQD-LEDs [34].
CQDs, Carbon quantum dots; *LED*, light-emitting diodes.
Source: Reprinted with permission. Copyright 2018 Royal Society of Chemistry.

structured LED of ITO/PEDOT:PSS/PVK:GQDs//LiF/Al was developed. The detailed theoretical and experimental results indicated the formation of hybridization complex states between carbazole-based host materials and GQDs. This has been proved to be beneficial for generating white emissions. Despite providing an alternative pathway for preparing white light-emitting diode (WLEDs), the brightness was only 1 cd/m^2 due to the lack of any transport layer materials.

The oleophilic CQDs were prepared using anhydrous citric acid and hexadecylamine via single-step microwave-assisted carbonization [34]. With help of this, white and yellow LEDs having high brightness were fabricated. As the authors highlighted, the highest ever brightness could be achieved with this CQD-doped LED system (Fig. 1.26). The white CQD-LED showed a maximum brightness of 455.2 cd/m^2 whereas the yellow one showed brightness up to 339.5 cd/m^2. In this system, the CQDs are the guest, and poly(*N*-vinylcarbazole) (PVK) acts as the host. The PVK possesses a wide energy gap and good film-forming ability which can be attributed to the enhanced brightness of the LED system ruling out the usual luminescence quenching of the CQD-LEDs.

1.4 Conclusions and future aspect

The PL property of the carbon dots is undoubtedly the most intriguing yet the most intangible characteristic of these nanosystems. Even after 15 years of rigorous and exponentially growing research on carbon dots, the problem of understanding their fundamental photophysics is still open. This difficulty particularly arises from the large variability in carbon dot structures. The strong luminescence behavior is associated with excellent tunability and sensitivity toward the local environment, i.e., solvents, ions, pH. Another notable aspect is their coverage of the broad spectral range from ultraviolet to visible. This is responsible for the multicolor luminescence in the visible range even though both the absorption and emission efficiencies fade out at longer wavelengths. Luminescence is also characterized by high quantum yields, which, primarily rely on synthetic conditions and procedures. However, as evident by the recent research works, the carbon dots are undoubtedly one of the most versatile nanomaterials in terms of their properties and diverse range of applications that include but are not limited to biomolecule sensing, metal ion sensing, drug delivery, and optoelectronic devices. Apart from providing such a wide range of applications, the unique carbon dot photophysics egg us to explore the heterogeneity-driven optical behavior of a material. It remains unpredictable how a given carbon dot structure will come up with specific photophysical behavior. We believe this decade would get enriched with many more significant explorations that would better our understanding of this wonderful nanomaterial.

References

[1] C.L. Xia, S.J. Zhu, T.L. Feng, M.X. Yang, B. Yang, Evolution and synthesis of carbon dots: from carbon dots to carbonized polymer dots, Advancement of Science 6 (23) (2019).

[2] L. M, Optical properties of carbon dots: a review, Nanoacchitectonics 1 (1) (2020) 1−12.

[3] H.T. Li, X.D. He, Z.H. Kang, H. Huang, Y. Liu, J.L. Liu, et al., Water-soluble fluorescent carbon quantum dots and photocatalyst design, Angewandte Chemie International Edition 49 (26) (2010) 4430−4434.

[4] H.J. Sun, L. Wu, N. Gao, J.S. Ren, X.G. Qu, Improvement of photoluminescence of graphene quantum dots with a biocompatible photochemical reduction pathway and its bioimaging application, ACS Applied Materials & Interfaces 5 (3) (2013) 1174−1179.

[5] Z.X. Gan, S.J. Xiong, X.L. Wu, T. Xu, X.B. Zhu, X. Gan, et al., Mechanism of photoluminescence from chemically derived graphene oxide: role of chemical reduction, Advanced Optical Materials 1 (12) (2013) 926−932.

[6] H. Ding, X.-H. Li, X.-B. Chen, J.-S. Wei, X.-B. Li, H.-M. Xiong, Surface states of carbon dots and their influences on luminescence, Journal of Applied Physics 127 (23) (2020) 231101.

[7] F.A. Permatasari, H. Fukazawa, T. Ogi, F. Iskandar, K. Okuyama, Design of pyrrolic-N-rich carbon dots with absorption in the first near-infrared window for photothermal therapy, ACS Applied Nano Materials 1 (5) (2018) 2368−2375.

[8] S. Hu, A. Trinchi, P. Atkin, I. Cole, Tunable photoluminescence across the entire visible spectrum from carbon dots excited by white light, Angewandte Chemie International Edition 54 (10) (2015) 2970−2974.

[9] Y. Liu, L. Jiang, B. Li, X. Fan, W. Wang, P. Liu, et al., Nitrogen doped carbon dots: mechanism investigation and their application for label free CA125 analysis, Journal of Materials Chemistry B 7 (19) (2019) 3053−3058.

[10] X. Miao, D. Qu, D. Yang, B. Nie, Y. Zhao, H. Fan, et al., Synthesis of carbon dots with multiple color emission by controlled graphitization and surface functionalization, Advanced Materials 30 (1) (2018) 1704740.

[11] H. Ding, S.-B. Yu, J.-S. Wei, H.-M. Xiong, Full-color light-emitting carbon dots with a surface-state-controlled luminescence mechanism, ACS Nano 10 (1) (2016) 484−491.

[12] D.Y. Pan, J.C. Zhang, Z. Li, M.H. Wu, Hydrothermal route for cutting graphene sheets into blue-luminescent graphene quantum dots, Advanced Materials 22 (6) (2010) 734.

[13] S.K. Cushing, M. Li, F.Q. Huang, N.Q. Wu, Origin of strong excitation wavelength dependent fluorescence of graphene oxide, ACS Nano 8 (1) (2014) 1002−1013.

[14] Y.P. Sun, B. Zhou, Y. Lin, W. Wang, K.A.S. Fernando, P. Pathak, et al., Quantum-sized carbon dots for bright and colorful photoluminescence, Journal of the American Chemical Society 128 (24) (2006) 7756−7757.

[15] Z.X. Liu, Z.L. Wu, M.X. Gao, H. Liu, C.Z. Huang, Carbon dots with aggregation induced emission enhancement for visual permittivity detection, Chemical Communications 52 (10) (2016) 2063−2066.

[16] H. Yang, Y. Liu, Z. Guo, B. Lei, J. Zhuang, X. Zhang, et al., Hydrophobic carbon dots with blue dispersed emission and red aggregation-induced emission, Nature Communications 10 (1) (2019) 1789.

[17] P. Choudhury, P.K. Das, Carbon dots-stimulated amplification of aggregation-induced emission of size-tunable organic nanoparticles, Langmuir: The ACS Journal of Surfaces and Colloids 35 (32) (2019) 10582−10595.

[18] C. Wang, K. Jiang, Z. Xu, H. Lin, C. Zhang, Glutathione modified carbon-dots: from aggregation-induced emission enhancement properties to a “turn-on” sensing of temperature/Fe3 + ions in cells, Inorganic Chemistry Frontiers 3 (4) (2016) 514−522.

[19] V. Gude, A. Das, T. Chatterjee, P.K. Mandal, Molecular origin of photoluminescence of carbon dots: aggregation-induced orange-red emission, Physical Chemistry Chemical Physics: PCCP 18 (40) (2016) 28274−28280.

[20] Y. Zhang, P. Zhuo, H. Yin, Y. Fan, J. Zhang, X. Liu, et al., Solid-state fluorescent carbon dots with aggregation-induced yellow emission for white light-emitting diodes with high luminous efficiencies, ACS Applied Materials & Interfaces 11 (27) (2019) 24395−24403.

[21] Y. Su, Z. Xie, M. Zheng, Carbon dots with concentration-modulated fluorescence: aggregation-induced multicolor emission, Journal of Colloid and Interface Science 573 (2020) 241−249.

[22] W. Lv, M. Lin, R. Li, Q. Zhang, H. Liu, J. Wang, et al., Aggregation-induced emission enhancement of yellow photoluminescent carbon dots for highly selective detection of environmental and intracellular copper(II) ions, Chinese Chemical Letters 30 (7) (2019) 1410−1414.

[23] X. Wei, S. Mei, D. Yang, G. Zhang, F. Xie, W. Zhang, et al., Surface states induced photoluminescence enhancement of nitrogen-doped carbon dots via post-treatments, Nanoscale Research Letters 14 (1) (2019) 172.

[24] W.L. Wei, C. Xu, J.S. Ren, B.L. Xu, X.G. Qu, Sensing metal ions with ion selectivity of a crown ether and fluorescence resonance energy transfer between carbon dots and graphene, Chemical Communications 48 (9) (2012) 1284−1286.

[25] J. Tang, B. Kong, H. Wu, M. Xu, Y.C. Wang, Y.L. Wang, et al., Carbon nanodots featuring efficient FRET for real-time monitoring of drug delivery and two-photon imaging, Advanced Materials 25 (45) (2013) 6569−6574.

[26] J. Kudr, L. Richtera, K. Xhaxhiu, D. Hynek, Z. Heger, O. Zitka, et al., Carbon dots based FRET for the detection of DNA damage, Biosensors & Bioelectronics 92 (2017) 133−139.

[27] J.L. Wang, J.H. Wei, S.H. Su, J.J. Qiu, Novel fluorescence resonance energy transfer optical sensors for vitamin B-12 detection using thermally reduced carbon dots, New Journal of Chemistry 39 (1) (2015) 501−507.

[28] T. Feng, H.J. Chua, Y.L. Zhao, Reduction-responsive carbon dots for real-time ratiometric monitoring of anticancer prodrug activation in living cells, ACS Biomaterials Science & Engineering 3 (8) (2017) 1535−1541.

[29] Y. Kim, G. Jang, T.S. Lee, New fluorescent metal-ion detection using a paper-based sensor strip containing tethered rhodamine carbon nanodots, ACS Applied Materials & Interfaces 7 (28) (2015) 15649−15657.

[30] Y.L. Hu, L. Zhang, X. Geng, J. Ge, H.F. Liu, Z.H. Li, A rapid and sensitive turn-on fluorescent probe for ascorbic acid detection based on carbon dots-MnO2 nanocomposites, Analytical Methods 9 (38) (2017) 5653−5658.

[31] D. Escudero, Revising intramolecular photoinduced electron transfer (PET) from first-principles, Accounts of Chemical Research 49 (9) (2016) 1816−1824.

[32] B. Zhao, Z.A. Tan, Fluorescent carbon dots: fantastic electroluminescent materials for light-emitting diodes, Advancement of Science 8 (7) (2021) 2001977.

[33] F. Wang, Y.H. Chen, C.Y. Liu, D.G. Ma, White light-emitting devices based on carbon dots' electroluminescence, Chemical Communications 47 (12) (2011) 3502−3504.

[34] J.C. Xu, Y.Q. Miao, J.X. Zheng, H. Wang, Y.Z. Yang, X.G. Liu, Carbon dot-based white and yellow electroluminescent light emitting diodes with a record-breaking brightness, Nanoscale 10 (23) (2018) 11211−11221.

The physical and chemical properties of carbon dots via computational modeling

2

Arup Chakraborty
Department of Chemistry, Institute of Nanotechnology and Advanced Materials, Bar-Ilan University, Ramat Gan, Israel

2.1 Introduction

Quantum dots (QDs) are zero-dimensional nanostructures which provide interesting electronic and optical properties because of quantum confinement. Semiconductor QDs are applicable for optoelectronics, biosensing, and bioimaging due to their tunable fluorescence emission properties. When primarily heavy metals, such as Cd, Pb, and Hg, are used, there is, however, a drawback to using semiconductor QDs. On the contrary, carbon-based QDs are low toxic, cost-effective, have better fluorophores than other organic counterparts, have good solubility, and provide high quantum yields [1−3]. Hence, the carbon dots (CDs) have received attention within materials research for these advantages in the last two decades. Furthermore, these CDs are applied in energy storage devices, catalysis, optoelectronics, sensors, biomedicine, and quantum computations (see Fig. 2.1) [4]. Modeling QDs provides atomistic insights for these applications. Furthermore, these exciting properties of QDs are mainly because of quantum confinement which we discuss in this chapter.

CDs are categorized mainly based on their atomic structures. State-of-the-art computational techniques help unlock the structure−properties relation of these CDs. Furthermore, the properties of the CDs strongly depend on the type of atoms that saturate the dangling bonds or the surface functionalization group, which controls the band gap of CDs.

2.2 Different carbon dots

Carbon zero-dimensional dots can be categorized into several groups (see Fig. 2.2) based on their structures. These dots can be either crystalline or amorphous. Broadly, the CDs are graphene quantum dots (GQDs), graphitic carbon nitride quantum dots (CNQDs), carbon nanodots (CNDs), carbon quantum dots (CQDs), and carbonized polymer dots (CPDs), as shown in Fig. 2.2. Beyond these primary QDs, N- and S-doped CDs were also studied widely. The GQDs consisting of a few

Carbon Quantum Dots for Sustainable Energy and Optoelectronics. DOI: https://doi.org/10.1016/B978-0-323-90895-5.00012-6
© 2023 Elsevier Ltd. All rights reserved.

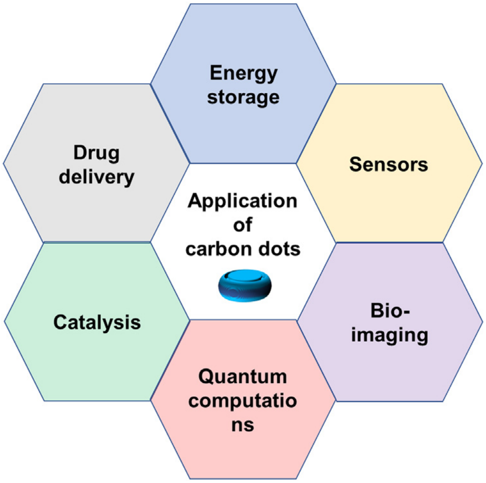
Energy storage
Drug delivery
Sensors
Application of carbon dots
Catalysis
Bio-imaging
Quantum computations

Figure 2.1. The schematic diagram for their applications in different fields of CDs. *CDs*, Carbon dots.

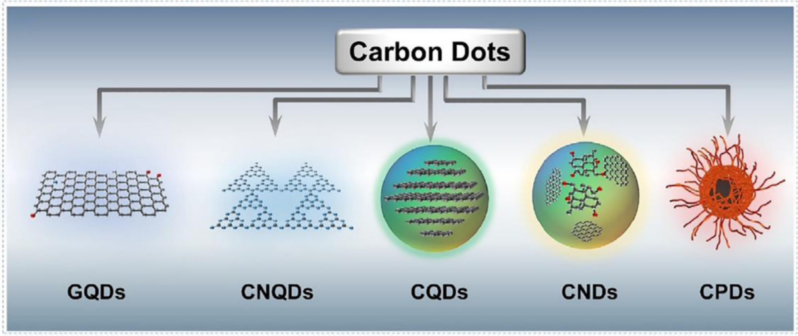
Carbon Dots
GQDs
CNQDs
CQDs
CNDs
CPDs

Figure 2.2 Schematic models of different types of carbon dots.
Source: Reproduced from S. Li, et al., The development of carbon dots: from the perspective of materials chemistry. Materials Today, 51 (2021) 188–207, with permission from Elsevier.

graphene layers are mainly prepared from graphene or graphite materials [2]. CNQDs are analog to GQDs, and the difference comes from their elemental contents. The CQDs have a crystalline core based on the mixture of sp^3 and sp^2 hybridization, unlike GQDs. The GQDs could have a diameter of up to 40 nm, while CQDs have a diameter of 10 nm. On the other hand, CNDs have an amorphous core. The CPDs have carbonized core with aggregation or cross-linking of linear polymers. This chapter mainly discusses a range of theoretical and computational studies on the different properties of CDs.

2.3 Computational methods applied to study the properties of carbon dots

State-of-the-art computational tools help obtain atomic insights into material properties missing in experimental studies. This section discusses several theoretical and computational methods for studying CD properties [5]. Fig. 2.3 shows that we can categorize the methods in different domains ranging from semi-empirical and classical approaches to higher-level multireference methods with increasing computational costs. The structure could be found using force field-based (classical) simulation, whereas electronic properties are obtained from quantum mechanics, based on Hartree-Fock theory or density functional theory (DFT) with proper exchange-correlation functional (generalized gradient approximation [GGA], *meta*-GGA, hybrid functional, etc.). One needs higher-level theory like time-dependent DFT to treat optical excitation, where the excited state and excitonic effect are described more accurately. For better results, one can choose a multireference method or coupled cluster method (CCSD(T)), but it is restricted to the small size of the system due to the enormous computational costs [5]. In the following section, we discuss different fascinating properties of CDs with applied computational methods.

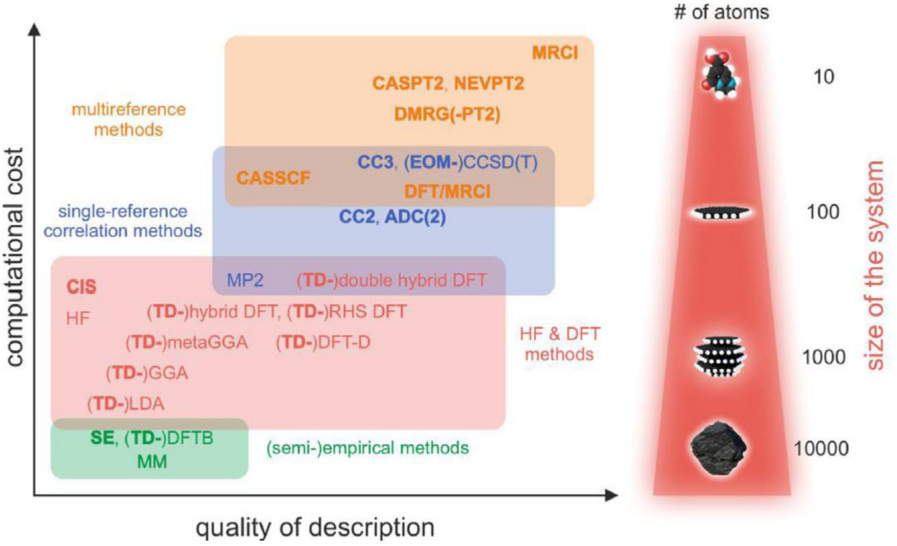
computational cost
quality of description
multireference methods
single-reference correlation methods
HF & DFT methods
(semi-)empirical methods
MRCI
CASPT2, NEVPT2
DMRG(-PT2)
CASSCF
CC3, (EOM-)CCSD(T)
DFT/MRCI
CC2, ADC(2)
MP2
(TD-)double hybrid DFT
CIS
HF
(TD-)hybrid DFT, (TD-)RHS DFT
(TD-)metaGGA
(TD-)DFT-D
(TD-)GGA
(TD-)LDA
SE, (TD-)DFTB
MM
# of atoms
10
100
1000
10000
size of the system

Figure 2.3 A schematic representation of system size versus computational cost. *Source:* Reproduced from M. Langer, et al., Progress and challenges in understanding of photoluminescence properties of carbon dots based on theoretical computations. Applied Materials Today, 22 (2021) 100924, with permission from Elsevier.

2.4 Theoretical studies of different properties of carbon quantum dots

2.4.1 Electronic structure

The electronic properties of CDs depend on the effect of quantum confinement and the surface passivating species. These two factors determine the energy gap between the highest occupied molecular orbital (HOMO) state and the lowest unoccupied molecular orbital (LUMO) state, as shown in Fig. 2.4. GQDs have a nonzero band gap because of excitons in graphene. The main controllers for the energy gap are the bonding between C atoms like GQDs in the core region of the CDs and its surface species.

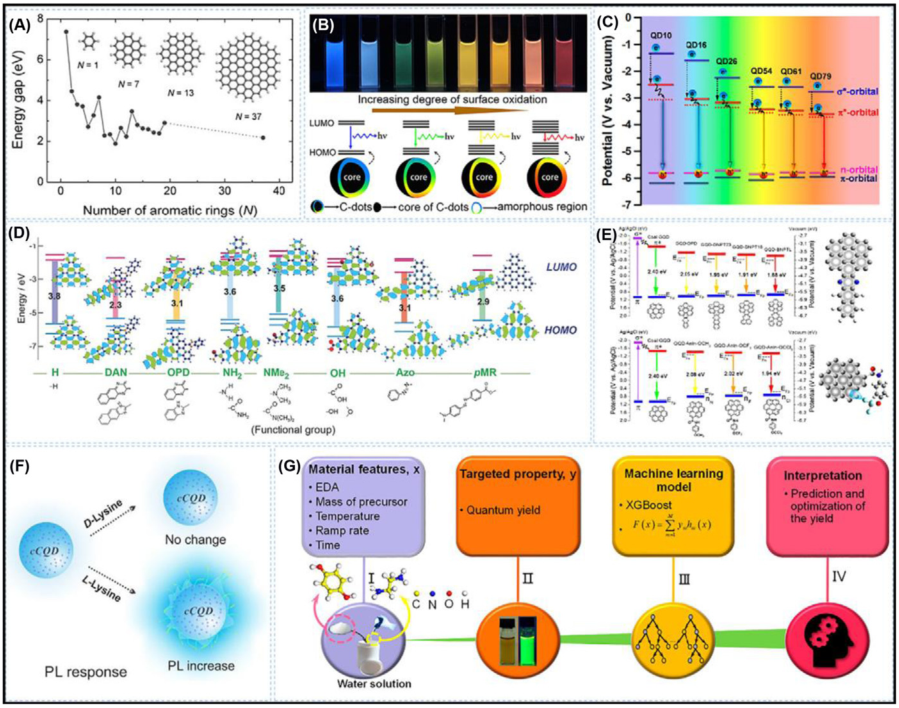
(A)
Energy gap (eV)
0
2
4
6
8
N = 1
N = 7
N = 13
N = 37
0
10
20
30
40
Number of aromatic rings (N)
(B)
Increasing degree of surface oxidation
LUMO
HOMO
hv
core
C-dots
core of C-dots
amorphous region
(C)
Potential (V vs. Vacuum)
0
-1
-2
-3
-4
-5
-6
-7
QD10
QD16
QD26
QD54
QD61
QD79
σ*-orbital
π*-orbital
n-orbital
π-orbital
(D)
Energy / eV
-1
-3
-5
-7
3.8
2.3
3.1
3.6
3.5
3.6
3.1
2.9
LUMO
HOMO
H
DAN
OPD
NH₂
NMe₂
OH
Azo
pMR
(Functional group)
(E)
Ag/AgCl (eV)
Vacuum (eV)
Coal GQD
GQD-OPD
2.40 eV
2.15 eV
1.95 eV
1.91 eV
1.88 eV
2.40 eV
2.08 eV
2.02 eV
1.94 eV
Potential (V vs. Ag/AgCl)
Potential (V vs. Vacuum)
(F)
eCQD
D-Lysine
L-Lysine
No change
PL increase
PL response
(G)
Material features, x
• EDA
• Mass of precursor
• Temperature
• Ramp rate
• Time
Targeted property, y
• Quantum yield
Machine learning model
• XGBoost
• $F(x)=\sum_{m=1}^{M} y_m h_m(x)$
Interpretation
• Prediction and optimization of the yield
I
II
III
IV
C N O H
Water solution

Figure 2.4 (A) Relation between the energy gap vs the size of the aromatic ring. (B) Variation of energy gap with degrees of oxidation. (C) The effect of the introduction of oxygen atoms on the energy gap. (D) The impact of the introduction of nitrogen atoms on the energy gap. (E) The effect of introducing an electron-donating functional group or domain size of sp^2 hybridization. (F) Modification of PL after D-Lysine and L-Lysine. (G) Synthesis of CDs guided by machine learning.
Source: Reproduced from S. Li, et al., The development of carbon dots: from the perspective of materials chemistry. Materials Today, 51 (2021) 188–207, with permission from Elsevier.

The design principles of different CDs with several parameters are schematically depicted in Fig. 2.4, as shown by Li et al. [2]. The CDs have GQDs as core and surface functional groups. In Fig. 2.4A, with the increasing size of the aromatic ring, the band gap decreases due to the effect of quantum confinement. The sp^2 domain size also increases with the growing length of the aromatic rings. Similarly, the energy gap of CDs reduces upon an increment of oxidation at the surface of the CDs. Incorporating oxygen atoms into the sp^2 region generates an *n*-orbital level, which causes n-π* transition (Fig. 2.4B and C). Furthermore, nitrogen functionalization at the surface of CQDs changes the HOMO and LUMO positions and hence the energy gap as shown in Fig. 2.4D. This nitrogen-containing surface group could donate electrons, and it may generate *n*-orbital between π and π* that affect the photoluminescence (PL).

Chirality is another factor that affects CDs' electronic and chemical properties, as explained in Fig. 2.4F. Chirality in CDs, modified by chiral ligands (e.g., amino acid), enhances their chemical stability and optical properties.

The state-of-the-art computational approach could help to design and control the electronic and optical properties and develop CDs. Han et al. recently showed from computation using machine learning (ML) technique that their advanced ML-based method can design the CDs with higher quantum yield [6].

2.4.2 Optical properties

The optical properties of any material depend entirely on its electronic structure, as discussed above. Several optical processes are observed in CDs, as shown in Fig. 2.5. These optical processes are only within the singlet state of CDs. PL and absorption depend entirely on the transition between two electronic states obeying selection rules. In general, the emission mechanism in CDs is exciton-dependent, and this occurs in three different ways, namely emissions due to the quantum confinement effect of the 0D QDs, emissions due to more prominent surface states, and emissions due to molecular states.

Strong absorption occurs in CDs due to the transition between π to π* of the phenyl rings. This absorption of light belongs to the ultraviolet region. On the contrary, lower absorption by the transition between *n* to π* from C-C or C-O bonds lies in the visible and near-infrared region. The PL phenomenon is observed between two singlet states following internal conversion between nonradiative singlet states.

The excitation-dependent PL or fluorescence is the most promising phenomenon observed in CDs [3]. Due to excitation-dependent PL, a wide range of multicolor emissions makes CDs more useful in optoelectronic applications. These long-ranged emission processes occur from the transition between several surface defect states to ground states. On the contrary, the tunable PL in semiconductor QDs mainly arises from the changing size of the particle due to the quantum confinement effect. Several groups showed a direct relationship between surface state-to-PL. Hence, one can generate particular color of PL by modifying surface defect states from passivating agents in CDs. Fu et al. had shown that the luminescence in

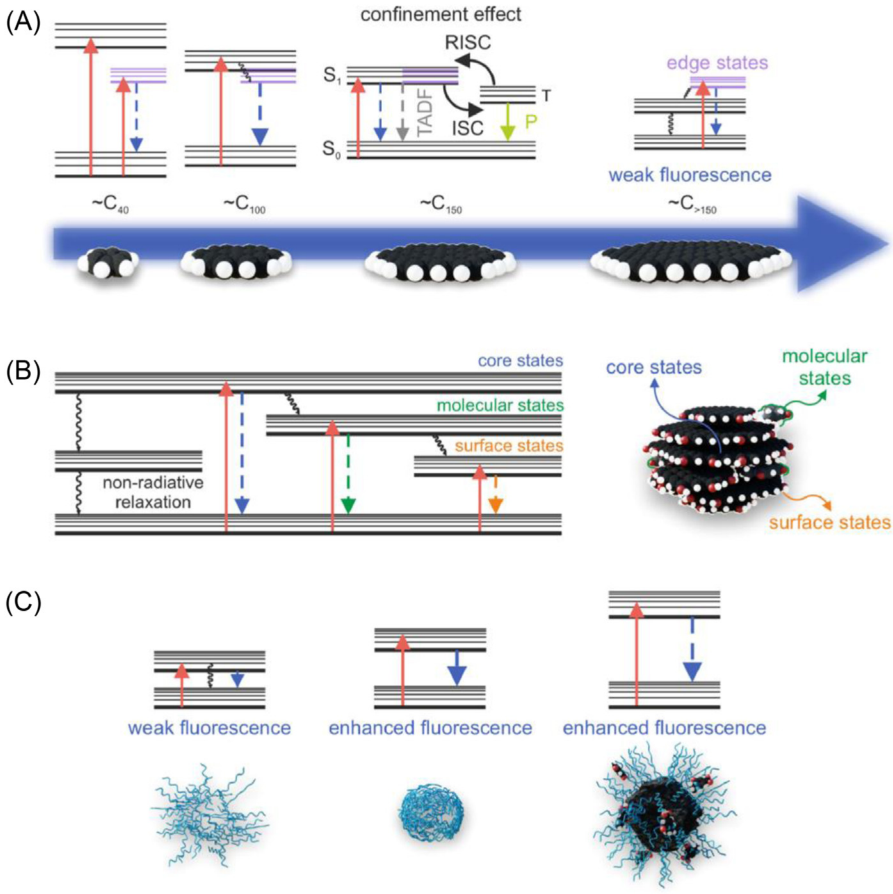
(A)
confinement effect
RISC
S_1
S_0
TADF
ISC
T
P
edge states
weak fluorescence
~C_{40}
~C_{100}
~C_{150}
~$C_{>150}$
(B)
core states
molecular states
surface states
non-radiative relaxation
core states
molecular states
surface states
(C)
weak fluorescence
enhanced fluorescence
enhanced fluorescence

Figure 2.5 Different possible PL and fluorescence mechanisms. (A) Effect of quantum confinement; (B) multicomponent PL between core, molecular, and surface states; (C) effect of crosslink-enhanced emission.
Source: Reproduced from M. Langer, et al., Progress and challenges in understanding of photoluminescence properties of carbon dots based on theoretical computations. Applied Materials Today, 22 (2021) 100924, with permission from Elsevier.

CDs could be controlled by adjusting the structure of emitting surface species [7]. For example, they showed two-dimensional polycyclic aromatic hydrocarbons (PAHs) containing carbons having sp^2 hybridization, which mimic the nanodomains of CDs. Luo et al. also showed luminescence tuning in aryl functionalized GQDs, where aryl residues make covalent bonds with surface carbon atoms [8].

Furthermore, several photophysical processes were observed in the CDs, namely electrochemiluminescence, chemical luminescence, Foster resonance energy transfer (FRET), etc.

2.4.3 Electrocatalytic properties

Beyond the PL application, the CDs have plenty of applications in energy storage via electrocatalytic processes. The advantages of using CDs as an electrocatalytic agent are that they are nontoxic, economically cheap, have large surface area, high conductivity, and reasonable charge transfer possibilities (see Fig. 2.6) [9]. These include oxygen reduction reaction (ORR), oxygen evolution reaction (OER), CO_2 reduction, hydrogen evolution reaction (HER), etc. [10].

To know the intermediate steps of any electrocatalytic phenomena such as OER, ORR, HER, etc., we can calculate free energies for all steps using DFT, and details of the approach could be found in Ref. [11]. In DFT, we calculate Gibbs free energy from the following formula.

$$\Delta G = \quad \Delta E + \quad \Delta ZPE - T \cdot \Delta S$$

where ΔG, ΔE, ΔZPE, T, and ΔS are changes in Gibbs free energy for the reaction, change in binding energies for the reaction, change in zero-point energy, temperature, and change in entropy, respectively. All the parameters are calculated from DFT or the gas-phase database.

There are very few theoretical studies on the electrocatalytic properties of CDs. We here discuss a few of the recent studies. W. A. Saidi explored ORR activity from first-principles calculations for N-doped GQDs, where pyridine and graphitic nitrogen are the most active sites with comparatively low overpotential [12].

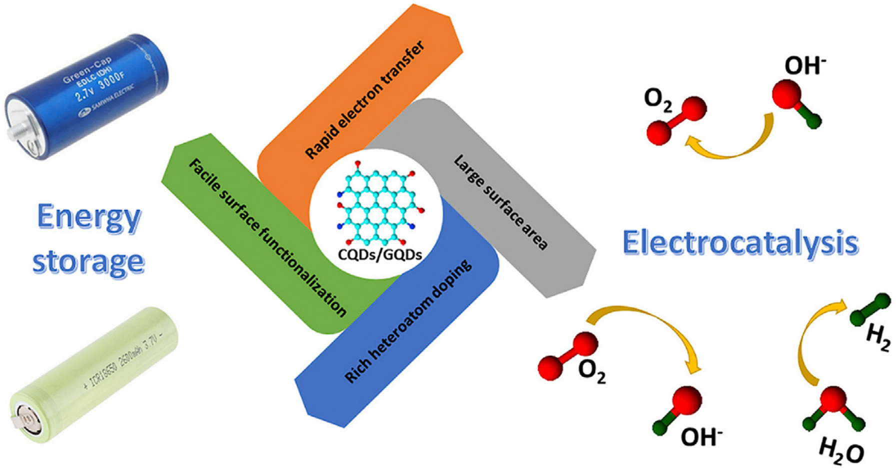
Green-Cap
EDLC(DH)
2.7V 3000F
SAMWHA ELECTRIC
Energy storage
+ ICR18650 2600mAh 3.7V -
Rapid electron transfer
Facile surface functionalization
Large surface area
Rich heteroatom doping
CQDs/GQDs
Electrocatalysis
O_2
OH^-
O_2
OH^-
H_2
H_2O

Figure 2.6 Schematic representation of various electrocatalytic properties of CQDs and GQDs. *GQDs*, Graphene quantum dots; *CQDs*, carbon quantum dots.
Source: Reproduced from V. C. Hoang, K. Dave, V. G. Gomes, Carbon quantum dot-based composites for energy storage and electrocatalysis: Mechanism, applications and future prospects. Nano Energy, 66 (2019) 104093, with permission from Elsevier.

Li et al. showed that CDs could be used as a promising electrocatalyst for ORR [13]. These CDs can easily combine with noble metals, metal oxides, and other organic solvents. These integrated complexes help the electrocatalytic process through possible charge separation, opening new reactive sites and reducing the reaction's activation barrier. The GQDs combined with carbon nitride form nanohybrid, which helps in ORR. Hence, the CQDs could provide promising electrocatalytic applications.

The CDs combined with transition metal compounds such as CoP provide better OER activity, where the overpotential is lowered by 400 mV compared to pure CoP [10].

In fossil fuels, nitrogen-doped GQDs with the wrapping of Au nanoparticles help to reduce CO_2 in the natural carbon cycle. This is due to the enhancement of the absorption of the carboxylic group at the N site of the pyridine ring of N-doped GQDs [14].

Furthermore, CDs can be used for HER activity, such as Ru with CDs hybrid, which requires only 10 mV of overpotential [15].

Therefore, CDs are promising as electrocatalysts due to their inherent properties, as shown in Fig. 2.6, and are nontoxic and inexpensive, as discussed earlier.

2.4.4 Transport properties

Beyond the interesting optical properties, CDs, especially GQDs, also show exciting transport properties. The electronic and transport properties of nanostructures like QDs depend on the QDs' confined geometry. The quantum confinement of the CDs avails of exciting phenomena like quantum interference, resonant tunneling, and localization. Recently, Gonzalez et al. found a resonant behavior for the conductance of the GQDs using tight-binding Hamiltonian and Green's function (Landauer-Buttiker formalism) with the real space renormalization technique [16]. This can be controlled by changing their geometry, and the negative differential conductance appears upon applying low gate and bias voltage values.

Furthermore, the spin state beyond the charge transport in GQDs can be used as qubits in quantum computation, which is the future for superfast computations. The GQDs have advantages over semiconductor QDs like GaAs QDs because of the weaker spin-orbit coupling due to the low atomic weight, which provides a much longer spin coherence time, unlike GaAs [17,18]. The GQDs also have a larger spin g-factor (c. 2), so qubit manipulation could be done much faster than GaAs [19]. A simple illustration of the long-range interaction via Klein tunneling between spin qubits of QDs embedded within a graphene sheet is presented in Fig. 2.7. To understand the behavior of spin qubits in GQDs, one can use the model Hamiltonian approach considering spin-orbit coupling and electron-phonon coupling within it. More details about spin qubits and their interaction in different graphene and semiconductor QDs could be found in Ref. [17–19].

2.4.5 Kondo effect in carbon quantum dots

The conduction electrons get scattered due to magnetic impurities in the materials, for which resistivity at zero temperature diverges. This phenomenon is known as

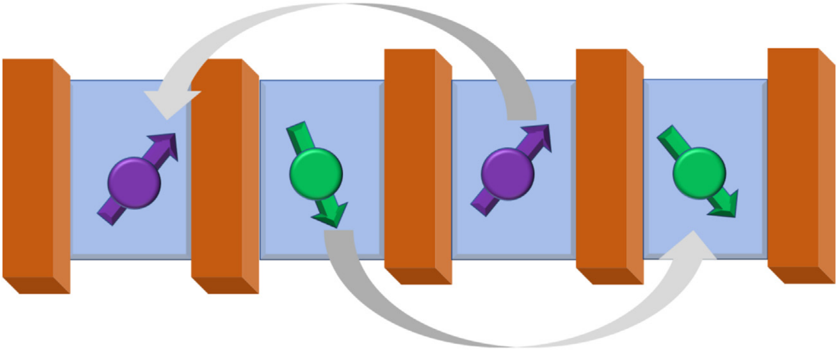

Figure 2.7 Schematic illustration of long-distance interaction via Klein tunneling (shown by the gray arrows) between qubits of GQDs. The purple/green dots are the quantum dots, the brown bars are the barriers, the blue sheet is graphene sheets. Purple/green arrows show spin qubits in each quantum dot [20]. *GQDs*, Graphene quantum dots.

the Kondo effect. The first time experimentally Kondo effect in QDs was observed in 1998, confirming theoretical predictions [21]. In the case of GQDs, Kurzmann et al. showed the presence of the Kondo effect from the two-electron triplet ground states with small spin-orbit coupling [22].

2.5 Summary and outlook

CDs are most beneficial compared to other semiconductor counterparts for their low cost and nontoxic nature. CDs offer fascinating properties like electronic, optical, electrocatalytic, transport, etc. CDs' quantum confinement effect and surface functionalization groups influence these properties. Theoretical and computational modeling of CDs paves the way for understanding these properties which we have briefly discussed in this chapter. Here, we have provided atomistic insights based on several theoretical and computational studies. This chapter has elucidated how the fluorescence and PL of CDs occur due to transition between different electronic states and due to mixed sp^2-sp^3 hybridization, how CDs help in the electrocatalytic process by increasing reactive sites and reducing energy barrier, and the possibility of spin qubit interaction in CDs useful for quantum computations.

However, there are many challenges in fabricating and modeling devices with CDs. For instance, surface functionalization is crucial for getting optimized electronic and optical properties. Various approaches were attempted to handle these challenges. From a modeling perspective, we have to be careful in choosing methods for calculating specific properties. *There is scope* for improvement in synthesis as well as in the understanding of the properties of CDs. Finally, CDs are promising for their future applications in the different fields of optoelectronics, electrocatalyst, quantum computations, drug delivery, etc.

References

[1] Y. Wang, A. Hu, Carbon quantum dots: synthesis, properties and applications, Journal of Materials Chemistry C 2 (34) (2014) 6921−6939.

[2] S. Li, et al., The development of carbon dots: from the perspective of materials chemistry, Materials Today 51 (2021) 188−207.

[3] R. Jelinek, Carbon quantum dots: synthesis, properties and applications. Carbon Nanostructures, Springer, Switzerland, 2017.

[4] B. Wang, et al., Carbon dots as a new class of nanomedicines: opportunities and challenges, Coordination Chemistry Reviews 442 (2021) 214010.

[5] M. Langer, et al., Progress and challenges in understanding of photoluminescence properties of carbon dots based on theoretical computations, Applied Materials Today 22 (2021) 100924.

[6] Y. Han, et al., Machine-learning-driven synthesis of carbon dots with enhanced quantum yields, ACS Nano 14 (11) (2020) 14761−14768.

[7] M. Fu, et al., Carbon dots: a unique fluorescent cocktail of polycyclic aromatic hydrocarbons, Nano Letters 15 (9) (2015) 6030−6035.

[8] P. Luo, et al., Aryl-modified graphene quantum dots with enhanced photoluminescence and improved pH tolerance, Nanoscale 5 (16) (2013) 7361−7367.

[9] L. Tian, et al., Carbon quantum dots for advanced electrocatalysis, Journal of Energy Chemistry 55 (2021) 279−294.

[10] V.C. Hoang, K. Dave, V.G. Gomes, Carbon quantum dot-based composites for energy storage and electrocatalysis: mechanism, applications and future prospects, Nano Energy 66 (2019) 104093.

[11] J.K. Nørskov, et al., Origin of the overpotential for oxygen reduction at a fuel-cell cathode, The Journal of Physical Chemistry. B 108 (46) (2004) 17886−17892.

[12] W.A. Saidi, Oxygen reduction electrocatalysis using N-doped graphene quantum-dots, The Journal of Physical Chemistry Letters 4 (23) (2013) 4160−4165.

[13] Q. Li, et al., Nitrogen-doped colloidal graphene quantum dots and their size-dependent electrocatalytic activity for the oxygen reduction reaction, Journal of the American Chemical Society 134 (46) (2012) 18932−18935.

[14] J. Fu, et al., Low overpotential for electrochemically reducing CO_2 to CO on nitrogen-doped graphene quantum dots-wrapped single-crystalline gold nanoparticles, ACS Energy Letters 3 (4) (2018) 946−951.

[15] W. Li, et al., Carbon-quantum-dots-loaded ruthenium nanoparticles as an efficient electrocatalyst for hydrogen production in alkaline media, Advanced Materials 30 (31) (2018) 1800676.

[16] J.W. González, et al., Transport properties of graphene quantum dots, Physical Review B 83 (15) (2011) 155450.

[17] B. Trauzettel, et al., Spin qubits in graphene quantum dots, Nature Physics 3 (3) (2007) 192−196.

[18] R. Hanson, et al., Spins in few-electron quantum dots, Reviews of Modern Physics 79 (4) (2007) 1217−1265.

[19] P. Recher, B. Trauzettel, Quantum dots and spin qubits in graphene, Nanotechnology 21 (30) (2010) 302001.

[20] V. Fal'ko, Quantum information on chicken wire, Nature Physics 3 (3) (2007) 151−152.

[21] D. Goldhaber-Gordon, et al., Kondo effect in a single-electron transistor, Nature 391 (6663) (1998) 156−159.

[22] A. Kurzmann, et al., Kondo effect and spin−orbit coupling in graphene quantum dots, Nature Communications 12 (1) (2021) 6004.

3 Synthesis of carbon quantum dots

Ankita Saha[1], *Lopamudra Bhattacharjee*[2] *and*
Rama Ranjan Bhattacharjee[3]
[1]Amity School of Applied Sciences, Amity University, Kolkata, West Bengal, India, [2]PSG Institute of Advanced Studies, Coimbatore, Tamil Nadu, India, [3]Department of Chemistry, Sister Nivedita University, Kolkata, West Bengal, India

3.1 Introduction

The excellent physical and chemical properties of carbogenic nanosystems (fullerenes, carbon nanotubes, carbon quantum dots, graphene sheets, and nanodiamonds) have inspired researchers to conduct extensive studies with such materials. The expected outcome possesses great potential for a wide variety of applications.

Carbogenic nanosystems have been extensively studied since the discovery of carbon nanotubes (CNTs). Despite the fact that CNTs have enormous potential in electronic applications, large-scale synthesis of such materials has been difficult. Existing methods are time-consuming, involve high production costs, and produce insufficient yields. CNTs also suffer from dispersion issues. The material is difficult to functionalize and hence shows limited dispersion abilities. Only a few solvents have been reported to be used as dispersion medium but they are mostly high boiling solvents. CNTs also suffer from issues related to impurities or the presence of adsorbed solvents. Researchers who use sonication for CNT dispersion in a given medium, report itching of amorphous carbon from the material and hence conducting properties are altered.

3.1.1 Carbon quantum dots

Carbon quantum dots (CQDs) may emerge as a cost-effective alternative to CNTs due to their ease of synthesis and high yield. CQDs have recently gained popularity as a potential substitute to CNTs for feasible applications. CQDs, which are entirely composed of carbon atoms, are abundant on the earth and are not harmful to the environment or human health. CQDs have various properties such as optical fluorescence and electrical conductance. These QDs are also used in combination with oxides such as TiO_2, SiO_2, Cu_2O, and ZnO for catalysis via electrochemical reaction or energy transfer. CQDs primarily exhibit properties based on relative hybridization volume as a combination of sp^2 and sp^3 hybridizations. Because of the abundance of trap states, the QDs could be used effectively as charge carrier pockets or quantum wells.

Carbon Quantum Dots for Sustainable Energy and Optoelectronics. DOI: https://doi.org/10.1016/B978-0-323-90895-5.00014-X
© 2023 Elsevier Ltd. All rights reserved.

Extensive efforts have been made for the development of nontoxic or less toxic and water dispersible fluorescent QDs as alternatives to the semiconductor-based QDs. Carbon-based nanostructures (e.g., CNTs, fullerenes, etc.) including CQDs and graphene nanosheet of less than 100 nm in size, which are known as graphene quantum dots (GQDs) have already been developed. Various methods have been demonstrated in the preparation of fluorescent CQDs. Electrochemical oxidation processes, chemical oxidation methods, hydrothermal methods, and carbonizing organic molecules are some important methods for the preparation of CQDs. Carbon-based QDs derived from adaptable resources such as graphene materials, graphite, as well as from various carbon resources, such as banana juice, citric acid, carbon soot, glucose, egg material, and so on, exhibit high quantum yield (QY) depending on their synthesis procedure and surface passivation nature. Most of the developed procedures are unsuitable because of high cost of the equipment required, low yield, and the complex procedure. Most of the obtained CQDs have relatively low QY in comparison to conventional semiconductor-based QDs. Nowadays efforts are made to increase fluorescence QYs of CQDs by passivating them with large organic molecules and polymers. Doping them with various heteroatoms also has drawn attention due to their tunable properties.

3.1.1.1 Structure of carbon quantum dots

Though there is considerable literature on CQDs, the exact structure of these fascinating materials is still unknown.

Until now, graphene and graphene oxide QDs have been reported to be synthesized from graphite nanoparticles through conventional Hammer's method and few of its modifications as shown in Fig. 3.1. Fig. 3.1 shows the synthesis process schematically.

From the figure it is clear that the final structure of the graphene oxide nanomaterial was easy to predict and it is mainly composed of arrays of sp^2 carbons with few defects as shown in the figure. The issue with CQDs is that the final structure

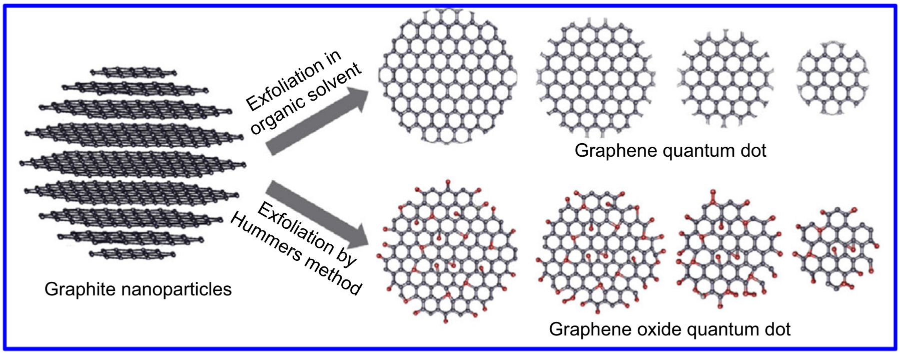
Exfoliation in organic solvent
Graphene quantum dot
Exfoliation by Hummers method
Graphite nanoparticles
Graphene oxide quantum dot

Figure 3.1 A schematic route showing synthesis of graphene oxide quantum dots and graphene quantum dots from graphite nanoparticles by exfoliation.

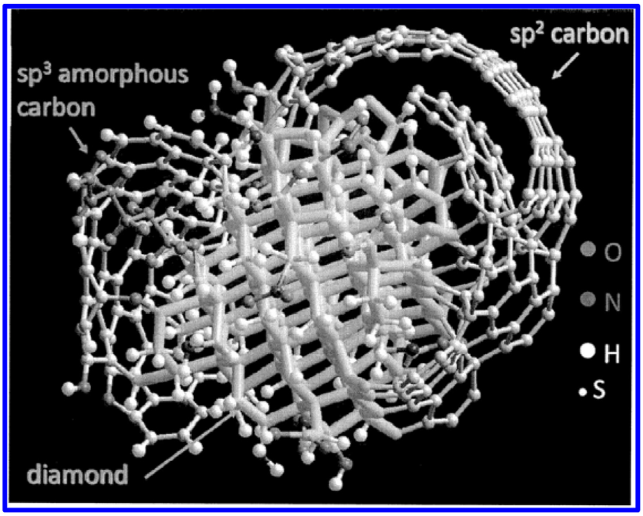

Figure 3.2 Schematic representation of the structure of CQDs. *CQDs*, Carbon quantum dots. Courtesy: w.w.w.

of the material is difficult to assign as the source of the materials (mostly organic materials like citric acid, etc.) do not retain any identity. Thus, a hypothetical structure of CQDs has been proposed in Fig. 3.2.

It is assumed that CQDs might consist of various allotropic forms of carbon where either one may be prevalent. The structure may have all three different hybridization areas (sp, sp^2, and sp^3) or a diamond-like crystal structure as shown in Fig. 3.2. Some researchers have also predicted that CQDs are composed of discrete sp^2 islands separated or dispersed over sp^3 medium. From the application point of view, it is reasonable to state that the occurrence of more and more sp^2 islands would be preferable as it will lower the transition energy and impose better-conducting properties and tunable emission in the near infrared region. Thus the challenge for chemists is to synthesize CQDs with more sp^2 domains or more continuous sp^2 domains.

3.1.1.2 Principles of synthesis

To synthesize fluorescent CQDs, a range of different methods have been established. Some simple but ineffective preparative strategies have also been created, such as:

- Directly oxidizing candle soot into fluorescent CQDs.
- Electrochemical change of CNTs into highly fluorescent nanocrystals of carbon.
- Breaking of nonluminescent graphene sheets into blue fluorescent GQDs hydrothermally.
- Incomplete thermal degradation of presynthesized citrate salts into fluorescent CQDs.

Multistep techniques are time-consuming and complicated, but they are very much effective at producing strong green luminescent carbon materials.

3.2 Basic techniques for carbon quantum dot preparation

The preparation of CQDs has made great progress in recent years. According to the carbon precursor used, the synthesis methods of CQDs can be classified into two methods: top-down and bottom-up approaches. The top-down approach was excessively used during the early periods of research, and usually, big-size carbon materials were cut and stripped by physical or chemical methods to make CQDs of long-range order and to make macroscopic connections. In the bottom-up method, small organic molecules are chemically polymerized into CQDs. These two methods can fulfill the different demands of small particle size and magnificent optical features of CQDs to a certain extent.

3.2.1 Top-down approach

The top-down approach involves the fragmentation of large materials into small-sized structures or particles (in nm range). This approach is inherently simpler and relies on the removal or segmentation of bulk materials or the miniaturization of bulk manufacturing processes to produce the desired structure with suitable attributes. This top-down approach can further be classified into two main groups: physical methods and chemical methods.

3.2.1.1 Physical methods

Arc discharge method

Arc discharge method was one of the earliest approaches used to synthesize CNTs. In this method, the graphite electrodes (anode and cathode) are used which are placed very close to each other in an inert atmosphere. By conducting high amounts of current, the source carbon materials can be vaporized from the positive electrode, which condenses again and deposited on the surface of the chamber or over the cathode substrate. Application of high current will produce a hard and impure material with some free nanotubes. Therefore, the lowest possible current needs to be applied. With arc discharge method, individual CNTs of many hundred microns length could be produced. Metal oxide nanoparticles, fullerenes, graphene oxides, CNTs, and CNFs are synthesized by the arc discharge methods using alternating current (AC) or direct current (DC); however, DC imparts higher yields of CNTs especially for multiwalled CNTs which are deposited on the cathode. This method has only led to low production of single-walled nanotubes (SWNT). But large-scale SWNTs production can be carried out in electric arc discharge apparatus, where the arc is created in a reactor between two electrodes under helium atmosphere (660 mbar). The cathode and anode are both graphite rods with sizes 40 mm length × 16 mm diameter and 100 mm length × 6 mm diameter, respectively. In anode, a hole with size 40 mm length × 6 mm diameter is drilled and then filled with a mixture of graphite powder and metallic catalyst. The arc discharge is produced with a 100 A current; 30 V voltage drop between the electrodes is controlled with continuous translation of the anode by keeping fixed distance (~3 mm) between it and the cathode. The catalysts used in this method are some mixtures of Ni–Co, Co–Y, or Ni–Y in various atomic percentages; these are known to produce a chain of fascinating carbon nanostructures. The best results were obtained from the mixture of 4.2 at.% Ni and 1 at.% Y. Both single-shell and multi-shell CNTs are synthesized by arc discharge method where iron plays the role of catalyst. Here the evaporation chamber is replete with a mixture of gas consisting of methane gas and inert argon gas. A DC current of 200 A is passed through the electrodes. Single-shell tubes of 1 nm are formed in the gas phase whereas the multi-shell tubes grow on the surface of carbon cathode.

CNTs having very small diameters and a single atomic layer thickness can also be formed by cobalt and carbon vaporization in arc generators. These tubes form a web-like deposit and blend with fullerene-containing soot, which gives rubbery texture.

B, N-doped GQDs (B/N-GQDs) of 4–6 nm size can be synthesized by arc discharge process using graphite electrodes and chemical shearing in the atmosphere of hydrogen (H_2), diborane (B_2H_6), helium (He), and H_2, He, ammonia (NH_3) mixtures, respectively. Besides that, CQDs and CQDs–TiO_2 composite can be produced by direct current arc discharge between graphite electrodes of high purity. Here TiO_2 plays a vital role in enhancing the photolytic activity of CQDs and slowing down the electron–hole recombination rate. Under the catalysis of visible light, the prepared CQDs–TiO_2 composite shows stronger applicability than TiO_2 [1].

Laser ablation

Laser ablation is a procedure where solid materials can be removed from the surface of that solid material upon irradiation of a laser beam. Higher flux converts the materials into plasma, whereas in presence of lower flux the material evaporates or sublimes by absorbing heat energy. The advantages of this process are:

- It is simple.
- It is rapid.
- The end product has easily tunable surface properties.

The carbon target was prepared by hot-pressing a mixture of graphite powder and cement, followed by roasting, curing, and annealing in argon flow. For ablation, a Q-switched Nd:YAG laser (10 Hz, 1064 nm) was used, where water vapor carrying argon gas passes through the carbon target at 900°C and 75 kPa. As a result, aggregated carbon nanoparticles (CNPs) of different sizes are produced. As the sample does not exhibit any detectable photoluminescence, surface passivation of CQDs is done by attaching simple organic species such as amine-terminated polyethylene glycol (PEG_{1500N}) and poly(propionylethyleneimine-coethyleneimine)

(PPEI-EI). The surface passivation of carbon dots (CDs) with the help of organic moieties imparts bright luminescence emission [2,3]. Fluorescent CQDs can also be made with laser irradiation of a suspension of graphite power dispersed in three different organic solvents: diamine hydrate, diethanolamine, and PEG_{200N}. The surface properties of the CQDs could be revised by varying organic solvents in order to accomplish tunable light emission [4,5].

CQDs of visible and tunable photoluminescence can be prepared through laser ablation of nanocarbon particles of some common organic solvents such as ethanol, acetone, or water. Here the raw nanoparticles are smaller than 50 nm in average size and have a turbostratic structure. After ultrasonication, the suspension is dropped into a glass made cell which is coated with quartz for laser irradiation. An Nd:YAG pulsed laser consisting of a second harmonic wavelength (532 nm) is used to excite the suspension. After that the supernatant solution containing the CQDs is obtained by centrifuging the suspension. The nanostructure of carbon had changed to a kind of core–shell structure after laser irradiation [5,6]. The experimental setup is illustrated in Fig. 3.3.

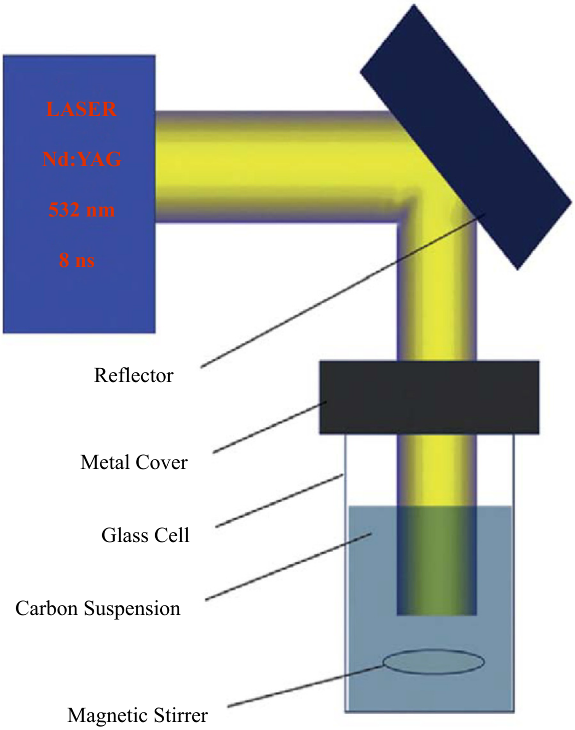

Figure 3.3 Schematic illustration of laser ablation experimental setup.
Source: Adapted from X. Li, H. Wang, Y. Shimizu, A. Pyatenko, K. Kawaguchi, N. Koshizaki. Chemical Communications, 47 (2011) 932–934.

Toluene also acts as a carbon precursor to make CDs by employing the unfocused laser irradiation approach in which the key step is further ablation of intermediate graphene. An Nd:YAG nonfocusing pulsed laser of 1064 nm wavelength was used to illuminate the liquid through a quartz window. Argon gas was used to protect the reaction and maintain a safe air pressure. In this approach, graphene is generated as an intermediate. By adjusting input laser intensity, controllable preparation of CQDs with discrete optical properties can be realized. Fig. 3.4 reveals a schematic illustration of a device which shows real-time supervision of the fluorescent change and provides a new approach for controllable synthesis of fluorescent nanomaterials [7,8].

But this process also has some disadvantages as follows:

- Low quantum yield.
- Surface modification is required.
- Size cannot be controlled.
- Energy consuming.

Plasma treatment

Plasma treatment is the process of refining the surface of various materials utilizing nonequilibrium gas plasmas. Nonequilibrium plasmas having depleted degrees of ionization, also known as low-temperature plasmas or cold plasmas, consist of free radicals, electronically excited atomic and molecular species, electrons, and ions. These hyperactive plasma species interact with material surfaces nonthermally. It may also be possible that these react with and bond with different substrate surfaces or associate together to produce a very thin layer of plasma and alter consequently the surface phenomenon. The plasma-treated nanotubes or nanoparticles with appropriate surface

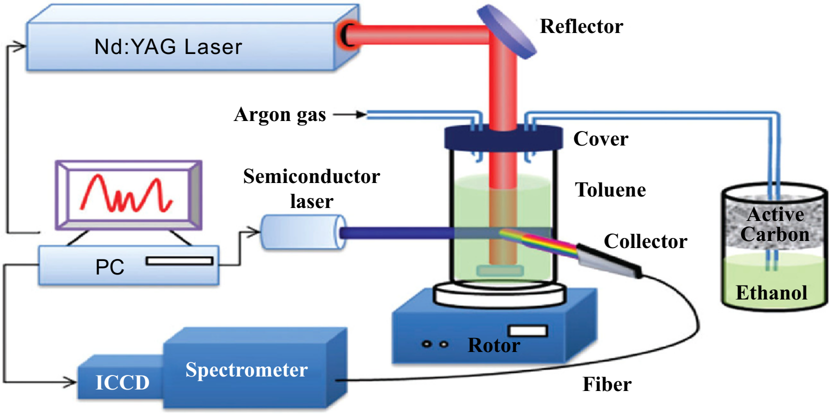

Figure 3.4 The schematic illustration of the experimental setup for controllable synthesis of fluorescent nanomaterials.

Source: Adapted from H. Yu, X. Li, X. Zeng, Y. Lu, Chemical Communications, 52 (2016) 819–822.

functionalities can make strong interaction with fluid molecules and thus disperse into the base liquid to create stable suspension. Those nonequilibrium plasmas, that is, low-temperature plasmas, which can be easily created by electrical discharges under reduced pressures (e.g., 10 mTorr–10 Torr), are composed of electronically excited atomic, molecular, ionic, and free radical species. Depending on the composition of gas or plasma chemistry, these hyperactive plasma species react with materials having a clean surface, link to different substrates, or associate to form a thin nanoscale layer of plasma coat and alter consequently the characteristics of the surface [9].

Oxygen plasma is helpful to selectively convert the topmost layer of multilayer samples. Oxygen plasmas generated at both microwave (MW) and radio frequency (RF) are used to treat CNTs. Strong spatially uniform PL can be succeeded in single-layer graphene on substrates by selective plasma oxidation (oxygen plasma treatment). Remarkably, bi- and multilayer flakes remain nonluminescent, while their elastic scattering spectra indicate the formation of sandwich-like structures containing unetched layers [5,10,11]. Briefly, samples of graphene which are formed by micro-cleavage of graphite on a silicon substrate are exposed to oxygen: argon (1:2) RF plasma (0.04 mbar, 10 W) for increasing time (1–6 seconds). The optical and structural changes were monitored by elastic light scattering and Raman spectroscopy [12,13].

CNPs can be synthesized from benzene and the surface passivation of these nanoparticles is done by grafting primary amine functional groups in one combined step in a plasma reactor having low power supply. The functionalization process is merged into the synthesis process by taking advantage of free radicals generated by a submerged arc helium atmosphere plasma to supply ethylenediamine directly after the plasma to functionalize the CNPs. The dispersibility of those CNPs in aqueous solution is dramatically improved compared to the CNPs solely synthesized from benzene [14].

3.2.1.2 Chemical methods

Electrochemical synthesis

This technique is one of the most acceptable top-down methods of producing CQDs with comparatively bigger carbonaceous materials such as graphene, graphite, carbon fiber, etc. The advantages of the electrochemical method are as follows:

- Ease of the process.
- Abundance of precursor materials.
- Potential for large-scale production.
- Cheap process.
- Greener synthetic protocol.

However, laborious purification processing of formed particles can be considered as a main disadvantage of this method.

Electrochemical synthesis is performed through oxidation–reduction reactions in electrolytic cells. Carbon nanocrystals (NCs), which give off strong blue luminescence, can be synthesized by electrochemical treatment of MWCNTs. The electrochemical preparation of carbon NCs is performed in a degassed acetonitrile solution with tetrabutylammonium perchlorate (TBAP) which acts as supporting electrolyte. MWCNTs used here are developed on carbon paper by chemical vapor deposition (CVD) method. In the electrochemical cell, a Pt wire acts as a counter electrode and an Ag/$AgClO_4$ wire acts as a reference electrode [5,15].

A cavity microelectrode (CME) is applicable for the synthesis of hybrid composites made of conducting polymer poly(N-methylpyrrole) and CNTs electrochemically. This electrode imparts proper nanometric coating of the polymer on the surface of CNT, without using any additive-like surfactant molecule. The CME helps to characterize the existence of the polymer covering on the CNT surface by the cyclic voltammetry (CV) method [16].

The single carbon source that can be used for the production of fluorescent CDs by one-pot electrochemical carbonization under basic conditions is alcohol having low molecular weight. Here two Pt sheets are used as the auxiliary working electrodes, and a calomel electrode kept on a Luggin capillary is used as the reference electrode. The electrolyte is NaOH/EtOH [17]. The electrochemical oxidation of alcohols in alkaline solution results in the formation of a large number of carbonium ions, alkoxy radicals, and hydroxyl free radicals [18,19]. CDs are produced by electrochemical oxidation and dehydration of ethanol at a suitable potential. The applied potential controls the size of the CDs. The higher the applied potential, the greater the number of alcohol molecules oxidized and free radicals and carbonium ions that might be produced to undergo crosslinking and dehydration to form CNPs, leading to larger CDs [17].

Chemical ablation/oxidation

Strong oxidizing acids such as hydrogen peroxide, nitric acid, and sulfuric acid carbonize small organic molecules to carbonaceous materials, which can be further cut into small sheets by controlled oxidation. Various types of carbon precursors can be used in this method which makes the method more facile and more accessible. But there are some drawbacks of this process such as:

- Harsh reaction conditions.
- Involving more than one step.
- Nanoparticle size is not retained.

The concentration-dependent CDs can be obtained by the reaction of coal pitch powder with the mixed solution of hydrogen peroxide (H_2O_2) and formic acid (HCOOH) without any heating. But this preparation process is very hazardous if heated due to the liberation of toxic gases. So the small crystalline carbons can be exfoliated from coal pitch with the mixture of H_2O_2 and HCOOH and then can be grown up by their assembly. In a typical experiment, the abovementioned compounds are mixed in an open flask by vigorous stirring, and then coal pitch powder of mild temperature is added to the mixed solution. Subsequently, the resultant muddy is stirred for 20 hours without any external heating. Then the unreacted powder is removed by centrifugation, and the suspension is obtained which contains CDs [7,20].

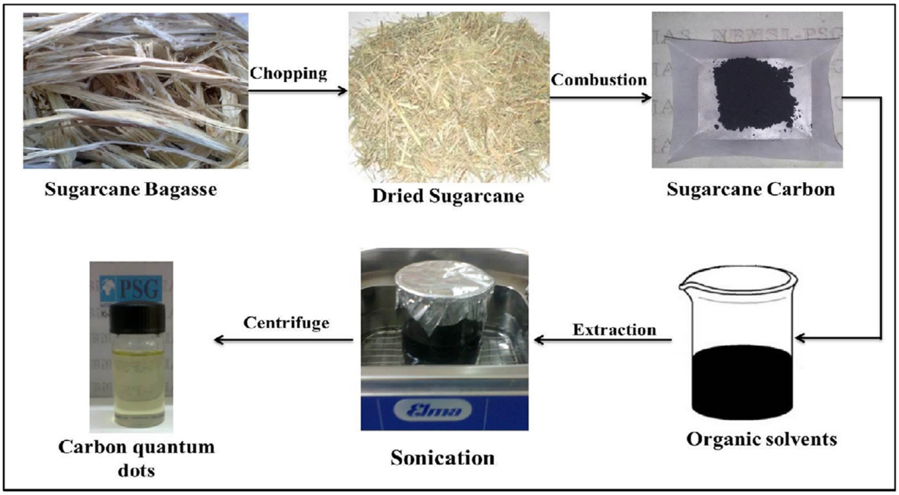

Figure 3.5 Schematic diagram of the synthesis of CQDs from sugarcane bagasse pulp. *Source*: Adapted from S. Thambiraj, D.R. Shankaran. Applied Surface Science, 390 (2016) 435–443.

Excitation-independent fluorescent CDs are also synthesized by the oxidation of carbon fibers (CFs) in nitric acid (HNO_3) under reflux condition followed by ultrafiltration. The photoluminescence properties of CDs are primarily determined by their size and amount of surface oxidation which can be modified by fluctuating temperature, reaction time, and nitric acid concentration [7,21].

Fluorescent CDs can be synthesized by chemical oxidation of sugarcane carbon followed by exfoliation. Sugarcane dry pulp is one of the vital solid wastes obtained from agriculture. It is useful as a natural source for mass production of carbon-based nanomaterials because it is plentiful, low priced, environment friendly. The sugarcane bagasse pulp is cut into tiny pieces and dried in sunlight for 6 days so that combustion of the pulp occurs at 60°C in the open atmosphere to form carbon. The yielded carbon is added to toluene and continuously stirred for one day at room temperature to achieve complete dispersion. Then, the ultrasonication of the dispersed carbon solution is done for 1 hour followed by centrifugation for 30 minutes at room temperature. After that the black precipitate is removed and the supernatant liquid is collected. Ethanol is added to dilute the supernatant liquid and the CDs are collected (Fig. 3.5) [22].

3.2.2 Bottom-up approach

Bottom-up approach is suitable for assembly and building short-ranged orders at nanoscale dimensions. Bottom-up or self-assembly nanofabrication methods use physical or chemical forces or forces which operate on the nanoscale to bring together the basic units to form bigger structures. Since the size of components during nanofabrication decreases, the bottom-up approach provides a major alternative to top-down technology.

3.2.2.1 Microwave-assisted method

CQDs can be prepared from organic compounds upon microwave irradiation which is a fast and cost-effective method. Fluorescent self-passivated CQDs can be formed by using PEG as both the carbon precursor and solvent in different atmospheres including O_2, CO_2, N_2, and air by microwave irradiation method (Fig. 3.6). Oxygen can be used in expediting the synthesis of CQDs from PEG and can significantly influence the properties of the CQDs using PEG as a single component precursor without passivation reagent. In the microwave-assisted formation of CQDs, PEG undergoes successive reactions, including dehydrogenation, polymerization, cyclization, and aromatization [23]. This process has a limitation in that the size of the synthesized nanoparticles cannot be controlled properly. But still, this method is one of the most convenient methods because of its rapidity, cost-effectiveness, sustainability, and scalability.

3.2.2.2 Hydrothermal method

CQDs can be synthesized by low-temperature hydrothermal carbonization which is easily achieved in the one-step green method using the cabbage as the natural carbon source. The surfaces of procured CQD are rich with a hydroxyl group (OH^-) as well as nitrogen and so no further modification is required [24]. The synthesis route is shown in Fig. 3.7. This process is very cheap, rapid, nontoxic, and eco-friendly. But the sizes of the QDs cannot be maintained thoroughly.

Highly green-fluorescent CDs are synthesized by one-step hydrothermal treatment of orange juice at comparatively low temperature (120°C) and in less time (150 minutes). The mechanism for the formation of CDs includes hydrothermal carbonization of the greater constituents of orange juice, mainly glucose, sucrose, fructose, ascorbic acid, and citric acid. The synthesis procedure has been illustrated in Fig. 3.8. The interesting part of this synthesis method is that neither strong acid nor postsynthetic surface passivation is required. The starting material can be obtained from a single

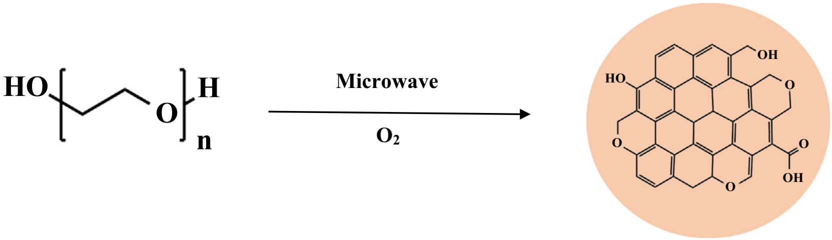

Figure 3.6 Microwave-assisted synthesis of CQDs from polyethylene glycol. *CQDs*, Carbon quatum dots.

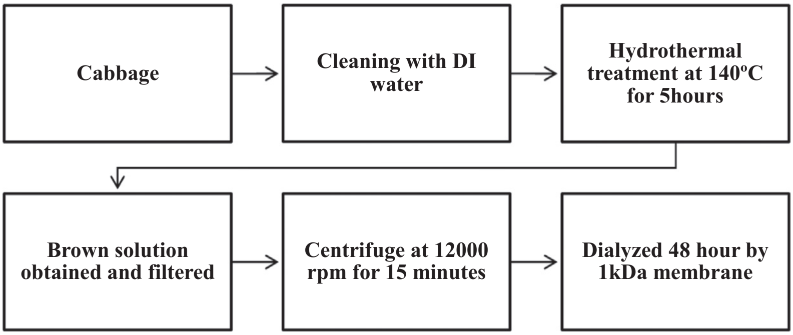
Cabbage
Cleaning with DI water
Hydrothermal treatment at 140°C for 5hours
Brown solution obtained and filtered
Centrifuge at 12000 rpm for 15 minutes
Dialyzed 48 hour by 1kDa membrane

Figure 3.7 Schematic presentation of the synthesis procedure of CQD using cabbage with the hydrothermal treatment. *CQDs*, Carbon quatum dots.

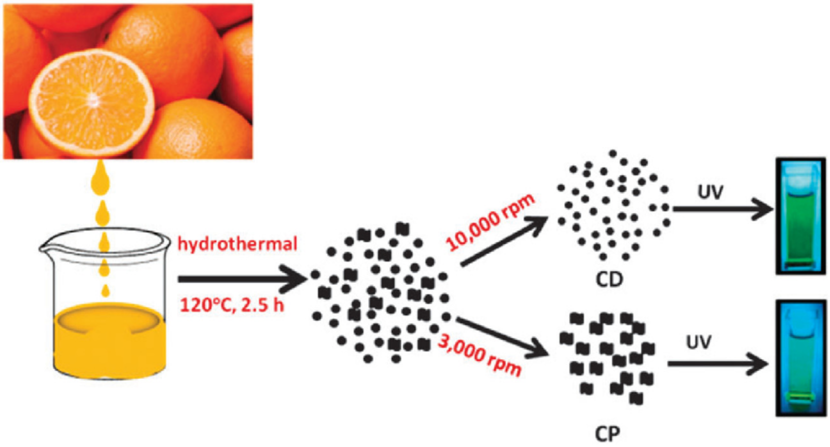
hydrothermal
120°C, 2.5 h
10,000 rpm
3,000 rpm
UV
CD
UV
CP

Figure 3.8 Illustration of formation of CDs from hydrothermal treatment of orange juice. *Source*: S. Sahu, B. Behera, T.K. Maiti, S. Mohapatra, Chemical Communications, 48 (2012) 8835–8837.

natural source and the synthesis method is cost-effective and green. As the synthesized CDs are functionalized with carboxylic acid, hydroxyl, carbonyl, and epoxy groups, they are highly water soluble without being chemically modified [24,25].

Besides orange juice, waste orange peels are also employed as a carbon source to synthesize fluorescent CDs. The orange peels are processed by the hydrothermal carbonization at a mild temperature (180°C). The carbonization process and functionalization process take place through the dehydration reaction of the orange peels, which results in the formation of fluorescent carbon particles with very small size (in nm range). The prepared hydrothermal CDs contain a large quantity of oxygen functional groups at their surface [26].

Similarly strawberry juice is treated hydrothermally in one step to synthesize fluorescent nitrogen-doped carbon nanoparticles (FNCNPs) with N_2 content of 6.88%. These FNCNPs are used for sensitive and selective detection of Hg^{2+} [27]. The hydrothermal approach of grass at 180°C also leads to the creation of photoluminescent, water-soluble, carbon-rich, nitrogen-doped, polymer nanodots which can detect Cu^{2+} from water samples [28].

3.2.2.3 Ultrasound-assisted method

The ultrasound-assisted approach for CQDs procurement exploits the ultrasonic wave of high energy to break carbon compounds into nanoparticles in the presence of alkali, acid, or oxidant, which is regarded as a novel technique of CQDs synthesis. The use of energetic ultrasonic waves bypasses the need for complex posttreatment processes, therefore realizing the effortless synthesis of CQDs with smaller sizes. Monodispersed water-soluble fluorescent CNPs are prepared directly from $C_6H_{12}O_6$ by a one-step ultrasonic treatment under acidic or alkaline conditions (Fig. 3.9). The hydroxyl groups available on the CNP surface make them water soluble [7,29]. Potato starch can play the role of carbon precursor to produce water-soluble CQDs via an acid-assisted ultrasonic route [30].

High-quality PEG-functionalized functional carbonaceous nanomaterials (FCNs) are synthesized via a dehydration reaction of cigarette ash and thiol group-containing PEG through a facile one-pot ultrasonic irradiation treatment [31]. The synthesis procedure is shown in Fig. 3.10.

Fluorescent nitrogen-doped CQDs (N-CQDs) can be produced from dopamine which undergoes ultrasonic treatment in presence of dimethylformamide for 8 hours. The CQDs exhibit water stability and dispersibility, bright fluorescence in different ionic strength and pH, high photostability, and low cytotoxicity [32].

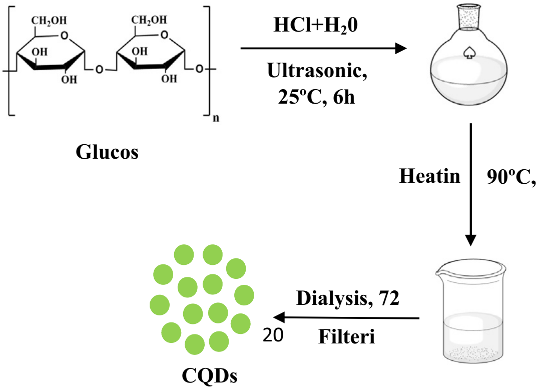

Figure 3.9 The synthesis illustration of the CQD. *CQDs*, Carbon quatum dots.

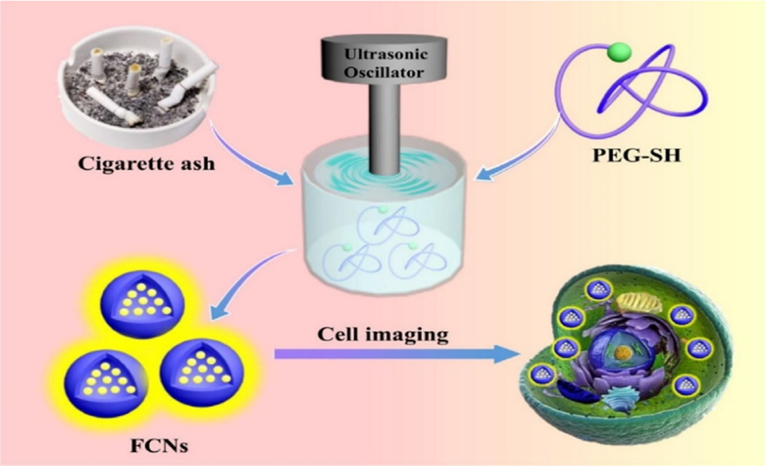

Figure 3.10 Schematic showing the preparation of PEG-functionalized FCNs.
Source: H. Huang, Y. Cui, M. Liu, J. Chen, Q. Wan, Y. Wen, et al., Journal of Colloid and Interface Science, 532 (2018) 767–773.

3.3 Conclusion

CQDs are such materials that can be efficiently synthesized and scalable in many ways. The chapter provide us with in-depth knowledge and help to elaborate chemistry of CQD synthesis that is required both in laboratory and industry. This is important as it provides improved quality of these materials, mainly focusing on the green chemistry aspect of it. The synthesis has been detailed in this chapter via both top-down and bottom-up approaches. In short, the readers will be satisfied in getting a thorough and detailed description of all the synthetic protocols and the fundamental chemistry behind each of the protocols.

References

[1] N. Biazar, R. Poursalehi, H. Delavari, AIP Conference Proceedings 1920 (2017) 020033. 2018.
[2] Y.-P. Sun, B. Zhou, Y. Lin, W. Wang, K.A.S. Fernando, P. Pathak, et al., Journal of the American Chemical Society 128 (2006) 7756–7757.
[3] Y. Wang, A. Hu, Journal of Materials Chemistry C 2 (2014) 6921–6939.
[4] S.-L. Hu, K.-Y. Niu, J. Sun, J. Yang, N.-Q. Zhao, X.-W. Du, Journal of Materials Chemistry 19 (2009) 484–488.
[5] H. Li, Z. Kang, Y. Liu, S.-T. Lee, Journal of Materials Chemistry 22 (2012) 24230–24253.
[6] X. Li, H. Wang, Y. Shimizu, A. Pyatenko, K. Kawaguchi, N. Koshizaki, Chemical Communications 47 (2011) 932–934.

[7] M. Pan, X. Xie, K. Liu, J. Yang, L. Hong, S. Wang, Nanomaterials 10 (2020) 930.
[8] H. Yu, X. Li, X. Zeng, Y. Lu, Chemical Communications 52 (2016) 819−822.
[9] Y.J. Kim, Q. Yu, H. Ma, Encyclopedia of Microfluidics and Nanofluidics, Springer, 2013, pp. 1−17.
[10] T. Gokus, R.R. Nair, A. Bonetti, M. Böhmler, A. Lombardo, K.S. Novoselov, et al., ACS Nano 3 (2009) 3963−3968.
[11] J. Shen, Y. Zhu, X. Yang, C. Li, Chemical Communications 48 (2012) 3686−3699.
[12] C. Casiraghi, A. Hartschuh, E. Lidorikis, H. Qian, H. Harutyunyan, T. Gokus, et al., Nano Letters 7 (2007) 2711−2717.
[13] A.C. Ferrari, J.C. Meyer, V. Scardaci, C. Casiraghi, M. Lazzeri, F. Mauri, et al., Physical Review Letters 97 (2006) 187401−187404.
[14] H. Jiang, F. Chen, M.G. Lagally, F.S. Denes, Langmuir: The ACS Journal of Surfaces and Colloids 26 (2010) 1991−1995.
[15] J. Zhou, C. Booker, R. Li, X. Zhou, T.-K. Sham, X. Sun, et al., Journal of the American Chemical Society 129 (2007) 744−745.
[16] M. Bozlar, F. Miomandre, J. Bai, Carbon 47 (2009) 80−84.
[17] J. Deng, Q. Lu, N. Mi, H. Li, M. Liu, M. Xu, et al., A European Journal 20 (2014) 4993−4999.
[18] G. Sundholm, Electroanalytical Chemistry and Interfacial Electrochemistry 31 (1971) 265−267.
[19] S.N. Raicheva, M.V. Christov, E.I. Sokolova, Electrochimica Acta 26 (1981) 1669−1676.
[20] X. Meng, Q. Chang, C. Xue, J. Yang, S. Hu, Chemical Communications 53 (2017) 3074−3077.
[21] L. Bao, C. Liu, Z.-L. Zhang, D.-W. Pang, Advanced Materials 27 (2015) 1663−1667.
[22] S. Thambiraj, D.R. Shankaran, Applied Surface Science 390 (2016) 435−443.
[23] Y. Zhao, S. Zuo, M. Miao, RSC Advances 7 (2017) 16637−16643.
[24] A.-M. Alam, B.-Y. Park, Z.K. Ghouri, M. Park, H.-Y. Kim, Green Chemistry 17 (2015) 3791−3797.
[25] S. Sahu, B. Behera, T.K. Maiti, S. Mohapatra, Chemical Communications 48 (2012) 8835−8837.
[26] A. Prasannan, T. Imae, Industrial & Engineering Chemistry Research 52 (2013) 15673−15678.
[27] H. Huang, J.-J. Lv, D.-L. Zhou, N. Bao, Y. Xu, A.-J. Wang, et al., RSC Advances 3 (2013) 21691−21696.
[28] S. Liu, J. Tian, L. Wang, Y. Zhang, X. Qin, Y. Luo, et al., Advanced Materials 24 (2012) 2037−2041.
[29] H. Li, X. He, Y. Liu, H. Huang, S. Lian, S.-T. Lee, et al., Carbon 49 (2011) 605−609.
[30] R. Qiang, S. Yang, K. Hou, J. Wang, New Journal of Chemistry 43 (2019) 10826−10833.
[31] H. Huang, Y. Cui, M. Liu, J. Chen, Q. Wan, Y. Wen, et al., Journal of Colloid and Interface Science 532 (2018) 767−773.
[32] M. Lu, L. Zhou, Materials Science and Engineering: C 101 (2019) 352−359.

Further reading

S. Dey, A. Govindaraj, K. Biswas, C.N.R. Rao, Chemical Physics Letters 595−596 (2014) 203−208.
Available from: https://www.britannica.com/technology/nanotechnology/Nanofabrication.

S. Iijima, T. Ichihashi, Nature 363 (1993) 603−605.
J.P. Raval, P. Joshi, D.R. Chejara, Applications of Nanocomposite Materials in Drug Delivery, Woodhead Publishing, 2018, pp. 203−216.
M.A. Virji, A.B. Stefaniak, Comprehensive Materials Processing 8 (2014) 103−125.
L. Yang, Nanotechnology-Enhanced Orthopedic, Woodhead Publishing, 2015, pp. 97−120.

Characterization and physical properties of carbon quantum dots

4

Sujatha D.[1,2], *Pardhasaradhi Nandigana*[1,2], *P. Sriram*[1,2] *and*
Subhendu K. Panda[1,2]
[1]CSIR—EMF Division, Central Electrochemical Research Institute, Karaikudi,
Tamil Nadu, India, [2]Academy of Scientific & Innovative Research (AcSIR), Ghaziabad,
Uttar Pradesh, India

4.1 Introduction

Carbon-based materials such as fullerenes (C60), carbon nanotubes (CNTs), carbon nanodots (CNDs), activated carbons, and graphene have constituted an emerging field in research for decades. In this chapter, various carbon allotropes are explored and these are shown in Fig. 4.1 [1]. Carbon quantum dots (CQDs) also belong to carbon family and these were discovered during the purification of single-walled carbon nanotubes in 2004 [2], which have zero dimension and diameter of around 1−10 nm in size. CQDs have their own optical, electrical, and mechanical properties and exhibit characteristic strong florescence. CQDs possess many physical properties such as nano size, high thermal and electrical conductivity, long-term fluorescence stability, and good thermal stability. CQDs also possess good water solubility, photobleaching resistance, and excellent photo and chemical stability, excellent biocompatibility, low toxicity, and magnetism [3−6]. Incorporation of appropriate functional groups and heteroatoms leads to desired tailored applicability. This chapter aims to present a comprehensive overview of physical properties of CQDs and their characterization. According to their nature of the cores, CQDs are classified into three types: graphene quantum dots (GQDs), polymer dots (PDs), and CNDs (Fig. 4.2) [7].

Carbon nanomaterials can be classified in several ways: dimensionality, that is., zero-dimensional (0D), one-dimensional (1D), and two-dimensional (2D) structures [1,8] (Table 4.1).

GQDs have a certain crystallinity due to the presence of a carbon core with an average lattice parameter of 0.24 nm corresponding to (100) spacing of single graphene dots on lacey support sheets. Out of the two types of CNDs, carbon nanoparticles do not show any crystal lattice whereas evident crystal lattice are present in CQDs. CQDs have a typical interlayer gap of 0.34 nm, which corresponds to crystalline graphite spacing of (002) [9]. PDs are cross-linked polymers formed by aggregation/assembly of linear nonconjugated polymers. PDs can also be formed by

Carbon Quantum Dots for Sustainable Energy and Optoelectronics. DOI: https://doi.org/10.1016/B978-0-323-90895-5.00007-2
© 2023 Elsevier Ltd. All rights reserved.

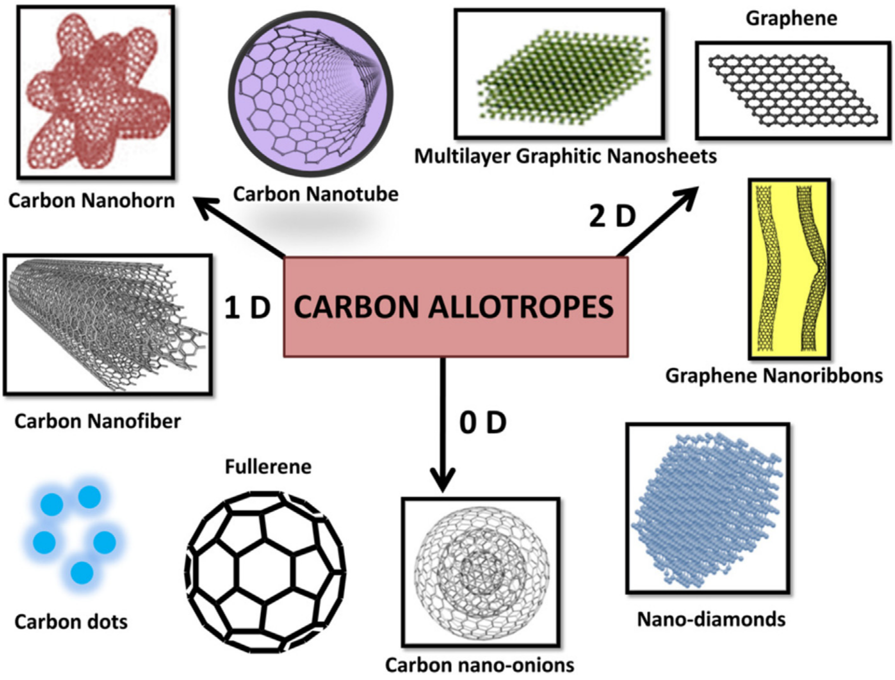
Carbon Nanohorn
Carbon Nanotube
Multilayer Graphitic Nanosheets
Graphene
2 D
1 D
CARBON ALLOTROPES
Graphene Nanoribbons
Carbon Nanofiber
0 D
Fullerene
Carbon dots
Carbon nano-onions
Nano-diamonds

Figure 4.1 Carbon materials classification as carbon allotropes [1].
Source: Adapted with permission from P. Karfa, S. De, K. C. Majhi, R. Madhuri, P. K. Sharma, Functionalization of carbon nanostructures, Comprehensive Nanoscience and Nanotechnology 1–5 (2019) 123–144, doi: 10.1016/B978-0-12-803581-8.11225-1.

Graphene quantum dots (GQDs)
Polymer dots (PDs)
Carbon Nano Dots (CNDs)

Figure 4.2 Classification of CQDs. *CQDs*, Carbon quantum dots.

the carbon core and grafted polymer chains. In all kind of carbon dots (CDs), there is the presence of modified chemical groups, such as oxygen-based, amino-based, polymer chains, and others on the surface which are interconnected [7].

4.1.1 Carbon quantum dots

CQDs are generally known for luminescence property and also exhibit tunable fluorescence emission which is significant for many new applications, such as electro-optical, bioimaging, photonic materials, energy harvesting, etc. Fig. 4.3 shows fluorescent nature according to the energy structure of CQDs. CQDs have a sp^2-hybridized carbon core with hydrogen atoms or functional groups such as $-NH_2$, $-OH$, $-COOH$, etc. in the shell layers [10]. Originally, CQDs were

Table 4.1 Classification of carbon allotropes structures [1,8].

Nanostructures	Structure
Fullerenes	C60 (0D) consists of 60 sp^2 carbon atoms arranged serially in hexagons and pentagons order to form a spherical structure
Carbon nanotubes (CNT)	Sp^3 hybridization (1D) wall or layered structure (SWCNT, double-walled carbon nano tubes, multi-walled carbon nano tubes)
Nanodiamonds	Complex structure with inner diamond core and outer amorphous carbon shell (0D)
Carbon nanodots	High degree of carbonization with no display of the crystalline or polymeric structures and quantum confinement effect
Graphene quantum dots	Anisotropic graphene fragments that are made up of single or multiple layers of graphene sheets that form graphene networks in their arrangement
Carbonized polymer dots	Carbon and aggregated polymer cross-linked nanohybrids having a central carbonized core encased by polymeric chains or functional groups
Carbon quantum dots (CQDs)	CQDs contain mixture of sp^3 and sp^2 carbon atoms (0D)

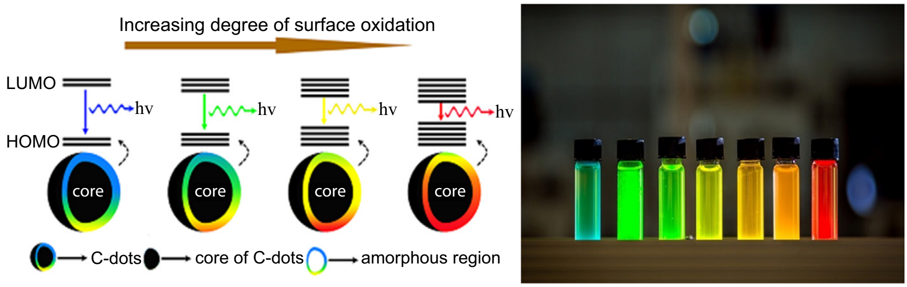

Figure 4.3 Fluorescent nature according to the energy structure of carbon quantum dots and next image shows fluorescence of carbon quantum dots from blue to red [12,13].
Source: Reproduced with permission from H. Ding, S. B. Yu, J. S. Wei, H. M. Xiong, Full-color light-emitting carbon dots with a surface-state-controlled luminescence mechanism, ACS Nano 10 (1) (2013) 484–491, doi: 10.1021/acsnano.5b05406; E. Feature, "Carbon Quantum Dots Found and Isolated from Egg Yolk Oil," Scientific Reports 7 (2017) 1–7, https://www.azoquantum.com/Article.aspx?ArticleID = 53.

prepared by the chemical functionalization and organic molecules which logically led as surface functionalized as small carbon nanoparticles [10]. Fig. 4.3. shows energy band structure interms of increasing surface oxidation level with respect to decreasing energy bandgap resulting in fluorescence obtained from blue-to-red region. According to Yuan et al., the direct bandgap imprints high-quality fluorescence CQDs [11].

CQDs are made up of nontoxic element carbon, and these are applicable for applications like biological imaging, solar cell, and manufacturing photonic device. CQDs are termed as "universe nanoparticles" and these carbon-based photophysical properties exhibit light emission. The photophysical characteristics of CQDs are improved by chemical and physical alterations, resulting in a revamp in a variety of applications. Such approaches provide structurally and compositionally well-defined pathway to synthesize CQDs [14]. According to research sources, high energy impact results in the formation of fluorescent CQDs, which is the result of a synthetic technique that involves the crystalline organization of carbon core fragments and surface functionalization of CQDs [15]. The unique photoluminescence (PL) properties of CQDs with core and surface states are shown in Fig. 4.4.

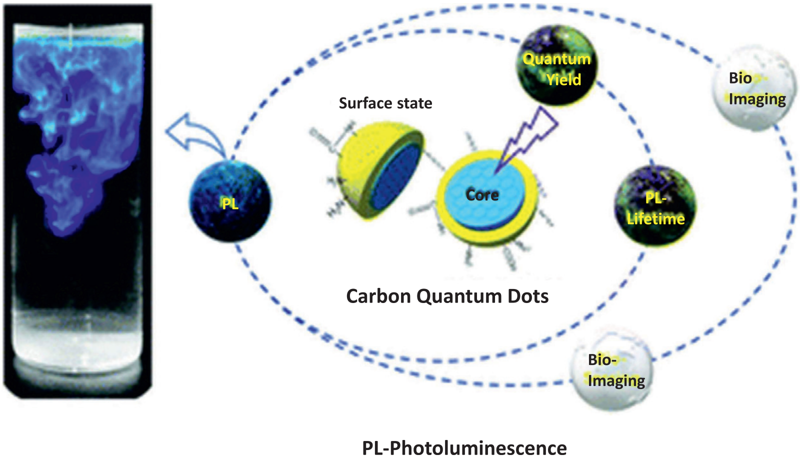

Figure 4.4 Structures and photoluminescence of CQDs and its lifetime. *CQDs*, Carbon quantum dots.
Source: Adapted with permission from K. J. Mintz, Y. Zhou, R. M. Leblanc, Recent development of carbon quantum dots regarding their optical properties, photoluminescence mechanism, and core structure, Nanoscale 11 (11) (2019) 4634–4652, doi: 10.1039/c8nr10059d.

Various analytical approaches are used to analyze CQDs and their physical characteristics by emphasizing their crystalline structure and the presence of functional units on their surface [7,15]. Various analytical approaches, including X-ray powder diffraction (XRD), high-resolution transmission electron microscopy (HRTEM), and Raman spectroscopy, etc., can be used to confirm CQDs. Fourier-transform infrared (FTIR), X-ray photoelectron spectroscopy (XPS), and elemental analysis EDAX can be used to assess the grafting of chemical groups [7]. The TEM of CQDs reveals essential details on particle shape, size distribution, and crystalline structure, whereas HRTEM reveals the core's periodicity, which reflects its crystalline nature. Raman spectroscopy can determine the structural characteristics of CQDs. XPS gives particular information on the atomic units on its surface, whereas FTIR reveals different functional units by capturing characteristic vibrational bands [4].

4.1.2 Structure of carbon quantum dots

As mentioned above, CQDs belong to the carbon family and have zero dimension with highly crystalline structures. In recent years, researchers have made chemical and physical changes to CQDs in order to improve their applications such as fluorescence, quantum yield (QY), and other physicochemical applications such as photo (electro) catalytic performances [12]. As per scientific records, shape of CQDs may be circular or elliptical; some possess quadrate, triangular, and hexagonal structures also which is confirmed by HRTEM, scanning electron microscopy (SEM), and XRD [16]. Here the chemical structure and electronic structure of the CQDs are discussed. Fig. 4.5 shows the generalized structure of CQDs with the common surface functional groups including carboxyl, hydroxyl, and amino groups exhibited in outermost shell and dopants like O, N, S, and others are present in the carbon structures.

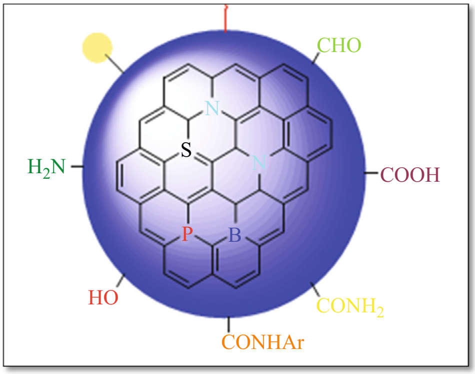

Figure 4.5 Generalized structure of carbon quantum dots.
Source: Reproduced with permission from B. Gayen, S. Palchoudhury, J. Chowdhury, Carbon dots: a mystic star in the world of nanoscience, Journal of Nanomaterials 2019 (2019), doi: 10.1155/2019/3451307.

4.1.2.1 Chemical and electronic structures of carbon quantum dots

The chemical structure of CQD is shown in Fig. 4.6. Unlike the graphene type sp^2 hybridization, diamond-like sp^3-hybridized carbon insertions are present in the CD nanoparticles. CQDs have surface functional groups and are amorphous and crystalline in form. Because the dots include graphene lattices, they resemble a single or layered graphene crystalline structure. Therefore, CDs can be viewed as a highly defected composition of coexisting aromatic and aliphatic regions [17].

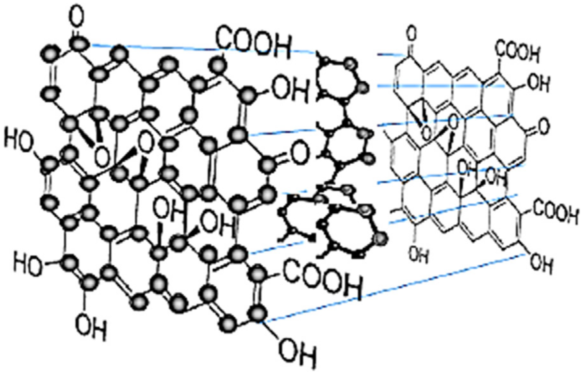

Figure 4.6 Schematic chemical structure of CQDs [18]. *CQDs*, Carbon quantum dots. *Source*: Adapted with permission from A. P. Demchenko, M. O. Dekaliuk, Novel fluorescent carbonic nanomaterials for sensing and imaging, Methods and Applications in Fluorescence 1 (4) (2013). doi: 10.1088/2050-6120/1/4/042001.

The molecular orbital hypothesis explains the electronic structure of CQDs, which commonly shows n→π* and π→π* transitions due to their easily accessible transition energies. In CQDs, the π state can be ascribed to the aromatic sp^2-hybridized carbon in their core and n state can be ascribed to functional groups containing electron lone pairs such as amides, amines, carbonyls, and thiols. When the number of aromatic rings increases, the energy gap between π states decreases gradually, just as in the case of π-conjugation in organic molecules. The electron transition from the n states of functional groups to the π* states of aromatic rings can occur through the bonding of the n→π* transition, which is feasible due to the electron lone pairs of the functional groups that are bound to aromatic sp^2-hybridized carbon [17].

4.1.3 Types

CQDs are majorly classified into two types: hydrophilic and hydrophobic (Fig. 4.7).

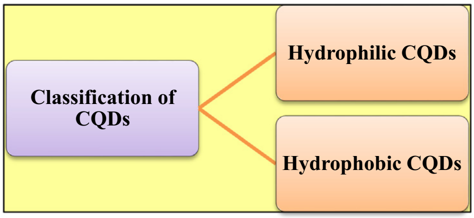

Figure 4.7 Scheme of classification of CQDs. *CQDs*, Carbon quantum dots.

4.1.3.1 Hydrophobic carbon quantum dots

Hydrophobic CQDs are prepared by using nonpolar solvents (organic solvents), containing carboxyl and carbonyl functional groups, using top-down approach. It generally consists of carbohydrate as carbon source with some nonpolar solvents like octadecylamine and octadecane. So, it helps to reduce bulk amount of carbon source in the CQDs [19]. It is simpler to integrate hydrophobic CQDs into diverse matrices for the production of multifunctional particles.

4.1.3.2 Hydrophilic carbon quantum dots

Hydrophilic CQDs are prepared from aqueous solutions using a bottom-up technique, which consists of functional groups like epoxy and hydroxyl on the basal planes or at surfaces. These hydrophilic CQDs are particularly soluble in water and other polar solvents, which distinguishes them from other carbon-based nanomaterials. Hydrophilic CQDs are also nontoxic and biocompatible. These CQDs have a high hydrophilicity due to the presence of different functional groups such as carbonyl, hydroxyl, epoxy, carboxylic acid, amino, and ether on the surface of sp^2-hybridized CQDs [9,20,21].

Again, CQDs can be classified into two types: undoped and doped.

Undoped carbon quantum dots

The regular CQDs contain carbon (C) with hydrogen (H) and oxygen (O) atoms and are mostly undoped with sp^2 and sp^3 configurations. The natural or synthesized precursors as carbon source for the preparation provide simple and easy form of CQDs with surface passivation. Surface passivation is the development of a thin layer of insulation to cover the outside surface of CQDs and it can be done by several synthesis techniques. Surface contaminants can be removed to improve their optical characteristics. According to the findings of the elemental analysis, pure CQDs included 55.57 wt.% carbon and 35.60 wt.% oxygen, whereas $NaBH_4$-reduced CQDs contained 56.80 wt.% carbon and 34.88 wt.% oxygen [22,23]. The absence and presence of fringe like structures for the dopants emphasize the undoped and doped CQDs respectively as shown in Fig. 4.8.

Doped carbon quantum dots

CQDs are doped and co-doped to improve their physical and optical characteristics. Heteroatom doping in CQDs improves the properties through lone pairs of electrons. Nonmetallic dopants, in particular, increase their QY by minimizing the energy gap between the orbital and the nonbonding (n) orbital of carbon, whereas metallic dopants change the band structure during the carbonization or dehydration process by chelating to functional groups. Functional groups including heteroatoms such as oxygen, nitrogen, sulfur, phosphorus, and boron may be present in some situations [6,10]. Fig. 4.9 depicts doping of various elements into the CQDs.

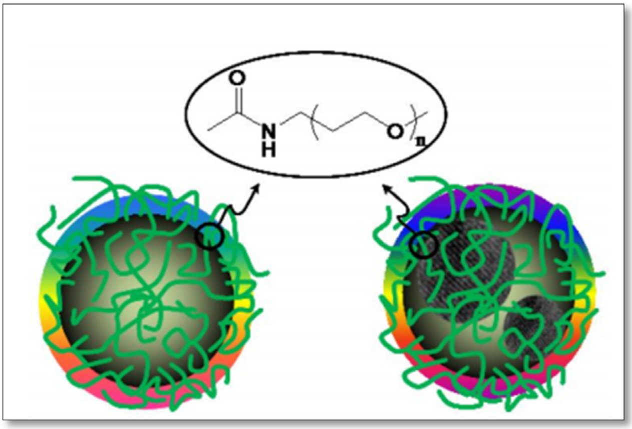

Figure 4.8 Illustration of undoped and doped CQDs [24]. *CQDs*, Carbon quantum dots. *Source*: Reproduced with permission from L. Cao et al., Competitive performance of carbon 'quantum' dots in optical bioimaging, Theranostics 2 (3) (2012) 295−301, doi: 10.7150/thno.3912.

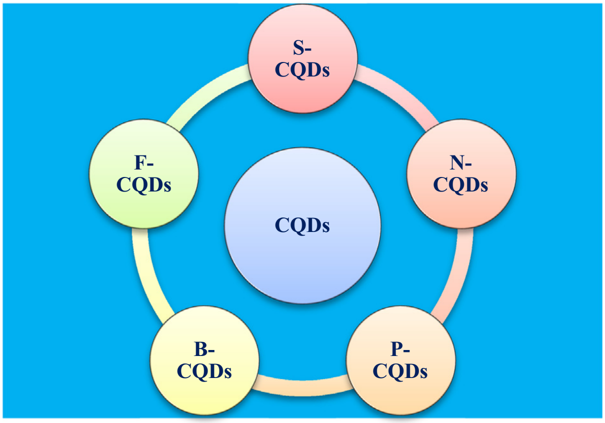

Figure 4.9 Schematic representation of various doped CQDs. *CQDs*, Carbon quantum dots.

4.2 Physical properties

The size-dependent physical properties such as absorbance, PL, magnetic behavior, melting and boiling point, particle size and morphology, density, tensile nature, conductivity, heat absorption, etc. of CQDs play a vital role in their different applications. These properties are mainly controlled by the synthesis procedure as both the carbon core and the surface passivation play critical role in controlling such parameters. CQDs are generally quasi-spherical in shape, and depending on the precursors and synthetic pathways utilized, they can be crystalline or amorphous carbon with a variety of adjustable surface groups [6]. TEM and SEM can be used to analyze the morphology, size distribution, and particle size of CQDs. If the particle size varies from 1 to 20 nm, SEM is used; however, if the measurement surpasses the resolution of SEM, TEM can provide greater resolving power [10]. CQDs uniform dispersion and spherical shape with its agglomeration are analyzed by TEM, and the lateral size distribution in particle size and lattice fringes may measure by HRTEM. The uniformity, 2D and 3D topographic structure can be observed by atomic force microscopy (AFM). The peak width decreases as the relative intensity of the XRD peak increases, indicating that CQDs carbonation and crystallinity are improving [25]. Thus, XRD technique provides a valuable information on the particle size, crystal structure, and purity of CQDs [21]. CQDs are primarily made up of carbon atoms, with oxygen, nitrogen, and maybe other dopants added depending on the elements present as well as reaction circumstances such as time and temperature. Depending on which materials are integrated into the carbon network and surface state, the actual structure of spherical CQDs might vary in complexity. Moreover, the parameters of the particle formation are determined directly by its various heating methods [23]. The chemical bonds and compositions of CQDs were revealed using the XPS and FTIR methods. XPS can identify the C, O, and N elements present in CQDs, while FTIR can see functional groups such as carbonyl, hydroxyl, carboxyl, amide, and amino groups on the surface of CQDs [25]. Mechanical qualities of CQDs include elongation at break, tensile strength, scratch hardness, toughness, flexibility, and impact resistance [26]. Elasticity (or flexibility) of CQDs was examined at several pH levels, including cycling between acidic and basic states, and CQDs were shown to be able to keep their structure and fluorescence ability when exposed to an excitation source [27]. CQDs have an aromatic carbonized structure that increases their strength, and their peripheral polar functional groups generate strong physiochemical interactions that boost their elasticity and toughness [26]. The surface-functionalized CQDs exhibit variable PL behavior in response to changes in their surroundings, allowing them to operate as sensors for monitoring changes in pH or temperature within and around the defined target. The sensitivity to pH was attributed to hydrogen bonding between the surrounding ions and the surface functional groups of CQDs [27]. The density of CQDs can be observed as 1.0032 g/mL. CQDs whose density may be greatly boosted by co-doped sulfur atoms provide important scientific insights into CQD fluorescence enhancement mechanisms [28]. CQDs possess high purity and good water solubility [29]. Many carboxyl moieties present on CQDs surface impart excellent solubility in water. Citric acid is an important organic acid with strong water solubility that is often employed as a carbon source to synthesize CQDs [29–31].

Generally, CQDs possess tunable emission fluorescence in 450–550 nm range. CQDs are chemically modified and have their surfaces passivated using a variety of organic, polymeric, inorganic, and biological materials. The fluorescence as well as the physical features of the surface were improved by this passivation. When aqueous solutions of N-CQDs are excited at 360 nm, CQDs show a bright luminescence centered at 450 nm [25]. CQDs exhibit ferromagnetism property, that is, CQDs have a substantial, positive susceptibility to an externally applied magnetic field, as well as a strong attraction to it and the ability to maintain their magnetic characteristics when the external field is withdrawn [26]. The magnetic result implies all the spins contribute to the magnetism, including those at the particle surface [26,32]. Fluorescent CQDs in aqueous media are mostly transparent in appearance and emit color under UV light. It is also observed that at elevated temperatures the CQD solutions turns to yellow color and on cooling to room temperature again it turns to transparent color [33,34]. CQDs possess good electrical conductivity and it is enhanced by doping with N, S, metals, and conducting polymers. The electrical conductivity and current density of the N-CQDs—graphene oxide (GO) hybrid catalyst is significantly improved due to the well-connected junctions of GO and N-CQDs, which allow electrons to be readily and swiftly transported. The edge-filled element dopant in the hybrid catalyst leads to a significant increase in electrical conductivity as well as large surface area when compared to standard Pt—C catalysts [34]. The electrical features of CQDs include a significant inherent dipole moment and huge bandgap. These can efficiently collect visible light energy, generate electron—hole pairs, rapidly separate electrons and holes, and minimize electronic loss, allowing them to quickly and effectively execute optically electrical impulses, and also electrical impulse transformation and transmission. These excellent electrical characteristics benefit logic gates, transistors, solar cells, ultrafast optical switches, quantum computing, etc. [35]. CQDs have excellent thermal stability and can withstand temperatures of up to 800°C, enabling for a wide range of applications in high-temperature conditions [36]. Javed et al. calculated thermal stability of CQDs up to 1000°C [37]. Furthermore, CQDs aromatic carbonaceous structure and peripheral polar hydroxyl groups cause substantial physiochemical interactions with the matrix, which improves heat stability [38]. The functionalities allow the surfaces of CQDs to take on either a hydrophilic or hydrophobic character, resulting in the required thermodynamic stability in various solvents [17]. CQDs show good ionic stability in a high ionic strength solution [30]. CQDs exhibit high chemical stability varied by physical and chemical modulations [31]. Mansuriya et al. highlighted the long-term chemical stability of CQDs owing to their ability to connect strongly with catalysts via electrostatic interactions [39].

4.2.1 Physiochemical properties (catalytic)

The conductivity of the CQDs mostly depends on the size, shape, heteroatom doping, and changes in surface functional groups which possess a large surface area and quick charge transfer phenomena. Hence it can be applicable for the photo (electro)catalytic applications. Organic groups facilitate water molecule adsorption and improve coordinating sites with metal ions, resulting in the formation of CQD-hybridized catalyst. CQDs may be employed as efficient confined electron acceptors in metal organic frameworks to isolate photogenerated carriers from core metallic nanoparticles, boosting their photocatalytic activity significantly [22]. The demand for clean, long-lasting energy has spawned a burgeoning branch of chemical study. Photocatalysts based on CQDs can be driven by sunlight to efficiently push forward the chemical processes required to degrade toxic organic dyes and pollutants into smaller, more ecologically friendly molecules, or to photosplit water to generate hydrogen for clean energy production [27] (Fig. 4.10) [40].

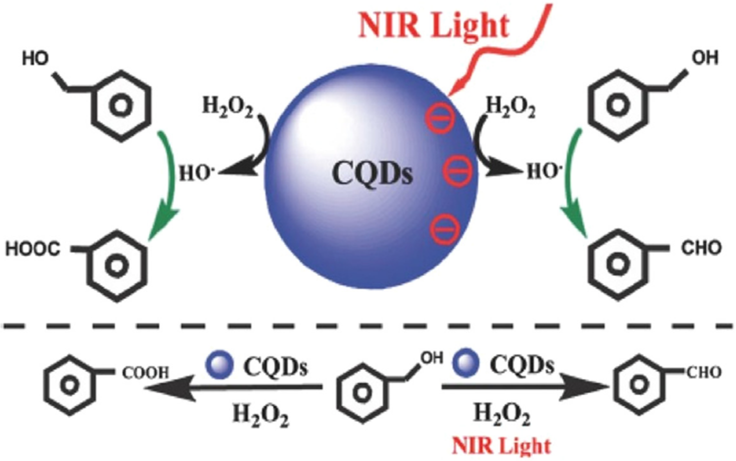

Figure 4.10 Photocatalytic mechanism of CQDs [40]. *CQDs*, Carbon quantum dots. *Source*: Reproduced with permission from Z. Zhang, T. Zheng, X. Li, J. Xu, H. Zeng, Progress of carbon quantum dots in photocatalysis applications, *Particle and particle systems characterization*, vol. 33, no. 8, Wiley-VCH Verlag, 2016, pp. 457–472, doi: 10.1002/ppsc.201500243.

Heteroatoms, such as N-CQDs, S-CQDs, and P-CQDs, play vital role by electronic structures in engineering field as well as act as reactive catalytic sites during the electrocatalytic process. This physiochemical reaction can be classified into three divisions as shown in Fig. 4.11A and Fig. 4.12.

Carbon-based materials, especially CQDs, have gained a great deal of interest in the fields of energy storage and conversion as a result of emerging environmental concerns. The functional groups (e.g., $-OH$, $-COOH$, $-NH_2$) on the surface of CQDs can be utilized as active centers for transition metal ions. Enhanced electron transport through internal interactions might increase the electrocatalytic efficiency of heteroatom-doped CQDs with several components. CQDs hybridized with other inorganic materials, such as metal sulfides, layered double hydroxides (LDHs), and metal phosphides, can be utilized as excellent electrocatalytic materials for oxygen reduction reaction (ORR), hydrogen evolution reaction (HER), oxygen evolution reaction (OER), and carbon dioxide reduction reaction (CO_2 RR) [41]. Mostly reported carbon-based materials usually respond to ORR, meanwhile doping CQDs with other binary/ternary metal endowed with transition metal dichalcogenides enhances their HER and OER activity. Figs. 4.10, 4.11B, and 4.12 show photocatalytic reactions, types of catalytic reactions, and various applications of composite CQDs, respectively.

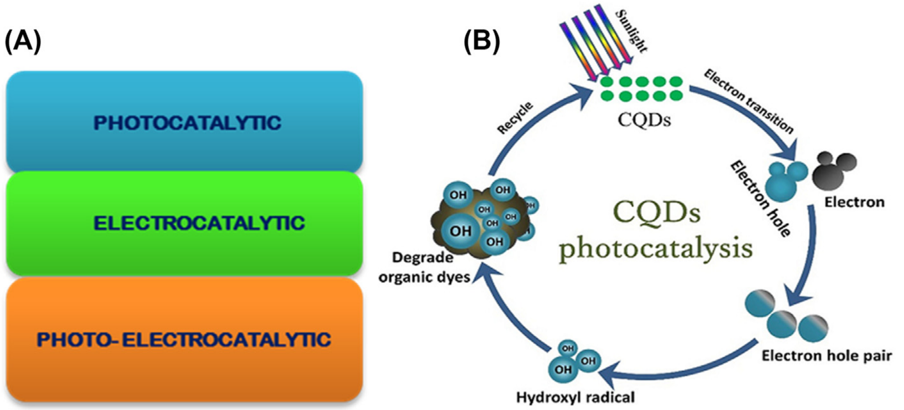
(A)
PHOTOCATALYTIC
ELECTROCATALYTIC
PHOTO-ELECTROCATALYTIC
(B)
Sunlight
CQDs
Electron transition
Electron hole
Electron
Electron hole pair
Hydroxyl radical
Degrade organic dyes
Recycle
CQDs photocatalysis
OH

Figure 4.11 (A) Different catalytic reactions of CQDs. (B) schematic illustration of the photocatalytic degradation of organic pollutants using CQDs as photocatalyst. *CQDs*, Carbon quantum dots.
Source: Reproduced with permission from U. Abd, L. Yong, C. Yin, E. Mahmoudi, A review of carbon quantum dots and their applications in wastewater treatment, Advances in Colloid and Interface Science 278 (2020) 102124, doi: 10.1016/j.cis.2020.102124.

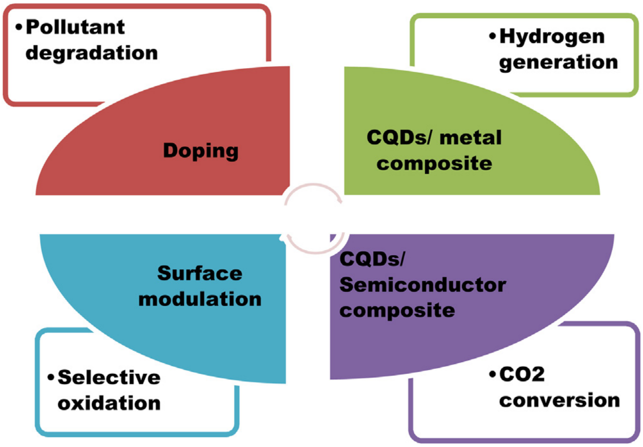
•Pollutant degradation
Doping
•Hydrogen generation
CQDs/ metal composite
Surface modulation
•Selective oxidation
CQDs/ Semiconductor composite
•CO2 conversion

Figure 4.12 Composite and hybrid structures of CQDs showing different applications. *CQDs*, Carbon quantum dots.

4.2.2 Optical properties

CQDs show some of the significant optical properties, such as absorption, PL, fluorescence, etc., which are mostly depend on their size and the surface properties. We can control the particle size, shape, and other parameters in different synthesis routes. Fig. 4.13A shows fluorescence of multicolor bandgap fluorescent CQDs

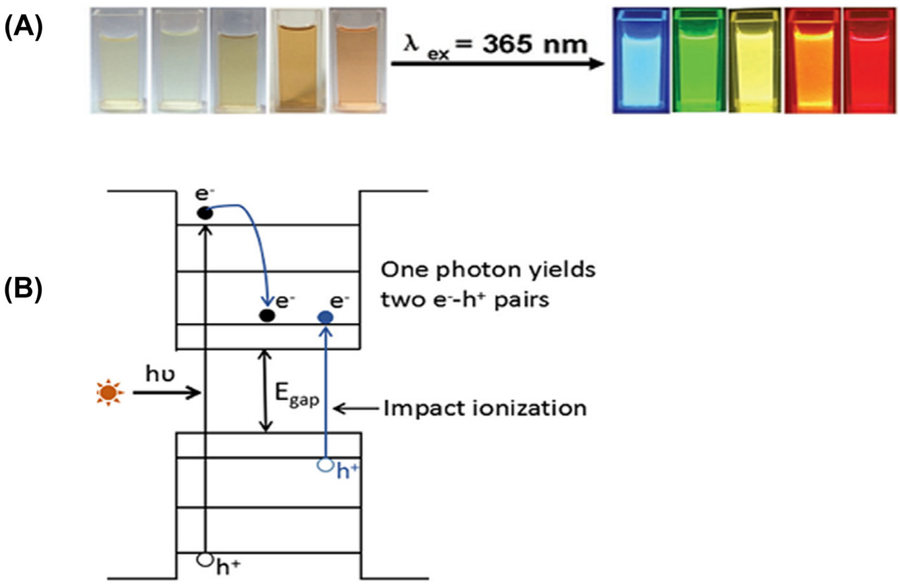

Figure 4.13 (A) Optical properties of MCBF-CQDs exhibiting various colors under UV light [43]. (B) Enhanced electron–hole pairs (excitons) multiplication in CQDs [44]. *CQDs*, Carbon quantum dots.
Source: From with permission (A) T. Yuan, et al., "Carbon quantum dots: an emerging material for optoelectronic applications," Journal of Materials Chemistry C 7 (23) (2019) 6820–6835, doi: 10.1039/c9tc01730e; (B) A. Luque, A. Martí, A. J. Nozik, "Solar Cells Based on Quantum Dots : Multiple Exciton Generation and Intermediate Bands," vol. 32, Cambridge University Press, 2007, pp. 236–241.

synthesized through hydrothermal method at different time periods that showed different colors from blue to red under UV light. Fig. 4.13B shows phenomena of enhanced electron–hole pairs. In further sections, we have elaborately explained optical properties such as absorption, PL, fluorescence, etc. (Fig. 4.14) [42].

4.2.2.1 Absorption

UV–visible spectrophotometer is generally used to measure the CQDs capacity to absorb light in the UV–visible region, with the highest absorption peak occurring at 230 nm and a tail beginning at ~300 nm that involves electron lone pairs. The absorption peak position can be influenced by oxygen in CQDs, and by doping [45]. CQDs possess optical absorption peaks caused by the n* transition of sp^2-conjugated carbon as well as the n- transition of hybridization in the UV–visible region. Heteroatoms such as N, S, and P hybridized might be accountable for the optical absorption peaks of CQDs, and optical absorbance is influenced by the surface passivation or modification procedure. CQDs can be produced as red, green, or blue luminous. These CQDs absorption transitions observed as redshifted, owing to the reduced form of electronic

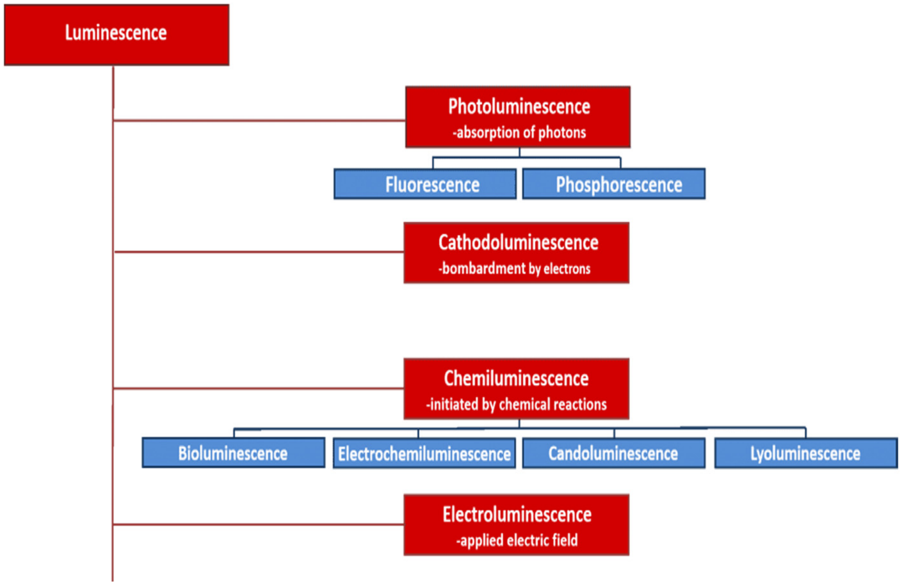
Luminescence
Photoluminescence
-absorption of photons
Fluorescence
Phosphorescence
Cathodoluminescence
-bombardment by electrons
Chemiluminescence
-initiated by chemical reactions
Bioluminescence
Electrochemiluminescence
Candoluminescence
Lyoluminescence
Electroluminescence
-applied electric field

Figure 4.14 Classification of luminescence and their energy sources.
Source: Edinburgh Instruments, Fluorescence, phosphorescence, photoluminescence differences. Photoluminescence Differences. 2012, [Online]. Available: https://www.edinst.com/blog/photoluminescence-differences/.

band gaps compared to others [46]. The absorption band was characteristic of an aromatic and it correlated to the p—p* transition of carbon bonds $C=C$, with faint peak at 310 nm owing to the p—p* transition of $C=O$ [47].

4.2.2.2 Photoluminescence

PL plays a vital role which can be manipulated by used precursors along with various synthesis methods. There are several reports on CQDs showing variety of PL wavelengths ranging from visible to near-infrared (NIR). CQDs have unique emission wavelength and intensity as distinctive properties, depending on the size and the surface functionality [17]. Mostly, the CQDs exhibit a wide and excitation-dependent PL emission spectrum that can be easily tuned by varying the concentration, where the PL strength of the CQDs increases at first and then decreases gradually as the concentration increases. The PL emission wavelength is mostly greater than that of the excitation wavelength [41]. Many researchers demonstrated that PL is strong when the size of the CQDs are well controlled as well as when CQDs are well passivated [48]. Fig. 4.15A illustrates the spectral response of CQDs with glucose/NaOH, whereas Fig. 4.15B depicts the spectral response of CQDs with glucose/HCl. Under UV and visible excitation, the respective visible emission of CQDs is across the blue-to-red range of wavelength [49].

Generally, PL can be further classified into two types: fluorescence and phosphorescence.

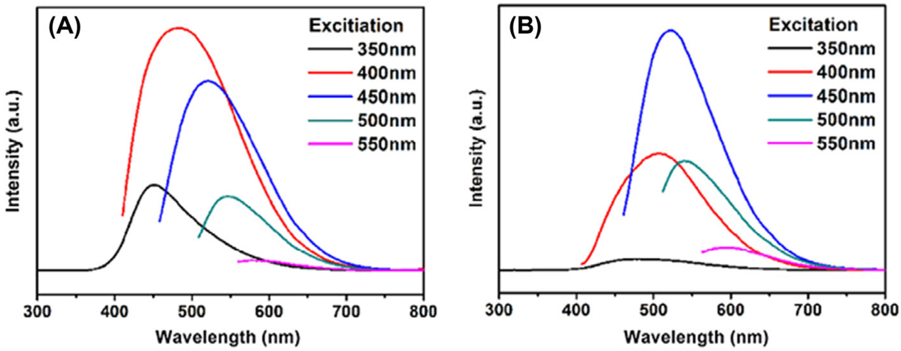

Figure 4.15 (A) CQDs prepared from glucose/NaOH, and (B) CQDs prepared from glucose/HCl [49]. *CQDs*, Carbon quantum dots.

Fluorescence

- Bandgap transitions attributed by conjugated p-domains.
- Surface defects.

Generally, p-domains rich in p-electrons which are involved in sp^2 hybridization are responsible for fluorescence in CQDs. The fluorescence mechanism caused by CQDs surface-related defects are based on the ratio of the surface to volume, that is, smaller sizes attribute to a large surface-to-volume ratio, which attribute to a greater number of surface defects that result in enhanced fluorescence. In another approach, by passivation of the surface functional groups −COOH and epoxy of the CQDs by −CONHR and −CNHR with alkylamines, the surface defect-related green emission disappears and the intrinsic blue emission is observed to be greatly enhanced [43]. Surface defects such as oxygen-containing functional groups, as well as sp^3- and sp^2-hybridized carbons, can act as excitons capture centers, resulting in surface-related defect state fluorescence. According to density-functional theory simulations, the carboxyl groups on the sp^2-hybridized carbons can cause considerable local distortions and minimize the energy gap. After the reduction of these oxygen-containing functional groups, the optical characteristics may be entirely altered, such as drastically different fluorescence emission bands and intensity distributions. Red-shift of fluorescence peak positions appear with the increase of the excitation wavelength [38].

Phosphorescence

CQDs have demonstrated the intriguing ultra-long lifetime and room temperature fluorescence. The researchers employed phosphoric acid in combination with ethanolamine or EDA and observed phosphorescence for up to 10 s. Mansuriya et al. measured the lifespan of CQDs phosphorescence using ethanolamine and EDA to be 1.46 and 1.39 s, respectively [39]. The phosphorescence was quenched in solution and only detected in the solid form and this was also ascribed to the phosphorous doping into the CQDs structure, which created the extended lifespan emission. The researchers also exhibited phosphorescence in CQDs without phosphorous doping; these CQDs phosphorescence were with a lifespan of 1045 ms (glucose, trihydrofluoride, and trimethylamine) and 747 ms (glucose, trihydrofluoride, and trimethylamine) (glucose and aspartic acid) [50]. Huang et al. also demonstrated the preparation of CQDs from citric acid and urea, then passivating them using cyanuric acid. Furthermore, in the phosphorescence of CQDs, hydrogen bonding plays a vital role [40]. Interestingly, CQDs displayed phosphorescence in an aqueous solution with a lifespan of 687 ms, which is significantly longer than the solid powder which is around 253 ms. Increased stiffness introduced by hydrogen bonding of water and cyanuric acid of CQDs increases the phosphorescence lifespan in the aqueous solution [51]. Lim et. al. reported that the synthesis of CQDs using folic and citric acids exhibited excellent phosphorescence lifespan of about 705 ms at pH 11.5 [52]. The phosphorescence was improved by increasing the conjugation of the electrons and de-protonating the carboxylic groups at a basic pH. The lifespan and QY of phosphorescence were considerably boosted as a result of this, in addition to the intraparticle hydrogen bonding [6]. Fig. 4.16 shows wavelength versus intensity plot for phosphorescence and fluorescence of CQDs.

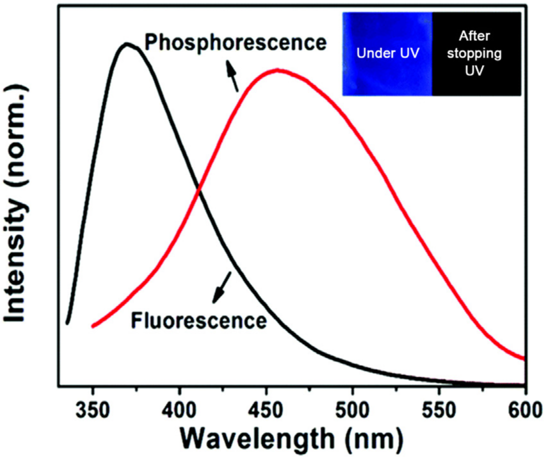

Figure 4.16 Phosphorescence of CQDs analyzed by wavelength versus intensity plot [50]. *CQDs*, Carbon quantum dots.

4.2.2.3 Electroluminescence

Because semiconductor nanocrystals are well known for exhibiting electroluminescence (EL), it is no surprise that CQDs have sparked a flurry of interest in EL research that might be useful in electrochemical domains. The emission color of CQD-based light-emitting diodes may be adjusted by the driving current. Under varying working voltages, watchable EL colors detected from the identical CQDs range from blue to white [53]. The researchers developed two theories based on the conjugated p-domain bandgap emission and the edge effect generated by another surface defect to better explain the luminescence mechanism of CQDs [25]. The quantum confinement effect (QCE) of p-conjugated electrons in the sp^2 atomic framework determines the EL properties of the fluorescence emission of CQDs from the conjugated p-domain, which may be changed by changing the size, shape, and edge configuration. Surface flaws such as sp^2 and sp^3-hybridized carbon, as well as other surface defects of CQDs, cause fluorescence emission, and even fluorescence intensity and peak position are connected to this defect [52,54].

4.2.2.4 Up-converted photoluminescence

In addition to traditional PL emission, in recent investigations, several CQDs have demonstrated up-converted PL (UCPL) emission. In contrast to regular PL, in UCPL the emission wavelength is shorter than the excitation wavelength. To explain such UCPL properties in CQDs, there are two kinds of mechanisms proposed by several researchers such as multiphoton active process and anti-Stokes PL. Researchers discovered that CQDs made by laser ablation had significant luminescence in the NIR (800 nm) with two-photon excitation, implying that they have UCPL characteristics [33]. In addition to their PL emission, Liu et al. analyzed that CQDs possess UCPL characteristics where the emission is in the range of 450–750 nm, where they are excited by a long-wavelength light from 700 to 1000 nm as shown in Fig. 4.17 [49]. The UCPL of CQDs can be attributed to the multiphoton activation process; this feature of CQDs can be used for a variety of applications, including in vivo bioimaging, because bioimaging at longer wavelengths is usually preferred due to improved photon tissue penetration and lower background auto fluorescence [17].

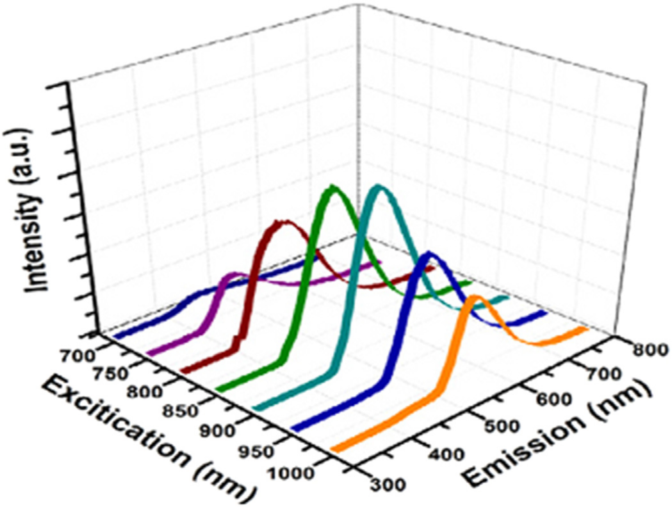

Figure 4.17 Up-converted photoluminescence (UCPL) spectra of CQDs at different excitation wavelengths. *CQDs*, Carbon quantum dots.
Source: Adapted with permission from H. Li, et al., One-step ultrasonic synthesis of water-soluble carbon nanoparticles with excellent photoluminescent properties, Carbon 49 (2) (2011) 605–609, doi: 10.1016/j.carbon.2010.10.004.

4.2.3 Photoinduced electron transfer

CQDs could be quenched efficiently by either electron acceptors or electron donors in the solution [46]. Despite the fact that this light-induced electron transfer property of CQDs has lately been extensively reported, direct evidence and the essence of photoinduced charge separation in CQDs have yet to be achieved. Through redox reactions, some indirect experimental proof was gained. PL decay experiments of CQDs using the known electron acceptor 2,4-dinitrotoluene (−0.9 V vs NHE) and electron donor N, N-diethylaniline corroborated this feature (DEA, 0.88 V vs NHE) [17]. Photoinduced electron transfer capabilities of CQDs offer up new possibilities for their possible applications. Irradiating a CQD solution with a noble metal (e.g., silver, gold, or platinum) salt causes the noble metal to form and deposit on the surface of the CQDs. Because the noble metal has a high electron affinity, it absorbs electrons from the connected CQDs, interrupting radiative recombination once more, resulting in the very effective static suppression of fluorescence emissions seen [17].

4.2.4 Biological properties

One of the most essential aspects of CQDs is their biocompatibility, which may be achieved in the field of bioimaging due to their low toxicity and luminous qualities in living systems. CQDs that are made by decomposing citric acid monohydrate and diethylene glycol bisphosphate have high fluorescence characteristics and minimal cytoxicity during imaging (3-aminopropyl) [52]. These CQDs are considered as important for their application in cell labeling and imaging. Herein, we investigate the cytotoxicity of CQDs at the diverse time and concentrations [55]. The biocompatibility of CQDs, along with the wide range of surface functionalization methods, has opened up new possibilities for gene delivery. CQDs perform better than organic dyes because of their reduced cytotoxicity [26]. Metal-sensing capabilities of CQDs have been demonstrated with improved selectivity and sensitivity. Diagnostics is another major use of CQDs in biomedicine, and semiconductive quantum dots have been employed for in vivo disease diagnosis [16]. Bioimaging of HeLa cells is shown in Fig. 4.18.

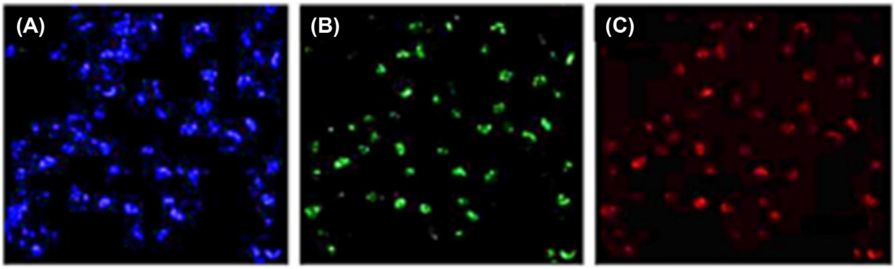

Figure 4.18 Bioimaging of HeLa cells. (A) Excitation at 405 nm causes blue emission. (B) Excitation at 458 nm produces green emission. (C) Excitation at 514 nm causes red emission. *Source*: Adapted with permission from B. D. Mansuriya, Z. Altintas, Carbon dots: classification, properties, synthesis, characterization, and applications in health care-an updated review (2018−2021), Nanomaterials 11 (2021) 10, doi: 10.3390/nano11102525.

4.3 Characterization

4.3.1 Structural characterization

Structure analysis and characterization focuses on contribution of significant components such as crystal structure, structural parameters, and position of the functional groups as these have important effects on the characteristics and properties of the material. These are generally known to be structure–activity or structure–property. In other words, these are collectively termed as structural characterization techniques—namely, XRD, SEM, TEM, Raman, XPS, FTIR, AFM, UV–vis, etc.

4.3.1.1 X-ray powder diffraction

XRD is an efficient analytical approach for determining material's crystal structure, unit cell size, crystal spacing, and phase identification. CQDs are both amorphous and crystalline in nature which can be confirmed by XRD results; this may depend on the synthesis procedure. Zhang et al. reported the XRD pattern of CQDs shows the diffraction peak at 20.5° of 2θ reflecting the crystalline graphitic structure (Fig. 4.19A) [56]. Monte et al. reported low intense diffraction peak centered at 20°

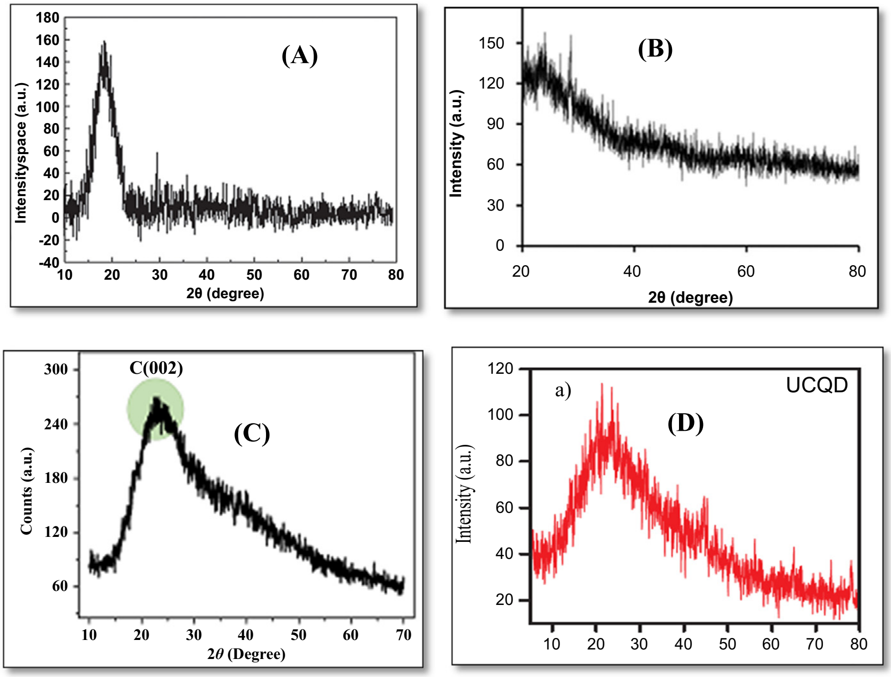

Figure 4.19 (A) XRD pattern of crystalline CQDs [56], (B) XRD pattern of amorphous CQDs [57], (C) shows high degree of C (002) plane for the partial graphitic and the amorphous nature of N-CQDs [58]. (D) XRD pattern of UCQD [45]. *CQDs*, Carbon quantum dots.

of 2θ which corresponds to amorphous carbon phase (Fig. 4.19B) [57]. Xiao et al. successfully synthesized N-CQD characterized by using XRD which exhibits the broad peak centered at 2θ = 24°. For the partly graphitic and amorphous character of N-CQDs, this spectrum is attributed to disordered high degree of carbon plane (002) (Fig. 4.19C) [58]. In XRD pattern for undoped CQDs, as shown in the Fig. 4.19D, the diffraction peak is observed at 2θ = 22.4° reflecting to amorphous nature [45].

4.3.1.2 Scanning electron microscope

An SEM gives information about surface morphology, granular orientation, crystallographic information, and chemical composition of CQDs. The morphology of CQDs clearly shows spherical and spongy nature and the size of about 50–60 nm, as shown in Fig. 4.20A [47]. Also Fig. 4.20B shows SEM image of M-CQDs around 100 nm [51]. The surface morphology of the CQDs cannot be obtained at higher magnifications in the SEM, hence we can go for the TEM as it gives good surface morphology and further crystal information.

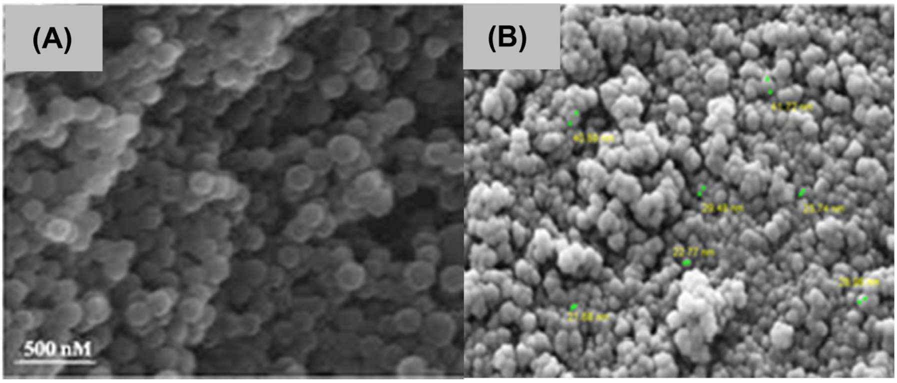

Figure 4.20 SEM images of (A) CQDs [47] and (B) M-CQDs [51]. *CQDs*, Carbon quantum dots.

4.3.1.3 Transmission electron microscope

TEM is a technique where a beam of electrons is transmitted through an ultrathin specimen. These electrons are interacting with the atoms in the material which gives magnified and focused image onto an imaging device which can be detected by a sensor or a camera. The principal approach for visualizing CQDs is TEM, which provides crucial information on particle shape, size distribution, and crystalline structure. Thambiraj et al. observed HRTEM by adding a drop of CQDs solution in copper grid and coating it. After the grid dried thoroughly, it was investigated using energy-dispersive X-ray spectroscopy (EDS) with a 200 kV acceleration voltage [59]. Because TEM has a high resolution of 0.1 to 0.2 nm, it may be utilized to determine the ultrastructure of CQDs [60]. TEM indicates that the CQDs are near spherical in shape and uniformly distributed, which are in range between 2.4 and 4.7 nm in diameter [61]. In determination of crystallinity, two types of lattice fringes are used, that is, in-plane lattice spacing and interlayer spacing, respectively. According to Zou et al., interlayer spacing typically focused at around 0.34 nm, while in-plane lattice spacing focused at 0.24 nm [62]. Thambhiraja et al. claimed that the HRTEM image obviously indicates that the CQDs are smaller in size, approximately spherical in form, and monodispersed, with particle size distributions examined. The author observed CQDs that have a graphite-like structure and produce 87.18 wt.% high purity carbon [59]. Fig. 4.21A shows the TEM image of CQDs are spherical and monodisperse, and the particle size of the CQDs is 2.5 ± 0.5 nm, and Fig. 4.21B shows particle size of CQDs corresponding to the (102) crystal planes of sp^2 graphitic carbon. Fig. 4.21C shows selected area electron diffraction (SAED) pattern of CQDs.

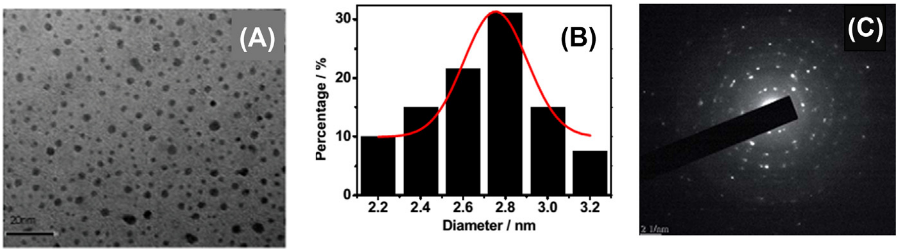

Figure 4.21 (A) TEM image of CQDs, (B) histogram of size distribution [56], and (C) SAED pattern CQDs. *CQDs*, Carbon quantum dots.
Source: Adapted with permission from B. De, B. Voit, N. Karak, Carbon dot reduced Cu2O nanohybrid/hyperbranched epoxy nanocomposite: mechanical, thermal and photocatalytic activity, RSC Advance 4 (102) (2014) 58453–58459, doi: 10.1039/c4ra11120f.

Precisely, crystal size and crystalline nature of CQDs can be studied by using SAED pattern. As reported by Chen et al., bright spots in the SAED pattern of the TEM analysis indicate the presence of CQDs and determine the type of CQDs as amorphous or poor crystalline [63].

4.3.1.4 Raman spectroscopy

Raman scattering is used as very basic analytical tool for detecting CQD formation. A standard Raman spectrum has two peaks, one for the D band and the other for the G band. The D band is about 1350/cm and is attributed to disordered sp^2 carbons, whereas the G band is about 1600/cm and is attributed to crystalline graphite carbons in-plane E_{2g} stretching vibration mode [15]. The ratio of the D and G intensities of the characteristic Raman bands can be utilized to examine structural characteristics such as crystallinity and the relative concentration of core over surface carbon atoms [15]. Wang et al. demonstrated two predominant peaks at 1340 and 1590/cm attributed to the disordered D and crystalline G bands as shown in Fig. 4.22A and intensity ratio of

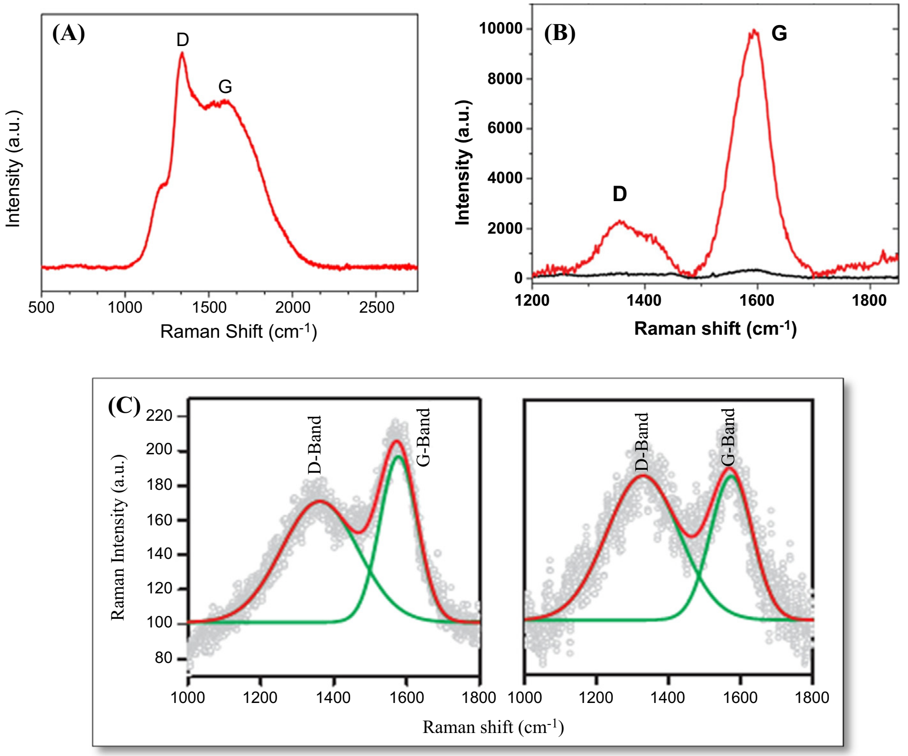

Figure 4.22 (A) Raman spectroscopy of CQDs peak at 1340 and 1590/cm. (B) CQDs show graphitic nature. (C) UCQDs and N-CQDs. *CQDs*, Carbon quantum dots.
Source: Adapted with permission from Refs. (A) [3]; (B) [65]; (C) [45].

the D-band and G-band (I_D/I_G) of the CQDs was about 1.3, indicating a large amount of amorphous nature in CQDs [3]. Kumar et al. analyzed that the occurrence of pristine CQDs is indicated by the strong and intense Raman peak of the G-band observed at 1578/cm in comparison to the weak peak of the D-band at 1331/cm, and the ratio of intensities of ID/IG was determined to be 0.59, confirming the CQDs purity [64]. Yongsheng and his coworkers explained CQDs through Raman peak G-band at 1590/cm and weaker D-band peaks around 1357 and 1418/cm shown in Fig. 4.22B and concluded CQDs are predominantly graphitic based on G peak strength [65].

Ramar and co-authors proved that Raman spectroscopy is a nondestructive procedure for detecting and evaluating nanostructures that is rapid, precise, and powerful. The authors recorded Raman spectra for UCQDs and N-CQDs using a Lorentzian fit, and computed an I_D/I_G intensity ratio of 0.86, which indicates the cleanliness of the UCQDs and is inversely related to the common size of the sp^2 crystalline region. At the same time, N-CQDs are extremely sensitive to strain effects in the sp^2 system, with an I_D/I_G intensity ratio of 0.854, which is nearly identical to that of UCQDs (see Fig. 4.22), D and G band of UCQDs and N-CQDs [45].

4.3.1.5 X-ray photoelectron spectroscopy

XPS gives information of particular atomic units on surface of CQDs. With monochromatized Al Ka radiation, the spectral analysis reveals unique nitrogen-, oxygen-, and carbon-bonded units shown on the CQDs surface [66]. XPS is a technique for analyzing primarily C and O components, with minimal N and S element XPS can be used to determine the chemical structure and content of CQDs, according to Wang et al. The XPS survey spectra of CQDs showed three typical strong peaks at 284.7, 399.4, and 531.9 eV, which were commonly assigned to C1s, N1s, and O1s, respectively, showing that CQDs largely comprised C (73.18%), N (7.23%), and O (19.59%) elements, as shown in Fig. 4.23A. Four peaks occurred at 284.3, 285.1, 286.4, and 288.4 eV in the C1s spectra (Fig. 4.23B), originating from the sp_2 C−C/C = C, C−N, C−O, C = O groups, respectively [67]. The N1s band of CQDs (Fig. 4.23C) may be deconvoluted into two peaks at 399.4 and 400.9 eV, which correspond to the pyrrolic N and amine groups, respectively. The primary component of N-CQDs was pyrrolic N, which produced through the dehydrolysis reaction

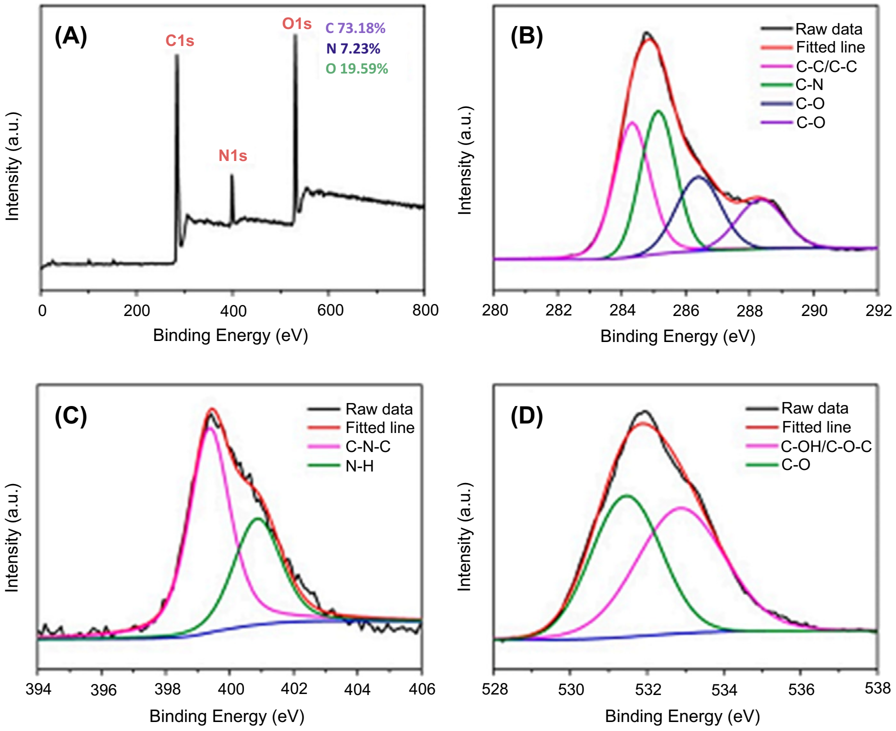

Figure 4.23 XPS spectrum of CQDs, (A) XPS full-survey spectrum of CQDs, (B) high-resolution XPS spectrum for C1s, (C) N1s and (D) O1s. *CQDs*, Carbon quantum dots. *Source*: Adapted with permission from X. Wang, et al., Green preparation of fluorescent carbon quantum dots from cyanobacteria for biological imaging, Polymers (Basel) 11 (2019) 4, doi: 10.3390/polym11040616.

between carboxyl and amine groups. Previous reports have proposed that the pyrrolic N is likely to improve electronic cloud density of CQD surfaces, resulting in an enhancement in luminescence efficiency [68]. In the O1s spectra (Fig. 4.23D), the peaks at 531.5 and 532.9 eV are assigned to the binding energies of $C=O$ and $C-O$, respectively [69]. Dong et al. experimented with NSCQDs and observed the high-resolution scan of the C1s region gives information that C was present in various chemical environments. By using their experiments, concluding s^2p XPS peaks occurred at 163.4 and 164.6 eV, nearer to the $s^2p^{2/3}$ and $s^2p^{1/3}$ positions for their spin-orbit couplings [24]. Thus, the creation of doping N and S in NSCQDs as well as amide N on the surface of NSCQDs were clearly indicated by C1s, O1s, N1s, and s^2p XPS spectra, which both considerably contributed to the fluorescence increase of NSCQDs. As a result of these findings, carboxyl and hydroxyl groups were most likely generated on the surface of NSCQDs [70]. Overall, the resultant CQDs contained multiple O- and N-related functional groups that paves the way for their excellent water solubility and fluorescence emission [3].

4.3.1.6 Fourier-transform Infrared

FTIR spectroscopy is used to investigate the chemical bonding, surface functional groups, and structure of CQDs. The spectra of the CQDs were measured in the wavenumber ranging from 400 to 4000/cm. Meiqin et al. investigated CQDs and found oxygen functionalities peaks at 3450 (OH stretching vibrations), 2927/cm, 1407/cm (CH stretching vibrations), 1726/cm ($C=O$ stretching vibrations), and 1639/cm ($C=C$ stretching vibrations) as shown in Fig. 4.24A [71]. Fig. 4.24B

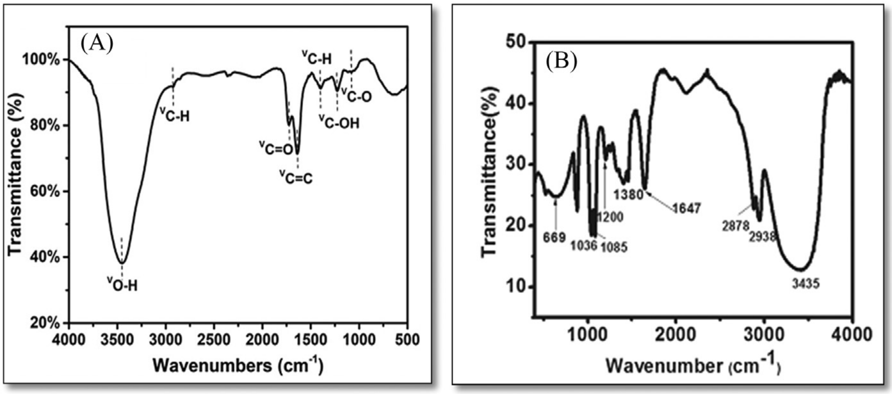

Figure 4.24 (A and B) FTIR spectrum of CQDs [72,73]. *CQDs*, Carbon quantum dots. *Source*: Adapted with permission from M. He, J. Zhang, H. Wang, Y. Kong, Y. Xiao, W. Xu, Material and optical properties of fluorescent carbon quantum dots fabricated from lemon juice via hydrothermal reaction, Nanoscale Research Letters 13 (2018), doi: 10.1186/s11671-018-2581-7; A. F. Shaikh, M. S. Tamboli, R. H. Patil, A. Bhan, J. D. Ambekar, B. B. Kale, Bioinspired carbon quantum dots: an antibiofilm agents, Journal of Nanoscience and Nanotechnology 19(4) (2018) 2339–2345, doi: 10.1166/jnn.2019.16537.

shows that broad peak around 3435/cm is due to hydrogen bonding that can be concluded that there is existence of hydroxyl groups on the surface of the CQDs. Also, the peaks at 1085 and 1046/cm contribute to the asymmetric and symmetric stretching vibration of C−O−C, and the peak around 669−900/cm attributed to the aromatic out of plane of C−H bending [29].

4.3.1.7 Atomic force microscopy

AFM used to identify topographic height in 2D and 3D structures [29]. Thambiraj et al. studied the surface topography of the CQDs which are decorated on the UV-treated silicon wafer. CQDs have average sizes of 3−5 nm and a surface roughness of less than 5 nm, in a counting scale. The CQDs' histogram exhibited an average roughness of 4.2 nm [61]. The height profiles display that the typical topographic height difference of the N-CQDs approached 2 nm, as illustrated in Fig. 4.25, reveals the small spherical morphology of the N-CQDs [19].

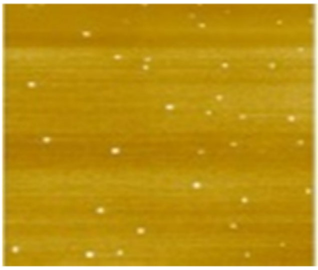

Figure 4.25 AFM images of N-CQDs. *CQDs*, Carbon quantum dots.
Source: Adapted with permission from L. Cao, et al., Competitive performance of carbon 'quantum' dots in optical bioimaging, Theranostics 2(3) (2012) 295−301, doi: 10.7150/thno.3912.

4.3.1.8 UV−vis spectra

UV−visible spectra frequently show apparent optical absorption in the UV−visible region; the CQDs exhibits absorption spectra of around 260−323 nm. Surface passivation of CQDs with various compounds leads to a shift in absorbance to longer wavelength according to the findings. The optimal emission wavelength red shifts as particle size increases [52].

Fig. 4.26A shows UV absorption spectra of N-CQDs. As shown in the figure, the absorption peak around 249 nm due to the $\pi \rightarrow \pi^*$ electronic transition of aromatic C − C bonds and another peak occur around 355 nm from the $n \rightarrow \pi^*$ electronic transitions of the C = C and C − N bonds, ascribed due to the N heteroatoms induced resulted in the formation of excited defect surface states [34,58]. Four typical sizes of CQDs by white and UV light are shown in Fig. 4.26B. CQDs' radiated colors are bright and vivid enough to be seen with the naked eye [68]. At 360 nm,

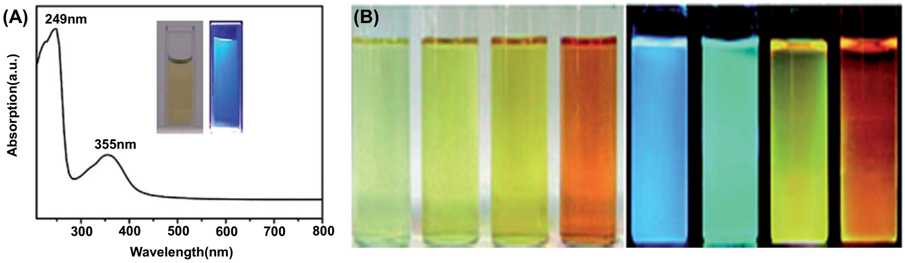

Figure 4.26 (A) The UV−vis absorption spectra of N-CQDs in aqueous solution are shown: (B) white (left; ordinary lamp; hues are pale green, pale yellow, yellow, and red, respectively) and UV light illuminate four common sizes of CQDs (right; 365 nm; from left to right the colors are blue, green, yellow, and red, respectively) [33,66]. *CQDs*, Carbon quantum dots.

CQD has a significant UV−visible absorption peak [62]. Two peaks at 200 and 420 nm are obtained in N-CQDs [51].

4.3.2 Photophysical analysis

Excitation-dependent PL, also known as excitation-dependent fluorescence emission, is perhaps the most remarkable attribute of CQDs. Typical excitation-dependent luminescence spectra are shown, along with the accompanying colors. The multicolor features of CQDs are highlighted by their wide spectrum range and relatively high emission peak intensities. Indeed, one of the distinctive aspects of CQDs is that the emission color can be changed according to the excitation wavelength, which has implications in a variety of applications.

4.3.2.1 Photoluminescence

PL is size-dependent optical absorption, which is one of the most interesting aspects of CQDs. It is one of the remarkable characteristics of CQDs that depends on emission wavelength and intensity, as different emissive traps exist at the surface of CQD [67].

Ding et al. claimed that changing the emissive trap sites on identical particles of the same size has a greater impact on the excitation wavelength of CQDs PL. The QCE theory applicable for the PL of CQDs [12]. When the size of a material is smaller than the Bohr excitons radius and within the same order of magnitude as the de Broglie wavelength of the electron, QCE occurs, resulting in a discrete size-dependent energy bandgap between the valence and conduction bands [68]. As a result of the absorption of a photon, one electron from the valence band's HOMO is promoted to the conduction band LUMO, resulting in fluorescence, which blue shifts with decreasing particle size. Zhou et al. showed that the fluorescence of oxidized CQDs was size dependent, with both excitation and emission spectra showing a red shift when CQDs molecular weight increases [6]. Another study clarifies the visible PL of GQDs of various shapes and sizes and confirms the size and shape dependence of PL. The PL emission red-shifted as the size of GQDs increases. Furthermore, maximal absorption occurred at longer wavelengths within the same size range, and intensity declined as GQD size increased. The edge states of CQDs were also governed by their shape with increasing armchair edges appearing as the size climbed above 17 nm, at which time overall shape shifted from circular to polygonal. As a result, the emission intensity as the size of the particle grew larger than 17 nm. Fig. 4.27A shows the PL emission spectrum of CQDs stimulated from 245 to 395 nm, Fig. 4.27B shows PL decay lifetime profile of the CQDs as excitation wavelength at 337 nm and emission wavelength at 437 nm, and Fig. 4.27C shows corresponding PL emission spectra of the eight samples, with peaks at 440, 458, 517, 553, 566, 580, 594, and 625 nm. Another potential explanation for PL is that it is caused by the presence of surface energy traps on surface imperfections

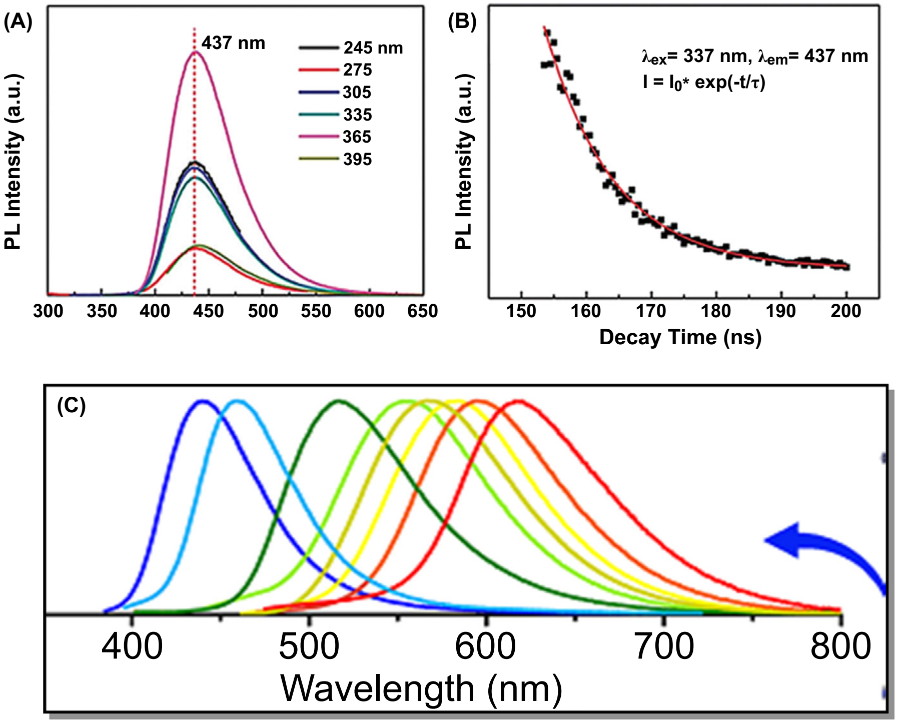

Figure 4.27 (A) PL emission spectrum of CQDs excited between 245 and 395 nm. (B) PL decay lifetime profile of CQDs. (C) The eight samples PL emission spectra, with maxima at 440, 458, 517, 553, 566, 580, 594, and 625 nm. *CQDs*, Carbon quantum dots.
Source: Adapted with permission from H. Ding, S. B. Yu, J. S. Wei, H. M. Xiong, Full-color light-emitting carbon dots with a surface-state-controlled luminescence mechanism, ACS Nano, 1 0(1) (2016) 484–491. doi: 10.1021/acsnano.5b05406; V. A. Online, et al., Nitrogen-doped, carbon-rich, highly photoluminescent carbon dots from ammonium citrate †, Nanoscale 6 (2014) 1890–1895, doi: 10.1039/c3nr05380f.

caused by the passivation process. Furthermore, the optical behavior of CQDs may be determined by the dispersion of various emissive sites on the optical characteristics of the produced CQDs solution in pH 6.9 phosphate buffer as analyzed by Xu et al.

4.3.2.2 Fluorescence

As shown in Fig. 4.28A, the position of the emission peaks varies from 428 to 510 nm as the excitation wavelength increases from 330 to 470 nm, and the fluorescence intensity increases to a maximum and then gradually falls. It means that the CQDs are affected by the wavelength of stimulation. The highest emission peak is redshifted because the CQDs have the general properties of quantum dots, such as size effects, point defects, edge effects, and so on [66]. The maximum excitation wavelength and the maximum fluorescence wavelength of N-CQDs are 350 and 445 nm, respectively. Such excitation wavelength-dependent emission character is derived from the π*→n electronic transitions of the surface-attached C = C and C$-$NH$_2$ bonds, which indicates that the fluorescence band can be tuned by adjusting the excitation wavelength without changing CQDs size. Fig. 4.28D$-$G shows the

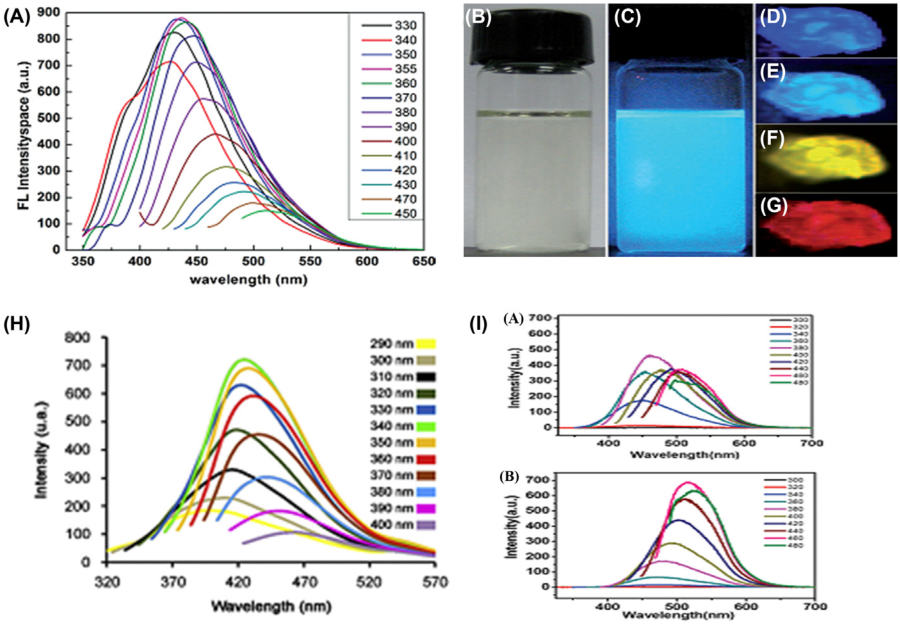

Figure 4.28 (A) Fluorescence spectrum of CQDs at different excitation wavelength and (B, C) represents the CQDs under normal light and under excitation at 365 nm. (D$-$G) The CQD images captured with a fluorescent microscope at several excitation wavelengths 360, 390, 470, and 540 nm, respectively. (H) The variation in the emission peak positions by varying the excitation wavelength, and (I-A and B) fluorescence emission of CQDs observed in water and ethanol respectively. *CQDs*, Carbon quantum dots.
Source: Adapted with permission from Refs. [57,58,66,67].

fluorescent microscope images of CQDs under excitations at 360, 390, 470 and 540 nm, respectively. Fig. 4.28I,A and B shows the fluorescence of CQDs under different excitation wavelengths in water and ethanol as solvents, respectively. From the figures it can be observed that for both the solvents the peak intensity increases with increase in the excitation wavelength. For aqueous system, the peak intensity reaches the maximum at 380 nm whereas increases upto 460 nm in ethanol solvent. The peak intensity for the same CQDs in ethanol as solvent shows higher values as compared to the water-dispersed CQDs. N-CQDs have an average fluorescence lifespan of 15.0 ns, which is close to the maximum value [71]. N-CQDs have a higher QY than 80%, since N-CQDs are stable over a pH range (4−11), high ion strength (2 M KCl), and 4 h of continuous UV light irradiation, making them ideal for preservation and transit. Dry N-CQDs powder can be redispersed in water multiple times without aggregating in solution, and no significant changes in fluorescence spectra are detected. N-CQDs that have an extremely long fluorescence lifespan, a high QY, and outstanding stability can be used in a variety of biomedical applications.

4.3.2.3 Forster resonance energy transfer

The fluorescence phenomena of Forster resonance energy transfer (FRET) have shown in CQDs. FRET is a nonradiative energy transfer between two fluorophores that are physically near to each other (fluorescence donor and acceptor). As a result, the approach is beneficial in determining the structural characteristics of materials, particularly biological molecules. FRET has been used to detect changes in intramolecular distances caused by protein folding processes by embedding the donor and acceptor molecules within the lipid bilayer framework. In a lipid bilayer system, containing hydrophobic CQDs that can serve as energy donors to two different acceptor molecules, each excited at a different wavelength. In some cases, the CQDs could also serve as a FRET acceptor for the donor molecules. Fig. 4.29 demonstrates the feasibility of FRET interaction of CQDs with riboflavin for determining the concentration of the organic molecule. From Fig. 4.29A it can be seen that there is a good overlap of the absorbance spectrum of the riboflavin with the emission spectrum of the CQDs excited at 380 nm. This overlap is essential for the FRET interaction between the two entities, where the CQD serves as the donor and the riboflavin acts as the acceptor. As shown in Fig. 4.29B when the riboflavin concentration is increased gradually, the emission intensity of CQDs at 440 nm gradually decreased, whereas the riboflavin peak at 520 nm increased gradually, demonstrating the FRET interaction between the two. As the FRET efficiency is depending on the concentration of the riboflavin molecules and the excitation wavelength of the CQDs, the FRET process efficiency can be calculated by $E_{FRET} = [(F_0\text{-}F)/F_0] \times 100$ (where F and F_0 represent the fluorescence intensity at 440 nm of CQDs in presence and absence of the riboflavin, respectively). The calculated FRET efficiency is plotted and explained in Fig. 4.29C. FRET has also been used to monitor membrane remodeling. CQDs have a wide range of excitation/emission wavelengths and can act as both donors and acceptors in FRET investigations. These characteristics construct a single CQDs species that can function as an energy donor to a variety of acceptors by simply changing the excitation wavelength [71].

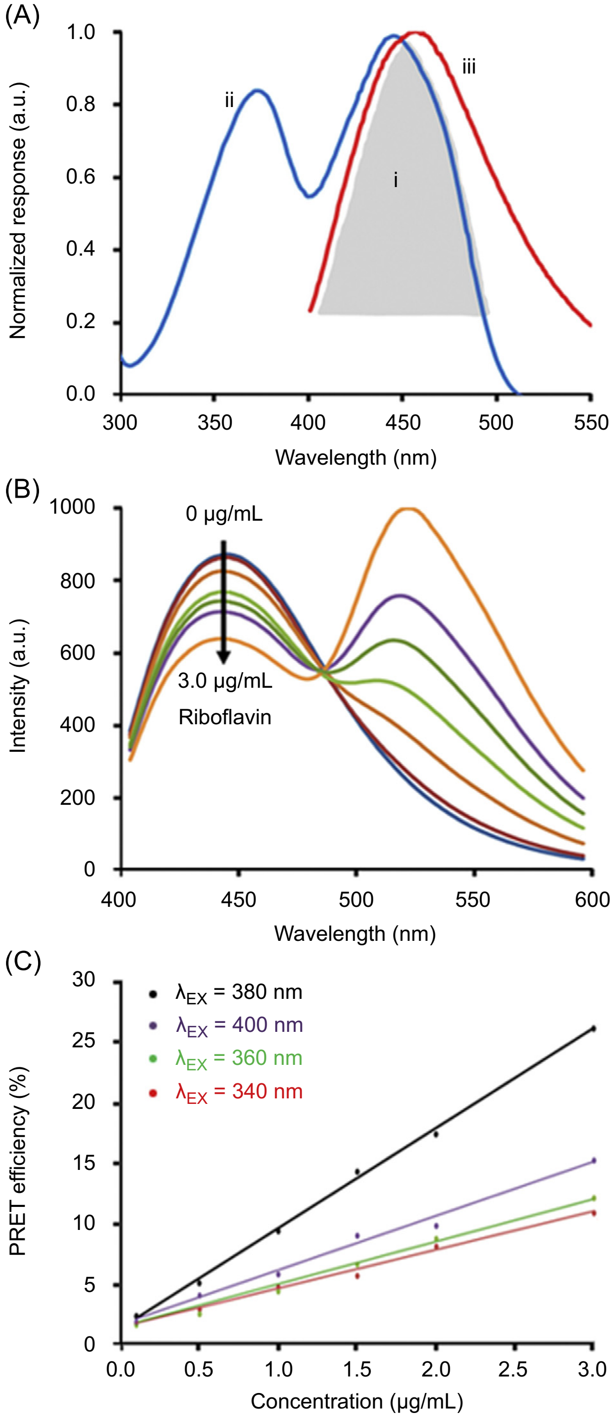
(A)
Normalized response (a.u.)
1.0
0.8
0.6
0.4
0.2
0.0
ii
i
iii
300
350
400
450
500
550
Wavelength (nm)
(B)
Intensity (a.u.)
1000
800
600
400
200
0
0 μg/mL
3.0 μg/mL
Riboflavin
400
450
500
550
600
Wavelength (nm)
(C)
PRET efficiency (%)
30
25
20
15
10
5
0
λ_{EX} = 380 nm
λ_{EX} = 400 nm
λ_{EX} = 360 nm
λ_{EX} = 340 nm
0.0
0.5
1.0
1.5
2.0
2.5
3.0
Concentration (μg/mL)

(*Continued*)

4.3.3 Stability of carbon quantum dots

The influence of UV light irradiation on acidic or basic and ionic strength conditions of the PL intensity was explored due to the necessity of fluorescence stability for CQDs. CQDs are exposed to UV light (365 nm) for 60 min after being manufactured and the results show that the PL intensity displayed low fluctuation with exposure time. Furthermore, with the pH increasing from 4 to 10, there was no significant change in the PL intensity, in both acidic and neutral environments; the intensity of the radiated light remained unchanged as the pH value increased [71]. Another similar study has reported that the fluorescence stability of CQDs remains unchanged after 30 days which indicate that the CQDs can be used for various applications without reducing their reactivity and effectiveness [29]. Mostly scientists experimented when the NaCl concentration reached 0.1 M; these findings were in line with prior research on the properties of CDs. The results of the foregoing investigations show that CQDs have a high degree of stability, and their outstanding fluorescence is ideal for biological imaging applications [67].

4.4 Conclusions

CQDs have high fluorescence, tunable excitation-dependent PL activity, and excellent photostability across a wide pH range due to their unique physical, chemical, optical, and electrical properties. Confined size, shape, surface functional groups, and doping on CQDs determine and provide the tunability to the physical and chemical properties of the CQDs, which in turn provide remarkable electrochemical, photophysical, electroluminescence, high hardness, good density, and solubility features. There are so many characterization techniques used to study various physical and chemical properties of the CQDs such as XRD for crystallinity, SEM and TEM for morphology, and the surface functionality by FTIR spectroscopy, Raman spectroscopy, and XPS. CQDs have strong, inert, and stable luminous characteristics that might be useful in optoelectronics and bioimaging applications.

Figure 4.29 (A) The integral overlap region (i), the riboflavin absorption (ii), and the CDs emission spectra (iii). (B) Fluorescence spectra of CDs in the presence of different amounts of riboflavin, lex¼ 380 nm. (C) The efficiency of the FRET process as a function of the riboflavin concentration with the excitation wavelength of the CDs/riboflavin varying from 340 to 400 nm.

Source: Adapted with permission from S. S. Monte-Filho, S. I. E. Andrade, M. B. Lima, M. C. U. Araujo, Synthesis of highly fluorescent carbon dots from lemon and onion juices for determination of riboflavin in multivitamin/mineral supplements, Journal of Pharmaceutical Analysis 9 (3) (2019) 209–216, doi: 10.1016/j.jpha.2019.02.003.

References

[1] P. Karfa, S. De, K.C. Majhi, R. Madhuri, P.K. Sharma, Functionalization of carbon nanostructures, Comprehensive Nanoscience and Nanotechnology 1−5 (2019) 123−144. Available from: https://doi.org/10.1016/B978-0-12-803581-8.11225-1.

[2] X. Xu, et al., Electrophoretic analysis and purification of fluorescent single-walled carbon nanotube fragments, Journal of the American Chemical Society 126 (40) (2004) 12736−12737. Available from: https://doi.org/10.1021/ja040082h.

[3] X. Wang, et al., Green preparation of fluorescent carbon quantum dots from cyanobacteria for biological imaging, Polymers (Basel) 11 (4) (2019). Available from: https://doi.org/10.3390/polym11040616.

[4] R. Jelinek, Introductionno. 9783319439099 Carbon nanostructures, Springer International Publishing, 2017pp. 1−3.

[5] P.G. Luo, et al., Carbon 'quantum' dots for optical bioimaging, Journal of Materials Chemistry B 1 (16) (2013) 2116−2127. Available from: https://doi.org/10.1039/c3tb00018d.

[6] K.J. Mintz, Y. Zhou, R.M. Leblanc, Recent development of carbon quantum dots regarding their optical properties, photoluminescence mechanism, and core structure, Nanoscale (2019) 4634−465211, no. 11. Royal Society of Chemistry. Available from: https://doi.org/10.1039/c8nr10059d.

[7] S. Zhu, Y. Song, X. Zhao, J. Shao, J. Zhang, B. Yang, The photoluminescence mechanism in carbon dots (graphene quantum dots, carbon nanodots, and polymer dots): current state and future perspective, Nano Research 8 (2) (2015) 355−381. Available from: https://doi.org/10.1007/s12274-014-0644-3.

[8] T.J. Pillar-Little, N. Wanninayake, L. Nease, D.K. Heidary, E.C. Glazer, D.Y. Kim, Superior photodynamic effect of carbon quantum dots through both type I and type II pathways: detailed comparison study of top-down-synthesized and bottom-up-synthesized carbon quantum dots, Carbon 140 (2018) 616−623. Available from: https://doi.org/10.1016/j.carbon.2018.09.004.

[9] M.P. Ajith, S. Pardhiya, P. Rajamani, Carbon dots: an excellent fluorescent probe for contaminant sensing and remediation, Small (Weinheim an der Bergstrasse, Germany) 2105579 (2022) 1−27. Available from: https://doi.org/10.1002/smll.202105579.

[10] V.L. John, Y. Nair, T.P. Vinod, Doping and surface modification of carbon quantum dots for enhanced functionalities and related applications, Particle & Particle Systems Characterization 38 (11) (2021) 1−28. Available from: https://doi.org/10.1002/ppsc.202100170.

[11] F. Yuan, Z. Wang, X. Li, Y. Li, Z. Tan, L. Fan, Bright multicolor bandgap fluorescent carbon quantum dots for electroluminescent light-emitting diodes, Advanced Materials 29 (2017) 1604436. Available from: https://doi.org/10.1002/adma.201604436.

[12] H. Ding, S.B. Yu, J.S. Wei, H.M. Xiong, Full-color light-emitting carbon dots with a surface-state-controlled luminescence mechanism, ACS Nano 10 (1) (2016) 484−491. Available from: https://doi.org/10.1021/acsnano.5b05406.

[13] E. Feature, "Carbon quantum dots found and isolated from egg yolk oil,", Scientific Reports 7 (2017) 1−7 [Online]. Available from: https://www.azoquantum.com/Article.aspx?ArticleID = 53.

[14] B. Gayen, S. Palchoudhury, J. Chowdhury, Carbon dots: a mystic star in the world of nanoscience, Journal of Nanomaterials 2019 (2019) 3451307. Available from: https://doi.org/10.1155/2019/3451307.

[15] R. Jelinek, Characterization and physical properties of carbon-dotsno. 9783319439099 Carbon Nanostructures, 0, Springer International Publishing, 2017pp. 29−46.

[16] P. Bhartiya, A. Singh, H. Kumar, T. Jain, B.K. Singh, P.K. Dutta, Carbon dots: chemistry, properties and applications, Journal of the Indian Chemical Society 93 (7) (2016) 759–766.

[17] R. Wang, K.Q. Lu, Z.R. Tang, Y.J. Xu, Recent progress in carbon quantum dots: synthesis, properties and applications in photocatalysisno. 8 Journal of Materials Chemistry A, 5, Royal Society of Chemistry, 2017pp. 3717–3734.

[18] A.P. Demchenko, M.O. Dekaliuk, Novel fluorescent carbonic nanomaterials for sensing and imagingno. 4 Methods and applications in fluorescence, 1, IOP Publishing Ltd, 2013.

[19] M. Varisco, D. Zufferey, A. Ruggi, Y. Zhang, R. Erni, O. Mamula, Synthesis of hydrophilic and hydrophobic carbon quantum dots from waste of wine fermentation, Royal Society Open Science 4 (12) (2017). Available from: https://doi.org/10.1098/rsos.170900.

[20] M. Kováčová, E. Špitalská, Z. Markovic, Z. Špitálský, Carbon quantum dots as antibacterial photosensitizers and their polymer nanocomposite applications, Particle & Particle Systems Characterization 37 (1) (2020) 1–11. Available from: https://doi.org/10.1002/ppsc.201900348.

[21] Y.-P. Sun, Carbon dots: the classical synthesis and properties, Carbon Dots (2020) 69–107. Available from: https://doi.org/10.1007/978-3-030-41184-8_4.

[22] H. Liu, R. Shen, K. Song, H. Liu, Y. Li, Dramatic fluorescence enhancement of bare carbon dots through facile reduction chemistry, Chemphyschem: A European Journal of Chemical Physics and Physical Chemistry 13 (15) (2012) 3549–3555. Available from: https://doi.org/10.1002/cphc.201200018.

[23] M. Jorns, D. Pappas, A review of fluorescent carbon dots, their synthesis, physical and chemical characteristics, and applicationsno. 6 Nanomaterials, 11, MDPI AG, 2021.

[24] L. Cao, et al., Competitive performance of carbon ‘quantum’ dots in optical bioimaging, Theranostics 2 (3) (2012) 295–301. Available from: https://doi.org/10.7150/thno.3912.

[25] X. Wu, B. Zhao, J. Zhang, H. Xu, K. Xu, G. Chen, Photoluminescence and photodetecting properties of the hydrothermally synthesized nitrogen-doped carbon quantum dots, The Journal of Physical Chemistry C 123 (42) (2019) 25570–25578. Available from: https://doi.org/10.1021/acs.jpcc.9b06672.

[26] H.C. Yao, et al., Construction of magnetic-carbon-quantum-dots-probe-labeled apoferritin nanocages for bioimaging and targeted therapy, International Journal of Nanomedicine 11 (2016) 4423–4438. Available from: https://doi.org/10.2147/IJN.S108039.

[27] S. Dey, P. Chithaiah, S. Belawadi, K. Biswas, C.N.R. Rao, New methods of synthesis and varied properties of carbon quantum dots with high nitrogen content, Journal of Materials Research 29 (3) (2014) 383–391. Available from: https://doi.org/10.1557/jmr.2013.295.

[28] Y. Dong, et al., Carbon-based dots co-doped with nitrogen and sulfur for high quantum yield and excitation-independent emission, Angewandte Chemie International Edition 52 (30) (2013) 7800–7804. Available from: https://doi.org/10.1002/anie.201301114.

[29] U. Abd, L. Yong, C. Yin, E. Mahmoudi, A review of carbon quantum dots and their applications in wastewater treatment, Advances in Colloid and Interface Science 278 (102124) (2020). Available from: https://doi.org/10.1016/j.cis.2020.102124.

[30] J.Y. Liang, et al., Spectrochimica Acta Part A : molecular and biomolecular spectroscopy green fl uorescent carbon quantum dots as a label-free probe for rapid and sensitive detection of hematin, Spectrochimica Acta, Part A: Molecular and Biomolecular Spectroscopy 212 (2019) 167–172. Available from: https://doi.org/10.1016/j.saa.2019.01.001.

[31] H. Lin, J. Huang, L. Ding, Preparation of carbon dots with high-fluorescence quantum yield and their application in dopamine fluorescence probe and cellular imaging, Journal of Nanomaterials 2019 (2019) 5037243.

[32] J.P. Wilcoxon, no. 1 1st (ed.), Nanoparticles-preparation, characterization and physical properties, 3, Elsevier Ltd., 2012.

[33] J. Liu, X. Liu, H. Luo, Y. Gao, One-step preparation of nitrogen-doped and surface-passivated carbon quantum dots with high quantum yield and excellent optical properties, RSC Advance 4 (15) (2014) 7648−7654. Available from: https://doi.org/10.1039/c3ra47577h.

[34] N. Shaari, S.K. Kamarudin, R. Bahru, Carbon and graphene quantum dots in fuel cell application: An overview no. 2, International Journal of Energy Research, 45, John Wiley and Sons Ltd, 2021, pp. 1396−1424.

[35] N.K. Bakirhan, S.A. Ozkan, Quantum Dots as a New Generation Nanomaterials and Their Electrochemical Applications in Pharmaceutical Industry, Elsevier Inc, 2018.

[36] V. Rimal, S. Shishodia, P.K. Srivastava, Novel synthesis of high-thermal stability carbon dots and nanocomposites from oleic acid as an organic substrate, Applied Nanoscience 10 (2) (2020) 455−464. Available from: https://doi.org/10.1007/s13204-019-01178-z.

[37] M. Javed, et al., Carbon quantum dots from glucose oxidation as a highly competent anode material for lithium and sodium-ion batteries, Electrochimica Acta 297 (2019) 250−257. Available from: https://doi.org/10.1016/j.electacta.2018.11.167.

[38] F. Wang, S. Wang, Z. Sun, H. Zhu, Study on ultrasonic single-step synthesis and optical properties of nitrogen-doped carbon fluorescent quantum dots, Fullerenes Nanotub. Carbon Nanostructures 23 (9) (2015) 769−776. Available from: https://doi.org/10.1080/1536383X.2014.996287.

[39] B.D. Mansuriya, Z. Altintas, Carbon dots: classification, properties, synthesis, characterization, and applications in health care-an updated review (2018−2021), Nanomaterials 11 (10) (2021). Available from: https://doi.org/10.3390/nano11102525.

[40] Z. Zhang, T. Zheng, X. Li, J. Xu, H. Zeng, Progress of carbon quantum dots in photocatalysis applicationsno. 8 Particle and particle systems characterization, 33, Wiley-VCH Verlag, 2016pp. 457−472.

[41] X. Wang, Y. Feng, P. Dong, J. Huang, A mini review on carbon quantum dots: preparation, properties, and electrocatalytic application, Frontiers in chemistry, 7, Frontiers Media S.A, 2019.

[42] Edinburgh Instruments, Fluorescence, phosphorescence, photoluminescence differences. 2012, [Online]. Available: https://www.edinst.com/blog/photoluminescence-differences/.

[43] T. Yuan, et al., Carbon quantum dots: an emerging material for optoelectronic applications, Journal of Materials Chemistry C 7 (2019) 6820−6835no. 23. Royal Society of Chemistry. Available from: https://doi.org/10.1039/C9TC01730E.

[44] A. Luque, A. Martí, A. J. Nozik, “Solar Cells Based on Quantum Dots : Multiple Exciton Generation and Intermediate Bands,” vol. 32, Cambridge University Press, 2007, pp. 236−241.

[45] V. Ramar, S. Moothattu, K. Balasubramanian, Metal free, sunlight and white light based photocatalysis using carbon quantum dots from Citrus grandis: a green way to remove pollution, Solar Energy 169 (2018) 120−127. Available from: https://doi.org/10.1016/j.solener.2018.04.040.

[46] H. Li, R. Liu, S. Lian, Y. Liu, H. Huang, Z. Kang, Near-infrared light controlled photocatalytic activity of carbon quantum dots for highly selective oxidation reaction, Nanoscale 5 (8) (2013) 3289−3297. Available from: https://doi.org/10.1039/c3nr00092c.

[47] B.B. Rasulkhan, S.K. Ponnaiah, P. Periakaruppan, G. Venkatachalam, J. Balasubramanian, A new CQDs/f-MWCNTs/GO nanocomposite electrode for arsenic (10−12M) quantification in bore-well water and industrial effluents, New Journal of Chemistry 44 (42) (2020) 18149−18156. Available from: https://doi.org/10.1039/d0nj04252h.

[48] K. Dimos, Carbon quantum dots: surface passivation and functionalization, Current Organic Chemistry 20 (6) (2015) 682−695. Available from: https://doi.org/10.2174/1385272819666150730220948.

[49] H. Li, et al., One-step ultrasonic synthesis of water-soluble carbon nanoparticles with excellent photoluminescent properties, Carbon 49 (2) (2011) 605−609. Available from: https://doi.org/10.1016/j.carbon.2010.10.004.

[50] J. Tan, J. Zhang, W. Li, L. Zhang, D. Yue, Synthesis of amphiphilic carbon quantum dots with phosphorescence properties and their multifunctional applications, Journal of Materials Chemistry C 4 (42) (2016) 10146−10153. Available from: https://doi.org/10.1039/c6tc03027k.

[51] N. Sarmasti, A. Khazaei, J. Yousefi Seyf, High density sulfonated magnetic carbon quantum dots as a photo enhanced, photo-induced proton generation, and photo switchable solid acid catalyst for room temperature one-pot reaction, Research on Chemical Intermediates 45 (7) (2019) 3929−3942. Available from: https://doi.org/10.1007/s11164-019-03829-w.

[52] S.Y. Lim, W. Shen, Z. Gao, Carbon quantum dots and their applicationsno. 1 Chemical society reviews, 44, Royal Society of Chemistry, 2015pp. 362−381.

[53] Y. Xu, J. Liu, C. Gao, E. Wang, Applications of carbon quantum dots in electrochemiluminescence: a mini review, Electrochemistry communications, 48, Elsevier Inc, 2014, pp. 151−154.

[54] B.K. Walther, et al., Nanobiosensing with graphene and carbon quantum dots: recent advances, Materials Today, 39, Elsevier B.V, 2020, pp. 23−46.

[55] Z. Zhang, Y. Duan, Y. Yu, Z. Yan, J. Chen, Carbon quantum dots: synthesis, characterization, and assessment of cytocompatibility, Journal of Materials Science. Materials in Medicine 26 (7) (2015). Available from: https://doi.org/10.1007/s10856-015-5536-x.

[56] Y. Zhang, Y. Xiao, Y. Zhang, Y. Wang, Carbon quantum dots as fluorescence turn-off-on probe for detecting Fe3 + and ascorbic acid, Journal of Nanoscience and Nanotechnology 20 (6) (2019) 3340−3347. Available from: https://doi.org/10.1166/jnn.2020.17412.

[57] S.S. Monte-Filho, S.I.E. Andrade, M.B. Lima, M.C.U. Araujo, Synthesis of highly fluorescent carbon dots from lemon and onion juices for determination of riboflavin in multivitamin/mineral supplements, Journal of Pharmaceutical Analysis 9 (3) (2019) 209−216. Available from: https://doi.org/10.1016/j.jpha.2019.02.003.

[58] Q. Xiao, Y. Liang, F. Zhu, S. Lu, S. Huang, Microwave-assisted one-pot synthesis of highly luminescent N-doped carbon dots for cellular imaging and multi-ion probing, Microchimica Acta 184 (7) (2017) 2429−2438. Available from: https://doi.org/10.1007/s00604-017-2242-z.

[59] T. S, R.S. D, Green synthesis of highly fluorescent carbon quantum dots from sugarcane bagasse pulp, Applied Surface Science 390 (2016) 435−443. Available from: https://doi.org/10.1016/j.apsusc.2016.08.106.

[60] I. Singh, R. Arora, H. Dhiman, R. Pahwa, Carbon quantum dots: synthesis, characterization and biomedical applications, Turkish Journal Of Pharmaceutical Sciences 15 (2) (2018) 219−230. Available from: https://doi.org/10.4274/tjps.63497.

[61] Y. Chen, X. Qin, C. Yuan, Y. Wang, Switch on fluorescence mode for determination of l-cysteine with carbon quantum dots and Au nanoparticles as a probe, RSC Advance 10 (4) (2020) 1989−1994. Available from: https://doi.org/10.1039/c9ra09019c.

[62] P. Zuo, X. Lu, Z. Sun, Y. Guo, H. He, A review on syntheses, properties, characterization and bioanalytical applications of fluorescent carbon dots, Microchimica Acta (2016) 519−542. Available from: https://doi.org/10.1007/s00604-015-1705-3.

[63] B. De, B. Voit, N. Karak, Carbon dot reduced Cu2O nanohybrid/hyperbranched epoxy nanocomposite: Mechanical, thermal and photocatalytic activity, RSC Advance 4 (102) (2014) 58453−58459. Available from: https://doi.org/10.1039/c4ra11120f.

[64] D. Kumar, K. Singh, V. Verma, H.S. Bhatti, Synthesis and characterization of carbon quantum dots from orange juice, Journal of Bionanoscience 8 (4) (2014) 274−279. Available from: https://doi.org/10.1166/jbns.2014.1236.

[65] Y. Li, X. Zhong, A.E. Rider, S.A. Furman, K. Ostrikov, Fast, energy-efficient synthesis of luminescent carbon quantum dots, Green Chemistry: An International Journal and Green Chemistry Resource: GC 16 (5) (2014) 2566−2570. Available from: https://doi.org/10.1039/c3gc42562b.

[66] M. Farshbaf, S. Davaran, F. Rahimi, N. Annabi, R. Salehi, A. Akbarzadeh, Carbon quantum dots: recent progresses on synthesis, surface modification and applicationsno. 7 Artificial cells, nanomedicine and biotechnology, 46, Taylor and Francis Ltd, 2018pp. 1331−1348.

[67] Y. Zhang, et al., One-step synthesis of chiral carbon quantum dots and their enantioselective recognition, RSC Advance 6 (65) (2016) 59956−59960. Available from: https://doi.org/10.1039/c6ra12420h.

[68] L. Wang, et al., Full-color fluorescent carbon quantum dots, Science Advance 6 (2020) eabb6772 [Online]. Available from: http://advances.sciencemag.org/.

[69] V.A. Online, et al., Nitrogen-doped, carbon-rich, highly photoluminescent carbon dots from ammonium citrate †, Nanoscale 6 (2014) 1890−1895. Available from: https://doi.org/10.1039/c3nr05380f.

[70] L. Lin, Y. Luo, P. Tsai, J. Wang, X. Chen, Metal ions doped carbon quantum dots: synthesis, physicochemical properties, and their applications, TrAC - Trends in analytical chemistry, 103, Elsevier B.V, 2018, pp. 87−101. 10.1016/j.trac.2018.03.015.

[71] Q. Liang, W. Ma, Y. Shi, Z. Li, X. Yang, Easy synthesis of highly fluorescent carbon quantum dots from gelatin and their luminescent properties and applications, Carbon 60 (2013) 421−428. Available from: https://doi.org/10.1016/j.carbon.2013.04.055.

[72] M. He, J. Zhang, H. Wang, Y. Kong, Y. Xiao, W. Xu, Material and optical properties of fluorescent carbon quantum dots fabricated from lemon juice via hydrothermal reaction, Nanoscale Research Letters 13 (2018). Available from: https://doi.org/10.1186/s11671-018-2581-7.

[73] A.F. Shaikh, M.S. Tamboli, R.H. Patil, A. Bhan, J.D. Ambekar, B.B. Kale, Bioinspired carbon quantum dots: an antibiofilm agents, Journal of Nanoscience and Nanotechnology 19 (4) (2018) 2339−2345. Available from: https://doi.org/10.1166/jnn.2019.16537.

Surface engineering of carbon quantum dots

5

Ankita Saha[1], *Lopamudra Bhattacharjee*[2] *and*
Rama Ranjan Bhattacharjee[3]
[1]Amity School of Applied Sciences, Amity University, Kolkata, West Bengal, India,
[2]PSG Institute of Advanced Studies, Coimbatore, Tamil Nadu, India, [3]Department of
Chemistry, Sister Nivedita University, Kolkata, West Bengal, India

5.1 Introduction

Carbon allotropes and their analogs are highly hydrophobic in nature. Due to the catenation property, C-C bonds are very difficult to substitute keeping their chemical and physical properties intact. Hence, they are always limited to the same nature of their surface functionalities, which are related to surface chemistry.

For nanomaterials, surface properties are the most important issue. The main challenge for chemists is to tune surface properties for better dispersibility in a variety of solvent systems so that the surface chemistry and hence reactivity of the system is not compromised. Along with chemical properties, physical properties like optical and electronic properties are also influenced by the nature of the surface. One of the most important nanomaterials investigated so far is the carbon nanotube (CNT). They have attracted increased research attention due to their excellent mechanical and physical properties, tunable semiconductivity, low density, high modulus, and high electrical or thermal properties. CNT applications range from sensors, electronic devices, catalysis, and energy storage to superconductors and field emission devices depending on the surface functionalization as shown in Fig. 5.1. However, the major problem with CNTs is that they are prone to accumulate and develop clusters owing to high van der Waals pressure in between the tubes. Due to the robust C-C bonds, the solubility in standard solvents and CNTs' interaction with other compounds such as polymer or molecules are inadequate. Surface engineering of the CNT exterior is a promising means of conquering these difficulties and takes an essential place for the applications of CNTs.

5.1.1 Carbon nanotube versus carbon quantum dots

Since the innovation of CNTs, carbogenic nanosystems have been broadly looked into. Though CNTs have great potential in electronic applications, the synthesis of such material in extensive amounts has been challenging. The existing processes are tiresome and involve massive production costs and inadequate yields [1]. CNT also suffers from dispersion issues. The material is difficult to functionalize and

Carbon Quantum Dots for Sustainable Energy and Optoelectronics. DOI: https://doi.org/10.1016/B978-0-323-90895-5.00008-4
© 2023 Elsevier Ltd. All rights reserved.

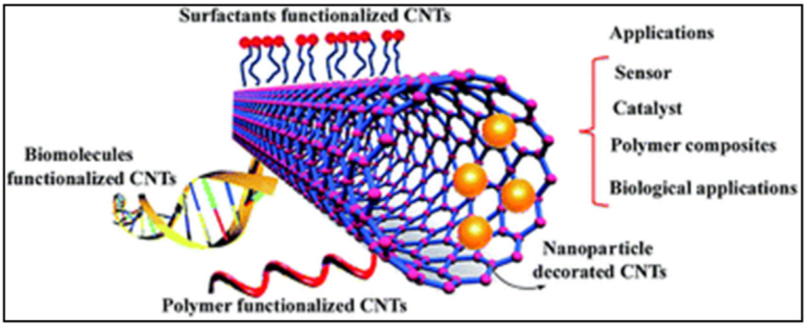
Surfactants functionalized CNTs
Applications
Sensor
Catalyst
Polymer composites
Biological applications
Biomolecules functionalized CNTs
Nanoparticle decorated CNTs
Polymer functionalized CNTs

Figure 5.1 Schematic representation of various surface functionalities in CQDs.
Source: RSC Advance, 2016, 6, 1099316–109935.

hence shows limited dispersion abilities. Only few solvents are reported to be used as dispersion medium but they are mostly high-boiling solvents. CNTs also suffer from issues related to impurities or presence of adsorbed solvents. Researchers, who use sonication for CNT dispersion in a given medium, report itching of amorphous carbon from the material and hence conducting properties are altered.

Carbon quantum dots (CQDs) may emerge as a cost-effective alternative to CNTs because CQDs can be synthesized using simple pyrolytic methods with high yields. CQDs are similar allotropes of carbon and possess interesting physical and chemical properties. The surface chemistry is very important and interesting as it influences the photoluminescent properties of the CQDs. In recent years, the PL properties of CQDs have attracted huge attention and are very unique compared to other nanomaterials. Literature suggests that the emission resources in CQDs arise from the blend of powerful quantum custody and surface flaw. The observable properties of such CQDs in suspension had been considerably reported in the past with biological applications and excellent quantum outcomes. The polymer presence on the CQD surface aids to enhance PL properties. The steady surface trap sites are the source of the potent emission in polymer-stabilized CQDs. From literature survey, it is evident that these surface trap sites create low-lying energy levels and facilitate effective radiative recombination. Polymer-passivated CQDs exhibit unique quantum yield and enhanced processability through control over size, crystallinity, and surface sites. Hence, it is crucial to study the observable properties of polymer-passivated CQDs in diverse environments. Several writers have reported PL of polymer-passivated CQDs in halt. Few have reported PL properties in fabricated structures, solid states, and polymer films. Detailed studies on concentration and environment effects on PL properties are still rare. There is no report on the effect of dispersion medium or fabricated structures on optical properties of polymer-stabilized CQDs. Studies on photobleaching or photoblinking and dark fraction of CQDs have not been reported too. Apart from emission properties, CQDs also have interesting electronic properties. These highly emitting CQDs have been continuously used in the bioimaging study and also in the field of light-emitting diodes.

5.1.2 Fundamentals of surface engineering in carbogenic allotropes

Carbogenic allotropes and their related nanomaterials tend to cluster uncontrollably. Therefore, it results in massive surface energy and stabilizes numerous p—p electron reactions between the tubes. Feeble dispersibility and their difficulty of dispersibility in solvents and other material matrices like polymerics and ceramics have limited their applications. The potential applications of CQDs need detailed engineering of the carbon atoms present on the surface to form processable and adjust their properties. For solving the issues, two separate techniques are used to distribute CQDs, namely chemical and mechanical techniques. The mechanical methods involve increased shear mixing, increased impact mixing, rubbing and grating, ultrasonication, and many more. Now the mechanical methods can separate the CQDs from each other, but can also break up nanodomains, decreasing their size during processing. Thus, these may be time-consuming and ineffective approaches.

Caution: Here a matter of concern needs to be understood and clarified: During mechanical agitation and other processes, it is observed that the properties of the CQDs are degraded. The reason behind such detoriation of properties is related to the dissolution or destruction of amorphous portions and regions in the structure. The same thing happens for CNTs and has been well reported. Despite that, many students and researchers often do not understand the effects of sonication and other mechanical treatments of nanomaterials. They should understand that nanomaterials have infant crystals, that is, the crystals are not fully grown, they are not robust, and fully crystalline. Hence, extensive use of very high mechanical sintering can be lethal for nanomaterials, especially like CQDs.

Chemical methods are thus thought to be more effective for changing the surface modification of CQDs, thereby improving their wetting or adhesion characteristics and dispersion stability. These procedures are aimed to modify the surface phenomena of the CQDs either covalently or noncovalently. Engineered CQDs may have different electrical, optical, or mechanical properties than that of the original nanotubes. As a consequence, it is a captivating domain for functionalizing CQDs for a wide range of applications.

5.2 Methodology

5.2.1 Hydrothermal carbonization

Hydrothermal carbonization, a propitious technique among all surface passivation technologies, is a chemical process for the conversion of organic compounds to structured carbons. This process can be classified into two basic constituents based on the application of temperature. The high-temperature method occurs from 300°C to 800°C, allowing multiwalled CNTs, graphic carbon materials, fullerenes, activated carbon materials, and carbon spheres with different nanostructures to be synthesized. The low-temperature hydrothermal carbonization process is performed

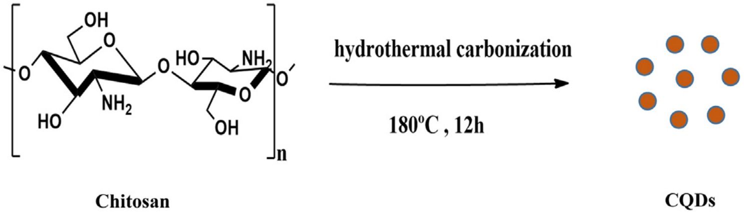

Figure 5.2 A schematic illustration of the preparation procedure of CQDs by hydrothermal carbonization of chitosan [4].

below 300°C to synthesize functional carbonaceous materials where carbon spheres have been obtained as main products via dehydration reaction followed by polymerization reaction [2,3].

5.2.1.1 Amino-functionalized fluorescent carbon quantum dots

Highly amino-functionalized fluorescent CQDs can be synthesized by low-temperature hydrothermal carbonization of chitosan. Here the formation of CQDs and their surface functionalization take place simultaneously during hydrothermal carbonization, which occurs through the dehydration of chitosan (Fig. 5.2). The functional groups make them water-soluble and reduce their potential bio-toxicity. The advantage of this one-step synthetic method is that no acid solvent or surface passivation reagent is needed and this occurs in an aqueous solution. The process is very cheap, absolutely green [4].

The transparent yellowish CQDs solution is clear under sunlight, whereas it shows strong blue luminescence under UV light. Some defect sites on the surface of CQDs can be created due to the surface modification. These defects trap the radiative recombination of the excitons resulting in high fluorescence emission. The CQDs show low cytotoxicity and do not pose any significant toxic effects. This result concludes that CQDs can be used in a high concentration for bioimaging or other medical applications.

5.2.1.2 Branched polyethylenimine functionalized carbon quantum dots

The branched polyethylenimine (BPEI)–CQDs can be synthesized by low-temperature (<200°C) carbonization of citric acid (CA) in the presence of BPEI. This is basically an easy one-step bottom-up synthesis method. The temperature should not be higher than 200°C, to avoid the degeneration of BPEI. Here CA is used as the carbon precursor because of its facile low carbonization temperature (<200°C). Since BPEI plays a role in surface passivation of CQDs with some amines, it helps to detect different analytes with the other free amines due to its polyamine structure. It can be used as capping and functionalizing reagent. The principle of the synthesis of BPEI functionalized CQDs is shown in Fig. 5.3.

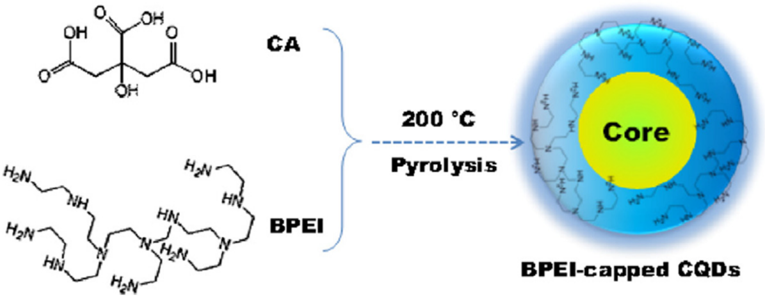

Figure 5.3 Synthesis route of BPEI functionalized CQDs (BPEI-CD) [5].

The polyamine functionalized CQDs can both selectively recognize trace amount of certain metal ions, such as Cu^{2+} ion with high FL quantum yield. The amino groups at the surface of the CQDs can bind the Cu^{2+} to form cupric amine, resulting in a selective and strong quenching of the CQDs' FL via a so-called inner filter effect, and give a very sensitive signal response, providing their promising application in analytical chemistry [5,6].

5.2.1.3 Amino-functionalized carbon quantum dots

Amino-functionalized CQDs can also be prepared from anhydrous CA and diethylenetriamine by a low-temperature (200°C) hydrothermal approach. Then the synthesized CQDs can be attached covalently to 4-carboxyphenylboronic acid (CPBA) to form CPBA-CQD (Fig. 5.4).

The CPBA functional groups are reactive toward vicinal diols. So they can covalently bridge the highly toxic catechol with the vicinal diol structures and as a result, the fluorescence gets quenched significantly via the static quenching mechanism [7].

5.2.1.4 Spiropyran-functionalized carbon quantum dots

Fluorescent CQDs can be synthesized by the low-temperature hydrothermal carbonization of ethylenediaminetetraacetic acid disodium salt (EDTA.2Na). Then the synthesized CQDs are functionalized with spiropyran by linking them covalently. Spiropyran, a photoisomeric dye, is known for its photochromic properties that provide this molecule with the ability of functionalizing some low dimensional materials like CNTs, noble metal nanoclusters, and semiconductor quantum dot. These spiropyran-functionalized materials have extensive use in medical and technology areas. To synthesize spiropyran-functionalized CQDs, the functionalization of the CQDs with ethylenediamine (EDA) is needed at first. So to synthesize EDA-CQD, excess amount of EDA is added to the CQD solution, activated by N-Hydroxysuccinimide (NHS) for 1 hour. Then, carboxyl containing spiropyran is treated with EDA-CQD to functionalize them with spiropyran. Spiropyran-functionalized CQDs show reversible fluorescence modulation, excellent photoreversibility, high stability, and relatively fast photoresponsivity. This suggests that

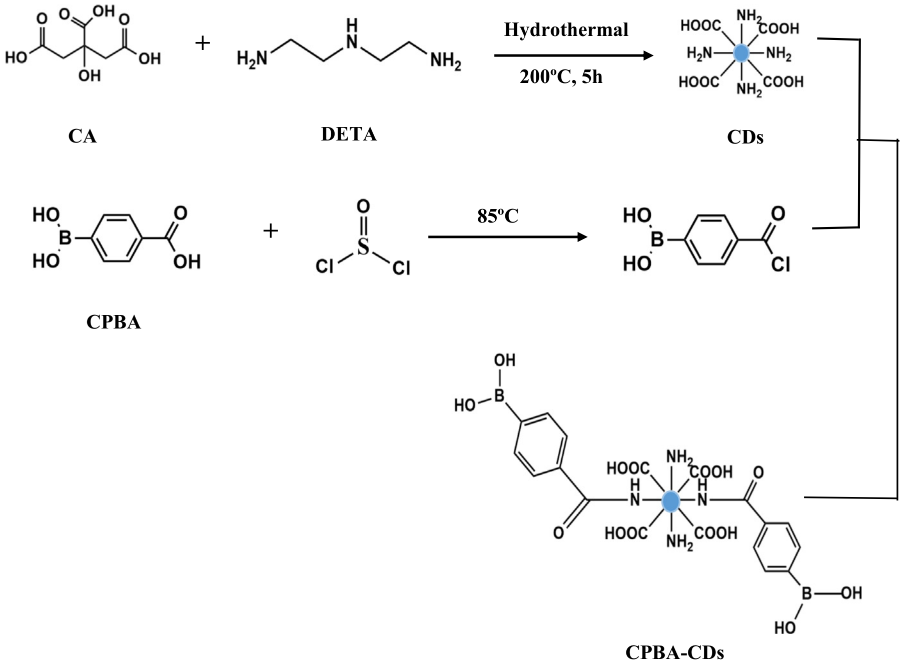

Figure 5.4 Synthesis route of CPBA functionalized CQDs (CPBA-CD) [7].

the photoresponsive spiropyran-functionalized CQDs can be potentially applied in biological imaging and labeling, reversible data storage/erasing, as well as individual light-dependent nanoscale devices [8].

5.2.2 Microwave-assisted pyrolysis

The thermal decomposition of matter at elevated temperatures in an inert atmosphere is known as pyrolysis. Microwave-assisted pyrolysis is a special type of pyrolysis that comprises microwave dielectric heating and temperatures as high as 800°C. The traditional surface engineering process of nanoparticles usually embraces multiple steps and makes the processing time-consuming. But the microwave-assisted pyrolysis process is very fast [9].

5.2.2.1 Hyperbranched polyethylenimine and isobutyric amide functionalized C-dots

Strong photoluminescent polyethylenimine (PEI) functionalized C-dots (CD-PEI) have been synthesized directly via microwave pyrolysis of glycerol in the presence of hyperbranched PEI under 700 W microwaves for 10 min. The role of PEI as the surface passivation agent will aid in the generation of C-dots, which will help in gene delivery and intensify fluorescent properties. In this synthetic route, the formation of

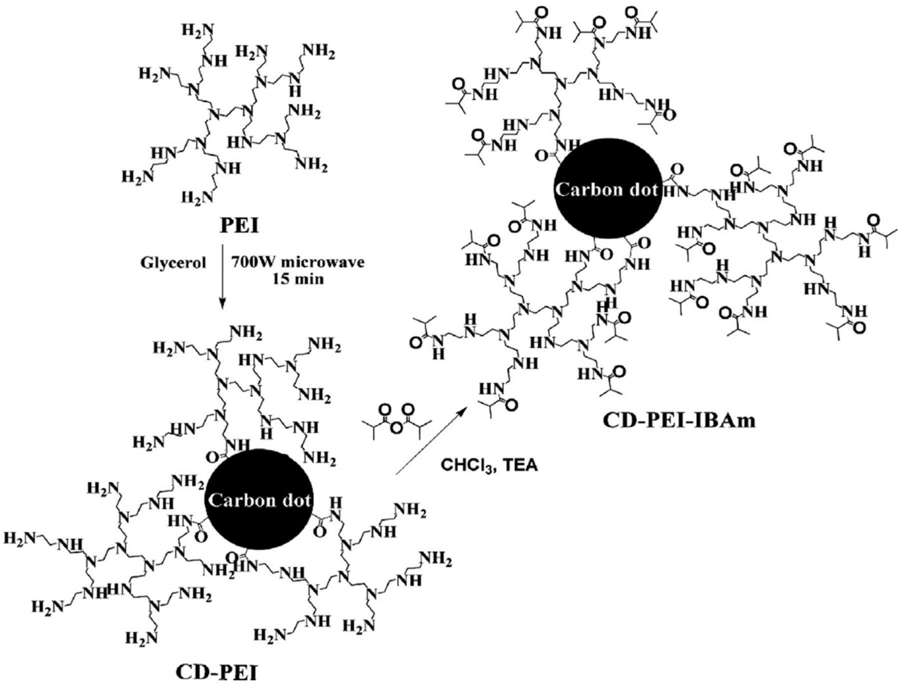

Figure 5.5 Synthesis of hyperbranched PEI and IBAm functionalized CD [10].

carbon nanoparticles and the surface passivation with PEI occur simultaneously in one pot. Isobutyric amide (IBAm) groups can be coupled with CD-PEI through the amidation reaction of isobutyric anhydride and HPEI moiety to produce multistimuli-responsive CD-PEI-IBAm (Fig. 5.5). This type of photoluminescent CQDs is able to host organic molecules as nanocarriers. Thus they are applicable in the area of drug delivery systems and biotechnology as "smart" materials [10].

5.2.2.2 Organosilane functionalized carbon quantum dots

For real device application, it is required to synthesize nontoxic and ecofriendly CQDs by embedding them in solid-state architectures or in a suitable solid matrix. Silica gel and organically functionalized silicates are significantly used as solid matrices because of their optical properties and inherent stability. But aggregation, low doping concentration, or phase separation during the preparation of polymer hybrid materials or silica gel make their use limited. So nanomaterials can be modified with organosilanes instead of silica gel after their formation. The highly luminescent amorphous CDs can be synthesized by the decomposition and pyrolysis of anhydrous CA, which produces gas and condensable vapors with the surface passivation reaction of the amine groups of N-(β-aminoethyl)-γ-aminopropylmethyldimethoxysilane (AEAPMS) and the carboxyl groups derived from the pyrolyzed

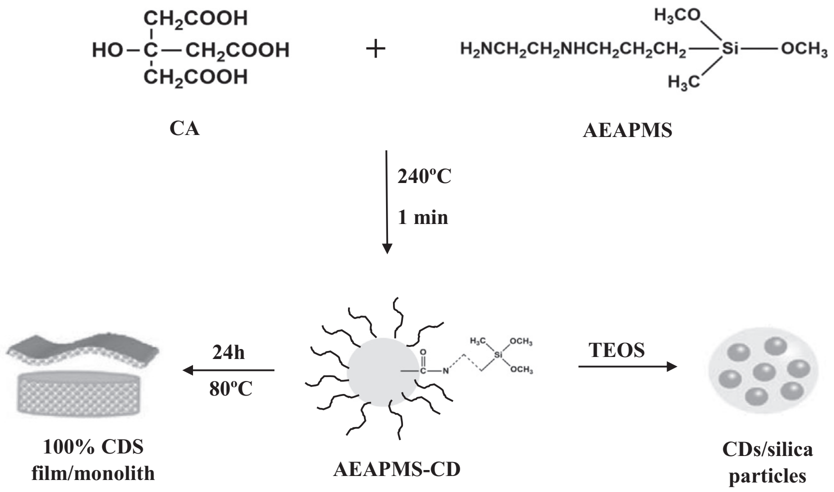

Figure 5.6 Synthesis route of organosilane functionalized CD [11].

species in 1 minute. Here AEAPMS acts as a coordinating solvent. The AEAPMS-CDs can be forged into pure CD monoliths or fluorescent films simply by charring them at 80°C for 24 h. Furthermore, the water-insoluble AEAPMS-CDs can be converted into water-soluble CDs/silica particles by treating them with tetraethylorthosilicate (TEOS) (Fig. 5.6). This silica precursor TEOS helps to hydrolyze and condense the terminal methoxysilane groups to form a silica overlayer [11,12].

Those biocompatible and nontoxic CDs/silica particles have promising implementations in different fields like medical diagnostics to catalysis and photovoltaics due to their cost-effectiveness, magnificent chemical stability, ready scalability, and special properties.

5.2.2.3 Organic dye-functionalized carbon quantum dot

Extremely fluorescent crystalline CQDs can be synthesized from sucrose upon 100 W microwave irradiation for 3 min 40 s in presence of phosphoric acid. Here, sucrose and phosphoric acid play the role of carbon precursor oxidizing agents. This type of CQDs exhibits bright green fluorescence upon excitation of UV light. To further modify the fluorescence property as well as to reduce the cytotoxicity of the synthesized carbon nanoparticles of the resulting CQDs, they are functionalized by different dyes, for instance rhodamine B, fluorescein, and α-naphthylamine. To functionalize those dyes, the CQDs should, at first, be activated by1-Ethyl-3-(3-dimethylaminopropyl)carbodiimide (EDC). Then those activated CQDs are treated with an ethanol solution of corresponding dyes to prepare CQD-Naph, FCQD, and CQD-Rh (Fig. 5.7).

The particles functionalized with fluorescein exhibit maximum fluorescence intensity. All of the above compounds, as well as CQDs, have been successfully implemented with minimal cytotoxicity into the erythrocyte-enriched proportion of

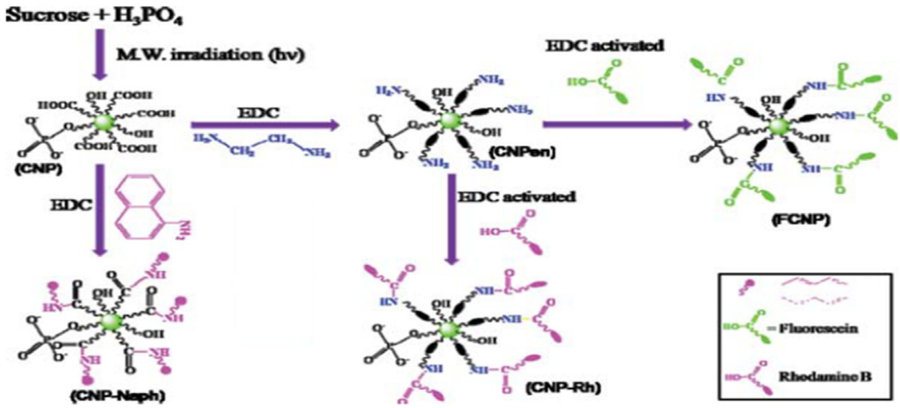

Figure 5.7 Synthesis of organic dyes (fluorescein, rhodamine B, and α-naphthylamine) functionalized CD [13].

healthy human blood cells. In the future, CQD-Naph could also be used as a unique material for bioimaging and drug delivery due to the following benefits:

- It manifests a very negligible amount of cytotoxicity among all the compounds.
- The synthesis procedure is way simpler than that of the FCQD.
- After entering living cells, it emits the brightest green fluorescence [13].

5.2.3 Sol–gel reaction

A novel ecofriendly molecularly imprinted polymer (MIP) can be produced by an effective one-pot sol–gel polymerization at room temperature. There are different types of methods to prepare MIP such as multi-step swelling polymerization, suspension polymerization, and precipitation polymerization. Sol–gel polymerization shows superiority over others as it manifests three advantages:

1. Thin films and/or bulk gels enable simple fabrication.
2. The ecosustainable reaction solvent (ethanol or water) differs from the general solvent (chloroform, acetonitrile, or toluene) used in the polymerization reactions mentioned above.
3. The reagents can be readily introduced within the porous and extensively cross-linked host structure without the problems of chemical or thermal degradation due to the mild proper polymerization conditions.

The surface of AEAPMS functionalized CDs can be modified with MIP matrix (CDs@MIP) by one-pot sol–gel molecular imprinting method at room temperature. Here dopamine (DA) is used as a template. Silica molecular imprinted nanospheres can be synthesized by hydrolysis and condensation reaction between CDs template molecules (DA), functional monomer (3-aminopropyl-triethoxysilane, APTES), and cross-linker (TEOS) in the presence of aqueous ammonia solution that acts as catalysis (Fig. 5.8). In the presence of light and air, as DA molecules are oxidized easily, the

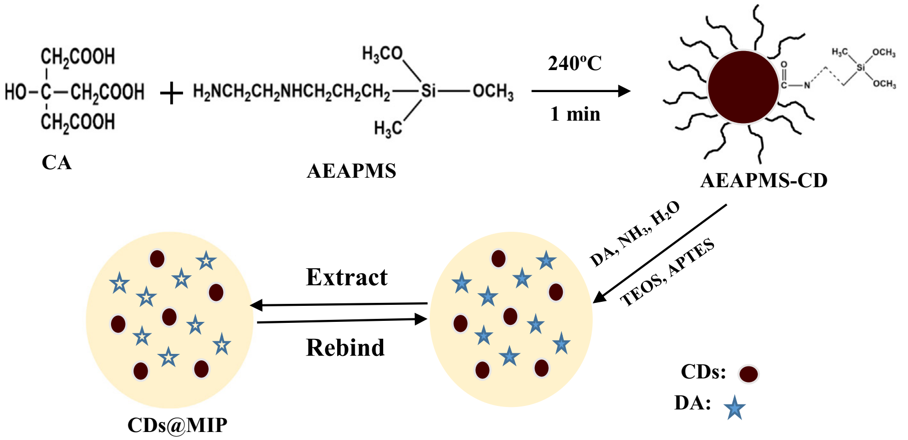
CA
AEAPMS
240°C
1 min
AEAPMS-CD
DA, NH₃, H₂O
TEOS, APTES
Extract
Rebind
CDs@MIP
CDs:
DA:

Figure 5.8 Synthesis of CDs@MIP [14].

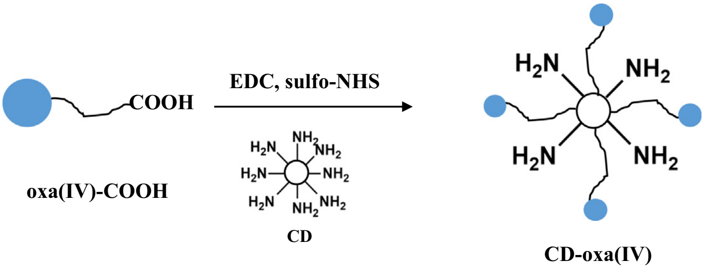
COOH
oxa(IV)-COOH
EDC, sulfo-NHS
CD
CD-oxa(IV)

Figure 5.9 Synthesis of CD-oxa(IV) [15].

reaction should perform in the dark inert (nitrogen) environment. These CDs@MIP are used to recognize DA in aqueous solutions and in human urine samples. Optical recognition of DA is significant in diagnoses, prohibition, and treatments of some neurological diseases; for example, Parkinson's disease, Schizophrenia, and Hunting-ton's disease [14].

5.2.4 Condensation reaction

The polyene polyamine (PEPA) functionalized CDs can be prepared by the hydrothermal carbonization of PEPA and CA at 170°C for 0.5−2 hours. This PEPA-CD is modified with the anticancer drug oxaplatin derivative oxa(IV)-COOH. The amino groups on the surface of the fluorescent CDs and the carbonyl groups of the oxa(IV)-COOH, undergoing the condensation reaction, result in the functionalization (Fig. 5.9). This functionalization induces the optical properties of CDs, so this

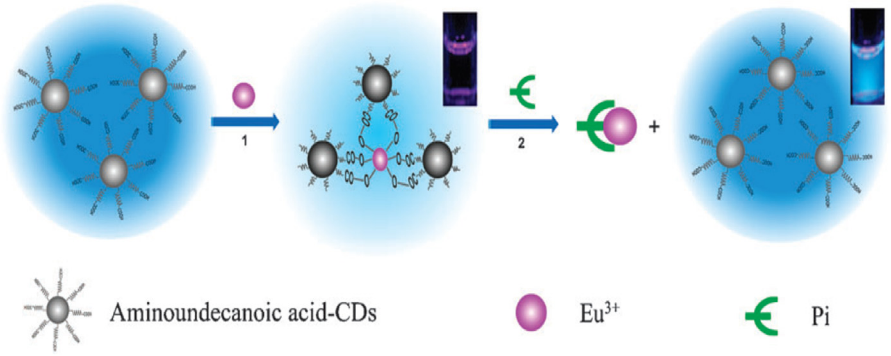

Figure 5.10 Schematic representation of Pi detection based on the off-fluorescence probe of carbon dots adjusted by Eu^{3+} [16].

CD-oxa(IV) is useful for fluorescent tracking. Besides that, due to the anticancer function of oxaplatin CD-oxa(IV), it has been an intense research focus in the medical field [15].

5.2.4.1 Europium-adjusted carbon dots

The CDs treated for the functionalization by europium (Eu^{3+}) are synthesized by the condensation reaction of CA and 11-aminoundecanoic acid. The availability of carboxylate groups on the surface of CDs makes them water-soluble. Europium is the most reactive element in the lanthanide series. Eu^{3+} is one of the rarest earth elements on earth and generally it occurs in the +3 oxidation state. Like other lanthanides, Eu^{3+} exhibits high coordination number i.e., C.N 6. It shows preference for the O-donor atoms and acts as bridging element between the neighboring carboxylate groups. So, Eu^{3+} can easily coordinate with the carboxylate groups attached on the surface of the CDs, resulting in the aggregation of the CDs. Thus, the presence of Eu^{3+} ion makes the fluorescence emission of CDs quenched through charge or energy-transfer process (Fig. 5.10). The Eu^{3+} functionalized CDs (CDs-Eu^{3+}) flaunt high selectivity towards phosphate (Pi) by showing specific fluorescence "turn on" response towards Pi [16].

5.2.5 Oxidation–polymerization reaction

The synthesis of a novel carbon dot–polyaniline (CD–PANI) complex can be done in the presence of hydrochloric acid and CD through an efficient one-pot chemical-oxidative polymerization reaction. At first, the CDs are synthesized by the dehydration reaction between D-(+)-glucose and concentrated sulfuric acid. Aniline monomer is treated under acidic conditions for the protonation of aniline molecule, i.e., for the emergence of anilinium ion. In the aqueous solution, the anilinium ions combine with COO- groups present on the surface of the CDs via charge–charge interactions and

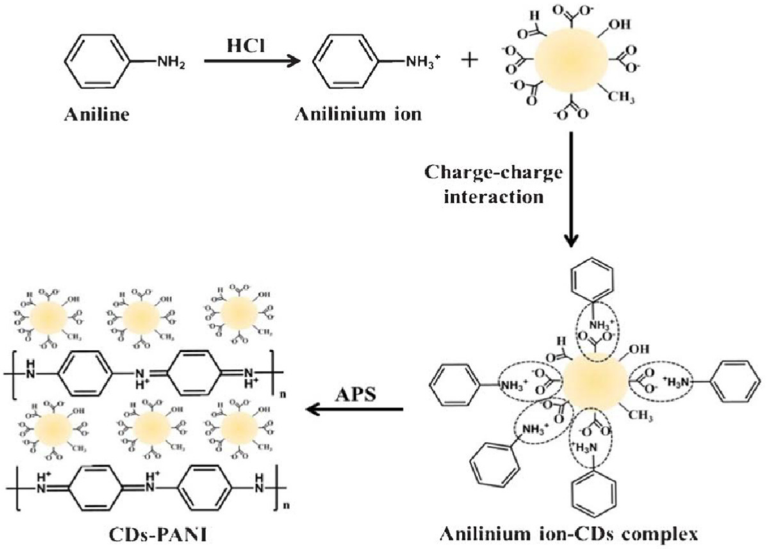

Figure 5.11 An illustration of the synthetic procedure for the preparation of CD–PANI [17].

form an anilinium ion–CD composite. The aniline monomers undergo polymerization reaction with the help of ammonium persulfate, which acts as the oxidant for 16 hours at room temperature, and CD–PANI is generated [17] (Fig. 5.11).

5.3 Conclusion

The chapter is based on the issues faced with the surface functionalization of carbonaceous nanostructures, with special emphasis on the use of CQDs and the facile surface engineering of the CQDs. The chapter details the several approaches taken for modifying the CQD surface and their advantage as well as disadvantages. Mostly, chemical-based approaches are discussed as it is understood that these materials are industrially important and hence required easy and scalable process for surface engineering. Lastly, mainly greener synthetic protocols have been stressed in the chapter, which provides a sustainable solution to nanotechnological advances for future applications of CQDs.

References

[1] Y. Wang, A. Hu, Journal of Materials Chemistry C 2 (2014) 6921–6939.
[2] M. Inagaki, 2014. Advanced materials science and engineering of carbon, Carbonization under pressure (pp. 67–85), Hindawi.

[3] S.T. Yoganandham, G. Sathyamoorthy, R.R. Renuka, Sustainable seaweed technologies, Emerging Extraction Techniques: Hydrothermal Processing, Elsevier, 2020, pp. 191−205. Available from:. Available from: https://www.sciencedirect.com/topics/chemistry/hydrothermal-carbonization.

[4] Y. Yang, J. Cui, M. Zheng, C. Hu, S. Tan, Y. Xiao, et al., Chemical Communications 48 (2012) 380−382.

[5] Y. Dong, R. Wang, H. Li, J. Shao, Y. Chi, X. Lin, et al., Carbon 50 (2012) 2810−2815.

[6] Y. Dong, R. Wang, G. Li, C. Chen, Y. Chi, G. Chen, Analytical Chemistry 84 (2012) 6220−6224.

[7] Q. Ye, F. Yan, D. Kong, J. Zhang, X. Zhou, J. Xu, et al., Sensors and Actuators B: Chemical 250 (2017) 712−720.

[8] B. Liao, P. Long, B. He, S. Yi, B. Ou, S. Shen, et al., Journal of Materials Chemistry C 1 (2013) 3716−3721.

[9] C. Liu, P. Zhang, X. Zhai, F. Tian, W. Li, J. Yang, et al., Biomaterials 33 (2012) 3604−3613.

[10] J.-Y. Yin, H.-J. Liu, S. Jiang, Y. Chen, Y. Yao, ACS Macro Letters 2 (2013) 1033−1037.

[11] F. Wang, Z. Xie, H. Zhang, C.-y. Liu, Y.-g. Zhang, Advanced Functional Materials 21 (2011) 1027−1031.

[12] X. Gao, K. Tam, K.M.K. Yu, S.C. Tsang, Small (Weinheim an der Bergstrasse, Germany) 1 (2005) 949−952.

[13] S. Chandra, P. Das, S. Bag, D. Laha, P. Pramanik, Nanoscale 3 (2011) 1533−1540.

[14] Y. Mao, Y. Bao, D. Han, F. Li, L. Niu, Biosensors and Bioelectronics 38 (2012) 55−60.

[15] M. Zheng, S. Liu, J. Li, D. Qu, H. Zhao, X. Guan, et al., Advanced Materials 26 (2014) 3554−3560.

[16] H.X. Zhao, L.Q. Liu, Z.D. Liu, Y. Wang, X.J. Zhao, C.Z. Huang, Chemical Communications 47 (2011) 2604−2606.

[17] Y. Mao, Y. Bao, L. Yan, G. Li, F. Li, D. Han, et al., RSC Advances 3 (2013) 5475−5482.

Photodetector applications of carbon and graphene quantum dots

6

Suvra Prakash Mondal[1] *and Tanmoy Majumder*[1,2]
[1]Department of Physics, National Institute of Technology, Agartala, Tripura, India,
[2]Department of Electronics and Communication Engineering, Tripura Institute of Technology, Agartala, Tripura, India

6.1 Introduction

One of the most abundant and environmental friendly elements in earth is carbon (C). Interestingly, 18% of our human body is consisted of carbon atoms. The carbon atoms can be bonded together in various ways and form different allotropes due its valency. Since 19th century, several research works have been conducted on the growth and properties of various carbon materials [1]. Nowadays, carbon-based nanomaterials such as graphene, fullerenes, carbon nanotubes, and carbon-based quantum dots (QDs) are investigated extensively for their interesting electrical, optical, and mechanical properties [2]. Semiconductor QDs such as CdSe, CdS, CdTe, PbS, PbSe, CuInS, CuInSe, etc. have been extensively investigated in various photodetectors and optoelectronic devices because of their excellent size, tuneable photoabsorption, and emission properties in broad spectral range due to quantum confinement effect [3–7]. Despite having superior photoaborption and quantum efficiency (QE), semiconductor QDs suffer from several bottlenecks like high level of toxicity, complex synthesis process, and high chemical precursor cost. Recently, zero-dimensional (0D) carbon nanomaterials like carbon quantum dots (CQDs) and graphene quantum dots (GQDs) have attracted much attention for their photoabsorption and emission properties similar to that of semiconductor QDs [8,9]. These 0D carbon nanomaterials can replace the conventional semiconductor QDs because of low toxicity, less synesis cost, chemical inertness, and environmental friendly nature [8–14]. GQDs are theoretically 0D graphene material and consist of atomically thin graphitic plane of 2 nm thick (generally 1 or 2 layers) of carbon atoms with lateral size within 10 nm [15]. Although graphene exhibits infinite exciton Bohr radius in theoretical point of view, GQDs exhibit several unique features such as nonzero bandgap owing to quantum confinement effect, excellent dispersibility, and copious active sites. On the other hand, CQDs are spherical carbon particles consisting of amorphous sp^3 carbon or crystalline sp^2 core surrounded by amorphous layers [16]. The typical diameter of CQDs is ~10 nm. It has been reported that GQDs are crystalline in nature compared to CQDs. CQDs usually exhibit

Carbon Quantum Dots for Sustainable Energy and Optoelectronics. DOI: https://doi.org/10.1016/B978-0-323-90895-5.00016-3
© 2023 Elsevier Ltd. All rights reserved.

relatively broad X-ray diffraction (XRD) peak due to amorphous carbon layers. Both GQDs and CQDs demonstrate very strong and size tuneable optical absorption and emission properties; therefore, these QDs have been applied in photodetectors [17–19], bioimaging [11], light-emitting diodes (LEDs) [20], chemical sensors [21], photoelectrochemical cells [22–26], solar cells [27] and photocatalytic [28] applications. These QDs are highly stable, chemically inert, possess excellent photostability, nontoxic, and overall less expensive. Due to unique size-dependent optical and electrical behaviors, GQDs and CQDs are attractive candidates for photosensitizer with semiconductors nanomaterials. In this chapter, we focus on the potential use of GQDs and CQDs for UV and broadband photodetector applications.

6.2 Synthesis of carbon quantum dots and graphene quantum dots

The synthesis of CQDs and GQDs can be done by two major nanomaterial growth techniques: top-down and bottom-up approaches. Top-down method involves direct cutting of bulk carbon materials into nanosized CQDs or GQDs via chemical or electrochemical exfoliation, laser ablation, ultrasonication techniques, etc. The major advantages of top-down approach are the large availability of raw carbon materials, and abundant oxygen-containing functional groups, which facilitate solubility and functionalization. However, the major bottlenecks of top-down methods are noncontrollable of size and shape, large defect states, low quantum yield, etc. In the bottom-up approach CQDs or GQDs can be grown from suitable molecular precursors, like small molecules and polymers using hydrothermal techniques, microwave-assisted growth, metal catalyzed methods, etc. In comparison to top-down approach, synthesis of CQDs or GQDs using bottom-up approach has several advantages, such as control size and morphology, less defects states, and high quantum yield. However, poor solubility and agglomeration issues are the major bottlenecks of this bottom-up approach.

6.2.1 Top-down synthesis process

Using top-down method, CQDs/GQDs can be easily grown from graphite powder, carbon nanotubes, carbon soot, graphite oxide, and charcoals, etc. by chemical oxidation, laser ablation, arc discharge, and electrochemical methods. At first, Xu et al. synthesized fluorescent CQDs while purifying single-walled carbon nanotubes (SWCNTs) using arc discharge [29]. Several researchers synthesized CQDs by laser ablation of graphite powder [29]. Ming et al. reported electrochemical synthesis of high-quality CQDs from graphite rods in aqueous medium. In their synthesis method, graphite rods were used as anode as well as cathode. A static DC potential of 15–60 V was applied between two electrodes [30]. Feng et al. reported the growth of CQDs from coke using green chemical oxidation process [31]. The relative quantum yield of such coke-based CQDs was 9.2% [31].

Dong et al. fabricated single layered GQDs using a simple hydrothermal etching method from single-walled carbon nanotubes (SWCNTs) [32]. Fig. 6.1A shows the schematic representation of growth of GQDs from SWCNTs. The average lateral size and height of GQDs estimated from transmission electron micrograph (TEM) and atomic force micrograph (AFM) were found to be 8 nm and 0.5 nm, respectively (Fig. 6.1B and C). Several researchers reported synthesis of GQDs from coal and coal tar pitch (CTP) [33–36].

Dong et al. synthesized single-layer GQDs from coal using chemical route [33]. GQDs were prepared from six coal samples with different grade. The schematic representation of growth of GQDs from coal powder is presented in Fig. 6.2A. The plane-view TEM micrograph presented in Fig. 6.2B indicates that the size of grown GQDs is approximately 10 nm. Fig. 6.2C shows the AFM topography of b-GQDs. The section analysis showed that the height of b-GQDs is 0.3–0.9 nm.

6.2.2 Bottom-up synthesis process

Both CQDs and GQDs can be grown by bottom-up synthesis process from small molecular precursors such as glucose, citric acid, ascorbic acid, chitosan, and different types of carbohydrates molecules using microwave heating, hydrothermal, solvothermal synthesis process, etc. [37–41]. Bourlinos et al. synthesized CQDs from ammonium citrate using one-step thermal decomposition method [42]. Liu et al. synthesized highly luminescent N doped CQDs using microwave pyrolysis method using citric acid and amine molecules as precursors [43]. S and N co-doped GQDs can be synthesized from citric acid and thiourea using hydrothermal methods [44]. Fig. 6.3 shows the schematic growth process of S,N co-doped GQDs.

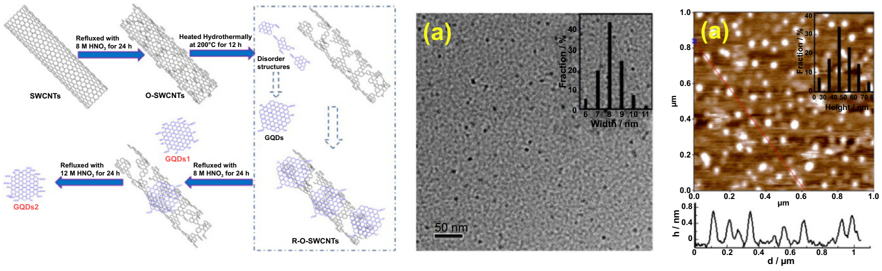

(A) (B) (C)

Figure 6.1 (A) Schematic representation for the growth of GQDs from SWCNTs. (B) Typical TEM micrograph of GQDs grown from SWCNTs. (C) AFM images of GQDs. The corresponding height profile is also present. GQDs, graphene quantum dots; SWCNTs, single-walled carbon nanotubes.
Reprinted with permission from Y. Dong, H. Pang, S. Ren, C. Chen, Y. Chi, and T. Yu, Etching single-wall carbon nanotubes into green and yellow single-layer graphene quantum dots, Carbon 64 (2013) 245–251. Copyright 2013, Elsevier.

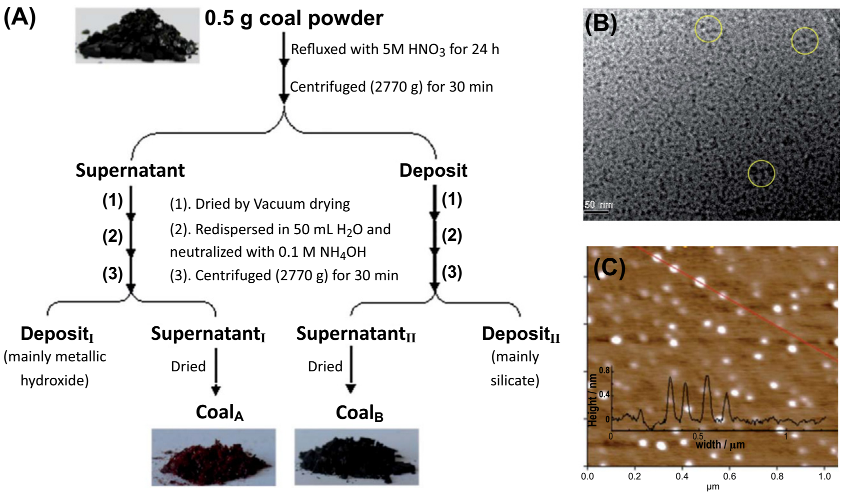
(A)
0.5 g coal powder
Refluxed with 5M HNO3 for 24 h
Centrifuged (2770 g) for 30 min
Supernatant
Deposit
(1)
(2)
(3)
(1). Dried by Vacuum drying
(2). Redispersed in 50 mL H2O and neutralized with 0.1 M NH4OH
(3). Centrifuged (2770 g) for 30 min
DepositI (mainly metallic hydroxide)
SupernatantI
SupernatantII
DepositII (mainly silicate)
Dried
CoalA
CoalB
(B)
50 nm
(C)
Height / nm
0.8
0.4
0
0.5
1
width / μm
0.0
0.2
0.4
0.6
0.8
1.0
μm

Figure 6.2 (A) Treatment procedures of coal samples. (B) TEM image. (C) AFM image of GQDs. *TEM*, transmission electron micrograph; *AFM*, atomic force micrograph; *GQDs*, graphene quantum dots.
Reproduced with permission from Y. Dong, J. Lin, Y. Chen, F. Fu, Y. Chi, and G. Chen, Graphene quantum dots, graphene oxide, carbon quantum dots and graphite nanocrystals in coals, Nanoscale 6 (2014) 7410–7415. Copyright 2014, Royal Society of Chemistry.

Qu et al. synthesized N doped and S, N co-doped GQDs using hydrothermal synthesis route [45]. In this method, citric acid was used as C source and urea, thiourea were used as N, S source, respectively. S and N doping enhanced optical absorption of GQDs in broad spectral range from UV to visible region. N doped GQDs can be synthesized from citric acid and urea using hydrothermal method [23]. Fig. 6.4A and B represents AFM and TEM images of NGQDs, respectively. From AFM and TEM study, it has been observed that NGQDs consist of 1–3 monolayers of graphene with size of 3–7 nm.

Tam et al. reported the growth of boron doped GQDs using hydrothermal method [46]. The B doped GQDs were synthesized from glucose in the presence of boric acid during hydrothermal reaction. The schematic growth process and TEM micrographs of B doped GQDs of lateral size is 4 nm are represented in Fig. 6.5A and B, respectively.

6.3 Optical absorption, emission, and electrical properties

Study of optical properties of CQDs and GQDs is very much important for their application in several optoelectronic devices like photodetectors, solar cell, photoelectrochemical cells, LEDs, etc. Most of the GQDs and CQDs exhibit two distinct

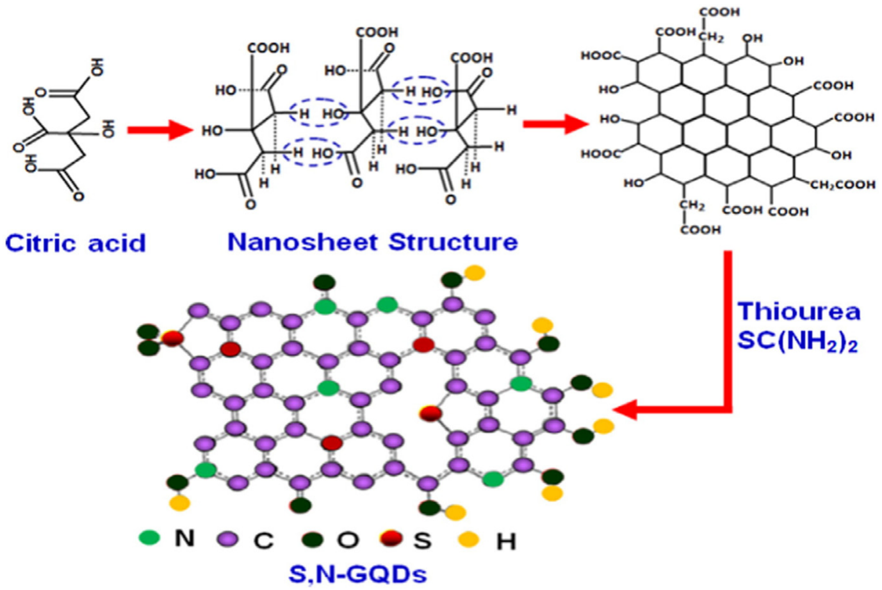
Citric acid
Nanosheet Structure
Thiourea
SC(NH₂)₂
N
C
O
S
H
S,N-GQDs

Figure 6.3 Schematic growth process of S, N co-doped GQDs [44]. *GQDs*, graphene quantum dots.
Reprinted with permission from J.J.L. Hmar, T. Majumder, S. Dhar, and S.P. Mondal, Sulfur and nitrogen Co-doped graphene quantum dot decorated ZnO nanorod/polymer hybrid flexible device for photosensing applications, Thin Solid Films 612 (2016) 274–283. Copyright 2016, Elsevier.

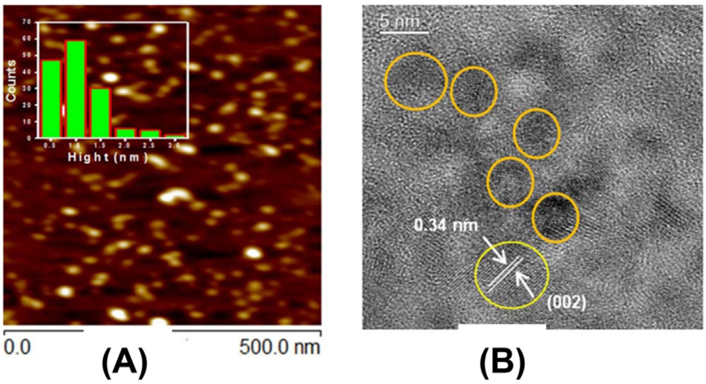
Counts
Hight (nm)
0.0
500.0 nm
(A)
5 nm
0.34 nm
(002)
(B)

Figure 6.4 (A) AFM micrograph of NGQDs. Height distribution plot is presented at inset. (B) HRTEM micrograph of NGQDs.
Reprinted with permission from T. Majumder, K. Debnath, S. Dhar, J. J. L. Hmar, and S. P. Mondal, Nitrogen-doped graphene quantum dot-decorated ZnO nanorods for improved electrochemical solar energy conversion, Energy Technology 4 (2016) 950–958. Copyright 2016, Wiley-VCH Verlag GmbH & Co.

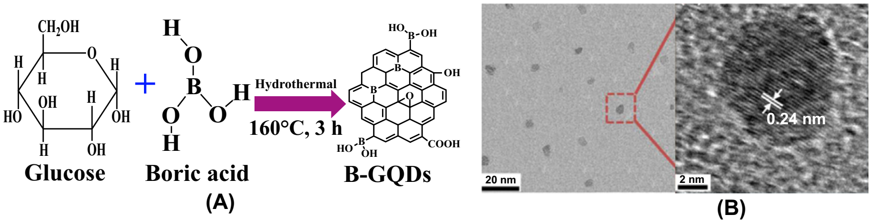

Figure 6.5 (A) Schematic grown scheme of boron doped GQDs (BGQDs). (B) TEM and HRTEM micrographs of BGQDs.
Reproduced with permission from T.V. Tam, S.G. Kang, K.F. Babu, E.-S. Oh, S.G. Lee, and W.M. Choi, Synthesis of B doped graphene quantum dots as a metal-free electrocatalyst for the oxygen reduction reaction, Journal of Materials Chemistry A 5 (2017) 10537–10543. Copyright 2017, Royal Society of Chemistry.

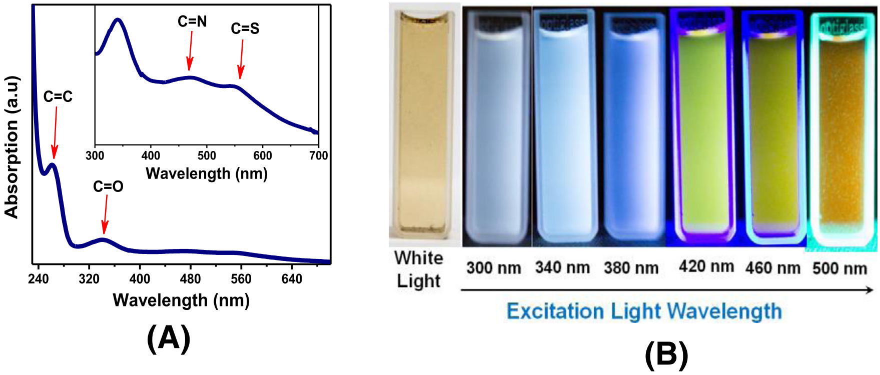

Figure 6.6 (A) Absorption spectrum of SNGQDs, C = N, C = S peaks are shown at inset. (B) Digital photograph of SNGQDs solution under incident of different wavelengths of light.
Reprinted with permission from T. Majumder, S. Dhar, P. Chakraborty, K. Debnath, S.P. Mondal, S, N co-doped graphene quantum dots decorated C doped ZnO nanotaper photoanodes for solar cells application, Nano 14 (2019) 1950012. Copyright 2019, World Scientific Publishing.

absorption peaks located nearly 220–240 nm and 320–360 nm, which lead to use of deep ultraviolet (DUV) photodetector. Commonly, the absorption peak at 220–250 nm is attributed to the $\pi-\pi^*$ transition of C = C bonds [47,48] and the peak at 320–360 nm is ascribed to $n-\pi^*$ transition of C = O bond [10,49,50]. The photoabsorption of GQDs and CQDs can be extended up to visible region by doping various elements like boron (B) [45], nitrogen (N) [23,51], sulfur (S) [44], phosphorus (P) [52,53], chlorine (Cl) [54], potassium (K) [55], sodium (Na) [56], etc. Co-doping of atoms into the GQD matrix also improves optical and electrical properties for certain applications [44,47,57]. Fig. 6.6A shows the optical absorption spectrum of S, N co-doped GQDs synthesized by Majumder et al. [26]. Along with

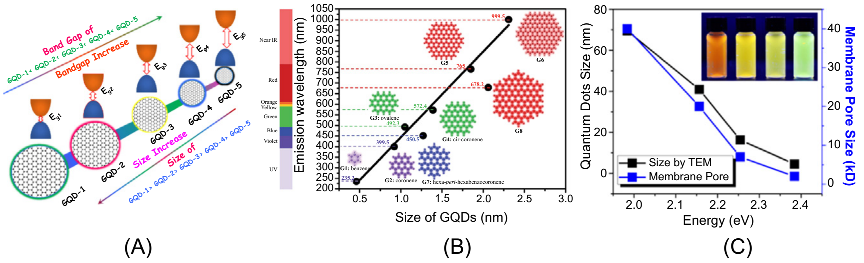

Figure 6.7 (A) Schematic illustration of variation of band gap of GQDs with size and morphology. (B) Emission wavelength (nm) plot as a function of diameter of GQDs using DFT method in vacuum. (C) Variation of band gap with the size of GQDs. PL emission from samples with various sizes of GQDs (inset). *DFT*, density-functional theory.
Reprinted with permission from R. Ye, Z. Peng, A. Metzger, J. Lin, J.K. Mann, K. Huang, et al., Bandgap engineering of coal-derived graphene quantum dots, ACS Applied Materials & Interfaces 7 (2015) 7041–7048. M.A. Sk, A. Ananthanarayanan, L. Huang, K.H. Lim, P. Chen, Revealing the tunable photoluminescence properties of graphene quantum dots, Journal of Materials Chemistry C 2 (2014) 6954–6960. Copyright 2014, Royal Society of Chemistry. Copyright 2015, American Chemical Society.

strong UV absorption, the spectrum shows visible photoabsorption in the wavelength region 450–600 nm due to the presence of C = N and C = S bonding.

Upon excitation of UV light, SNGQDs demonstrate excellent visible emission as depicted in Fig. 6.6B. Both GQDs and CQDs exhibit excellent photoluminescence (PL) behavior similar to semiconductor QDs, which is attractive for optoelectronic devices. However, due to the presence of surface traps, they demonstrate very low quantum yield. But it can be enhanced dramatically after surface passivation [20,58–60].

The optical as well as electrical nature of GQDs/CQDs can be modified by controlling the shape and size during the growth process. Fig. 6.7A shows the schematic representation of variation of band gap of GQDs with size. As the size decreases, the energy band gap increases similar to semiconductor QDs. Chen et al. established a relation between emission wavelength (band gap) and size of GQDs with the help of density-functional theory (DFT) [61]. Fig. 6.7B represents the variation of emission wavelength and size of GQDs using theoretical prediction. Despite a small deviation between theory and experimental results, the trend of variation of band gap with size of GQDs demonstrated good agreement with experimental results [61]. Fig. 6.7C shows the experimental study of variation of band gap with size by Ye et al. [61].

GQDs and CQDs often exhibit excitation-dependent PL emission. Fig. 6.8A and B show the excitation-dependent PL emission of NGQDs and SNGQDs at various excitation wavelengths (340–560 nm). Such red-shifted emission is attributed to the QDs size variation and presence of various impurity states. Electrical properties of CQDs/GQDs are similar to graphene oxide (GO) when it contains oxygenated functional groups. Such surface functional groups and doping of various elements also influence its electrical conductivity.

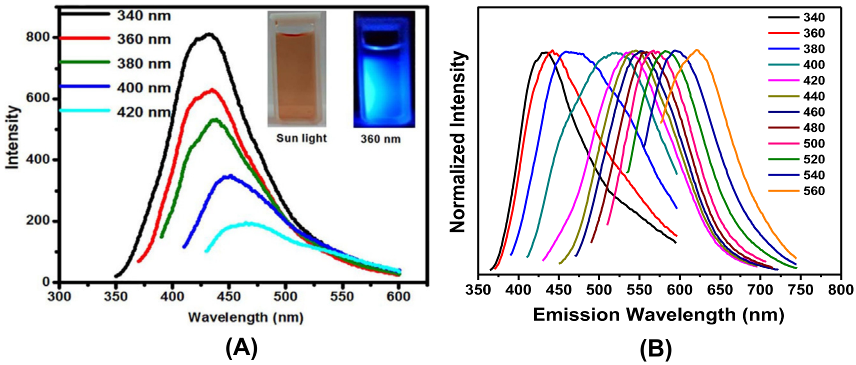

Figure 6.8 (A) PL spectra of NGQDs under excitation of light of wavelengths 340–420 nm. Photographs of NGQDs under sunlight and UV light (360 nm). (B) Normalized PL spectra of SNGQDs at various excitation wavelengths (340–560 nm).
Reprinted with permission from T. Majumder, S. Dhar, P. Chakraborty, K. Debnath, and S. P. Mondal, S, N co-doped graphene quantum dots decorated C doped ZnO nanotaper photoanodes for solar cells application, Nano 14 (2019) 1950012. T. Majumder, K. Debnath, S. Dhar, J. J. L. Hmar, S. P. Mondal, Nitrogen-Doped Graphene Quantum Dot-Decorated ZnO Nanorods for Improved Electrochemical Solar Energy Conversion, Energy Technology 4 (2016) 950–958. Copyright 2019, World Scientific Publishing; Copyright 2016, Wiley-VCH Verlag GmbH & Co.

6.4 Optoelectronics applications of carbon quantum dots and graphene quantum dots

0D carbon nanomaterials have been applied in wide range of optoelectronic devices due to their tuneable optical properties, large surface area, excellent charge transfer and transport, abundant active sites, and ease to integrate with semiconductor nanomaterials. GQDs/CQDs have been used by several researchers as photosensitizers in QD-sensitized solar cells, and studied as electron/hole transport layer in perovskite or organic solar cells. They have been also studied as active layers in dye-sensitized solar cells. For the applications of LEDs, GQDs are often utilized as electroluminescent phosphor, bandgap tuner, dopant materials in organic light emitter, and color converter. As GQDs are excellent photoabsorbers in wide spectral region, they have been studied as photosensitizers in photodetectors.

Tsai et al. studied a silicon-based heterojunction solar cell and improved power conversion efficiency up to 16.55% by utilizing GQDs [62]. Schematic representation of solar cell, top-view, and cross-sectional SEM images of the solar cell is presented in Fig. 6.9A–C, respectively. The IV characteristics of Si/GQDs solar cell are shown in Fig. 6.9D. After sensitization of GQDs, short circuit current density and photoconversion efficiency have been increased from 35.31 mA/cm^2 to 37.47 mA/cm^2 and from 14.77% to 16.55%, respectively. Song et al. reported eco-friendly and cost-effective GQD-based LED [63]. The schematic LED device structure, and energy band diagram is shown Fig. 6.9E. Electroluminescent image of

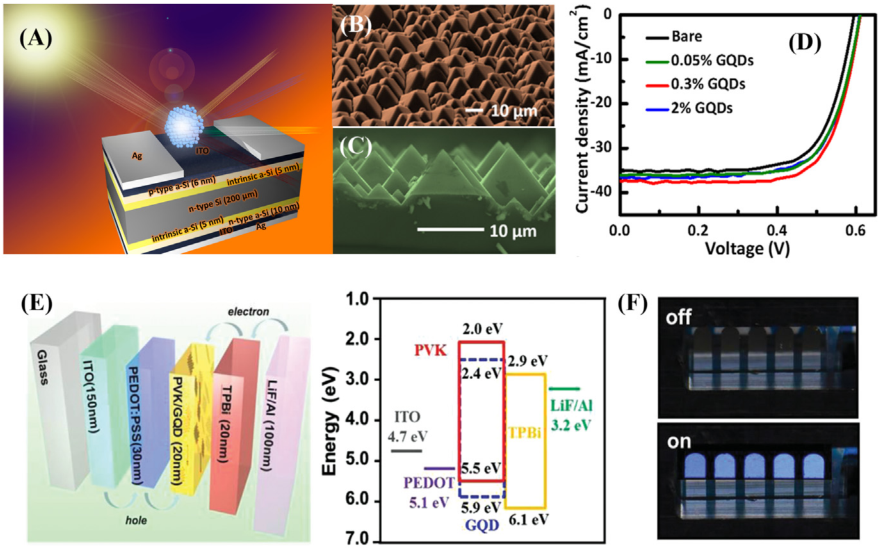
(A)
Ag
ITO
p-type a-Si (6 nm)
intrinsic a-Si (5 nm)
n-type Si (200 μm)
intrinsic a-Si (5 nm)
n-type a-Si (10 nm)
ITO
Ag
(B)
10 μm
(C)
10 μm
(D)
Current density (mA/cm²)
0
-10
-20
-30
-40
Bare
0.05% GQDs
0.3% GQDs
2% GQDs
0.0
0.2
0.4
0.6
Voltage (V)
(E)
electron
Glass
ITO(150nm)
PEDOT:PSS(30nm)
PVK/GQD (20nm)
TPBi (20nm)
LiF/Al (100nm)
hole
Energy (eV)
1.0
2.0
3.0
4.0
5.0
6.0
7.0
PVK
2.0 eV
2.4 eV
2.9 eV
ITO
4.7 eV
PEDOT
5.1 eV
5.5 eV
5.9 eV
GQD
TPBi
6.1 eV
LiF/Al
3.2 eV
(F)
off
on

Figure 6.9 (A) Schematic, (B) top-view SEM, (C) cross-section SEM image of Si/GQDs heterojunction solar cell. (D) IV characteristics of Si/GQD solar cell. (E) Schematic of GQD-based LED structure with energy band diagram. (F) Electroluminescent image of GQD-based LEDs.
Reprinted with permission from S. H. Song, M.-H. Jang, J. Chung, S. H. Jin, B. H. Kim, S.-H. Hur, et al., Highly efficient light-emitting diode of graphene quantum dots fabricated from graphite intercalation compounds, Advanced Optical Materials 11 (2014) 1016−1023. M.L. Tsai, W.C. Tu, L. Tang, T.C. Wei, W.-R. Wei, S.P. Lau, et al., Efficiency enhancement of silicon heterojunction solar cells via photon management using graphene quantum dot as downconverters, Nano Letters 1 (2016) 309−313. Copyright 2016, American Chemical Society. Copyright 2014, Wiley-VCH Verlag GmbH & Co.

GQD-based LEDs before and after bias is shown in Fig. 6.9F. The maximum luminescence has been observed ~1000 cd/m^2 at 16 V. In the present report, we focus on the study of various kinds of photodetectors using CQDs and GQDs.

6.5 Photodetector applications of carbon quantum dots and graphene quantum dots

Based on the sample geometry, CQDs/GQDs-based photodetectors can be classified into following three types of devices: (1) field effect transistor (FET)-based photodetectors, (2) CQDs or GQDs-sensitized nanomaterial-based UV and broadband photodetectors, and (3) polymer nanocomposite-based photodetectors. Depending upon photoabsorption, two major photodetectors were reported, namely UV photodetectors and broadband photodetectors.

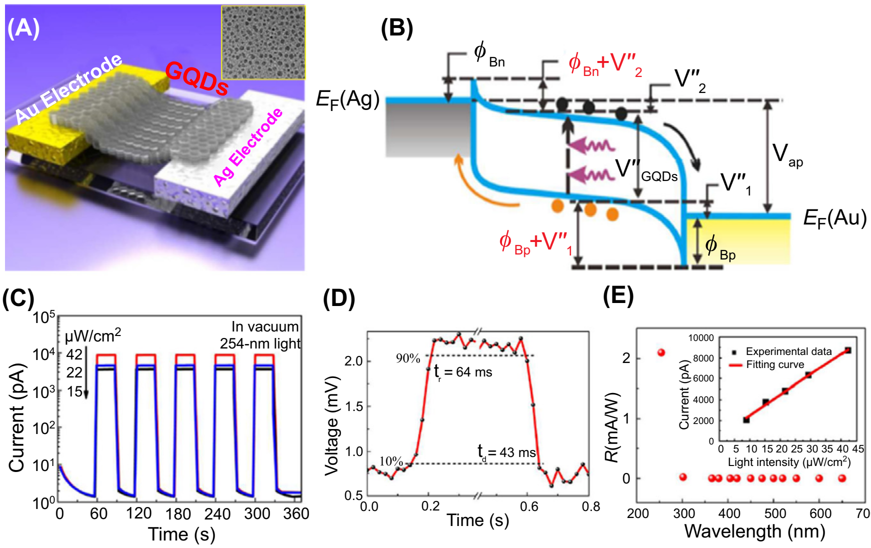

Figure 6.10 (A) Schematic device structure of DUV photodetector. (B) Energy band diagram and carrier transport mechanism in asymmetric Ag-Au electrodes. (C) Transient photoresponse of the device at various intensities of 254 nm UV light. (D) Rise and decay curve of transient photoresponse. (E) Responsivity plot of the photodetector at +5 V bias. The photocurrent variation with light intensity at +5 V bias is presented at inset. Reprinted with permission from Q. Zhang, J. Jie, S. Diao, Z. Shao, Q. Zhang, L. Wang, et al., Solution-processed graphene quantum dot deep-UV photodetectors, ACS Nano 2 (2015) 1561–1570. Copyright 2015, American Chemical Society.

6.5.1 FET-based photodetectors using carbon quantum dots and graphene quantum dots

FET-based photodetectors were studied by dispersing a thin layer of GQDs on insulating substrates like glass, quartz, SiO_2/Si, etc. Some researchers fabricated photodetector devices after depositing GQDs on graphene and transition metal dichalcogenide (TMD) films, which acted as fast electron transport layer due to their 2D geometry. However, in both types of devices, electrical contacts were made laterally using metal electrodes. Zhang et al. fabricated DUV photodetectors with fast-response time and high-sensitivity [64]. The photodetector device was fabricated after deposition of Ag and Au asymmetric electrodes on quartz substrates. Solution processed GQDs of size 4–5 nm and thickness 0.4–2.5 nm consisting of 1–4 layers of graphene were deposited on the electrodes. Fig. 6.10A represents the schematic diagram of device structure. Under DUV light, excitation carrier excited to LUMO of the GQDs and transported one GQD to another via hopping. Carrier transport mechanism in asymmetric Ag-Au electrodes under illumination is shown in Fig. 6.10B. Even after illumination of 254 nm UV light with weak intensity of 42 μW/cm², their device showed on/off ratio of ~6000. The response and recovery

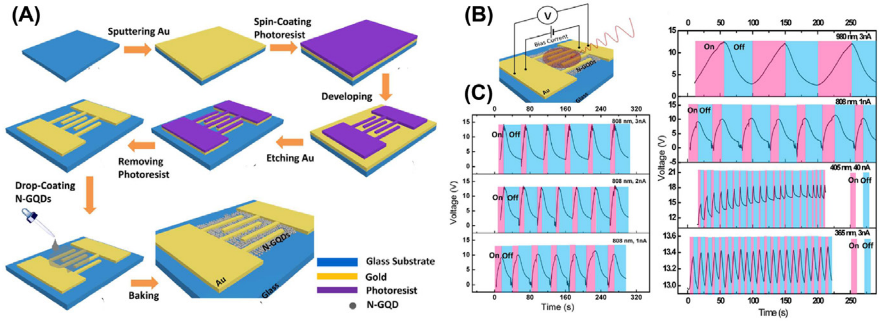

Figure 6.11 (A) Schematic representation of the photodetector fabrication process. (B) The schematic device structure of the photodetector under bias. (C) The transient photoresponse of NGQDs-based photodetector with various light sources and bias currents.
Reprinted with permission from L. Tang, R. Ji, X. Li, G. Bai, C.P. Liu, J. Hao, et al., Deep ultraviolet to near-infrared emission and photoresponse in layered N-doped graphene quantum dots, ACS Nano 6 (2014) 6312−6320. Copyright 2014, American Chemical Society.

time of the device were 64 Ms and 43 Ms, respectively. Fig. 6.10C shows transient photoresponse of the DUV device under various intensities (15−42 mW/cm^2) of 254 nm UV light in vacuum condition at +5 V bias. The estimation of rise and decay time from the transient photoresponse is presented in Fig. 6.10D. The photodetector demonstrated responsivity of 2.10 mA/W (Fig. 6.10E).

Materials that absorb light from spectral range covering DUV, visible, and near-infrared regions are attractive for broadband photodetectors. Such materials can also be applied in broadband modulators, solar cells, bioimaging, and optical fiber communications. Several research work have been conducted on broadband photodetection using a combination of low- and high-band gap semiconductors. However, fabrication of such detector using a single material is very much attractive due to simple device configuration. Tang et al. fabricated broadband photodetector in the wavelength range 300−1000 nm using chemically grown NGQDs [65]. The broadband photoabsorption of the detector was attributed to the layered structure of the NGQDs. Fig. 6.11A represents the schematic fabrication process of the device using photolithography. The photodetector device was fabricated by drop coating NGQDs on interdigitated gold electrodes (Fig. 6.11A). The photodetector under bias condition is presented in Fig. 6.11B. The photoresponse of NGQDs was monitored under different monochromatic light illuminations (Fig. 6.11C). The maximum responsivity of the detector was 325 V/W at 405 nm.

Tetsuka et al. synthesized o-phenylenediamine (OPD-GQDs) and diaminonaphthalene (DAN-GQDs) functionalized NGQDs with tailored optical properties and studied photodetection using graphene/NGQDs hybrid phototransistors [66]. The NGQD was deposited on the top of a graphene-based field-effect transistor. Fig. 6.12A shows the schematic representation of the photodetector, where p-Si with 90 nm SiO$_2$ layer was used as substrate, graphene used as carrier transport

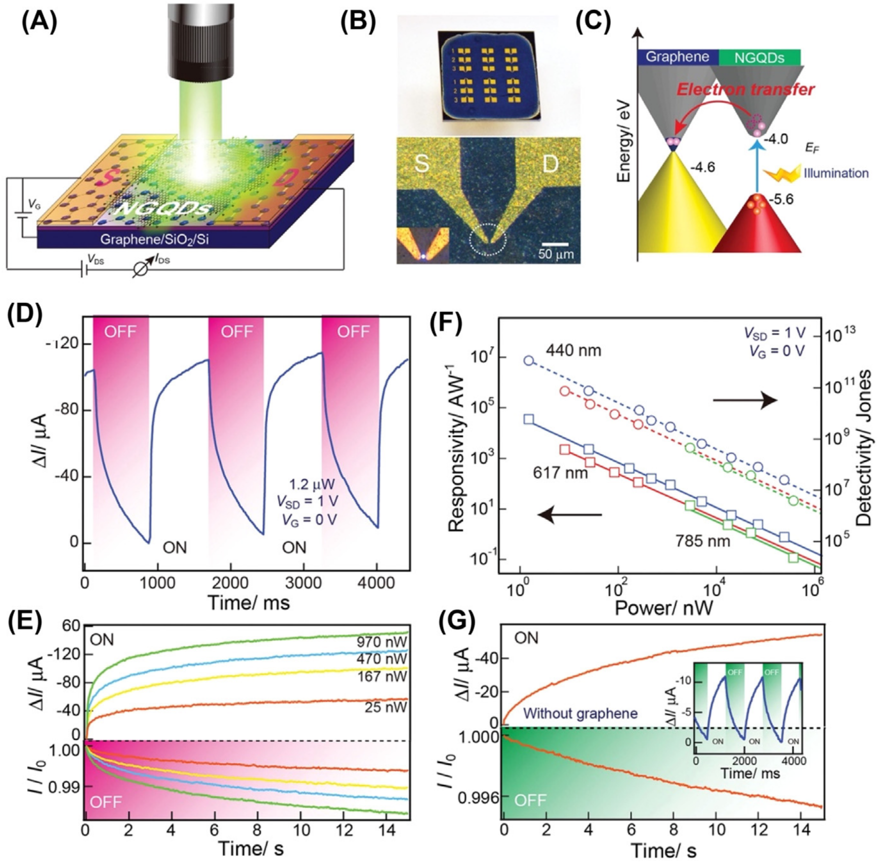

Figure 6.12 (A) Graphic diagram of a graphene/NGQDs FET-based phototransistor. (B) Digital photographic images of the devices. (C) Carrier transport mechanism at graphene/NGQDs junction under illumination. (D) Photocurrent response of the photodetector. (E) Variation of the response time with the excitation power of 25 to 970 nW. (F) Change in responsivity and detectivity with optical power (laser wavelengths 440−785 nm). (G) The on and off photocurrent response of the OPD-GQDs phototransistor without any graphene layer. Temporal photocurrent response is presented at inset.
Reprinted with permission from H. Tetsuka, A. Nagoya, T. Fukusumi, and T. Matsui, Molecularly designed, nitrogen-functionalized graphene quantum dots for optoelectronic devices, Advanced Materials 28 (2016) 4632−4638. Copyright 2016, Wiley-VCH Verlag GmbH & Co.

layer, and NGQDs used as photon absorption layer. The actual digital photograph of graphene/NGQDs phototransistor is shown in Fig. 6.12B. Fig. 6.12C illustrates the charge transfer mechanism from NGQDs to graphene layer under illumination. The temporal photoresponse under illumination of 440 nm laser light with intensity 1.2 μW is shown in Fig. 6.12D. The change in photocurrent with time under the excitation power varied from 25 to 970 nW for graphene/OPD-GQDs phototransistor is shown in Fig. 6.12E. Fig. 6.12F shows photoresponsivity and detectivity plots under different illumination power (laser wavelengths 440−785 nm). The photocurrent response under on/off condition of the phototransistor without any graphene layer is presented in Fig. 6.12G. Temporal photocurrent response is presented at inset. Graphene/NGQDs phototransistor demonstrated high photoconductive gain of $\approx 2\times 10^{10}$. Photoresponsivity and detectivity of the device increase linearly with the decrease of power of the incident laser of power 1.5 nW. The maximum photoresponsivity and detectivity were $\sim 3.5\times 10^{4}$ A/W and $\sim 1.2\times 10^{12}$ J, respectively. The same group also improved the device performance using a boron nitride nanosheets buffer layer for efficient charge separation, and transport of photogenerated carriers from NGQDs. The photodetector demonstrated photoresponsivity and detectivity of 2.3×10^{6} A/W and 5.5×10^{13} Jones, respectively, in the DUV range without any back-gate voltage [67]. Kim et al. studied graphene/GQD/graphene-based photodetector, which demonstrated strong responsivity in UV-Vis-NIR range [68]. Such GQD sandwiched between graphene layers photodetector showed detectivity $>10^{11}$ cm Hz1/2/W and responsivity 0.2−0.5 A/W in the UV to near infrared region.

Recently, 2D TMD materials such as MoS_2, WS_2, $MoSe_2$, WSe_2, and $MoTe_2$ have attracted much attention for photodetector application for their high carrier mobility, excellent tuneable band gap, and high ON/OFF ratio. But due to their 2D structure and atomically thin layers, the photoabsortion and emission are very limited. Therefore, the combination of 2D materials and QDs is particularly attractive for photodetector devices. As QDs are excellent photoabsorbers, they can inject photogenerated carriers into the 2D layers of TMDs efficiently, and the photogenerated carriers can be transported to the electrodes very fast due to the superior carrier mobility of 2D structures.

Nguyen et al. reported a hybrid nanostructure consisting of monolayer (ML) WSe_2 covered with NGQDs (WSe_2/NGQDs) thin films [69]. Fig. 6.13A and B represent the schematic diagram of ML WSe_2 FET device and optical photograph of ML WSe_2/NGQDs devices, respectively. Gate voltage characteristics of both devices at VDS = 1 V are shown in Fig. 6.13C. Fig. 6.13D shows schematic view of ML WSe_2/NGQD under light. Time-dependent photocurrent response of both devices is shown in Fig. 6.13E. FET characteristic transfer curves under dark and light illumination condition and along with different intensities of lights are presented in Fig. 6.13F and G. Photoresponsivity of WSe_2/N-GQD photodetector was reported to be about 480% higher compared to WSe_2-based photodetector. Such high responsivity is accredited to the charge transfer from NGQDs to WSe_2. Responsivity plots as a function of back-gate voltage and power density of ML WSe_2/N-GQD photodetector are shown in Fig. 6.13H and I, respectively. The highest photoresponsivity was found to be 2578 A/W at power density of 1.9 μW/cm^2. The rise and decay time of the photodetector was found to be smaller than 0.5 s (Fig. 6.13J). Change in responsivity with back-gate voltage and bias voltage of ML WSe_2/N-GQD under light of wavelength $\sim$405 nm is presented in Fig. 6.13K. It is reported that the responsivity of the WSe_2/NGQD photodetector is stable under ambient experimental condition up to 30 days. Chen et al. reported the photodetector properties of GQDs deposited MoS_2 on thin film based phototransistors [70].

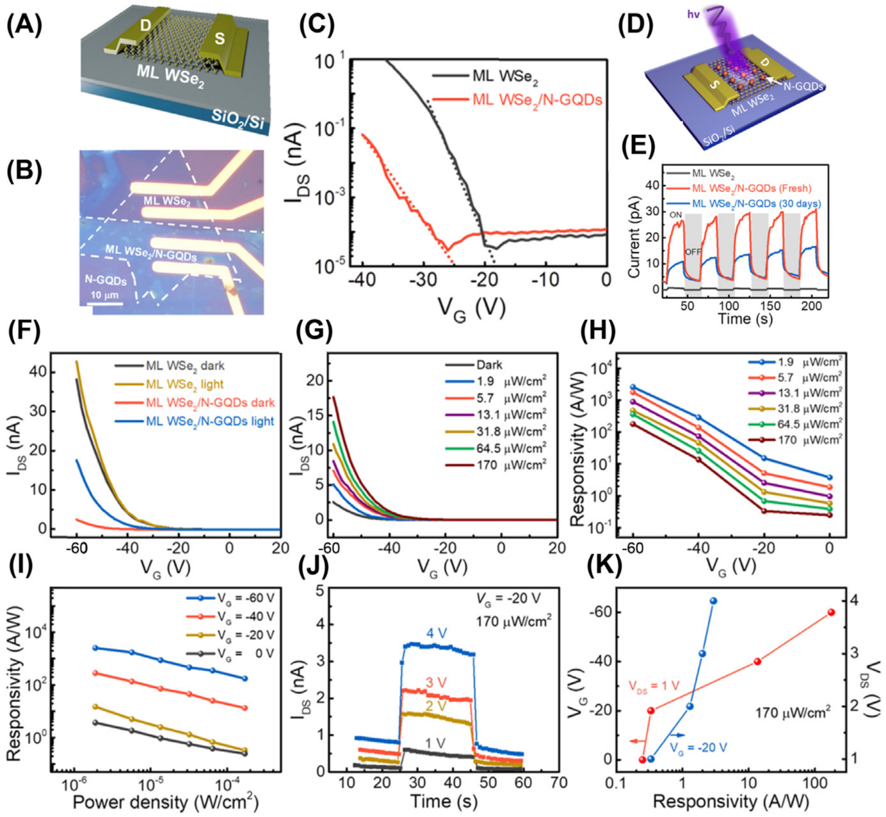

Figure 6.13 (A) Schematic image of monolayer (ML) WSe_2 FET device. (B) Optical microscopy image of ML WSe_2 FET and ML WSe_2/NGQDs devices. (C) Gate voltage characteristics at $V_{DS} = 1$ V. (D) Schematic view of ML WSe_2/NGQD under light. (E) Time-dependent photocurrent response of both devices at $V_{DS} = 1$ V and VG = 0 V. Transfer curves of ML WSe_2 and ML WSe_2/N-GQD devices (F) under dark and light and (G) under illumination of different intensities of lights. (H) Responsivity plots vs back-gate voltage plots of the ML WSe_2/N-GQD photodetector at various intensities. (I) Responsivity plots vs power density plots of ML WSe_2/N-GQD photodetector. (J) Transient photocurrent of ML WSe_2/N-GQD photodetector under different bias voltage. (K) Change in responsivity with gate and bias voltage of ML WSe_2/N-GQD under light of wavelength ~405 nm. Reprinted with permission from N.D. Nguyen, M.O. Hye, T.D. Ngoc, S. Bang, S.J. Yoon, and M.S. Jeong, Highly enhanced photoresponsivity of a monolayer WSe2 photodetector with nitrogen-doped graphene quantum dots, ACS Applied Materials & Interfaces 10 (2018) 10322–10329. Copyright 2018, American Chemical Society.

The phototransistor devices were fabricated on SiO_2/Si substrates as shown in Fig. 6.14A. MoS_2-GQDs device was fabricated after drop casting of GQDs solution on the MoS_2 layer followed by heat treatment at 70°C. The attachment of GQDs onto MoS_2 film creates an *n-n* type van der Waals heterostucture, which

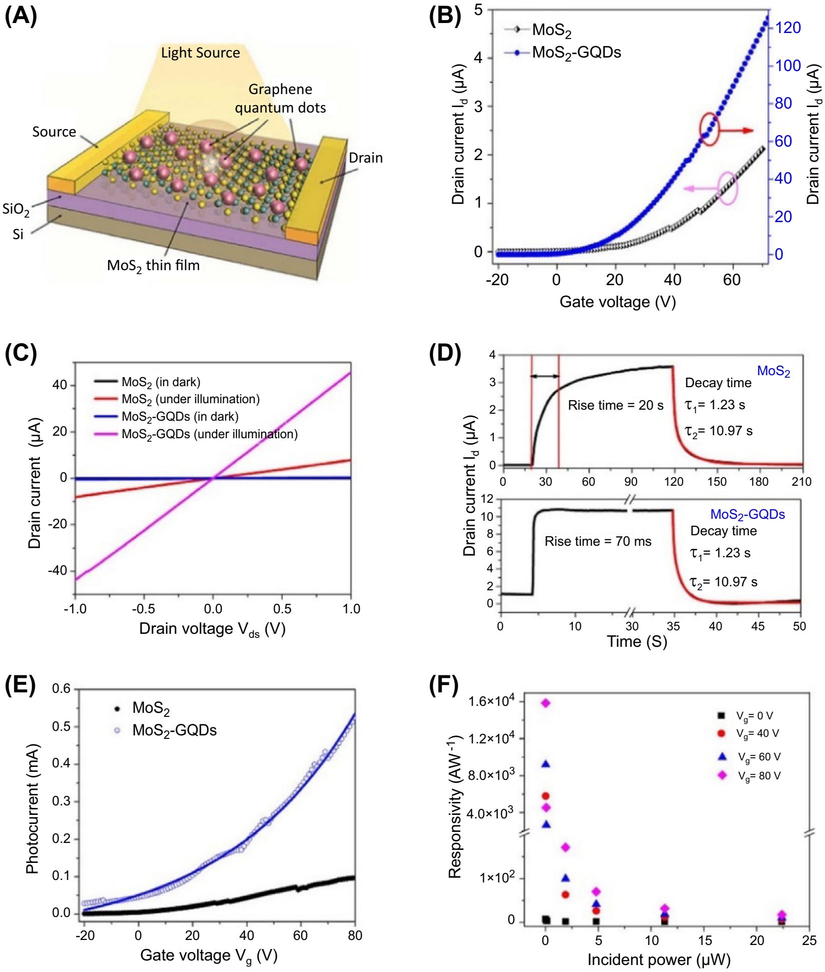

Figure 6.14 (A) Schematic device structure of a MoS_2/GQDs phototransistor. (B) Transfer curves of MoS_2 and MoS_2-GQDs devices with source-drain voltage: Vds = 1 V. (C) Drain current (Id) vs source-drain voltage (Vds) under light and dark. Laser wavelength ~ 405 nm with power ~ 17 μW. (D) Temporal photoresponse of MoS_2 and MoS_2/GQDs devices. (E) Variation of photocurrent vs gate voltage for both device under light of power ~30.1 μW. (F) Variation photoresponsivity with incident light power at different back-gate voltage.
Reprinted with permission from C. Chen, H. Qiao, S. Lin, C.M. Luk, Y. Liu, Z. Xu, et al., Highly responsive MoS2 photodetectors enhanced by graphene quantum dots, Scientific Reports 5 (2015) 11830. Copyright 2015, Springer Nature.

significantly improved the carrier mobility through the injection of photogenerated electrons from GQDs to MoS_2. Fig. 6.14B shows the transfer curves of MoS_2 and MoS_2-GQDs devices with source-drain voltage (V_{ds}) ~1 V. The drain current (I_d) vs source-drain voltage (V_{ds}) of both devices under light and dark is plotted in

Fig. 6.14C. After deposition of GQDs, the rise time of the photodetector was improved from 20 s to 70 Ms (Fig. 6.14D). The MoS_2-GQDs phototransistor device also demonstrated superior gate voltage dependent photocurrent under incident power ~30.1 μW (laser wavelength ~405 nm) (Fig. 6.14E).

The device demonstrated photoresponsivity of 1.6×10^4/AW with a photogain of 2.4×10^7 (Fig. 6.14F). The improvement of photodetection in MoS_2-GQDs phototransistor was explained on the basis of tunneling effect, the re-absorption of photons, and holes transfer from GQDs to MoS_2. Sun et al. fabricated heterojunction photodetector using p-type monolayer of WSe_2 and n-type Si substrate [71]. The WSe_2 layer was deposited by physical vapor deposition. The photodetector properties were elevated by incorporating GQDs on the WSe_2/Si heterojunction by drop coating of GQDs solutions. The GQDs/WSe_2/Si heterojunction showed responsivity of ~707 mA/W and detectivity of ~ 4.51×10^9 Jones. The device demonstrated response time of 0.2 Ms [71]. The superior photodetector performance of WSe_2/Si heterojunction after introduction of GQDs is attributed to strong light absorption and long carrier lifetimes. Wu et al. studied N-CQDs/graphene hybrid composites for UV photodetector application [72]. Photodetector was fabricated by spin-coating NCQDs on single layer graphene film deposited on SiO_2/p-type Si substrate. Negative responsivity up to 2.5×10^4/AW was observed under UV light of wavelength 375 nm.

6.5.2 Carbon quantum dots or graphene quantum dots-sensitized nanomaterial-based photodetectors

Several researchers applied GQDs or CQDs as photosensitizers similar to semiconductors QDs with nanorods and nanowires for enhancing the photoconducting properties of the device. These 0D carbon materials create favorable band alignment between the QDs and semiconductors and enhance the charge carrier transport to the electrodes. Dhar et al. studied a Schottky junction UV photodetector using ZnO nanorods (ZnO NRs) and conducting polymer poly 3,4-ethylenedioxythiophene: polystyrene sulfonate (PEDOT:PSS) junction [18,19]. The photodetector properties of such inorganic/organic heterojunction was enhanced after attachment of GQDs with ZnO NRs. Top-view SEM micrographs of ZnO NRs before and after spin coating of PEDOT:PSS are presented in Fig. 6.15A and B, respectively. Plane-view TEM micrographs of GQDs and GQDs decorated ZnO NRs are shown in Fig. 6.15C and D, respectively. The absorption and emission spectra are depicted in Fig. 6.15E and F. Due to strong UV absorption, both GQDs and NGQDs are attractive as photosensitizer with metal oxide semiconductors like TiO_2, ZnO, In_2O_3, etc. To demonstrate the photodetector behaviors of GQDs and NGQDs-sensitized nanorods, the following samples were prepared. The studied samples were (1) FTO/ZnO NRs/PEDOT:PSS/Ag (S1), (2) FTO/GQD decorated ZnO NRs/PEDOT:PSS/Ag (S2), and (3) FTO/NGQD decorated ZnO NRs/PEDOT:PSS/Ag (S3). Fig. 6.15G represents the *J-V* characteristics of S3 sample at dark condition and the illustration of the device is presented at inset. Under white light illumination, the reverse

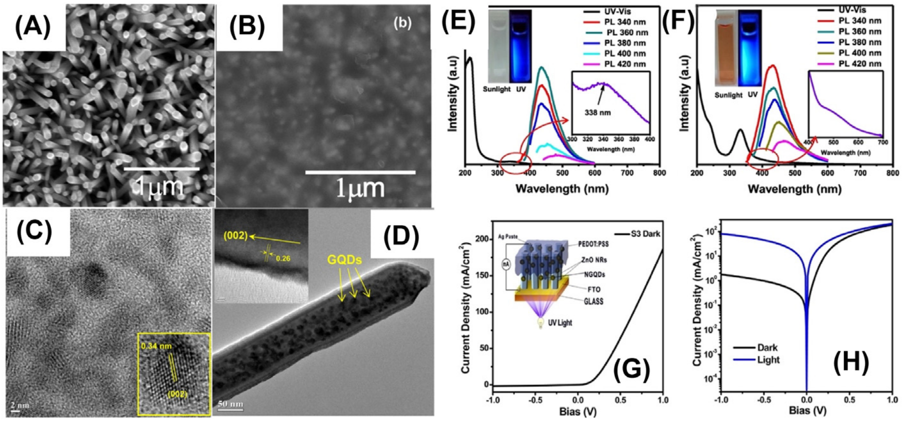

Figure 6.15 SEM image of ZnO nanorods (A) before and (B) after spin coating of PEDOT: PSS layer. (C) Plane-view TEM image of GQDs. Inset: HRTEM image of a GQD. (D) TEM image of GQDs coated ZnO NRs. Inset: HRTEM image of ZnO nanorods. Absorption and PL spectra of (E) GQDs and (F) NGQDs. Insets: Digital photographs of GQD and NGQD solutions. (G) J-V plot of S3 at dark condition. Inset: Schematic diagram of UV detector (S3 sample). (H) J-V plot in semilogarithmic scale of sample S3 under dark and light of intensity 80 mW/cm^2.

Reprinted with permission from S. Dhar, T. Majumder, S.P. Mondal, Graphene Quantum Dot-Sensitized ZnO Nanorod/Polymer Schottky Junction UV Detector with Superior External Quantum Efficiency, Detectivity, and Responsivity, ACS App. Mater. Interfaces 8 (2016) 31822–31831. Copyright 2016, American Chemical Society. S. Dhar, T. Majumder, and S.P. Mondal. Phenomenal improvement of external quantum efficiency, detectivity and responsivity of nitrogen doped graphene quantum dot decorated zinc oxide nanorod/polymer Schottky junction UV detector, Materials Research Bulletin 95 (2017) 198–203. Copyright 2016, Elsevier; T. Majumder, S.P. Mondal, Advantages of nitrogen-doped graphene quantum dots as a green sensitizer with ZnO nanorod based photoanodes for solar energy conversion, Journal of Electroanalytical Chemistry 769 (2016) 48–52, Copyright 2016, Elsevier.

saturation current of the device changes rapidly, as shown in Fig. 6.15H. Transient photoresponse of all samples under illumination of wavelength ~340 nm of power 0.38 mW/cm^2 is depicted in Fig. 6.16A. The on/off ratio for S3 detector was found to be three times and 78 times higher compared to S2 and S1 samples, respectively.

Responsivity and detectivity plots of S1, S2, and S3 samples are plotted in Fig. 6.16A–C, respectively. The responsivity and detectivity were found maximum at 340 nm wavelength for all samples. The responsivity values for S1, S2, and S3 samples are 3, 36, and 158 A/W, respectively. The detectivity values of above samples are 3.81×10^{11}, 1.72×10^{12}, and 8.75×10^{12} Hz$^{1/2}$/W, respectively. It is obvious that NGQD modified detector demonstrated higher photocurrent, responsivity, and detectivity in comparison with GQD modified and pristine ZnO NR detectors due to strong UV absorption of NGQDs. The photodetector performance of S3 sample was further improved by increasing the electrical conductivity of PEDOT:PSS

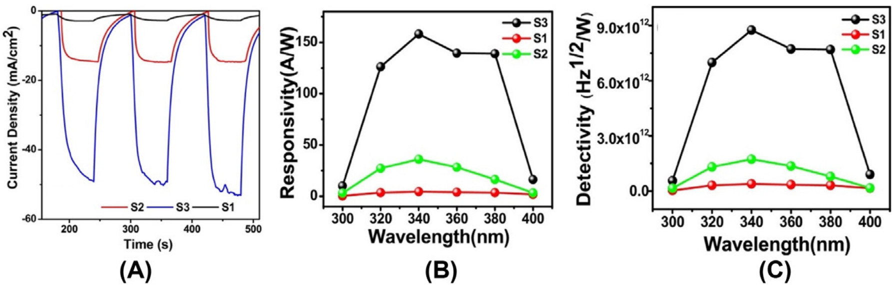

Figure 6.16 (A) Time-dependent photocurrent (J-t plot) of S1, S2, and S3 devices at 1 V bias and under UV light of wavelength 340 nm. (B) Responsivity and (B) detectivity plots for S1, S2, and S3 samples at 1 V bias.
Reprinted with permission from S. Dhar, T. Majumder, and S.P. Mondal. Phenomenal improvement of external quantum efficiency, detectivity and responsivity of nitrogen doped graphene quantum dot decorated zinc oxide nanorod/polymer Schottky junction UV detector, Materials Research Bulletin 95 (2017) 198–203. Copyright 2016, Elsevier.

polymer. The maximum responsivity was ~247 A/W at 340 nm wavelength at −1 V bias.

Xie et al. reported self-powered photodetector using CQD coated silicon nanowire (Si NW) core-shell heterojunction [73]. Vertical Si NW array was prepared by Ag-assisted chemical-etched process. Fig. 6.17A shows the schematic representation of the device structure. The CQD/Si NW core-shell heterojunction demonstrated rectifying nature with rectification ratio of 10^3 at ± 0.8 V under dark. The power conversion efficiency of the device was found to be 9.10% under AM 1.5 G irradiation. Fig. 6.17B shows IV plots of the sample in dark and under irradiation of light of wavelength 600 nm of intensity 100 mW cm^2. The device exhibited high photocurrent upto 0.1 mA at zero bias. The photosensitivity (I_{light}/I_{dark}) of the sample was found to be $\sim 3 \times 10^3$ (Fig. 6.17C). The rise time and fall time were obtained 20 and 40 μs, respectively (Fig. 6.17D). The transient photoresponse of Si NW array/CQD heterojunction photodetector under incidence of pulsed light of frequencies of 500, 1000, and 2200 Hz is presented in Fig. 6.17E. The device demonstrated responsivity of 353 mA/W.

Ghosh et al. fabricated GQD decorated ZnO nanorods based on UV photodetector with high photoresponsivity and detectivity at low applied potential [74]. In their study, GQDs, CQDs, GO, and RGO were prepared using solution growth process and sensitized with ZnO NRs grown on FTO substrates. UV photodetector properties were studied using all samples, and a comparative study was demonstrated. I-V characteristics of GQD/ZnO NRs at various intensities of 365 nm UV light are presented in Fig. 6.18A. The schematic device configuration is also shown at the inset of Fig. 6.18A. Responsivity vs wavelengths plot of optimized GQD/ZnO NRs device along with control sample is presented in Fig. 6.18B. The highest photoresponsivity and detectivity are $\sim 6.92 \times 10^4$ A/W and $\sim 1.78 \times 10^{15}$ Jones, respectively under 10 μW illumination of UV light at 2 V bias.

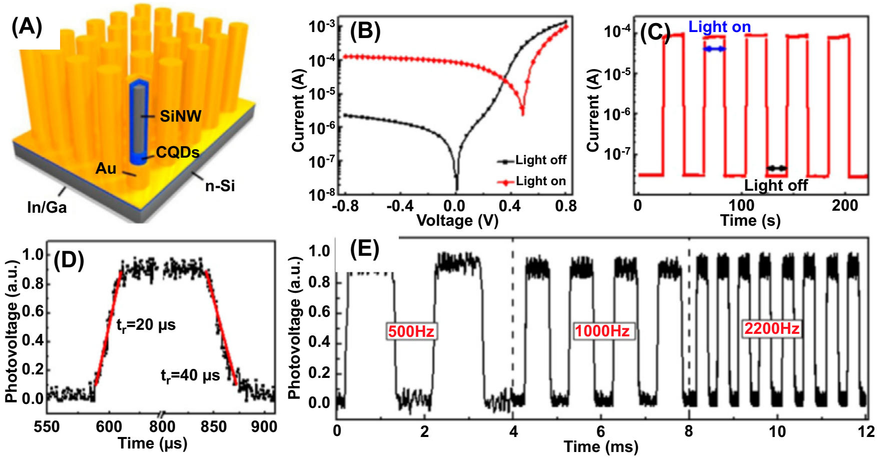

Figure 6.17 (A) Schematic diagram of the Si nanowire/CQD device. (B) I-V characteristics of Si NW array/CQD heterojunction under dark and illumination of light of 600 nm wavelength. (C) Transient photoresponse under on/off light. (D) Calculation of rise time and fall time. (E) Transient photoresponse of Si NW/CQD heterojunction under incident of pulsed light of frequencies of 500, 1000, and 2200 Hz.
Reprinted with permission from C. Xie, B. Nie, L. Zeng, F.X. Liang, M.Z. Wang, L. Luo, et al., Core shell heterojunction of silicon nanowire arrays and carbon quantum dots for photovoltaic devices and self-driven photodetectors, ACS Nano 8 (2014) 4015–4022. Copyright 2014, American Chemical Society.

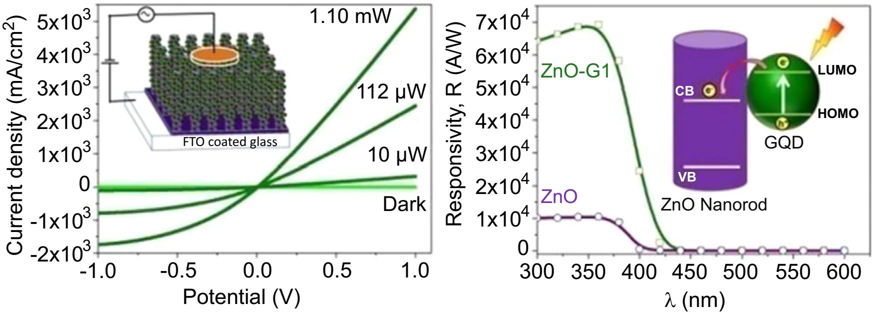

(A) **(B)**

Figure 6.18 (A) IV characteristics of GQD/ZnO NRs photodetector under incident of UV (~365 nm) light of different intensities. The schematic diagram of the device is shown at inset. (B) Responsivity vs wavelength plots of ZnO NRs and GQD/ZnO NRs. The schematic presentation of electron transfer is shown at inset.
Reprinted with permission from D. Ghosh, S. Kapri, and S. Bhattacharyya, Phenomenal ultraviolet photoresponsivity and detectivity of graphene dots immobilized on zinc oxide nanorods. ACS Applied Materials & Interfaces 8 (2016) 35496–35504. Copyright 2016, American Chemical Society.

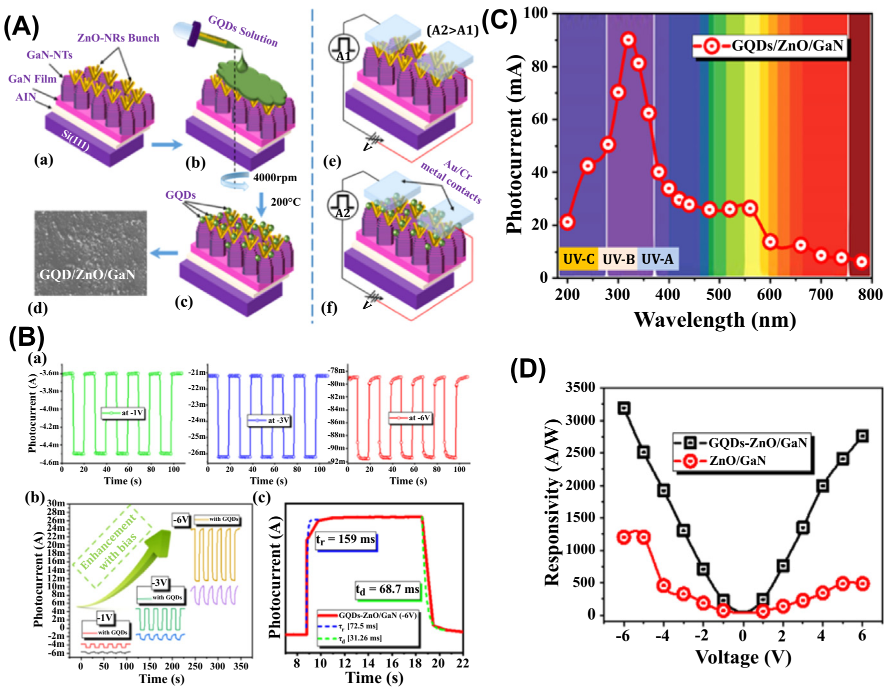

Figure 6.19 (A) Schematic representation for the device fabrication and electrical contacts of the GQD-sensitized ZnO NR/GaN-NT heterostructure. (B) Time-dependent photocurrent of GQD-sensitized UV detector and calculation of rise time and decay time. (C) Photocurrent vs wavelength plot of the GQD-sensitized ZnO/GaN-based device. (D) Responsivity vs applied bias plot for the ZnO NR/GaN and GQD decorated ZnO NR/GaN-NT UV photodetector.

Reprinted with permission from L. Goswami, N. Aggarwal, R. Verma, S. Bishnoi, S. Husale, R. Pandey, et al., Graphene quantum dot-sensitized ZnO-nanorod/gan-nanotower heterostructure-based high performance UV photodetectors, ACS Applied Materials & Interfaces 12 (2020) 47038–47047. Copyright 2020, American Chemical Society.

Goswami et al. studied UV photodetector properties of GQDs-sensitized ZnO-nanorod grown on GaN nanotower (GaN-NT) [75]. Fig. 6.19A displays the schematic representation of growth and electrical contacts of UV photodetector. Fig. 6.19B shows the time-dependent photocurrent of GQD-ZnO NR/GaN-NT heterostructure. The rise time and fall time estimated from time dependent photocurrent curve are 159 and 68.7 Ms, respectively (Fig. 6.19B). The spectral response of the sample demonstrated UV current compared to other regions because of incorporation of GQDs (Fig. 6.19C). The plot of responsivity versus applied bias plot for the ZnO NR/GaN and GQD-ZnO NR/GaN-NT UV device is presented in Fig. 6.19D. The fabricated device demonstrated responsivity of $\sim 3.2 \times 10^3$ A/W at -6 V with enhancement of $\sim 265\%$ compared to control sample. They also observed low noise equivalent power of 5×10^{-14} cm W $Hz^{-1/2}$ in comparison

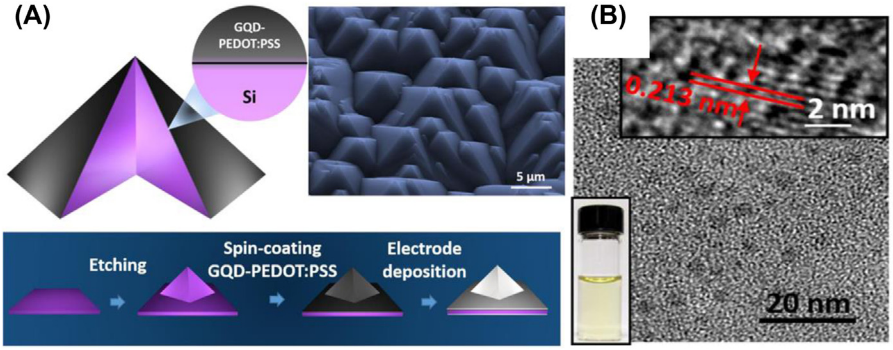

Figure 6.20 (A) The schematic growth process of the hybrid device. Inset: Top-view SEM image of the sample. (B) TEM micrograph of GQDs. Insets: HRTEM image of GQD and digital photograph of GQD solution.
Reprinted with permission from M.L. Tsai, D.S. Tsai, L. Tang, L.J. Chen, S.P. Lau, J.H. He, Omnidirectional harvesting of weak light using a graphene quantum dot-modified organic/silicon hybrid device, ACS Nano 11 (2017) 4564−4570. Copyright 2017, American Chemical Society.

with unsensitized sample. The device also demonstrated higher switching speed at ~50 fW intensity.

Liu et al. prepared UV photodetector using isotype heterojunction by growing n-ZnO NRs on n-GaN thin films [76]. To enhance UV photoabsorption, GQDs were spin coated on ZnO NRs. Transient photoresponse was studied under exposure of 365 nm UV light, and rise and decay times were 100 and 120 Ms, respectively [77]. The detectivity and photoresponsivity of the device were ~10^{12} Jones and 34 mA/W, respectively, at 10 V bias. Photosensing properties of GQDs-sensitized ZnO NRs were also studied by several researchers. Yang and co-workers observed higher photocurrent under UV light illumination in GQDs-coated ZnO NR compared to pristine ZnO [78]. The photosensitivity of coated ZnO NR was obtained to be 150 times higher than that of ZnO NR at 5 V.

6.5.3 Polymer nanocomposite-based photodetectors

Tsai and his co-researchers studied self-powered organic/inorganic hybrid photodetector device consisting of GQDs-modified PEDOT:PSS deposited on micropyramidal Si nanostructures [79]. Fig. 6.20A shows the schematic diagram of fabricated device and top-view SEM micrograph of the device (inset). The TEM micrograph of GQDs is shown in Fig. 6.20B. Fig. 6.21A and B illustrate IV characteristics of GQD-PEDOT:PSS/ micropyramid Si hybrid and micropyramid Si and planner Si devices upon illumination of 532 nm light, respectively. All the devices exhibited similar photocurrent nature within voltage −1 to 0.75 V above light intensity 25.2 μW. The responsivity of the photodetector was increased upto 1.02 A/W at intensity 2.52 μW, which is 57 times higher compared to PEDOT:PSS/Si device [79]. The detectivity of

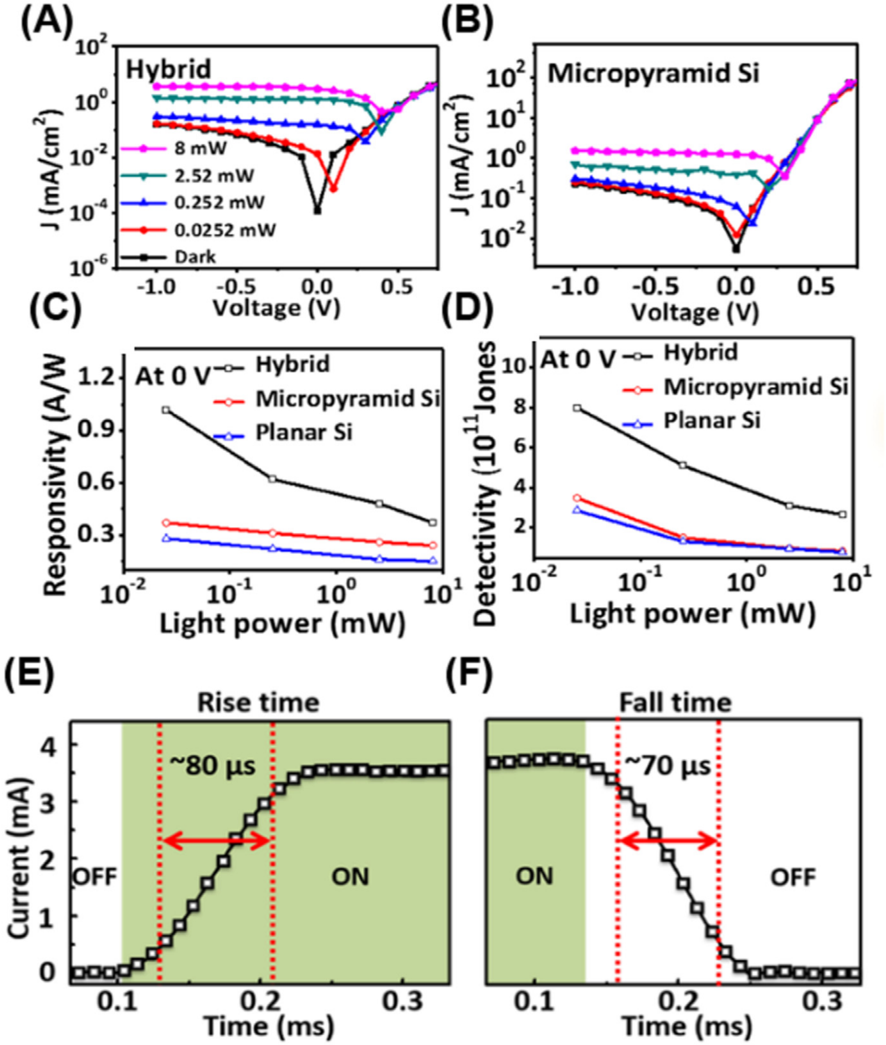

Figure 6.21 I-V characteristics of (A) GQDs modified PEDOT:PSS hybrid micropyramidal Si and micropyramidal Si measured under dark and light of wavelength ~ 532 nm with various intensity of light. (C) Responsivity vs light power and (D) detectivity vs light power plots of the hybrid, micropyramidal and planar Si photodetector devices at 0 V. The estimation of rise time (E) and (F) fall time of the GQDs modified PEDOT:PSS hybrid micropyramidal Si photodetector at 0 V under 850 nm light illumination.
Reprinted with permission from M.L. Tsai, D.S. Tsai, L. Tang, L.J. Chen, S.P. Lau, and J.H. He, Omnidirectional harvesting of weak light using a graphene quantum dot-modified organic/silicon hybrid device, ACS Nano 11 (2017) 4564−4570. Copyright 2017, American Chemical Society.

Table 6.1 A comparison list of all graphene quantum dots and carbon quantum dots based photodetectors and their performances.

Material	Detectivity cm $Hz^{1/2}/W$	Responsivity A/W	Spectral region	Structure	References
Au/GQDs/Ag	9.59×10^{11}	2.1×10^{-3}	UV	Field effect transistor based photodetectors	[64]
NGQDs	–	325	UV-Vis-NIR		[65]
Graphene/NGQDs	1.2×10^{12}	3.5×10^{4}	Vis-NIR		[66]
Graphene/NGQD/BN	5.5×10^{13}	2.3×10^{6}	UV-Vis-NIR		[67]
Graphene/GQD/graphene	$>10^{11}$	0.5	UV-Vis-NIR		[68]
WSe_2/NGQDs	–	2578	UV		[69]
MOS2-GQDs	–	1.6×10^{4}	Vis		[70]
WSe_2/Si/GQDs	4.51×10^{9}	0.707	Vis		[71]
NCQD/graphene	–	2.5×10^{4}	UV		[72]
ZnO/GQD/PEDOT:PSS	1.3×10^{12}	36	UV	GQDs/CQDs-sensitized nanomaterial based photodetectors	[19]
ZnO/NGQD/PEDOT:PSS	8.7×10^{12}	158	UV		[18]
CQDs/Si	–	–	Vis		[73]
GQDs/Si NP	–	0.31	UV-Vis-NIR		[81]
GQDs/Si NW	11.9×10^{12}	40.6	UV-Vis-NIR		[82]
GQDs/ZnO NRs	–	–	UV		[77]
GQDs/ZnO NRs	1.78×10^{15}	6.62×10^{4}	UV		[74]
GQDs/ZnO NR/GaN NT	5×10^{14}	3.2×10^{3}	UV		[75]
GQDs/ZnO NR/GaN NT	10^{12}	34×10^{-3}	UV		[76]
NCQDs/ZnO NR	–	–	UV-Vis		[78]
GQDs-PEDOT:PSS/Si	8×10^{11}	1.02	Vis	GQDs/CQDs and polymer nanocomposite- based photodetectors	[79]
CQD/ZnO/PVK	8.33×10^{12}	0.14	UV		[80]
ZnO/PVA/GQDs	–	26.6	UV		[83]

the hybrid device under 532 nm illumination was 8×10^{11} Jones without any bias voltage (Fig. 6.21C and D). The rise and fall times of the photoresponse were ~80 and ~70 μs, respectively, at 0 V bias under illumination of 850 nm light (Fig. 6.21E and F). The group also demonstrated low-light infrared sensing with the hybrid photodetector at 850 nm, which is attractive for possible application in optical communication and biological imaging.

Lee et al. fabricated UV photodetector using mixture of CQDs and ZnO NRs as hybrid photoactive layer [80]. Such hybrid photodetector exhibited detectivity of 8.33×10^{12} J at wavelength 365 nm and intensity of 1 mW/cm^2. The maximum photoresponsivity was 0.14 A/W at 350 nm wavelength under 5 V bias. The photodetector performances of reported GQDs/CQDs-based devices are summarized and listed in Table 6.1.

6.6 Conclusions

We have discussed the potential use of GQDs and CQDs for photodetector applications. Numerous methods for the synthesis of the GQDs and CQDs have been reviewed. The unique optical properties of the GQDs and CQDs have been discussed. From the reported literatures, we have observed that most of the studies have been done for UV photodetector application. Broadband photodetection in the UV-Vis-NIR range using GQDs or CQDs has also been reported by some researchers. It has been observed that, among the reported photodetectors, FET-based detectors demonstrated higher responsivity, detectivity, and response time. However, real-life application of GQDs/CQDs-based photodetectors is still a challenging task and more research work needs to be done in this particular area. Reproducibility, consistency of experimental results, and batch fabrication of photodetector devices are very much essential for real-life applications.

References

[1] B.C. Brodie, On the atomic weight of graphite, Philosophical transactions of the Royal Society of London 149 (1859) 249−259.

[2] A.C. Power, B. Gorey, S. Chandra, J. Chapman, Carbon nanomaterials and their application to electrochemical sensors: a review, Nanotechnology Reviews 7 (2018) 19−41.

[3] S. Dhar, P. Chakraborty, T. Majumder, S.P. Mondal, CdS-decorated Al-doped ZnO nanorod/polymer schottky junction ultraviolet-visible dual-wavelength photodetector, ACS Applied Nano Materials 1 (2018) 3339−3345.

[4] M.M. Rahman, M.R. Karim, H.F. Alharbi, B. Aldokhayel, T. Uzzaman, H. Zahir, Cadmium selenide quantum dots for solar cell applications: a review, Chemistry − An Asian Journal 16 (2021) 902−921.

[5] A.D. Iacovo, C. Venettacci, L. Colace, L. Scopa, S. Foglia, PbS Colloidal quantum dot photodetectors operating in the near infrared, Scientific Reports 6 (2016) 37913.

[6] N. Sukharevska, D. Bederak, V.M. Goossens, J. Momand, H. Duim, D.N. Dirin, et al., Scalable PbS quantum dot solar cell production by blade coating from stable inks, ACS Applied Materials & Interfaces 13 (2021) 5195−5207.

[7] M. Dolatyari, A. Rostami, S. Mathur, A. Klein, Trap engineering in solution processed PbSe quantum dots for high-speed MID-infrared photodetectors, Journal of Materials Chemistry C 7 (2019) 5658−5669.

[8] R. Guo, F. Huang, K. Zheng, T. Pullerits, J. Tian, CuInSe2 quantum dots hybrid hole transfer layer for halide perovskite photodetectors, ACS Applied Materials & Interfaces 10 (2018) 35656−35663.

[9] M. Bacon, S.J. Bradley, T. Nann, Graphene quantum dots, Particle & Particle Systems Characterization 31 (2014) 415−428.

[10] X.T. Zheng, A. Ananthanarayanan, K.Q. Luo, P. Chen, Glowing graphene quantum dots and carbon dots: properties, syntheses, and biological applications, Small (Weinheim an der Bergstrasse, Germany) 11 (2015) 1620−1636.

[11] X. Tan, Y. Li, X. Li, S. Zhou, L. Fan, S. Yang, Electrochemical synthesis of small-sized red fluorescent graphene quantum dots as a bioimaging platform, Chemical Communications 51 (2015) 2544−2546.

[12] L. Fan, M. Zhu, X. Lee, R. Zhang, K. Wang, J. Wei, et al., Direct synthesis of graphene quantum dots by chemical vapor deposition, Particle & Particle Systems Characterization 30 (2013) 764−769.

[13] Z. Zhang, J. Zhang, N. Chen, L. Qu, Graphene quantum dots: an emerging material for energy-related applications and beyond, Energy & Environmental Science 5 (2012) 8869−8890.

[14] J. Shen, Y. Zhu, X. Yang, C. Li, Graphene quantum dots: emergent nanolights for bioimaging, sensors, catalysis and photovoltaic devices, Chemical Communications 48 (2012) 3686−3699.

[15] D. Wang, J.-F. Chen, L. Dai, Recent advances in graphene quantum dots for fluorescence bioimaging from cells through tissues to animals, Particle and Particle Systems Characterization 5 (2015) 515−523.

[16] X. Li, M. Rui, J. Song, Z. Shen, H. Zeng, Carbon and graphene quantum dots for optoelectronic and energy devices: a review, Advanced Functional Materials 25 (2015) 4929−4947.

[17] S. Dhar, T. Majumder, P. Chakraborty, S.P. Mondal, DMSO modified PEDOT:PSS polymer/ZnO nanorods Schottky junction ultraviolet photodetector: photoresponse, external quantum efficiency, detectivity, and responsivity augmentation using N doped graphene quantum dot, Organic Electronics 53 (2018) 101−110.

[18] S. Dhar, T. Majumder, S.P. Mondal, Phenomenal improvement of external quantum efficiency, detectivity and responsivity of nitrogen doped graphene quantum dot decorated zinc oxide nanorod/polymer Schottky junction UV detector, Materials Research Bulletin 95 (2017) 198−203.

[19] S. Dhar, T. Majumder, S.P. Mondal, Graphene quantum dot-sensitized ZnO nanorod/polymer Schottky junction UV detector with superior external quantum efficiency, detectivity, and responsivity, ACS Applied Materials & Interfaces 8 (2016) 31822−31831.

[20] R. Sekiya, Y. Uemura, H. Murakami, T. Haino, White-light-emitting edge-functionalized graphene quantum dots, Angewandte Chemie International Edition 53 (2014) 5619−5623.

[21] Z. Qian, J. Zhou, J. Chen, C. Wang, C. Chen, H. Feng, Nanosized N-doped graphene oxide with visible fluorescence in water for metal ion sensing, Journal of Materials Chemistry 21 (2011) 17635−17637.

[22] T. Majumder, S.P. Mondal, Advantages of nitrogen-doped graphene quantum dots as a green sensitizer with ZnO nanorod based photoanodes for solar energy conversion, Journal of Electroanalytical Chemistry 769 (2016) 48−52.

[23] T. Majumder, K. Debnath, S. Dhar, J.J.L. Hmar, S.P. Mondal, Nitrogen-doped graphene quantum dot-decorated ZnO nanorods for improved electrochemical solar energy conversion, Energy Technology 4 (2016) 950−958.

[24] T. Majumder, S. Dhar, K. Debnath, S.P. Mondal, Role of S, N Co-doped graphene quantum dots as a green photosensitizer with Ag-doped ZnO nanorods for improved electrochemical solar energy conversion, Materials Research Bulletin 93 (2017) 214−222.

[25] T. Majumder, S. Dhar, P. Chakraborty, K. Debnath, S.P. Mondal, Advantages of ZnO nanotaper photoanodes in superior photoelectrochemical properties of nitrogen doped graphene quantum dot sensitized, Journal of Electroanalytical Chemistry 813 (2018) 92−101.

[26] T. Majumder, S. Dhar, P. Chakraborty, K. Debnath, S.P. Mondal, S, N co-doped graphene quantum dots decorated C doped ZnO nanotaper photoanodes for solar cells application, Nano 14 (2019) 1950012.

[27] T. Majumder, S.P. Mondal, Graphene quantum dots as a green photosensitizer with carbon doped ZnO nanorods for quantum dot sensitized solar cell applications, Bulletin of Materials Science 42 (2019) 65.

[28] Y. Zhang, D. Maa, Y. Zhang, W. Chen, S. Huanga, N-doped carbon quantum dots for TiO_2-based photocatalysts and dye-sensitized solar cells, Nano Energy 2 (2013) 545−552.

[29] X.Y. Xu, R. Ray, Y.L. Gu, H.J. Ploehn, L. Gearheart, K. Raker, et al., Electrophoretic analysis and purification of fluorescent single-walled carbon nanotube fragments, Journal of the American Chemical Society 126 (2004) 12736−12737.

[30] H. Ming, Z. Ma, Y. Liu, K.M. Pan, H. Yu, F. Wang, et al., Large scale electrochemical synthesis of high quality carbon nanodots and their photocatalytic property, Dalton Transactions (Cambridge, England: 2003) 41 (2012) 9526−9531.

[31] X. Feng, Y. Zhang, A simple and green synthesis of carbon quantum dots from coke for white light-emitting devices, RSC Advances 9 (2019) 33789−33793.

[32] Y. Dong, H. Pang, S. Ren, C. Chen, Y. Chi, T. Yu, Etching single-wall carbon nanotubes into green and yellow single-layer graphene quantum dots, Carbon 64 (2013) 245−251.

[33] Y. Dong, J. Lin, Y. Chen, F. Fu, Y. Chi, G. Chen, Graphene quantum dots, graphene oxide, carbon quantum dots and graphite nanocrystals in coals, Nanoscale 6 (2014) 7410-7415.

[34] M. Li, C. Yu, C. Hu, W. Yang, C. Zhao, S. Wang, et al., Solvothermal conversion of coal into nitrogen-doped carbon dots with singlet oxygen generation and high quantum yield, Chemical Engineering Journal 320 (2017) 570−575.

[35] R. Ye, Z. Peng, A. Metzger, J. Lin, J.K. Mann, K. Huang, et al., Bandgap engineering of coal-derived graphene quantum dots, ACS Applied Materials & Interfaces 7 (2015) 7041−7048.

[36] Q. Liu, J. Zhang, H. He, G. Huang, B. Xing, J. Jia, et al., Green preparation of high yield fluorescent graphene quantum dots from coal-tar-pitch by mild oxidation, Nanomaterials 8 (2018) 844.

[37] J. Gu, X. Zhang, A. Pang, J. Yang, Facile synthesis and photoluminescence characteristics of blue-emitting nitrogen-doped graphene quantum dots, Nanotechnology 27 (2016) 165704.

[38] Y. Dong, J. Shao, C. Chen, H. Li, R. Wang, Y. Chi, et al., Blue luminescent graphene quantum dots and graphene oxide prepared by tuning the carbonization degree of citric acid, Carbon 12 (2012) 4738−4743.

[39] L. Wang, Y. Wang, T. Xu, H. Liao, C. Yao, Y. Liu, et al., Gram-scale synthesis of single-crystalline graphene quantum dots with superior optical properties, Nature Communications 5 (2014) 5357.

[40] L. Tang, R. Ji, X. Li, K.S. Teng, S.P. Lau, Size-dependent structural and optical characteristics of glucose-derived graphene quantum dots, Particle & Particle Systems Characterization 6 (2013) 523−531.

[41] S. Kumar, S.K.T. Aziz, O. Girshevitz, G.D. Nessim, One-step synthesis of N doped graphene quantum dots from chitosan as a sole precursor using chemical vapor deposition, The Journal of Physical Chemistry C 122 (2018) 2343−2349.

[42] B. Bourlinos, A. Stassinopoulos, D. Anglos, R. Zboril, M. Karakassides, E.P. Giannelis, Surface functionalized carbogenic quantum dots, Small (Weinheim an der Bergstrasse, Germany) 8 (2008) 455−458.

[43] X. Zhai, P. Zhang, C. Liu, T. Bai, W. Li, L. Dai, et al., Highly luminescent carbon nanodots by microwave-assisted pyrolysis, Chemical Communications 48 (2012) 7955−7957.

[44] J.J.L. Hmar, T. Majumder, S. Dhar, S. P. Mondal, Sulfur and nitrogen Co-doped graphene quantum dot decorated ZnO nanorod/polymer hybrid flexible device for photosensing applications, Thin Solid Films 612 (2016) 274−283.

[45] D. Qu, M. Zheng, P. Du, Y. Zhou, L. Zhang, D. Li, et al., Highly luminescent S, N Co-doped graphene quantum dots with broad visible absorption bands for visible light photocatalysts, Nanoscale 5 (2013) 12272−12277.

[46] T.V. Tam, S.G. Kang, K.F. Babu, E.-S. Oh, S.G. Lee, W.M. Choi, Synthesis of B doped graphene quantum dots as a metal-free electrocatalyst for the oxygen reduction reaction, Journal of Materials Chemistry A 5 (2017) 10537−10543.

[47] L. Tang, R. Ji, X. Cao, J. Lin, H. Jiang, X. Li, et al., Deep ultraviolet photoluminescence of water-soluble self-passivated graphene quantum dots, ACS Nano 6 (2012) 5102−5110.

[48] D. Qu, Z. Sun, M. Zheng, J. Li, Y. Zhang, G. Zhang, et al., Three colors emission from S, N Co-doped graphene quantum dots for visible light H_2 production and bioimaging, Advanced Optical Materials 3 (2015) 360−367.

[49] M. Zhang, L.L. Bai, W.H. Shang, W.J. Xie, H. Ma, Y.Y. Fu, et al., Facile synthesis of water-soluble, highly fluorescent graphene quantum dots as a robust biological label for stem cells, Journal of Materials Chemistry 22 (2012) 7461−7467.

[50] G.S. Kumar, R. Roy, D. Sen, U.K. Ghorai, R. Thapa, N. Mazumder, et al., Amino-functionalized graphene quantum dots: origin of tunable heterogeneous photoluminescence, Nanoscale 6 (2014) 3384−3391.

[51] H.X. Wang, J. Xiao, Z. Yang, H. Tang, Z.T. Zhu, M. Zhao, et al., Rational design of nitrogen and sulfur co-doped carbon dots for efficient photoelectrical conversion applications, Journal of Materials Chemistry A 3 (2015) 11287−11293.

[52] M.K. Barman, B. Jana, S. Bhattacharyya, A. Patra, Photophysical properties of doped carbon dots (N, P, and B) and their influence on electron/hole transfer in carbon dots−nickel (II) phthalocyanine conjugates, The Journal of Physical Chemistry C 118 (2014) 20034−20041.

[53] J. Zhou, X. Shan, J. Ma, Y. Gu, Z. Quin, J. Chen, et al., Facile synthesis of P-doped carbon quantum dots with highly efficient photoluminescence, RSC Advances 4 (2014) 5465−5468.

[54] X. Li, S.P. Lau, L. Tang, R. Ji, P. Yang, Multicolour light emission from chlorine doped graphene quantum dots, Journal of Materials Chemistry C 1 (2013) 7308−7313.

[55] F. Qian, X. Li, L. Tang, S.K. Lai, C. Lu, S.P. Lau, Potassium doping: tuning the optical properties of graphene quantum dots, AIP Advances 6 (2016) 075116.

[56] N.U. Ain, M.O. Eriksson, S. Schmidt, M. Asghar, P.C. Lin, P.O. Holtz, et al., Tuning the emission energy of chemically doped graphene quantum dots, Nanomaterials 6 (2016) 198.

[57] M. Favaro, L. Ferrighi, G. Fazio, L. Colazzo, C.D. Vaentin, C. Durante, et al., Single and multiple doping in graphene quantum dots: unraveling the origin of selectivity in the oxygen reduction reaction, ACS Catalysis 5 (2015) 129−144.

[58] X. Wei, S. Mei, D. Yang, G. Zhang1, F. Xie, W. Zhang, et al., Surface states induced photoluminescence enhancement of nitrogen-doped carbon dots via post-treatments, Nanoscale Research Letters 14 (2019) 172.

[59] P.H. Luo, Z. Ji, C. Li, G.Q. Shi, Aryl-modifed graphene quantum dots with enhanced photoluminescence and improved PH tolerance, Nanoscale 5 (2013) 7361−7367.

[60] Y.N. Hao, H.L. Guo, L. Tian, X.F. Kang, Enhanced photoluminescence of pyrrolic-nitrogen enriched graphene quantum dots, RSC Advances 5 (2015) 43750−43755.

[61] M.A. Sk, A. Ananthanarayanan, L. Huang, K.H. Lim, P. Chen, Revealing the tunable photoluminescence properties of graphene quantum dots, Journal of Materials Chemistry C 2 (2014) 6954−6960.

[62] M.L. Tsai, W.C. Tu, L. Tang, T.C. Wei, W.-R. Wei, S.P. Lau, et al., Efficiency enhancement of silicon heterojunction solar cells via photon management using graphene quantum dot as downconverters, Nano Letters 1 (2016) 309−313.

[63] S.H. Song, M.-H. Jang, J. Chung, S.H. Jin, B.H. Kim, S.-H. Hur, et al., Highly efficient light-emitting diode of graphene quantum dots fabricated from graphite intercalation compounds, Advanced Optical Materials 11 (2014) 1016−1023.

[64] Q. Zhang, J. Jie, S. Diao, Z. Shao, Q. Zhang, L. Wang, et al., Solution-processed graphene quantum dot deep-UV photodetectors, ACS Nano 2 (2015) 1561−1570.

[65] L. Tang, R. Ji, X. Li, G. Bai, C.P. Liu, J. Hao, et al., Deep ultraviolet to near-infrared emission and photoresponse in layered N-doped graphene quantum dots, ACS Nano 6 (2014) 6312−6320.

[66] H. Tetsuka, A. Nagoya, T. Fukusumi, T. Matsui, Molecularly designed, nitrogen-functionalized graphene quantum dots for optoelectronic devices, Advanced Materials 28 (2016) 4632−4638.

[67] H. Tetsuka, A. Nagoya, S.-I. Tamura, Graphene/nitrogen-functionalized graphene quantum dot hybrid broadband photodetectors with a buffer layer of Boron Nitride Nanosheets, Nanoscale 47 (2016) 19677−19683.

[68] C.O. Kim, S.W. Hwang, S. Kim, D.H. Shin, S.S. Kang, J.M. Kim, et al., High-performance graphene quantum-dot photodetectors, Scientific Reports 4 (2014) 5603.

[69] N.D. Nguyen, M.O. Hye, T.D. Ngoc, S. Bang, S.J. Yoon, M.S. Jeong, Highly enhanced photoresponsivity of a monolayer WSe2 photodetector with nitrogen-doped graphene quantum dots, ACS Applied Materials & Interfaces 10 (2018) 10322−10329.

[70] C. Chen, H. Qiao, S. Lin, C.M. Luk, Y. Liu, Z. Xu, et al., Highly responsive MoS2 photodetectors enhanced by graphene quantum dots, Scientific Reports 5 (2015) 11830.

[71] M. Sun, Q. Fang, D. Xie, Y. Sun, L. Qian, J. Xu, et al., Heterostructured graphene quantum dot/Wse2/Si photodetector with suppressed dark current and improved detectivity, Nano Research 11 (2017) 3233.

[72] X. Wu, B. Zhao, J. Zhang, H. Xu, K. Xu, G. Chen, Photoluminescence and photodetecting properties of the hydrothermally synthesized nitrogen-doped carbon quantum dots, The Journal of Physical Chemistry C 123 (2019) 25570−25578.
[73] C. Xie, B. Nie, L. Zeng, F.X. Liang, M.Z. Wang, L. Luo, et al., Core shell heterojunction of silicon nanowire arrays and carbon quantum dots for photovoltaic devices and self-driven photodetectors, ACS Nano 8 (2014) 4015−4022.
[74] D. Ghosh, S. Kapri, S. Bhattacharyya, Phenomenal ultraviolet photoresponsivity and detectivity of graphene dots immobilized on zinc oxide nanorods, ACS Applied Materials & Interfaces 8 (2016) 35496−35504.
[75] L. Goswami, N. Aggarwal, R. Verma, S. Bishnoi, S. Husale, R. Pandey, et al., Graphene quantum dot-sensitized zno-nanorod/gan-nanotower heterostructure-based high performance UV photodetectors, ACS Applied Materials & Interfaces 12 (2020) 47038−47047.
[76] D. Liu, H.J. Li, J. Gao, S. Zhao, Y. Zhu, P. Wang, High-performance ultraviolet photodetector based on graphene quantum dots decorated ZnO nanorods/GaN film isotype heterojunctions, Nanoscale Research Letters 13 (2018) 261.
[77] B. Yang, J. Chen, L. Cui, W. Liu, Enhanced photocurrent of a ZnO nanorod array sensitized with graphene quantum dots, RSC Advances 5 (2015) 59204−59207.
[78] R. Wang, J. Lu, Y. Lin, High-performance nitrogen doped carbon quantum dots: facile green synthesis from waste paper and broadband photodetection by coupling with ZnO nanorods, Journal of Alloys and Compounds 813 (2020) 152201.
[79] M.L. Tsai, D.S. Tsai, L. Tang, L.J. Chen, S.P. Lau, J.H. He, Omnidirectional harvesting of weak light using a graphene quantum dot-modified organic/silicon hybrid device, ACS Nano 11 (2017) 4564−4570.
[80] S.W. Lee, K.J. Choi, B.H. Kang, J.S. Lee, S.W. Kim, J.B. Kwon, et al., Low dark current and improved detectivity of hybrid ultraviolet photodetector based on carbon-quantum-dots/zinc-oxide-nanorod composites, Organic Electronics 39 (2016) 250−257.
[81] S. Kim, D.H. Shin, J. Kim, C.W. Jang, S.S. Kang, J.M. Kim, et al., Energy transfer from an individual silica nanoparticle to graphene quantum dots and resulting enhancement of photodetector responsivity, Scientific Reports 6 (2016) 27145.
[82] I. Mihalache, A. Radoi, R. Pascu, C. Romanitan, E. Vasile, M. Kusko, Engineering graphene quantum dots for enhanced ultraviolet and visible light p-Si nanowire-based photodetector, ACS Applied Materials & Interfaces 9 (2017) 29234−29247.
[83] S.S. Mousavi, B. Sajad, M.H. Majlesara, Fast response ZnO/PVA nanocomposite-based photodiodes modified by graphene quantum dots, Materials & Design 162 (2019) 249−255.

Photovoltaic application of carbon quantum dots

7

Prashant Kumar[1], *Arup Mahapatra*[1,2], *Sandeep Kumar*[1] *and*
Basudev Pradhan[1,2]
[1]Department of Energy Engineering, Central University of Jharkhand, Ranchi, Jharkhand, India, [2]Centre of Excellence (CoE) in Green and Efficient Energy Technology (GEET), Central University of Jharkhand, Ranchi, Jharkhand, India

7.1 Introduction

With the advent of civilization, the energy demand grew rapidly. However, the present primary source of energy, i.e., fossil fuels are limited in stock and are highly responsible for global warming and other environmental crisis. These reasons have driven mankind to look for renewable sources of energy to mitigate the global energy crisis. With its vast potential, easy exploitability, quiet production, and nondetrimental impact on the environment, solar energy is the best choice among the renewable energy resources to serve the sustainable growth agenda of the 21st century. Energy from the sun could be harnessed by photovoltaic technology, i.e., direct conversion of sunlight into electricity with the help of a photovoltaic device also known as a solar cell. In a typical solar cell, electron–hole pair is generated after absorption of an incident photon which assists in driving current in the external circuit so that power is extracted from the device. There are many types of solar cells which work on various photovoltaic principles and whose efficiency improvement is the only way by which solar power could be used effectively. Unfortunately, commercially successful silicon-based photovoltaic technology is still restricted to mass-scale acceptability to common people due to high cost-to-energy output ratios and it also uses environmentally health-hazardous materials in the device fabrication process. So it is necessary to look into biocompatible materials with greener technology for low-cost photovoltaic devices. In this direction, emerging semiconducting carbon quantum dots (CQDs), which have recently become very popular and versatile materials, can play important role in photovoltaic devices due to their unique advantageous features of high luminescence, good water solubility, excellent photostability, robust chemical inertness, and facile modifiability. CQDs have an edge over other conventional semiconductors [1]. These excellent properties, to some extent, are a result of functionalization and passivation of CQDs with various groups along with their intrinsic properties [2]. The remarkable electronic characteristics of CQDs as donors and acceptors of electrons, resulting in electrochemical luminescence and chemiluminescence make them very useful for application in photovoltaic conversion. Moreover, facile synthetic

Carbon Quantum Dots for Sustainable Energy and Optoelectronics. DOI: https://doi.org/10.1016/B978-0-323-90895-5.00017-5
© 2023 Elsevier Ltd. All rights reserved.

methods, size control, and modification strategies make them very eminent for these applications [3]. In this chapter, the application of CQDs in photovoltaic conversion has been discussed across the different types of solar cells in different roles. The overall performance of a photovoltaic device is characterized by open-circuit voltage (V_{OC}), short-circuit current density (J_{SC}), and fill factor (FF). These parameter values are calculated from the current density—voltage characteristics (J—V) of the device under normally 100 mW/cm^2 AM 1.5 G illumination conditions. The FF is calculated as $FF = (V_{\max} \times J_{\max})/(V_{OC} \times J_{SC})$, where $V_{\max}$ and $J_{\max}$ are voltage and current density corresponding to the maximum power of the J—V curve in the fourth quadrant. The power conversion efficiency (η) of the photovoltaic devices is calculated by following equation:

$$\eta(\%) = \frac{J_{SC} \times V_{OC} \times FF}{P_{in}} \times 100$$

where P_{in} is the incident light intensity. The performance of the photovoltaic device is also quantified on a macroscopic level with the external quantum efficiency (EQE) parameter. The EQE is the ratio between the number of photogenerated charge carriers backing to the photocurrent and the number of incident photons. The EQE is given as:

$$EQE = \frac{\Delta J_{SC}}{q \Delta \phi_{\lambda}}$$

where ΔJ_{SC} is the incremental short-circuit current density generation by a photovoltaic device due to incremental photon flux of $\Delta \phi_{\lambda}$ at wavelength λ and q is the electronic charge. These parameters provide throughout characteristics of the device and help in fabricating an efficient photovoltaic device. CQDs, being a material with unique optoelectronic property, have application in dye-sensitized solar cells, solid-state solar cells, organic solar cells (OSCs), and polymer solar cells that have been elaborated with correlating impact on photovoltaic parameters in the next sections.

7.2 Carbon quantum dots in dye-sensitized solar cells

Dye-sensitized solar cells (DSSCs) have attracted much attention as a viable, promising, cost-effective thin-film technology since it was first reported by Regan and Grätzel in 1991 [4—6]. A typical DSSC consists of titanium dioxide (TiO_2) nanoparticles coated photoanode, light-absorbing dye molecules which generate photoelectrons, an electrolyte containing a redox couple for electron transfer, and a counter electrode (CE). The sensitizer or dye plays a crucial role in the overall process. Therefore, various synthetic dyes as well as natural dyes and quantum dots as sensitizer have been explored extensively. At present, most successful DSSCs typically use ruthenium complex as a photosensitizer with so far maximum power conversion efficiency of 11.9%. However, these dye molecules are very expensive due to their cumbersome synthesis process and use of rare earth metals. This led the scientific community to look for a suitable and environmentally friendly alternative. In this direction, CQDs are one of the premier alternatives. For the first time, Mirtchev et al. used CQDs as a sensitizer in DSSC [7]. After which, it got wide recognition and was used in every component of the DSSC device, such as a sensitizer, cosensitizer, electrolyte, and CE for improved performances which are briefly discussed here.

7.2.1 Carbon quantum dots as sensitizer

CQDs derived from natural extracts have been investigated as sensitizers in DSSC application due to their strong absorbance in the visible light spectrum. CQD-based dye has been studied as a potential replacement of the highly toxic and costlier ruthenium-containing dye. Until now, several studies have reported using CQDs as a sensitizer as well as a cosensitizer in combination with other materials. The theoretical simulation has been performed by Yan et al. and it is calculated that their highest occupied molecular orbital (HOMO) and lowest unoccupied molecular orbital (LUMO) energy levels were -5.3 and -3.80 eV, respectively [8]. These values indicate that the CQDs have the potential to be used as a sensitizer in DSSCs because it perfectly matches with the energy levels of TiO_2 and electrolyte. In a typical quantum dot-based DSSCs, photosensitizer CQDs absorb photon energy and reach to the excited state which is demonstrated in Fig. 7.1. The excited

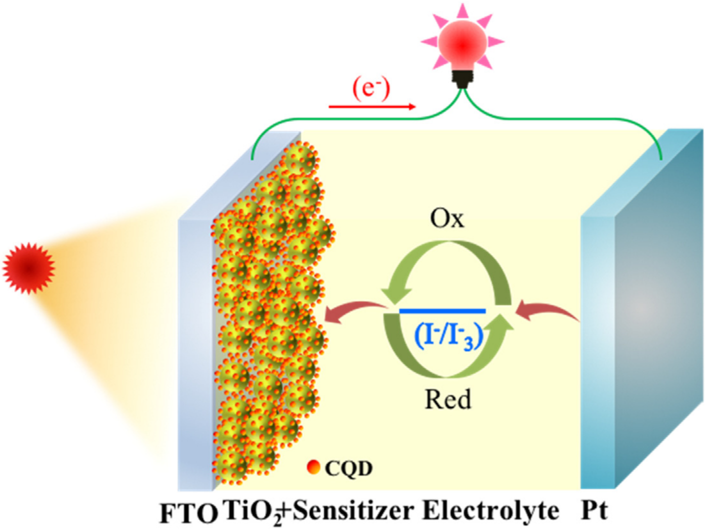

Figure 7.1 Schematic device structure of CQD-based dye-sensitized solar cell. *CQDs*, Carbon quantum dots.

sensitizer transfers photoelectron to the external electrode via the semiconductor which is mostly TiO_2. On the other hand, the oxidized sensitizer is getting back to the neutral state by accepting one electron from I_3^-/I^- electrolyte which is received through the platinum CE (Pt). In 2011, Mirtchev et al. demonstrated first water soluble colloidally stable CQDs as a sensitizer in DSSCs with power conversion efficiency (PCE) of 0.13% with V_{OC} of 380 mV, J_{SC} of 0.532 mA/cm^2, and *FF* of 64% as proof of concept. They found that CQDs consist of Sp^2 hybridization core capped with hydroxyl, carboxyl, and sulfonate groups through core and surface properties analysis via Fourier transform infrared spectroscopy (FTIR), nuclear magnetic resonance (NRM), and X-ray photoelectron spectroscopy (XPS) studies. This makes it function as an electron acceptor/donor, and provides an efficient conducting platform for electrons thus functioning as of electron funnel/carrier/bridge [7]. In a pivotal work, Guo et al. synthesized CQDs from bee pollen (B-CQDs), citric acid (C-CQDs), and glucose (G-CQDs) via hydrothermal methods and used as a sensitizer for solar cell application (Fig. 7.2A). The transmission electron microscopy (TEM) images of these three CQDs show spherical morphology with an average particle size of 2.4 nm (B-CQDs), 2.4 nm (C-CQDs), and 5.2 nm (G-CQDs) (Fig. 7.2B–E). Fig. 7.2F shows the current density–voltage (*J–V*) curves of three kinds of CQDs-based DSSC devices along with uncoated pure TiO_2. Among three of them, the highest efficiency of around 0.11% was achieved in the case of B-CQDs with higher J_{SC} and V_{OC} compared to other devices [9]. The observed increase in V_{OC} was due to the smaller size of the B-CQDs which was governed by the quantum size effect and the higher J_{SC} value was due to broad absorbance spectra and strong electron transfer from B-CQDs. But in the case of C-CQD-based device performance is low though it was in similar size because of the higher surface defect and internal recombination which limits the photogenerated carrier movement.

CQDs are also doped with nitrogen to generate a large of number of active sites which help in fast carrier transportation along with bandgap tunability for better solar cell performance. In another work, Huang et al. have reported DSSCs with PCE of around 0.45% and FF of 60% from nitrogen self-doped CQDs as sensitizer via the one-pot hydrothermal method from *Allium fistulosum* [10]. The typical *J–V* curve of the nitrogen-doped CQDs (NCQDs) sensitized solar cells is shown in Fig. 7.2G. Wang et al. synthesized the green NCQDs via direct pyrolysis of citric acid (CA) and ammonia as shown schematically in Fig. 7.3A [11]. They have demonstrated that the absorbance spectra of NCQDs can be tuned by controlling the mass ratio of reactants which was confirmed from XPS analysis. They observed that when mass ratio is 1:4 (ammonia:CA), the NCQDs process highest visible absorption which is shown in UV–vis spectra of both NCQDs and nitrogen-free CQDs (Fig. 7.3B). It is due to the strong chemical reaction between excess ammonia and overheated NCQDs, which eliminates water molecules from the NCQDs surface.

The absorbance spectra of optimal NCQDs solution not only shows a strong peak of absorption at 335 nm but also shows broad absorption in visible spectra extended to 550 nm. In general, 335 nm peak corresponds to $n-\pi^*$ transition of

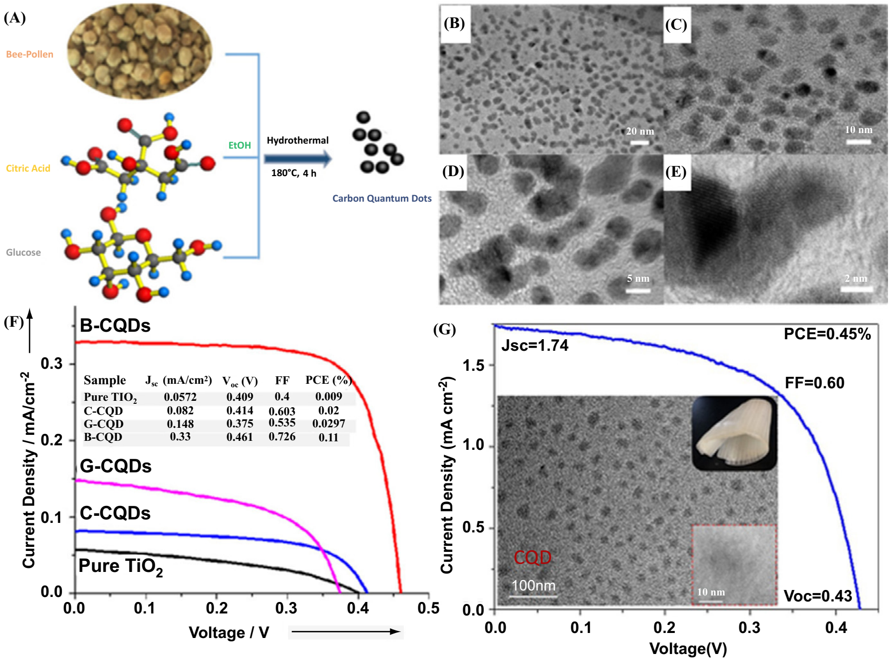

Sample	J_{sc} (mA/cm²)	V_{oc} (V)	FF	PCE (%)
Pure TIO_2	0.0572	0.409	0.4	0.009
C-CQD	0.082	0.414	0.603	0.02
G-CQD	0.148	0.375	0.535	0.0297
B-CQD	0.33	0.461	0.726	0.11

Figure 7.2 (A) Synthesis scheme of CQDs from various sources. (B—E) High-resolution TEM images of B-CQDs (B, C), C-CQDs (D), and G-CQDs (E). Scale bar in (B) 20 nm, (C) 10 nm, (D) 5 nm, (E) 2 nm. (F) *J—V* characteristics of curves and main device parameters for CQD-sensitized solar cells. (G) *J—V* characteristics of NCQDs-sensitized solar cells. Inset shows TEM images of CQDs and fistulosum. *CQDs*, Carbon quantum dots; *TEM*, transmission electron microscopy.
Source: (A—F) Reproduced with permission from X. Guo, H. Zhang, H. Sun, M.O. Tade, S. Wang, Green synthesis of carbon quantum dots for sensitized solar cells, ChemPhotoChem (1) (2017) 116—119. (G) Reproduced with permission from P. Huang, S. Xu, M. Zhang, W. Zhong, Z. Xiao, Y. Luo, Green allium fistulosum derived nitrogen self-doped carbon dots for quantum dot-sensitized solar cells, Materials Chemistry and Physicsater (240) (2020) 122158.

C = O bonds and on the other hand broader absorption peak in visible range is due to presence of amino groups in NCQDs. NCQDs also show blue light under UV lamp (365 nm) irradiation as depicted in the inset of Fig. 7.3B. The enhanced visible light absorbance in NCQDs is beneficial for DSSC application. It can be noted that the presence of N-dopant in NCQD creates additional energy levels between π of carbon and π* of oxygen, which improves in the absorption of visible low energy photons and generates photoexcited charge carrier compared to n-free CQDs illustrated in Fig. 7.3C. These processes in turn result in more photoexcited electrons that transfer to the conduction band of TiO_2 resulting in enhanced photovoltaic

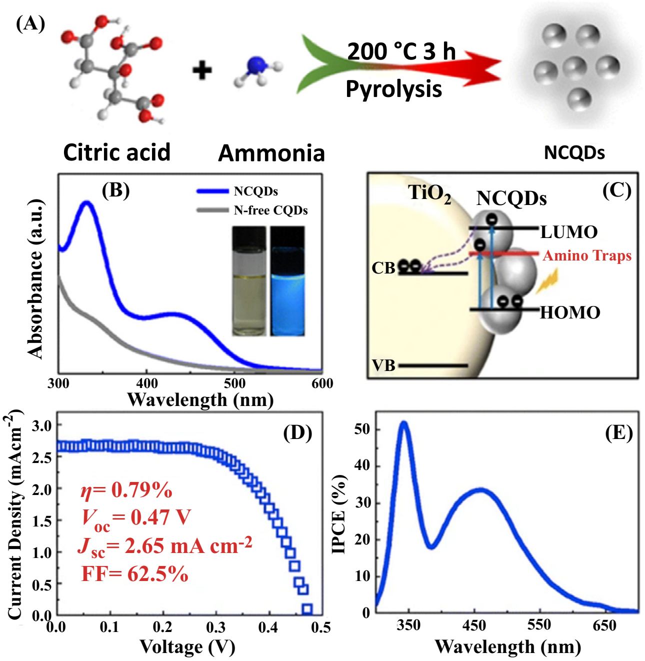

Figure 7.3 (A) Preparation of NCQDs using citric acid and ammonia via direct pyrolysis method. (B) UV−vis spectra of NCQDs and N-free CQDs. Insets showing the photographs of NCDs aqueous solution photographs under UV lamp irradiation (right) and day light (left). (C) Schematic illustration of photoinduced transfer of electron between CQDs and TiO_2. (D) J−V curve and (E) IPCE spectra of nitrogen-doped CQDs (NCQDs)-sensitized solar cells [11]. *CQDs*, Carbon quantum dots; *IPCE*, incident photon-to-electron conversion efficiency; *NCQDs*, nitrogen-doped carbon quantum dots.
Source: Published under creative commons CC BY.

performance which is reflected in the *J−V* curve of NCQDs-based DSSC device under 100 mW/cm^2 AM 1.5 G illumination intensity shown in Fig. 7.3D. The overall PCE of around 0.79% is measured with a V_{OC} of 0.47 V, J_{SC} of 2.65 mA/cm^2, and *FF* of 62.5%. Fig. 7.3E depicts 34% incident photon-to-electron conversion efficiency (IPCE) of NCQD-based DSSCs with over 10% between 400 and 550 nm. Further, Zhang et al. improved the efficiency of CQD-based DSSCs to 0.87% by in situ growing of CQDs of 2−6 nm size on a TiO_2 photoanode for effective charge transfer between CQDs and TiO_2 [12].

It has been noted that DSSCs with only CQDs as sensitizers exhibit poor PCE values as a consequence of narrow spectral response and weaker affinity amongst CQDs and mesoscopic TiO_2. On the other hand, state-of-art ruthenium complex (N719 dye) also shows narrow spectral absorption and serious electron−hole recombination issue. To overcome this issue, different research groups have explored combining CQDs with organic dye as a cosensitizer which ultimately

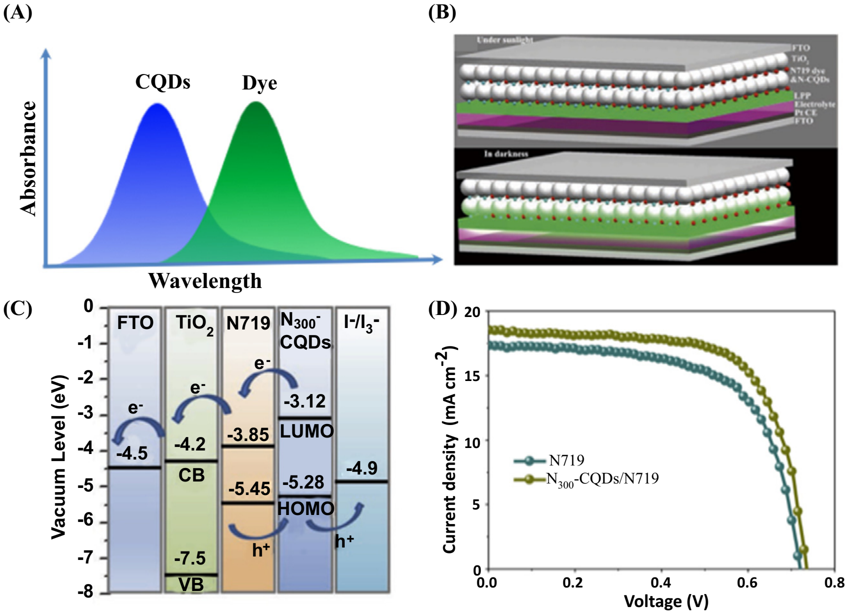

Figure 7.4 (A) Schematic illustration of cosensitizer of CQDs with dye. (B) Schematic of the N300-CQDs and N719 cosensitized DSSCs device with a m-TiO_2/LPP photoanode. (C) Corresponding energy level diagram to illustrate charge transfer process, distribution and charge transfer processes. (D) *J*—*V* curves of characteristics of optimized DSSCs with N719 dye and N300-CQDs/N719 under solar irradiation (100 mW/cm^2, AM 1.5G). *DSSCs*, Dye-sensitized solar cells. *LPP*, long persistent phosphors.

Source: Reproduced with permission from Y. Zhao, J. Duan, B. He, Z. Jiao, Q. Tang, Improved charge extraction with N-doped carbon quantum dots in dye-sensitized solar cells, Electrochimica Acta (282) (2018) 255—262.

widened the absorption of light ranging from visible to near-infrared regions along with fast photogenerated carrier extraction as illustrated in Fig. 7.4A. Zhu et al. reported enhanced PCE of 8.19% using cosensitizer of polyethylene glycol (PEG)-modified CQDs (PEG-m-CQDs) and N719 dye [14]. They have further pushed the efficiency to 9.89% with the same cosensitizer with transparent metal selenide CE modified with green light-emitting long persistent phosphors (LPPs). The main purpose of LPPs is to harvest scattered light from the surrounding and emit green photofluorescence for several hours at dark-light conditions. In another research, Zhao et al. demonstrated DSSCs with cosensitizer NCQDs and N719 dye. Fig. 7.4B shows the schematic device of cosensitized solar device, and the corresponding energy band diagram is shown in Fig. 7.4C which reflects proper energy levels alignment for fast photocarrier generation and better charge transport. Fig. 7.4D validates the optimal *J*—*V* characteristic of N719 dye and also cosensitizer NCQDs/N719 dye. They have reported DSSCs with PCE of around 9.29% using cosensitizer

Table 7.1 Performance of photovoltaic devices with carbon quantum dots as sensitizer and cosensitizer.

Role	Materials	V_{OC} (V)	J_{SC} (mA/cm^2)	FF (%)	PCE (%)	References
Sensitizer	CQDs	0.38	0.53	64	0.13	[7]
	CQDs	0.461	0.33	72	0.11	[9]
	NCQDs	0.43	1.74	60	0.45	[10]
	NCQDs	0.47	2.65	63	0.79	[11]
	CQDs	0.43	6.47	31	0.87	[12]
	N719	0.708	17.3	64.9	8.09	[13]
Cosensitizer	CQDs/N719	0.721	17.01	68	8.19	[14]
	Cubic CQDs/N719	0.721	16.60	73.5	8.68	[16]
	NCQDs/N719	0.736	18.6	67.9	9.29	[13]
S-CQDs/metal selenide CE	Sulfer-CQD[a]	0.715	0.771	16.6	9.15	[17]

of NCQDs with N719 dye. Whereas DSSCs with only N719 dye exhibit PCE of around 8.09% [13]. This significant enhancement is due to upconversion and fast hole extraction properties of NCQDs. Recently, Shejale et al. reported PCE of 8.78% using a cophotoactive layer of NCQDs and N719 dye. They have prepared photoanode by incorporating NCQDs in TiO_2 after that N719 dye was absorbed. In this process, NCQDs are efficiently anchored to TiO_2 via a large number of carboxylic group sites which enhances the photogenerated carrier transport [15]. The detail performances of photovoltaic devices with CQDs as sensitizer and cosensitizer are shown in Table 7.1.

7.2.2 Carbon quantum dots as counter electrode

The CE is another major component in DSSCs which especially contributes to the electrocatalytic performances. The standard CE utilized in high-performing DSSCs is platinum (Pt) which is deposited onto transparent conductive oxide coated glass substrate due to high catalytic activity toward iodine reduction. Even so, Pt is a very expensive material, so researchers are looking for alternative substitutes which are cheap and easily processable. However, CQDs have been extensively used as a photosensitizer in DSSCs, due to their interesting electronic properties which make them a favorable candidate as additives with other materials in CE. Lee et al. synthesized exceptionally porous polyaniline (PANI) using carbon nanodots (CNDs) as a nucleating agent and demonstrated their use as CE in DSSCs [18]. High number of porous sites increases the reactant diffusion for improved electrocatalytic activity. CNDs are caped with highly active aniline which ultimately increases the surface area, facilitates the generation of head-to-tail dimers, and improves the degree of para-coupling in the molecular structure of PANI. Consequently, PANI–CND films show high electrical conductivity of 774 S/cm. The PANI–CND fabricated CEs in DSSCs exhibited PCE as high as 7.45% than those with only platinum ($\eta = 7.37\%$) and pristine PANI CEs ($\eta = 5.60\%$). Dao et al. reported the use of carbon dot-Au nanoraspberries (Cdot-Au NRs) as CE in ZnO nanowire/CdS/CdSe(QDs) solar cell with 5.4% PCE, whereas Au-sputtered CE exhibited PCE of 3.6% and C dot exhibited remarkably low PCE of 0.18%. Such improved performance of the QDSCs with C dot-Au NR-based CE is accredited to its more larger surface area than that of Au-sputtered CE, resulting in an increased in number of the electrocatalytic active sites with improved charge transfer and reduced series resistance [19].

On the other hand, bifacial DSSCs have been fabricated to harvest solar energy from both sides of the device which is a major attraction to the scientific community because of optimum utilization of solar radiation within the same fabrication cost. In this case, semitransparent CE is required upon shining by sunlight; however, the preferred Pt electrode has transparency below 40% in general, yielding an efficiency lower up to 3%–4% in final solar cell devices. For bifacial DSSCs, CQDs can be an important player. Zhu et al. demonstrated that improvement in the bifacial DSSCs by the integration of CQDs with transparent CoSe is an effective strategy to enhance the catalytic activity of a CE and rear efficiency of corresponding bifacial DSSCs [20]. Fig. 7.5A shows the schematic device diagram of bifacial DSSCs, and the corresponding energy band diagram is shown in Fig. 7.5B. Upon illumination through the front side, the photons that enter from the fluorine-doped tin oxide (FTO) glass are absorbed by organic N719 dye molecules to release electrons to TiO_2. These exciting dyes go back to the ground state after accepting an electron from I^-/I_3^- electrolyte. When light enters through the rear side of the device, the photons pass through the transparent CE and excite the CQDs according to the same mechanism to transfer an electron to LUMO level of alloy CE. Overall, the CQDs perform three functions: first UV and near-infrared light absorption for downconversion and upconversion channel respectively; second, it helps CE for better electron collection from the external circuit; and third it serves as the better electron donor to accelerate the reduction from electrolyte in the oxidation state. To achieve this, high transmittance of rear CE is very much critical. As presented in Fig. 7.5C, both CQDs-CoSe and CoSe-only CEs have outstanding optical transparencies ($>60\%$) at 400–1000 nm and are almost slimmer. Fig. 7.5D shows *J–V* curves of DSSCs devices with different CEs under dark and light illumination conditions from both sides of the devices with simulated sunlight irradiation. Using only CoSe tailed as CE, a front efficiency of 8.06% and a rear efficiency of 5.18% were reported for the CoSe tailored solar cell, which are both at a high level for bifacial DSSCs. By using the CQDs-CoSe CE, the front efficiency is increased to 9.08% whereas rear efficiency went up to 7.01%. The enhancement in efficacy in the front is due to the reabsorption of unabsorbed visible light across the photoanode and electrolyte by the CQDs, maximizing electron concentration at the CoSe electrode. Interestingly, about 35% enhancement of PCE in rear-side illumination of bifacial DSSC was observed due to excellent catalytic activity of the CQDs-CoSe CE. Zhang et al. also performed surface functionalization of CQDs to obtain

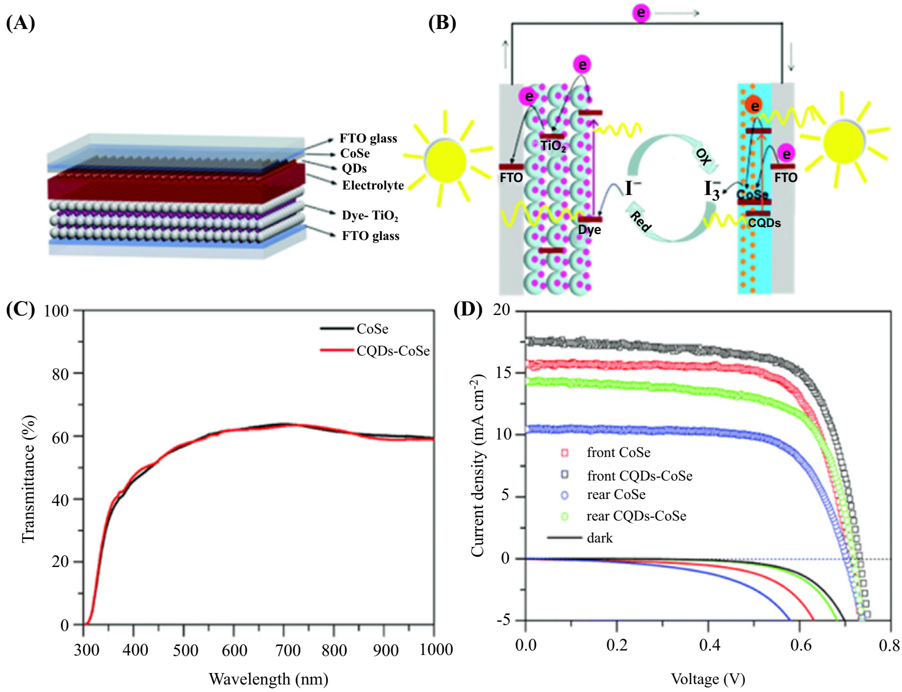

Figure 7.5 Schematic of (A) bifacial DSSCs, (B) charge carrier transfer processes under the illumination from the front or rear side. (C) Transmittance spectra of CoSe and CQDs-CoSe CEs. (D) *J–V* characteristics of bifacial DSSCs with different CEs. *CE*, Counter electrode; *CQDs*, carbon quantum dots; *DSSCs*, dye-sensitized solar cells.
Source: Reproduced with permission from W. Zhu, Y. Zhao, J. Duan, Y. Duan, Q. Tang, B. He, Carbon quantum dot tailored counter electrode for 7.01%-rear efficiency in a bifacial dye-sensitized solar cell, Chemical Communications (53) (2017) 9894–9897.

S-CQDs to enhance the electron density and used as CE in bifacial DSSCs with the front and rear sides PCE of 9.15% and 6.26%, respectively [17]. CQDs also used as an electrolyte to replace the volatile electrolyte have been looked upon so that its application for wider application is not hampered.

7.3 Carbon quantum dots in organic solar cells

Various advantages of OSCs such as low cost, lightweight, mechanical flexibility, and solution processability made them a potential candidate as a recently developed alternative source of energy harvesting. A typical OSC is composed of donor and acceptor material as an active layer sandwiched between cathode and anode. So far, most successful OSCs are in bulk heterojunction device architecture where acceptor and donor materials are mixed at the nanoscale level and placed between cathode and anode [21,22]. Overall, the operation of the device remains the same in all the device structures. The incident photons are absorbed by the active materials and generate excitons (loosely bound electron−hole pairs) which are dissociated at the donor−acceptor interface followed by transport to the respective electrode for the generation of electricity. Till date, the major challenges of OSCs have been their efficiency and stability to which incorporation of CQDs has contributed considerably. Complex production, a tendency to aggregation, and heterogeneous sizes of the organic molecule have made interfacial layers kinetically unfavorable for charge transportation, thus making most of the organic photovoltaic devices poorly performing devices. Despite that, Yang et al. reported a low-cost and low-cytotoxic inverted polymer solar cell with CQDs as the cathode interlayer (CIL) and the photoactive layer of PTB7-Th:$PC_{71}BM$ [23]. The device achieved a PCE of 8.13%, outperforming the control device without CQDs (4.14%). Parameters like V_{OC} and FF increase with the incorporation of CIL, thus enhancing electron extraction and hole-blocking. Values of series resistance (R_S) and the shunt resistance (R_{SH}) confirm this speculation and hence justify the results [23]. In another research, Yan et al. reported first-time synthesis of OSCs with graphitically structured fluorescent CQDs via chemical vapor deposition [24]. Synthesized material showed excellent crystallinity and the solar cell was further fabricated using the solution-processed CQDs as electron transport layer (ETL) as depicted in device structure (Fig. 7.6A) with the corresponding energy band structure (Fig. 7.6B). Device exhibited almost similar optimized PCE as that of P3HT:$PC_{61}BM$, PTB7:$PC_{61}BM$, and PTB7-TH:$PC_{71}BM$. After integration of CQD ETLs, devices reached to optimum PCE of 3.11%, 6.85%, and 8.23%, respectively. Fig. 7.6C shows the $J-V$ curves of PTB7-Th:$PC_{71}BM$ devices with various ETLs. It is clear from the curves that CQDs incorporated devices exhibited enhanced device performances when compared to the reference device untreated with ETL or methanol whereas its performance was comparable with LiF-based devices. The enhanced device performances are due to the low series resistance in the devices with CQDs, exhibiting a superior interfacial contact between the contact electrode and polymer by taking advantage of this ETL. Their study revealed that CQDs-based devices are thermally stable at 80°C for more than 150 hours, which is three times larger than LiF-based devices as shown in Fig. 7.6D. As it is quite known that Li^- and F^- diffuse very quickly into the organic part, but it is very difficult for CQDs to diffuse because of higher molecular dimension. The CQDs could be used as ETL in organic solar devices with superior thermal stability.

Lim et al. reported improved photovoltaic device performance of the inverted polymer solar cells after using hybrid CQDs and absorption polymer materials. CQDs ease carrier extraction in the PV structures, and thus increase PCE by 30% at around 3.3% on use of 0.05 weight % of carbon compared with that of the reference device in PCE [25]. Cui et al. reported fabrication of polymer solar cell with device architecture ITO/ZnO/P3HT:C-CQDs/MoO_3/Al and ITO/ZnO/P3HT:C-CQDs:

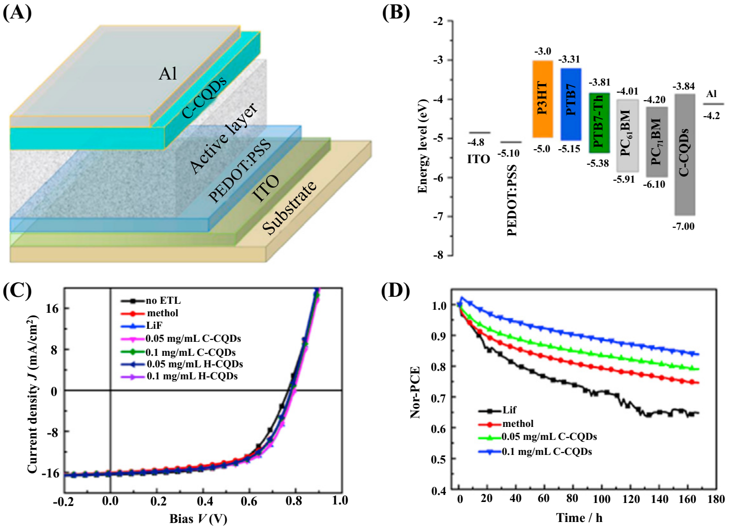

Figure 7.6 (A) Structure of device and (B) energy level alignment diagram of the solar device with CQDs as ETLs and P3HT:$PC_{61}BM$, PTB7:$PC_{61}BM$, or PTB7-Th:$PC_{71}BM$ as active layers. (C) $J-V$ curves of PTB7-Th:$PC_{71}BM$-based devices with different ETL. (D) Normalized PCE degradation of P3HT:$PC_{61}BM$ devices with various ETLs at the temperature of 80°C. *CQDs*, Carbon quantum dots; *ETL*, electron transport layer; *PCE*, power conversion efficiency.

Source: Reproduced with permission from L. Yan, Y. Yang, C.-Q. Ma, X. Liu, H. Wang, B. Xu, Synthesis of carbon quantum dots by chemical vapor deposition approach for use in polymer solar cell as the electrode buffer layer, Carbon (109) (2016) 598–607.

$PC_{61}BM/MoO_3/Al$ with varying concentration of CQDs. The PCE went up to 0.29% and 3.67% with incorporation of CQD in P3HT:CQDs and P3HT:CQDs: $PC_{61}BM$ configuration at varying carbon concentration of 5% and 7.5%, respectively. This increment could be due to the increased absorption and decreased impedance after incorporation of CQDs [26].

A highly efficient tandem solar device, consisting of hole transport layer (HTL) and polyethyleneimine (PEI) polyelectrolyte, was reported by Kang et al. in single junction. Efficiency up to 9.49% was recorded after CQDs-doped PEI was used as ETL in between ITO and photoactive layer which is almost 10% higher than only pristine PEI-based solar cell [27]. Device structure (schematic) of tandem organic solar device with CQDs is shown in Fig. 7.7A, and cross-section TEM of the real tandem solar cell to identify different constituted layers with proper estimation of thickness of each layers is shown in Fig. 7.7B. The $J-V$ characteristics of single-junction and tandem solar device with and without CQD doping on PEI are shown in Fig. 7.7C, and the corresponding EQE spectra of devices is shown in Fig. 7.7D. For the tandem solar cell, the PCE rose as high as 12.13% using CQDs-doped PEI as intermediate tunnel junction connection layer between two sub cells, which is approximately 15% higher than only pristine PEI as a layer. The reason behind the

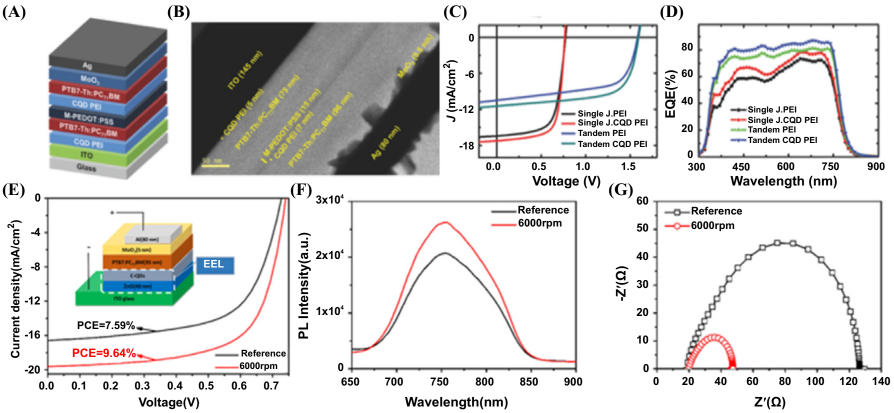

Figure 7.7 (A) Tandem cell architecture. (B) TEM image of tandem cell with CQD-doped PEI cross sectional view. (C) *J*−*V* curves of single-junction and tunnel-junction tandem cell with and without CQD-doped PEI. (D) Corresponding EQE spectra of devices [27]. (E) *J*−*V* plots of organic solar device in inverted structure with and without with CQD EEL on ZnO layer. Inset shows illustration of typical device structure. (F) Photoluminescence spectra for samples with layer structure of ITO/EEL(40 nm)/PTB7(50 nm)/MoO_3(5 nm)/Al(10 nm) under photoexcitation of 500 nm at room temperature. (G) Nyquist plot of the CQD-based devices and reference devices [28]. *CQD*, Carbon quantum dot; *EEL*, electron extraction layer; *EQE*, external quantum efficiency; *TEM*, transmission electron microscopy.
Source: (A−D) R. Kang, S. Park, Y.K. Jung, D.C. Lim, M.J. Cha, J.H. Seo, et al., High-efficiency polymer homo-tandem solar cells with carbon quantum-dot-doped tunnel junction intermediate layer, Advanced Energy Materials (8) (2018) 1702165. (E−G) Reproduced with permission from R. Zhang, M. Zhao, Z. Wang, Z. Wang, B. Zhao, Y. Miao, et al., Solution-processable ZnO/carbon quantum dots electron extraction layer for highly efficient polymer solar cells, ACS Applied Materials & Interfaces (10) (2018) 4895−4903.

increment is due to electron extraction properties in single-junction solar devices and improved series connection in tandem devices. In another research, Liu et al. reported improved energy transfer and charge transport property with CQDs in polymer solar cells in the inverted configuration. The PCE of doped devices increased to 7.05%, an improvement of around 28.2% compared with that of contrast devices. Significant enhancement in FF and a slight improvement in J_{SC} were observed after the use of CQDs [29].

Wang et al. synthesized N, S-doped CQDs (N,S-CQDs) and used them for photovoltaic application with ZnO ETL and got higher power conversion efficiency of around 9.31% without S-shape kink in the current density − voltage curves as of in reference device. The efficient surface modification for ZnO is to downplay light soaking effect in inverted OSCs. After placing of the N,S-CQDs on ZnO, roughness and surface energy reduce, thereby facilitating the transport and collection of photogenerated carriers [30]. In another research, an increase in PCE was reported by Lim et al. after incorporation of CQD/polyethylenimineethoxylated (PEIE) composites at interfacial layer with an electron extraction property in PTB7:PC_{71}BM-based solar cell got PCE of 8.34% [31]. They have reported that the significant improvement in device performance is due to the strong ultraviolet (UV) and visible range (300−780 nm) light absorbance due to CQDs reflected in the external quantum efficiency measurement. Inverted polymer solar cell with PCE of 9.64% has been reported by Zhang et al. applying CQDs electron extraction layer (EEL) on ZnO layer, which is 27% higher than control device as shown in Fig. 7.7E; inset shows typical device structure [28]. The contribution of increment is due to the incorporation of bilayer ZnO/CQDs EEL which suppresses the exciton quenching by ZnO passivation of the surface defects in EEL leading to an improved dissociation of an exciton, reduced recombination of charge as manifested in the PL spectra of Fig. 7.7F, and thus resulting in higher J_{SC} in CQDs-based devices. It was further verified by the electric impedance spectroscopy measurement through Nyquist plots displayed in Fig. 7.7G at zero bias under dark conditions. In comparison with the reference device, OSCs with ZnO/CQDs layer display a smaller diameter as compared to the reference device, indicating a very low contact resistance and lower transport resistance which results to an efficient photogenerated carrier extraction probability.

7.4 Carbon quantum dots in solid-state solar cells

The word "solid" in solid-state solar cells in itself reveals the fact that the device comprise all solid components. Solid-state solar cells are the evolved version of the earlier mentioned DSSCs [32]. It has been developed by minimizing the limitations like volatility and leakage of liquid electrolyte in DSSCs, which is leading to decreased device performance and stability. Liquid electrolyte peels off the mesoporous layer, thus dilapidating the overall device. A standard solid-state solar device is composed of photoanode, CE, and metal oxide nanoparticle sensitized with dye placed between them. It basically mimics the principle on which DSSCs work. CQDs have been explored as photosensitizer not only in DSSCs but also in solid-state solar cells. Advancement in the solid-state solar cell technology got restricted due its limitation as high cost output ratio, supplemented with use of hazardous element generally toxic in nature in spite of its unrivaled device stability and longevity. Briscoe et al. reported first-time green biomass-based CQDs for solid-state nanostructured solar cells. ZnO nanorods sensitized with three biomass, chitin, chitosan, and glucose, and their performance dependence on functional groups is studied. A layer combination of chitosan and chitin-derived CQDs produces the high efficiency of 0.077% [33]. NCQDs has been investigated by Carolan et al. Environmentally friendly, facile, rapid method techniques have been used such that their bandgap structure is suitable for photovoltaic application. An efficiency of 0.8% with an open-circuit voltage of 1.8 V was achieved. This improvement in efficiency was mainly attributed to the highly crystalline NCQD and the nondependence of CQD size on starting conditions [34].

Xie et al. fabricated a cost-effective heterojunction photovoltaic device with silicon nanowire (SiNW) array/CQDs core-shell by direct coating of Ag-assisted

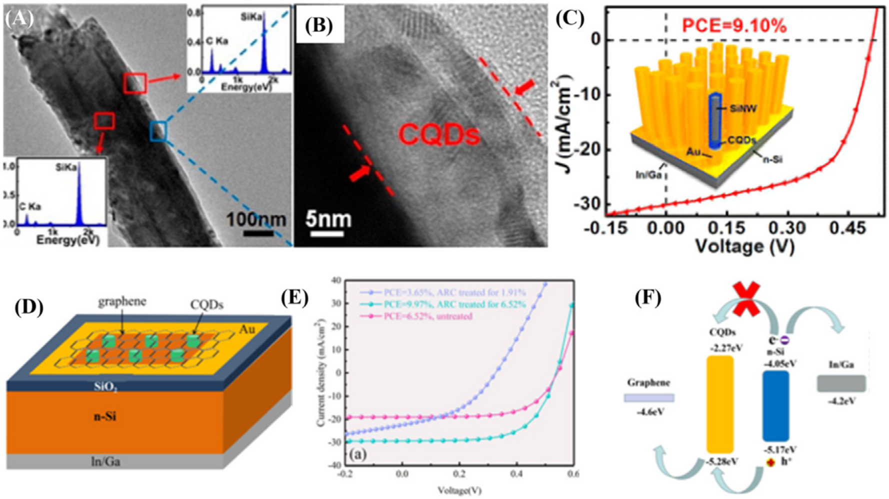

Figure 7.8 (A) TEM images of CQDs-coated SiNWs. EDS analysis of the CQD-coated SiNWs. In insets (B) high-resolution TEM images of individual SiNWs coated with CQDs. (C) *J*–*V* characteristic of CQDs coated silicon nanowire based solar cell. Inset shows schematic diagram of SiNW array/CQDs heterojunction device. (D) Illustration of the Gr/CQDs/Si solar cells. (E) *J*–*V* curves of Gr/CQDs/n-Si schottky solar cell before and after ARC treatment. (F) Energy band diagram of Gr/CQDs/n-Si device with photogenerated charge carrier movement in devices. *CQDs*, Carbon quantum dots; *EDS*, energy-dispersive X-ray spectroscopy; *SiNWs*, silicon nanowire.
Source: (A–C) Reproduced with permission from C. Xie, B. Nie, L. Zing, F.-X. Liang, M.-Z. Wang, L. Luo, et al., Core–shell heterojunction of silicon nanowire arrays and carbon quantum dots for photovoltaic devices and self-driven photo detectors, ACS Nano (8) (2014) 4015–4022. (D–F)Reproduced with permission from C. Geng, Y. Shang, J. Qiu, Q. Wang, X. Chen, S. Li, et al., Carbon quantum dots interfacial modified graphene/silicon Schottky barrier solar cell, Journal of Alloys and Compounds (835) (2020) 155268.

chemically etched SiNW arrays with CQDs [35]. Fig. 7.8A shows a typical TEM image of a CQDs coated SiNW. It is clear from the images that the SiNW fully covered by the CQDs thin film of a thickness of about 23 nm, corresponding to the ~5 layers of CQDs. Additionally, CQDs are closely attached to SiNW surface without pinhole area as revealed from high-resolution TEM images as presented in the Fig. 7.8B which were also further confirmed with energy-dispersive X-ray spectroscopy analysis in the insets of Fig. 7.8A, pointing uniform coverage of CQDs on SiNWs. The heterojunction exhibited a rectifying behavior with a rectification ratio of 10^3 at 0.8 V in the dark and efficiency as high as 9.10% under AM 1.5 G irradiation along with a barrier height of 0.75 eV shown in Fig. 7.8C. The thickness of device participated vitally in determining device performance. Device is sensitive to 600 nm photoirradiation under zero bias with greater photosensitivity and quicker response speed. Enhanced PCE of graphene/silicon Schottky barrier solar cell was reported by Geng et al. by CQD-based interface engineering. Fig. 7.8D shows a schematic diagram of the Gr/CQDs/Si solar cells [36]. The efficiency reached 9.97% of nano-TiO_2 coated Gr/CQDs/Si solar cells where the CQDs size was 4−7 nm at the interlayer thickness of around 26 nm with V_{OC} of 0.51 V, J_{SC} of 29.33 mA/cm^2, and *FF* of 66.59% as shown in the *J*−*V* characteristics in Fig. 7.8E. The TiO_2 acts as an anti-reflecting coating. The interlayer serves as an electron blocking layer as well as HTL simultaneously and decreases charge recombination and reverse saturation current as demonstrated in the energy band diagram (Fig. 7.8F). Efficiency improvement in crystalline silicon module was reported by Dai et al. after incorporation of CQDs which in turn tunes solar absorption spectra. Hydrothermally synthesized fluorescent CQDs mixed in VAE (vinyl acetate-ethylene) forms an emulsion which has good sticking quality and exhibits luminescent downshifting. The I_{SC} and EQE of the module increase to 17.86% at 2 wt.% of Si-CQDs after utilization of UV light [37]. Pelayo et al. reported improvement of silicon solar cell efficiency by employing the photoluminescent, downshifting effects of CQDs and CdTe quantum dots. Results show that there is a modest increase in the efficiency when the CQDs and CdTe QDs [with/without poly(methyl methacrylate(PMMA)] are incorporated regardless of the refluxing time employed during QD synthesis [38]. Moreover, CQDs help in increasing current collection and diminish parasitic recombination.

7.5 Carbon quantum dots in perovskite solar cells

Owing to their inherent structural property, perovskite-based solar cells are one of the most promising third-generation solar cells which have achieved a PCE of 25.6% in single junction just a little more than a decade since its inception [39]. The perovskite solar cell (PSC) comprises an active layer of perovskite material sandwiched between the electron and HTL on a transparent conducting oxide substrate with back metal contact at the other end. Depending on the arrangement of layers, PSCs could be of *n-i-p* or *p-i-n* configuration. In a typical PSC, incident photon energy absorbed by the perovskite materials generates exciton which gets separated within the perovskite layer or heterojunction interface to form electron and hole followed by transported through ETL and HTL, respectively. To facilitate the charge extraction and transportation processes, various strategies and techniques have been adopted which contribute to the efficient functioning of the overall device. On the other hand, CQDs have been widely used in PSCs as hole extraction material and almost research advancement revolves around it. CQDs, being a *p*-type semiconductor and its application as a HTL, have contributed significantly to the improved performance of the PSCs. The CQDs increase conductivity, reduce hysteresis, downshift band structure in material, and thus improve device performances. CQDs play a significant role in the passivating grain boundary, and increase crystallinity and ion mobility. Han et al. reported FTO/cp-TiO_2/mp-TiO_2/$MAPbI_3$-CQDs/carbon structure device. *J*−*V* curve of the device recorded the variation in PCE from 10.7% to 13.3% with an increasing concentration of CQD.

The CQD not only played a vital part in hole extraction from $MAPbI_3$ layer but also passivated trap states at $MAPbI_3$-CDQs interface film, thus leading to reduced recombination and interface loss, and increased grain size and efficiency [40]. Recently, hydrothermally synthesized CQDs were used to get ITO/HTL/Perovskite/PCBM/BCP/Ag, *p-i-n* configuration by Kim et al. $J-V$ curves of devices with bare NiO HTL and NiO:CQD HTL exhibited highest PCE of 16.42 ± 0.392% at a ratio of 95:5 [41]. Forward and reverse scan showed were recorded with an efficiency of 15.34% and 16.03% for bare NiO, and 16.75% and 16.91% for NiO:CQD::95:5, respectively. The hysteresis reduced significantly from 4.5% to less than 1% NiO. After inclusion of CQDs energy band alignment of NiO down shifts providing a justified orientation to the ITO work function and band edges of the perovskite layer. Electrical characteristics of HTL got improved because of CQDs which assisted in the improved charge conductance and decreased the series resistance (R_s) of the PSCs to 6.12 Ω cm^2 for NiO and 4.25 Ω cm^2 for NiO:CQD. Long-term stability of PCEs was achieved under ambient atmospheric conditions, and the CQD-incorporated NiO-based PSCs retained ~70% of its initial efficiency even after 192 hours. In another research by Paulo et al. group from Spain reported methyl ammonium lead iodide($MAPbI_3$) based perovskite solar devices with CQDs as HTL for improved PCE of 3%. The investigation reveals limitations such as poor perovskite coverage over the mp-TiO_2 surface lower efficiency as confirmed by environmental scanning electron microscopy (ESEM) analysis [42]. Hao et al. reported an increase of almost 24.6% in PCE after optimized addition of 10 wt.% CQDs in ITO/TiO_2(CQD)/Perovskite/spiro-OMeTAD/Au cell architecture [43]. The champion device exhibits V_{OC} of around 1.14 V, a J_{SC} up to 21.36 mA/cm^2, a FF of 78%, with high PCE of 18.9%. This significant improvement in efficiency could be accredited to efficient charge carrier extraction and injection in PSCs, especially between the TiO_2 and perovskite layers. The CQDs increase the electronic coupling between the $CH_3NH_3PbI_{3-x}Cl_x$ and TiO_2 ETL interface as well as energy levels that contribute to electron extraction. It was also observed that CQDs/TiO_2 combination improves V_{OC} and J_{SC} simultaneously when compared to standalone TiO_2 devices. A theoretical study performed by Matta et al. reveals about efficient charge transfer mechanism between the C-Dot/PbI_2 system interfaces when compared to that of CQDs/MAI system interface [44]. The study found that C-dots with functionalized -OH and -COOH moieties which acts as the potential hole transfer entity for PSCs. It was also found that the bonding position on the C-dot impacts the bandgap and band edge positions. This opens up the avenue to explore and tune the band alignment of C-dots to get desired value for other solar cells applications. The valance band maximum (VBM) levels for C-dots are found to be more suitable for the purpose of efficient hole transportation after considering the minimum driving force that is required for an effective hole transporting material. Zou et al. reported hole-transport material (HTM)-free CQDs incorporated PSCs. The observations revealed the effects of CQDs on the TiO_2 nanosheet-based and HTM-free PSCs performance. At CQD content of 0.1% (optimized values) the PSC exhibited 60% higher J_{SC} up to 16.40 mA/cm^2 and an efficiency of 7.62%. The reason behind this improvement could be due to excellent conductivity resulting from the heterogeneous nuclei of

CQDs in course of perovskite crystallization, which increases the number of perovskite nuclei and forms a fine perovskite grain, for increased coverage on the substrate. Moreover, CQDs help in the efficient transportation of the photo-excited electrons, thus accelerating the separated and mobilized charge carriers [45]. Mat et al. fabricated the device with PCE of 18.24% withholding its initial PCE of around 73.4% after 48 hours of aging under 80% relative humidity dark room temperature condition. The results reveal the CQDs passivation mechanism on the grain boundaries and its role as the nucleation site to improve the crystallinity of the perovskite, thus reducing the recombination of charge carrier at the grain boundaries. Carbonyl functional groups on CQDs could reduce down the perovskite crystal growth, resulting in larger size of perovskite grains. Moreover, CQDs can passivate the uncoordinated lead ions at grain boundaries of perovskite by functional groups such as hydroxyl and carbonyl to decrease nonradiative recombination [45]. Maxim et al. reported the downconversion effect with the use of CQDs to substantially convert fraction of incident UV light to visible light for optimized photovoltaic applications. After embedding CQDs on PMMA the PSCs exhibited improved PCE of 17.29% and 17.86% for forward and reverse bias, respectively, especially resulting increased FF and photocurrent density [46].

High efficiency of around 22.77%, has been attained by Hui et al. by the use of inexpensive carboxylic acid and red CQDs (hydroxyl-rich) (RCQs)-doped SnO_2. This could be accredited to the doped ETL which has highest electron mobility for modified SnO_2, i.e., 1.73×10^{-2} $cm^2/V/s$. They have fabricated $Cs_{0.05}(MA_{0.17}FA_{0.83})_{0.95}Pb(I_{0.83}Br_{0.17})_3$, a planar-type PSCs on both the SnO_2 and SnO_2-RCQs ETLs with ITO/SnO_2/perovskite/spiro-OMeTAD/MoO_3/Au structure which is depicted in Fig. 7.9A. The device upon optimization displayed superior performance, with V_{OC} of 1.14 V, J_{SC} of 24.1 mA/cm^2, and FF of 83%, resulting is an excellent PCE reaching 22.77% as compared to 19.15% PCE of the control device PSC based on the SnO_2 at 1 vol.% of SnO_2-RCQs ETL as shown in the typical $J-V$ curve in Fig. 7.9B. The common problem in the PSCs is hysteresis behavior in the $J-V$ curve. Fig. 7.9C shows $J-V$ hysteresis of PSCs based upon SnO_2-RCQs with a significant reduction within $\approx 1\%$ as compared to pure SnO_2 ETL-based devices. This improvement is much likely due to improved electron mobility of RCQs-SiO_2 ETL. The stabilized output (steady-state) with PCE of 21.50% and J_{sc} of 21.50 mA/cm^2 of SnO_2-RCQs-based devices at which maximum power point ($V_{max} \approx 1$ V) was achieved for 120 hours of testing is shown in Fig. 7.9D. The enhancement in EQE spectra of SnO_2-RCQs-based PSC devices was reported over the entire visible range with integrated J_{SC} of 22.7 mA/cm^2 as shown in Fig. 7.9E. The device shows environmental stability without encapsulation, retaining up to 95% of initial PCE at 25°C after 1000 hours, when exposed to lesser relative humidity of 40%–60% as compared to SnO_2-based device which holding 80% as depicted in Fig. 7.9F. The improved performance of SnO_2-RCQs-based device is due to RCQs which reduces Gibbs free energy of SnO_2 surface and acts as nucleation center for perovskite crystal development. Alongside, RCQs can efficiently bond with incompletely coordinated Pb^{2+} ions of the perovskites to support high-quality formation of film which is depicted in Fig. 7.9G. The passivation conclusively leads to improved crystalline phase purity over large areas with enhanced uniformity and

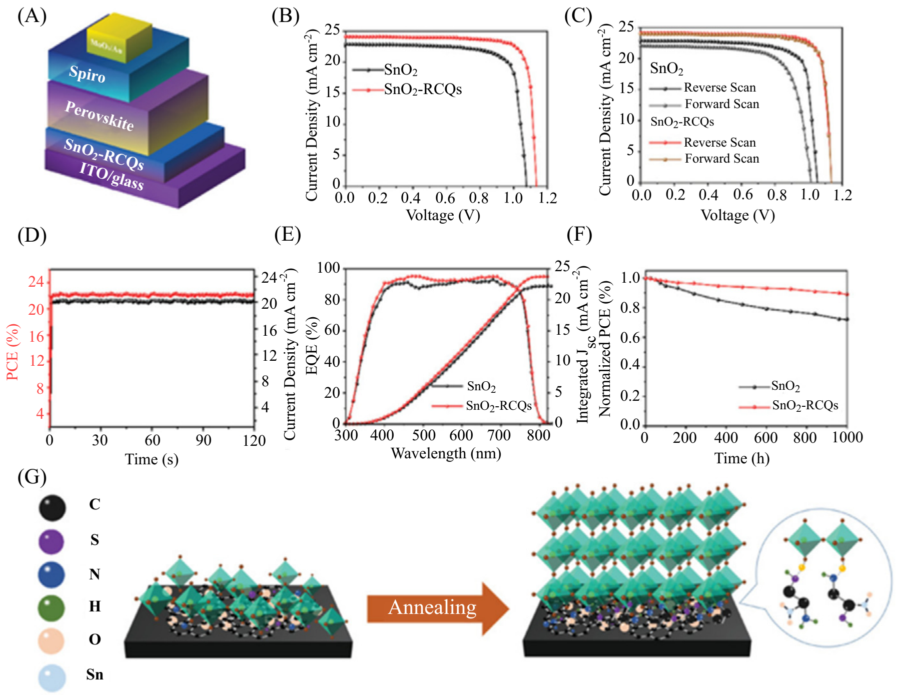

Figure 7.9 (A) Schematic of device structure used in this study. (B) Current density vs voltage (*J*−*V*) plot of the champion perovskite devices based on SnO_2 and SnO_2-RCQs ETLs under the illumination of 1 sun AM 1.5 G. (C) *J*−*V* plot for forward and reverse scans in case of both the champion devices. (D) Photocurrent and efficiency of the PSCs on the SnO_2-RCQs ETL at the at 1.0 V (maximum power point). (E) EQE and current density plot of both of the champion perovskite solar cells. (F) PCE (normalized) of PSCs based on two ETLs without encapsulation as function of time at 25°C in ambient environment (dark) with relative humidity of 40%−60%. (G) Perovskite crystal growth mechanism in RCQs doped SnO_2 (ETLs) precursor solution. *EQE*, External quantum efficiency; *ETL*, electron transport layer; *PCE*, power conversion efficiency; *PSC*, perovskite solar cell.

Source: Reproduced with permission from W. Hui, Y. Yang, Q. Xu, H. Gu, S. Feng, Z. Su, et al., Red-carbon-quantum-dot-doped SnO_2 composite with enhanced electron mobility for efficient and stable perovskite solar cells, Advanced Materials (32) (2020) 1906374.

reduced traps/defects at ETL/perovskite interface attributed to higher performances [47]. PCE of 8.29% was recorded by Zhou et al. after sensitization of cesium lead bromide ($CsPbBr_3$) inverse opal PSC with CQD. The inorganic $CsPbBr_3I$ shows a slow photon effect from tunable bandgaps exhibiting optical responses novel in nature as it has a broad light absorption range, higher charge transfer rate, and facilitates electron−hole extraction, thus resulting in improved PCE [48]. Lio et al. reported an increase in PEC of 12.08% and 28.7% after integration of CQDs and CQDs with red phosphorus quantum dots (RPQDs), respectively. This increase could be due to the setting up of intermediate energy levels around TiO_2/$CsPbBr_3$ and $CsPbBr_3$/carbon interfaces with

CQDs and RPQDs, respectively. The interface modification increases charge extraction and passivation effect contributing to a highest PCE of around 8.20% and 7.14% for FTO/c-TiO_2/m-TiO_2/CQDs/$CsPbB_3$/RPQDs/carbon configurations and FTO/c-TiO_2/m-TiO_2 /CQDs/$CsPbBr_3$/carbon configurations, respectively [49]. On the other hand, these all-inorganic PSCs are very stable more than 1056 hours and 80% relative humidity, which indicates a good environmental stability toward future commercialization.

7.6 Carbon quantum dots in all-weather solar cells

All-weather solar cells are an important strategy to supplement intermittent energy supply. For the past few years, all-weather solar cell has gripped the tremendous attention of the scientific community. They provide a solution to challenges posed by state-of-the-art solar cells and provide energy supply during dark-light conditions, rainy, cloudy, and foggy weather. Its structure resembles to that of DSSCs with an extra layer coating of advanced material to improve the spectral range utilization of solar radiation, thus facilitating maximized long hour energy harvest without compromising the PCE. Like DSSC, it consists of mesoporous nanoparticles coated photoanode, light-absorbing dye molecules, an electrolyte containing a redox couple, and a CE [50]. Meng et al. reported use of CQD-sensitized m-TiO_2/LPP photoanodes in all-weather solar cells [51]. Optical storage phenomena exhibited by photoanode of the device under illumination and monochromatic green light excitation in dark makes it worthy for all-weather photovoltaic application. The optimized yields are around 7.97% in case of dark PCE along with its several hour consistency in electricity output. Green-emitting LPP absorbs down-converted as well as up-converted light for electricity generation in dark atmosphere, thus remarkably widening light absorption range. In another research, Yang et al. reported all-weather solar cells with the incorporation of LPP in CQD-based solar cells. The efficiency rose as high as 14.8% in dark with good long-term stability [52]. The possible mechanism behind this is an increment in conjugated degree of CQDs varying concerning heating time range and hence altering the quantum confinement in CQDs. Tang et al. reported low-cost, environment friendly carbohydrates (glucose, maltol, and sucrose) based CQDs with all-weather solar cells applications. With glucose, maltol, and sucrose as CQD sources, the device yielded efficiency values of 0.14%, 0.11%, and 0.12%, respectively. Attribution to such low efficiency is due to the weak affinity of CQDs and the TiO_2 surface. After incorporation of LPP, the efficiency increased as high as 14.5%, 15.1%, and 13.5% for the solar cells with glucose, maltose, and sucrose sources, respectively [53].

7.7 Summary and perspective

CQDs have been successfully investigated in different types of photovoltaic devices with different capacities due to their excellent photophysical properties. The interesting features of CQDs make them highly compatible luminescent material with optoelectronic applicability superior to conventionally used materials from the past. Despite such impressive contribution and progresses in solar cells performances, all the CQD synthesis processes along with the purification processes need to be relooked to separate out reaction by-products, followed by a judicial investigation of every component which is necessary for further enhancement. Standard characterization protocols with careful statistical comparison need to be followed to resolve the revealed properties of CQDs. The longer device stability of CQD-based photovoltaic devices is also one of the rising concerns that demands significant research efforts. The doping with heteroatoms in the core of CQDs or functionalizing at the surface is very much necessary for further advancement of the electronic and optoelectronic features in CDQs efficient light harvesting. The CQD-based photovoltaic cells need to be highly stable due to their continuous exposure to light under ambient conditions for commercial application. CQDs are an excellent new player in photovoltaic devices with the potential to go greener and suitable for low-cost high-efficient solar cell applications.

Acknowledgments

This work is partially supported by Science and Engineering Research Board (SERB) (Project No.: SB/FTP/PS-148/2013, SR/S2/RJN-55/2012, and CRG/2021/007016), Department of Science and Technology, Government of India.

References

[1] J.B. Essner, G.A. Baker, The emerging roles of carbon dots in solar photovoltaics: a critical review, Environmental Science: Nano 4 (2017) 1216−1263.

[2] Y. Wang, A. Hu, Carbon quantum dots: synthesis, properties and applications, Journal of Materials Chemistry C 2 (2014) 6921−6939.

[3] T. Yuan, T. Meng, P. He, Y. Shi, Y. Li, X. Li, et al., Carbon quantum dots: an emerging material for optoelectronic applications, Journal of Materials Chemistry C 7 (2019) 6820−6835.

[4] B. O’regan, M. Grätzel, A low-cost, high-efficiency solar cell based on dye-sensitized colloidal TiO_2 films, Nature 353 (1991) 737−740.

[5] A. Mahapatra, P. Kumar, J. Bhansare, S.M. Surapaneni, A. Sen, B. Pradhan, Development of dye-sensitized solar cell using *M. philippensis* (kamala tree) fruit extract: a combined experimental and theoretical study, International Journal of Energy Research 45 (2021) 21509−21515.

[6] A. Mahapatra, P. Kumar, B. Pradhan, Improved performance of cadmium sulfide-sensitized solar cells by interface engineering, Journal of Materials Science: Materials in Electronics 31 (2020) 6274−6278.

[7] P. Mirtchev, E.J. Henderson, N. Soheilnia, C.M. Yip, G.A. Ozin, Solution phase synthesis of carbon quantum dots as sensitizers for nanocrystalline TiO 2 solar cells, Journal of Materials Chemistry 22 (2012) 1265−1269.

[8] X. Yan, X. Cui, B. Li, L.-s Li, Large, solution-processable graphene quantum dots as light absorbers for photovoltaics, Nano Letters 10 (2010) 1869−1873.

[9] X. Guo, H. Zhang, H. Sun, M.O. Tade, S. Wang, Green synthesis of carbon quantum dots for sensitized solar cells, ChemPhotoChem 1 (2017) 116−119.

[10] P. Huang, S. Xu, M. Zhang, W. Zhong, Z. Xiao, Y. Luo, Green allium fistulosum derived nitrogen self-doped carbon dots for quantum dot-sensitized solar cells, Materials Chemistry and Physics 240 (2020) 122158.

[11] H. Wang, P. Sun, S. Cong, J. Wu, L. Gao, Y. Wang, et al., Nitrogen-doped carbon dots for “green” quantum dot solar cells, Nanoscale Research Letters 11 (2016) 1−6.

[12] Q. Zhang, G. Zhang, X. Sun, K. Yin, H. Li, Improving the power conversion efficiency of carbon quantum dot-sensitized solar cells by growing the dots on a TiO_2 photoanode in situ, Nanomaterials 7 (2017) 130.

[13] Y. Zhao, J. Duan, B. He, Z. Jiao, Q. Tang, Improved charge extraction with N-doped carbon quantum dots in dye-sensitized solar cells, Electrochimica Acta 282 (2018) 255−262.

[14] W. Zhu, J. Duan, Y. Duan, Y. Zhao, Q. Tang, Efficiency enhancement of hybridized solar cells through co-sensitization and fast charge extraction by up-converted polyethylene glycol modified carbon quantum dots, Journal of Power Sources, 367 (2017) 158−166.

[15] K.P. Shejale, A. Jaiswal, A. Kumar, S. Saxena, S. Shukla, Nitrogen doped carbon quantum dots as Co-active materials for highly efficient dye sensitized solar cells, Carbon 183 (2021) 169−175.

[16] D. Dou, J. Duan, Y. Zhao, B. He, Q. Tang, Cubic carbon quantum dots for light-harvesters in mesoscopic solar cells, Electrochimica Acta 275 (2018) 275−280.

[17] Y. Zhang, Y. Zhao, J. Duan, Q. Tang, S-doped CQDs tailored transparent counter electrodes for high-efficiency bifacial dye-sensitized solar cells, Electrochimica Acta 261 (2018) 588−595.

[18] K. Lee, S. Cho, M. Kim, J. Kim, J. Ryu, K.-Y. Shin, et al., Highly porous nanostructured polyaniline/carbon nanodots as efficient counter electrodes for Pt-free dye-sensitized solar cells, Journal of Materials Chemistry A 3 (2015) 19018−19026.

[19] V.-D. Dao, P. Kim, S. Baek, L.L. Larina, K. Yong, R. Ryoo, et al., Facile synthesis of carbon dot-Au nanoraspberries and their application as high-performance counter electrodes in quantum dot-sensitized solar cells, Carbon 96 (2016) 139−144.

[20] W. Zhu, Y. Zhao, J. Duan, Y. Duan, Q. Tang, B. He, Carbon quantum dot tailored counter electrode for 7.01%-rear efficiency in a bifacial dye-sensitized solar cell, Chemical Communications 53 (2017) 9894−9897.

[21] S. Liu, J. Yuan, W. Deng, M. Luo, Y. Xie, Q. Liang, et al., High-efficiency organic solar cells with low non-radiative recombination loss and low energetic disorder, Nature Photonics 14 (2020) 300−305.

[22] B. Pradhan, S. Albrecht, B. Stiller, D. Neher, Inverted organic solar cells comprising low-temperature-processed ZnO films, Applied Physics A 115 (2014) 365−369.

[23] Y. Yang, X. Lin, W. Li, J. Ou, Z. Yuan, F. Xie, et al., One-pot large-scale synthesis of carbon quantum dots: efficient cathode interlayers for polymer solar cells, ACS Applied Materials & Interfaces 9 (2017) 14953−14959.

[24] L. Yan, Y. Yang, C.-Q. Ma, X. Liu, H. Wang, B. Xu, Synthesis of carbon quantum dots by chemical vapor deposition approach for use in polymer solar cell as the electrode buffer layer, Carbon 109 (2016) 598−607.

[25] H. Lim, K.S. Lee, Y. Liu, H.Y. Kim, D.I. Son, Photovoltaic performance of inverted polymer solar cells using hybrid carbon quantum dots and absorption polymer materials, Electronic Materials Letters 14 (2018) 581−586.

[26] B. Cui, L. Yan, H. Gu, Y. Yang, X. Liu, C.-Q. Ma, et al., Fluorescent carbon quantum dots synthesized by chemical vapor deposition: an alternative candidate for electron acceptor in polymer solar cells, Optical Materials 75 (2018) 166−173.

[27] R. Kang, S. Park, Y.K. Jung, D.C. Lim, M.J. Cha, J.H. Seo, et al., High-efficiency polymer homo-tandem solar cells with carbon quantum-dot-doped tunnel junction intermediate layer, Advanced Energy Materials 8 (2018) 1702165.

[28] R. Zhang, M. Zhao, Z. Wang, Z. Wang, B. Zhao, Y. Miao, et al., Solution-processable ZnO/carbon quantum dots electron extraction layer for highly efficient polymer solar cells, ACS Applied Materials & Interfaces 10 (2018) 4895−4903.

[29] C. Liu, K. Chang, W. Guo, H. Li, L. Shen, W. Chen, et al., Improving charge transport property and energy transfer with carbon quantum dots in inverted polymer solar cells, Applied Physics Letters 105 (2014) 131. 131.

[30] Y. Wang, L. Yan, G. Ji, C. Wang, H. Gu, Q. Luo, et al., Synthesis of N, S-doped carbon quantum dots for use in organic solar cells as the ZnO modifier to eliminate the light-soaking effect, ACS Applied Materials & Interfaces 11 (2018) 2243−2253.

[31] H. Lim, Y. Liu, H.Y. Kim, D.I. Son, Facile synthesis and characterization of carbon quantum dots and photovoltaic applications, Thin Solid Films 660 (2018) 672−677.

[32] B. Lee, J. He, R.P. Chang, M.G. Kanatzidis, All-solid-state dye-sensitized solar cells with high efficiency, Nature 485 (2012) 486−489.

[33] J. Briscoe, A. Marinovic, M. Sevilla, S. Dunn, M. Titirici, Biomass-derived carbon quantum dot sensitizers for solid-state nanostructured solar cells, Angewandte Chemie International Edition 54 (2015) 4463−4468.

[34] D. Carolan, C. Rocks, D.B. Padmanaban, P. Maguire, V. Svrcek, D. Mariotti, Environmentally friendly nitrogen-doped carbon quantum dots for next generation solar cells, Sustainable Energy & Fuels 1 (2017) 1611−1619.

[35] C. Xie, B. Nie, L. Zing, F.-X. Liang, M.-Z. Wang, L. Luo, et al., Core−shell heterojunction of silicon nanowire arrays and carbon quantum dots for photovoltaic devices and self-driven photo detectors, ACS Nano 8 (2014) 4015−4022.

[36] C. Geng, Y. Shang, J. Qiu, Q. Wang, X. Chen, S. Li, et al., Carbon quantum dots interfacial modified graphene/silicon Schottky barrier solar cell, Journal of Alloys and Compounds 835 (2020) 155268.

[37] D. Dai, X. To, X. Li, T. Live, F. Han, Tuning solar absorption spectra via carbon quantum dots/VAE composite layer and efficiency enhancement for crystalline Si solar module, Progress in Photovoltaics: Research and Applications 27 (2019) 283−289.

[38] E. Pelayo, A. Zarzuela, R. Lopez, E. Saucedo, R. Rules, A. Ayton, Silicon solar cell efficiency improvement employing the photoluminescent, down-shifting effects of carbon and CdTe quantum dots, Materials for Renewable and Sustainable Energy 5 (2016) 5.

[39] A. Mahapatra, S. Kumar, P. Kumar, B. Pradhan, Recent progress in perovskite solar cells: challenges from efficiency to stability, Materials Today Chemistry 23 (2022) 100686.

[40] J. Han, Y. Zhou, X. Yin, H. Nan, M. Tai, Y. Gu, et al., An excellent modifier: carbon quantum dots for highly efficient carbon-electrode-based methylammonium lead iodide solar cells, Solar RRL 3 (2019) 1900146.

[41] J.K. Kim, D.N. Nguyen, J.-H. Lee, S. Kang, Y. Kim, S.-S. Kim, et al., Carbon quantum dot-incorporated nickel oxide for planar pin type perovskite solar cells with enhanced efficiency and stability, Journal of Alloys and Compounds 818 (2020) 152887.

[42] S. Paulo, G. Stoica, W. Cambarau, E. Martinez-Ferrero, E. Palomares, Carbon quantum dots as new hole transport material for perovskite solar cells, Synthetic Metals 222 (2016) 17−22.

[43] H. Li, W. Shi, W. Huang, E.-P. Yao, J. Han, Z. Chen, et al., Carbon quantum dots/TiO x electron transport layer boosts efficiency of planar heterojunction perovskite solar cells to 19%, Nano Letters 17 (2017) 2328–2335.

[44] S. Kasi Matta, C. Zhang, A.P. O'Mullane, A. Du, Density functional theory investigation of carbon dots as hole-transport material in perovskite solar cells, Chemphyschem: A European Journal of Chemical Physics and Physical Chemistry 19 (2018) 3018–3023.

[45] H. Zou, D. Guo, B. He, J. Yu, K. Fan, Enhanced photocurrent density of HTM-free perovskite solar cells by carbon quantum dots, Applied Surface Science 430 (2018) 625–631.

[46] A.A. Maxim, S.N. Sadyk, D. Aidarkhanov, C. Surya, A. Ng, Y.-H. Hwang, et al., PMMA thin film with embedded carbon quantum dots for post-fabrication improvement of light harvesting in perovskite solar cells, Nanomaterials 10 (2020) 291.

[47] W. Hui, Y. Yang, Q. Xu, H. Gu, S. Feng, Z. Su, et al., Red-carbon-quantum-dot-doped SnO_2 composite with enhanced electron mobility for efficient and stable perovskite solar cells, Advanced Materials 32 (2020) 1906374.

[48] S. Zhou, R. Tang, L. Yin, Slow-photon-effect-induced photoelectrical-conversion efficiency enhancement for carbon-quantum-dot-sensitized inorganic CsPbBr3 inverse opal perovskite solar cells, Advanced Materials 29 (2017) 1703682.

[49] G. Liao, J. Duan, Y. Zhao, Q. Tang, Toward fast charge extraction in all-inorganic CsPbBr3 perovskite solar cells by setting intermediate energy levels, Solar Energy 171 (2018) 279–285.

[50] Q. Tang, All-weather solar cells: a rising photovoltaic revolution, Chemistry–A European Journal 23 (2017) 8118–8127.

[51] Y. Meng, Y. Zhang, W. Sun, M. Wang, B. He, H. Chen, et al., Biomass converted carbon quantum dots for all-weather solar cells, Electrochimica Acta 257 (2017) 259–266.

[52] J. Yang, Q. Tang, Q. Meng, Z. Zhang, J. Li, B. He, et al., Photoelectric conversion beyond sunny days: all-weather carbon quantum dot solar cells, Journal of Materials Chemistry A 5 (2017) 2143–2150.

[53] Q. Tang, W. Zhu, B. He, P. Yang, Rapid conversion from carbohydrates to large-scale carbon quantum dots for all-weather solar cells, ACS Nano 11 (2017) 1540–1547.

Light-emitting diode application of carbon quantum dots

8

Morteza Sasani Ghamsari[1] *and Ashkan Momeni Bidzard*[2]
[1]Photonics and Quantum Technologies Research School, Nuclear Science and Technology Research Institute, Tehran, Iran, [2]Department of Basic Sciences, Abadan Faculty of Petroleum Engineering, Petroleum University of Technology, Abadan, Iran

8.1 Introduction

Nowadays, carbon quantum dots (CQDs) with tunability in the bandgap, excitation-independent emission, and high-fluorescence quantum yields have received much attention. Due to the unique optical properties of CQDs and their biocompatibility, cost-effectiveness, and exceptional electronics, they have received much attention [1–10]. Over the past two decades, different top-down and bottom-up methods consisting of electrochemical synthesis [11–14], arc discharge [15–17], pulsed laser ablation/passivation [18–22], microwave-assisted synthesis [23–28], and hydrothermal and solvothermal methods [29–35] have been developed for the synthesis of CQDs with better optical characteristics. One of the important aspects is that the CQDs can emit full-color fluorescence covering the whole visible spectrum. Researchers showed that the quantum confinement and surface functionalization effects can be applied to tailor the optical properties of CQDs [33–47]. These optical properties make CQDs promising materials for a wide range of applications in light-emitting diodes (LEDs) [48–73] and lasers [74–82]. Especially, stable wavelength-tunable fluorescence from the visible to near-infrared (NIR) makes the CQDs an excellent building block for all types of LEDs. This chapter provides a survey of the recent research achievements in synthesis and tunable optical properties of CQDs which can apply to LEDs. We mainly focus on stable full-color fluorescence emissions of CQDs due to the quantum confinement and surface functionalization effects. We hope that the present chapter will stimulate interest in further investigations on carbon nanoparticle-based LEDs.

8.2 Synthesis methods of functionalized carbon quantum dots

Nowadays, different top-down and bottom-up approaches are employed to synthesize CQDs such as electrochemical synthesis, arc discharge, pulsed laser ablation/passivation, microwave-assisted synthesis, and hydrothermal and solvothermal methods.

Carbon Quantum Dots for Sustainable Energy and Optoelectronics. DOI: https://doi.org/10.1016/B978-0-323-90895-5.00011-4
© 2023 Elsevier Ltd. All rights reserved.

8.2.1 Electrochemical synthesis

Recently, the researchers developed electrochemical methods as commercial and environment-friendly techniques for the synthesis of the CQDs. These methods have advantages such as low cost, high productivity, good reproducibility, simple one-step operation, and easy posttreatments [11–14]. In this approach, carbon-containing materials such as graphite rods, carbon fiber, and carbon nanotubes can be used as electrode materials [12]. Fig. 8.1 shows an experimental setup of this process. It should be noticed that the electrode materials, electrolytes, and the applied potential play critical roles in the production of monodisperse CQDs by electrochemical methods. CQDs with different sizes and surface functionalization can be obtained by controlling these parameters [13,14].

8.2.2 Arc discharge

The synthesis of CQDs via electrical discharge has been employed as a simple and straightforward process [15–17]. In this method, two graphite electrodes are immersed into water or organic solutions, and the CQDs are produced by electrical discharge applied between electrodes [15,16]. A usual setup of the electrical discharge in liquids was illustrated in Fig. 8.2. This technique provides advantages of the control ability for the size and surface characteristics of the final nanoparticles product and the possibility to scale up the synthesis of CQDs by changing the discharge regimes and parameters. Especially, surface engineering of the synthesized CQDs with various functional groups in solutions leads to the enhancement of optical properties of the CQDs.

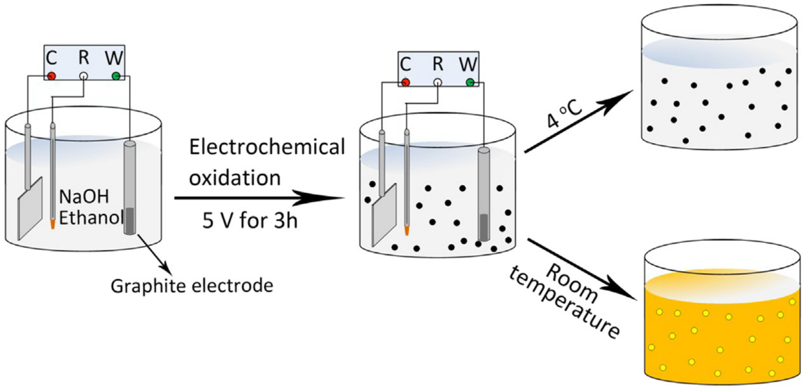

Figure 8.1 Experimental setup for the electrochemical synthesis of CQDs. *CQDs*, Carbon quantum dots.
Source: Reproduced with permission from M. Liu, et al., Carbon quantum dots directly generated from electrochemical oxidation of graphite electrodes in alkaline alcohols and the applications for specific ferric ion detection and cell imaging. *Analyst* 141 (9) (2016) 2657–2664.

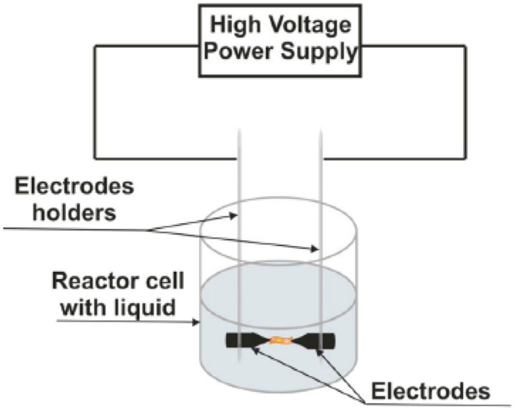

Figure 8.2 Electrical discharge in liquids for production of CQDs. *CQDs*, Carbon quantum dots.
Source: Reproduced with permission from A. Nevar, et al., Carbon nanodots with tunable luminescence properties synthesized by electrical discharge in octane. *Carbon Letters* 31 (1) (2021) 39–46.

8.2.3 Pulsed laser ablation/passivation technique

The synthesis of CQDs in solution using laser ablation is an attractive method owing to advantages such as simple, fast, and chemically clean operation [18–20]. In this process, as shown in Fig. 8.3, we use an intense laser beam focused on the surface of a carbon-based target material immersed in a liquid media. The ablation process is performed using ultrafast single-pulse and double-pulse laser irradiations [18–20]. The laser and material parameters have a crucial influence on the CQD size distribution as well as their surface characteristics which are critical factors for the optical properties of CQDs. Furthermore, the laser fragmentation of colloidal carbon micro/nanoparticles has been used to prepare the well-dispersed CQDs [21,22].

8.2.4 Microwave-assisted synthesis

Microwave irradiation was developed as a powerful technique for the one-pot synthesis of CQDs [23–28]. In this method, large-scale production of the CQDs can be achieved by using cheap, accessible, and natural materials as the green carbonaceous precursor [28]. The microwave-assisted reaction allows easy production of the high photoluminescence (PL) monodispersed CQDs with promising potential for optics-related applications [28]. A schematic of this process is shown in Fig. 8.4. In addition, it has been shown that microwave irradiation of CQDs can lead to a decrease in their surface defects, which results in a decrease in the nonradiative transitions. Therefore, PL enhancement can be observed [25].

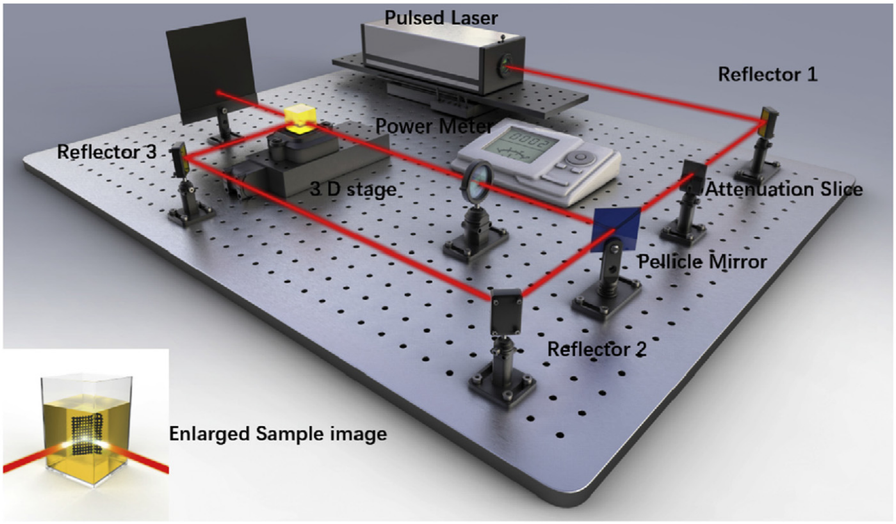
Pulsed Laser
Reflector 1
Power Meter
Reflector 3
3 D stage
Attenuation Slice
Pellicle Mirror
Reflector 2
Enlarged Sample image

Figure 8.3 Schematic diagram of the pulsed laser ablation process in liquids.
Source: Reproduced with permission from L. Cui, et al., Synthesis of homogeneous carbon quantum dots by ultrafast dual-beam pulsed laser ablation for bioimaging. *Materials Today Nano* 12 (2020) 100091.

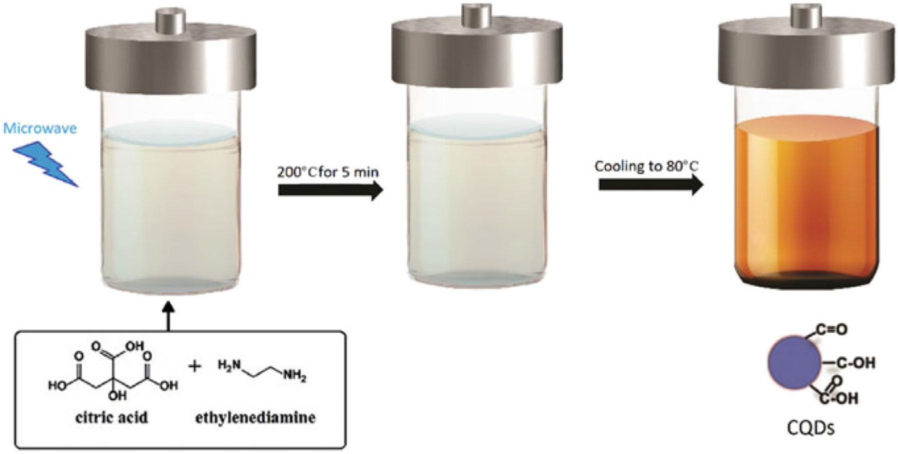
Microwave
200°C for 5 min
Cooling to 80°C
citric acid
ethylenediamine
C=O
C-OH
C-OH
CQDs

Figure 8.4 Schematic of the microwave-assisted method for production of CQDs. *CQDs*, Carbon quantum dots.
Source: Reproduced with permission from H. Behboudi, et al., Carbon quantum dots in nanobiotechnology, in nanomaterials for advanced biological applications (p. 145–179), Springer (2019).

8.2.5 Hydrothermal and solvothermal synthesis

Hydrothermal carbonization has been introduced as the most effective way for the large-scale synthesis of surface-functionalized CQDs [29–33]. Different types of precursors such as small molecules of polymers or food commodities (e.g., milk, fruit) to wastes (waste microorganisms) can be used in this technique [33]. Size distribution controllability and surface modifications of CQDs are the predominant characters of CQDs synthesized by this method, which have great importance for their applications [29]. Fig. 8.5 shows the proposed formation mechanism of CQDs in this process. Furthermore, the solvothermal method can be applied to synthesize the CQDs with full-spectrum emission. Due to the effect of solvent-related reactions, the tuning in the bandgap and PL are predicted [25,34,35].

8.3 Optical properties of carbon quantum dots

Previously, we emphasized that CQDs are a new class of carbon nanoparticles with sizes less than 10 nm that were discovered in 2004 and have received increasing attention over the past decade due to unique optical properties for optoelectronic applications [1–10]. Scientists have made great efforts to develop fluorescent CQDs with full-color tunable emission across the entire visible spectrum [33–47,83–85]. The emission wavelength of CQDs can be tuned by controlling their size, shape, surface passivation, and functionalization. However, there has been a long-standing debate about the PL mechanism. But, the proposed origins of CQD emission are the quantum confinement effect and electron–hole radiative recombination in carbon cores, surface defects, molecular states, and surface energy traps [33–47,83–85]. The CQDs with low toxicity, low-cost green synthesis methods, and exceptional tunable fluorescence emissions can be alternatives to conventional semiconductor quantum dots. Therefore, it is of great scientific effort to understand their optical properties for various device applications.

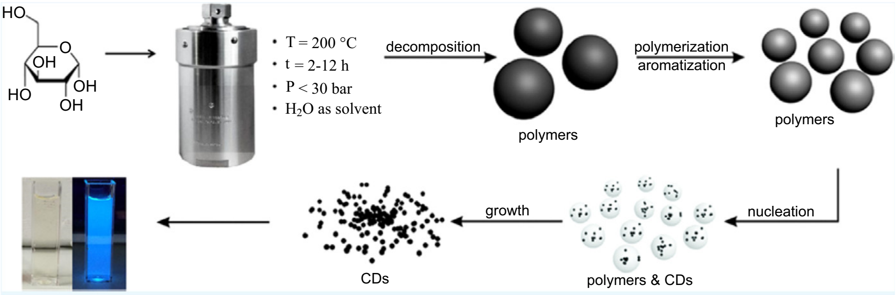

Figure 8.5 Formation mechanism of CQDs in the hydrothermal synthesis process [29]. *CQDs*, Carbon quantum dots.

8.3.1 Optical absorption

The UV−visible optical absorption of CQDs has been reported to have prominent UV absorption (230−320 nm) with a tail extending into the visible region due to the π-conjugated electrons in the core of CQDs and their surface chemical groups [8−10,37−40]. The broad peak at ~230 nm could be assigned to the π−π* transition of aromatic C = C bonds, whereas the n−π* transition of C = O bonds or other surface groups may result in the shoulder at ~300 nm [8−10]. Based on the quantum confinement effect, with the increase in size of CQDs a gradual redshift in excitonic absorption band from blue to red can be achieved and shown in Figs 8.6 and 8.7. In Fig. 8.6A, daylight photographs and UV excited fluorescence images of multicolor bandgap fluorescent CQDs are presented. In Fig. 8.6B, UV−visible optical absorption can be found. In Fig. 8.6C, D, the normalized PL spectra and time-resolved luminescence measurement of the CQDs are respectively illustrated. The changes of HOMO and LUMO energy levels as a function of the CQDs size are shown in Fig. 8.6E. In Fig. 8.7A and B, the daylight photographs, UV excited fluorescence images of the narrow bandwidth emission triangular CQDs ethanol solution are indicated, respectively. Fig. 8.7C shows the normalized UV−visible optical absorption and Fig. 8.7D indicates the normalized luminescence spectra of the blue, green, yellow, and red narrow bandwidth emission triangular CQDs, respectively.

Furthermore, surface functional groups on CQDs, i.e., C−OH, C = O, O−C = O, C = N, and C = S can also contribute to their absorption features. Studies showed that the surface functional groups provide the surface states formation that their energy levels are between π and π* states of C = C. These surface states thereby induce new absorption bands for possible electron transitions [8−10]. The redshifted absorption bands can play a crucial role in the tunable multiwavelength emissions from surface passivated CQDs.

8.3.2 Photoluminescence emissions from ultraviolet to near-infrared regions

The wavelength-tunable fluorescence across the entire visible to NIR spectrum makes CQDs promising materials for a wide range of applications. The physical mechanisms underlying the PL of the CQDs are mainly due to their size, shape, and surface functionalization [33−47,83−85].

8.3.2.1 Photoluminescence emission due to quantum confinement effect

The size-related quantum confinement effect has been introduced as a main PL mechanism of CQDs [46,47,83−85]. Yuan et al. have reported full spectrum bright multicolor fluorescent CQDs originated from their bandgap transitions [84]. Fig. 8.6 shows the redshift in fluorescence emission of CQDs with the size distribution of 1−7 nm, indicating the quantum confinement effect and the red-shifted

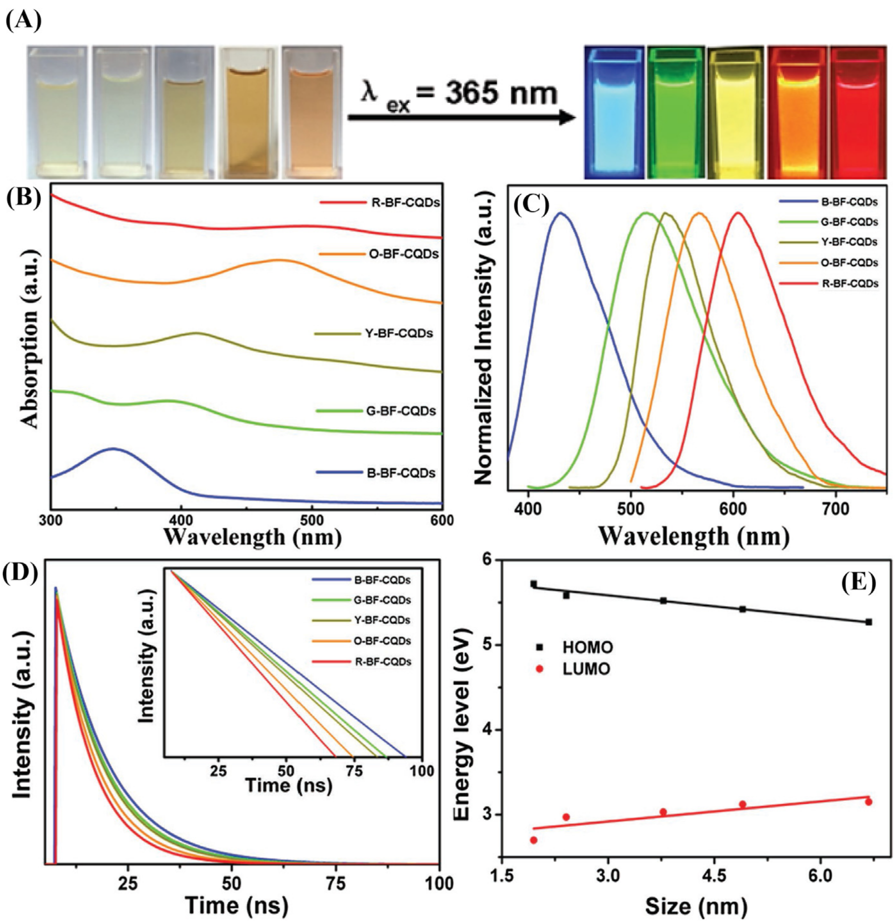

Figure 8.6 (A) Daylight photographs (left) and UV excited fluorescence images (right) of multicolor bandgap fluorescent CQDs. (B) UV−visible optical absorption, (C) normalized PL spectra, and (D) time-resolved luminescence measurement of the CQDs. (E) The changes of HOMO and LUMO energy levels as a function of the CQDs size. *CQDs*, Carbon quantum dots.

Source: Reproduced with permission from F. Yuan, et al., Bright multicolor bandgap fluorescent carbon quantum dots for electroluminescent light-emitting diodes. *Advanced Materials*, 29 (3) (2017) 1604436.

excitonic absorption bands of the CQDs [84]. Furthermore, the Yuan group has reported the synthesis of triangular CQDs with high color purity, narrow bandwidth, and tunable wavelength emission across the whole visible spectrum [85]. Fig. 8.7 depicts the excitonic absorption and highly tunable emission peaks originated from band-edge transitions in the triangular CQDs.

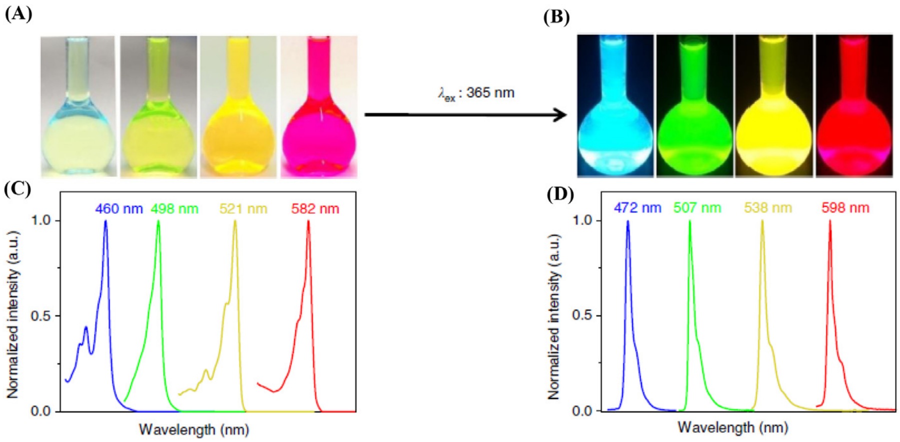

Figure 8.7 (A) Daylight photographs, and (B) UV excited fluorescence images of the narrow bandwidth emission triangular CQDs ethanol solution. (C) The normalized UV−visible optical absorption and (D) normalized luminescence spectra of the blue, green, yellow, and red narrow bandwidth emission triangular CQDs, respectively.
Source: Reproduced with permission from F. Yuan, et al., Engineering triangular carbon quantum dots with unprecedented narrow bandwidth emission for multicolored LEDs. *Nature communications*, 9 (1) (2018) 1−11.

8.3.2.2 Photoluminescence emission due to surface passivation and functionalization effect

The surface characteristics engineering of CQDs is one of the main remaining challenges with the significant influences on their optical properties, especially tunable full-color fluorescence emission [33−46]. Wang et al. reported that in the solvothermal synthesis method, the formed fluorophores by the solvent-related reactions could lead to the full-spectrum emission of CQDs by PL bandgap tuning [34]. Ding et al. have reported production of the CQDs with tunable emission across the entire visible spectrum by mainly controlling the content of graphitic nitrogen and oxygen-containing surface functional groups [35]. Shao et al. have presented experimental and theoretical evidence demonstrating that the LUMO − HOMO energy gap of the amino-functionalized CQDs may decrease with an increase in the number of amino (NH_2) surface groups, resulting in the PL redshift and full-spectrum emission [36]. Jiang et al. have reported that tuning the surface state of CQDs by increased surface oxidation and carboxylation can result in the redshift and multicolor PL emission [37]. Xu et al. have shown that the formation of different surface level states by hydrogen bonds between the surfaces of the CDs and different solvents can result in multicolor luminescent CQDs [38]. Furthermore, it has been reported that multi-emission luminescence in carbon dots can originate from multi-energy states assigned to the bandgap state, surface defect state, and molecular state [40]. The optical images of multicolor fluorescent CQDs with different molecular weights and at various oxidation times and corresponding fluorescence emission spectra of the CQDs under excitation of 360 nm are shown in Fig. 8.8A. In Fig. 8.8B, the influence of size of CQDs and their surface oxidation on the PL properties are shown.

It is evident that the surface states of CQDs have arisen from both sp^3- and sp^2-hybridized carbons and the surface functional groups [41,42]. Generally, the surface states-related fluorescence aspect may include the size of CQDs, their surface functional groups, and defects and heteroatom doping [41,42]. Experimental results indicate that the strong coupling interaction of carbon cores with carboxyl and carbonyl surface functional groups can alter the energy gaps of CQDs, resulting in the size-dependent PL ascribed to the surface states. It has been shown that diverse surface defects with different energy levels formed due to the oxygen-containing functional groups (epoxide, hydroxyl, carbonyl, and carboxyl). This kind of CQDs surface defect can result in multicolor emissions covering the visible light spectrum [41,42]. The process of tunable PL emission of CQDs due to oxygen-related surface defect state is shown in Fig. 8.9. In addition, the surface state emission intensity can be enhanced by the formation of the nitrogen-related surface functional group such as amino, pyridinic, hydrazine, or graphitic nitro. Also, they result in red-shifted emission and tunable multiwavelength PL from CQDs [41,42]. It was figured out that the CQDs doping with a heteroatom such as sulfur, phosphorus, boron, and fluorine, has also been introduced as an effective way for significant enhancement of their fluorescence intensity and redshift of emission wavelength [41,42].

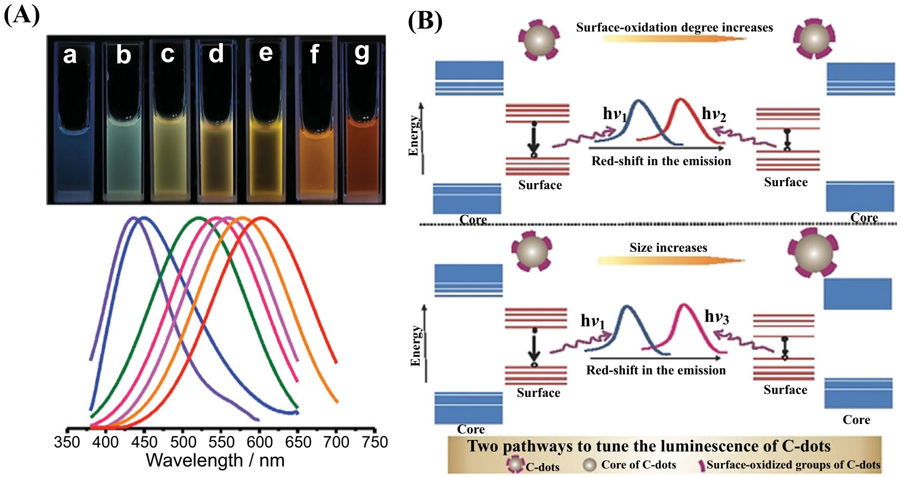

Figure 8.8 (A) Top: Optical images of multicolor fluorescent CQDs with different molecular weights and at various oxidation times. Bottom: Corresponding fluorescence emission spectra of the CQDs under excitation of 360 nm. (B) The influence of size of CQDs and their surface oxidation on the PL properties.
Source: Reproduced with permission from L. Bao, et al., Photoluminescence-tunable carbon nanodots: surface-state energy-gap tuning. *Advanced Materials*, 27 (10) (2015) 1663−1667.

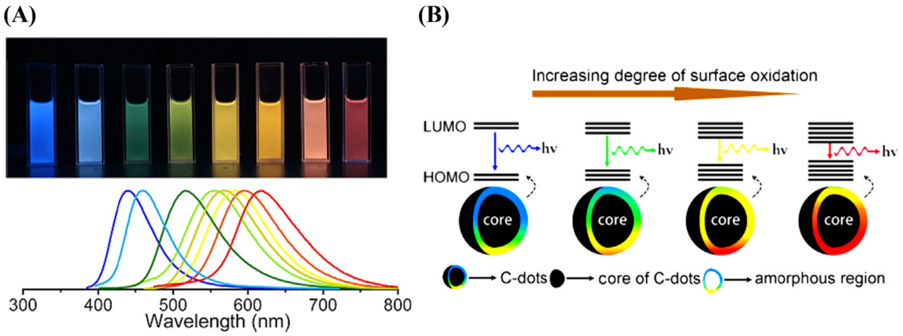

Figure 8.9 (A) UV excited fluorescence images of CQDs with corresponding luminescence spectra. (B) A model that presents the influence of different degrees of surface oxidation on the tunable PL of CQDs.
Source: Reprinted (adapted) with permission from H. Ding, et al., Full-color light-emitting carbon dots with a surface-state-controlled luminescence mechanism. *ACS Nano*, 10 (1) (2016) 484–491. Copyright {2016} American Chemical Society.

8.3.2.3 Up-conversion photoluminescence

In recent years, the CQDs with different surface functional groups have been introduced as effective spectral converters through broadband up-conversion of NIR/visible photons to higher energy photons [86–95]. The CQDs can exhibit multiple photon absorption in the three NIR windows (650–2000 nm), resulting in efficient visible light emission applicable for photoelectrode systems and bioimaging [87–90]. Fig. 8.10 shows the up-conversion fluorescence of CQDs. Under 800 nm fs-laser excitation, a transferring from the NIR light to visible light occurred [90]. Moreover, CQDs are confirmed to have the visible up-conversion PL property, capable of improving the visible/ultraviolet light photocatalytic performance of different materials [91–94]. It should be noted that the normal fluorescence due to the second-order grating diffraction of the exciting source may be incorrectly referred to as up-conversion fluorescence of CQDs [95].

8.3.3 Electroluminescence

The obtained wavelength-tunability from visible to NIR emission of CQDs has stimulated worldwide interest in developing efficient CQDs-based light-emitting devices for low-cost applications [48–53]. In light-emitting devices, an electroluminescence (EL) process occurs due to the electronic excitation. When CQDs are used in the light-emitting devices, the emission is observed by PL photoexcitations at multiple wavelengths. It has been shown that the CQDs with EL emission covering the entire visible spectrum can act as the emissive layer for achieving high-performance white LEDs [48,49]. Zhang et al. have reported switchable

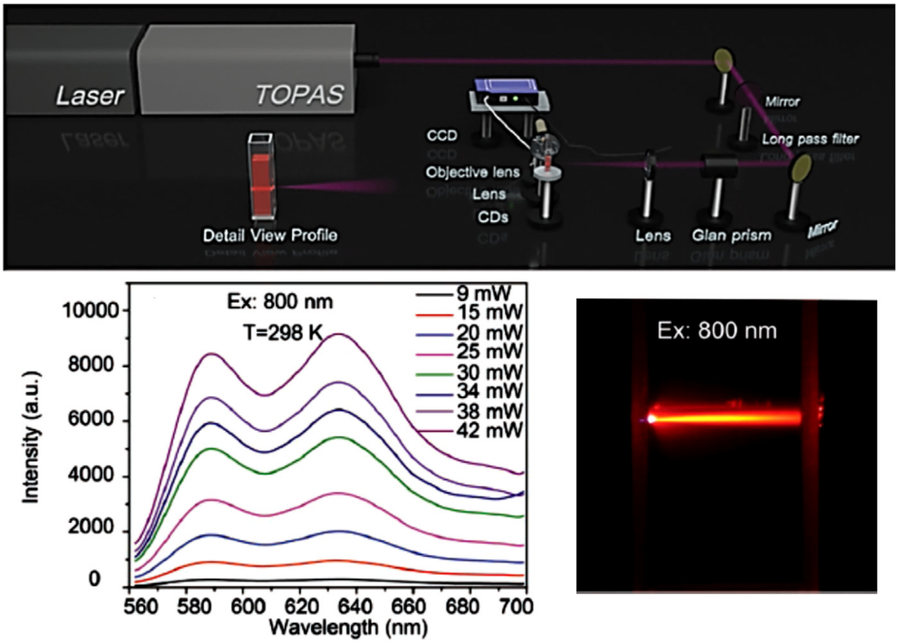

Figure 8.10 Setup and PL spectra of the CQDs excited by 800 nm fs-laser with different excitation intensities.
Source: Reproduced with permission from K.K. Liu, et al., Efficient red/near infrared emissive carbon nanodots with multiphoton excited upconversion fluorescence. *Advanced Science*, 6 (17) (2019) 1900766.

multicolor blue, cyan, magenta, and white EL emissions from the same CQDs by controlling the applied voltage (6–9 V) and injecting current density [50]. Mo et al. have presented low-voltage multicolor EL from CQDs/Si heterostructures including three distinct peaks at 438, 540, and 600 nm originating from the intrinsic CDs core, the C = O, and C–N surface groups, respectively [51]. As seen in Fig. 8.11, the CQDs with multicolor bright bandgap EL emission across the whole visible spectrum can be applied as an active emissive layer for the monochrome LEDs [84].

8.4 Carbon quantum dots device applications

8.4.1 Light-emitting diodes

In the last decade, the full-color fluorescent CQDs have been demonstrated as excellent materials to fabricate multicolor LEDs [48–73]. Two different strategies are followed for fabrication of CQDs-based LED devices. In the first one, CQDs are used as fluorescent materials of active emitters. In the second one, the CQDs

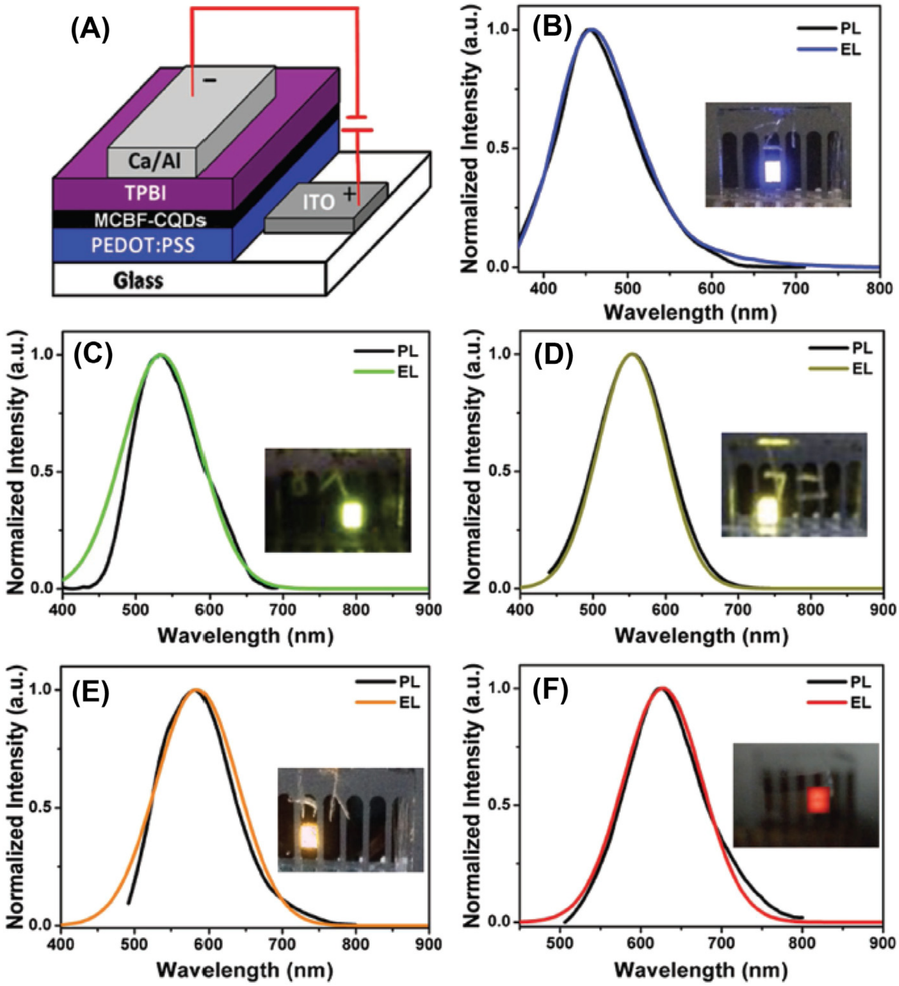

Figure 8.11 (A) Schematic view of CQDs-based LED device structure. Comparison of normalized EL and PL spectra of (B) blue, (C) green, (D) yellow, (E) orange, and (F) red emissions from CQDs thin films. The corresponding monochrome CQDs-based LEDs emissions are shown in the insets of (B–F).
Source: Reproduced with permission from F. Yuan, et al., Bright multicolor bandgap fluorescent carbon quantum dots for electroluminescent light-emitting diodes. *Advanced Materials*, 29 (3) (2017) 1604436.

are employed as color-converting phosphors [54,55]. Consequently, worldwide attention has been focused on using emitting layer CQDs in EL LEDs [48–63]. Fig. 8.12 illustrates schematics of CQDs-based EL LED with a middle emission layer of CQDs or CQDs/polymers host–guest complexes surrounded by interface transport layers and electrodes [54]. In the last decade, many investigations have

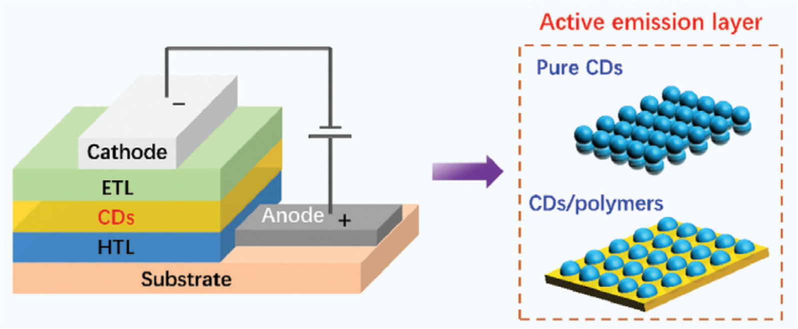

Figure 8.12 Schematic of the typical device structure of CQDs-based LEDs [54].

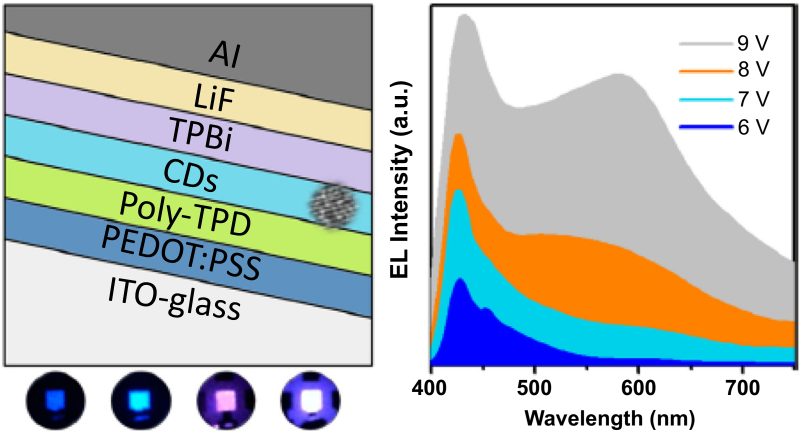

Figure 8.13 The device structure, EL spectra, and true color photographs of multicolor CQDs-LEDs operated under different voltages of 6−9 V.
Source: Reprinted (adapted) with permission from X. Zhang, et al., Color-switchable electroluminescence of carbon dot light-emitting diodes. *ACS Nano*, 7 (12) (2013) 11234−11241. Copyright {2013} American Chemical Society.

been focused on EL LEDs based on the pure/doped CQDs serving as an emissive layer with potential application for flat-panel displays and solid-state lighting [54].

Wang et al. demonstrated the CQDs-based white light-emitting device for the first time in 2011 [48]. Fig. 8.13 shows a CQDs-based color-switchable LED with multicolor blue, cyan, magenta, and white emissions achieved by tuning the applied voltage (6−9 V) and injecting current density [50]. Mo et al. have reported low-voltage and multicolor EL LEDs by using fluorescent CQDs as the active emitter [51]. Yuan et al. have presented monochrome LEDs in the blue-red spectral region in which the emission layer includes CQDs with multicolor bandgap fluorescent (see Fig. 8.11) [84]. Fluorescent CQDs with short-chain passivation and good film-forming ability applied as the emitting layer for the fabrication of EL LEDs that emit blue light under the voltage of 6–9 V [52]. Veca et al. have fabricated LED devices utilizing EL CQDs as the active layer, emitting white light with a bluish color [53].

Feasible strategies have been proposed to achieve high-performance CQDs-based LEDs with improved performance. These strategies include high-quality synthesis of CQDs with solid-state fluorescent, room temperature phosphorescence, thermally activated delayed fluorescence, and optimization of the LED device structure [54]. Wang et al. have reported EL LEDs by using CQDs as emitters which emit green and orange emissions with central wavelengths of 498 and 560 nm, respectively [56]. They have demonstrated adjustable correlated color temperature white LEDs by combining CQDs with blue, green, and orange emissions [56]. Paulo-Mirasol et al. have reported a CQDs-based LED in which the active emitter layer exhibits white light emission at a driving voltage of 5 V due to the recombination processes within the CQDs [57]. High-performance EL warm white LEDs have been developed using red bandgap emission CQDs passivated by strong electron-donating groups [58]. Feng et al. have employed dual-peak-emissive CQDs with blue and yellow-green emissions to fabricate solid-state full-color and white phosphor LEDs which is applicable for display and lighting [59].

In recent years, as promising candidates for the construction of deep blue LEDs, CQDs have been introduced that are important for solid-state lighting and display [60–63]. Fig. 8.14 shows a fabrication design and emission properties of bright deep blue LEDs based on the CQDs as the active emission layer [60]. Wang et al. have demonstrated high-efficiency ultra-bright pure blue LEDs by utilizing oxygen and nitrogen co-doped CQDs as the active emission layer [61]. Using CQDs emitting layer, many investigations focus on the fabrication of blue CQDs-based LEDs in which a sandwich structure between different transport layers and electrodes are formed [62]. Xu et al. have reported ultrahigh brightness blue EL LED based on the CQDs that exhibited the highest luminance performance compared to other monochromatic blue CQDs-LEDs [63]. The fluorescent CQDs can be employed as a color converting phosphors to enhance the light emission efficiency in LEDs [64,65]. Kim et al. have constructed white LED by utilizing yellow-emitting CQDs as an effective color converting phosphors, as shown in Fig. 8.15 [64]. Furthermore, it has been demonstrated that the CQDs interlayer can improve the electrical and EL performance of the quantum dot and perovskite LEDs [66–68]. Fig. 8.16 depicts the EL properties of quantum dot-based LEDs with/without CQDs interlayer, indicating higher brightness and significant improvement of LED performance by using the CQDs interlayer [66]. Fluorescent CQDs with blue and green emission bands have been used as a single converter to the fabrication of white LEDs under UV excitation at 365 nm [69]. By using the solid-state green emissive CQDs as a color converter, white and yellow LEDs with the emission maximum of 565 and 590 nm were fabricated [70]. Lan et al. have used the red light-emitting CQDs as phosphor-converted materials to construct warm white LED with a high color rendering index [71].

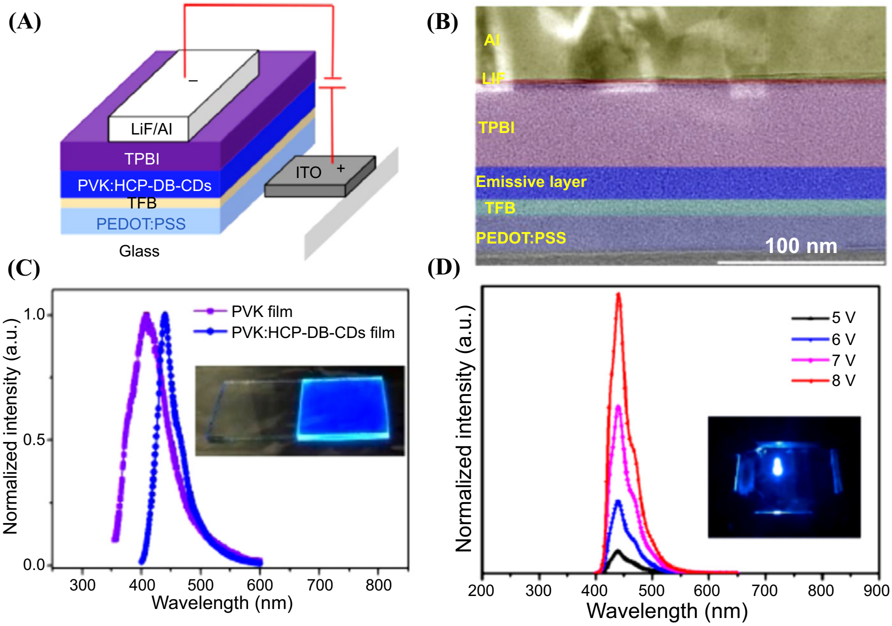

Figure 8.14 (A) Device structure and (B) cross-sectional TEM image of high-color-purity deep-blue (HCP-DB) CQDs-based LEDs. (C) The normalized luminescence of perovskite (PVK) and PVK:HCP-DB-CQD films. The corresponding UV photographs of these films are shown in the insets. (D) The normalized EL spectra of the HCP-DB-CD-based LEDs at different applied voltage of 5–8 V.

Source: Reproduced with permission from F. Yuan, et al., Bright high-colour-purity deep-blue carbon dot light-emitting diodes via efficient edge amination. *Nature Photonics*, 14 (3) (2020) 171–176.

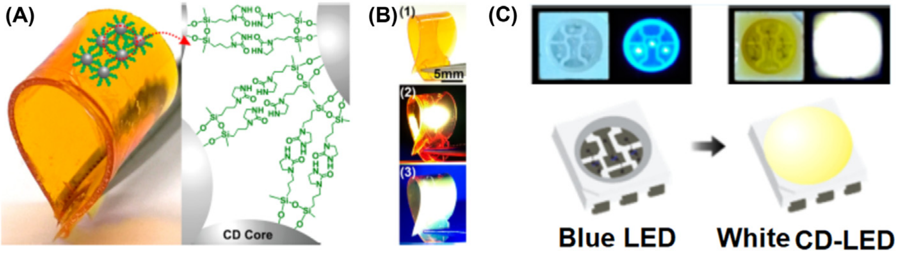

Figure 8.15 (A) Schematic illustration of functionalization of CDs with tethered imidazolidinones (IS-CDs). (B) The photograph of IS-CD sample under (1) room light, (2) 405 nm laser, and (3) 460 nm blue light. (C) The bare blue LED (left) and white CD-LED (right) under room light.

Source: Reproduced with permission from T.H. Kim, et al., Yellow-emitting carbon nanodots and their flexible and transparent films for white LEDs. *ACS Applied Materials & Interfaces*, 8 (48) (2016) 33102–33111.

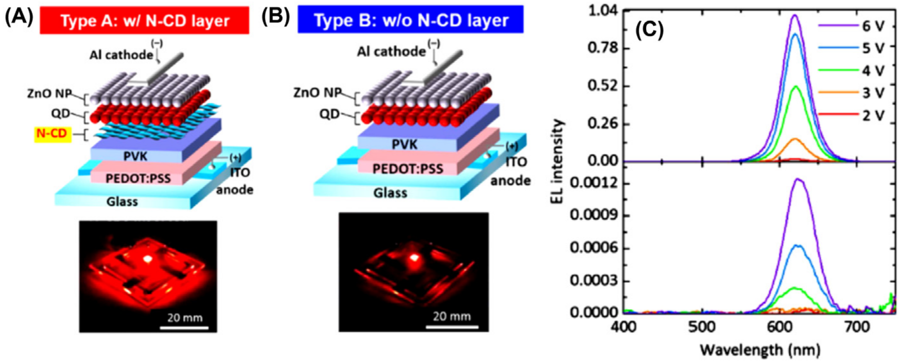

Figure 8.16 Schematic illustrations of quantum dot based LEDs (QD-LEDs) (A) with and (B) without nitrogen-doped CQDs, respectively. The photographs of red emission depict higher brightness of LED performance by using the CQDs interlayer. (C) The upper and lower panels shows EL spectra of QD-LEDs with and without nitrogen-doped CQDs, respectively.
Source: Reproduced with permission from Y.R. Park, et al., Quantum-dot light-emitting diodes with nitrogen-doped carbon nanodot hole transport and electronic energy transfer layer. *Scientific Reports*, 7 (1) (2017) 1–13.

Furthermore, nitrogen and sulfur co-doped red emissive CQDs have been developed into fluorescent hydrogels to fabricate warm white LEDs [72]. Li et al. have demonstrated white LEDs by using highly efficient CQDs phosphors with hybrid fluorescence/phosphorescence dual-emission that exhibited the highest quantum yield value compared with ever reported white-light-emitting CQDs-based materials [73].

8.4.2 Optical gain and lasing

The result of recent investigations on quantum dot lasers indicates the potential of CQDs as a gain medium for lasing [74–82]. First, in 2012, Zhang et al. showed lasing emission in the visible spectrum by using CQDs onto the surface of optical fiber as the laser gain media [74]. Qu et al. have reported light amplification and green lasing emission from CQDs ethanol aqueous solution in a linear long Fabry–Perot cavity, as shown in Fig. 8.17 [75]. Han et al. have shown that CQDs with strong and ultranarrow bandwidth orange emission can be used as the gain medium for a whispering gallery mode microcavity laser [76]. Xi et al. have presented monochrome CQDs-based random lasing with stable full-color emission under a low excitation threshold which is valuable for lighting technology [77,78]. They have demonstrated random lasers with ultrastable, highly efficient, low-thresholds, and narrow bandwidth lasing emissions ranging from blue to red can be obtained using triangular CQDs [77,78]. Furthermore, CQDs laser have constructed by sandwiching CQDs film between a quartz substrate and a dielectric mirror in which lasing emission achieved via three-photon excitation [79]. Yadav et al. have reported

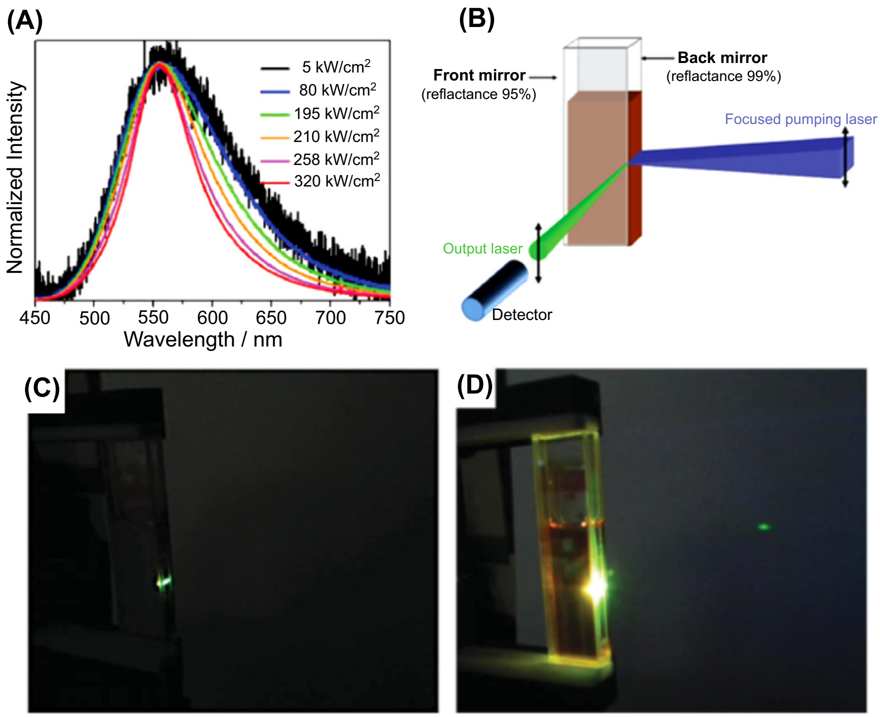

Figure 8.17 (A) Normalized green lasing emission of CQDs ethanol aqueous solution under various optically pumped pulse densities. (B) The corresponding schematic of optical pumping and output of the CQDs-based laser. The green lasing emission from CQDs-based laser pumped by 355 nm laser at (C) 30 kW/cm^2 and (D) 190 kW/cm^2.
Source: Reproduced with permission from S. Qu, et al., Amplified spontaneous green emission and lasing emission from carbon nanoparticles. *Advanced Functional Materials*, 24 (18) (2014) 2689−2695.

lasing emission at 587 nm (linewidth of 3.2 nm) from CQDs−rhodamine B composite under the optical pumping with the wavelength of 532 nm and 1.86 mJ pump energy [80]. Prakash et al. have demonstrated Fabry−Perot lasing and white light emission from CQDs − NaCl crystals as a nontoxic green source [81]. Moreover, by using red emissive CQDs−epoxy composite as the gain medium, random lasing emission at 612 nm and Fabry−Perot lasing were achieved from a microcavity at room temperature and high temperatures (250°C), respectively [82].

8.5 Summary

Over the past decade, CQDs have attracted worldwide interest. CQDs have optoelectronic applications owing to desirable electronic and optical properties, cost-effectiveness, and biocompatibility. The wavelength-tunable fluorescence across the entire visible spectrum makes CQDs promising materials for a wide range of optoelectronic devices. Especially, full-color fluorescent CQDs have been demonstrated as excellent materials to develop multicolor LEDs that are valuable for lighting technology. Thus, it is of great scientific effort to study the optical properties of the CQDs for various device applications. This chapter presents a review of the recent research achievements in synthesis and optical properties of CQDs, focusing on stable full-color fluorescence emissions arising from the quantum confinement and surface functionalization effects. First, the conventional top-down and bottom-up approaches are commonly applied to synthesize CQDs. These methods consist of electrochemical synthesis, arc discharge, pulsed laser ablation/passivation, microwave-assisted synthesis, and hydrothermal and solvothermal processes that have been presented in the chapter. Then, the optical properties of CQDs were studied and discussed. The CQDs device applications as recent achievements in using the CQDs in LEDs and lasers have been evaluated. We hope that the present chapter will stimulate interest for further investigations on carbon nanoparticles-based LEDs.

References

[1] J. Liu, R. Li, B. Yang, Carbon dots: a new type of carbon-based nanomaterial with wide applications, ACS Central Science 6 (12) (2020) 2179–2195.
[2] P. He, et al., Recent advances in white light-emitting diodes of carbon quantum dots, Nanoscale 12 (8) (2020) 4826–4832.
[3] L. Wang, et al., Full-color fluorescent carbon quantum dots, Science Advances 6 (40) (2020) eabb6772.
[4] M.J. Molaei, The optical properties and solar energy conversion applications of carbon quantum dots: a review, Solar Energy 196 (2020) 549–566.
[5] L. Tian, et al., Carbon quantum dots for advanced electrocatalysis, Journal of Energy Chemistry 55 (1) (2020) 279–294.
[6] A. Nair, et al., Natural carbon-based quantum dots and their applications in drug delivery: a review, Biomedicine & Pharmacotherapy 132 (2020) 110834.
[7] P. Das, et al., Acoustic cavitation assisted synthesis and characterization of photoluminescent carbon quantum dots for biological applications and their future prospective, Nano-Structures & Nano-Objects 25 (2021) 100641.
[8] T. Yuan, et al., Carbon quantum dots: an emerging material for optoelectronic applications, Journal of Materials Chemistry C 7 (23) (2019) 6820–6835.
[9] K.J. Mintz, Y. Zhou, R.M. Leblanc, Recent development of carbon quantum dots regarding their optical properties, photoluminescence mechanism, and core structure, Nanoscale 11 (11) (2019) 4634–4652.
[10] H. Luo, et al., Manipulating the optical properties of carbon dots by fine-tuning their structural features, ChemSusChem 12 (19) (2019) 4432–4441.
[11] L. Tian, et al., The influence of inorganic electrolyte on the properties of carbon quantum dots in electrochemical exfoliation, Journal of Electroanalytical Chemistry 878 (2020) 114673.

[12] M. Liu, et al., Carbon quantum dots directly generated from electrochemical oxidation of graphite electrodes in alkaline alcohols and the applications for specific ferric ion detection and cell imaging, Analyst 141 (9) (2016) 2657−2664.

[13] X. Li, Z. Zhao, Facile ionic-liquid-assisted electrochemical synthesis of size-controlled carbon quantum dots by tuning applied voltages, RSC Advances 4 (101) (2014) 57615−57619.

[14] J. Deng, et al., Electrochemical synthesis of carbon nanodots directly from alcohols, Chemistry−A European Journal 20 (17) (2014) 4993−4999.

[15] F. Chao-Mujica, et al., Carbon quantum dots by submerged arc discharge in water: synthesis, characterization, and mechanism of formation, Journal of Applied Physics 129 (16) (2021) 163301.

[16] A. Nevar, et al., Carbon nanodots with tunable luminescence properties synthesized by electrical discharge in octane, Carbon Letters 31 (1) (2021) 39−46.

[17] I.F. Andhika, S. Hastuti, T.E. Saraswati, The surface characteristics of carbon nanoparticles produced via submerged arc discharge in ethanol/water, AIP Conference Proceedings 2296 (1) (2020) 020069.

[18] D. Reyes, et al., Laser ablated carbon nanodots for light emission, Nanoscale Research Letters 11 (1) (2016) 1−11.

[19] L. Cui, et al., Synthesis of homogeneous carbon quantum dots by ultrafast dual-beam pulsed laser ablation for bioimaging, Materials Today Nano 12 (2020) 100091.

[20] V. Nguyen, et al., Double-pulse femtosecond laser ablation for synthesis of ultrasmall carbon nanodots, Materials Research Express 7 (1) (2020) 015606.

[21] C. Doñate-Buendia, et al., Fabrication by laser irradiation in a continuous flow jet of carbon quantum dots for fluorescence imaging, ACS Omega 3 (3) (2018) 2735−2742.

[22] X. Li, et al., Preparation of carbon quantum dots with tunable photoluminescence by rapid laser passivation in ordinary organic solvents, Chemical Communications 47 (3) (2010) 932−934.

[23] G. Jeong, et al., Microwave-assisted synthesis of multifunctional fluorescent carbon quantum dots from A4/B2 polyamidation monomer sets, Applied Surface Science 542 (2021) 148471.

[24] A. Dager, et al., Ultrafast synthesis of carbon quantum dots from fenugreek seeds using microwave plasma enhanced decomposition: application of C-QDs to grow fluorescent protein crystals, Scientific Reports 10 (1) (2020) 1−15.

[25] K.M. Omer, et al., Photoluminescence enhancement via microwave irradiation of carbon quantum dots derived from solvothermal synthesis of L-arginine, New Journal of Chemistry 43 (2) (2019) 689−695.

[26] T. Yu, et al., A rapid microwave synthesis of green-emissive carbon dots with solid-state fluorescence and pH-sensitive properties, Royal Society Open Science 5 (7) (2018) 180245.

[27] H. Behboudi, et al., Carbon quantum dots in nanobiotechnology, Nanomaterials for advanced biological applications, Springer, 2019, pp. 145−179.

[28] J. Wang, et al., Large-scale green synthesis of fluorescent carbon nanodots and their use in optics applications, Advanced Optical Materials 3 (1) (2015) 103−111.

[29] N. Papaioannou, M.-M. Titirici, A. Sapelkin, Investigating the effect of reaction time on carbon dot formation, structure, and optical properties, ACS Omega 4 (26) (2019) 21658−21665.

[30] Z. Han, et al., Hydrothermal synthesis of carbon dots and their application for detection of chlorogenic acid, Luminescence: The Journal of Biological and Chemical Luminescence 35 (7) (2020) 989−997.

[31] Y. Xie, et al., One-step hydrothermal synthesis of fluorescence carbon quantum dots with high product yield and quantum yield, Nanotechnology 30 (8) (2019) 085406.

[32] Y. Yang, et al., Dual-emission ratiometric fluorescent detection of dinotefuran based on sulfur-doped carbon quantum dots and copper nanocluster hybrid, Sensors and Actuators B: Chemical 321 (2020) 128534.

[33] L. Li, T. Dong, Photoluminescence tuning in carbon dots: surface passivation or/and functionalization, heteroatom doping, Journal of Materials Chemistry C 6 (30) (2018) 7944−7970.

[34] Y. Wang, Y. Li, L. Feng, Exploring solvent-related reactions and corresponding band gap tuning strategies for carbon nanodots based on solvothermal synthesis, The Journal of Physical Chemistry Letters 11 (2020) 10439−10445.

[35] H. Ding, et al., Solvent-controlled synthesis of highly luminescent carbon dots with a wide color gamut and narrowed emission peak widths, Small (Weinheim an der Bergstrasse, Germany) 14 (22) (2018) 1800612.

[36] M. Shao, et al., Continuous synthesis of carbon dots with full spectrum fluorescence and the mechanism of their multiple color emission, Lab on a Chip 19 (23) (2019) 3974−3978.

[37] K. Jiang, et al., Preparation of multicolor photoluminescent carbon dots by tuning surface states, Nanomaterials (Basel, Switzerland) 9 (4) (2019) 529.

[38] X. Xu, et al., Red, orange, yellow and green luminescence by carbon dots: hydrogen-bond-induced solvation effects, Nanoscale 13 (14) (2021) 6846−6855.

[39] S.Y. Lim, W. Shen, Z. Gao, Carbon quantum dots and their applications, Chemical Society Reviews 44 (1) (2015) 362−381.

[40] P. Zhu, et al., Origins of efficient multiemission luminescence in carbon dots, Chemistry of Materials 31 (13) (2019) 4732−4742.

[41] L. Ai, et al., Insights into photoluminescence mechanisms of carbon dots: advances and perspectives, Science Bulletin 66 (8) (2021) 839−856.

[42] H. Ding, et al., Surface states of carbon dots and their influences on luminescence, Journal of Applied Physics 127 (23) (2020) 231101.

[43] W. Liang, et al., Evaluation of commercial “carbon quantum dots” sample on origins of red absorption and emission features, C 5 (4) (2019) 70.

[44] L. Bao, et al., Photoluminescence-tunable carbon nanodots: surface-state energy-gap tuning, Advanced Materials 27 (10) (2015) 1663−1667.

[45] H. Ding, et al., Full-color light-emitting carbon dots with a surface-state-controlled luminescence mechanism, ACS Nano 10 (1) (2016) 484−491.

[46] B. Zhi, et al., Synthesis, applications and potential photoluminescence mechanism of spectrally tunable carbon dots, Nanoscale 11 (43) (2019) 20411−20428.

[47] M.S. Ghamsari, et al., Wavelength-tunable visible to near-infrared photoluminescence of carbon dots: the role of quantum confinement and surface states, Journal of Nanophotonics 10 (2) (2016) 026028.

[48] F. Wang, et al., White light-emitting devices based on carbon dots’ electroluminescence, Chemical Communications 47 (12) (2011) 3502−3504.

[49] C. Qi, et al., Toward near-white electroluminescence with enhanced blue emission from carbon dots in PEDOT: PSS/ZnO organic/inorganic hybrid heterojunctions, Journal of Luminescence 224 (2020) 117230.

[50] X. Zhang, et al., Color-switchable electroluminescence of carbon dot light-emitting diodes, ACS Nano 7 (12) (2013) 11234−11241.

[51] X. Mo, et al., Low-voltage multicolor electroluminescence from all-inorganic carbon dots/Si-heterostructured light-emitting diodes, Journal of Materials Science 54 (11) (2019) 8492−8503.
[52] Y. Ding, et al., Synthesis of short-chain passivated carbon quantum dots as the light emitting layer towards electroluminescence, RSC Advances 7 (46) (2017) 28754−28762.
[53] L.M. Veca, et al., Electroluminescence of carbon 'quantum' dots−from materials to devices, Chemical Physics Letters 613 (2014) 40−44.
[54] B. Zhao, Za Tan, Fluorescent carbon dots: fantastic electroluminescent materials for light-emitting diodes, Advanced Science 8 (7) (2021) 2001977.
[55] P. Lagonegro, U. Giovanella, M. Pasini, Carbon dots as a sustainable new platform for organic light emitting diode, Coatings 11 (1) (2021) 5.
[56] X. Wang, et al., Carbon-dot-based white-light-emitting diodes with adjustable correlated color temperature guided by machine learning, Angewandte Chemie International Edition 60 (22) (2021) 12585−12590.
[57] S. Paulo-Mirasol, E. Martínez-Ferrero, E. Palomares, Direct white light emission from carbon nanodots (C-dots) in solution processed light emitting diodes, Nanoscale 11 (23) (2019) 11315−11321.
[58] H. Jia, et al., Electroluminescent warm white light-emitting diodes based on passivation enabled bright red bandgap emission carbon quantum dots, Advanced Science 6 (13) (2019) 1900397.
[59] T. Feng, et al., Color-tunable carbon dots possessing solid-state emission for full-color light-emitting diodes applications, ACS Photonics 5 (2) (2018) 502−510.
[60] F. Yuan, et al., Bright high-colour-purity deep-blue carbon dot light-emitting diodes via efficient edge amination, Nature Photonics 14 (3) (2020) 171−176.
[61] X. Wang, et al., Ultra-bright and stable pure blue light-emitting diode from O, N Co-doped carbon dots, Laser & Photonics Reviews 15 (3) (2021) 2000412.
[62] F. Chen, et al., Blue quantum dot-based electroluminescent light-emitting diodes, Materials Chemistry Frontiers 4 (5) (2020) 1340−1365.
[63] J. Xu, et al., Ultrahigh brightness carbon dot−based blue electroluminescent LEDs by host−guest energy transfer emission mechanism, Advanced Optical Materials 6 (14) (2018) 1800181.
[64] T.H. Kim, et al., Yellow-emitting carbon nanodots and their flexible and transparent films for white LEDs, ACS Applied Materials & Interfaces 8 (48) (2016) 33102−33111.
[65] R. Guo, T. Li, S. Shi, Aggregation-induced emission enhancement of carbon quantum dots and applications in light emitting devices, Journal of Materials Chemistry C 7 (17) (2019) 5148−5154.
[66] Y.R. Park, et al., Quantum-dot light-emitting diodes with nitrogen-doped carbon nanodot hole transport and electronic energy transfer layer, Scientific Reports 7 (1) (2017) 1−13.
[67] M.B. Alam, et al., Carbon quantum dot as electron transporting layer in organic light emitting diode, ChemistrySelect 4 (25) (2019) 7450−7454.
[68] Z. Wang, et al., Multifunctional p-type carbon quantum dots: a novel hole injection layer for high-performance perovskite light-emitting diodes with significantly enhanced stability, Advanced Optical Materials 7 (24) (2019) 1901299.
[69] X. Chen, et al., Blue and green double band luminescent carbon quantum dots: synthesis, origin of photoluminescence, and application in white light-emitting devices, Applied Physics Letters 118 (15) (2021) 153102.

[70] E. Liu, et al., Highly emissive carbon dots in solid state and their applications in light-emitting devices and visible light communication, ACS Sustainable Chemistry & Engineering 7 (10) (2019) 9301−9308.

[71] X. Lan, et al., A facile microwave-assisted synthesis of highly crystalline red carbon dots by adjusting the reaction solvent for white light-emitting diodes, Nanotechnology 31 (21) (2020) 215704.

[72] Y. Liu, et al., Multicolor tunable highly luminescent carbon dots for remote force measurement and white light emitting diodes, Chemical Communications 55 (81) (2019) 12164−12167.

[73] Q. Li, Y. Li, S. Meng, J. Yang, Y. Qin, J. Tan, et al., Achieving 46% efficient white-light emissive carbon dot-based materials by enhancing phosphorescence for single-component white-light-emitting diodes, Journal of Materials Chemistry C 9 (21) (2021) 6796−6801.

[74] W. Zhang, et al., Observation of lasing emission from carbon nanodots in organic solvents, Advanced Materials 24 (17) (2012) 2263−2267.

[75] S. Qu, et al., Amplified spontaneous green emission and lasing emission from carbon nanoparticles, Advanced Functional Materials 24 (18) (2014) 2689−2695.

[76] Z. Han, et al., Highly efficient and ultra-narrow bandwidth orange emissive carbon dots for microcavity lasers, Nanoscale 11 (24) (2019) 11577−11583.

[77] Z. Xi, et al., Highly efficient and stable full-color random lasing emission based on carbon quantum dots, Acta Chim Sin 76 (6) (2018) 460.

[78] F. Yuan, et al., Ultrastable and low-threshold random lasing from narrow-bandwidth-emission triangular carbon quantum dots, Advanced Optical Materials 7 (2) (2019) 1801202.

[79] W. Zhang, et al., Realization of multiphoton lasing from carbon nanodot microcavities, Nanoscale 9 (18) (2017) 5957−5963.

[80] A. Yadav, et al., Lasing behavior of surface functionalized carbon quantum dot/RhB composites, Nanoscale 9 (16) (2017) 5049−5054.

[81] S. Prakash, et al., Carbon dot-NaCl crystals for white-light generation and fabry-perot lasing, Chemistry−An Asian Journal 16 (7) (2021) 783−792.

[82] Y. Ni, et al., Transformation of random lasing to Fabry−Perot lasing: observation of high temperature lasing from carbon dots, Nanoscale 13 (16) (2021) 7566−7573.

[83] Y.-P. Sun, et al., Quantum-sized carbon dots for bright and colorful photoluminescence, Journal of the American Chemical Society 128 (24) (2006) 7756−7757.

[84] F. Yuan, et al., Bright multicolor bandgap fluorescent carbon quantum dots for electroluminescent light-emitting diodes, Advanced Materials 29 (3) (2017) 1604436.

[85] F. Yuan, et al., Engineering triangular carbon quantum dots with unprecedented narrow bandwidth emission for multicolored LEDs, Nature Communications 9 (1) (2018) 1−11.

[86] J. Ren, et al., Precisely controlled up/down-conversion liquid and solid state photoluminescence of carbon dots, Advanced Optical Materials 6 (14) (2018) 1800115.

[87] X. Zhang, et al., Carbon quantum dots serving as spectral converters through broadband upconversion of near-infrared photons for photoelectrochemical hydrogen generation, Journal of Materials Chemistry A 1 (38) (2013) 11529−11533.

[88] Y.H. Chien, et al., NIR-responsive nanomaterials and their applications; upconversion nanoparticles and carbon dots: a perspective, Journal of Chemical Technology & Biotechnology 93 (6) (2018) 1519−1528.

[89] D. Li, et al., Thermally activated upconversion near-infrared photoluminescence from carbon dots synthesized via microwave assisted exfoliation, Small (Weinheim an der Bergstrasse, Germany) 15 (50) (2019) 1905050.

[90] K.K. Liu, et al., Efficient red/near infrared emissive carbon nanodots with multiphoton excited upconversion fluorescence, Advanced Science 6 (17) (2019) 1900766.

[91] Y. Hu, et al., Visible-light upconversion carbon quantum dots decorated TiO_2 for the photodegradation of flowing gaseous acetaldehyde, Applied Surface Science 440 (2018) 266−274.

[92] Y. Deng, et al., Visible−ultraviolet upconversion carbon quantum dots for enhancement of the photocatalytic activity of titanium dioxide, ACS Omega 6 (6) (2021) 4247−4254.

[93] K.M. Omer, N.N. Mohammad, S.O. Baban, Up-conversion fluorescence of phosphorous and nitrogen co-doped carbon quantum dots (CDs) coupled with weak LED light source for full-spectrum driven photocatalytic degradation via ZnO-CDs nanocomposites, Catalysis Letters 148 (9) (2018) 2746−2755.

[94] J. Wang, Y. Zhu, L. Wang, Synthesis and applications of red-emissive carbon dots, The Chemical Record 19 (10) (2019) 2083−2094.

[95] X. Wen, et al., On the upconversion fluorescence in carbon nanodots and graphene quantum dots, Chemical Communications 50 (36) (2014) 4703−4706.

Nanoelectronic applications of carbon quantum dots

9

M. Shiva Subramani[1], *Soumyo Chatterjee*[2] *and Kallol Mohanta*[1]
[1]Nanotech Research Innovation and Incubation Centre (NRIIC), PSG Institute of Advanced Studies (PSG IAS), Peelamedu, Coimbatore, Tamil Nadu, India, [2]School of Physical Sciences (SPS), Indian Association for the Cultivation of Science (IACS), Jadavpur, Kolkata, West Bengal, India

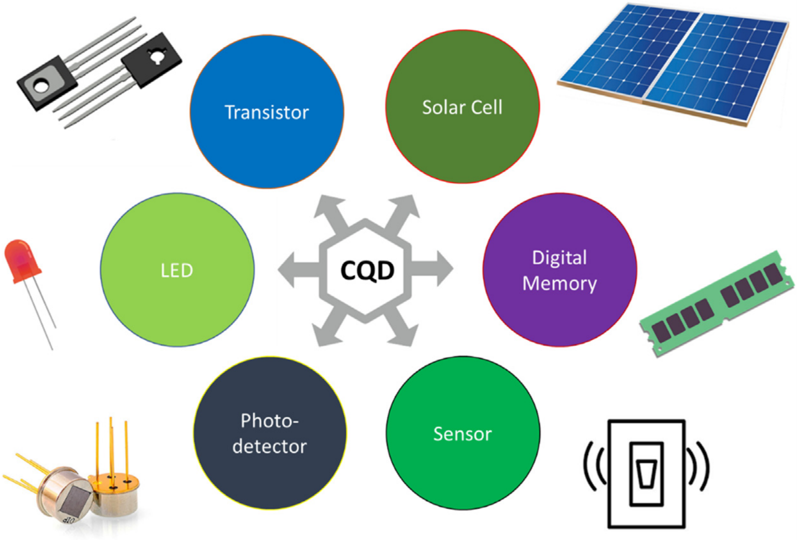

TOC picture

9.1 General introduction

As the development of semiconductor technology has increased exponentially in the past two decades, both miniaturization in sizes and performance have been improved. With the advent of nanotechnology, designing a material in nanoscale and controlling its properties are thereby propelling this fast development. When it comes to daily utilization, the materials have to satisfy both the ecological and economical prospects other than its beneficial semiconducting properties. Over the time, we have seen that many semiconductors have been developed through nanotechnology and organic

Carbon Quantum Dots for Sustainable Energy and Optoelectronics. DOI: https://doi.org/10.1016/B978-0-323-90895-5.00010-2
© 2023 Elsevier Ltd. All rights reserved.

synthesis, but most of them failed to combine all the advantageous and requisite attributes. Of late, carbon nanomaterials found some foothold to be used as components in commercial semiconductor industry. The most successful carbon nanomaterial for the industrial application till date is various types of carbon nanotubes (CNTs) due to their amazing conducting properties and longitudinal structures. In recent developments, CQDs play a vital role in multiple areas from bio application to nanoelectronics application due to their fluorescent property, photostability, photoluminescence, etc. CQDs have good aqueous dispersibility, apposite biocompatibility, entailed non-toxicity, and fantastic optical properties which mark them as one of the emergent materials for different types of applications.

The first CQDs were discovered accidently by Xu et al. in 2004 during purification of single-walled CNTs [1]. After this discovery by arc discharge by Xu and team, several different ways have been used to synthesize cost-effective, highly manipulative, and scaled-up CQDs from various carbon precursors [2–4]. As the CQDs can accommodate several useful functional groups with different compositions and structures, they are appropriate for various applications. Coming to the synthesis process, they are prepared by both top-down and bottom-up approaches. Top-down methods are used to grind down the macroscopic carbon structures into CQDs. Some of the top-down methods are arc discharge, laser ablation, electrochemical and oxidation, and ultrasonication. Contrarily, bottom-up methods are used for synthesizing the CQDs from carbonaceous molecules through hydrothermal, pyrolysis, ultrasonics and dehydration/direct heating techniques with polymerization and canbonizations. The advantages of using CQDs in applications like electronics include high-mobility carrier, high stability in air and optoelectronics systems, optical transmission, etc. [5].

The carbon atoms in CQDs are in mixed hybridized states though mostly consists of sp^2 hybridization. Based on the fringes seen in transmission microscope images, the CQDs have a “d” spacing of 0.34 nm corresponding to the (002) interlayer spacing of carbon [6]. CQDs are generally prepared through simple pyrolysis or hydrothermal processes, which is one of the vantage point for the CQDs applications, but these simplified synthesis processes leave a lot many defect sites. The defects are mainly found at the boundaries between the volumes of different hybridized states of carbons. However, these surface defects are mostly responsible for the interesting photoluminescence properties of the CQDs [7]. These passivated surface defect sites are the energy/charge trap sites causing the unique optical and electrical features of CQDs [8]. As in case of other semiconducting nanomaterials, the optical properties of CQDs are fascinating and most interesting features for industrial applications and experimental research.

CQDs are prepared from various carbonaceous precursors including organic and biomaterials [2,4,9–12]. The synthesis processes of CQDs are simple and do not require complex instrumentation. At the same time, these processes use minimal energy consumption. The filtration methods of the CQDs are also nominal and do not expend much use of water or organic solvents. These attributes enable to evolve several green synthesis processes with harmless by-products [11,12]. This is another positive quality of CQDs due to which we may soon see the utilization of CQDs in industry is increasing.

However, the scope of this chapter is not to address the synthesis or the characteristics of CQDs rather it is to find different electronical aspects and applications of CQDs in the field of electronics. Again, since some more chapters are discussing solar cell, light-emitting diode (LED), and supercapacitor applications, we will try to confine ourselves in this chapter to the possible rest of the applications. While studying the development and utilizations of CQDs in recent years it has been found that these nanomaterials are being used for digital memory devices, thin-film transistors, photodetectors, electronic sensors, etc. apart from the solar cells and LEDs. We will try to present a glimpse of basics of these applications and then attempt to elaborate how CQDs are being utilized for these applications. As stated earlier, we would like to consciously avoid the discussion of solar cells, LEDs, and in some extent of photodetectors but these may come in small segments since sometimes the usage of CQDs in one application promotes its advantageous role for another. The structure of CQDs and thereby their properties are similar to its elder sibling, CNTs; thus, a comparison of the performance for particular applications between CQDs and CNTs is inevitable. We shall bring in such assessments wherever it seems appropriate.

9.2 Memory devices

Memory device research has been very active from the last decade. Business analysts predict that the total digital memory demand will surpass by 3×10^{24} bits in commercial semiconductor industry by 2040 [13]. In simple words, a semiconductor device stores memory by trapping and de-trapping the charges in the form of “1” and “0” bits, i.e., “ON” and “OFF” states, respectively in a single memory cell [14]. An array of memory cells is connected in a typical memory system to form a 2D array. Both the storage node and the select device, two fundamental components of memory cells in these arrays, have an impact on scaling limits. In principle, the storage nodes can be scaled down to less than 10 nm for several emerging resistance-based memories [15]. Memory density is therefore limited by the select device, which are usually planar transistors. Vertical select transistors can be used to achieve the highest 2D memory density possible. Providing cost-effective memory devices to the electronics industry, such as cellphones, computers, and other industries, can be considered as the semiconductor industry’s first driver, and as a result, the primary contribution to maintaining Moore’s law [16].

9.2.1 Classifications of memory devices

In terms of data retention time, electrical-driven memory can be divided into two categories: volatile memory and nonvolatile memory. Volatile memory responds to program operations transiently before returning to its original state. In dynamic random-access memory (DRAM), the recorded data can only be preserved for a short period of time and will dissipate shortly after powering off. When an external voltage is removed from nonvolatile memory, the programmed state will remain for a relatively long time. Usually, the writing and erasing of a memory bit is checked over several cycles, this is called write-read-erase-read (WRER) cycle [17]. There are two common categories in which the nonvolatile memory effect is studied: (1) two electrode based resistive switching (RS) devices and (2) three electrode based transistor type devices. Flash memory based on field effect transistor (FET) is also a well-studied data storage device [18]. We use flash memory in our daily lives because it is compatible with complementary metal-oxide−semiconductor (CMOS) circuitry. Its reliability in terms of storage capacity, cyclic operation, and long data retention time have been proven through countless research studies.

Memory applications have been proposed for a variety of carbon allotropes, such as amorphous carbon, diamond-like carbon, CQDs, CNTs, and graphitic carbon. In the basic device, current pulses are used to change the resistance of an electrode/carbon/electrode capacitor. One of the switching mechanisms proposed in this line relies on the creation and destruction of conductive sp^2 bonds in an insulating carbon matrix consisting of sp^3 bonds [15]. An entirely different approach is taken by a redox-based nano ionic random access memory (RAM), which operates on a change in resistance of the “MIM” structure, which is composed of an insulating or resistive material “I” sandwiched between two electron conductors “M,” which may be different. Cation (or anion) migration is responsible for this change, as are redox processes that involve both electrode and insulation materials [15]. The electrochemical metallization mechanism, valence change mechanism, and thermochemical mechanism are the three main classes. In the switching mechanisms of these three ReRAM classes, thermal and electrochemical forces compete. There is a wide range of novel memory devices operating on alternative principles with CQDs that have been reported in this context in great detail. Moreover, some of them are nearing the premanufacturing stage of their development [19] (Fig. 9.1).

An electric bias voltage couples solid-state ionic and electronic transport levels, resulting in memory effects. Under vacuum at 100°C, CQD films were prepared by drop-casting colloidal solution. CQDs and their composites show a significant resistance hysteresis that is stable over a large number of cycles [20]. Thermal treatments, which remove shallow trapping states, account for this stability. The charge-trapping states associated with the CQDs determine this memory effect in both cases, which is quite significant when considering the device’s dimensions. As a result, CQD composites exhibit memory effects at high temperatures. It was found that the transport mechanisms in bare and functionalized CQDs differed significantly. These findings indicate that bare CQDs could be used in memory devices at room temperature, while functionalized CQDs could be used in devices with enhanced functionality at higher working temperatures [20] (Fig. 9.2).

Arvind et al. reported that CQDs have temperature-dependent current trap layers, which are synthesized by laser ablation methods and used for memory applications [21]. They have shown the photocurrent and photo-persistent conductivity with temperature variation with two different wavelengths of 325 and 633 nm. Here the building up of photocurrent saturation is controlled by two things, namely carrier generations and carrier capture rates. The monotonic decrease of saturation photocurrent was identified by increasing the temperature.

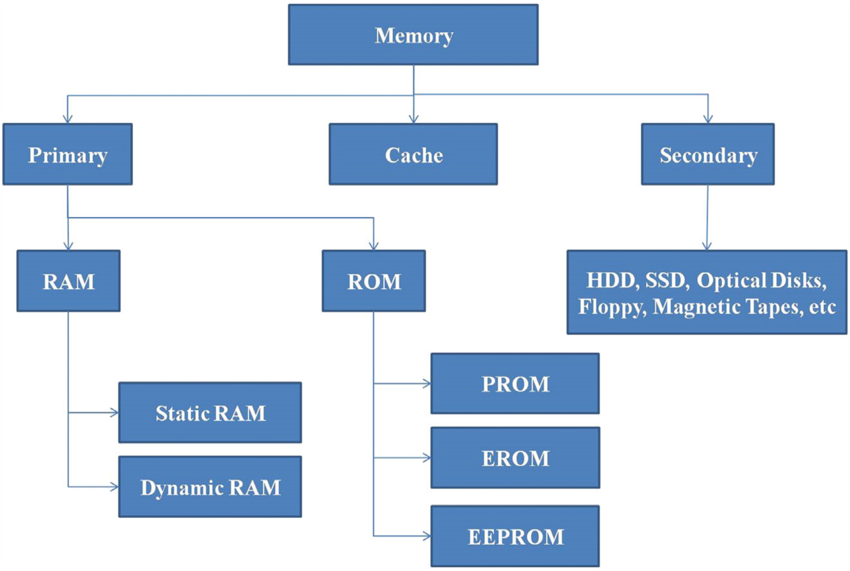
Memory
Primary
Cache
Secondary
RAM
ROM
HDD, SSD, Optical Disks, Floppy, Magnetic Tapes, etc
Static RAM
Dynamic RAM
PROM
EROM
EEPROM

Figure 9.1 Classification of memory types.

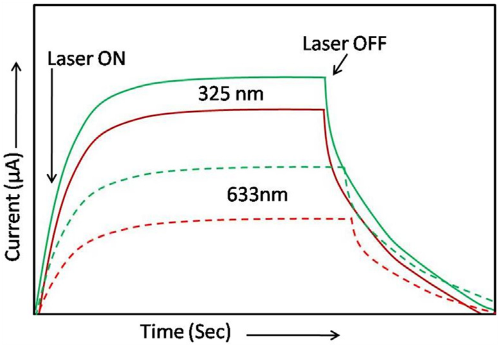

Figure 9.2 Light excitation dependence of photoinduced current and persistent photoconductivity. The laser ON and OFF times have been indicated by arrow marks. *Source*: Reproduced with permission from A. Singh, A. Nivedan, S. Kumar and S. Kumar, *Journal of Applied Physics*, 126 (2019), 225102.

9.2.2 Random access memory

For the phototunable memory behaviors of bio-RAM, two distinct mechanisms have been proposed [13]. First, the photovoltaic effect, in which an electron–hole pair can be created in CQDs by absorbing photons with higher energy than the band gap's value. An electric field divides the excitons at the interface between CQDs and its counterpart. As a result, CQDs act as a local gate for the photogenerated electrons.

It has been found that Al and Au electrodes in bio-memories show write once read multiple (WORM) characteristics, while Ag-based devices exhibit reversible bipolar-RS due to diffusive propagation of Ag ions into the biomaterial layer and formation of filaments. These effects are attributed to the RS effects of photonic memory devices that use an inactive anode (Al or Au) or a conductive filament (Ag).

Charge-trapping centers are one of the essential components for RS. Therefore, creating these centers by incorporating appropriate nanoparticles within electrically inert or dielectric matrix would be a strategy to found RS in a composite material. Now if these nanoparticles can be excited with external fields other than electrical, then there would be an additional control over the switching or memory aspect of that device [19] (Fig. 9.3).

With nitrogen-doped CQD particles in polyvinylpyrrolidone (PVP) films, a phototunable memory has been achieved. The phototunability property of the device not only allow to have an extra control on device response, it also enhances the storage density. In such devices, the memory can be written by light pulses and for this particular case the light irradiation duration modifies the bias requirement for the writing the memory. This behavior has been attributed to the creation of conducting carbonaceous island in the CQDs by powerful UV radiation, which in turn served as hopping spots during the charge transition [19].

When a thin film of this material could be developed on a flexible substrate, a potential application of wearable information encrypted device would be realized. That device would not only store the information, it would also be encrypted with suitable electromagnetic irradiation. The storage device as demonstrated in this reference has RRAM arrays based on the CQD−PVP nanocomposite and is an illustration of futuristic neuromorphic computation apparatus [22] (Fig. 9.4).

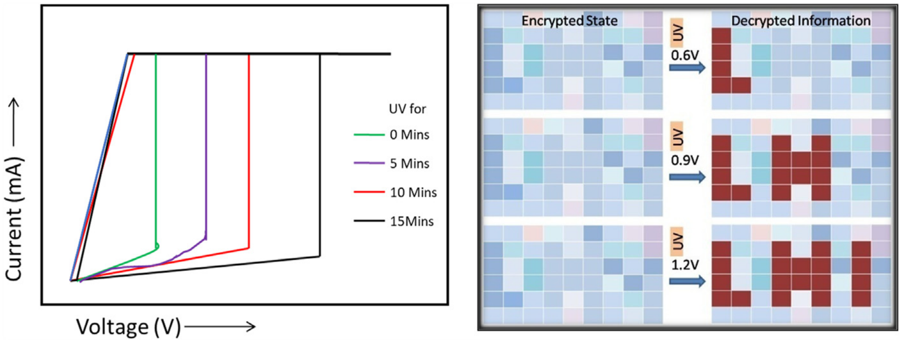

Figure 9.3 The effects of UV irradiation on RS behaviors with different UV irradiation times (0, 5, 10, and 15 min). (A) The UV irradiation represented the process of information encryption, in which three regions (the image "L," "I," and "H") underwent 15, 10, and 5 min UV irradiation, respectively. (B) Demonstration of the encrypted image storage in our RRAM array.

Source: Reproduced with permission from Y. Lin, X. Zhang, X. Shan, T. Zeng, X. Zhao, Z. Wang, et al., *Journal of Materials Chemistry C*, 8 (2020) 14789−14795.

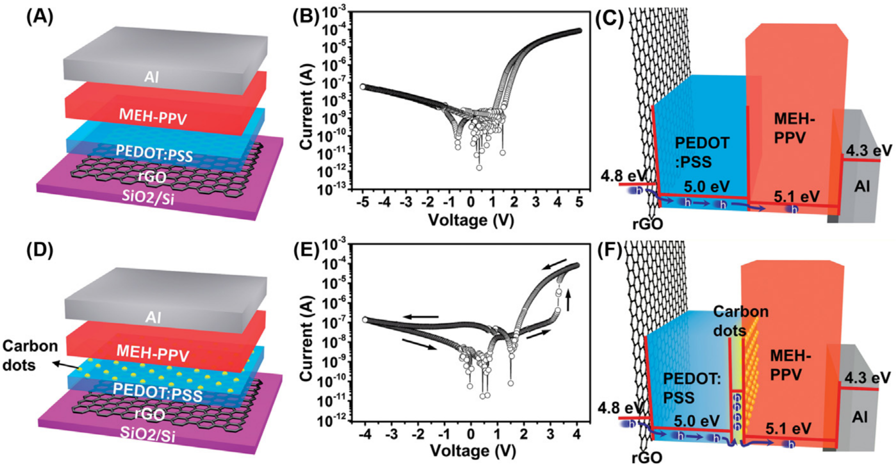

Figure 9.4 (A) Schematic structure, (B) typical I−V characteristics, and (C) energy band diagram of the rectifying device. (D) Schematic structure, (E) typical I−V characteristics (the arrows represent the sweep directions), and (F) energy band diagram of the rectifying memory device.

Source: Reproduced with permission from H. Lu, Y. Chen, Q. Chang, S. Cheng, Y. Ding, J. Chen, et al., *RSC Advances*, 8 (2018) 13917−13920.

A junction between MEH-PPV (poly[2-methoxy-5-(2′-ethylhexyloxy)-1,4-phenylene vinylene]) and PEDOT:PSS (poly(3,4-ethylenedioxythiophene)-poly(styrenesulfonate)) is generally a rectifying junction since this is like polymer version of metal−semiconductor Schottky junction. However, an interesting fact has been observed when a layer of CQDs has been inserted within these two polymer layers. This change in device configuration introduces the memory characteristics into this rectifying device. Moreover, when reduced graphene oxide (rGO) was used as anode instead of ITO, a longer endurance had been observed. This introduction memory is surely due to the CQDs, and the feature of charge trapping at CQD sites is the most responsible for this exhibition [23].

Important indicators of nonvolatile data storage capacity in memory are retention characteristics. The retention characteristics of device were measured by recording IDS at the 1 and 0 states vs time. At state 1, the negative reading of IDS slowly increased during the whole measurement process, and this dissipation of trapped charges in the inert polymer layer is attributed to the internal conduction pathways that form from dipoles, moisture, and ions. However, at the 0 state.

IDS exhibit almost no significant change during the entire testing process, which is due to the discrete distribution and electron-withdrawing capability of the CQDs. It shows that the memory on/off ratio of the present memory reaches 50% of the initial after 10^4 s, which indicates a long retention time of the device [24,25]. In summary, we have demonstrated a strategy to achieve an organic field-effect transistor memory (OFETM) based on a CQDs−PVP hybrid nanolayer as a charge-trapping layer, and the operating mechanism is discussed in detail. In our experiment, the CQDs prepared by the one-step microwave-assisted hydrothermal method have excellent electron-withdrawing properties. Embedding the CQDs into the PVP layer can improve the positive storage performance of the OFETM device. By optimizing the concentration of CQDs doped into the PVP matrix, the device A presents bidirectional memory characteristics. As a result, a large memory window of 8.41 V and a data retention time up to 10^4 s is realized (Fig. 9.5).

The formation and dissolution of conducting filaments across the switching layer widely account for the operation mechanism of RRAM devices. In a nonlinear RRAM cell with very low operating current for high-density vertical resistive memory (VRRAM), oxidized CQD (OCQD)−GO nanocomposites films showed robust low resistance states (LRSs) with long retention times. The switching mechanism in GO was found to be governed by the migration of oxygen functional groups in the switching layer of the OCQD−GO nanocomposite. With the increase of compliance current (CC), the retention time has increased substantially. This may be due to increase in the oxygen migration energy barrier. Also, the concentration of oxidized CQD particles in the films reduces the switching time in these devices [26] (Fig. 9.6).

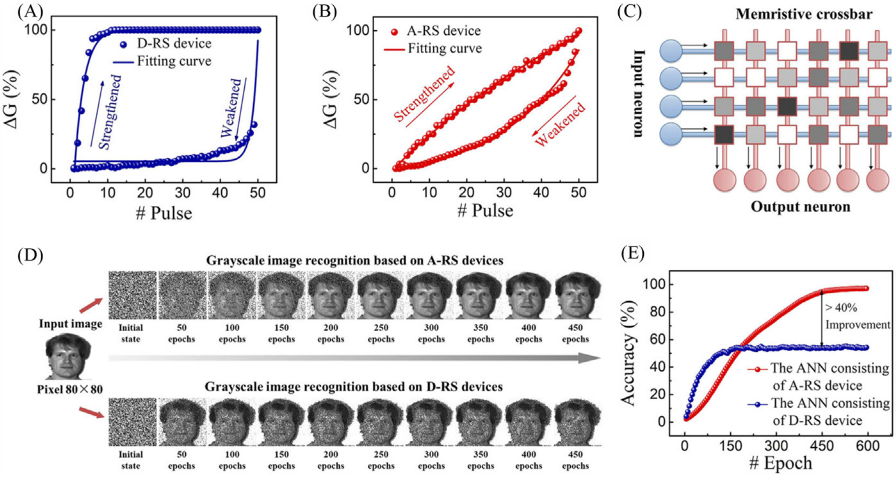

Figure 9.5 Comparison of pattern recognition simulated in the artificial neuromorphic networks (ANNs) comprising the digital-type RS (D-RS) and analog-type RS (A-RS) devices. (A, B) Conductance potentiation/depression of the devices with (A) D-RS and (B) A-RS behaviors. The A-RS device was obtained with 10 min UV irradiation. (C) Neuromorphic system simulator built with an 80 × 80 memristive crossbar array. (D) Evolution of images during the learning process of ANNs based on D-RS (lower) and A-RS (upper) memristors. The synaptic weights of memristive synapses are randomly initialized before they are trained to learn the input image. (E) Learning accuracy as a function of number of epochs for the memristive ANNs consisting of D-RS and A-RS devices.
Source: Reproduced with permission from Y. Lin, Z. Wang, X. Zhang, T. Zeng, L. Bai, Z. Kang, et al., *NPG Asia Materials*, 12 (2020), 64.

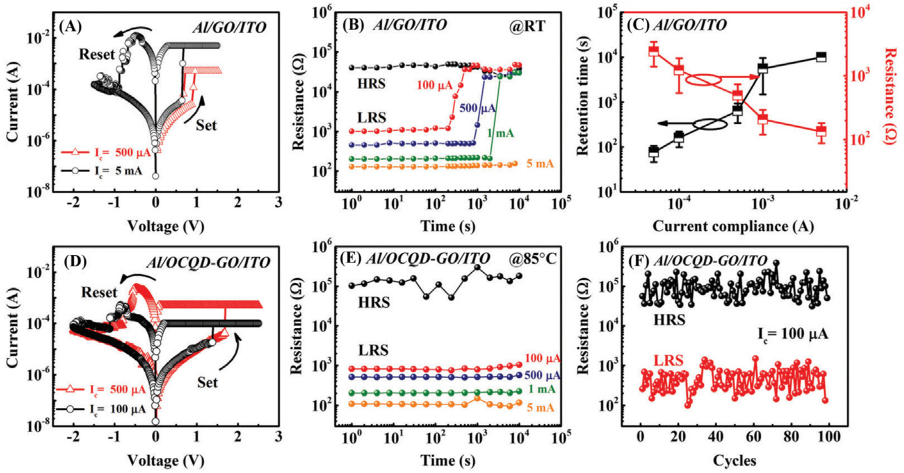

Figure 9.6 Panels (A) and (B) show the RS behavior and retention characteristics, respectively, of the Al/GO/ITO device under the different CCs. (C) The dependence of LRS and retention time for various CCs. Measured I−V curves (D) and retention characteristics (E) of the Al/OCQD−GO/ITO devices under different CCs. (F) The evolution of the HRS (high resistance state)/LRS with 100 consecutive RS cycles under a CC of 100 μA. The resistance values were read at 0.1 V.

Source: Reproduced with permission from M. Qi, L. Bai, H. Xu, Z. Wang, Z. Kang, X. Zhao, et al., *Journal of Materials Chemistry C*, 6 (2018) 2026−2033.

One good thing worth noting is that the CQDs are highly dispersible in water and in alcohols which makes them easy to coat on various substrates including the flexible ones through printing methods as well as other simple coating processes such as spin-coating or spray-coating. Making CQD nanocomposites with inorganic or organic molecules realizes suitable active material for memory device and the active material in such cases can be tailor-made according to needs since there could be virtually countless combinations. This suppleness allows to add multifunctionality in the memory devices which can be simply made through solution-based methods (Fig. 9.7).

The devices show a ferroelectric-like hysteretic I−V characteristic. The polarization charges can form an additive reverse and produce a nonzero current I_{SC} at zero-bias and a nonzero voltage V_{OC} when the current is zero. The values of I_{SC} and V_{OC} increase as the applied field increases and attains a saturation at a sufficiently high external field. The device with additional CQDs layer shows an enlarged window, which is attributed to the enhanced spatial ordering of electric dipole moments between the organic molecules and CQDs under applied external field. Though the alternation of dipole moments can be fatigued due to slow charge transfusions within organic−inorganic interfaces but the device demonstrated a switching reliability for several thousand cycles in a succession of periodic pulses without any performance degradation [27] (Fig. 9.8).

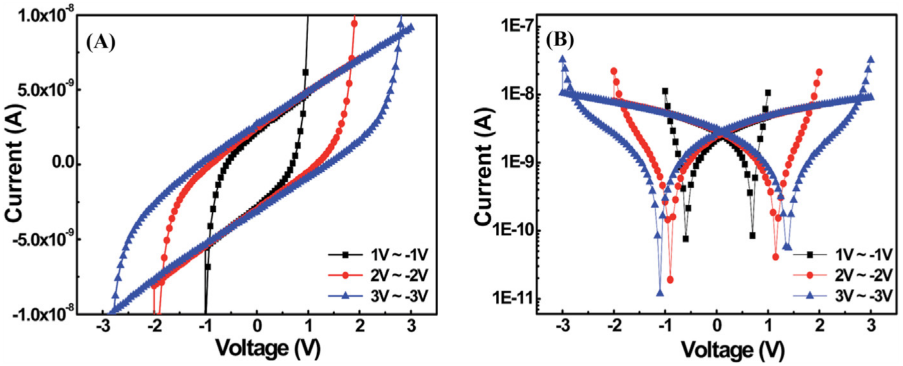

Figure 9.7 (A) The linear I−V curves in the cyclic multiple-valued voltage sweeping from +1 to −1 V, +2 to −2 V and +3 to −3 V for the device Al/PMMA/CDs/PEDOT:PSS/ITO, respectively. (B) The corresponding semi-log plots of (A).
Source: Reproduced with permission from X. Zhang, J. Xu, S. Shi, X. Wang, X. Zhao, P. Zhou, et al., *RSC Advances*, 6 (2016), 58733−58739.

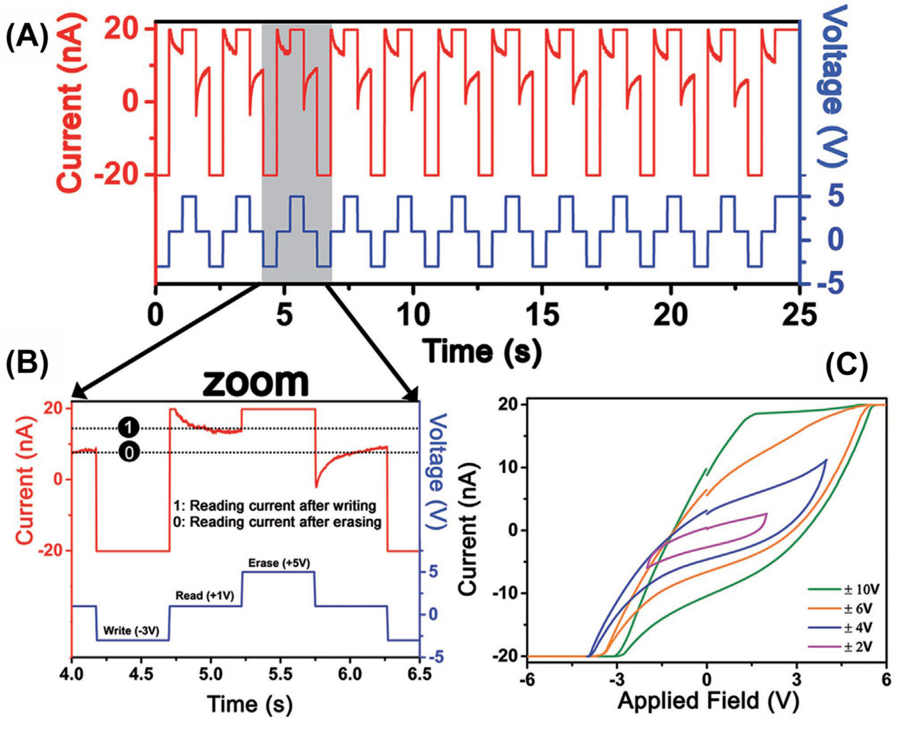

Figure 9.8 (A) Typical current response to WRER cycles for the CNP-PANI device of single contact area between probe and device layer. (B) One single WRER cycle is zoomed in. The current (red) versus voltage (blue) response for a certain period of pulses (0.5 s) was monitored, which showed a significant current difference between the “1” and “0” states. (C) Current hysteresis curves have been shown with different sweeping voltages, indicating the charge-trapping behavior of the device layer.
Source: Reproduced with permission from S. Goswami, S. Nandy, A. N. Banerjee, A. Kiazadeh, G. R. Dillip, J. V. Pinto, et al., *Advanced Materials*, 29 (2017) 1703079.

CQD—polyaniline (PANI) composite is another example of CQD-based memory material. Goswami et al. have shown that the composite material is suitable for "electrotyping"—a term that defines spatially localized memory by charge injection method [28]. Electrotyping happens due to charge trapping at specific sites and the process is carried out by a conducting atomic force microscope (AFM) probe. The probe was used for charge injection, string and after that diffusion of that charge. It has been found that the CQDs sufficiently increase the charge-storing capacity of the conducting polymer which act as the matrix and is prone to disperse the charges fell into this matrix. However, using CQDs, it has been made possible to attain several WRER cycles on an area as small as 20 nm, which was the point contact of the AFM tip on the CQD−PANI composite film. Thus, it would be possible to achieve a memory bit size (spatial) even lower than 20 nm using thinner probes by this electrotyping method.

9.3 Transistors

9.3.1 Basics of transistor

A transistor is a three terminal current-driven semiconductor device that can be used to control the flow of current in an electronic circuit. Transistors can be used to either amplify a weak signal, as an oscillator, or as a switch. Owing to such a versatile range of functionalities, transistors are used as one of the basic building blocks of integrated circuits in a wide array of modern day electronic devices.

The name "transistor" originates from the phrase "transfer of resistor," which essentially points toward the modification of resistance of the device under external effects (current or voltage) while in operation. The three terminals of a transistor can be considered to form a couple of channels (*vide infra*) and a small signal (voltage or current) is applied between one pair (input channel) to control a much larger signal at another pair of terminals (output channel). Such a "gain" hence allows producing a stronger output signal from transistor, which is proportional to the input signal, and thus it acts as an amplifier. Alternatively, the transistor can be used to turn current on or off in a circuit as an electrically controlled switch, where the amount of current is determined by other circuit elements.

Transistors can be basically divided into two major categories: bipolar junction transistors (BJT) and field effect transistors (FET). In a BJT, the three terminals are labeled as base, collector, and emitter and as the term bipolar suggests, the current carriers are both electrons and holes. Depending upon their configuration, BJTs can be further classified as NPN or PNP-type transistors and between these two the NPN is preferred for the sake of convenience. Under a typical operation, a small current is fed to the input channel that is formed between the base and the emitter. Since the junction is forward biased, the electrons (holes) flow from the emitter to base and holes (electrons) from the base to emitter. It is worthy to state here that although the emitter electrons (holes) become minority carriers in the base, due to the narrow thickness of the base only a little portion of the charge carriers are lost in recombination process and the carriers are then drawn toward the collector−base junction which is kept under reverse biased. So, essentially the base terminal serves as a controller to regulate or switch a much larger current in the output channel formed between the collector and emitter terminals and such an operation makes BJTs a current controlled device.

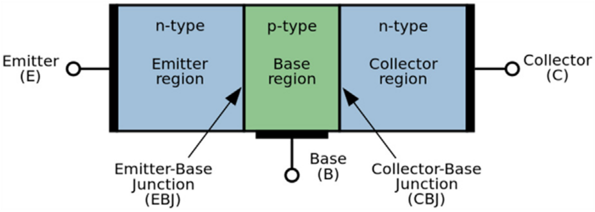
n-type
Emitter region
p-type
Base region
n-type
Collector region
Emitter (E)
Collector (C)
Emitter-Base Junction (EBJ)
Base (B)
Collector-Base Junction (CBJ)

For an FET, on the other hand, the terminals are labeled as gate, source, and drain, and a voltage at the gate can control a current between source and drain. So unlike BJTs, an FET is a voltage or field controlled device and its operation is based around the concept that charge on a nearby object can attract charges within a semiconductor channel. Based on the nature of the semiconductor (*n*-type or *p*-type) forming the channel, the conduction process in an FET takes place through movement of either electron or hole and FET is hence called a unipolar device.

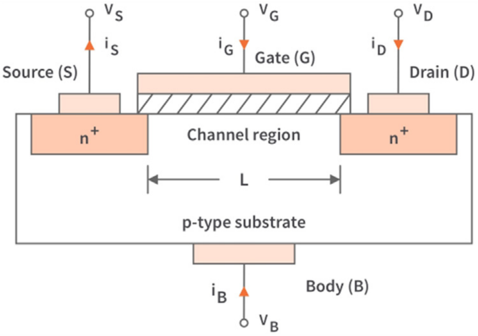
V_S
i_S
Source (S)
V_G
i_G
Gate (G)
V_D
i_D
Drain (D)
n^+
Channel region
n^+
L
p-type substrate
i_B
Body (B)
V_B

While in operation, the gate electrode in a FET, due to its close proximity to the channel, can control the flow of carriers (electrons or holes) flowing from the source to drain by controlling the size and shape of the conductive channel. So, in this way, by the application of a voltage to the gate, the conductivity between the drain and source terminals of an FET can be modulated. The semiconductor channel where the current flow occurs may be either p-type or n-type. This gives rise to two types or categories of FET known as p-channel and n-channel FETs.

9.3.2 Carbon quantum dots used in transistor applications

Among various QDs in transistor applications, CQDs have emerged as viable candidates for conventional inorganic nanocrystals owing to their low cost, low toxicity, and long-term stability. Typically, the structure of CQDs is defined as the quasi-spherical graphitic nanoparticle with various types of surface functional groups (e.g., aldehydes, carboxylic acids, hydroxides, etc.) and with a proper choice of these surface ligands during device processing, such CQD-based transistors can be foreseen to revolutionize the use of QDs as the active layer in FETs.

Typically, to fabricate a QD-based FET device, either a bottom-gate or a top-gate configuration is considered. For the bottom-gate configuration, a highly doped silicon wafer is usually used as a gate electrode and it is separated from the QD film with a dielectric (e.g., SiO_2) layer. On top of the substrate, two electrodes, source and drain, are formed following different techniques such as optical lithography, thermal evaporation, and so on. On the other hand, in the top-gate configuration, after the deposition of the electrodes and QD films a dielectric layer (e.g., SiO_2, Al_2O_3, or an ion gel) is formed on top and this dielectric layer separates the top gate from the QD film. So, essentially for application of QDs in FET devices, a good quality of the thin film is a prerequisite and with CQDs formed through various approaches such as arc discharge, electrochemical oxidation, hydrothermal, hot injection and so on, a very uniform surface coverage with homogeneous distribution can be achieved with thin film form.

In a pioneering effort with CQDs in transistor application, Kwon et al. have reported charge transport phenomenon in films of amine-capped CQDs as the channels of FETs [29]. In their effort, colloidal CQDs were synthesized following a modified version of the micelle-assisted method, and to demonstrate the role of ligand length on charge transport, the as-synthesized CQDs were ligand exchanged with several shorter-tailed primary amines. Under modulation of the gate voltage, the CQD FETs exhibited ambipolar transport behavior with high electron and hole mobilities and the conduction mechanism could be described by the nearest-neighbor hopping model (Fig. 9.9).

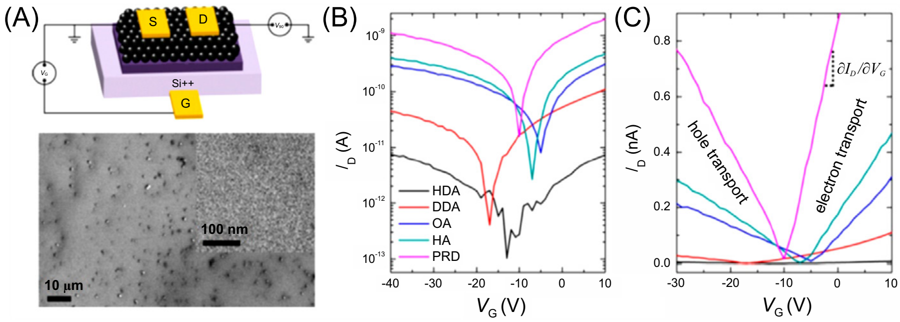

Figure 9.9 (A) Schematic of the FET and SEM images of the CQD channel (HA-CQD). Transfer characteristics of a series of the CQD FETs on (B) semilogarithmic and (C) linear plots at V_{SD} (source-drain voltage) = −30 V. The channel length and width are 150 and 1500 μm, respectively. The color coding is the same for both graphs.
Source: Reproduced with permission from W. Kwon, S. Do, D. C. Won and S.-W. Rhee, *ACS Applied Materials & Interfaces*, 5 (2013) 822−827.

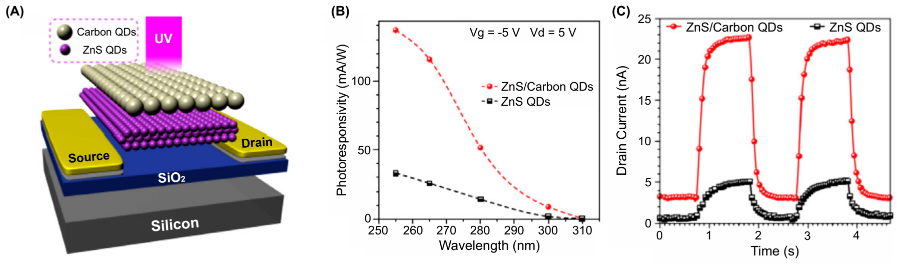

Figure 9.10 (A) Schematic illustration of the phototransistor fabricated with the ZnS/carbon QDs. (B) Photoresponse performance of bare ZnS and ZnS/carbon QD phototransistors. (C) Time response behavior of the devices under 255 nm UV light.
Source: Reproduced with permission from W. J. Kuang, Z. P. Wang, H. Liu, Y. F. Ding, Q. M. Xu, R. H. Guo, et al., *IEEE Photonics Technology Letters*, 32 (2020) 204–207.

CQDs have also been demonstrated as a promising material in field-effect phototransistors. In this regard, Zhu et al. reported formation of graphene quantum dots (GQDs) with promising light absorption properties through chemical vapor deposition (CVD) technique toward their application in hybrid phototransistors with indium gallium zinc oxide (IGZO) as the channel layer. Such devices when exposed to ultraviolet illumination yielded almost 10 times larger photocurrent compared to than that of IGZO one [30]. In a recent report, Kuang et al. have incorporated vertical ZnS/CQD heterojunction structure as a light-absorbing layer in FET structure and showed that introduction of the CQDs can significantly improve the photodetection performance of the devices compared to the pristine ZnS QDs [31]. By using a gate-field modulation, the phototransistor can be operated in the depletion mode with a large detectivity of 1.45×10^{10} cm $Hz^{1/2}/W$, enhanced photoresponsivity, high external quantum efficiency, and shorter response time (0.2 s) that could be attributed to the enhanced carrier separation at the heterojunction interface owing to the high mobility of the channel materials leading to fast charge carrier transport coupled with the strong light-absorbing properties of the semiconductors (Fig. 9.10).

CQDs have found their clinical application in the form of electrochemical biosensors. Such devices are typically designed with a biorecognition element integrated with an electrochemical signal transducer such as electrode and FET. The semiconductor channel in these FET-based biosensors is composed of a biorecognition element in contact with the analyte environment and the source-drain current is found to be proportional to the analyte concentration. Dong et al. demonstrated the promising performance of carbon dot-modified liquid-exfoliated graphene FET as an alternative DNA methylation (DNAm) sensor in determining *SEPT9* methylation in colorectal cancer patients [32]. The qualification and quantification of trace amount of cancer biomarkers is of vital importance for the early diagnosis. The carbon dots were found to enhance the DNAm sensitivity of the FETs and overall the FET-based biosensor exhibited the advantages of high sensitivity because an FET sensor is composed of a sensor and an amplifier. The results moreover inferred a good agreement to the traditional route of methylation evaluation and interestingly

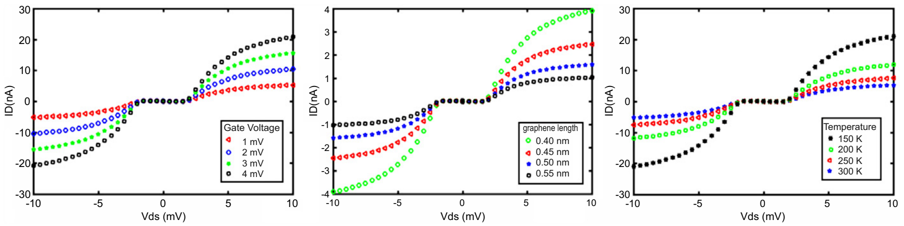

Figure 9.11 The current vs voltage curves of proposed model of DQD SET for (A) different gate voltages, graphene length is 1 nm and temperature is 300 K; (B) different graphene lengths, applied gate voltage is 1 mV and temperature is 300 K; and (C) different temperature, gate voltage is 1 mV and graphene length is 1 nm.
Source: Reproduced with permission from V. Khademhosseini, D. Dideban, M. Ahmadi and R. Ismail, *ECS Journal of Solid State Science and Technology*, 9 (2020) 021003.

it offered an improved diagnostic value which is even higher than the traditional PCR-based methylation method. The effort hence introduced the FET-based system as an efficient alternative avenue for evaluating DNAm in the target genes of colorectal cancer. Huang et al. developed a novel electrochemical sensor based on Pb^{2+}-dependent DNAzyme assisted signal amplification and GQD-ionic liquid-nafion (GQDs-IL-NF) composite film for detection of carcinoembryonic antigen (CEA) [33]. CEA is also one of the most promising tumor markers for diagnosing cancer, and the as developed sensors with excellent biocompatibility and low toxicity provided high electrochemical response signals resulting in high selectivity, good reproducibility, and acceptable stability in CEA detection.

Apart for FET devices, CQDs have also shown potential in fabrication of single-electron transistor (SET) as a fast current switching device by tunneling of electrons. Khademhosseini et al. reported fabrication and characterization of GQD SET devices where graphene was used as a material of SET island with high electron mobility [34]. The results evidenced a direct dependence of SET current on the gate voltage and an influence of graphene length and temperature on the current. Simulation studies and a comparison of single graphene quantum dot and double GQDs moreover indicated that with increasing number of quantum dot in SET, its performance and speed can be improved (Fig. 9.11).

9.4 Sensors

CQDs play important roles in wide range of sensors beginning from optical sensors, biosensors, water purity sensors, etc. [35]. CQDs and their dopants/derived materials improved sensing characteristics, e.g., response times and regenerations. CQDs have shown promising fluorescent probes in the detection of small bioanalytes such as antibacterial drugs, dopamine (DA), ascorbic acid (AA), glucose, etc. [36–39].

Metal ions are responsible for several chemical reactions. When they take part in the reaction exchange of electrons come about. It is sometime important

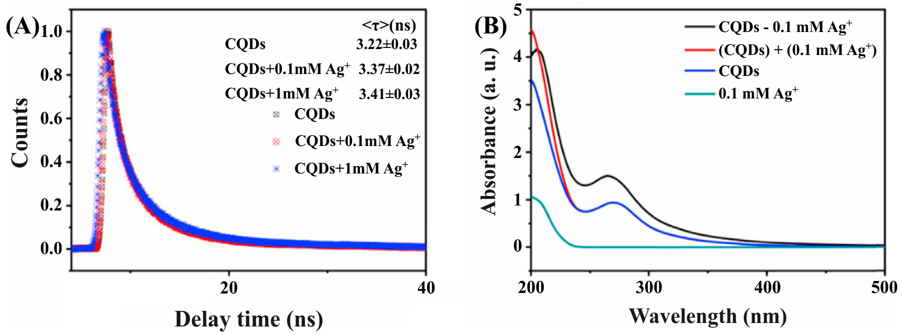

Figure 9.12 (A) Fluorescence decay traces of CQDs with addition of different concentration of Ag + solution; (B) UV−vis absorption spectra of CQDs (blue), Ag + (green), CQDs−Ag + system (black), and summed UV−vis absorption spectrum between CQDs and Ag + (red), respectively.

Source: Reproduced with permission from M. J. Molaei, *Talanta*, 196 (2019) 456−478.

to know whether a particular reaction occurs or not especially for fast-action drug deliveries. An optical sensor is useful to flag the occurrence of the reaction in such cases. CQDs are nontoxic and highly fluorescent. They can be synthesized by simple hydrothermal process. Tagging CQDs with metal ions could make a simple yet useful optical sensor for chemical reactions if the reactivity of the metal ions is preserved and electron exchange takes place with the CQDs. Here is an example of binding CQDs to Ag^+ ion [40]. The binding of the quantum dot to the ion is confirmed from the UV-Vis characteristics. But when the Ag^+ ion converts the functional group (−CONH −) from spirolactam structure to an open-ring amide, the fluorescence of the attached CQDs decreases. This is a static fluorescence quench since the fluorescence life time does not alter much (Fig. 9.12).

In a similar line of mechanism, ferric ions can be detected by CQDs. The presence of iron ions in water has been detected through a fast process. CQDs have been conjugated with ZnO/CdS core-shell nanoparticles. The detection process depends on the static quenching of fluorescence of the CQDs but there were interfering noise due to cations present in the sample though thermodynamic analysis showed that the interaction between the conjugated nanoparticles and ferric ions is hydrophobic in nature [41]. Also, at high temperature the sensor reliability is questionable (Fig. 9.13).

The hygroscopic property of the CQDs has been used for relative humidity sensors [42]. The CQDs for this case have been synthesized through pyrolysis method. These CQDs have quite high bandgap, and the sensor is based on the capacitive response. CQDs are the principal dielectric of this capacitor. With humidity the dielectric constant of the CQDs is altering and likewise the capacitance of the capacitor is changing. This type of sensor is very sensitive and can detect incredibly low humidity within a small time.

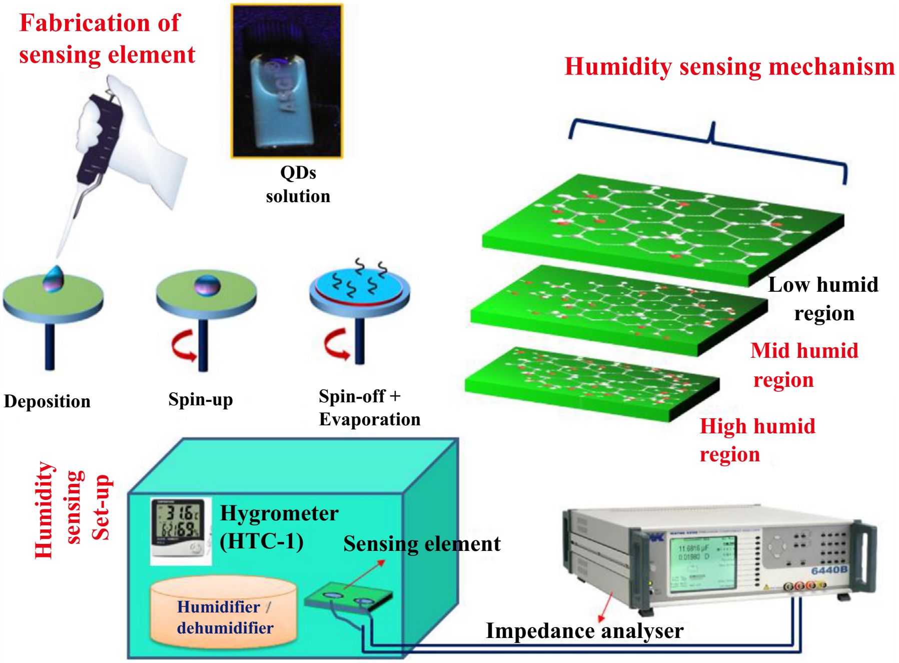
Fabrication of sensing element
QDs solution
Humidity sensing mechanism
Low humid region
Mid humid region
High humid region
Deposition
Spin-up
Spin-off + Evaporation
Humidity sensing Set-up
Hygrometer (HTC-1)
Sensing element
Humidifier / dehumidifier
Impedance analyser
6440B

Figure 9.13 Schematic of carbon quantum dot synthesis and humidity sensor fabrication and data acquisition setup.
Source: Reproduced with permission from P. Chaudhary, D. K. Maurya, S. Yadav, A. Pandey, R. K. Tripathi and B. C. Yadav, *Sensors and Actuators B: Chemical*, 329 (2021) 129116.

CQDs can also be used as the chemosensor material. Methotrexate is a chemotherapeutic agent found in environment due to its usage to treat different types of cancer. However, this toxic drug can cause other deadly diseases such as pneumonitis or cirrhosis. This drug when exposed to environment remains undetectable in the ecosystem and requires sophisticated instrumentation or complex research experimentation. The N, S co-doped CQDs bind with the methotrexate through (1) hydrogen bonding and (2) $\pi-\pi$ stacking. These types of adhesion between materials causes inner filter effect and results in a quenching of fluorescence for a particular excitation wavelength. Through this method methotrexate has been detected in a small resolution amount in wastewater and extracellular fluids [43].

In the above examples of the recently developed sensors, CQDs play an important role to improve the sensing parameters. Today, our science has been developed in such a position that detection/sensing a particular entity or event is not difficult, but the main concern remains the response and recovery times. CQDs used in the cases have contributed positively to build up these characteristics due to their excellent optical and exceptional electrical properties. The CQDs are unique in sense that these are an agglomerate of differently hybridized carbonaceous volumes within a particle and posses many defects. These defects are inherent, and also a range of surface passivation interject the defects. Though there are beneficial features of CQDs to be used as sensing material, the drawback of it is its hygroscopicity. As has been already mentioned on several occasions in this chapter that CQDs are highly hygroscopic, this can be shown even from the surface interaction simulation study using DFT based on B3LYP at diffused and polarized basis [42,44]. The water in the sensor kills the sensing ability of the device and deteriorates the device's life time.

9.5 Carbon quantum dot laser

Due to the presence of shallow energy levels and deep-lying discrete energy levels within the energy bands, CQDs show an excitation independent emission. This feature of CQDs arises from its nonuniform hybridization and surface defect states. Instead of high quantum yields, excitation wavelength-independent (λ_{ex}-independent) photoluminescence characteristics of CQDs are utilized for CQD-based light amplification [45]. It has been known that the fluorescence quantum yield becomes large when the photoluminescence properties of any matter are wavelength dependent. Such CQDs do not show lasing action. Whereas the CQDs with λ_{ex}-independent photoluminescence demonstrate spontaneous emission and in-phase amplification a CQD-based laser though the threshold remained low.

Reference

[1] X. Xu, R. Ray, Y. Gu, H.J. Ploehn, L. Gearheart, K. Raker, et al., Electrophoretic analysis and purification of fluorescent single-walled carbon nanotube fragments, Journal of the American Chemical Society 126 (2004) 12736−12737.

[2] N.K. Khairol Anuar, H.L. Tan, Y.P. Lim, M.S. So'aib, A review on multifunctional carbon-dots synthesized from biomass waste: design/fabrication, characterization and applications, Abu Bakar 9 (2021). Available from: https://doi.org/10.3389/fenrg.2021.626549.

[3] S. Tajik, Z. Dourandish, K. Zhang, H. Beitollahi, Q.V. Le, H.W. Jang, et al., Carbon and graphene quantum dots: a review on syntheses, characterization, biological and sensing applications for neurotransmitter determination, RSC Advances 10 (2020) 15406−15429.

[4] M. Kurian, A. Paul, Recent trends in the use of green sources for carbon dot synthesis – a short review, Carbon Trends 3 (2021) 100032.

[5] B. De, Carbon dots and their polymeric nanocomposites, in: N. Karak (Ed.), Nanomaterials and Polymer Nanocomposites, Elsevier, 2019, pp. 217−260. Available from: https://doi.org/10.1016/B978-0-12-814615-6.00007-2.

[6] H.-H. Huang, K.K.H. De Silva, G.R.A. Kumara, M. Yoshimura, Structural evolution of hydrothermally derived reduced graphene oxide, Scientific Reports 8 (2018) 6849.

[7] L. Bhattacharjee, R. Manoharan, K. Mohanta, R.R. Bhattacharjee, Conducting carbon quantum dots – a nascent nanomaterial, Journal of Materials Chemistry A 3 (2015) 1580–1586.

[8] M.J. Molaei, A review on nanostructured carbon quantum dots and their applications in biotechnology, sensors, and chemiluminescence, Talanta 196 (2019) 456–478.

[9] Y. Wang, A. Hu, Carbon quantum dots: synthesis, properties and applications, Journal of Materials Chemistry C 2 (2014) 6921–6939.

[10] R. Wang, K.-Q. Lu, Z.-R. Tang, Y.-J. Xu, Recent progress in carbon quantum dots: synthesis, properties and applications in photocatalysis, Journal of Materials Chemistry A 5 (2017) 3717–3734.

[11] S. Iravani, R.S. Varma, Green synthesis, biomedical and biotechnological applications of carbon and graphene quantum dots. A review, Environmental Chemistry Letters 18 (2020) 703–727.

[12] R. Das, R. Bandyopadhyay, P. Pramanik, Carbon quantum dots from natural resource: a review, Materials Today Chemistry 8 (2018) 96–109.

[13] Z. Lv, Y. Wang, Z. Chen, L. Sun, J. Wang, M. Chen, et al., Phototunable biomemory based on light-mediated charge trap, Advanced Science 5 (2018) 1800714.

[14] C. Wu, R. Buyya, Cloud storage basics, in: C. Wu, R. Buyya (Eds.), Cloud Data Centers and Cost Modeling, Morgan Kaufmann, 2015, pp. 425–495. Available from: https://doi.org/10.1016/B978-0-12–801413-4.00012-X.

[15] R.J.M. Palma, J.M.M. Duart (Eds.), Novel advanced nanomaterials and devices for nanoelectronics and photonics, Nanotechnology for Microelectronics and Photonics, Nanophotonics, Elsevier, 2017.

[16] J. Ajayan, D. Nirmal, S. Tayal, S. Bhattacharya, L. Arivazhagan, A.S.A. Fletcher, et al., Nanosheet field effect transistors – a next generation device to keep Moore's law alive: An intensive study, Microelectronics Journal 114 (2021) 105141.

[17] X. Wang, K.-C. Chang, Z. Zhang, Q. Liu, L. Li, S. Ma, et al., Performance enhancement and mechanism exploration of all-carbon-nanotube memory with hydroxylation and dehydration through supercritical carbon dioxide, Carbon 173 (2021) 97–104.

[18] M.C. Petty, Organic electronic memory devices, in: O. Ostroverkhova (Ed.), Handbook of Organic Materials for Optical and (Opto)electronic Devices, Woodhead Publishing, 2013, pp. 618–653. Available from: https://doi.org/10.1533/9780857098764.3.618.

[19] Y. Lin, X. Zhang, X. Shan, T. Zeng, X. Zhao, Z. Wang, et al., Photo-tunable organic resistive random access memory based on PVP/N-doped carbon dot nanocomposites for encrypted image storage, Journal of Materials Chemistry C 8 (2020) 14789–14795.

[20] I. Mihalache, L.M. Veca, M. Kusko, D. Dragoman, Memory effect in carbon quantum DOT–PEG1500N composites, Current Applied Physics 14 (2014) 1625–1632.

[21] A. Singh, A. Nivedan, S. Kumar, S. Kumar, Impurity assisted hopping conduction and persistent photoconductivity in disordered carbon nanoparticle film, Journal of Applied Physics 126 (2019) 225102.

[22] W. Wu, Biodegradable polymer nanocomposites for electronics, in: Y. Zhou, G. Ding (Eds.), Polymer Nanocomposite Materials: Applications in Integrated Electronic Devices, Wiley, 2021, pp. 53–75.

[23] H. Lu, Y. Chen, Q. Chang, S. Cheng, Y. Ding, J. Chen, et al., Polymer–carbon dot hybrid structure for a self-rectifying memory device by energy level offset and doping, RSC Advances 8 (2018) 13917–13920.

[24] Y. Lin, Z. Wang, X. Zhang, T. Zeng, L. Bai, Z. Kang, et al., Photoreduced nanocomposites of graphene oxide/N-doped carbon dots toward all-carbon memristive synapses, NPG Asia Materials 12 (2020) 64.

[25] W. Zhang, X. Guo, J. Yin, J. Yang, Organic field-effect transistor memory device based on an integrated carbon quantum dots/polyvinyl pyrrolidone hybrid nanolayer, Electronics 9 (2020).

[26] M. Qi, L. Bai, H. Xu, Z. Wang, Z. Kang, X. Zhao, et al., Oxidized carbon quantum dot−graphene oxide nanocomposites for improving data retention of resistive switching memory, Journal of Materials Chemistry C 6 (2018) 2026−2033.

[27] X. Zhang, J. Xu, S. Shi, X. Wang, X. Zhao, P. Zhou, et al., Ferroelectric-like hysteresis effect observed in carbon quantum dots sandwiched between PMMA and PEDOT:PSS hybrid film, RSC Advances 6 (2016) 58733−58739.

[28] S. Goswami, S. Nandy, A.N. Banerjee, A. Kiazadeh, G.R. Dillip, J.V. Pinto, et al., "Electro-typing" on a carbon-nanoparticles-filled polymeric film using conducting atomic force microscopy, Advanced Materials 29 (2017) 1703079.

[29] W. Kwon, S. Do, D.C. Won, S.-W. Rhee, Carbon quantum dot-based field-effect transistors and their ligand length-dependent carrier mobility, ACS Applied Materials & Interfaces 5 (2013) 822−827.

[30] H. Zhu, A. Liu, F. Shan, W. Yang, W. Zhang, D. Li, et al., One-step synthesis of graphene quantum dots from defective CVD graphene and their application in IGZO UV thin film phototransistor, Carbon 100 (2016) 201−207.

[31] W.J. Kuang, Z.P. Wang, H. Liu, Y.F. Ding, Q.M. Xu, R.H. Guo, et al., ZnS/carbon quantum dot heterojunction phototransistors for solar-blind ultraviolet detection, IEEE Photonics Technology Letters 32 (2020) 204−207.

[32] D. Dong, J. Zhang, R. Zhang, F. Li, Y. Li, Y. Jia, Multiprobe assay for clinical SEPT9 methylation based on the carbon dot-modified liquid-exfoliated graphene field effect transistor with a potential to present a methylation panorama, ACS Omega 5 (2020) 16228−16237.

[33] J.-Y. Huang, L. Zhao, W. Lei, W. Wen, Y.-J. Wang, T. Bao, et al., A high-sensitivity electrochemical aptasensor of carcinoembryonic antigen based on graphene quantum dots-ionic liquid-nafion nanomatrix and DNAzyme-assisted signal amplification strategy, Biosensors and Bioelectronics 99 (2018) 28−33.

[34] V. Khademhosseini, D. Dideban, M. Ahmadi, R. Ismail, Current analysis of single electron transistor based on graphene double quantum dots, ECS Journal of Solid State Science and Technology 9 (2020) 021003.

[35] M. Li, T. Chen, J.J. Gooding, J. Liu, Review of carbon and graphene quantum dots for sensing, ACS Sensors 4 (2019) 1732−1748.

[36] S. Thangamani, H.P. Mahendran, R.R. Bhattacharjee, S. Jeyaraj, K. Mohanta, Assessment of dihydropyrimidinone-based nanocomposites as multifunctional anti-cancer drug, Materials Advances 2 (2021) 3385−3393.

[37] Z. Hassanvand, F. Jalali, M. Nazari, F. Parnianchi, C. Santoro, Carbon nanodots in electrochemical sensors and biosensors: a review, ChemElectroChem 8 (2021) 15−35.

[38] S. Mohapatra, R.K. Das, Dopamine integrated B, N, S doped CQD nanoprobe for rapid and selective detection of fluoride ion, Analytica Chimica Acta 1058 (2019) 146−154.

[39] X. Liang, N. Li, R. Zhang, P. Yin, C. Zhang, N. Yang, et al., Carbon-based SERS biosensor: from substrate design to sensing and bioapplication, NPG Asia Materials 13 (2021) 8.

[40] X. Zhao, S. Liao, L. Wang, Q. Liu, X. Chen, Facile green and one-pot synthesis of purple perilla derived carbon quantum dot as a fluorescent sensor for silver ion, Talanta 201 (2019) 1−8.

[41] Z. Nan, C. Hao, X. Zhang, H. Liu, R. Sun, Carbon quantum dots (CQDs) modified ZnO/CdS nanoparticles based fluorescence sensor for highly selective and sensitive detection of Fe (III), Spectrochimica Acta Part A: Molecular Biomolecular Spectroscopy 228 (2020) 117717.

[42] P. Chaudhary, D.K. Maurya, S. Yadav, A. Pandey, R.K. Tripathi, B.C. Yadav, Ultrafast responsive humidity sensor based on roasted gram derived carbon quantum dots: experimental and theoretical study, Sensors and Actuators B: Chemical 329 (2021) 129116.

[43] Y. Zhao, S. Zou, D. Huo, C. Hou, M. Yang, J. Li, et al., Simple and sensitive fluorescence sensor for methotrexate detection based on the inner filter effect of N, S co-doped carbon quantum dots, Analytica Chimica Acta 1047 (2019) 179−187.

[44] R.E. Ambrusi, J.M. Arroyave, M.E. Centurión, M.S. Di Nezio, M.F. Pistonesi, A. Juan, et al., Density functional theory model for carbon dot surfaces and their interaction with silver nanoparticles, Physica E: Low-Dimensional Systems and Nanostructures 114 (2019) 113640.

[45] Y. Zhang, Y. Hu, J. Lin, Y. Fan, Y. Li, Y. Lv, et al., Excitation wavelength independence: toward low-threshold amplified spontaneous emission from carbon nanodots, ACS Applied Materials & Interfaces 8 (2016) 25454−25460.

Carbon quantum dot-based nanosensors

10

Ankita Saha[1], *Lopamudra Bhattacharjee*[2] *and*
Rama Ranjan Bhattacharjee[3]
[1]Amity School of Applied Sciences, Amity University, Kolkata, West Bengal, India, [2]PSG Institute of Advanced Studies, Coimbatore, Tamil Nadu, India, [3]Department of Chemistry, Sister Nivedita University, Kolkata, West Bengal, India

10.1 Introduction to nanosensors

A sensor is a gadget that identifies a variable quantity, usually electronically or optically, and transforms the data into specific signals. The requirements of sensors are selectivity, diversity, sensitivity, stability, and accuracy of information extracted. Sensors have huge applications in everyday life, with applications like monitoring volatile organic compounds (VOCs) for face recognition. Sensors are used to monitor various industrial processes. Nanosensors function similarly to conventional sensors, but the technical and structural difference is that nanosensors use nanomaterials as their active sensing agent.

Nanomaterials perform better as sensor elements than their bulk counterpart as sensing is mostly a surface phenomenon. Nanomaterials are more reactive because nanomaterials have improved surface area. Breaking of bonds between atoms takes place to make them nanodimensional. More surface area signifies more surface energy. Material with high energy will always be unstable so it will share the energy with other sources. In the case of nanomaterials with a size of approximately 2 nm, the ratio of the surface atom to bulk atom is about 50%. The same affect the crystallographic properties also. For example, the main difference between (111), (110), and (100) facets in materials depends on the surface energy. On the surface of many materials, the atoms possess dangling or unsatisfied bonds that are available for bonding with any other atoms or molecules. The surface atoms are always under strain where the directed force is always towards the bulk. This is energetically controlled. The bond distance between the surface and subsurface atoms is smaller than that between bulk atoms. As each facet has characteristic surface energy, the interaction energy will depend on how many broken chemicals bonds one material possess on its surface. For example, for metals with structure face centered cubic (FCC):

- {100} facets would have four broken chemical bonds,
- {110} surfaces has 5 broken chemical bonds and
- {111} has 3.

Carbon Quantum Dots for Sustainable Energy and Optoelectronics. DOI: https://doi.org/10.1016/B978-0-323-90895-5.00006-0
© 2023 Elsevier Ltd. All rights reserved.

Solid-state sensors with nanocomponent depend on the interfacial reaction that occurs on the surface. Nanoparticles have large surface area than the bulk one. It enhances the number of reaction site for the reaction to occur. Surface atom is more unstable (and reactive). This instability related to their position on the lattice that forces the atoms to unbounded to their neighbor atoms or molecules. For nanoparticles, as the surface/bulk atoms ratio increase, the instability (and reactivity) also increases. Therefore, surface chemistry, synthesis process, and size are very important issues for handling nanoparticles and designing nanosensors.

Nanosensors are applied for detecting physical and chemical phenomena in portions difficult to access, for identifying biomolecules in cellular materials, and for detecting gases and VOCs in the industry and environment. There are two types of nanosensors: chemical and mechanical. Nanosensors that detect chemicals or chemical reactions function by detecting the change in the electrical conductivity of the nanomaterial once an active analyte is detected. Many nanomaterials have a certain value of electrical conductivity, which will reduce upon interaction with a molecule. It is this detectable change that is measured. However, the mechanism in which nanosensors work is very different. Nanomaterials that are used in mechanical nanosensors deviate from their electrical conductivity when the material is physically changed and this physical change creates a substantial response. This response can also be measured with an attached capacitor.

10.2 Chemical sensing

Chemical sensors are used in many applications for:

- food technology,
- environmental checking of quality of air and water,
- industrial leak detection,
- Aerospace, includeing chemical analysis of soil and atmospheric constituents,
- Military and anti-terrorism applications.

Few other environmental applications include the use of a chemoresistor sensor to detect insect attack. The chemoresistor includes a conducting polymer being the active layer with nanoparticle or other dopants incorporated within the matrix. The sensor detects specific VOCs produced by plants, such as when attacked by herbivores. Detecting these volatile phytochemicals helps detect insect attack at early stages of plant growth. The ability to detect important molecules, such as disease-related molecules, proteins, nucleic acids, pathogens, and cells, is important not only for disease diagnosis in the early stages but also for environmental and agricultural research and industrial development.

10.2.1 Fluorescence-based chemical sensing

In case of chemical sensing, the widely used phenomenon in chemical sensors is fluorescence. Fluorescent molecules and bulk materials are often used in sensor applications. These sensors are conventional in nature and often experience issues related to photobleaching, photoreduction, photodegradation, photoblinking, and other light induced chemical and physical changes. We have observed the effect of light on fluorescent dyes when they are kept out in the open. These cause concerns for use of fluorescent dyes as active sensor material in environmental sensors. Another issue with conventional fluorescent molecules is that their optical properties cannot be tuned and are not robust. Hence, the need for nanomaterials to replace conventional fluorescent materials has been felt and their robustness and tunability as well as strong fluorescence signal help them get better recognition as chemical sensor materials.

10.2.1.1 *Reasons for strong emission characteristics in nanoparticles*

It has been observed that conventional fluorescent materials have certain limitations. Hence, it is important that they can be replaced with nanomaterials. The exciton decay (i.e., electron–hole pair recombination) in fluorescent nanomaterials occurs almost exclusively through the band edge fluorescence emission to give a sharp and intense peak (Fig. 10.1). The factors favoring and strengthening this radiative-exciton decay path are as follows:

- High transition probability: Momentum matching is not applicable for both the inter and intra-band radiative transitions.
- Prevention of nonradiative exciton decay: The excited electrons and holes quickly move to their most stable positions through the small nonradiative decay pathways.
- Noncritical excitation: The exciting radiation frequency can cover a wide range starting from the absorption onset frequency. Thus, photoexcitation to produce the excitons in nanoparticles is favorable.
- Prevention of nonradiative electron–hole recombination through surface passivation: The surface dangling orbitals and surface defects acting as the traps of excited electrons and holes may lead to the nonradiative pathway of electron–hole recombination to weaken the band edge emission.

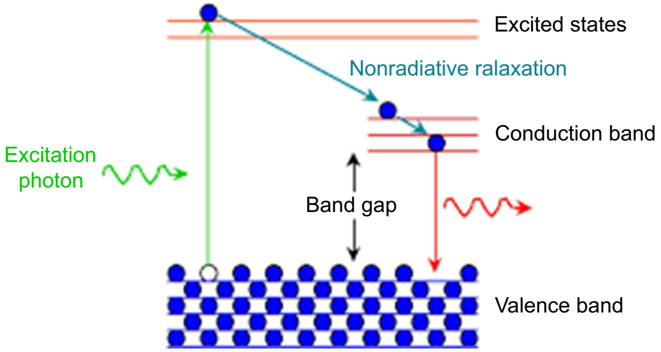

Figure 10.1 Schematic representation of the band edge and other transitions.

- Prevention of red-shifted defect fluorescent emission through surface passivation: The trapped electrons and holes by the surface dangling orbitals and surface defects may undergo the radiative recombination to produce low-energy defect fluorescent emission which reduces the intensity of the band edge fluorescent emission. The same can be avoided through surface passivation for carbon quantum dots (CQDs), as we will see in the next sections.

10.2.2 Chemical sensors: nanoparticles as superior components

Nanosensors are sensing devices with at least one of their sensing dimensions ranging between 1 and 100 nm. Nanomaterials used in the designing of nanosensors devices are generally nanotubes, polymeric nanomaterials, nanowires, and nanothin films. Carbon-based nanomaterials like CQDs, fullerenes, carbon nanotubes (CNTs), etc. have gained great interest in wide range of applications including bioimaging, industrial sensing, and environmental monitoring. The superior physicochemical, spectral, and optical characteristics of noble metal nanoparticles have also allowed the preparation of new biosensors. Anisotropic metal oxide nanoparticles form a promising class of active sensor components due to their easy fabrication, chemical stability, easy preparation, and scale-up protocol.

The following properties and related topics should be considered during the manufacturing of nanomaterials:

- Providing the chemistry of specific interactions with specific analytes by attaching functional molecules on surface.
- Attaining the electrochemically active sites through controlling the size and shape of nanomaterials during formation steps.
- Improving the specificity and stability by optimization mixed metallic nanomaterials.
- Designing novel nanocrystals with never seen before selectivity by structure–property relationship between the activity and the surface structure.
- Offering platform for the nonconventional electrocatalytic properties by improving the selectivity and sustainability of the nanosensors.
- Improving the electrochemical properties through the invention of highly conductive, chemically and mechanically stable surface and significant surface area of substrate materials.

10.2.3 CQDs: fluorescent sensor material

CQDs are currently viewed as promising organic fluorophores as they are composed of carbon, oxygen, and nitrogen. Investigations on the structure of CQDs reveal the presence of isolated sp^2 island separated or dispersed in between sp^3 regions. The CQDs can be compared with organic nanoparticles composed of molecular aggregates that emit solid-state fluorescence.

10.2.3.1 Fluorescence from CQDs

The isolated carbon nano-domains possess suitable band energy gaps and thus can emit variable-frequency emissions through electron–hole radiative recombination.

Fluorescence is one of the most fascinating features of CQDs for both fundamental science and applications. Fluorescence in CQDs has been thought to arise from excitons of carbon, quantum confinement effects in aromatic structure and free zigzag sites, and/or oxygenous emissive traps. Here we will discuss each mechanism separately. Application of CQDs as chemical sensors can be best understood if we clearly understand the underlying reasons for fluorescence.

Radiative recombination in small nano-domains

As per the structure of CQDs envisaged in previous chapters, it can be said that the isolated sp^2 nano-domains within the carbon-oxygen sp^3 matrix lead to the localization of e-h pairs, facilitating radiative recombination in small nano-domains (Fig. 10.2).

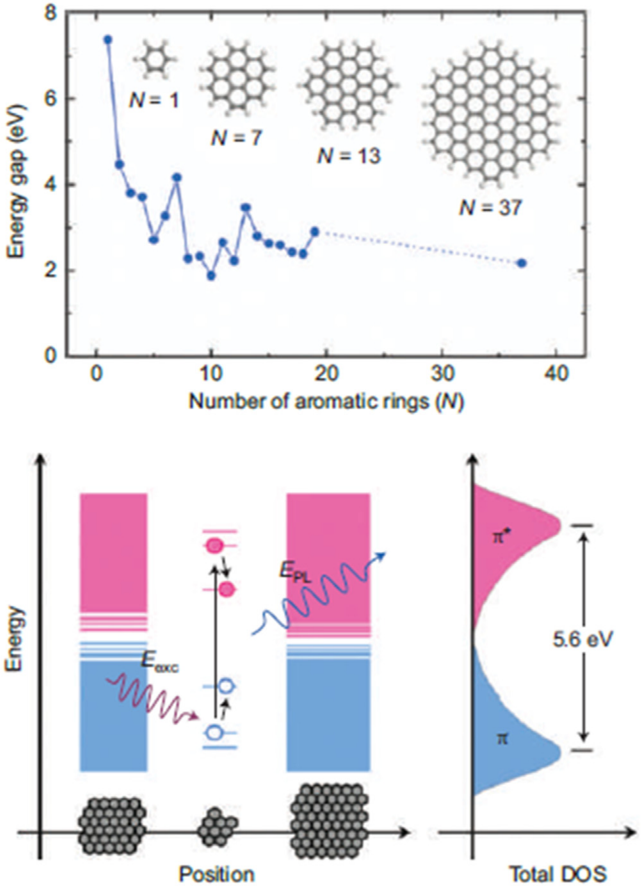

Figure 10.2 Schematic representation of sp^2 islands in CQDs and the band gap generated due to the discrete islands (https://doi.org/10.1038/nchem.907).

The emission band gap is determined by the size of sp^2 nano domains. It can be understood from Fig. 10.2 that the size of sp^2 domain determines the resonance length of the electron. Going by the laws of electron confinement,

$$E = n^2h^2/8mL^2$$

The larger the dimension of sp^2 domain, the smaller is the energy gap, as shown in the above figure. Corresponding emission will be within the visible and NIR region as observed for CQDs.

Free zigzag sites with a carbine-like triplet ground state

From previous chapters, we have understood that CQDs have sp^2 domains separated by sp^3 domains. At the edges of these sp^2 domains, various terminal C = O and C-O groups are present that contribute to the emission properties of CQDs, and will be discussed further as shown in Fig. 10.3. The periphery of these sp^2 domains generally consists of zigzag and chair edges. In a chemically derived CQD, free edges coexist with functionalized edges. These free zigzag sites are carbene-like, with a triplet ground state being most common, whereas free armchair sites are carbyne-like, with a singlet ground state most common. The carbene centers at zigzag sites are stabilized by virtue of localization of itinerant p electrons through s−p coupling.

Literature suggests that both phenomena contribute to the interesting emission properties of CQDs. However, the competition between sides as well as the detailed emission origin and mechanism still remain unclear and debatable. Fluorescence of CQDs has been studied by various techniques but the intrinsic mechanism and origin of the fluorescence have not been completely understood yet.

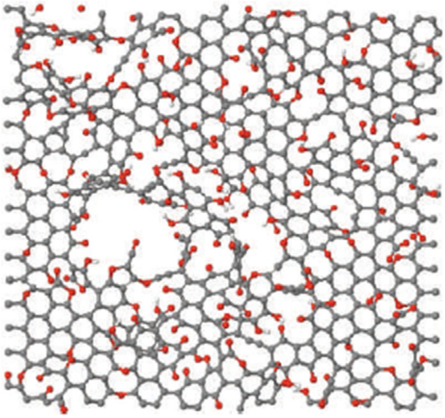

Figure 10.3 Schematic representation of various defects and edges in a CQD nano-domain terminated with oxygen moieties (in red) (https://doi.org/10.1038/nchem.907). *CQD*, Carbon quantum dot.

10.2.3.2 The basis of fluorescence sensing by CQDs

The structure of CQDs is not always clearly elucidated due to the various sources or precursors from which they are derived as well as the little control over the population of various hybrid structures that might be present in the CQD. It also depends on the relative ratio of those hybrid states and their distribution. Hence, the change in fluorescence properties, either shifting of the emission peak towards red or blue region of visible spectra or the quenching of the same, can be the modes in which sensing mechanism can be derived. As per the recent literature on the sensing by CQDs, most reports are based on the quenching of fluorescence triggered by the addition of a particular analyte and its preferential selectivity towards that particular analyte. Hence, we will discuss the various different quenching mechanisms of CQDs and how they are applied for specific sensing applications. Further, we will discuss few specific sensing applications of CQDs especially as pH sensor and metal ion sensor.

Quenching and sensing

The CQDs have unique merits such as good photostability, excellent water dispersibility, cell permeability, low toxicity, and biocompatibility. CQDs have been used in various applications such as bioimaging, detecting analytes, and drug delivery [1,2] in comparison with other organic probes and quantum dots (QDs) of the CdSe type [3–7]. These applications were based on the principle that the interactions between analytes and CQDs either decrease the fluorescence by quenching or increase fluorescence by suppressing the quenching effect. Quenching mechanisms of CQDs include static quenching, dynamic quenching, energy transfer, photoinduced electron transfer (PET), and inner filter effect (IFE) [8]. The energy transfer is divided into Förster resonance energy transfer, Dexter energy transfer, and surface energy transfer.

Static quenching occurs when a nonfluorescent ground-state complex is formed through the interaction between CQDs and quencher. Dynamic quenching can be explained as an effect where the excited state returns to the ground state by the collision between the quencher and CQDs due to energy transfer or charge transfer [9].

The IFE mechanism of CQDs is different from static and dynamic quenching mechanism of CQDs. The IFE occurs when the absorption spectrum of the quencher in the detection system overlaps the excitation or emission spectra of CQDs. It does not require to modify the CQDs.

Static quenching occurs when a nonfluorescent ground-state complex is formed through the interaction between CQDs and quencher. The complex immediately returns to the ground state without emission of a photon when the complex absorbs light [9].

For static quenching $\tau^0/\tau = 1$. The formation of the ground-state complex can result in the change of the absorption spectrum of the CQDs. A rise of temperature can cause the decline of the stability of the ground-state complex, so reduces the effect of static quenching [8–10] (Fig. 10.4).

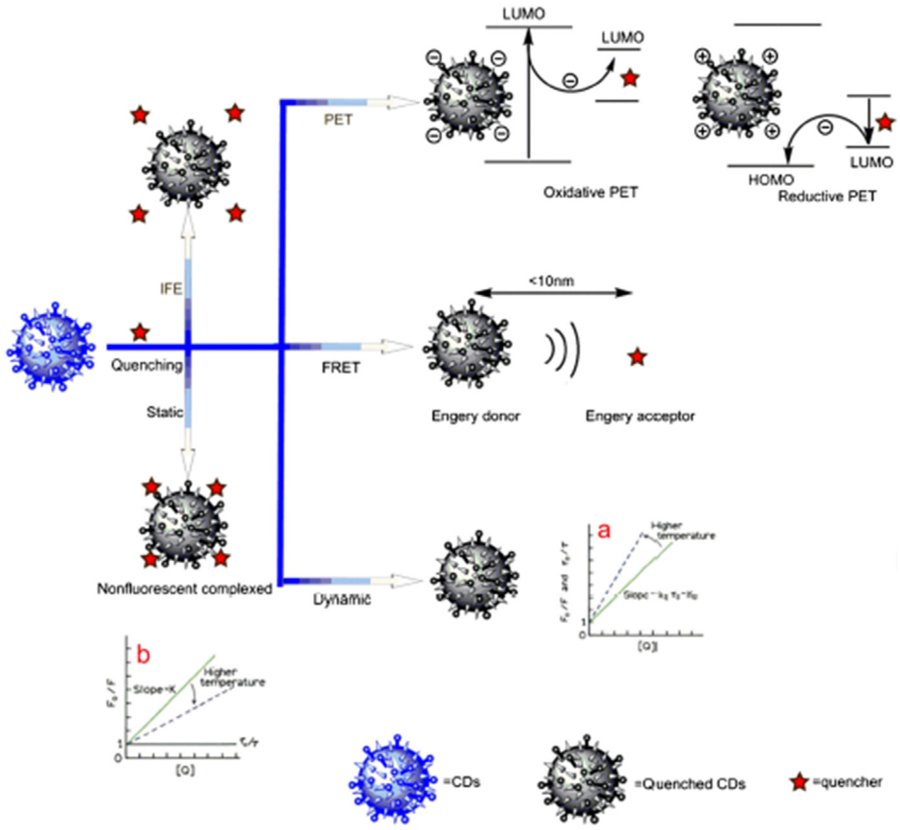
LUMO
LUMO
PET
Oxidative PET
HOMO
LUMO
Reductive PET
IFE
Quenching
Static
FRET
<10nm
Engery donor
Engery acceptor
Nonfluorescent complexed
Dynamic
a
Higher temperature
b
Slope=K
Higher temperature
[Q]
[Q]
=CDs
=Quenched CDs
=quencher

Figure 10.4 Quenching mechanisms of fluorescent CDs which is used in the process of detecting analytes (https://doi.org/10.1007/s00604-017-2318-9).

Dynamic quenching can be explained as an effect where the excited state of CQDs returns to the ground state by the collision between the quencher and CQDs due to energy transfer or charge transfer [9]. These have different characteristics compared to static quenching. (1) Dynamic quenching only affectes the excited states of the CQDs, so no changes in the absorption spectra CQDs are observed. (2) The lifetime of CQDs would change in the absence and presence of quencher. (3) A rise of temperature can lead to the increase of the effect of dynamic quenching.

10.2.4 pH sensor

The graphene quantum dots (GQDs) emit strong fluorescence most likely because of the presence of high concentration of free zigzag sites owing to the nano-domains. The emission spectra with two sharp peaks observed in the GQDs are similar to that of triplet carbene in diarylmethylmethylenes. The emission mechanism based on the

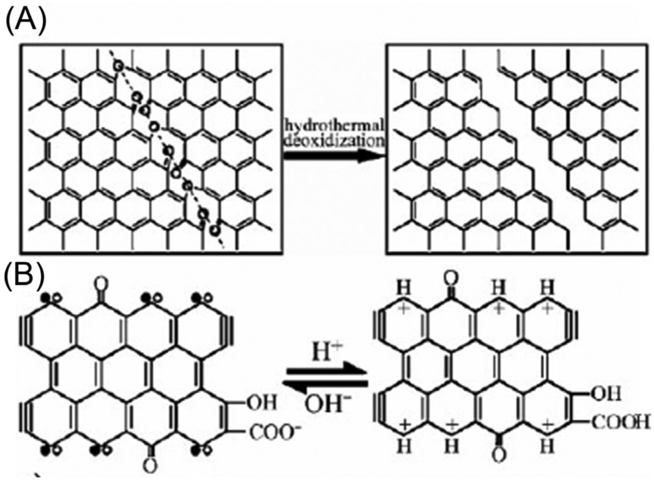

Figure 10.5 (A) Mechanism for the hydrothermal cutting of oxidized graphene sheets (GSs) into GQDs: a mixed epoxy chain composed of epoxy and carbonyl pair groups (left) is converted into a complete cut (right) under the hydrothermal treatment. (B) Models of the GQDs in acidic (right) and alkali (left) media. The two models can be converted reversibly depending on pH. The pairing of σ (•) and p (o) localized electrons at carbene-like zigzag sites and the presence of triple bonds at the carbyne-like armchair sites are represented (https://doi.org/10.1002/adma.200902825).

emissive free zigzag sites is further supported by the observed pH-dependent fluorescence and is fundamental to understanding the role of GQDs as pH sensors. Under alkaline conditions, the GQDs emit strong fluorescence, whereas, under acidic conditions, the fluorescence is nearly completely quenched (Fig. 10.5). If pH is switched repeatedly between 13 and 1, the fluorescence intensity varies reversibly. This reversible phenomenon can be well understood based on the proposed structural models (Fig. 10.5) and the fluorescence mechanism of the GQDs. Under acidic conditions, the free zigzag sites of the GQDs are protonated, forming a reversible complex between the zigzag sites and protons. Thus, the emissive triple carbene state is broken and becomes inactive in PL. However, under alkaline conditions, the free zigzag sites are restored, thereby leading to the restoration of PL.

Literature indicates that the blue fluorescence from a CQD is pH-dependent. That is, the fluorescence is strong enough to be observable by the naked eye at high pH levels, whereas it is nearly quenched at low pH conditions.

10.2.4.1 Role of surface groups in pH sensor applications of CQDs

Previous observations of fluorescence from pure CQDs and functionalized carbonaceous nanomaterials have been attributed to the presence of oxygen-containing functional groups. The abundant oxygen-containing functional groups not only passivate the surface of the CQDs but also lead to fluorescence due to various fluorophores. In spite of the controversial character of the fluorescence origins in CQDs, the involvement of surface traps in the radiative transition of carbon dots has been widely accepted. Surface functional groups, e.g., C-O, C = O, C-OH, can introduce trapping states with different energy levels, making CQDs emit light that varies with excitation energy. Thus, it can be speculated that the excitation dependence of the CQD fluorescence could be controlled through engineering the above-mentioned surface states of CQDs. As an extreme case, if all surface states are completely passivated, the emission is believed to take place only through the radiative transition of sp^2 carbon, probably the p to p* transition, which will obviously result in excitation independence due to the single transition mode with a certain energy. However, the observed enhancement of blue fluorescence of CQDs in few cases with reduction suggests that oxygen functional groups can be excluded as the origin. Instead, the creation of localized sp^2 clusters and structural defects during reduction are more likely to be responsible for the origin and enhancement in blue fluorescence.

10.2.4.2 Few more examples of pH sensing with CQDs

CQDs, synthesized from ethylenediamnine-tetraacetic acid (EDTA) salt via one-step low-temperature pyrolysis reaction, exhibit unique photoluminescence (PL) that is strongly reliant on pH. The intensity of PL remains constant in a neutral medium, i.e., in the pH range of 5.5–8. But in a basic medium, the intensity starts increasing moderately from pH 8 to 13, whereas it decays gradually in an acidic medium with pH depleting from 5.5 to 1. The absorbance spectra of that CQDs are

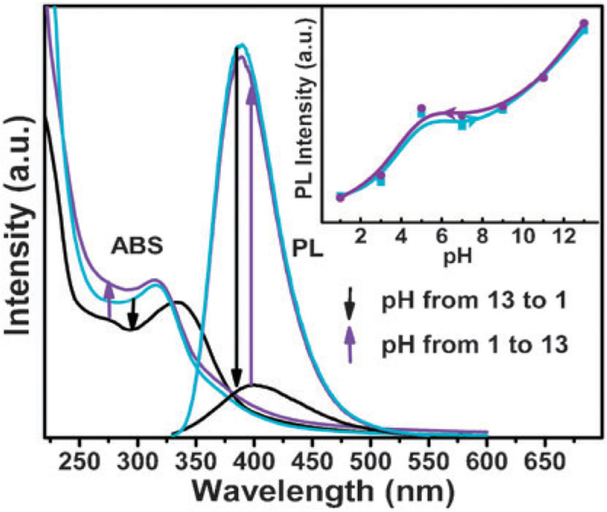

Figure 10.6 pH-dependent UV-vis absorption and PL spectra when pH is switched between 13 and 1. Insert: dependence of PL intensity on pH (changed from 13 to 1 and then from 1 to 13) (https://doi.org/10.1039/c000114g).

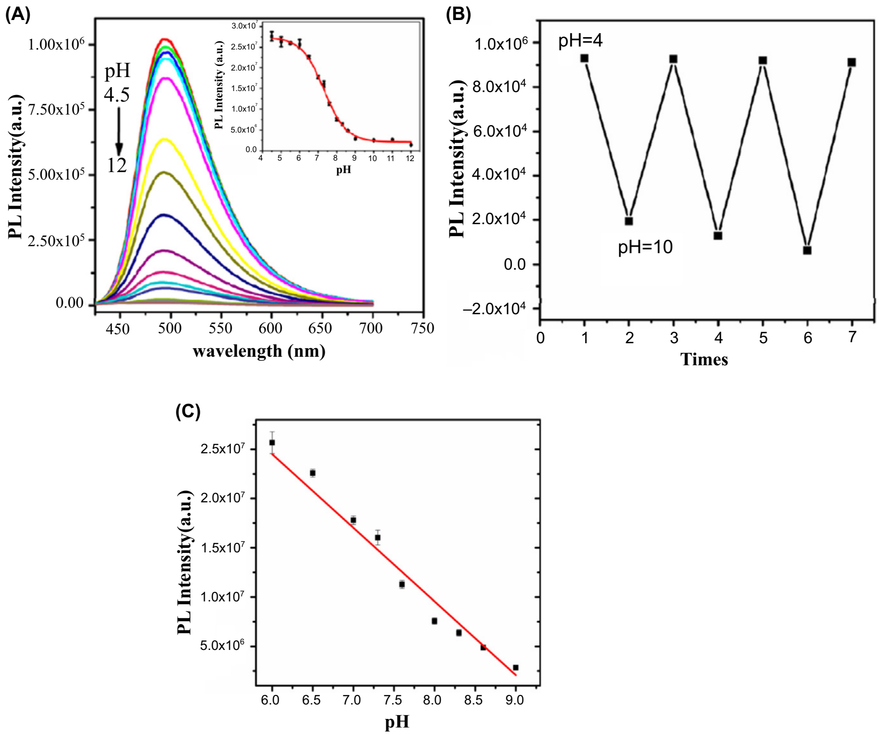

Figure 10.7 (A) The PL spectra of CQDs excited at 400 nm as the pH increases from 4.5 to 12. The inset displays sigmoidal fitting of pH-dependent fluorescence intensity. (B) PL intensity of CQDs upon cycling the pH value seven times between 4 and 10. (C) A linear relationship between PL intensity and pH (from 6.0 to 9.0) (https://doi.org/10.3390/s19173801).

found to be weak in the entire spectral region. It is observed that there is a slight red shift in both the PL and absorption peak when the pH is modulated from 13 to 1. But as soon as the pH value is changed to 13, both the PL spectra and the corresponding absorption spectra are restored indicating that the PL spectra gets quenched in an acidic medium and restored in alkaline medium The reversible pH-dependent PL behavior of CQD indicates that the fluorescence probe present in the nanoparticle should contain basic sites pertinent to the blue emission.

The reverse phenomenon is observed for highly fluorescent green carbon dots prepared by hydrothermal process of 3,5-diaminobenzoic acid (Fig. 10.6). Under acidic condition, it exhibits strong fluorescence intensity and under basic medium the intensity decreases rapidly with the increase in pH from 4.5 to 12. A linear relationship between PL intensity and pH is observed in the neutral range of pH (pH = 6.0−9.0). The protonation-deprotonation of amino and carboxyl groups on the surface of CQDs is responsible for the emission enhancement PL spectroscopy (Fig. 10.7).

10.2.5 Effect of solvent: sensing dielectric of surrounding medium

Considering the effect of solvent on the fluorescence properties of CQDs, the effect of solvent polarity on the energy of the sp^2 nano-domains can be considered. The effect of solvent polarity on the band gap of CQDs can be related to semiconductors in the same way as that for semiconducting nanomaterials. Also the effect of surface functional groups present on the CQDs can play an important role in selective sensing under different dielectric mediums.

10.2.5.1 Few more examples of solvent sensing

A unique chitosan-carbon dot functionalized by bipyridine-based heterocyclic molecule, 4-(pyridine-2-yl)-3H-pyrrolo[2,3-c]quinolone (PPQ), is used to detect trace amount of water in organic solvents. This fluorescence-based nanosensor provides sensitive detection by exhibiting fluorescence "turn on" response towards water. The PPQ-CQD shows maximum fluorescence intensity in an aqueous medium but the fluorescence emission is quenched selectively in presence of organic solvents like ethanol, DCM (dichloromethane), THF (tetrahydrofuran), DMF (dimethylformamide), DMSO (dimethyl sulfoxide), and toluene. The PET process from the nitrogen of PPQ group to the carboxyl groupfluorophore (CD) makes the PPQ-CD nonfluoroscent as the electrons from LUMO cannot return to the ground state by radiative process. The enhancement in fluorescence emission in presence of water is attributed to the formation of hydrogen-bonded complex between the quinoline nitrogen of PPQ and the carboxylate group of CD. Due to the protonation of N atom of PPQ, the energy of HOMO of donor PPQ becomes lower compared to that of CQDs which prevents the PET process, and the intensity of PL spectra increases (Fig. 10.8).

Green terbium ions-functionalized red CQD doped hybrid material (Tb^{3+}@p-CQDs/MOF) are also used as fluorescent probe to detect water content in organic solvents.

10.2.6 Doped CQDs in sensors: metal ion detection

Nitrogen-doped PEGylated (PEG) CQDs are functionalized with dithiothreitol (DTT) to detect Hg^{2+} ion in water sample at an ultralow level. The fluorescence emission of DTT/CD in aqueous solution is selectively quenched upon addition of Hg^{2+} owing to the formation of chelate complex between Hg^{2+} with NH_2 and thiol group present on the surface of CQDs due to the electron transfer reaction. However, there is no significant spectral change in presence of other metal ions (Fig. 10.9).

Besides, other N-doped CQDs can also be synthesized by the pyrolysis reaction of carbon precursor chitosan, condensation agent acetic acid, and N-dopant 1,2-ethylenediamine. N-doped CQDs exhibit significant fluorescence quenching in the presence of ferric ion (Fe^{3+}) due to the strong interaction between phenolic

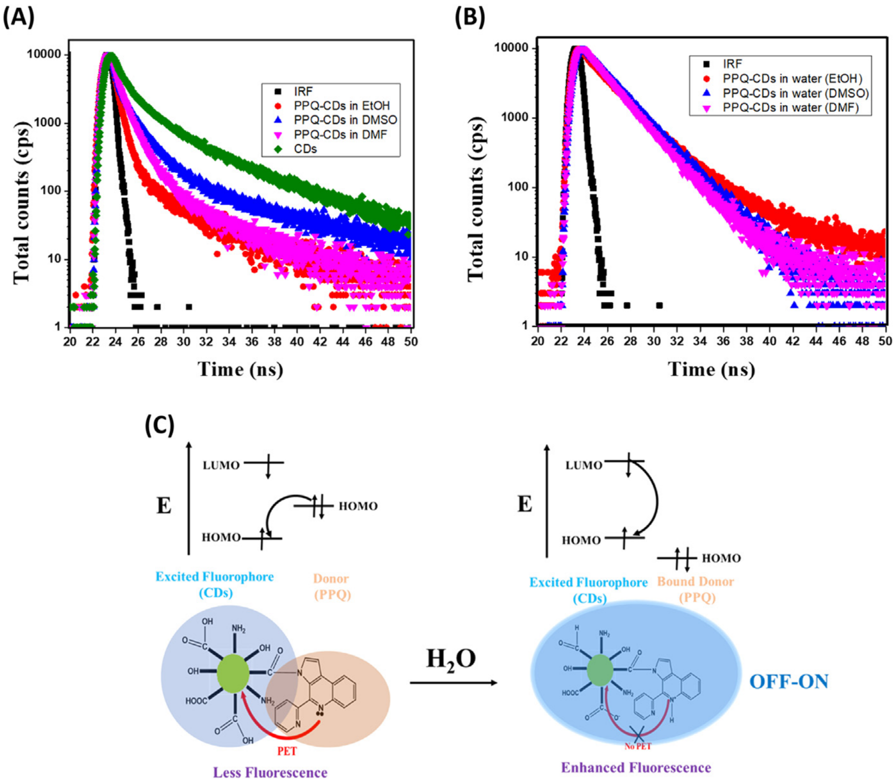

Figure 10.8 Time-resolved fluorescence decay curves of (A) as-prepared CQDs in water and PPQ-CQDs in different organic solvents and (B) PPQ-CQDs in organic solvents followed by addition of 68% water (v/v) in each of them. The emission was collected at 450 nm upon 340 nm excitation. (C) Fluorescence enhancement mechanism in terms of molecular orbitals of the acceptor (CQDs) and the donor (PPQ) (https://doi.org/10.1021/acsomega.9b01208).

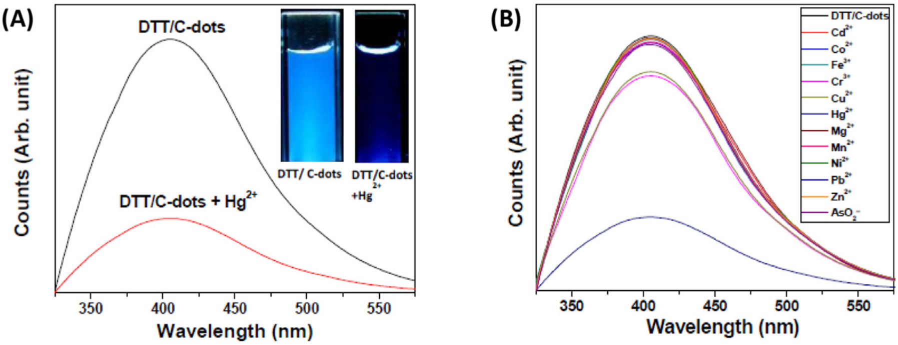

Figure 10.9 (A) Extensive fluorescence quenching of DTT/C-dots was observed upon addition of 50 μM of Hg^{2+} (inset shows the UV lamp images of DTT/C-dots without and with addition of Hg^{2+}), (B) fluorescence intensity of DTT/C-dots in the presence of various other metal ions (50 μM) individually to the DTT/C-dots (https://doi.org/10.1039/C5CC03019F).

hydroxyl and/or amine groups of N-CQDs. Hence, N-CQD is applicable for the specific and sensitive detection of Fe^{3+} in biological systems. Sulfur (S)- N doped CQDs can be prepared from a cheap green source garlic by hydrothermal process using EA, Na_2SO_4, and $Na_2S \cdot 9H_2O$. The fluorescence emission of S-N doped CQDs significantly gets quenched in presence of Fe^{3+} ion attributed to the coordination between carboxyl group present of the surface of CQD and Fe^{3+} ion.

10.2.6.1 Red emitting carbon dots for specific metal ion detection

Nitrogen-doped red-emitting carbon dots (N-CQDs) can be synthesized from p-phenylenediamine (p-PD) in the presence of aminobenzoic acid and nitric acid through the hydrothermal method. This derivative flaunts high selectivity for the detection of palladium (Pd^{2+}) and indium (In^{3+}) in aqueous medium by showing specific fluorescence "turn off" response with a slight blue shift and "turn on" response with a red shift towards Pd^{2+} and In^{3+} respectively due to the interaction of hydroxyl groups of CQDs with these ions. The red emission basically depends on the lone pair of oxygen atoms. The more oxygen content on the surface of CQDs, the more is the degree of surface oxidation. The amount of oxidation is associated with red emission of CQDs. The emission wavelength becomes red shifted with the increase in surface oxidation. Due to the adduct formation between N-CQD and Pd^{2+}, the amount of lone pair of electrons of oxygen atom reduces causing a decrease in fluorescence emission. Moreover, when N-CQD is excited, the splitting of vacant d orbital of Pd^{2+} takes place which prevents the fluorescence emission of N-CQD in radiative pathways. Thus, the intensity of PL spectra gets quenched. As In^{3+} contains filled d orbital, during In^{3+}-N-CQD adduct formation $-$OH groups do not share lone pairs with In^{3+}. Therefore, the availability of lone pair is more in this case, which leads to the enhancement of radiative combination rate of N-CQD. As a result, the intensity of fluorescence emission increases. These excess lone pairs of electrons create new higher energy states, decreasing the band gap of N-CQDs, suggesting a red-shifted emission (Fig. 10.10).

10.2.7 Gas sensing with conducting carbon dots

Apart from optical property, CQDs have interesting conducting properties that can be used for sensing gases and VOCs. Because of the small size of nanotubes, nanowires, or nanoparticles, a few gas molecules are sufficient to change the electrical properties of the sensing elements. This allows the detection of a very low concentration of chemical vapors. The goal is to have small, inexpensive sensors that can sniff out chemicals just as dogs are used in airports to smell the vapors given off by explosives or drugs.

The capability of producing small, inexpensive sensors that can quickly identify a chemical vapor provides a kind of nano-bloodhound that does not need sleep or exercise which can be useful in a number of ways. An obvious application is to mount these sensors throughout an airport, or any facility with security concerns, to

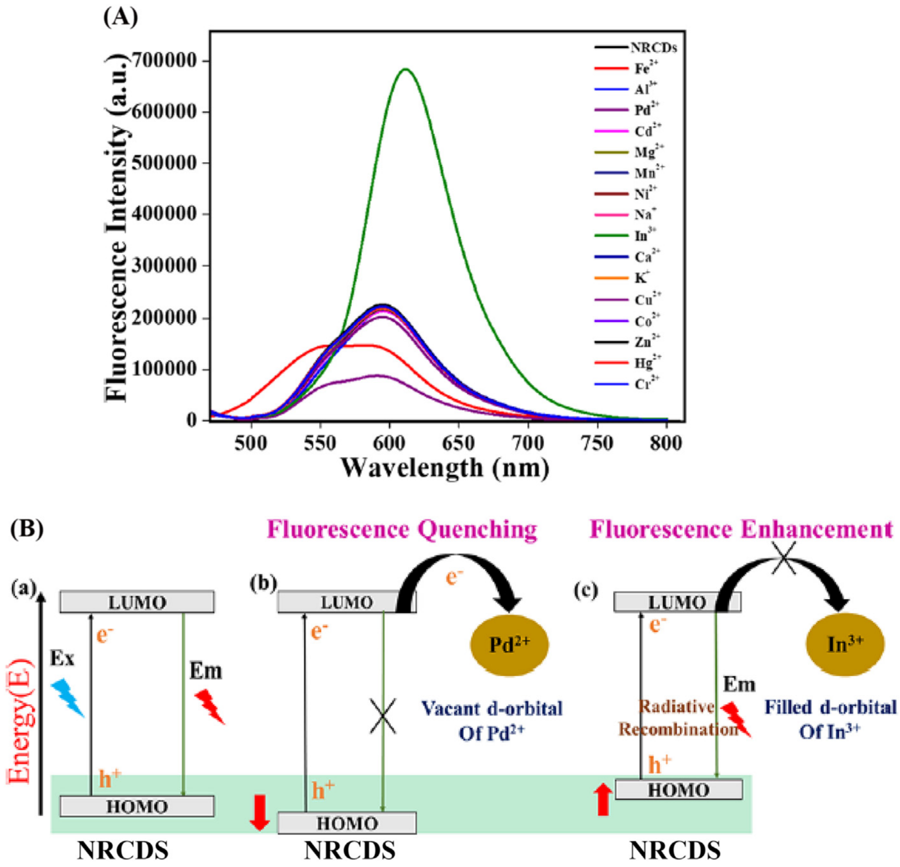

Figure 10.10 (A) Time-resolved fluorescence decay curves of non-radiative carbon dots (NRCDs) (1 mg/mL) with and without the addition of 500 μL of 10^{-3} M In^{3+} and Pd^{2+}; the emission was collected at 600 nm upon 440 nm excitation. (B) Schematic illustration of the proposed energy levels and electron transition diagrams of (A) free NRCDs and NRCDs with (B) Pd^{2+} and (c) In^{3+} (https://doi.org/10.1021/acsomega.0c00883).

check for vapors given off by explosive devices. These sensors can also be useful in industrial plants that use chemicals in manufacturing to detect the release of chemical vapors. When hydrogen fuel cells come into use, in cars or other applications, a sensor that detects escaped hydrogen could be very useful in warning of a leak. This technology should also make possible inexpensive networks of air quality monitoring stations to improve the tracking of air pollution sources.

Conducting property of CQD has not been explored much till date. Our group has reported conducting property of individual polymer passivated CQDs, which is the first ever report on conductivity of individual CQD. We have used surface spreading resistance (SRI) imaging mode to probe individual conducting particle by scanning probe microscopy. Fluorescence excitation spectra of the CQDs showed

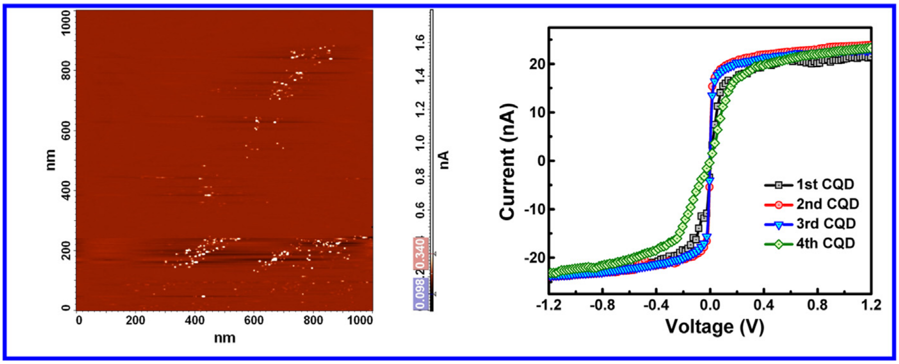

Figure 10.11 SRI images of PSS-CQDs. White spots in the 2-D image indicate conducting PSS passivated CQDs (left) I-V characteristics of individual PSS-CQDs(right) (https://doi.org/10.1039/C4TA05491A).

evidence of low-lying energy states responsible for excitation-dependent fluorescence properties. Current-voltage (I-V) characteristics of individual polystyrene sulfonate stabilized CQDs (PSS-CQDs) exhibited linear behavior at low bias and a sudden jump in current value as the bias crossed zero voltage. Cyclic voltammetry was used to determine band gap of the CQDs. Conducting AFM image of each CQDs and I-V data of each CQDs have been produced below (Fig. 10.11).

Still, there is very limited report on conducting properties of CQDs. Such studies are important for the fundamental understanding of the conducting phenomenon observed with the CQDs and further improvements can be made in the tunability of conducting nanocomposites.

10.2.7.1 Designing of gas sensors using carbonaceous nanomaterials

CQDs are generally obtained as powder and hence it is difficult to design sensors. It has to go with polymeric materials as composites. Insulating polymers can dampen the electrical properties of conducting CQDs. Hence, conducting polymer composites with CQDs are largely sought for.

Conducting polymers like PPy have been used to design gas and VOC sensors. These show excellent current–voltage characteristics which is used for sensing applications. The LUMO level of these polymers accepts free electrons from various gases and VOCs, and their HOMO electrons can share vacant orbitals of gaseous analytes. Such molecular interactions changes I-V characteristics, resulting in sensing properties.

It has been often observed that incorporation of nanomaterials within conducting polymer matrix enhances sensitivity of such sensors. Nanomaterials, due to their enhanced surface activity, induce active sites in the polymer for fast adsorption of gases that enable the sensing properties of the parent conducting polymer. The use of carbonaceous nanomaterials like C60, CNT, CQDs, etc. within conducting polymers has shown tremendous enhancement in sensor applications. The main idea behind such composites is that the carbonaceous nanomaterials are generally hydrophobic and hence they bond strongly to conducting polymers, which are also generally hydrophobic in nature. Further, a particular case observed for C60 is discussed that will help us understand the effect of CQDs on the properties of conducting polymers.

10.2.7.2 Effect of CQDs on the electrical properties of conducting polymers

It was reported in literature that incorporation of C60 within PPy resulted in enhanced I-V characteristics. C60 has sp^2 carbon with a strained configuration. The structure of the material has similarities with that of CQDs which do not have extended sp^2 domains as that of C60 but analogous similarities can be assumed. It was observed that C60 works as p-dopant in conducting polymer matrix while being n-type doped itself. That is, the electron is transferred from polymeric chain to LUMO of C60, charging it in the process. The ionic state created a further positively charged polaron in the PPy chain. The fluorescence in the doped PPy was observed to be remarkably suppressed and absorption spectra dramatically changed confirming the doping effect.

10.2.8 A VOC sensor based on CQDs

GQDs were the first reported carbonaceous QDs and were synthesized from graphite nanoparticles by the use of chemical and physical methods. A perfect graphene sheet is not fluorescent due to absence of electronic band gap caused by continuous π conjugation. Therefore, to introduce electronic band gap and hence fluorescence emission in graphene, much effort has been given to make the π network in the graphene from infinite to finite. In other words, the isolate conjugated π domains are structurally similar to large aromatic molecules within the graphene sheet. Advantages of the composite material were its low cost and simple fabrication. Polyaniline-GQD (PANI−GQDs) nanocomposite was prepared by in situ electrochemical polymerization of an aniline monomer in the presence of GQD, and it showed good catalytic activity in promoting tri-iodide reduction. The fluorine-doped tin oxide (FTO) coated glass was immersed into the solution of the aniline and GQD during the polymerization. Dye sensitized solar cell (DSSC) composed of the PANI−GQD nanocomposite electrode exhibits an energy conversion efficiency of 1.6%. The presence of synergistic effect of PANI and GQD led to the higher electrochemical catalytic activity of PANI−GQD nanocomposite than that of pristine PANI. As a result, better photovoltaic performance was observed for DSSCs based on the PANI−GQD electrode as compared to that of the DSSC sample based on the PANI electrode.

The above-mentioned reports motivated us to further explore the conducting properties of CQDs. The aim of the present work was to improve the conducting properties of PSS-CQDs by incorporating of polypyrrole (PPy) on the CQD surface, thereby stabilizing the PPy-coated CQD (CQD-PPy) colloidal particles as a water-based stable writable semiconducting ink. A unique surface-confined autocatalytic process has been developed to grow PPy over the CQD surface. Highly water dispersible CQD-PPy in aqueous suspension behaved as semiconducting ink. Literature suggests that conducting polymer has been used as active chemo-resistive material to sense rancidity in snacks. Changes in concentration of VOCs emitted by the food items can provide valuable information about its contamination. PPy-based gas sensor has been developed for detecting and monitoring the organic volatiles produced from wheat bread during storage. PPy has been extensively used as chemoresistive sensor material where the difference in sensing activity was compared with respect to the manner in which different analytes respond to resistance at fixed voltage. These polymer-based sensors can sense a particular analyte, but cannot differentiate between similar types of analytes. Thus, PPy shows change in resistance in presence of a VOC, but the change can be observed at any fixed voltage and for all VOCs. Thus, there is a need to modify the property of PPy so that it can sense and differentiate a volatile compound, which will help to differentiate VOCs. This can be applied to differentiate between flavors from different brands of snacks.

Oxidative rancidity of fats such as lard, shortenings, salad, and cooking oils refers to the undesirable odors and flavors which develop when such products are exposed to the oxygen in the air. Products containing these fats, including but not limited to food products such as fish, poultry, meat, frozen vegetables, and dry milk, can become rancid as the fats in the products react to air. The polyunsaturated fatty acid portions of these foods react with oxygen to form peroxides. The peroxides decompose to yield a complex of mixtures, including aldehydes, ketones, and other volatile products. These products are responsible for "rancid" odors and flavors. Hence, we thought of studying the ink on three types of important aldehydes mostly found in food stuff. Hexanal, heptanal, and octanal are the three types of aldehydes that are different from each other in terms of number of carbon atoms in the main chain.

10.2.8.1 Nanotechnology applications using CQDs for Gas/VOC sensing: a case study

A composite material of CQD and NiO (CQD@NiO) is used as an efficient sensing tool for the detection of methane (CH_4) gas. The composite for the detection of CH_4 works at the optimum temperature of 150°C. The chemical reaction behind the detection mechanism is:

$$CH_4 + 4O^- = 4H_2O + CO_2 + 4e^-$$

At first, on the surface of CQD@NiO, the adsorption of oxygen (O_2) takes place by reducing to O^- followed by a formation of a hole accumulation layer (HAL). As the edges of NiO have polygonal structure, it is highly efficient to capture O_2. Due to the deposition of CQD on NiO nanoparticles layer, a hetero-junction potential barrier is formed between the two layers, which acts as a potential CH_4 gas adsorption site. By increasing the rate adsorption of gas molecules, the thickness of the HAL decreases gradually. After the completion of the reaction, electron flow occurs from the CQD to NiO followed by a reduction in the hole concentration of NiO. Then O^- and CH_4 undergo redox reaction which results in an attenuation of the HAL and as enhancement in resistance as well. Thus, the detection of methane gas takes place.

10.3 Conclusion

The chapter deals with the basic properties of CQDs that lead to the utilization of these nanomaterials as active components in chemical sensors. Basic properties and characteristics of nanosensors have been introduced in this chapter along with the features of nanosesnors in general. The chapter also explains why nanomaterials are superior in properties and applications as sensors compared to bulk materials. The important features of CQDs lead to its application as a chemical sensor and has been discussed in detail in this chapter. Especially, the structure−property relationship in CQDs has been detailed here. Finally, few case studies on the application of CQDs for pH, solvent, and metal ion detection have been discussed. The chapter ends with the electrochemical property of CQDs, its origin, and chemical sensing of VOCs and gases using CQDs along with a few case studies.

References

[1] N. Parvin, T.K. Mandal, Dually emissive P,N-co-doped carbon dots for fluorescent and photoacoustic tissue imaging in living mice, Microchimica Acta 184 (4) (2017) 1117−1125.
[2] Y. Lin, B. Yao, T. Huang, S. Zhang, X. Cao, W. Weng, Selective determination of free dissolved chlorine using nitrogen-doped carbon dots as a fluorescent probe, Microchimica Acta 183 (7) (2016) 2221−2227.
[3] S.N. Baker, G.A. Baker, Luminescent carbon nanodots: emergent nanolights, Angewandte Chemie 49 (2010) 6726−6744.
[4] B. Cao, C. Yuan, B. Liu, C. Jiang, G. Guan, M.Y. Han, Ratiometric fluorescence detection of mercuric ion based on the nanohybrid of fluorescence carbon dots and quantum dots, Analytica Chimica Acta 786 (2013) 146−152.
[5] G.H.G. Ahmed, R.B. Laíño, J.A.G. Calzón, M.E.D. García, Highly fluorescent carbon dots as nanoprobes for sensitive and selective determination of 4-nitrophenol in surface waters, Microchimica Acta 182 (1−2) (2015) 51−59.
[6] E.S. Speranskaya, N.V. Beloglazova, P. Lenain, S.S. De, Z. Wang, S. Zhang, et al., Polymer-coated fluorescent CdSe-based quantum dots for application in immunoassay, Biosensors and Bioelectronics 53 (2014) 225−231.
[7] R. Wang, X. Wang, Y. Sun, Aminophenol-based carbon dots with dual wavelength fluorescence emission for determination of heparin, Microchimica Acta 184 (1) (2017) 187−193.

[8] A. Iqbl, Y. Tian, X. Wang, D. Gong, Y. Guo, K. Iqbal, et al., Carbon dots prepared by solid state method via citric acid and 1,10-phenanthroline for selective and sensing detection of Fe^{2+} and Fe^{3+}, Sensors and Actuators B 237 (2016) 408−415.

[9] J.R. Lakowicz, Principles of fluorescence spectroscopy, Springer, Maryland, USA, 2006.

[10] W. Liu, H. Diao, H. Chang, H. Wang, T. Li, W. Wei, Green synthesis of carbon dots from rose-heart radish and application for Fe^{3+} detection and cell imaging, Sensors and Actuators B 241 (2017) 190−198.

Carbon dots: biomedical applications

11

Ashwathi A. Madhavan[1], *Ranjita Ghosh Moulick*[2] and
Jaydeep Bhattacharya[1]
[1]NanoBiotechnology Lab, School of Biotechnology, Jawaharlal Nehru University,
New Delhi, Delhi, India, [2]Amity Institute of Integrative Science and Health,
Amity University Gurgaon, Panchgaon, Haryana, India

11.1 Carbon dots: structure and functionalization

The structure of carbon dots (C-dots) is highly debated as, to this date, no absolute structure has been defined. Due to the poor understanding of the structure, explaining the source of optical properties of C-dots has also been enigmatic. C-dots are quasi-spherical particles consisting of predominantly sp2 hybridized carbon as in graphene along with some sp3 hybridized regions. The nanostructure core is proposed to be spherical, consisting majorly of graphitic fragments, and the surface is rich in functional groups [1,2]. The elemental composition, apart from the core carbon in C-dots, varies largely depending on the source and routes of synthesis. The carbon source and method for synthesis largely determine the fluorescence/photoluminescence properties of the resultant C-dots, which in turn is defined by the arrangement of carbon core and extent of functionalization. A recent study based on modeling predictions backed up by experimental evidence has propounded that greater functionalization results in disordered or amorphous C-dots rather than crystalline C-dots [3].

The surface passivation and functionalization are important postsynthetic treatments for C-dots in order to improve its optical properties and enhance their biocompatibility. Surface passivation refers to the removal of surface contaminants and covering of the surface with inert substance in order to improve the fluorescence emissions. Passivation is done through the application of a thin layer of chemicals like polyethylene glycol (PEG). Surface passivation had been found to effectively increase the QY comparable to the levels of other fluorescent imaging probes [4,5]. Surface functionalization, on the other hand, involves the introduction of functional groups to the C-dots' surface, which induces surface defects. Apart from modulating the fluorescence profiles of C-dots, functionalization also allows the binding of ligand molecules particularly relevant to image-guided therapies and delivery at the target sites. Functionalization has been shown to improve the photostability, biocompatibility, and photoreversibility of C-dots [6].

Carbon Quantum Dots for Sustainable Energy and Optoelectronics. DOI: https://doi.org/10.1016/B978-0-323-90895-5.00018-7
© 2023 Elsevier Ltd. All rights reserved.

11.2 Biosynthesis of carbon dots

C-dots can be synthesized by top-down and bottom-up approaches. To account for the biomedical applications of C-dots, many researchers have been studying the biosynthesis of C-dots from green sources. The green synthesis approach makes use of sources that contain a combination of proteins and carbohydrates. To date, fruit juice [7,8], *Ocimum sanctum* [9], sweet pepper [10], milk [11], turmeric leaves [12], lotus root [13], corriander leaves [14], and prawn shells [15] are among a plethora of other green and environment friendly carbon sources.

Pyrolysis, caramelization, microwave-assisted synthesis, and hydrothermal synthesis are commonly employed for the synthesis of C-dots from natural sources. The formation of C-dots from natural sources is known to occur through chemical reactions that include hydrolysis, dehydration, and degradation. Hydrolysis results in the formation of a mixture of amino acids that undergoes polymerization and condensation, followed by carbonization to form the core of the C-dots structure [16]. An optional surface passivation/functionalization/doping step improves the surface state of the C-dots and hence enhances the optical properties. C-dots synthesized through this method have been successfully studied for various applications including catalysis [17], bioimaging [8,18], and biosensing [19].

11.3 Bioimaging applications of carbon dots

Bioimaging is a process by which biological events are studied noninvasively in real time with the use of a source such as fluorescence, light, X-ray, electrons, positrons, ultrasound, or magnetic resonance. With bioimaging tools, scientists can gain information on the 3D structure of a specimen, cell structures can be analyzed, molecular events can be understood, and multicellular organisms can be visualized. Understanding the cellular structures and molecular events can greatly improve our knowledge and therefore is an obligatory tool for scientists working in the relevant field of biology. A number of imaging modalities are currently used in medical diagnoses which includes optical imaging (OI), computed tomography imaging, positron emission tomography, and magnetic resonance imaging (MRI). Among them, OI is the most commonly used, pertaining to high sensitivity, high resolution, and ease of analysis [20]. Development of high-speed sensitive photodetectors and powerful lasers have revolutionized OI of biological systems and inclusion of fluorescent nanoparticles as imaging probes further increased the spatiotemporal resolution and sensitivity [21]. The unique tuneable optical properties coupled with adaptable surface functionalization and ability to incorporate therapeutic molecules makes nanoparticles an excellent bioimaging tool. Among different metallic and organic nanoparticles, quantum dots (QDs) and C-dots are noted for their excellent fluorescence properties. Owing to the high toxicity profiles of QDs, C-dots have recently emerged as a reliable biocompatible tissue imaging tool which is believed to bring revolutionary developments in the field of bioimaging [22–26].

11.3.1 Carbon dots: optical properties

The fluorescence/photoluminescence of C-dots can be varied by changing the size; for example, a red shift in the fluorescence emission was observed with increase in size [27]. Apart from the quantum effects due to bandgap transitions in the conjugated π bonds, defects due to functionalization, element doping, and presence of fluorophores attribute to the varied emission wavelengths and quantum yield of C-dots fluorescence/photoluminescence. Thus, both carbon core state and surface state contribute to the fluorescence emission in C-dots though it is still debatable and specific to the synthetic routes to larger extents.

C-dots typically exhibit two absorption bands, one at 274 nm attributed to the π-π* transitions in $C=C$ and the second at 330 nm, accounting to the n-π* transitions in the functionalized $C=O$ regions. For C-dots with extended sp2 graphite-like networks, the bandgap among the conjugated π electrons is proposed to be the source of fluorescence. Surface functionalization also enables to conjugate fluorophores like dyes, which add to the C-dots' core fluorescence. Element doping further enhances the QY for C-dots consisting only of carbon and oxygen [28].

Photoluminescence, on the other hand, arises largely due to the surface-state electronic transitions. Increasing the surface oxidation and increasing the size of conjugated π electron cloud, by increasing the particle core size, results in decreased energy gap and hence tunes the photoluminescence towards higher wavelengths [29]. Basically, the elemental composition and the core graphitic conformation modulate the optical properties of C-dots.

11.4 Biomedical applications of carbon dots

Despite the fact that bioimaging is the most important biomedical use of C-dots, the high surface area-to-volume ratio and presence of functional groups have recognized C-dots as a potent tool for biosensing and drug targeting. C-dots-based systems have recently been utilized to successfully detect heavy metals [9], glucose [30], proteins [31], DNA [32], and other substances and ions, apart from their utility in drug delivery, gene delivery, antibacterial and antiviral properties, and so forth [33]. C-dots have also demonstrated promise in drug delivery (Fig. 11.1).

Image-guided treatment is a promising new use for C-dots. Several research studies have been conducted to investigate the use of C-dots conjugated with particular targetting ligands and therapeutic compounds to certain tissues or cellular organelles [35,36]. Image-guided tissue engineering, on the other hand, entails the production of scaffolds or hydrogels infused with C-dots for targeted tissue regeneration. Because of the existence of C-dots, noninvasive imaging of in vivo created tissue is possible [37].

11.4.1 Drug delivery

Drug delivery systems (DDSs) necessitate the creation of systems capable of delivering drugs to particular targets in the body through definite interaction.

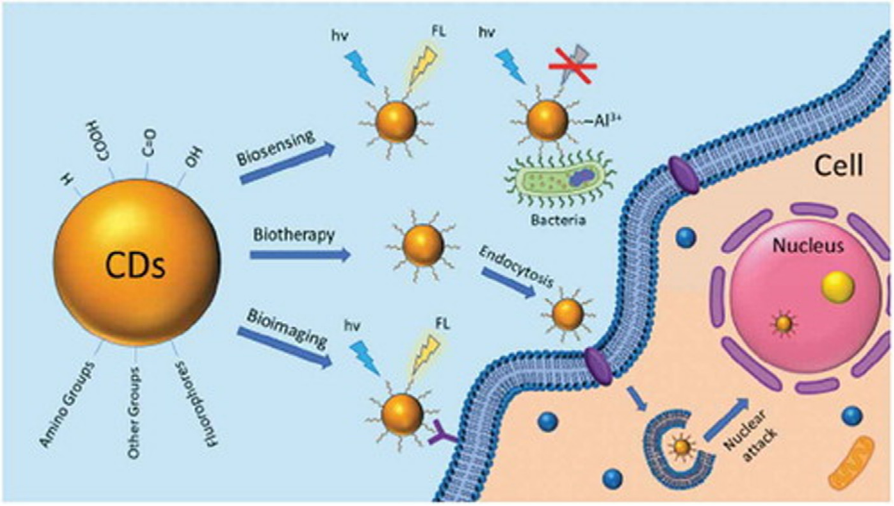

Figure 11.1 Schematic representation of various applications of C-dots [34].

DDS efficacy in terms of drug absorption, distribution, and excretion can be improved by using nanostructured materials conjugated with the medication(s) [38]. The use of nanotechnology in DDSs has facilitated drug targeting to a specific cell or tissue, drug delivery with low water solubility, simultaneous delivery of two or more drugs or therapeutic modality for different therapy, transfer of large macromolecule drugs, and drug site monitoring using imaging agents on the drug carrier [39].

For drug delivery purposes, C-dots have recently attracted considerable interest due to their excellent characteristics, such as fluorescence emission, small size and permeability of cell membranes, low toxicity and biocompatibility, as well as water solubility, ease of manufacture, and possible functionalization and drug loading capabilities. C-dots have been used in DDSs by a number of researchers [40]. According to Karthik et al. [41], Qucbl was covalently bound to nitrogen-containing C-dots, which was confirmed by fourier transform infrared spectroscopy spectroscopy. In vitro, drug-loaded C-dots aggregates were found in the cytoplasm and nucleus. Drug-anchored C-dots were studied in vitro using dopamine hydrochloride (DA). The DA release for the C-dots–DA combination lasted 60 h, compared to the control DA alone, and was found to be biocompatible for Neuro 2A cells [38].

Because of their greater drug loading capacity, hollow nanostructures have piqued the interest of researchers in drug delivery applications. Xu et al. [42] and Yang et al. [43] in vitro studies with doxorubicin (DOX) loaded C-dots demonstrated that cells quickly took up C-dots-DOX and released in a controlled pH-dependent manner. Fluorescence microscopy indicated that C-dots-DOX were internalized and were primarily detected in the cytoplasm of A549 cells. However, DOX was also discovered in the cell nucleus, indicating that the C-dots were successful in releasing DOX into the nucleus [32]. C-dots utilized in DDSs have the ability to become magnetic, allowing them to be employed for multimodal responses like magnetic resonance imaging (MRI) as well as drug administration and fluorescence imaging. The combination of MRI and fluorescence imaging would benefit from MRI's superior tissue penetration and spatial resolution, as well as the simplicity of microscopic tissue inspection provided by fluorescent imaging.

Magneto fluorescent C-dots were created by doping C-dots with Eu3 + , Mn2 + , and Gd3 + ions. In the presence of a magnetic field, unpaired electrons in transition metal dopants generate a magnetic moment. DOX was loaded onto magneto fluorescent C-dots, which were then used to deliver medicines to HeLa cells. A particular study used passivated C-dots with polyamine-containing organosilane molecules to deliver DOX, while another used organophilic C-dots to deliver curcumin to HeLa cells with high loading efficiency and rapid penetration and a third used nanoparticles to deliver the anticancer drug doxorubicin [44]. C-dots were created hydrothermally from pasteurized milk in order to deliver Lisinopril (Lis) to HeLa cells [45]. C-dots/calcium alginate hydrogel film was prepared for studying the vancomycin distribution in the gastrointestinal system [46], DOX delivery was measured using C-dots/mesoporous silica nanocarriers, [47] surface passivated and functionalized C-dots for DOX delivery to MCF-7 [48] are some important examples to be mentioned.

C-dots have been used in multifunctional platforms for drug delivery, MRI agents, as well as simultaneous codelivery of two or more medicines. Multifunctional DDS of C-dots containing DOX, as well as heparin as auxiliary medicament, have been procured for delivery to A549 cells [49]. The researchers used single-walled carbon nanotubes coated with Fe_3O_4@C-dots and conjugated with an aptamer to combine photothermal therapy, chemotherapy, and photodynamic therapy. The magnetic gadolinium oxide—iron oxide core having mesoporous silica shell gated with boronic acid functionalized C-dots have been synthesized for the delivery of the anticancer drug 5-fluorouracil [50].

11.4.2 Crossing blood-brain barrier

The size of the nanoparticles is a critical criterion for using any form of nanostructure in live biological applications. In order to be used in a living creature, the nanoparticles must be significantly smaller than their size. Smaller nanoparticles would avoid obstructing blood vessels and being removed by the reticulo endothelial system. Due to the blood—brain barrier (BBB), it is difficult to deliver imaging probes to brain cancers. It depends on the probes' size and surface characteristics whether they can penetrate the BBB. Drug delivery to the brain is further hampered by BBB characteristics that prohibit medicines, foreign proteins, compounds, and peptides from crossing it. Khan and co-authors have demonstrated that it is possible to administer drugs to the brain by using nanoparticles and QDs that cross the BBB, such as C-dots [51—54]. C-dots may sneak past the BBB if they are not functionally adorned. To create polymer-coated C-dots of different sizes (between 5 and 15 nm) that could penetrate glioma cells in vitro and be employed for glioma fluorescence imaging in vivo, researchers adopted the solvothermal technique. According to the blood—tumor barrier (BTB) of malignant glioma microvasculature, the C-dots produced were able to pass through it. C-dots having a hydrophilic polymer coating increased the blood circulation time and subsequently tumor targeting potential [47].

11.4.3 Gene delivery

Diseases can be treated using exogenous DNA encoding a missing or faulty gene product. Because of this, the use of appropriate gene vectors is a crucial component of gene therapy. Delivery of DNA has been done with nanoparticles [55], QDs, and peptides [56] as well as QDs alone [57]. Due to their biocompatibility, low toxicity, strong fluorescence emission, wide excitation spectrum, and sustained photoluminescence, C-dots may be a superior platform for gene transfer. They were shown to have a higher transfection efficiency than conventional plasmid DNA condensing methods. Caveolae- and clathrin-mediated endocytosis can transport C-dots/pDNA complexes into cells. Du et al. [58] assembled the negatively charged siRNAs and positively charged C dots to form a complex. In a reducing environment, folate-conjugated reducible polyethyleneimine passivated C-dots acted as efficient siRNA carriers. Kim and colleagues have also employed C-dots as a gene vector for the fibroblast chondrogenesis. The plasmid SOX9 was condensed using C-dots to generate nanoparticles between 10 and 30 nm in size. In addition to great solubility and minimal cytotoxicity, these nanoparticles exhibit fluorescent emission (Zhi-Ping Zhang and co-authors).

11.5 Biosensing applications using carbon dots

Biomolecular analysis is critical for clinical treatment security, food safety, environmental monitoring, and diagnosis [59]. Currently, optical and electronic biosensors have gained high importance for being a low-cost and user-friendly alternative of the high-end expensive complex instruments [60–62]. QDs have played a key role in the development of fluorescence-based optical biosensors. But, due to their inherited toxicity, most of the use has been restricted as chemical sensors and in vitro applications. C-dots, because of their great extent of biocompatibility, have recently attracted a lot of interest. C-dots have been shown to have good fluorescence performance with particular surface functional groups, allowing them to link with target analytes by different interactions such as electrostatic contact, conjugation, or electron transferring, resulting in C-dots' fluorescence turn-on or turn-off. Furthermore, C-dots have high electrical conductivity, strong dispersibility, and a wide specific surface area, which are favorable for biological molecules loading on their surface, making them ideal fluorescent probes for detecting inorganic ions and bio molecules. RBD-GQDs (rhodamine-functionalized graphene quantum dots), for example, were utilized as a Fe^{3+} turn-on fluorescence sensor with a detection limit of 0.02 μM. The RBD-GQDs fluoresced orange red, which was enhanced by the addition of Fe^{3+} ions due to the spirolactam ring of RBD being switched by Fe^{3+} ions. According to further study, the RBD-GQDs could penetrate the CSC membrane and react with internal Fe^{3+} ions. In addition to metal ions, C-dots have been used to detect other compounds. For the detection of peroxynitrites in live cells, researchers have developed a nanoprobe based on triphenylphosphonium modified C dots in 2015. Wu et al. [63] developed that peroxynitrite inhibits C-dots fluorescence via photo-induced electron transfer. Furthermore, this nanoprobe is equipped with a mitochondrial characteristic that makes it universal and well-targetable against a wide variety of cancer cells. Fluorescence quenching and recovery due to temperature aggregation was examined by Wang et al. in 2016. Fluorescence of C-dots switched off due to the interaction between the surface group and glutathione (GSH). The fluorescence was noticed again when the switch was turned on because of increase in temperature. It is also crucial in the cancer diagnostic and detection process. These GQDs are visible to the naked eye and respond to all pH values from 1 to 14. Their fluorescence was shown to be temperature-sensitive, suggesting that they may be used as dual pH and temperature probes in complex settings such as biological medium or even in vivo. It was created in 2017 by Gao and colleagues by electrolysis of graphite rods dipped in sodium p-toluene sulfonate acetonitrile. As we know that the extracellular environment of solid tumors is acidic, the pRF-GQDs were able to detect the microenvironment and showed a substantial change in fluorescence between green and blue. These findings suggest that pRF-GQDs might be utilized in fluorescence-guided cancer surgery and diagnostics. In the field of biosensing, Peng et al. made major contributions by synthesizing hydrophilic and organophilic C-dots by simple one-pot solvothermal method. When exposed to 365 nm UV light, the C-dots dissolved in both water and ethanol, and showed a stunning white and blue fluorescence, respectively. Aqueous solution as well as living cells may be detected using the C-dots, which are highly water soluble and biocompatible. A team of researchers led by W. L. Gao mixed citric acid and neutral red as precursor that led to red-fluorescent solution and solid, respectively. Using the fluorescence they were successful in detecting noble metal ions in PC12 cells and zebrafish [65] (Fig. 11.2).

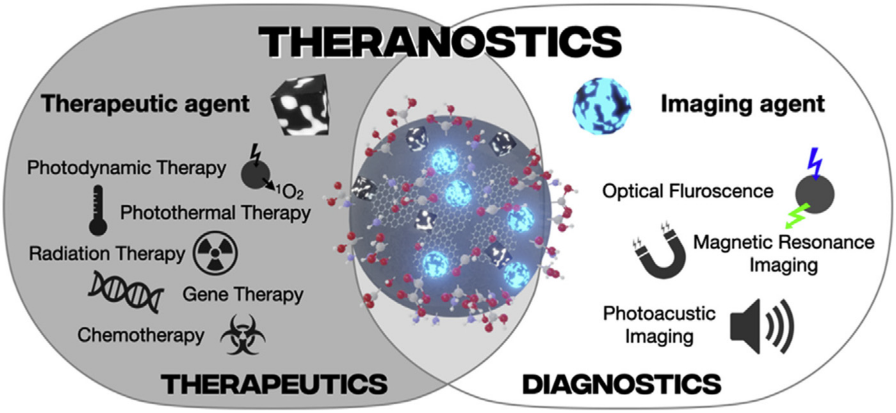

Figure 11.2 Schematic representation of therapeutics, diagnostics, and theranostics of C-dots (*Journal of Food and Drug Analysis* 2020;28:677–695).

11.6 Future scope and challenges

C-dots, due to their exceptional biocompatibility and optical properties, present with tremendous applications in the biomedical field. Owing to tunable fluorescence/photoluminescence, high quantum yield, high photostability, resistance to photobleaching, increased water solubility, and ease of synthesis, C-dots are reliable alternative to semiconductor QDs and traditional fluorescent dyes. In vitro and in vivo imaging studies have shown promising results for C-dots as fluorescent imaging probes and contrast agents. Image-guided therapy and image-guided tissue engineering are complimentary applications of C-dots, which holds great promise in the future. With clinical studies in the future for in vivo bioimaging in humans, C-dots are expected to transform the field of biomedical sciences.

Hazardous heavy metal semiconductor QDs is not preferred to be used in biological applications due to their toxicity. C-dots have negligible toxicity in the human body, and they emit fluorescence in the near-infrared region of the light spectrum. They are also better than semiconductor QDs with respect to the simplicity of production and possibility of functionalization. C-dots offer a wide range of biological applications, including in vivo and in vitro bioimaging, drug administration, gene transfer, and cancer therapy. However, to determine their blood circulation, toxicity, and conjugation in multifunctional systems for simultaneous bioimaging and drug/gene delivery, further research is needed. Surface coating, functionalization, N-doping, and synthesis technique have high impact on the optical properties of C-dots. It is therefore important to study the impact of synthesis parameters and doping in order to obtain the requisite high QY with biocompatibility. C-dots, as opposed to semiconductor QDs, are often more appealing for biological applications.

C-dots, despite being discovered by accident, continue to get substantial attention in a variety of disciplines due to their intrinsic characteristics. They exhibit a strong photoluminescence and are easily dispersed in water. They are commonly utilized in cellular imaging, catalysis, electronics, biosensing, power, small molecule detection, targeted medication administration, and other biomedical applications (Gao et al.). The subject of nanotheranostics is rapidly expanding as a result of advancements in material science, molecular biology, nanotechnology, and formulation development. C-dots-based theranostic drugs have the potential to substantially improve the management of a wide range of illnesses, including infections, inflammation, neurological disorders, cardiovascular disease, focused therapy, and therapeutic impact monitoring (Gao et al.). Oncology is one of the fields where C-dot theranostic systems have been intensively studied. However, C-dot theranostic systems have a long way to go, just combining imaging agents, medicines, and targeting ligands within C-dots is insufficient. Liposome-like C-dots are one of the prospective new carbon-based substances that can perform several tasks [64]. Liposome-like C-dots, which are made up of thousands of individual C-dots, have a higher fluorescence intensity than individual C-dots. They may be used to carry medicines such as doxorubicin (an anticancer agent) and efficiently enter cancer tissues, just as conventional C-dots. The biocompatible and stable liposome-like C-dots may also be utilized to load different cancer medicines that are either hydrophobic or hydrophilic. There are still a few issues that necessitate thorough examination of C-dots. To overcome these issues, comprehensive studies must be conducted that address in vivo safety, pharmacokinetics, distribution, and component compatibility. The impact of C-dots manufacturing methods on the stability of each component, as well as the creation of scalable C-dot production, is critical. All of these problems must be solved before C-dots are used in theranostic applications on a regular basis.

References

[1] P. Yang, J. Zhao, L. Zhang, L. Li, Z. Zhu, Intramolecular hydrogen bonds quench photoluminescence and enhance photocatalytic activity of carbon nanodots, Chemistry – A European Journal 21 (2015) 8561–8568. Available from: https://doi.org/10.1002/chem.201405088.

[2] K.A.S. Fernando, S. Sahu, Y. Liu, W.K. Lewis, E.A. Guliants, A. Jafariyan, et al., Carbon quantum dots and applications in photocatalytic energy conversion, ACS Applied Materials & Interfaces 7 (2015) 8363–8376. Available from: https://doi.org/10.1021/acsami.5b00448.

[3] K.J. Mintz, M. Bartoli, M. Rovere, Y. Zhou, S.D. Hettiarachchi, S. Paudyal, et al., A deep investigation into the structure of carbon dots, Carbon 173 (2021) 433–447. Available from: https://doi.org/10.1016/j.carbon.2020.11.017.

[4] Y.P. Sun, B. Zhou, Y. Lin, W. Wang, K.A.S. Fernando, P. Pathak, et al., Quantum-sized carbon dots for bright and colorful photoluminescence, Journal of the American Chemical Society 128 (2006) 7756–7757. Available from: https://doi.org/10.1021/ja062677d.

[5] N. Arsalani, P. Nezhad-Mokhtari, E. Jabbari, Microwave-assisted and one-step synthesis of PEG passivated fluorescent carbon dots from gelatin as an efficient nanocarrier for methotrexate delivery, Artificial Cells, Nanomedicine, and Biotechnology 47 (2019) 540–547. Available from: https://doi.org/10.1080/21691401.2018.1562460.

[6] R.S.A. Sonthanasamy, S. Fazry, B.M. Yamin, A.M. Lazim, Surface functionalization of highly luminescent carbon nanodots from *Dioscorea hispida* with polyethylene glycol and branched polyethyleneimine and their in vitro study, Journal of King Saud University - Science 31 (2019) 768–779. Available from: https://doi.org/10.1016/j.jksus.2018.05.004.

[7] H. Ding, Y. Ji, J.S. Wei, Q.Y. Gao, Z.Y. Zhou, H.M. Xiong, Facile synthesis of red-emitting carbon dots from pulp-free lemon juice for bioimaging, Journal of Materials Chemistry B 5 (2017) 5272–5277. Available from: https://doi.org/10.1039/c7tb01130j.

[8] C. Dias, N. Vasimalai, M.P. Sárria, I. Pinheiro, V. Vilas-Boas, J. Peixoto, et al., Biocompatibility and bioimaging potential of fruit-based carbon dots, Nanomaterials 9, 199 (2019). Available from: https://doi.org/10.3390/nano9020199.

[9] A. Kumar, A.R. Chowdhuri, D. Laha, T.K. Mahto, P. Karmakar, S.K. Sahu, Green synthesis of carbon dots from *Ocimum sanctum* for effective fluorescent sensing of Pb2 + ions and live cell imaging, Sensors and Actuators B: Chemical 242 (2017) 679–686. Available from: https://doi.org/10.1016/j.snb.2016.11.109.

[10] B. Yin, J. Deng, X. Peng, Q. Long, J. Zhao, Q. Lu, et al., Green synthesis of carbon dots with down- and up-conversion fluorescent properties for sensitive detection of hypochlorite with a dual-readout assay, Analyst 138 (2013) 6551–6557. Available from: https://doi.org/10.1039/c3an01003a.

[11] L. Wang, H.S. Zhou, Green synthesis of luminescent nitrogen-doped carbon dots from milk and its imaging application, Analytical Chemistry 86 (2014) 8902–8905. Available from: https://doi.org/10.1021/ac502646x.

[12] A. Saravanan, M. Maruthapandi, P. Das, J.H.T. Luong, A. Gedanken, Green synthesis of multifunctional carbon dots with antibacterial activities, Nanomaterials 11 (2021) 1–11. Available from: https://doi.org/10.3390/nano11020369.

[13] D. Gu, S. Shang, Q. Yu, J. Shen, Green synthesis of nitrogen-doped carbon dots from lotus root for Hg(II) ions detection and cell imaging, Applied Surface Science 390 (2016) 38–42. Available from: https://doi.org/10.1016/j.apsusc.2016.08.012.

[14] A. Sachdev, P. Gopinath, Green synthesis of multifunctional carbon dots from coriander leaves and their potential application as antioxidants, sensors and bioimaging agents, Analyst 140 (2015) 4260–4269. Available from: https://doi.org/10.1039/c5an00454c.

[15] G. Gedda, C.Y. Lee, Y.C. Lin, H.F. Wu, Green synthesis of carbon dots from prawn shells for highly selective and sensitive detection of copper ions, Sensors and Actuators B: Chemical 224 (2016) 396–403. Available from: https://doi.org/10.1016/j.snb.2015.09.065.

[16] C. Zhu, D. Du, J. Tang, Z. Zhu, Y. Zhai, Z. Li, et al., Red carbon dots: Optical property regulations and applications, Materialstoday 30 (2019) 52–79. Available from: https://doi.org/10.1016/j.mattod.2019.05.003.

[17] C. Zhu, J. Zhai, S. Dong, Bifunctional fluorescent carbon nanodots: Green synthesis via soy milk and application as metal-free electrocatalysts for oxygen reduction, Chemical Communications 48 (2012) 9367–9369. Available from: https://doi.org/10.1039/c2cc33844k.

[18] X. Zhao, J. Zhang, L. Shi, M. Xian, C. Dong, S. Shuang, Folic acid-conjugated carbon dots as green fluorescent probes based on cellular targeting imaging for recognizing cancer cells, RSC Advance 7 (2017) 42159–42167. Available from: https://doi.org/10.1039/c7ra07002k.

[19] X. Qin, W. Lu, A.M. Asiri, A.O. Al-Youbi, X. Sun, Green, low-cost synthesis of photoluminescent carbon dots by hydrothermal treatment of willow bark and their application as an effective photocatalyst for fabricating Au nanoparticles-reduced graphene oxide nanocomposites for glucose detection, Catalysis Science and Technology 3 (2013) 1027–1035. Available from: https://doi.org/10.1039/c2cy20635h.

[20] D. Qu, X. Wang, Y. Bao, Z. Sun, Recent advance of carbon dots in bio-related applications, Journal of Physics: Materials 3, 2 (2020). Available from: https://doi.org/10.1088/2515-7639/ab7cb9.

[21] F.W. Pratiwi, C.W. Kuo, B.C. Chen, P. Chen, Recent advances in the use of fluorescent nanoparticles for bioimaging, Nanomedicine: Nanotechnology, Biology, and Medicine 14 (2019) 1759–1769. Available from: https://doi.org/10.2217/nnm-2019-0105.

[22] Y. Liu, P. Le, S.J. Lim, L. Ma, S. Sarkar, Z. Han, et al., Enhanced mRNA FISH with compact quantum dots, Nature Communications 9 (2018) 1–8. Available from: https://doi.org/10.1038/s41467-018-06740-x.

[23] A.M. Chizhik, S. Stein, M.O. Dekaliuk, C. Battle, W. Li, A. Huss, et al., Super-resolution optical fluctuation bio-imaging with dual-color carbon nanodots, Nano Letters 16 (2016) 237–242. Available from: https://doi.org/10.1021/acs.nanolett.5b03609.

[24] G. Nocito, G. Calabrese, S. Forte, S. Petralia, C. Puglisi, M. Campolo, et al., Carbon dots as promising tools for cancer diagnosis and therapy, Cancers (Basel) (2021) 13, 1991. Available from: https://doi.org/10.3390/cancers13091991.

[25] S. Pandey, D. Bodas, High-quality quantum dots for multiplexed bioimaging: a critical review, Advances in Colloid and Interface Science 278 (2020) 102137. Available from: https://doi.org/10.1016/j.cis.2020.102137.

[26] H. Ali, S. Ghosh, N.R. Jana, Fluorescent carbon dots as intracellular imaging probes, Wiley Interdisciplinary Reviews: Nanomedicine Nanobiotechnology (2020). Available from: https://doi.org/10.1002/wnan.1617.

[27] C. Yi, Y. Pan, Y. Fang, Surface engineering of carbon nanodots (C-dots) for biomedical applications, Novel nanomaterials for biomedical, environmental and energy applications, Elsevier, 2018, pp. 137−188. Available from: https://doi.org/10.1016/B978-0-12−814497-8.00005−9.

[28] F. Yan, Z. Sun, H. Zhang, X. Sun, Y. Jiang, Z. Bai, The fluorescence mechanism of carbon dots, and methods for tuning their emission color: a review, Microchim. Acta (2019) 186, 583. Available from: https://doi.org/10.1007/s00604-019-3688-y.

[29] L. Bao, C. Liu, Z.L. Zhang, D.W. Pang, Photoluminescence-tunable carbon nanodots: surface-state energy-gap tuning, Advanced Materials 27 (2015) 1663−1667. Available from: https://doi.org/10.1002/adma.201405070.

[30] W. Shi, Q. Wang, Y. Long, Z. Cheng, S. Chen, H. Zheng, et al., Carbon nanodots as peroxidase mimetics and their applications to glucose detection, Chemical Communications 47 (2011) 6695−6697. Available from: https://doi.org/10.1039/c1cc11943e.

[31] H. Dai, C. Yang, Y. Tong, G. Xu, X. Ma, Y. Lin, et al., Label-free electrochemiluminescent immunosensor for α-fetoprotein: performance of nafion-carbon nanodots nanocomposite films as antibody carriers, Chemical Communications 48 (2012) 3055−3057. Available from: https://doi.org/10.1039/c1cc16571b.

[32] Q. Wang, et al., Hollow luminescent carbon dots for drug delivery, Carbon 59 (2013) 192−199.

[33] S. Iravani, Rajender, S. Varma, Green synthesis, biomedical and biotechnological applications of carbon and graphene quantum dots. A review, Environmental Chemistry Letters 18 (2020) 703−727. Available from: https://doi.org/10.1007/s10311-020-00984-0.

[34] M.C. Kim, et al., Polyethyleneimine-associated polycaprolactone—Superparamagnetic iron oxide nanoparticles as a gene delivery vector, Journal of Biomedical Materials Research Part B 105 (1) (2017) 145−154.

[35] Z. Wang, H. Liao, H. Wu, B. Wang, H. Zhao, M. Tan, Fluorescent carbon dots from beer for breast cancer cell imaging and drug delivery, Analytical Methods 7 (2015) 8911−8917. Available from: https://doi.org/10.1039/c5ay01978h.

[36] L.M.T. Phan, A.R. Gul, T.N. Le, M.W. Kim, S.K. Kailasa, K.T. Oh, et al., One-pot synthesis of carbon dots with intrinsic folic acid for synergistic imaging-guided photothermal therapy of prostate cancer cells, Biomaterials Science 7 (2019) 5187−5196. Available from: https://doi.org/10.1039/c9bm01228a.

[37] M. Vedhanayagam, I.S. Raja, A. Molkenova, T.S. Atabaev, K.J. Sreeram, D.W. Han, Carbon dots-mediated fluorescent scaffolds: recent trends in image-guided tissue engineering applications, International Journal of Molecular Sciences 22 (2021) 5378. Available from: https://doi.org/10.3390/ijms22105378.

[38] M.S. Khan, et al., Controlled delivery of dopamine hydrochloride using surface modified carbon dots for neuro diseases, Colloids Surf., B 134 (2015) 140−146.

[39] O.C. Farokhzad, R. Langer, Impact of nanotechnology on drug delivery, ACS Nano 3 (1) (2009) 16−20.

[40] A.R. Chowdhuri, et al., Carbon dots embedded magnetic nanoparticles@chitosan@metal organic framework as a nanoprobe for pH sensitive targeted anticancer drug delivery, ACS Applied Materials & Interfaces 8 (26) (2016) 16573−16583.

[41] S. Karthik, et al., Photoresponsive quinoline tethered fluorescent carbon dots for regulated anticancer drug delivery, Chemical Communications 49 (89) (2013) 10471−10473.

[42] C. Xu, et al., Magnetically targeted co-delivery of hydrophilic and hydrophobic drugs with hollow mesoporous ferrite nanoparticles, RSC Advance 8 (28) (2018) 15326−15335.
[43] J. Yang, et al., Multifunctional zinc-based hollow nanoplatforms as a smart pH-responsive drug delivery system to enhance in vivo tumor-inhibition efficacy, Materials & Design 139 (2018) 172−180.
[44] Y. Shu, et al., Ionic liquid mediated organophilic carbon dots for drug delivery and bioimaging, Carbon 114 (2017) 324−333.
[45] V.N. Mehta, et al., Green synthetic approach for synthesis of fluorescent carbon dots for lisinopril drug delivery system and their confirmations in the cells, Journal of Fluorescence 27 (1) (2017) 111−124.
[46] N. Sarkar, et al., Carbon quantum dot tailored calcium alginate hydrogel for pH responsive controlled delivery of vancomycin, European Journal of Pharmaceutical Sciences: Official Journal of the European Federation for Pharmaceutical Sciences 109 (2017) 359−371.
[47] Y. Wang, et al., Fluorescent carbon dot-gated multifunctional mesoporous silica nanocarriers for redox/ enzyme dual-responsive targeted and controlled drug delivery and real-time bioimaging, European Journal of Pharmaceutics and Biopharmaceutics: Official Journal of Arbeitsgemeinschaft fur Pharmazeutische Verfahrenstechnik e.V 117 (2017) 105−115.
[48] B. Ma, et al., Prolonged fluorescence lifetime of carbon quantum dots by combining with hydroxyapatite nanorods for bio-applications, Nanoscale 9 (6) (2017) 2162−2171.
[49] M. Zhang, et al., pH-Sensitive N-doped carbon dots−heparin and doxorubicin drug delivery system: preparation and anticancer research, RSC Advance 7 (15) (2017) 9347−9356.
[50] R.K. Das, et al., Magnetic mesoporous silica gated with doped carbon dot for site-specific drug delivery, fluorescence, and MR imaging, Langmuir: the ACS Journal of Surfaces and Colloids 34 (18) (2018) 5253−5262.
[51] J. Gu, K. Al-Bayati, E.A. Ho, Development of antibodymodified chitosan nanoparticles for the targeted delivery of siRNA across the blood-brain barrier as a strategy for inhibiting HIV replication in astrocytes, Drug Delivery and Translational Research 7 (4) (2017) 497−506.
[52] N. Huang, et al., Efficacy of NGR peptide-modified PEGylated quantum dots for crossing the blood−brain barrier and targeted fluorescence imaging of glioma and tumor vasculature, Nanomedicine: Nanotechnology, Biology, and Medicine 13 (1) (2017) 83−93.
[53] A.V. Kabanov, E.V. Batrakova, Polymer nanomaterials for drug delivery across the blood brain barrier, Neuroimmune pharmacology, Springer, 2017, pp. 847−868.
[54] M.M. Patel, B.M. Patel, Crossing the blood−brain barrier: recent advances in drug delivery to the brain, CNS Drugs 31 (2) (2017) 109−133.
[55] M.S. Huh, et al., Polysaccharide-based nanoparticles for gene delivery, Topics in Current Chemistry 375 (2) (2017) 31.
[56] I. Fernandez-Pĩneiro, et al., Development and characterisation of chondroitin sulfate- and hyaluronic acid-incorporated sorbitan ester nanoparticles as gene delivery systems, European Journal of Pharmaceutics and Biopharmaceutics 125 (2018) 85−94.
[57] X. Huang, et al., Characterization of calcium phosphate nanoparticles based on a PEGylated chelator for gene delivery, ACS Applied Materials & Interfaces 9 (12) (2017) 10435−10445.
[58] B. Du, et al., Lipid-coated gold nanoparticles functionalized by folic acid as gene vectors for targeted gene delivery in vitro and in vivo, ChemMedChem 12 (21) (2017) 1768−1775.
[59] S.P. Song, Y. Qin, Y. He, Q. Huang, C.H. Fan, H.Y. Chen, Functional nanoprobes for ultrasensitive detection of biomolecules, Chemical Society Reviews 39 (2010) 4234−4243.

[60] U. Resch-Genger, M. Grabolle, S. Cavaliere-Jaricot, R. Nitschke, T. Nann, Quantum dots versus organic dyes as fluorescent labels, Nature Methods 5 (2008) 763.

[61] S.A. Gomes, C.S. Vieira, D.B. Almeida, J.R. SantosMallet, R.F. Menna-Barreto, C.L. Cesar, et al., CdTe and CdSe quantum dots cytotoxicity: a comparative study on microorganisms, Sensors 11 (2011) 11664−11678.

[62] C.E. Bradburne, J.B. Delehanty, K. Boeneman Gemmill, B.C. Mei, H. Mattoussi, K. Susumu, et al., Cytotoxicity of quantum dots used for in vitro cellular labeling: role of QD surface ligand, delivery modality, cell type, and direct comparison to organic fluorophores, Bioconjugate Chemistry 24 (2013) 1570−1583.

[63] X.X. Wu, S.S. Sun, Y.H. Wang, J.L. Zhu, K. Jiang, Y.M. Leng, et al., A fluorescent carbon-dots-based mitochondria-targetable nanoprobe for peroxynitrite sensing in living cells, Biosensors & Bioelectronics 90 (2017) 501−507.

[64] C.X. Wang, K.L. Jiang, Q. Wu, J.P. Wu, C. Zhang, Green synthesis of red-emitting carbon nanodots as a novel "turn-on" nanothermometer in living cells, Chemistry − A European Journal 22 (2016) 14475−14479.

[65] X. Bao, Y. Yuan, J.Q. Chen, B.H. Zhang, D. Li, D. Zhou, et al., In vivo theranostics with near-infrared-emitting carbon dots—highly efficient photothermal therapy based on passive targeting after intravenous administration, Light: Science & Applications 7 (2018) 91.

Bioimaging applications of carbon quantum dots

12

Akanksha Kumari[1], *Jaydeep Bhattacharya*[2] *and Ranjita Ghosh Moulick*[1]
[1]Amity Institute of Integrative Science and Health, Amity University Gurgaon, Panchgaon, Haryana, India, [2]NanoBiotechnology Lab, School of Biotechnology, Jawaharlal Nehru University, New Delhi, Delhi, India

12.1 Introduction

Biological science has achieved a greater understanding with expansion in technologies in the past few years and will continue to grow in future. Advancements in the field of technology have played significant role to ease the struggles of biologists all over the world. One such example is bioimaging. As the name suggests, bioimaging is a noninvasive, real-time technique that let us visualize and speculate ongoing biological process at the cellular or molecular level in vivo or in vitro. Microscope is one of the most primitive bioimaging tools that has been used by biologists. Discovery of microscope introduced us to the living world of air, water, our bodies, and to the things that are not visible to the naked eye [1]. Discovery of cell by Robert Hooke and A. V. Leeuwenhoek might not have been possible without a microscope. However, microscope was not enough to inspect cellular components, as most of the time they are optically transparent. Scientists further came up with the idea of staining or probe tagging methods to enhance the contrast or signal in the samples. These imaging agents further provided the opportunity to link the signal to the biological events. Hans Christian Gram, a Danish bacteriologist, first introduced the crystal violet dye for differential staining and established Gram staining technique [2]. It has been noted that not only various improvements in the microscopy techniques were introduced at different timeline but also advancements were made in the direction of synthesis of new dyes and imaging agents. These molecules were designed to have an early impression about the disease sites, deformity, therapeutic responses, or progression [3]. For example, the invention of the fluorescence microscopy was the hallmark of the imaging technique. However, in the beginning, its application was limited to naturally occurring fluorescent samples. Later, florescent dyes were synthesized to stain the various biological samples that enriched the system. Two scientists, Coons and Kaplan, connected this concept with labeled antibodies to examine antigen–antibody interaction, which is said to be a major breakthrough in the field of immunohistochemistry. Moreover, with the advent of the green fluorescence protein (GFP) and other analogs, monitoring intracellular events within the live cell became easier (Fig. 12.1).

Carbon Quantum Dots for Sustainable Energy and Optoelectronics. DOI: https://doi.org/10.1016/B978-0-323-90895-5.00001-1
© 2023 Elsevier Ltd. All rights reserved.

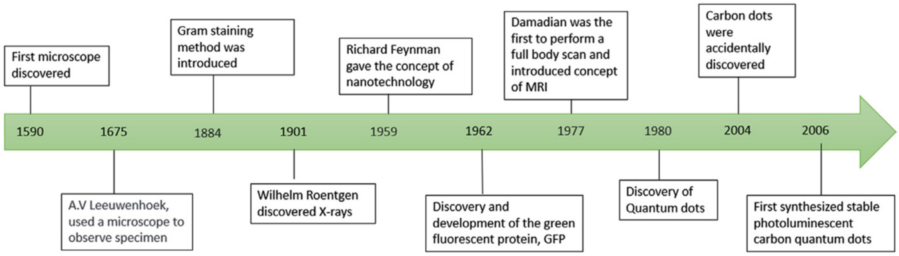
First microscope discovered
1590
1675
A.V Leeuwenhoek, used a microscope to observe specimen
Gram staining method was introduced
1884
1901
Wilhelm Roentgen discovered X-rays
Richard Feynman gave the concept of nanotechnology
1959
1962
Discovery and development of the green fluorescent protein, GFP
Damadian was the first to perform a full body scan and introduced concept of MRI
1977
1980
Discovery of Quantum dots
Carbon dots were accidentally discovered
2004
2006
First synthesized stable photoluminescent carbon quantum dots

Figure 12.1 A brief timeline of important discoveries related to the bioimaging field.

12.2 Development of various bioimaging modalities

The conventional bioimaging techniques include modalities mostly based on the use of electrons, positrons, magnetic resonance, temperature, X-rays, ultrasounds, etc. The early biomedical imaging was developed using ionizing electromagnetic radiation X-ray. And till now it is a popular method to diagnose any abnormalities in the body tissues, especially bones. High density bones absorb most of the X-rays and turn to be bright in image, while muscles, the soft tissues, absorb less of it and looks grayish. However, 2-D imaging of X-ray technique does not provide complete figure of the internal body. Therefore, imaging from different angles is required to understand the 3-D environment. In X-ray computed tomography (CT) scan, X-rays are projected from different angles and thus generate more detailed pattern of the internal body structure. It is more efficient to diagnose abnormalities such as tumors, infections, clotting, etc. However, to distinguish soft tissue types in patients, contrast dyes are injected for better functional imaging [3]. Magnetic resonance imaging (MRI) is more efficient in making pictures of soft tissues as compared to CT scan [4]. Though it is similar to CT scan, it uses radiowaves instead of X-rays for imaging. MRI is operated on very strong magnetic field and aligns the protons inside the body to the field. Different tissues take different time to align depending on its constituent. The detector senses the energy released by the proton and results in contrasting images after administration of an agent containing gadolinium [5]. Another bioimaging modality is radionuclide imaging in which images are obtained using radioactive emission-detecting camera that identify emissions of injected radionuclides. These injected radionuclides get distributed unevenly based on tissues in body and get accumulated in tissues with abnormalities. Positron emission tomography (PET) and single photon emission computed tomography (SPECT) are commonly used techniques for this kind of imaging that vary prominently on the type of radiotracers used. PET produces positrons to measure signals, while SPECT directly rrecognizes gamma rays, emitted during radioactive decay of tracer [2].

Optical imaging modalities include use of light for imaging. There are several tools available for optical imaging, such as optical microscopy, fluorescence microscopy, bioluminescence microscopy, etc. This technique is cost-effective, user-friendly, and safe. It has only one disadvantage, i.e., deep tissues cannot be imaged due to low energy of photons. Thermal imaging is another rapidly growing modality in the field of biomedical imaging. All objects with a temperature above 0 Kelvin emit infrared radiations. These radiations are released with different energy and are directly proportional to the temperature of the respective bodies. Thermal camera can sense temperature ddifferences among objects and create thermal images [6]. Thermal imaging is used in diagnosis of cancer, heart problems, brain imaging, and diabetes neuropathy, and in the recent pandemic situation of COVID-19, it is used to detect body temperature [7]. Thus, we can say that bioimaging techniques have been able to make considerable progress in their potential to image organs from anatomical to physiological level. Currently, there is a huge progress toward molecular imaging. Molecular imaging is defined as noninvasive visualization and characterization of biological activities at molecular level in a living subject [8]. Molecular imaging is not only confined to visualizing agents, there are few techniques as well that detect sounds to reconstruct images. For example, photoacoustic imaging provides detailed, high-resolution, clear images of biological systems, that too with no harmful radiations involved. It consumes laser induced soundwaves for signaling, which vary from tissues to tissues based on different chemical compositions. Basically, a laser source releases tuned pulses to the specimen, which is absorbed by tissue and the tissue expands due to heat. These disturbances create oscillations as soundwaves and an ultrasonic detector senses or "hears" it and processes an image. Another example is ultrasound molecular imaging. Development of specifically targeted ultrasound contrast agents have fueled this technique. Commonly used ultrasound molecular imaging contrast agents are functionalized gas-containing microbubbles that recognize biomolecules and attach. It is reported to be involved in clinical applications for early diagnosis and monitoring of cancer, myocardial ischemia, and inflammatory bowel diseases [9].

12.3 Requirement of imaging agents

Molecular imaging agents have made an enormous contribution to the field of molecular imaging. They are the essential components and are used in diagnosis of diseases, tracking disease progression, drug response, and biological studies. In the medical field, with advancement in personalized therapies and medications, there is a requirement of deep monitoring of the body state of a person before coming to a conclusion. Molecular imaging probe must also be able to reach its target and perform as per the expectation of linking imaging signal with the events. In addition, for an effective molecular imaging, highly sensitive contrast agents are required. Therefore, to optimize the best imaging results, atleast two among the following three components should be present: the target moity, signal component, and linker [8]. Hence, designing an imaging agent is important because ideally it should have high binding affinity, specificity, sensitivity, high contrast ratio, low immunogenicity, low toxicity, in vivo stability, fast clearance from blood circulation, easy excretion in urine, and be economical [8,10]. Though factors affecting pharmacokinetics attributes are unclear, it might be the biomolecule size, charge, and lipophilicity that play important roles for deciding the type of imaging agent.

12.4 Nanomaterials as imaging agents

It has been found that a variety of nanomaterials can be engineered as contrast agents. Since they offer many advantages in comparison to the traditional probes, such as control on physical properties, surface modification, and more circulation time, they can be exploited for various multimodal imaging and therapy combinations. For example, iron oxides are commonly used to synthesize magnetic nanoparticles. They are emerging in the field of drug delivery and bioimaging for their properties such as high surface area, metal rich moieties, and tuneable structural compositions. Iron oxide nanoparticles with improved size and composition have been used as contrast agents for MRI [11]. These particles are required to cover with biocompatible agents for biological purposes to prevent degradation of these particles and to avoid damage to body [12]. Gold nanoparticles are known for their highly sensitive optical and electronic properties and are used for Raman spectroscopic imaging for their ability to enhance Raman scattering. Plasmon resonance of gold nanoparticles is tuneable to increase optical response, which promotes efficiency of photoacoustic signaling [13–15]. Gold nanoparticles and tantalum oxide nanoparticles have been reported to carry higher X-ray attenuation coefficient, and are hence exploited for developing CT scan contrast agents [16–18]. Mesoporous silica nanoparticles are considered to be suitable carriers of fluorescent dyes for their high pore volume/surface area and tuneable pore size, which enhance loading capacity of fluorescent dyes and also provide protection to dyes [19–21]. Graphene-based nanomaterials are used in optical imaging involving fluorescence imaging or two-photon fluorescence imaging, radionuclide-based imaging, magnetic resonance imaging, photoacoustic imaging, Raman imaging, and multimodal imaging [22]. Various nucleic acid-functionalized nanomaterials like graphene, carbon nanotubes, silica particles, metal nanoparticles, magnetic nanoparticles, polyacrylamide nanoparticles and semiconductor QDs have also found profound applications in bioimaging [23]. Another well-known source for biological imaging is nanocluster-based probe. Nanoclusters are nanomaterials that comprise of upto 100 atoms and atleast one dimension between 1 and 10 nm, while nanoclusters with more than 1000 atoms are considered as nanoparticles [24]. Size of metal nanoclusters has been compared with Fermi wavelength of electrons [25], that is somewhere between a metal atoms and metal nanoparticles. In this intermediate size, they show significant difference in their properties such as better photoluminescence, photostability, and biocompatibility. Fluorescent platinum nanoclusters have been reported to be useful in bioimaging as they serve as fluorescent probes facilitating live cell imaging [26]. Besides, copper nanoparticles with excellent photoluminescent properties form nanoclusters and serve as intriguing probe for bioimaging and biosensing applications [27]. A promising fluorescent label is the silver nanocluster stabilized by glutathione as it is highly fluorescent and shows high stability in a varied range of pH with no bleaching over a long period of time [28]. Despite their excellent properties, nanoclusters face few challenges in their preparatory phase. It gets unmanageable to obtain desirable size of nanocluster and affect its size-dependent properties. Due to this, the quality of nanoclusters gets compromised and results in relatively low quantum yield (QY). There are also issues with metal nanocluster purification and high monodispersity [29].

QDs are artificially built nano-semiconductors. Although a part of nanoworld, they carry a few distinct features different from nanoparticles. QDs are smaller, mostly between 2 and 10 nm, while nanoparticle is the term given to particles comparatively larger in size, between 8 and 100 nm. The concept of QDs as semiconductor was theorized in 1970s, that if particles are at nanoscale level, quantum effects come into force and properties of particles can be controlled by changing their size and shape. When ultraviolet radiations hit tiny semiconductors, electrons excite and release energy in form of colorful lights. Due to their ability to produce colored light, they have applications in televisions, solar cells, biological labeling, etc. Compared with conventional dyes and fluorescent proteins, QDs give better resolution, stability against photobleaching, and can emit multicolors with a single light source. Graphene QDs with strong green-photoluminescent properties are being widely used for bioimaging applications [30]. Semiconductor QDs are being considered as a new class of fluorescent labels for molecular imaging. They are basically light-emitting photobleach-resistant nanometer scale particles with excellent optical and electronic properties serving in bioimaging applications [31]. The surface plasmon resonance of gold QDs has a lot of implications in biologically relevant imaging, for example, cellular and in vivo imaging [32].

12.5 Carbon quantum dots

Carbon is one of the most abundant and easily available elements on earth. However, it was underestimated for its basic properties such as low water solubility and weak fluorescence. In contrast, cDots are known for their good solubility and high luminescence, frequently called carbon nanolights [33]. It has strong chemical stability, easy modifications, and resistivity to photobleaching. In terms of biology, cDots show low toxicity and better biocompatibility, allowing their applications in bioimaging, biosensors, and drug delivery. cDots have properties of QDs along with some significant features that they carry from carbon. For example, their outstanding electrical properties are due to sp^2 carbon. Abundance of oxygenic groups on cDots surface makes them suitable for covalent bonding with other compounds during functionalization and also increases the solubility [34,35].

During the past few years, much progress has been achieved in the synthesis, properties, and applications of carbon-based QDs. Compared to traditional semiconductor QDs and organic dyes, photoluminescent carbon-based QDs are superior in terms of high (aqueous) solubility, robust chemical inertness, facile modification, and high resistance to photobleaching. The superior biological properties of carbon-based QDs, such as low toxicity and good biocompatibility, entrust them with potential applications in bioimaging, biosensor, and biomolecule/drug delivery. The outstanding electronic properties of carbon-based QDs as electron donors and acceptors, causing chemiluminescence and electrochemical luminescence, endow them with wide potentials in optronics, catalysis, and sensors.

12.6 Synthesis and modifications in carbon quantum dots

cDots can be made from many kinds of organic compounds, easily available in nature like onion, human fingernails [36,37], cotton [38], and coriander leaves [35,39]. Preparation of cDots might have to face few issues such as size nonuniformity, carbonaceous aggregation, and surface properties. Particle aggregation can be avoided using electrochemical synthesis or pyrolysis. Homogeneity in product is important for maintaining balanced properties among particles and post treatment processes such as dialysis, centrifugation, and gel electrophoresis can help in achieving it [34]. Numerous methods to synthesize cDots have been reported till date. These methods can be broadly categorized under "top-down" and "bottom-up" approaches. In "top-down" approaches, large materials (such as plants part) are broken into cDots. It includes chemical ablation, laser ablation, arc discharge, and electrochemical method (Fig. 12.2).

12.6.1 Chemical ablation

In this method, strong oxidizing acids break down organic molecules into carbonaceous matter through carbonization.

12.6.2 Electrochemical method

It is useful to isolate pure cDots from large organic molecules such as graphite, carbon nanotube. This method involves traditional electrolysis process using suitable electrolytes and electrodes [40]. Electrochemical carbonization is an efficient method to prepare cDots from bulky matter as precursor. There are few reports regarding usage of this method for small molecules for cDot synthesis.

12.6.3 Laser ablation

In laser ablation technique, large organic molecules get exposed to pulsated laser light. These laser radiations cause the release of carbon nanoparticles from these large

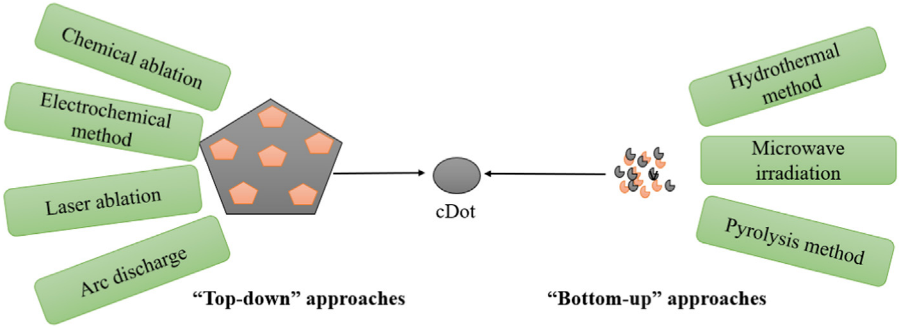

Figure 12.2 Approaches for synthesis of cDots. *cDot*, carbon dots.

structures. The laser ablation technique was first reported in 2006 by Sun et al. [41]. It is a commonly used technique for the synthesis of cDot with different sizes [42].

12.6.4 Arc Discharge method

Arc discharge method to synthesize cDots was discovered unintentionally, when Xu et al. were preparing single-walled carbon nanotubes (SWCNTs) [42,43]. Electric discharge between two graphite electrodes leads to the synthesis of cDots.

"Bottom-up" methods deal with adding raw material to grow it into cDots. "Bottom-up" techniques involve hydrothermal, microwave, and pyrolysis methods.

12.6.5 Hydrothermal method

In this method, organic compounds are sealed in hydrothermal reactors under high pressure and temperature conditions. The process is called hydrothermal carbonization or solvothermal carbonization. Natural sources such as banana juice [44], citric juice [45], chitosan, etc. can be used for making cDot using hydrothermal carbonization [34]. This process is considered to be most promising method for its easy, nontoxic, ecofriendly, and cost-effective route. Zhang et al. were first to report one-pot hydrothermal method using ascorbic acid as precursor [46].

12.6.6 Microwave irradiation

In this method, small organic precursors are carbonized using microwave radiations. Microwave-based technique is reported to be a low cost and fast synthesis process for cDot. cDots have been reported to be obtained from sucrose and diethylene glycol in a minute using microwave irradiation technique [47].

12.6.7 Pyrolysis method

It is a simple method to prepare cDot by chemical reactions in presence of strong acid/base under extremely high temperature [42].

12.7 Surface activation

Activating surface is the most important part to prepare a functional cDot. Without a proper activation, cDot might not be able to identify its target and fail to show response. Functionalization of surfaces could control nature of its surface based on hydrophobic or hydrophilic environment [48]. Unmodified carbon nanoparticles do not carry any kind of photoluminescence, whereas surface activation conducts its photoluminescent properties [49]. cDots' properties fluctuate dramatically by tuning their shape and doping with some heteroatoms such as nitrogen, oxygen, sulfur, and boron, particularly in the case of their photophysical and chemical properties [50].

There are many available methods to surface activation based on their interaction properties. Surface activation allow cDots to participate in diversified applications from biological field such as food safety, bioimaging, drug delivery to explosive detection, energy conversion, and chemical sensing [42,51].

12.7.1 Surface passivation

Surface passivation is a process of providing stability to cDot surface and increasing its shelf life. Bare surface of cDot is prone to get involved in unwanted reactions, which can lead to fading of its optoelectronic properties. Surface passivation can form a thin protective layer that can insulate cDots from direct exposure to impurities (Fig. 12.3B). Moreover, it can improve its florescence intensity. Many kinds of polymers and organic compounds can be used as passivation agent. Surface passivation agents must not contain chromophores for visible or near UV, so that they remain non emissive at visible wavelength, and confirming observed luminescence of passivated cDots [51].

12.7.2 Surface functionalization

Surface functionalization has major role in determining properties of cDots. Functional groups such as carboxyl, hydroxy, and amino are commonly used for cDot modification using covalent and noncovalent interactions. Covalent functionalization is suitable for better control in shape, size, and physical properties of cDots. Here researchers use covalent modification to add functional groups on cDot

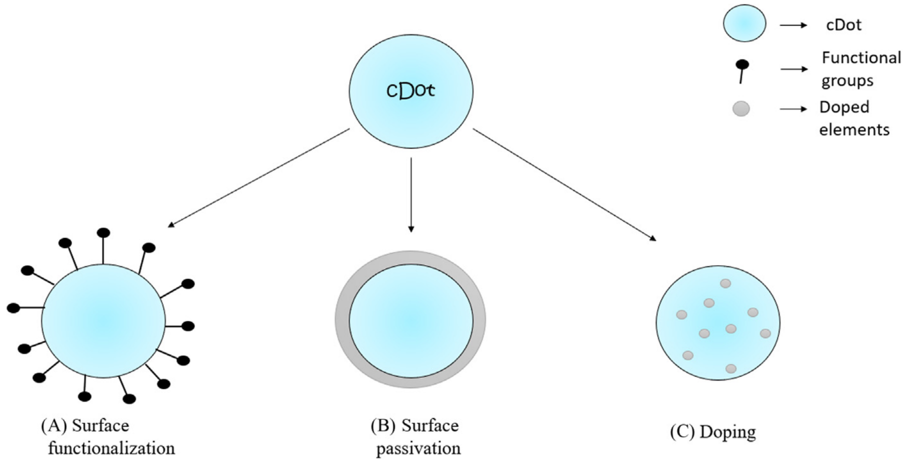

Figure 12.3 Surface activation of cDots. (A) Surface functionalization of cDot is shown with attached functional groups (black) on its surface. (B) Surface passivation is shown here where gray portion represents thin insulation around cDot. (C) Doping of cDots is illustrated in the figure where gray dots represent doping elements. *cDot*, carbon dots.

for targeting their molecule of interest as illustrated in Fig. 12.3A. It increases electron density on surface, which also alters the fluorescence spectrum of cDots. Specificity of reaction is one of most noteworthy features of covalently modified cDots, which can vary based on different functional groups. Based on reaction between different functional groups, it can be classified as amide, esterification, sialylation, sulfonylation, or copolymerization reaction. On other hand, noncovalent functionalization is based on electrostatic or π interactions of functional groups to cDots. Structural integrity is the leading advantage of noncovalent functionalization, since it has low negative effect on structure of cDots [52].

12.7.3 Doping

Doping is performed in cDots to monitor their properties, especially photoluminescence, by improving their fluorescence efficacy (Fig. 12.3C) [53]. Doped cDots are widely prepared using heteroatoms such as boron, nitrogen, phosphorous, sulfur, and fluorine [54]. Further, co-doping is also carried out using these heteroatoms. Hydrothermal method is commonly exploited for production of doped or co-doped cDots as compared to other synthesis methods. Precursors, preparatory methods, and type of doping have considerable influence on QY of cDots. As per reports, doped and co-doped cDots can be exploited in various applications including electronics, optical sensors, etc. [55]. Likewise, silicon-doped cDot developed by Qian et al. offered enhanced emission efficiency, low toxicity, resistance to photobleaching, and great biolabeling ability [56].

12.8 Properties of carbon quantum dots

An ideal QD-based bioimaging agent is expected to be target specific, accumulate at target location, easily operable, protect against photobleaching, nontoxic, and have high QY. cDots have acquired worldwide attention as imaging agent for achieving most of these features such as its facile synthesis, and properties including photostability, chemical stability, biocompatibility, tuneable photoluminescence, etc [57–59]. Small size, low toxicity, high hydrophilicity, biocompatibility, and excitation wavelength–dependent photoluminescence emission are prominent characters of cDots that can make them suitable for biomedical applications.

12.8.1 Fluorescence

There are two sources to develop fluorescence in cDots, viz. from bandgap transitions of conjugated π-domains and fluorescence associated from surface defects [60]. In the former mechanism to produce fluorescence, bandgap transitions are generated from conjugated π-domains and they are originated from π-electron rich sp^2 hybridized islands. It is being reported to be performed through reduction of graphene oxides using Hummer's method [61]. In such bandgap transitions, graphene sheets are single-layered to prevent interlayer quenching [62]. Secondly, fluorescence can also be developed from sites of surface defects that lack suitable sp^2 domain and can hold surface energy. The functionalized surface defects and hybridized carbon can follow such kind of fluorescence. Surface carrying multiple defective sites with different excitation and emission wavelength can have multicolor emission collectively [63,64] that is focused in blue and green range of visible light spectrum [65]. Moreover, surface activation by passivation or functionalization can make surface defect more stable and hence be helpful in achieving brighter fluorescence emissions [23]. cDots have unique property of tuneable fluorescence. Though even without surface passivation it carries tuneable emission, it reduces its QY due to unstable surface defects that cause decrease in radiative recombination. Passivation provides stability to sites of surface defects and promotes strong fluorescence emission.

12.8.2 Quantum yield

QY measures the efficiency to convert absorbed light into emitted light in the form of fluorescence. Often, fluorophores with high QY also release strong fluorescence, even at low concentration. Hence, high QY is also economically favorable as it reduces the quantity of fluorophores required for the process. Generally, bare cDots are reported to carry low QY (less than 10%). Surface activation using doping or surface functionalization can enhance their QY. Further, QY can be increased by doping of passivated cDots with inorganic dopants [66]. cDots with high fluorescence QY can show great performance in desirable applications, but efficient methods to synthesize high QY cDot are still under progress. Chemical doping with heteroatoms is one of the popular pathways to create cDots with tuneable intrinsic properties. A report showed synthesis of cDot with intense green emission under 420 nm excitation with high QY (46.4%). It was prepared using diammonium hydrogen citrate and urea, and these cDots carry low toxicity and biocompatible that make them suitable for future applications in cellular imaging [67]. A study was able to isolate cDots with ultrahigh QY (upto 94.5%) derived from folic acid using hydrothermal approach. These ultrabright cDots have ability to get executed in various biomedical applications [68]. Stable blue fluorescent nitrogen doped cDots with a very high QY (upto 81%) has been reported. This novel cDot is also synthesized using rapid one-step hydrothermal approach and has potential to be used in biomedical sensing applications for color switch sensing and imaging [69]. Cysteine-based cDots exhibit higher QY as compared to other amino acids [70,71].

12.9 cDot in bioimaging

cDot is better than semiconductor QDs in terms of optical properties, photochemical and chemical stability. Besides, carbon is prominently nontoxic and nature-friendly. These features make them a desirable choice in bioimaging applications for both in vivo and in vitro imaging such as various kind of cells and cell organelle imaging, and bioimaging-dependent drug delivery systems (Fig. 12.4) [72]. Generally, carbon cores of cDots do not show any cytotoxicity. However, agents used in surface passivation might lead to toxicity [63,73]. It is being suggested to execute low cytotoxicity agents for cDot passivation for safe in vivo imaging. cDots have potential to show multicolor emissions, which have great significance in bioimaging as it allows to control and select the excitation and emission wavelength [74]. Prior to bioimaging, usually cells are incubated with cDots to ensure that they enter the cells, which is reported to be temperature dependent. No cDots were found inside cells at temperature of 48°C [75]. Studies have suggested that cDots are probably internalizing in cells through endocytosis. Also, cDot intake might overcome by its interaction with cell membrane translocation peptides that let it cross the barrier [63]. A study reported synthesis of cDot using citric acid that possessed high fluorescence. They reported its role in real-time imaging,

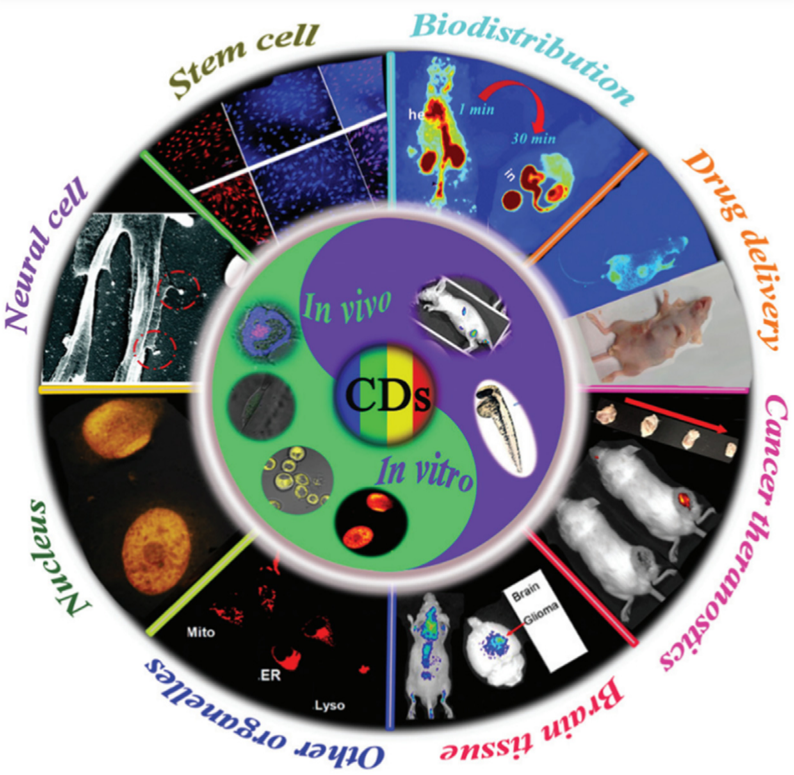
Stem cell
Biodistribution
1 min
30 min
he
in
Drug delivery
Cancer theranostics
Brain tissue
Brain
Glioma
Other organelles
Mito
ER
Lyso
Nucleus
Neural cell
In vivo
In vitro
CDs

Figure 12.4 Schematic representation of applications of fluorescent cDots in in vivo and in vitro bioimaging. *cDots*, carbon dots.
Reprinted with permission from H. Li, X. Yan, D. Kong, R. Jin, C. Sun, D. Du, et al. Recent advances in carbon dots for bioimaging applications. *Nanoscale Horizons* 5(2) (2020) 218−234, copyright 2019 Royal Society of Chemistry.

particularly for target-specific drug delivery of derivatives of hyaluronic acid in liver diseases [76]. Frasconi et al. developed labeling probe using carbon nano-onions for bioimaging and modified it by oxidation of surface defects for adding carboxyl group. It had high water dispersion, cell internalization ability, and target specificity [77]. In a study, *Escherichia coli* (bacteria), *Aspergillus aculeatus* (fungi), and *Fomitopsis* sp. (fungi) cells were used to test the application of three cDots in bioimaging. Three types of cDots (blue, green, and yellow) provided blue, green, and red color fluorescent signals with significant intensity for cell imaging at their respective excitation wavelengths, and they were easily internalized into cells via endocytosis (Fig. 12.5) [78].

12.9.1 In vitro imaging

cDots for in vitro bioimaging have been developing over time along with their application in drug delivery and biosensing. In regard to bioimaging, cDots have been emerging as an alternative due to their great optical properties along with low

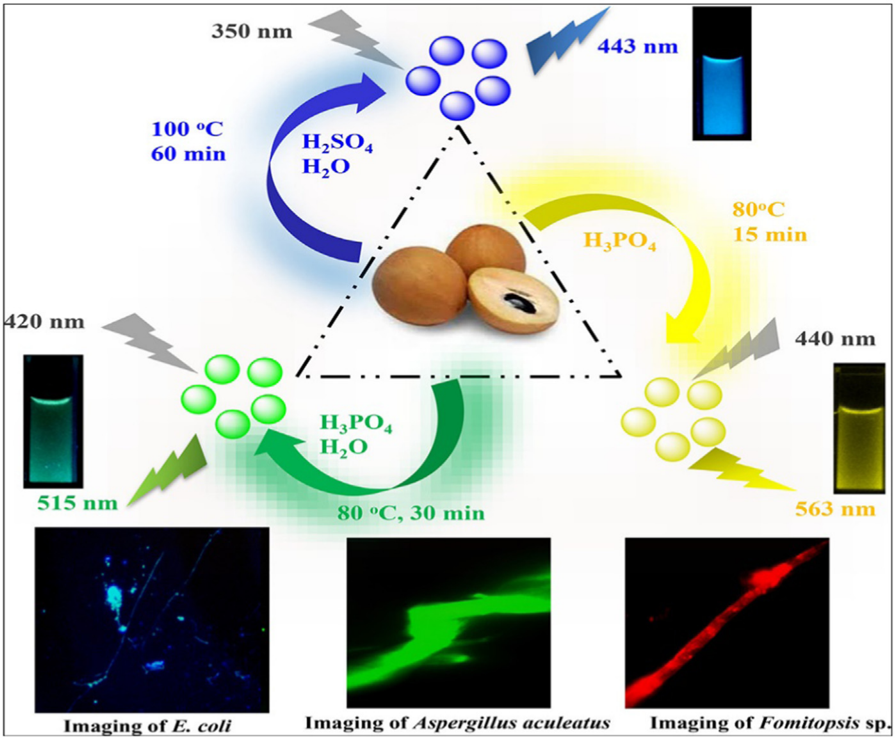
350 nm
443 nm
100 °C
60 min
H_2SO_4
H_2O
80°C
15 min
H_3PO_4
420 nm
440 nm
H_3PO_4
H_2O
515 nm
80 °C, 30 min
563 nm
Imaging of *E. coli*
Imaging of *Aspergillus aculeatus*
Imaging of *Fomitopsis* sp.

Figure 12.5 Imaging of various microbiota using C dots.
Reprinted with permission from M. Frasconi, V. Maffeis, J. Bartelmess, L. Echegoyen, and S. Giordani. Highly surface functionalized carbon nano-onions for bright light bioimaging. *Methods and Applications in Fluorescence* 3(4) (2015) 044005, copyright 2019 Elsevier Ltd.

toxicity levels. Optical properties of cDots have been suggested to be dependent strongly on local environment and surface chemistry. Synthesis process also play an important role in deciding their potential. Various synthesis processes have been available to develop cDots. Recently, cDot synthesis using natural resources has been gaining much attention for its easy, and economical route and provide water soluble cDot that is favorable for bioimaging purpose. Likewise, a study showed synthesis of aqueous cDot using spices, i.e., cinnamon, turmeric, red chilli, and black pepper by one-pot green hydrothermal method. These spices are known for their medicinal properties. cDots were characterized and showed high optical performance and QY of 43.6%. Results indicate cDot from spices are easily distinguishable when internalized in cells due to its self-fluorescence that is different from its background. It is suitable for in vitro imaging, preventing interference of unwanted autofluorescence of cells. Further, they reported that tumor inhibition can be observed while incubating cDots with tumor cells [79] (Table 12.1).

12.9.2 In vivo imaging

In vivo imaging agent is ideally expected to carry high fluorescence, be target specific, be nontoxic, have biocompatibility, and be resistant to photobleaching. Semiconductors based on QDs are extensively studied for bioimaging. However, they exhibit heavy metals such as cadmium that can be extremely toxic in in vivo imaging even at lower concentration [94]. Hence, cDots with nontoxic precursors have been studied as alternative. A sustainable process to produce high luminescent cDot has been reported by Huang et al., in which cDots were prepared using glycerol as carbon source and combined synthesis with surface functionalization and passivation in single step. cDots were directly fed to zebra fish for in vivo imaging. These cDots caused no harm and possessed improved cellular permeability [95]. In vivo bioimaging applications of cDot can reach out to diseases diagnosis and treatment. Likewise, exploitation of cDot for capping mesoporous silica particles to form drug delivery as well as cell imaging system has been reported in a study. These cDots were having low cytotoxicity and strong luminescence. This system has been observed to increase efficiency of anticancer drug loaded nanocomposite to kill cancer cells [96]. In order to treat brain associated critical diseases such as Alzheimer or brain cancer, target specificity and ability to crossing blood-brain barrier is a major concern. Various therapies are limited due to lack of ability to cross blood-brain barrier. cDots with size of <3 nm are observed to have ability to cross blood-brain barrier, targeting glioma cells [58,71]. Tryptophan-based cDots were developed and tested in zebra fish. These cDots are recognized by LAT1 transporters, which confirmed their potential to cross the blood-brain barrier [97] (Table 12.2).

12.9.3 Single-molecule imaging

cDots are being reported to be exploited as fluorescent label to examine single molecules individually. Single-molecule imaging involves localizing the position of particular molecule, which is considered to be a most popular approach to super resolution

Table 12.1 CDots (carbon dots) in in vitro bioimaging.

Type and source	Size (nm)	Quantum yield	Target cell line	Application	References
CDs, oxalic acid	2–5	28.7	SiLa cells	Cytotoxicity studies	[80]
CDs, camphor	2–6	35.26	SHSY5Y cells	Bioimaging and cytotoxicity	[81]
CDs, ethylene diamine	2–3	30.2	L929 cell line	Multicolor nanoprobe imaging	[82]
Nitrogen doped CDs, polyethyleneimine (PEI)	5	69	HeLa cells	Bioimaging	[83]
CDs, cumin	6–9	5.33	MCF-7 cells	Bioimaging	[84]
Reduced CDs, Lemon juice	4.6	28	HeLa cells	Bioimaging	[85]
Folic acid tagged CDs, dandelion and EDA	3.5	13.9	HepG-2, MCF-7 and PC-12 cells	Targeted bioimaging, differentiating cancerous and normal cells	[86]
CDs, beta-cyclodextrin and PEI	2–4	30	H1299 cells	Bioimaging	[87]
Nitrogen doped CDs, citric acid and PEI	2.6	51	293 T cells	Real time live cell imaging	[88]
CDs, fruit juice	2–5	7	Osteoblasts	Bioimaging	[89]
Silicon doped CDs, hydroquinone	7	19.2	HeLa cells	Bioimaging	[55]
CDs, curcumin and PEI	4–5	8.607	NIH 3T3, A549 and HCT-15 cells	Multicolor biolabeling	[90]
CDs, polyethylene glycol	2–4	3.5	HepG-2 cells	Bioimaging	[91]
Magnesium/nitrogen double doped CDs, citric acid	1–2	83	L929 cells	Bioimaging	[92]
Nitrogen doped CDs, citric acid	0.5–6	7–15	Retinal epithelial, lens epithelial and CHO cell lines	Bioimaging	[93]

Table 12.2 cDots (carbon dots) in in vivo bioimaging.

Type and source	Size (nm)	Quantum yield	Target tissue	Application	References
CDs, oxalic acid	2–5	28.7	Bean sprouts	Bioimaging	[98]
CDs, graphite, and carbon nanotubes	3–5	3–6	Nude mouse	Biodistribution	[99]
Nitrogen doped CDs, polyethylenic amine	5	69	BALB/c-nu mice	Bioimaging	[83]
ZnS doped CDs, PEG diamine	4–5	–	DBA/1 mouse	Bioimaging	[82]
Reduced CDs, lemon juice	4.6	28	Nude mouse	Bioimaging	[85]
CDs, curcumin, and PEI	4–5	8.607	Zebrafish embryos	Bioimaging	[91]
Nitrogen doped CDs, citric acid	0.5–6	7–15	Porcine ocular globes (ex vivo) Mice (post mortem)	Bioimaging	[99]
CDs, fruit juice	4–5	20–35	Zebrafish embryos	Bioimaging	[100]

imaging [101]. Previous studies showed cDots having properties such as excellent optical properties, photostability, and high photon count, making them suitable for single-molecule imaging. They have ability to fluctuate their intensity with ionic dark states, resembling conventional semiconductor QDs. A super-resolution imaging using optical fluctuation imaging was being carried out [102]. Recently, Khan et al. studied cDot with yellow emission for specific binding on RNA molecules in nucleolus of HeLa cells. cDots displayed superior optical properties, such as excitation independent emission and high QY. Intensity fluctuation with high photon count facilitated single molecule imaging. Hence, these studies are elucidating the cDots' applications in various areas of the field of bioimaging [103].

12.10 Conclusion

Fluorescence imaging enables visualization of biological processes and has been instrumental in the co-localization of a tracing molecule, gene expression analyses, enzyme activity, and calcium imaging. Fluorescent dyes have been extensively used for imaging applications for decades enabling scientists visualize and analyze biological events. Though organic fluorophores offer high QY, factors like photobleaching, low photostability, narrow excitation, and emission windows limit their practical applications. Semiconductor quantum dots, on the other hand, offer tuneable fluorescence emissions owing to the quantum confinement effect. QDs offer considerably higher fluorescence providing high sensitivity, and also are resistant to photobleaching compared to organic dyes and fluorescent proteins [31]. Though QDs are superior alternatives to organic dyes, toxicity and environmental hazard remain huge concerns and impede their use in in vivo imaging.

cDot in QDs is a new concept and has already begun to contribute in revolutionizing bioimaging. Apart from bioimaging, cDot has also unlocked new platforms in biomedical applications such as diseases diagnosis, drug delivery, biosensing, etc. Its luminescence, wide range of sources, nontoxicity, and biocompatibility are major reasons behinds its exploitation in biomedical field. Though bare cDot have low QY, its surface functionalization and passivation can enhance its QY to a great extent.

Since the accidental discovery in 2004 during the electrophoretic separation of SWCNTs [43], cDots have gained wide acceptance among scientists for use in bioimaging owing to their cost-effectiveness and easy synthesis, high surface-area-to-volume ratio, high QY, tunable optical properties [60], bio- and cytocompatibility, photostability, low interaction with proteins, and solubility in aqueous medium [104]. Since then, cDots have been referred to as the quantum sized carbon analogs with strong comparable photoluminescence and fluorescence [105]. High QY cDots can be synthesized from a range of sources, including natural precursors [106,107]. Relatively nontoxic pertaining to the organic core of cDots, surface functionalization makes cDots cyto-compatible in a range of cell types and they are also reported to be hemocompatible [108]. However, cDots still need to overcome few more limitations. Generally, preparation stages of cDots are multistep, tedious, and often expensive [79]. Moreover, cDots' stability is limited to few weeks of its synthesis. cDots precursors and their structure have impact on their electrical, chemical, and optical properties [80].

References

[1] Who Invented the Microscope? 2021. Livescience.Com. Available from: https://www.livescience.com/39649-who-invented-the-microscope.html.

[2] Z.-Y. Chen, Y.-X. Wang, Y. Lin, J.-S. Zhang, F. Yang, Q.-L. Zhou, et al., Advance of molecular imaging technology and targeted imaging agent in imaging and therapy, BioMed Research International 2014 (2014) 819324.

[3] U. Speck, Contrast agents: X-ray contrast agents and molecular imaging—a contradiction, Molecular Imaging I (2008) 167–175.

[4] MRI Vs. CT Scan | Health Images. 2021. Health Images. Available from: https://www.healthimages.com/mri-vs-ct-scan/.

[5] Magnetic Resonance Imaging (MRI). 2021. Nibib.Nih.Gov. Available from: https://www.nibib.nih.gov/science-education/science-topics/magnetic-resonance-imaging-mri.

[6] Vadivambal, R, and D S. Jayas. 2021. Bio-Imaging. Available from: https://www.taylorfrancis.com/books/9780429168147.

[7] Home - PMC - NCBI. 2021. Ncbi.Nlm.Nih.Gov. Available from: https://www.ncbi.nlm.nih.gov/pmc/articles.

[8] K. Chen, X. Chen, Design and development of molecular imaging probes, Current Topics in Medicinal Chemistry 10 (12) (2010) 1227–1236. Available from: https://doi.org/10.2174/156802610791384225.

[9] L. Abou-Elkacem, S.V. Bachawal, J.K. Willmann, Ultrasound molecular imaging: moving toward clinical translation, European Journal of Radiology 84 (9) (2015) 1685–1693. Available from: https://doi.org/10.1016/j.ejrad.2015.03.016.

[10] S.M. Okarvi, H.R. Maecke, Peptide applications in biomedicine, biotechnology and bioengineering. Peptide Applications in Biomedicine, Biotechnology and Bioengineering (2018) 431–483. Available from: https://doi.org/10.1016/B978-0-08-100736-5.00019-3.

[11] I. Fernández-Barahona, M. Muñoz-Hernando, J. Ruiz-Cabello, F. Herranz, J. Pellico, Iron oxide nanoparticles: an alternative for positive contrast in magnetic resonance imaging, Inorganics 8 (4) (2020) 28.

[12] S. Mirza, M.S. Ahmad, M.I.A. Shah, M. Ateeq, Magnetic nanoparticles: drug delivery and bioimaging applications, Metal nanoparticles for drug delivery and diagnostic applications, Elsevier, 2020, pp. 189–213. Available from: http://doi.org/10.1016/B978-0-12-816960-5.00011-2.

[13] N.J. Halas, S. Lal, W.-S. Chang, S. Link, P. Nordlander, Plasmons in strongly coupled metallic nanostructures, Chemical Reviews 111 (6) (2011) 3913–3961.

[14] W. Li, X. Chen, Gold nanoparticles for photoacoustic imaging, Nanomedicine 10 (2) (2015) 299–320.

[15] J. Guo, K. Rahme, Y. He, L.-L. Li, J.D. Holmes, C.M. O'Driscoll, Gold nanoparticles enlighten the future of cancer theranostics, International Journal of Nanomedicine 12 (2017) 6131. Available from: https://doi.org/10.2147/IJN.S140772.

[16] M.H. Oh, N. Lee, H. Kim, S.P. Park, Y. Piao, J. Lee, et al., Large-scale synthesis of bioinert tantalum oxide nanoparticles for X-ray computed tomography imaging and bimodal image-guided sentinel lymph node mapping, Journal of the American Chemical Society 133 (14) (2011) 5508–5515.

[17] J.F. Hainfeld, D.N. Slatkin, T.M. Focella, H.M. Smilowitz, Gold nanoparticles: a new X-ray contrast agent, The British Journal of Radiology 79 (939) (2006) 248–253.

[18] J. Kim, N. Lee, T. Hyeon, Recent development of nanoparticles for molecular imaging, Philosophical Transactions of the Royal Society A: Mathematical, Physical and Engineering Sciences 375 (2107) (2017) 20170022. Available from: https://doi.org/10.1098/rsta.2017.0022.

[19] S. Mura, J. Nicolas, P. Couvreur, Stimuli-responsive nanocarriers for drug delivery, Nature Materials 12 (11) (2013) 991–1003.

[20] C. Gimenez, C. de la Torre, M. Gorbe, E. Aznar, F. Sancenon, J.R. Murguia, et al., Gated mesoporous silica nanoparticles for the controlled delivery of drugs in cancer cells, Langmuir 31 (12) (2015) 3753–3762.

[21] F. Pratiwi, Wijaya, C.W. Kuo, S.-H. Wu, Y.-P. Chen, C.Y. Mou, et al., The bioimaging applications of mesoporous silica nanoparticles, The Enzymes 43 (2018) 123−153. Available from: https://doi.org/10.1016/bs.enz.2018.07.006.

[22] J. Lin, Y. Huang, P. Huang, Graphene-based nanomaterials in bioimaging, Biomedical Applications of Functionalized Nanomaterials (2018) 247−287.

[23] S. Hu, J. Liu, J. Yang, Y. Wang, S. Cao, Laser synthesis and size tailor of carbon quantum dots, Journal of Nanoparticle Research 13 (12) (2011) 7247−7252.

[24] G. Peng, M. Umair, I. Hussain, I. Javed, Nanosilver at the interface of biomedical applications, toxicology, and synthetic strategies, Metal Nanoparticles for Drug Delivery and Diagnostic Applications (2020) 119−139. Available from: https://doi.org/10.1016/B978-0-12-816960-5.00008-2.

[25] J. Zheng, P.R. Nicovich, R.M. Dickson, Highly fluorescent noble-metal quantum dots, Annual Review of Physical Chemistry 58 (2007) 409−431.

[26] S.-I. Tanaka, J. Miyazaki, D.K. Tiwari, T. Jin, Y. Inouye, Fluorescent platinum nanoclusters: synthesis, purification, characterization, and application to bioimaging, Angewandte Chemie 123 (2) (2011) 451−455.

[27] Y. An, Y. Ren, M. Bick, A. Dudek, E.H.-W. Waworuntu, J. Tang, et al., Highly fluorescent copper nanoclusters for sensing and bioimaging, Biosensors and Bioelectronics 154 (2020) 112078.

[28] G. Le, Xavier, C. Spies, N. Daum, G. Jung, M. Schneider, Highly fluorescent silver nanoclusters stabilized by glutathione: a promising fluorescent label for bioimaging, Nano Research 5 (6) (2012) 379−387.

[29] L. Zhang, E. Wang, Metal nanoclusters: new fluorescent probes for sensors and bioimaging, Nano Today 9 (1) (2014) 132−157.

[30] S. Zhu, J. Zhang, C. Qiao, S. Tang, Y. Li, W. Yuan, et al., Strongly green-photoluminescent graphene quantum dots for bioimaging applications, Chemical Communications 47 (24) (2011) 6858−6860.

[31] B.A. Kairdolf, A.M. Smith, T.H. Stokes, M.D. Wang, A.N. Young, S. Nie, Semiconductor quantum dots for bioimaging and biodiagnostic applications, Annual Review of Analytical Chemistry 6 (2013) 143−162.

[32] E. Hutter, D. Maysinger, Gold nanoparticles and quantum dots for bioimaging, Microscopy Research and Technique 74 (7) (2011) 592−604.

[33] S.N. Baker, G.A. Baker, Luminescent carbon nanodots: emergent nanolights, Angewandte Chemie International Edition 49 (38) (2010) 6726−6744.

[34] Y. Wang, A. Hu, Carbon quantum dots: synthesis, properties and applications, Journal of Materials Chemistry C 2 (34) (2014) 6921−6939. Available from: https://doi.org/10.1039/c4tc00988f.

[35] A. Kasouni, T. Chatzimitakos, C. Stalikas, Bioimaging applications of carbon nanodots: a review, C—Journal of Carbon Research 5 (2) (2019) 19. Available from: https://doi.org/10.3390/c5020019.

[36] T.G. Chatzimitakos, A.I. Kasouni, A.N. Troganis, C.D. Stalikas, Carbonization of human fingernails: toward the sustainable production of multifunctional nitrogen and sulfur codoped carbon nanodots with highly luminescent probing and cell proliferative/migration properties, ACS Applied Materials & Interfaces 10 (18) (2018) 16024−16032.

[37] T. Chatzimitakos, A. Kasouni, L. Sygellou, I. Leonardos, A. Troganis, C. Stalikas, Human fingernails as an intriguing precursor for the synthesis of nitrogen and sulfur-doped carbon dots with strong fluorescent properties: analytical and bioimaging applications, Sensors and Actuators B: Chemical 267 (2018) 494−501.

[38] X. Wen, L. Shi, G. Wen, Y. Li, C. Dong, J. Yang, et al., Green synthesis of carbon nanodots from cotton for multicolor imaging, patterning, and sensing, Sensors and Actuators B: Chemical 221 (2015) 769−776.

[39] A. Sachdev, P. Gopinath, Green synthesis of multifunctional carbon dots from coriander leaves and their potential application as antioxidants, sensors and bioimaging agents, Analyst 140 (12) (2015) 4260−4269.

[40] J. Zhou, C. Booker, R. Li, X. Zhou, T.-K. Sham, X. Sun, et al., An electrochemical avenue to blue luminescent nanocrystals from multiwalled carbon nanotubes (MWCNTs), Journal of the American Chemical Society 129 (4) (2007) 744−745.

[41] Y.-P. Sun, B. Zhou, Y. Lin, W. Wang, K.A. Shiral Fernando, P. Pathak, et al., Quantum-sized carbon dots for bright and colorful photoluminescence, Journal of the American Chemical Society 128 (24) (2006) 7756−7757.

[42] B. Gayen, S. Palchoudhury, J. Chowdhury, Carbon dots: a mystic star in the world of nanoscience, Journal of Nanomaterials 2019 (2019). Available from: https://doi.org/10.1155/2019/3451307.

[43] X. Xu, R. Ray, Y. Gu, H.J. Ploehn, L. Gearheart, K. Raker, et al., Electrophoretic analysis and purification of fluorescent single-walled carbon nanotube fragments, Journal of the American Chemical Society 126 (40) (2004) 12736−12737.

[44] B. De, N. Karak, A green and facile approach for the synthesis of water-soluble fluorescent carbon dots from banana juice, RSC Advances 3 (22) (2013) 8286−8290.

[45] S. Zhu, Q. Meng, L. Wang, J. Zhang, Y. Song, H. Jin, et al., Highly photoluminescent carbon dots for multicolor patterning, sensors, and bioimaging, Angewandte Chemie 125 (14) (2013) 4045−4049.

[46] B. Zhang, C.-Y. Liu, Y. Liu, A novel one-step approach to synthesize fluorescent carbon nanoparticles, European Journal of Inorganic Chemistry 28 (2010) 4411−4414.

[47] Y. Liu, N. Xiao, N. Gong, H. Wang, X. Shi, W. Gu, et al., One-step microwave-assisted polyol synthesis of green luminescent carbon dots as optical nanoprobes, Carbon 68 (2014) 258−264.

[48] J. Zuo, T. Jiang, X. Zhao, X. Xiong, S. Xiao, Z. Zhu, Preparation and application of fluorescent carbon dots, Journal of Nanomaterials 2015 (2015) 787862.

[49] M. Farshbaf, S. Davaran, F. Rahimi, N. Annabi, R. Salehi, A. Akbarzadeh, Carbon quantum dots: recent progresses on synthesis, surface modification and applications, Artificial Cells, Nanomedicine, and Biotechnology 46 (7) (2018) 1331−1348.

[50] M. Tuerhong, X.U. Yang, Y.I.N. Xue-Bo, Review on carbon dots and their applications, Chinese Journal of Analytical Chemistry 45 (1) (2017) 139−150.

[51] K. Dimos, Carbon quantum dots: surface passivation and functionalization, Current Organic Chemistry 20 (6) (2016) 682−695.

[52] F. Yan, Y. Jiang, X. Sun, Z. Bai, Y. Zhang, X. Zhou, Surface modification and chemical functionalization of carbon dots: a review, Microchimica Acta 185 (9) (2018) 1−34. Available from: https://doi.org/10.1007/s00604-018-2953-9.

[53] T.S. Atabaev, Doped carbon dots for sensing and bioimaging applications: a minireview, Nanomaterials 8 (5) (2018) 342.

[54] F. Li, D. Yang, H. Xu, Non-metal-heteroatom-doped carbon dots: synthesis and properties, Chemistry−A European Journal 25 (5) (2019) 1165−1176.

[55] G. Kandasamy, Recent advancements in doped/co-doped carbon quantum dots for multi-potential applications, C—Journal of Carbon Research 5 (2) (2019) 24. Available from: https://doi.org/10.3390/c5020024.

[56] Z. Qian, X. Shan, L. Chai, J. Ma, J. Chen, H. Feng, Si-doped carbon quantum dots: a facile and general preparation strategy, bioimaging application, and multifunctional

sensor, ACS Applied Materials & Interfaces 6 (9) (2014) 6797−6805. Available from: https://doi.org/10.1021/am500403n.

[57] M.J. Molaei, Carbon quantum dots and their biomedical and therapeutic applications: a review, RSC Advances 9 (12) (2019) 6460−6481. Available from: https://doi.org/10.1039/c8ra08088g.

[58] M. Zheng, S. Ruan, S. Liu, T. Sun, D. Qu, H. Zhao, et al., Self-targeting fluorescent carbon dots for diagnosis of brain cancer cells, ACS Nano 9 (11) (2015) 11455−11461.

[59] X.T. Zheng, A. Ananthanarayanan, K.Q. Luo, P. Chen, Glowing graphene quantum dots and carbon dots: properties, syntheses, and biological applications, Small 11 (14) (2015) 1620−1636.

[60] L.I. Cao, M.J. Meziani, S. Sahu, Y.-P. Sun, Photoluminescence properties of graphene vs other carbon nanomaterials, Accounts of Chemical Research 46 (1) (2013) 171−180.

[61] W.S. Hummers Jr, R.E. Offeman, Preparation of graphitic oxide, Journal of the American Chemical Society 80 (6) (1958). 1339-1339.

[62] T. Gokus, R.R. Nair, A. Bonetti, M. Bohmler, A. Lombardo, K.S. Novoselov, et al., Making graphene luminescent by oxygen plasma treatment, ACS Nano 3 (12) (2009) 3963−3968.

[63] S. Lim, W. Ying, Shen, Z. Gao, Carbon quantum dots and their applications, Chemical Society Reviews 44 (1) (2015) 362−381. Available from: https://doi.org/10.1039/c4cs00269e.

[64] M.J. Molaei, A review on nanostructured carbon quantum dots and their applications in biotechnology, sensors, and chemiluminescence, Talanta 196 (2019) 456−478.

[65] A.P. Demchenko, M.O. Dekaliuk, Novel fluorescent carbonic nanomaterials for sensing and imaging, Methods and Applications in Fluorescence 1 (4) (2013) 042001.

[66] S. Sadjadi, The utility of carbon dots for photocatalysis, Emerging carbon materials for catalysis, Elsevier, 2021, pp. 123−160. Available from: http://doi.org/10.1016/B978-0-12-817561-3.00004-4.

[67] W.U. Khan, D. Wang, W. Zhang, Z. Tang, X. Ma, X. Ding, et al., High quantum yield green-emitting carbon dots for Fe (III) detection, biocompatible fluorescent ink and cellular imaging, Scientific Reports 7 (1) (2017) 1−9. Available from: https://doi.org/10.1038/s41598-017-15054-9.

[68] H. Liu, Z. Li, Y. Sun, X. Geng, Y. Hu, H. Meng, et al., Synthesis of luminescent carbon dots with ultrahigh quantum yield and inherent folate receptor-positive cancer cell targetability, Scientific Reports 8 (1) (2018) 1−8. Available from: https://doi.org/10.1038/s41598-018-19373-3.

[69] Z. Yi, X. Li, H. Zhang, X. Ji, W. Sun, Y. Yu, et al., High quantum yield photoluminescent N-doped carbon dots for switch sensing and imaging, Talanta 222 (2021) 121663. Available from: https://doi.org/10.1016/j.talanta.2020.121663.

[70] A. Shore, Retraction: amino acid derived highly luminescent, heteroatom-doped carbon dots for label-free detection of Cd2 + /Fe3 + , cell imaging and enhanced antibacterial activity, RSC Advances 8 (69) (2018). 39784-39784.

[71] J.A. Jaleel, K. Pramod, Artful and multifaceted applications of carbon dot in biomedicine, Journal of Controlled Release 269 (2018) 302−321.

[72] H. Li, X. Yan, D. Kong, R. Jin, C. Sun, D. Du, et al., Recent advances in carbon dots for bioimaging applications, Nanoscale Horizons 5 (2) (2020) 218−234.

[73] Y. Wang, P. Anilkumar, L. Cao, J.-H. Liu, P.G. Luo, K.N. Tackett, et al., Carbon dots of different composition and surface functionalization: cytotoxicity issues relevant to fluorescence cell imaging, Experimental Biology and Medicine 236 (11) (2011) 1231−1238.

[74] C. Liu, P. Zhang, X. Zhai, F. Tian, W. Li, J. Yang, et al., Nano-carrier for gene delivery and bioimaging based on carbon dots with PEI-passivation enhanced fluorescence, Biomaterials 33 (13) (2012) 3604−3613.

[75] L. Cao, X. Wang, M.J. Meziani, F. Lu, H. Wang, P.G. Luo, et al., Carbon dots for multiphoton bioimaging, Journal of the American Chemical Society 129 (37) (2007) 11318−11319.

[76] E.J. Goh, K.S. Kim, Y.R. Kim, H.S. Jung, S. Beack, W.H. Kong, et al., Bioimaging of hyaluronic acid derivatives using nanosized carbon dots, Biomacromolecules 13 (8) (2012) 2554−2561. Available from: https://doi.org/10.1021/bm300796q.

[77] J.R. Bhamore, S. Jha, T.J. Park, S.K. Kailasa, Green synthesis of multi-color emissive carbon dots from Manilkara zapota fruits for bioimaging of bacterial and fungal cells, Journal of Photochemistry and Photobiology B: Biology 191 (2019) 150−155.

[78] M. Frasconi, V. Maffeis, J. Bartelmess, L. Echegoyen, S. Giordani, Highly surface functionalized carbon nano-onions for bright light bioimaging, Methods and Applications in Fluorescence 3 (4) (2015) 044005.

[79] N. Vasimalai, V. Vilas-Boas, J. Gallo, M. de Fátima Cerqueira, M. Menéndez-Miranda, J.M. Costa-Fernández, et al., Green synthesis of fluorescent carbon dots from spices for in vitro imaging and tumour cell growth inhibition, Beilstein Journal of Nanotechnology 9 (1) (2018) 530−544. Available from: https://doi.org/10.3762/bjnano.9.51.

[80] V. Mishra, A. Patil, S. Thakur, P. Kesharwani, Carbon dots: emerging theranostic nanoarchitectures, Drug Discovery Today 23 (6) (2018) 1219−1232.

[81] G. Oza, M. Ravichandran, V.-I. Merupo, S. Shinde, A. Mewada, J.T. Ramirez, et al., Camphor-mediated synthesis of carbon nanoparticles, graphitic shell encapsulated carbon nanocubes and carbon dots for bioimaging, Scientific reports 6 (1) (2016) 1−9.

[82] X. Zhai, P. Zhang, C. Liu, T. Bai, W. Li, L. Dai, et al., Highly luminescent carbon nanodots by microwave-assisted pyrolysis, Chemical Communications 48 (64) (2012) 7955−7957.

[83] J. Wang, P. Zhang, C. Huang, G. Liu, K.C.-F. Leung, Y.X.J. Wáng, High performance photoluminescent carbon dots for in vitro and in vivo bioimaging: effect of nitrogen doping ratios, Langmuir 31 (29) (2015) 8063−8073.

[84] V. Roshni, V. Gujar, H. Pathan, S. Islam, M. Tawre, K. Pardesi, et al., Bioimaging applications of carbon dots (C. dots) and its cystamine functionalization for the sensitive detection of Cr (VI) in aqueous samples, Journal of Fluorescence 29 (6) (2019) 1381−1392.

[85] H. Ding, Y. Ji, J.-S. Wei, Q.-Y. Gao, Z.-Y. Zhou, H.-M. Xiong, Facile synthesis of red-emitting carbon dots from pulp-free lemon juice for bioimaging, Journal of Materials Chemistry B 5 (26) (2017) 5272−5277.

[86] X. Zhao, J. Zhang, L. Shi, M. Xian, C. Dong, S. Shuang, Folic acid-conjugated carbon dots as green fluorescent probes based on cellular targeting imaging for recognizing cancer cells, RSC Advances 7 (67) (2017) 42159−42167.

[87] C. Yang, R.P. Thomsen, R. Ogaki, J. Kjems, B.M. Teo, Ultrastable green fluorescence carbon dots with a high quantum yield for bioimaging and use as theranostic carriers, Journal of Materials Chemistry B 3 (22) (2015) 4577−4584.

[88] S. Lu, S. Guo, P. Xu, X. Li, Y. Zhao, W. Gu, et al., Hydrothermal synthesis of nitrogen-doped carbon dots with real-time live-cell imaging and blood−brain barrier penetration capabilities, International Journal of Nanomedicine 11 (2016) 6325.

[89] X. Guo, Y. Zhu, L. Zhou, L. Zhang, Y. You, H. Zhang, et al., A facile and green approach to prepare carbon dots with pH-dependent fluorescence for patterning and bioimaging, RSC Advances 8 (66) (2018) 38091−38099.

[90] T. Pal, S. Mohiyuddin, G. Packirisamy, Facile and green synthesis of multicolor fluorescence carbon dots from curcumin: in vitro and in vivo bioimaging and other applications, ACS Omega 3 (1) (2018) 831–843.

[91] R.-J. Fan, Q. Sun, L. Zhang, Y. Zhang, A.-H. Lu, Photoluminescent carbon dots directly derived from polyethylene glycol and their application for cellular imaging, Carbon 71 (2014) 87–93.

[92] F. Li, C. Liu, J. Yang, Z. Wang, W. Liu, F. Tian, Mg/N double doping strategy to fabricate extremely high luminescent carbon dots for bioimaging, RSC Advances 4 (7) (2014) 3201–3205.

[93] B.B.̈ Karakoçak, J. Liang, S. Kavadiya, M.Y. Berezin, P. Biswas, N. Ravi, Optimizing the synthesis of red-emissive nitrogen-doped carbon dots for use in bioimaging, ACS Applied Nano Materials 1 (7) (2018) 3682–3692.

[94] S.-T. Yang, L. Cao, P.G. Luo, F. Lu, X. Wang, H. Wang, et al., Carbon dots for optical imaging in vivo, Journal of the American Chemical Society 131 (32) (2009) 11308–11309. Available from: https://doi.org/10.1021/ja904843x.

[95] Y.-F. Huang, X. Zhou, R. Zhou, H. Zhang, K.-B. Kang, M. Zhao, et al., One-pot synthesis of highly luminescent carbon quantum dots and their nontoxic ingestion by zebrafish for in vivo imaging, Chemistry–A European Journal 20 (19) (2014) 5640–5648.

[96] L. Zhou, Z. Li, Z. Liu, J. Ren, X. Qu, Luminescent carbon dot-gated nanovehicles for pH-triggered intracellular controlled release and imaging, Langmuir 29 (21) (2013) 6396–6403.

[97] K.J. Mintz, G. Mercado, Y. Zhou, Y. Ji, S.D. Hettiarachchi, P.Y. Liyanage, et al., Tryptophan carbon dots and their ability to cross the blood-brain barrier, Colloids and Surfaces B: Biointerfaces 176 (2019) 488–493.

[98] W. Lu, X. Gong, Z. Yang, Y. Zhang, Q. Hu, S. Shuang, et al., High-quality water-soluble luminescent carbon dots for multicolor patterning, sensors, and bioimaging, RSC Advances 5 (22) (2015) 16972–16979.

[99] H. Tao, K. Yang, Z. Ma, J. Wan, Y. Zhang, Z. Kang, et al., In vivo NIR fluorescence imaging, biodistribution, and toxicology of photoluminescent carbon dots produced from carbon nanotubes and graphite, Small 8 (2) (2012) 281–290.

[100] C. Dias, N. Vasimalai, M.P. Sárria, I. Pinheiro, V. Vilas-Boas, J. Peixoto, et al., Biocompatibility and bioimaging potential of fruit-based carbon dots, Nanomaterials 9 (2) (2019) 199.

[101] G. Patterson, M. Davidson, S. Manley, J. Lippincott-Schwartz, Superresolution imaging using single-molecule localization, Annual Review of Physical Chemistry 61 (2010) 345–367.

[102] A.M. Chizhik, S. Stein, M.O. Dekaliuk, C. Battle, W. Li, A. Huss, et al., Super-resolution optical fluctuation bio-imaging with dual-color carbon nanodots, Nano Letters 16 (1) (2016) 237–242.

[103] S. Khan, N.C. Verma, C. Nandi, C. Kanti, Carbon dots for single-molecule imaging of the nucleolus, ACS Applied Nano Materials (2018). Available from: https://doi.org/10.1021/acsanm.7b00175.

[104] G. Nocito, G. Calabrese, S. Forte, S. Petralia, C. Puglisi, M. Campolo, et al., Carbon dots as promising tools for cancer diagnosis and therapy, Cancers 13 (9) (2021) 1991.

[105] M. Bottini, C. Balasubramanian, M.I. Dawson, A. Bergamaschi, S. Bellucci, T. Mustelin, Isolation and characterization of fluorescent nanoparticles from pristine and oxidized electric arc-produced single-walled carbon nanotubes, The Journal of Physical Chemistry B 110 (2) (2006) 831–836.

[106] S. Chahal, N. Yousefi, N. Tufenkji, Green synthesis of high quantum yield carbon dots from phenylalanine and citric acid: role of stoichiometry and nitrogen doping, ACS Sustainable Chemistry & Engineering 8 (14) (2020) 5566−5575.

[107] Z. Deng, C. Liu, Y. Jin, J. Pu, B. Wang, J. Chen, High quantum yield blue-and orange-emitting carbon dots: one-step microwave synthesis and applications as fluorescent films and in fingerprint and cellular imaging, Analyst 144 (15) (2019) 4569−4574.

[108] A. Sharma, V. Panwar, V. Chopra, J. Thomas, S. Kaushik, D. Ghosh, Interaction of carbon dots with endothelial cells: implications for biomedical applications, ACS Applied Nano Materials 2 (9) (2019) 5483−5491.

Photocatalytic applications of carbon quantum dots for wastewater treatment

13

Umi Rabiatul Ramzilah P. Remli[1], *Azrina Abd Aziz*[1], *Lan Ching Sim*[2],
Minhaj Uddin Monir[3] *and Kah Hon Leong*[4]
[1]Faculty of Civil Engineering Technology, Universiti Malaysia Pahang, Kuantan, Pahang, Malaysia, [2]Department of Chemical Engineering, Lee Kong Chian Faculty of Engineering and Science, Universiti Tunku Abdul Rahman, Kajang, Selangor, Malaysia, [3]Department of Petroleum and Mining Engineering, Jashore University of Science and Technology, Jashore, Bangladesh, [4]Department of Environmental Engineering, Faculty of Engineering and Green Technology, Universiti Tunku Abdul Rahman, Jalan Universiti, Kampar, Perak, Malaysia

13.1 Overview on advanced oxidation process and photocatalysis

The excessive discharge of industrial effluent, worldwide production, and utilization of chemical products, as well as expanding world population contributes significantly to the increasing accumulation of bio recalcitrant organic pollutants in the environment [1]. In developing countries, this unpleasant trend is widespread due to the improper enforcement of environmental regulations and monitoring frameworks. A proportion of these organic pollutants remains unregulated and causes serious deterioration of the freshwater ecosystem. Presently, a large amount of various chemical pollutants containing wastewater are produced from domestic and industrial activities, which eventually pollute the environment [2,3]. Fresh, uncontaminated, and enough sanitary measures remain critical tohuman health and socioeconomic sustainability as these two are becoming endangered commodity at present [1,4,5]. In accordance with solving the present water crisis globally and acquiring more economic gain, an alternative for new water treatment technology that can completely remove organic pollutants is henceforth significant and necessary [6]. Owing to the expanding worldwide concern for environmental protection, advanced oxidation technology (AOT) pointed out the prominent role of a special class of oxidation technology defined as advanced oxidation process (AOPs) was developed. To date, studies have shown that AOPs still upheld as one of the favorable and reasonable methods for treating the water and wastewater to remove the contaminants [7–9]. AOPs stand out as one of the most environmentally friendly techniques used to remove bio recalcitrant organic pollutants that are not easily

Carbon Quantum Dots for Sustainable Energy and Optoelectronics. DOI: https://doi.org/10.1016/B978-0-323-90895-5.00004-7
© 2023 Elsevier Ltd. All rights reserved.

treatable by existing conventional treatment technologies due to their chemical stability [10]. The advantages and disadvantages of the existing water treatment method and photocatalytic system are summarized in Table 13.1.

AOPs allude to a set of chemical treatment procedures for removing organic pollutants in water and wastewater by oxidation. AOPs were first proposed for portable water treatment in the 1980s [9,11,12], which were then defined as oxidation processes involving the generation of hydroxyl radicals (OH-) in adequate amounts for water purification. The main mechanism of the AOPs function is the generation of highly reactive free radicals. AOPs include two phases of oxidation process: formation of strong oxidants (e.g., hydroxyl radicals) and the reaction of these oxidants with organic contaminants in water [13−15]. Table 13.2 depicts the oxidants used in different wastewater treatment techniques with corresponding oxidation potential values [16]. Among o them, OH- has stronger oxidation power than normally used oxidants and decomposes the organic compounds into moderately harmless compounds, such as CO_2, H_2O, or HCl.

To measure the effectiveness of the treatment, it is necessary to understand the selected type of AOPs, physical and chemical properties of pollutants, and operating parameters of the process. A variety of techniques were classified under the broad definition of AOPs. A list of possible techniques offered by AOPs are given in Fig. 13.1

Photocatalysis was included in the family of AOP, which enlisted many advantages and can likely provide solutions for many environmental problems faced by the modern world. This is because photocatalysis allocates a simple way of utilizing

Table 13.1 The advantages and disadvantages of existing water treatment technologies.

Water treatment technology	**Advantages**	**Disadvantages**
Biological	High reliability High load operation can be processed	Difficulty in securing stable process High level of sludge Operating management requires expertise
Coagulation/ precipitation	High efficiency of processing Low sites	Excessive sludge produced Difficult to maintain
Fenton	Wide coverage Treatment process is simple and easy to manage Effective colored discoloration of wastewater	High operating cost over the use of the Fenton's reagent Removal of the equipment needs iron salts
Photocatalytic advanced oxidation	Low operational and installation cost No sludge produces Possible for nonbiodegradable wastewater treatment	Limited lamp life when UV lamp is used Limitation on photocatalyst recovery facility

Source: Adapted from Lim, S.Y., Shen, W., & Gao, Z. (2015). Carbon quantum dots and their applications. Chemical Society Reviews, 44(1), 362–381. https://doi.org/10.1039/c4cs00269e.

Table 13.2 Different oxidizing agents used for water and waste water treatment and their redox potential.

Oxidizing agent	Oxidation potential (V)
Hydroxyl radical (OH^-)	2.80
Ozone (O_3)	2.07
Hydrogen peroxide (H_2O_2)	1.77
Perhydroxyl radical	1.70
Permanganate	1.68
Chlorine dioxide (ClO_2)	1.57
Chlorine (Cl_2)	1.36
Oxygen (O_2)	1.20

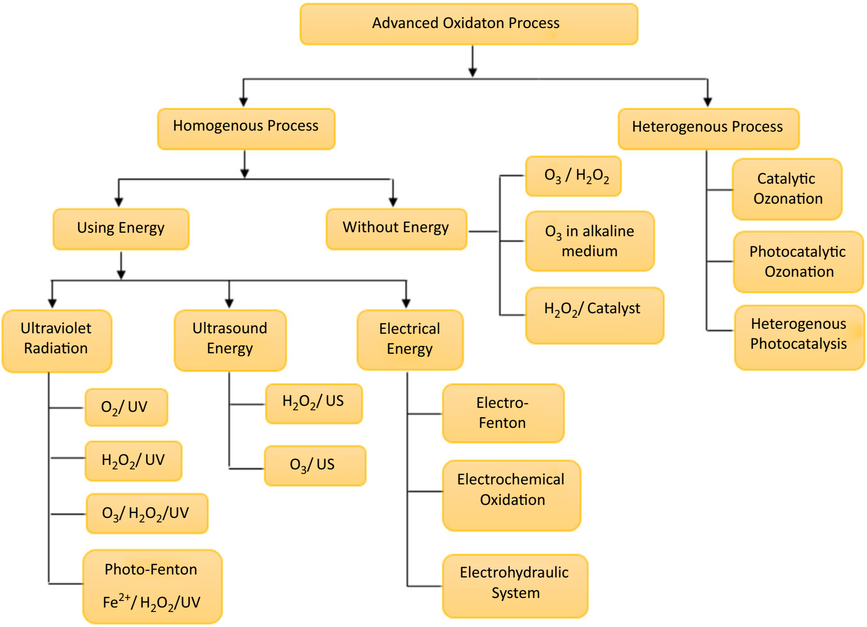
Advanced Oxidaton Process
Homogenous Process
Heterogenous Process
Using Energy
Without Energy
O_3 / H_2O_2
O_3 in alkaline medium
H_2O_2/ Catalyst
Catalytic Ozonation
Photocatalytic Ozonation
Heterogenous Photocatalysis
Ultraviolet Radiation
Ultrasound Energy
Electrical Energy
O_2/ UV
H_2O_2/ UV
O_3/ H_2O_2/UV
Photo-Fenton Fe^{2+}/ H_2O_2/UV
H_2O_2/ US
O_3/ US
Electro-Fenton
Electrochemical Oxidation
Electrohydraulic System

Figure 13.1 AOP classifications for wastewater treatment. AOP, *advanced oxidation process*.
Source: Adapted from Sharma, A., Ahmad, J., & Flora, S.J.S. (2018). Application of advanced oxidation processes and toxicity assessment of transformation products. Environmental Research, 167(April), 223–233. https://doi.org/10.1016/j.envres.2018.07.010.

light to induce chemical transformation. Although commercial uses of photocatalysis are related mainly to self-cleaning surfaces and pollution control, whether in aqueous solution or air, photocatalysis for water purification is a very potential studied application in recent years. The phenomenon of a photocatalytic splitting of water on TiO_2 electrode under ultraviolet light was first discovered by Fujishima and Honda in 1972 [17,18]. This event becomes notable as the beginning of a new era in heterogeneous photocatalysis. In general, photocatalysis is a combination of photochemistry and catalysis. The word "photocatalysis" comes from the Greek language and is divided into two parts: prefix "photo" means light and catalysis.

Catalysis is the process where a substance can control the rate of a chemical transformation of the reactants without being altered at the end [19]. The substance denoted here as a catalyst responsible for increasing the reaction rate by dropping the activation energy. Hence, in short, photocatalysis is a process where light and catalyst are concurrently utilized to support and accelerate the chemical reaction. There are two types of photocatalysis such as homogeneous and heterogeneous processes [20]. Metal complexes catalysts (transition metal complexes such as iron (Fe), copper (Cu), chromium (Cr), etc.) are mostly used in homogeneous photocatalytic methods. In the presence of light and heat, the higher oxidation states of metal ion complexes generate hydroxyl radicals, and they react with organic matter that destroys the toxic matters [17].

Compared to homogeneous photocatalysis, heterogeneous photocatalysis is a technically gifted method, normally being used to degrade various organic pollutants in wastewater [17,21]. Heterogeneous photocatalysis has many advantages compared to other method [17,22,23]. They are (1) complete mineralization, (2) no waste disposal, (3) low cost, and (4) necessity need mild temperature and pressure conditions. Photocatalysis technology involves catalyst, and several potential semiconductor photocatalyst was used like TiO_2, zinc oxide (ZnO), graphitic carbon, cadmium solenoid (CdS), etc. Semiconductor photocatalysis appears as a promising technology with many applications in environmental systems [20]. An outstanding semiconductor photocatalyst should work under visible and/or near UV-light, biologically and chemically inert, photostable, inexpensive, and nontoxic [17,21,23,24].

13.2 Mechanism of photocatalysis

Primarily, the photocatalytic reaction depends on the wavelength of light energy and the catalyst. The initial step of photocatalysis is the absorption of photons of light energy, which is sufficient to match the energy level of the photoactive material. Generally, semiconducting materials are used as a catalyst that perform sensitizers for the irradiation of light stimulated redox process due to their electronic structure and characterized by a filled valence band (VB) and a vacant conduction band (CB) [17,24]. Fig. 13.2 shows the schematic representation for basic principle of photocatalytic mechanism.

Several steps involved in the process of semiconductor photocatalyst are as follows [17,21,23,24]:

When the light energy in terms of photons strikes the surface of the semiconductor with energy of incident ray more or equivalent to the bandgap energy of the semiconductor, the VB electrons are agitated and excited to the CB of the semiconductor.

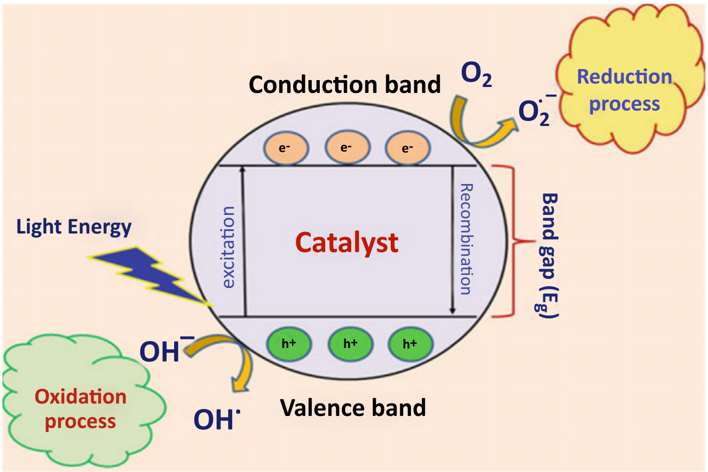

Figure 13.2 Schematic diagram for the basic principle of photocatalytic mechanism. *Source*: Adapted from Saravanan, R., Gracia, F., & Stephen, A. (2017). Nanocomposites for visible light-induced photocatalysis. 19—41. Springer. https://doi.org/10.1007/978-3-319-62446-4.

Holes would be performed in the VB of the semiconductor. These holes can oxidize donor molecules and react with water molecules to generate hydroxyl radicals. The hydroxyl (OH·) radicals have strong oxidizing power responsible for the degradation of the pollutants.

Meanwhile, the CB electron reacts with dissolved oxygen species to form superoxide ions. These electrons induced redox reactions.

During the oxidation mechanism, the photocatalyst surface that contains water was oxidized by the positive holes generated in the VB upon excitation of electrons to the CB by light irradiation. As a result, OH· was formed. Subsequently, these radicals then react with organic pollutants present in the water. On the off chance that oxygen is available when this procedure happens, the intermediate radicals in the organic compounds along with the oxygen molecules can encounter radical chain reactions and consume oxygen in some cases. At last, in such cases, the organic matter decomposes ultimately into carbon dioxide and water [17,23,24].

In the meantime, throughout the reduction process, the oxygen reduction happens in a pairing reaction [17,21]. Reduction of oxygen turn out to be an alternative to hydrogen generation because it is easily reducible substance. The CB electrons react with dissolved oxygen and form superoxide anions. These superoxide anions are then attached to the intermediate products in the oxidative reaction, creating peroxide or changing to hydrogen peroxide and then to water. Presumably, the reduction can occur more easily in the organic matter rather than in water. Thus, an increase in the concentration of organic matter tends to increase the number of positive holes, reducing the carrier recombination and improving the photocatalytic activity [17,24].

13.3 Photocatalysts material

During past decades, many researchers have focused on the reactions that take place on the illuminated surface of semiconductor photocatalysts like metal oxides, sulfides, and selenides, which portray a modest bandgap energy ranging from 1.1−3.8 eV between the CB and VB [24]. In the photocatalytic activity, the illumination of the semiconductor photocatalyst with UV light initiated the catalyst and established a redox reaction in the aqueous solution [25,26]. Semiconductors act as sensitizers for the light-induced redox processes due to their electronic structure of CB and VB.

The semiconductor photocatalyst absorbs impinging photons with energies equivalent to or higher than its bandgap energy. Every photon of the required energy (i.e., wavelength) that hits an electron in the occupied VB of the semiconductor atom can hoist that electron to the abandoned CB, leading to excited state CB electrons and positive VB holes [25]. As known, an ideal photocatalyst should be stable, inexpensive, nontoxic, and, of course, highly photoactive [24,25,27]. Another essential criterion for the degradation of organic compounds is the redox potential of the H_2O/OH couple $({}^{-}OH\ \cdot OH + e^{-};\ E = -2.8\ V)$ that lies within the bandgap of the semiconductor [28].

Fig. 13.3 shows the bandgap energy of various semiconductors that can be employed in the photocatalysis process [29]. As depicted in Fig. 13.1, the redox potential of VB and CB for various semiconductors varies between +4.00 to −1.5 V versus normal hydrogen electrode (NHE), respectively. In a photocatalytic reaction, the bottom of the photocatalyst's CB should be at more negative potential than the reduction potential of the substrate, while the top of the VB must be positioned more positively than the oxidation potential of the substrate in order for the reaction to occur simultaneously. Many organic compounds normally have more negative oxidation potentials than the valence potential of most semiconductor photocatalysts. Thus, it is thermodynamically possible for the organic pollutants to be oxidized by semiconductor photocatalyst [29].

13.4 Binary metal oxides

Several traditional metal oxides are broadly being studied because of their particular points of advantage. These include ZnO, ZrO_2, Fe_2O_3, and WO_3, which have been examined and used as photocatalysts to degrade organic pollutants [27,30]. However, these photocatalysts are regarded as unstable because of their intrinsic disadvantages to be utilized in the photocatalysis process. ZnO can be photocorroded easily under bandgap illumination by photogenerated electrons. On the other hand, WO_3, a stable photocatalyst, is not suitable for H_2 production due to its low CB level. Meanwhile, α-Fe_2O inherit the same problem as WO_3 and are not very stable in acidic solutions [27].

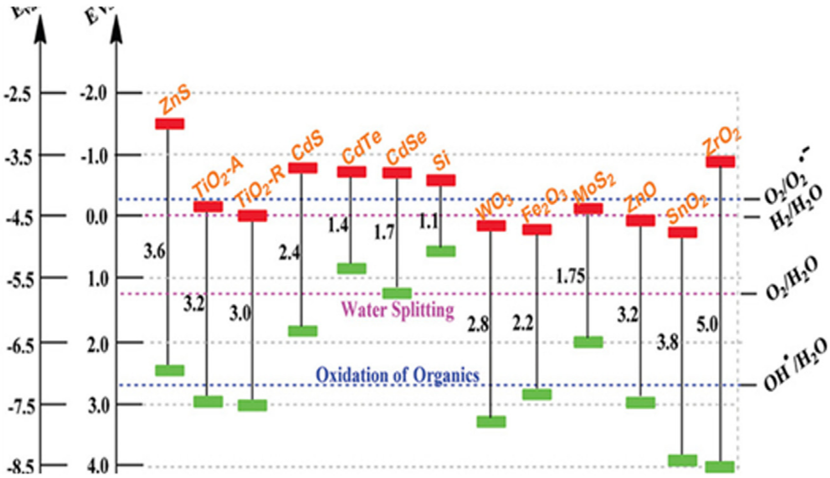

Figure 13.3 Energy band diagram of common semiconductors on the potential scale. *Source*: Adapted from A. Makama, M. Umar, and S. A. Saidu. CQD-based composites as visible-light active photocatalysts for purification of water. In Y. Yao (Ed.), *Visible-light photocatalysis of carbon-based materials*. IntechOpen (2018). https://doi.org/10.5772/intechopen.74245.

Apart from the traditional metal oxides mentioned in previous paragraph, TiO_2 is being widely used in materials around us. It is present in paints, cosmetics, and food products as well because of its high index of light reflection and nontoxic character. The main structure of TiO_2 is anatase, rutile, and brookite [17,31]. Among three structures, anatase TiO_2 is a promising candidate for photocatalytic activity, especially anatase nanoparticles (<14 nm), due to its large surface area [32−35]. In order to apply the semiconductor photocatalysts for water treatment, the following necessity must be fulfilled: complete mineralization without secondary pollution, repetitive cycles, and low costs for operations [16]. Therefore, the ideal photocatalyst that was chosen is TiO_2. It was recognized by Fujishima and Honda in 1972 as a strong oxidative and reductive property, which is inexpensive and can be synthesized easily in a laboratory. In addition, TiO_2 photocatalyst is very stable, both chemically and photochemically, safe and nontoxic as well as has strong resistance against acid and alkaline.

TiO_2 can not only maintain water solubility and self-degradable performance, but also does not undergo photocorrosion by itself because, under irradiation, the charge pair on the TiO_2 surface react with the solid lattice ions directly [16,36]. Generally, the possible mechanism underlying the TiO_2 photocatalyst has been widely reported in many reports and can be explained as [9,17].

$$\text{Semiconductor} + \text{Light Energy(hv)} \rightarrow \text{Semiconductor}\left(e^- + h^+\right) \tag{13.1}$$

$$\text{Dye} + \text{Semiconductor}\left(h^+\right) \rightarrow \text{Oxidation process} \tag{13.2}$$

$$\text{Semiconductor}\left(h^+\right) + \text{H}_2\text{O} \rightarrow \text{Semiconductor} + \text{H}^+ + \text{OH} \tag{13.3}$$

$$\text{Semiconductor}\left(h^+\right) + \text{OH}^- \rightarrow \text{Semiconductor} + \text{OH}^{\cdot} \tag{13.4}$$

$$\text{Dye} + \text{Semiconductor}(e^-) \rightarrow \text{Reduction process} \tag{13.5}$$

$$\text{Semiconductor}(e^-) + \text{O}_2 \rightarrow \text{Semiconductor} + \text{O}^{-2} \tag{13.6}$$

$$\text{O}_2^- + \text{H}^+ \rightarrow \text{HO}_2^{\cdot} \tag{13.7}$$

$$\text{HO}_2^{\cdot} + \text{HO}_2^{\cdot} \rightarrow \text{H}_2\text{O}_2 + \text{O}_2 \tag{13.8}$$

$$\text{H}_2\text{O}_2 + \text{O}_2^{\cdot -} \rightarrow \text{OH}^{\cdot} + \text{OH}^- + \text{O}_2 \tag{13.9}$$

$$\text{Dye} + \text{OH} \rightarrow \text{Degradation products} \tag{13.10}$$

However, this TiO_2 only acts under UV light irradiation which is only 5% available from the overall sunlight, and this drawback limits its performance in utilizing the solar energy resources [9]. On the other hand, unlike conventional semiconductor quantum dots with bandgap absorption, the absorption carbon dots extend from the broad UV/Vis spectral range to near IR, thus covering a significant portion of the solar spectrum. In short, with the fascinating view of their attractive optical properties and UV in particular, a nanocomposite of carbon quantum dots (CQDs) and TiO_2 is expected to realize the efficient usage of the full spectrum of sunlight. Other than harvesting harmless visible light and converting it to a shorter wavelength, which then excites TiO_2 to form electron–hole pair, it is believed that the CQDs in the nanocomposites facilitate the transfer of electrons from TiO_2, and the electrons can excite freely along the conducting paths of the CDQs allowing charge separation, stabilization, and hindering recombination, thus generating long-lived holes on the TiO_2 surface [36]. The longer-lived holes can enhance the photocatalytic activity of the TiO_2-CQDs nanocomposites.

13.5 Metal sulfides

Regularly, metal sulfides are considered potential and attractive candidates for visible light-responsive photocatalysis. Normally metal sulfides comprise 3p orbitals of S, resulting in a more occupied VB as well as narrower bandgap compared to metal oxides. Among the metal sulfides, studies have been focused on CdS, ZnS, and their solid solutions [27]. Although CdS has a suitable bandgap (2.4 eV) and is in good positions for light-assisted water splitting, the S^{2-} in CdS easily oxidized by photogenerated holes, which accompanied by the release of Cd^{2+} into the solution. This situation is same going to the ZnO. In fact, photocorrosion is a common problem for most metal sulfides photocatalyst, and urgent solutions are needed to tackle this limitation. Compared with ZnO and CdS, ZnS possesses too large bandgap (3.6 eV) that make them not efficient in responding to visible light. Therefore, based on much research on types of semiconductors such as photocatalysts, the general conclusion demonstrates that TiO_2 is more effective because of its characteristics. Table 13.3 summarizes the catalysts that have been used to treat dye wastewater.

13.6 Fundamentals of carbon quantum dots

Over the past decades, considerable efforts have been devoted for developing a facile and green method for synthesizing the CQDs. Appeared as a category of carbon-based nanomaterials that are usually quasispherical in shape, discrete, and lesser than 10 nm, it has allured enormous interest in many fields such as bioimaging, biosensing, electrocatalysis, photocatalysis, and nanomedicine [29,40]. For the first time, they were discovered accidently while purifying carbon nanotubes (CNTs) fabricated by the arc-discharge method [36,41]. Amorphous carbon is the main part of CQDs, together with nanocrystalline regions of sp^2-hybridized graphitic carbon. The main charecteristics of CQDs are strong blue photoluminescence (PL) and good visibility to near-infrared region (NIR) optical absorption, which make them promising candidates as photosensitizers for photocatalytic applications. CQDs can be fabricated by very simple and economical methods using a cheap and sustainable biomass sources like watermelon rinds (WMR), hair, and even cow manure [42]. In Malaysia, 20%–50% of fruits and vegetables are thrown away due to their short preservative duration, according to the research carried out by the Malaysian Agricultural Research and Development Institute (MARDI). In this context, the development of innovation and deployment of sustainable technologies to convert the fruit wastes into CQDs could be a promising strategy to enhance solid waste management.

Since discovery, CQDs have been considered potential substitutes of semiconductor QDs because of their interesting physical and chemical properties. There is mainly strong PL, which can be controlled by controlling the size and surface passivation. Surface passivation stabilizing the surface of QDs with thin organic materials can also further improve the fluorescence intensity of the CQDs. As CQDs contain mainly carbon and can interact with oxygen, it is very simple to attach different organic groups to their surfaces. These surface functionalizations control the photophysical and catalytic properties to enhance the applicability of these CQDs [43]. CQDs can be highly soluble in H_2O, which is usually desirable with adjustable hydrophilicity. As stated earlier, CQDs can be acquired from various

Table 13.3 List of catalysts that has been used to treat dye wastewater.

Catalysts	Dye concentration and volume	Target pollutant	Light source	Degradation (%) and reaction time	References
SiO_2-TiO_2	0.71 g/L 70 mL	Acid orange 7 (AO7)	High-pressure mercury lamp 2 mW/cm^2	40% 120 min	[37]
CdS	10 mg/L -1 20 mL	Rhodamine B (RhB)	500 W Mercury lamp	95% 60 min	
$F-TiO_2$	10 mg/L 80 mL	Methylene blue (MB)	400 W Halogen lamp with filter	91% 240 min	[38]
$N-TiO_2$	30 ppm 200 mL	Methylene blue (MB)	40 W Tungsten	93% 20 h	
C-dots/ZnO	Unknown	NBB azo dye	Unknown	84.3% 45 min	[39]
CQDs−ZnO	5×10^6	Rhodamine B (RhB)	Xenon arc lamp	83% 105 min	

cost-effective raw materials with diverse methods, while they are environmentally friendly and benign. Most CQDs exhibit chemical inertness, higher stability, and resistivity to photo-bleaching. Last but not least, CQDs possess two essential characteristics: lower cytotoxicity and exceptional biocompatibility that renders them superiority when compared to conventional semiconducting quantum dots and endows their potential for biological applicability [39,41,43].

Traditionally, as an example, semiconductors such as TiO_2 and CdS have been employed as photocatalysts. However, the use of these semiconductors is only absorptive or mostly in the UV range; hence, further research is required to be extended in the photon-harvesting visible region. Conceptually the use of semiconductor-carbon nanocomposite is similar as photocatalysts to take advantage of the optical absorption by nanoscale carbon in the visible spectrum. Cao and coworkers in 2011 had functionalized the surface of carbon nanoparticles with gold or platinum metal to drive photocatalytic process. The estimated quantum efficiency (QE) of the photoreduction of CO_2 to formic acid was significant by using semiconductor nanoparticles as photocatalysts, confirming the presence of photoinduced charge separation in CQDs as previously suggested by the fluorescence quenching behavior of CQDs with either electron donors or acceptors. It is also believed that CQDs could facilitate the transfer of electrons along the conducting paths of the CQDs, suppressing recombination and thus prolonging the lifetime of electrons and holes. Fig. 13.4 shows the schematic diagram of methylene blue (MB) degradation by CQDs. The CQDs first absorbed long-wavelength light (>600 nm), then emitted shorter wavelength light in the UV range, further exciting TiO_2 to produce photogenerated electrons and holes. Furthermore, CQDs existed as effective

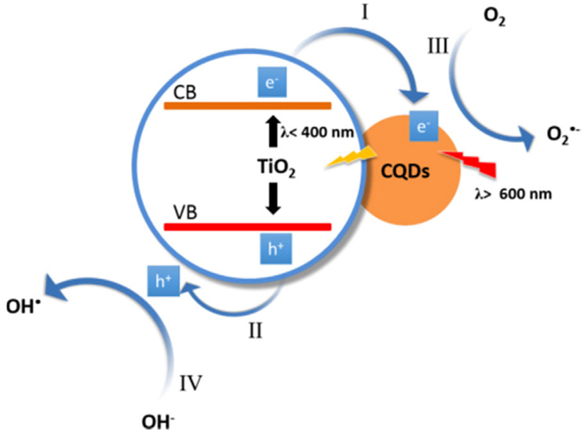

Figure 13.4 Schematic diagram of MB degradation by CQDs. MB, *Methylene blue*; CQDs, *carbon quantum dots*.

Source: Adapted from R. Miao, Z. Luo, W. Zhong, S. Y. Chen, T. Jiang, B. Dutta, et al. Mesoporous TiO_2 modified with carbon quantum dots as a high-performance visible light photocatalyst. *Applied Catalysis B: Environmental*, 189 (2016) 26–38. https://doi.org/10.1016/j.apcatb.2016.01.070.

electron reservoirs capable of trapping electrons emitted from TiO_2 CB [44]. As a result, electrons in the TiO_2 CB will migrate to CQDs (process I), where they will combine with molecular oxygen to create superoxide anion radicals (•), (process III). Meanwhile, photogenerated holes in the VB will travel to the TiO_2 surface (process II), where they will react with hydroxyl species to form active hydroxyl radicals (OH•) (process IV) [45]. Those very active radicals demonstrate extraordinary oxidizing capacity to organic molecules adsorbed on the surface of TiO_2 in a manner similar to the mechanism documented in the literature [46].

As reported by Prasannan and Imae in 2013, a simple and facile one-pot synthesis of fluorescent CQDs from orange waste peels using hydrothermal carbonization method at mild temperature (180°C) was developed. The prepared CQDs were combined with ZnO to degrade naphthol blue-black azo dye under UV irradiation, and excellent photocatalytic performance was observed. Residue from the brewing industry was successfully used as a carbon source to obtain luminescent CQDs through two facile synthetic procedures. The upconversion PL exhibited by CQDs and their staining pattern enables their future applications in cell-imagining experiments and provides a new tool for nucleoli studies linked with health and disease conditions through fluorescence microscopy. Liang and coworkers in 2014 fabricated high-quality blue, fluorescent CQDs from a dilute NH_4OH/water solution of forestry and agricultural biomass via one-step hydrothermal carbonization. They were successfully applied in bioimaging of murine embryonic stem cells. This low-cost and green chemistry method provides a feasible route for value-added and sustainable utilization of waste biomass. Nevertheless, the reported applications using biomass-derived CQDs in photodegradation of organic pollutants are, to some extent, limited since its pioneer research from Prasannan and Imae in 2013. Fluorescent carbon dots with a spherical shape and a diameter of 2−7 nm were produced by hydrothermal treatment of orange peels at 180°C. Under UV light irradiation, ZnO is doped with C-dots to facilitate the breakdown of NBB azo dye. The dye's time-course absorption spectra demonstrated that as the irradiation period increased, the dye's intensity effectively dropped due to dye degradation. Within the reported research, the degradation process takes 45 mins to completely degrade the dye [47]. Other agriculture wastes were also used in the synthesis of CQDs; however, most of them were used in applications other than photocatalysis, as per mentioned in Table 13.5. Therefore, it is highly desirable to explore cheap and easily available sources of carbon to synthesize CQDs with green and environmentally techniques to narrow the gap in the photocatalytic evaluation of CQDs.

13.7 Roles of carbon quantum dots in photocatalysis

13.7.1 Broaden the optical absorption range of photocatalyst

One of the key components, in order to acquire the useful efficiencies of photocatalysis process, is by enlarging the absorption of incident light irradiation of the photocatalysts, as reported in the previous studies [17,29,48,49]. However, owing to the wide bandgap semiconductor like TiO_2, a typical methodology for accomplishing this is photosensitizers. Photosensitizer is a molecule that produces a chemical change in another molecule in a photochemical process. A photosensitizer is excited by low-energy photons that create electrons which later gets into the CB of a wider bandgap photocatalyst. Nonetheless, ordinary photosensitizers used typically portrayed as costly, harmful, unstable, and polluting [29,50−54]. These disadvantages limit the practical and extensive scalable use of conventional photosensitizers. Consequently, it is necessary to locate an option photosensitizer material(s) that is free from these downsides and can harvest a larger portion of the light radiation. CQDs have all the earmarks of being such material with spectacular qualities such as easier producibility, being cheaper, nontoxic, green, stable, and widely abundant [29,36,55].

Moreover, CQDs not only exhibit stronger blue PL and decent optical absorption in the visible and NIR. but also exhibit upconversion PL properties which render them a suitably perfect candidate as photosensitizers for photocatalytic applicability [29,56−59]. From the previous studies, three possible photosensitization mechanisms have been proposed, involving the excitation of CQDs by a lower energy radiation for electrons (ecb^-) and holes ($\boldsymbol{h}vb^+$) generation at the first stage. Under good thermodynamic conditions, in order to initiate the reaction, the photogenerated ecb^- is injected into the CB of the wider bandgap photocatalyst as in Fig. 13.5A [29,40]. Next, with the fascinating upconversion PL properties of the CQDs, i.e., conversion of the longer wavelength light into a shorter wavelength can excite the wider bandgap photocatalyst to generate $ecb^-/\boldsymbol{h}vb^+$ pairs (Fig. 13.5B) [29,60]. Finally, incorporating CQDs into the semiconductor photocatalyst may lead to the bandgap narrowing of the semiconductor owing to the chemical bonding between the composite, resulting in the range extension of light absorption as in Fig. 13.5C [29,61].

For past few years, several works that have been reported proved that CQDs extend the optical absorption range of various wide and narrow bandgap photocatalysts into the visible range and even beyond that [29,38,39,62]. For instance, a recent publication reported by Ye et al. [63] showed that introducing CQDs into $BiVO_4$ to extend the light absorption range to entire visible light was successful when the resulting CQDs/$BiVO_4$ composite photocatalyst exhibited photocurrent density Jsc of 9.2 mA/cm^2. Meanwhile, Ren et al. [64] reported a victorious event after the integrating CQDs with $MoSe_2$, CQDs/$MoSe_2$ photocatalyst that is active in the entire range of solar spectrum. Otherwise, the upconversion PL property of CQDs was utilized to enhance the visibility and NIR response of narrow bandgap composite photocatalyst. For example, based on the previous research conducted by Liu et al. Wang et al. [65], the upconversion PL property of nitrogen-doped CQDs was utilized to improve the visible light and NIR response of graphitic carbon nitride (g-C_3N_4). In another work, Mao and coworkers [29] elevated the visible and NIR response of $Bi_{20}TiO_{32}$ by incorporating with CQDs. The resulting composite photocatalyst showed improved photocatalytic activity under the NIR region.

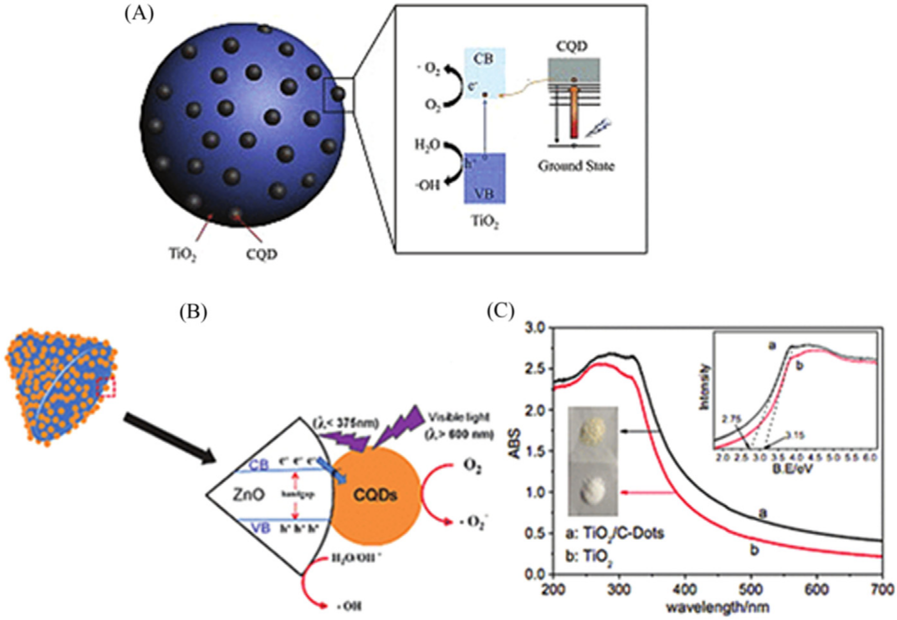
(A)
·O2
O2
H2O
·OH
CB
e-
h+
VB
TiO2
CQD
Ground State
TiO2
CQD
(B)
CB
ZnO
bandgap
VB
CQDs
(λ< 375nm)
Visible light (λ> 600 nm)
O2
·O2-
H2O/OH-
·OH
(C)
ABS
3.0
2.5
2.0
1.5
1.0
0.5
0.0
200
300
400
500
600
700
wavelength/nm
Intensity
B.E/eV
2.75
3.15
a
b
a: TiO2/C-Dots
b: TiO2

Figure 13.5 Schematic of the sensitization of CQDs based on (A) photoexcitation of CQDs (B) upconversion photoluminescence, and (C) narrowing of bandgap. CQDs, *carbon quantum dots*.
Source: Adapted from A. Makama, M. Umar, and S. A. Saidu. CQD-based composites as visible-light active photocatalysts for purification of water. In Y. Yao (Ed.), *Visible-light photocatalysis of carbon-based materials*. IntechOpen (2018). https://doi.org/10.5772/intechopen.74245.

13.7.2 Improved charge separation and electron transfer

In a photocatalytic system, the fundamental process limiting the QE is the massive recombination rate of photogenerated charge carriers [28,29]. Thus, to boost the performance of photocatalyst, it is necessary to enhance the charge carrier separation, which can result in minimization of recombination rate. Several strategies have been conducted to achieve these goals, including surface modification of the semiconductor photocatalyst with noble metals [29,66], a combination of two semiconductors with different electronic levels [29,67], and as well as using the related reagents to scavenge the photogenerated electron and holes [68,69].

Despite all the strategies listed, coupling carbon-based materials with semiconductor photocatalyst becomes a rising star due to their higher charge storage capacity and electrical conductivity. Recently, several reports have shown the positive effect of coupling CQDs with semiconductor [29,38,40,58,64,70]. For example, the intrinsic bandgap and stronger electron affinity in CQDs give them the ability to accept the photogenerated electron from an electron donor like a semiconductor with a more electronegative CB minimum. Then, the transferred electrons can move freely along the conducting paths of the CQDs allowing for the effective charge separation, stabilization, and anticipation of charge recombination. Longer-lived charge carriers have greater probability to induce transformations, thus representing enhancement of the QE of CQDs-based photocatalysts.

13.7.3 Allocate additional surface for adsorption and reaction

Alternatively, another important contribution of CQDs is that it improves the photocatalytic activity, which is its ability to cater to extra surface area for adsorption and reaction of substrate. As a nanomaterial, CQDs have a bigger surface area to volume proportion, and in this manner, its composite with different nanomaterials possibly gets a much-improvedsurface region, consequently expanding the adsorption limit. Like other carbon materials, adsorption capacity of CQD is originally from the flexible sp^2-bonded carbon structure and the extensive surface region. Since the outer surface of CQDs consists of plenty of oxygenated functional groups [29,36], its adsorption capacity relies upon its interaction with adsorbate. The aromatic rings of CQDs can form a π-π bond with original adsorbates consisting of aromatic structures to improve their adsorption. Other than that, the presence of other functional groups, for example, carbonyl, epoxy, hydroxyl, and amino gatherings on the outer surface of CQDs, advances the adsorption of a wide assortment of atoms and metal particles. Expanded adsorption of the target reactants on an outer surface of photocatalyst builds ashot of responding with photogenerated responsive oxidative species, in this manner improving photocatalytic activity of composite CQDs-based photocatalyst [29,71,72].

13.8 Synthesis route of carbon quantum dots

Over the past years, many progression have been attained in the synthesis, properties, and application of CQDs making them as a better candidates in catalysis application [41,55,73]. CQDs synthetic routes can be categorized into top-down and bottom-up methods [74].

13.8.1 Top-down method

In the top-down approach, preparation of CQDs involves larger carbon materials, such as graphite, soot, activated carbon, etc. [36]. Xu et al. in 2004 unfolded for the first time the example of fluorescent CQDs when they were purifying single-walled carbon nanotubes (SWCNTs) from arc-discharged soot. In order to obtain the CQDs, the arc-discharged soot was oxidized with nitric acid, then extracted using sodium hydroxide solution, and the black suspension from the extract was subjected to gel electrophoresis. Later on, in 2006 Sun and coworkers discovered the synthesis of CQDs through laser ablation of a carbon material utilizing argon as a carrier gas in the presence of water vapor. Even though nanosized carbon particles in various sizes were formed in the experiment, these CQDs gave no obvious fluorescence emissions. Thus, in favor of bright fluorescence, the sample was treated with acid oxidative followed by surface passivation. Subsequently, in 2007, Zhou et al. were the first group to describe an electrochemical method for CQDs preparation. It included developing multiwalled CNTs on a carbon paper, which was then embedded into an electrochemical cell that contained degassed acetonitrile with 0.1 M tetrabutylammonium perchlorate as the supporting electrolyte [36].

13.8.2 Bottom-up method

On the other hand, in the bottom-up methods, molecular precursors were used in the synthetization of CQDs via combustion/thermal treatments and supported synthetic and microwave synthetic routes [36]. For example, Liu's group in 2004 reported a synthetic procedure based on the use of modified silica spheres as carriers and resoles as carbon precursors. Bourlinos et al. outlined anfacile, one-step thermal decomposition method for getting fluorescent CQDs from ammonium citrate [75]. Apart from that, Zhu's team in 2009 revealed that CQDs are easily formed by heating a solution of polyethylene glycol (PEG) and saccharide in 500 W microwave oven for 2–10 min. Cost is one of the essential determinants of CQDs getting to be practical contenders for semiconductor quantum dots. Despite that, although all the above mentioned procedures were successful in preparing the CQDs, they noticeably suffer from some drawbacks because most of the methods require tedious processes with several steps, harsh chemical reactions, sophisticated instrumental setup, limited spectral efficiency, and low product yield which limit their wide application [76,77]. Table 13.4 includes the summary of the features of various synthetic methods preparation of CQDs that not being discussed above [41].

Therefore, it is necessary to find a green approach to synthesize CQDs neglecting the need for expensive materials and experimental setups. In search of readily available and abundant natural precursor as the carbon source coupled with green synthesis method of CQDs, the hydrothermal treatment appears attractive candidates due to its simple and low-cost synthesize of highly luminescent biofriendly CQDs [76].

13.9 Hydrothermal treatment of carbon quantum dots

Hydrothermal treatment is easy, low-cost, nontoxic, and environmentally friendly to synthesize carbon materials from different precursors. Typically, a solution of organic precursor is poured into a Teflon-line autoclave and put into an oven at a high temperature for the reaction to occur [41]. Previously, Mohapatra et al. and Sahu et al. [94] prepared highly PL CQDs with quantum yield of 26% in one step by hydrothermal treatment of orange juice and taken after by centrifugation [41,94]. Subsequently, in 2012 Liu et al. outlined a one-step synthesis of amino-

Table 13.4 Summary on features of different methods to synthesize CQDs (carbon quantum dots).

Synthesize method	Advantages	Disadvantages	References
Chemical ablation	More accessible, various sources	Harsh condition, drastic process, multiple steps, poor control over sizes	[78,79,80]
Electrochemical carbonization	Size and nanostructured are controllable, stable, one-step	Few small molecules precursor	[81]
Laser ablation	Rapid, effective, surface tunable	Low quantum yield, poor control over sizes, modification needed	[82]
Microwave irradiation	Cost-effective, eco-friendly, nontoxic	Poor control over sizes, high temperature for experiment	[83,84,85]
Chemical oxidation	Simple operation, large-scale production	Nonuniform distribution	[86,87]
Electrochemical oxidation	Controllable size, high product yield and purity, decent reproducibility	Complex process	[88]
Laser ablation	Controllable size and morphology	High cost, complex operation	[89,90]
Ultrasonic treatment	Simple operation	High cost, instrumental wastage	[91,92]
Thermal decomposition	Simple operation, cost-effective, solvent free, large-scale production	Nonuniform size distribution	[93]
Hydrothermal treatment	Cost-effective, eco-friendly, nontoxic	Poor control over size	Present work

functionalized fluorescent CQDs by hydrothermal carbonization of chitosan at 180°C for 12 h, and this amino-functionalized CQDs can be used directly as a novel bioimaging agent.

Herein, hydrothermal treatment is chosen as the method of preparation of CQDs since this study uses biomass as carbon source. Furthermore, biomass conversion occurs in a wet situation, so a high moisture content of the feed is not an issue. Thus, such a technique is considered appropriate for treating biomass with high moisture content, such as agricultural wastes which contain more than 50 wt.% of moisture in fresh condition [95]. However, concerning the experimental conditions of the hydrothermal treatment, ever since the existing studies have shown different results, it is difficult to predict the possibility of getting high-quality CQDs with specific characteristics [96]. Since temperature and reaction time affect the structural properties of synthesized CQDs, it is important to find an optimum temperature and reaction time to produce high-quality fluorescent nanoparticles CQDs. Theoretically, higher temperature and longer reaction time can produce larger sizes of nanoparticles compared to low temperature and these results are consistent with previous reported studies [96–98].

In recent years, a variety of biomass has been used as the carbon precursor in the preparation of CQDs, such as vegetables-derived CQDs, fruits-derived CQDs, and other sources, such as grass, soymilk, oatmeal, and other beverages [99]. Vegetables like coriander leaves, sweet potatoes, and carrot juices that are rich in vitamins, minerals, and other beneficial ingredients were used as carbon sources through hydrothermal treatment. In these studies, the prepared CQDs were uniformly distributed with nanodiameter in size but produced a low quantum yield, which is $<10\%$. Thus, in order to improve the quantum yield, another study was conducted by using onion waste as a carbon source using the same treatment method. This carbon source indeed increases the quantum yield of CQDs, but at the same time, the size of prepared CQDs also increases from 7 to 25 nm. Later, the study conducted using sweet pepper and cabbages as the carbon sources produced CQDs with narrow size distributions and increased quantum yield correspondingly. However, the preparation of CQDs using potatoes using different preparation methods showed better control of particle size, but the quantum yield was reduced in half [99].

Meanwhile, fruits containing lot of water, vitamins, and other components can also be used as carbon sources. Generally, CQDs prepared from fruits like pomegranate, sugarcane juice, apple juice, banana juice, and lemon juice produce particle sizes from 2 to 7 nm and have good photostability [99]. Besides the above several stated fruits, many kinds of fruits are used in CQDs preparation. In addition, fruits waste peel can also be used as a carbon source to prepare CQDs. For example, pomelo peels, orange peels, lemon peels, and WMR have been used in previous studies to produce a small size of CQDs in nanodiameter range. At present, the size distribution of CQDs prepared using biomass as a carbon source is relatively small and uniform, yet the heating temperature and heating time need to be improved accordingly for better control of size distribution. Table 13.5 illustrates the summary of hydrothermal treatment process of CQDs from various types of green precursors with their respective treatment condition as well as application.

Table 13.5 Summary of hydrothermal synthesize of CQDs (carbon quantum dots) from various type of green precursor.

Precursor	**Treatment condition**	**Application**	**Findings**	**References**
Sweet potato	Heating temp: 180°C Heating time: 18 h Centrifugation speed: 10,000 rpm	Fe^{3+} sensing and cell imaging	Size of CQDs = 2.5–5.5 nm XRD pattern = amorphous nature Absorption peak = 266 nm PL emission peak = red shifted (300–410 nm)	[100]
Soy milk	Heating temp: 180°C Heating time: not specified	Electrocatalysts for oxygen reduction	Size of CQDs = 13–40 nm XRD pattern = amorphous nature Absorption peak = 275 nm PL emission peak = red shifted	[101]
Oatmeal	Heating temp: 160°C–220°C Heating time: 1–7 h Centrifugation speed: 12,000 rpm	Cell imaging	Size of CQDs = 20–40 nm XRD pattern = amorphous nature Absorption peak = 280 nm PL emission peak = red shifted (410–504 nm)	[102]
Orange juice	Heating temp: 120°C Heating time: 150 min Centrifugation speed: 10,000 rpm	Bioimaging	Size of CQDs = 1.5–4.5 nm XRD pattern = amorphous nature Absorption peak = 288 nm PL emission peak = red shifted (390–455 nm)	[94]
Pomegranate juice	Heating temp: 170°C Heating time: 12 h	Cell imaging	Size of CQDs = 2–7 nm XRD pattern = amorphous carbon Absorption peak = 250–400 nm PL emission peak = red shifted (300–540 nm)	[103]
Coriander leaves	Heating temp: 240°C Heating time: 4 h	Sensors and bioimaging agents	Size of CQDs = 1.5–2.98 nm XRD pattern = amorphous carbon Absorption peak = 273 and 320 nm PL emission peak = red shifted (320–480 nm)	[104]

(*Continued*)

Table 13.5 (Continued)

Precursor	Treatment condition	Application	Findings	References
Cabbage	Heating temp: 180°C Heating time: 18 h Centrifugation speed: 12,000 rpm	Bioimaging	Size of CQDs = 2–6 nm XRD pattern = amorphous nature Absorption peak = 276 and 320 nm PL emission peak = red shifted (432–584 nm)	[76]
Pomelo Peel	Heating temp: 200°C Heating time: 3 h Centrifugation speed: 12,000 rpm	Hg2 + sensing	Size of CQDs = 2–4 nm XRD pattern = not involve Absorption peak = 280 nm PL emission peak = blue shifted (444–365 nm)	[105]
Watermelon Rinds	Heating temp: Heating time: Centrifugation speed	MB degradation	Size of CQDs = 3.18–4.67 nm XRD pattern = amorphous nature Absorption peak = 317 nm PL emission peak = red shifted (355 and 585 nm)	[106]

13.10 Watermelon rinds potential as carbon precursor

Citrullus lanatus or watermelon that belongs to the family of Cucurbitaceae is a major fruit found widely in tropics and subtropical regions [107–109]. Kalahari and Sahara deserts in Africa have been traced as the center of origin of these fruits and becoming the point of variegation to other parts of the world [107]. Watermelon normally has a large, round, oval, and sometimes oblong fruit shape, as well as smooth skin and dark green rind or pale green stripes that turn yellowish-green when ripe [108,110]. With *Citrullus lanatus* being one of the most important crops, it is consumed in almost all over the world due to its delicate taste and nutritional compositions resulting in annual production of 104,472,416 tons in 2011 [109].

In Malaysia, watermelon is an exceptionally well-known and famous short-term non-seasonal fruit in Malaysia, categorized under major fruits by the Ministry of Agriculture and Agro-based Industry, with an average production of 154,416 tons [111]. Watermelon fruit is composed of three main parts: flesh, seed, and rind. The components of watermelon are approximately divided into 68% flesh, 30% of rind, and 2% of seeds from the total weight [112,113]. The refreshing red flesh with pleasant smell and taste make them very popular in making juice as the thirst quencher and even desserts.

Despite its popularity, the outer WMR are regarded as waste that possesses no commercial value in daily life. WMR contain protein [108], carotenoids [109–112], cellulose [110–112], citrulline [109–112], pectin [112,114], and flavonoids [110,115]) with ample various functional groups such as carboxyl, hydroxyl, and amine that attracts cationic compounds rendering them as a potential candidate in treating dyes wastewater. Moreover, the antioxidant property of citrulline produces hydroxyl radicals that are a strong oxidizing agent that is suitable for the degradation process [110]. In addition, many researchers have speculated that flavonoids in WMR are probable scavengers of hydroxyl that can be utilized for photocatalytic activity [111,112,116].

13.11 Application of carbon quantum dots in photocatalysis

13.11.1 Application of carbon quantum dots-based composite in water purification

In recent years, a substantial number of studies have given an account of the application of CQDs-based composite for water purification due to the exceptional properties exhibited by the composite. CQDs have been doped with various metal oxides semiconductors like TiO_2, SiO_2, $MoSe_2$, Bi_2MoO_6, etc. Results found that they appear to be an excellent photocatalyst for the degradation of pollutants. This study will be focused on the CQDs coupled with TiO_2 since TiO_2 is the most popular semiconductor photocatalyst being used in many applications not limited to water purification only. Furthermore, this subtopic will also discuss the gap present in the previous study that use CQDs-TiO_2 composite photocatalyst. Table 13.6

Table 13.6 Summary of CQDs-TiO_2 photocatalyst used for wastewater purification.

CQDs composite	Targeted pollutant	Experimental conditions	Limitations	References
CQDs-TiO_2 (TiO_2 nanosheets)	Methylene blue (MB)	$>$420 nm light	-	[91]
CQDs-TiO_2 (nanotube array)	Methylene blue (MB)	500 W Xe lamp, $\leq$420-nm filter	– Harsh condition – Multiple steps – Poor control over size	[70]
CQDs-TiO_2 (TiO_2 nanotube)	Rhodamine B (RhB)	500 W Xe lamp, $\leq$420 nm filter	– Lower photocatalytic activity due to poor phase structure of CQDs and TiO_2 – Poor control over size	[38]
CQDs-TiO_2 (powder)	Methylene blue (MB)	$>$420 nm light	– Chemical usage as carbon source – Strict and tedious synthesize condition	[117]

summarizes some of the CQDs-TiO_2 composite that has been conducted as photocatalyst for the degradation variety of target pollutants [29].

As reported in Table 13.6, Sun et al. outlined the fabrication of CQDs-TiO_2 nanotubes photocatalyst with improved visible light absorption and photoelectrochemical response [70]. The result shows that the prepared composite of CQDs-TiO_2 nanotubes exhibited higher degradation efficiency than TiO_2 nanotubes arrays by 14% in 100 min under given experimental condition (MB = 15 mL, 5 mg/L). From this study, it was clear that CQDs-TiO_2 nanotubes composite enhanced photocatalytic activity when illuminated with visible light compared to TiO_2 nanotubes. Subsequently, in 2014, Yu and coworkers reported that CQDs-TiO_2 nanosheets (CQDs-TNS) and CQDs-P25 composite exposed an enhancement in photocatalytic activities, especially CQDs-TNS compared to CQDs-P25. Besides, an increasing amount of CQDs solution from 2.5 to 10 mL increases the degradation efficiency gradually from 27.2% to 95.4%, which indicates that utilization of a suitable amount of CQDs can effectively improve the visible light photocatalytic activity of TNS for RhB degradation [38].

Jun et al. attributed the improvement of the degrading efficiency of CQDs-TiO_2 powder, which is notably higher than the controlled pure TiO_2. At the point when the volume of CQDs utilized was 10 mL, catalytic activity is most noteworthy, up to 90%, which is almost 3.6 times higher than that of pure TiO_2. It is fascinating that, with the increase in CQDs from 5 to 10 mL, the catalytic activity of the CQDs-TiO_2 increased drastically due to improved absorbance of visible light and increased separation efficiency of photogenerated charge carriers. However, further increment of CQD content to 15 mL leads to an apparent decrease in photocatalytic performance due to the distribution of CQDs on the surface of TiO_2 [40].

Even though the reported studies successfully improved the visible light photocatalytic efficiency, the research gap still involves combining TiO_2 with CQDs derived from biomass as the carbon precursor, and the utilization of harmless sunlight irradiation for photocatalytic activity needs to be explored. This is because, the former studies were done using graphite rod and I-ascorbic acid as the precursor. The precursor is not cost-effective, not easily available, and meanwhile, the usage of chemicals as the precursor is considered not environmentally friendly [29,38,40,70]. The previous studies also involved harsh and multiple steps procedures, which were time-consuming and sometimes produced poor phase structure and bigger size of photocatalyst that effect the photocatalytic activity [29,40,70].

References

[1] J.O. Tijani, O.O. Fatoba, G. Madzivire, L.F. Petrik, A review of combined advanced oxidation technologies for the removal of organic pollutants from water, Water, Air, & Soil Pollution 225 (9) (2014) 2102. Available from: https://doi.org/10.1007/s11270-014-2102-y.

[2] M. Anjum, R. Miandad, M. Waqas, F. Gehany, M.A. Barakat, Remediation of wastewater using various nano-materials, Arabian Journal of Chemistry 12 (2016) 4897–4919. Available from: https://doi.org/10.1016/j.arabjc.2016.10.004.

[3] I. Oller, S. Malato, J.A. Sánchez-Pérez, Combination of advanced oxidation processes and biological treatments for wastewater decontamination—A review, Science of The Total Environment 409 (20) (2011) 4141−4166. Available from: https://doi.org/10.1016/j.scitotenv.2010.08.061.

[4] N.A. Wardrop, A.G. Hill, M. Dzodzomenyo, G. Aryeetey, J.A. Wright, Livestock ownership and microbial contamination of drinking-water: evidence from nationally representative household surveys in Ghana, Nepal and Bangladesh, International Journal of Hygiene and Environmental Health 221 (1) (2018) 33−40. Available from: https://doi.org/10.1016/j.ijheh.2017.09.014.

[5] C.J. Houtman, Emerging contaminants in surface waters and their relevance for the production of drinking water in Europe, Journal of Integrative Environmental Sciences 7 (4) (2010) 271−295. Available from: https://doi.org/10.1080/1943815X.2010.511648.

[6] K.M. Reza, A. Kurny, F. Gulshan, Parameters affecting the photocatalytic degradation of dyes using TiO_2: a review, Applied Water Science 7 (4) (2017) 1569−1578. Available from: https://doi.org/10.1007/s13201-015-0367-y.

[7] S. Sharma, V. Dutta, P. Singh, P. Raizada, A. Rahmani-Sani, A. Hosseini-Bandegharaei, et al., Carbon quantum dot supported semiconductor photocatalysts for efficient degradation of organic pollutants in water: a review, Journal of Cleaner Production 228 (2019) 755−769. Available from: https://doi.org/10.1016/j.jclepro.2019.04.292.

[8] M.N. Chong, B. Jin, C.W.K. Chow, C. Saint, Recent developments in photocatalytic water treatment technology: a review, Water Research 44 (10) (2010) 2997−3027. Available from: https://doi.org/10.1016/j.watres.2010.02.039.

[9] Y. Deng, R. Zhao, Advanced oxidation processes (AOPs) in wastewater treatment, Current Pollution Reports 1 (3) (2015) 167−176. Available from: https://doi.org/10.1007/s40726-015-0015-z.

[10] R. Lakshmipathy, N.C. Sarada, Methylene blue adsorption onto native watermelon rind: batch and fixed bed column studies, Desalination and Water Treatment 57 (23) (2016) 10632−10645. Available from: https://doi.org/10.1080/19443994.2015.1040462.

[11] W.H. Glaze, Drinking-water treatment with ozone, Environmental Science & Technology 21 (3) (1987) 224−230. Available from: https://doi.org/10.1021/es00157a001.

[12] W.H. Glaze, J.-W. Kang, D.H. Chapin, The chemistry of water treatment processes involving ozone, hydrogen peroxide and ultraviolet radiation, Ozone: Science & Engineering 9 (4) (1987) 335−352. Available from: https://doi.org/10.1080/01919518708552148.

[13] A. Stocking, R. Rodriguez, T. Browne, D. Ph, 3.0 Advanced oxidation processes, Evaluation 32 (9−10) (2011) 1031−1041. Available from: https://doi.org/10.1002/cite.200750374.

[14] S.C. Ameta, Chapter 1 − Introduction, in: S.C. Ameta, R. Ameta (Eds.), Advanced oxidation processes for waste water treatment, Academic Press, 2018, pp. 1−12. Available from: https://doi.org/10.1016/B978-0-12-810499-6.00001-2.

[15] M.A. Oturan, J.-J. Aaron, Advanced oxidation processes in water/wastewater treatment: principles and applications. A review, Critical Reviews in Environmental Science and Technology 44 (23) (2014) 2577−2641. Available from: https://doi.org/10.1080/10643389.2013.829765.

[16] S.Y. Lee, S.J. Park, TiO_2 photocatalyst for water treatment applications, Journal of Industrial and Engineering Chemistry 19 (6) (2013) 1761−1769. Available from: https://doi.org/10.1016/j.jiec.2013.07.012.

[17] R. Saravanan, F. Gracia, A. Stephen, Nanocomposites for visible light-induced photocatalysis, Springer, 2017, pp. 19–41. Available from: https://doi.org/10.1007/978-3-319-62446-4.

[18] A. Ibhadon, P. Fitzpatrick, Heterogeneous photocatalysis: recent advances and applications, Catalysts 3 (1) (2013) 189–218. Available from: https://doi.org/10.3390/catal3010189.

[19] A. Kumar, A.R. Chowdhuri, D. Laha, T.K. Mahto, P. Karmakar, S.K. Sahu, Green synthesis of carbon dots from Ocimum sanctum for effective fluorescent sensing of Pb^{2+} ions and live cell imaging, Sensors and Actuators, B: Chemical 242 (2017) 679–686. Available from: https://doi.org/10.1016/j.snb.2016.11.109.

[20] R. Saravanan, M.M. Khan, V.K. Gupta, E. Mosquera, F. Gracia, V. Narayanan, et al., ZnO/Ag/CdO nanocomposite for visible light-induced photocatalytic degradation of industrial textile effluents, Journal of Colloid and Interface Science 452 (2015) 126–133. Available from: https://doi.org/10.1016/j.jcis.2015.04.035.

[21] S. Rehman, R. Ullah, A.M. Butt, N.D. Gohar, Strategies of making TiO_2 and ZnO visible light active, Journal of Hazardous Materials 170 (2) (2009) 560–569. Available from: https://doi.org/10.1016/j.jhazmat.2009.05.064.

[22] A. Fujishima, K. Honda, Electrochemical photolysis of water at a semiconductor electrode, Nature 238 (5358) (1972) 37–38. Available from: https://doi.org/10.1038/238037a0.

[23] A. Fujishima, T.N. Rao, D.A. Tryk, Titanium dioxide photocatalysis, Journal of Photochemistry and Photobiology C: Photochemistry Reviews 1 (1) (2000) 1–21. Available from: https://doi.org/10.1016/S1389-5567(00)00002-2.

[24] M.M. Khan, S.F. Adil, A. Al-Mayouf, Metal oxides as photocatalysts, Journal of Saudi Chemical Society 19 (5) (2015) 462–464. Available from: https://doi.org/10.1016/j.jscs.2015.04.003.

[25] D. Beydoun, R. Amal, G. Low, S. McEvoy, Role of nanoparticles in photocatalysis, Journal of Nanoparticle Research 1 (4) (1999) 439–458. Available from: https://doi.org/10.1023/A:1010044830871.

[26] Y. Zhang, J.C. Crittenden, D.W. Hand, D.L. Perram, Fixed-bed photocatalysts for solar decontamination of water, Environmental Science & Technology 28 (3) (1994) 435–442. Available from: https://doi.org/10.1021/es00052a015.

[27] J.C. Colmenares, R. Luque, J.M. Campelo, F. Colmenares, Z. Karpiński, A.A. Romero, Nanostructured photocatalysts and their applications in the photocatalytic transformation of lignocellulosic biomass: an overview, Materials 2 (4) (2009) 2228–2258. Available from: https://doi.org/10.3390/ma2042228.

[28] M.R. Hoffmann, S.T. Martin, W. Choi, D.W. Bahnemann, Environmental applications of semiconductor photocatalysis, Chemical Reviews 95 (1) (1995) 69–96. Available from: https://doi.org/10.1021/cr00033a004.

[29] A. Makama, M. Umar, S.A. Saidu, CQD-based composites as visible-light active photocatalysts for purification of water, in: Y. Yao (Ed.), Visible-light photocatalysis of carbon-based materials, IntechOpen, 2018. Available from: https://doi.org/10.5772/intechopen.74245.

[30] I.K. Konstantinou, V.A. Sakkas, T.A. Albanis, Photocatalytic degradation of propachlor in aqueous TiO_2 suspensions. Determination of the reaction pathway and identification of intermediate products by various analytical methods, Water Research 36 (11) (2002) 2733–2742. Available from: https://doi.org/10.1016/s0043-1354(01)00505-x.

[31] O. Carp, C.L. Huisman, A. Reller, Photoinduced reactivity of titanium dioxide, Progress in Solid State Chemistry 32 (1–2) (2004) 33–177. Available from: https://doi.org/10.1016/j.progsolidstchem.2004.08.001.

[32] S.H. Hyun, S.Y. Jo, B.S. Kang, Surface modification of γ-alumina membranes by silane coupling for CO_2 separation, Journal of Membrane Science 120 (2) (1996) 197−206. Available from: https://doi.org/10.1016/0376-7388(96)00160-3.

[33] S. Leong, A. Razmjou, K. Wang, K. Hapgood, X. Zhang, H. Wang, TiO2 based photocatalytic membranes: a review, Journal of Membrane Science 472 (2014) 167−184. Available from: https://doi.org/10.1016/j.memsci.2014.08.016.

[34] B. Samuneva, V. Kozhukharov, C. Trapalis, R. Kranold, Sol-gel processing of titanium-containing thin coatings - Part I Preparation and structure, Journal of Materials Science 28 (9) (1993) 2353−2360. Available from: https://doi.org/10.1007/BF01151665.

[35] A. Stoyanova, H. Hitkova, A. Bachvarova-Nedelcheva, R. Iordanova, N. Ivanova, M. Sredkova, Synthesis and antibacterial activity of TiO_2/ZnO nanocomposites prepared via nonhydrolytic route, Journal of Chemical Technology and Metallurgy 48 (2) (2013) 154−161.

[36] S.Y. Lim, W. Shen, Z. Gao, Carbon quantum dots and their applications, Chemical Society Reviews 44 (1) (2015) 362−381. Available from: https://doi.org/10.1039/C4CS00269E.

[37] T. Cetinkaya, L. Neuwirthová, K.M. Kutláková, V. Tomášek, H. Akbulut, Synthesis of nanostructured TiO_2/SiO_2 as an effective photocatalyst for degradation of acid orange, Applied Surface Science 279 (2013) 384−390. Available from: https://doi.org/10.1016/j.apsusc.2013.04.121.

[38] X. Yu, J. Liu, Y. Yu, S. Zuo, B. Li, Preparation and visible light photocatalytic activity of carbon quantum dots/TiO_2 nanosheet composites, Carbon 68 (2014) 718−724. Available from: https://doi.org/10.1016/j.carbon.2013.11.053.

[39] A. Prasannan, T. Imae, One-pot synthesis of fluorescent carbon dots from orange waste peels, Industrial and Engineering Chemistry Research 52 (44) (2013) 15673−15678. Available from: https://doi.org/10.1021/ie402421s.

[40] J. Ke, X. Li, Q. Zhao, B. Liu, S. Liu, S. Wang, Upconversion carbon quantum dots as visible light responsive component for efficient enhancement of photocatalytic performance, Journal of Colloid and Interface Science 496 (2017) 425−433. Available from: https://doi.org/10.1016/j.jcis.2017.01.121.

[41] Y. Wang, A. Hu, Carbon quantum dots: synthesis, properties and applications, Journal of Materials Chemistry C 2 (34) (2014) 6921−6939. Available from: https://doi.org/10.1039/c4tc00988f.

[42] V. Sharma, P. Tiwari, S.M. Mobin, Sustainable carbon-dots: recent advances in green carbon dots for sensing and bioimaging, Journal of Materials Chemistry B 5 (45) (2017) 8904−8924. Available from: https://doi.org/10.1039/c7tb02484c.

[43] K. Dimos, Carbon quantum dots: surface passivation and functionalization, Current Organic Chemistry 20 (2016) 682−695. Available from: https://doi.org/10.2174/1385272819666150730220948.

[44] H. Zhang, H. Huang, H. Ming, H. Li, L. Zhang, Y. Liu, et al., Carbon quantum dots/Ag_3PO_4 complex photocatalysts with enhanced photocatalytic activity and stability under visible light, Journal of Materials Chemistry 22 (21) (2012) 10501−10506. Available from: https://doi.org/10.1039/C2JM30703K.

[45] L. Zhang, J. Lian, L. Wu, Z. Duan, J. Jiang, L. Zhao, Synthesis of a thin-layer MnO_2 nanosheet-coated Fe_3O_4 nanocomposite as a magnetically separable photocatalyst, Langmuir 30 (23) (2014) 7006−7013. Available from: https://doi.org/10.1021/la500726v.

[46] R. Miao, Z. Luo, W. Zhong, S.Y. Chen, T. Jiang, B. Dutta, et al., Mesoporous TiO_2 modified with carbon quantum dots as a high-performance visible light photocatalyst, Applied Catalysis B: Environmental 189 (2016) 26−38. Available from: https://doi.org/10.1016/j.apcatb.2016.01.070.

[47] B. Thangaraj, P.R. Solomon, S. Ranganathan, Synthesis of carbon quantum dots with special reference to biomass as a source – a review, Current Pharmaceutical Design 25 (13) (2019) 1455–1476. Available from: https://doi.org/10.2174/1381612825666190618154518.

[48] T. Zhang, X. Wang, X. Zhang, Recent progress in TiO_2-mediated solar photocatalysis for industrial wastewater treatment, International Journal of Photoenergy 2014 (March) (2014) 607954. Available from: https://doi.org/10.1155/2014/607954.

[49] G. Rothenberger, P. Comte, M. Gra, A contribution to the optical design of dye-sensitized nanocrystalline solar cells, Fuel and Energy Abstracts 40 (6) (1999) 398. Available from: https://doi.org/10.1016/s0140-6701(99)98992-0.

[50] T. Sakai, D. Mersch, E. Reisner, Photocatalytic hydrogen evolution with a hydrogenase in a mediator-free system under high levels of oxygen nss, Angewandte Chemie International Edition 52 (2013) 12313–12316. Available from: https://doi.org/10.1002/anie.201306214.

[51] X. Zhang, Y. Lin, J. Wu, J. Jing, B. Fang, Improved performance of CdSe/CdS/PbS co-sensitized solar cell with double-layered TiO_2 films as photoanode, Optics Communications 395 (C) (2017) 117–121. Available from: https://doi.org/10.1016/j.optcom.2016.05.026.

[52] K. Maeda, G. Sahara, M. Eguchi, O. Ishitani, Hybrids of a ruthenium(II) polypyridyl complex and a metal oxide nanosheet for dye-sensitized hydrogen evolution with visible light: effects of the energy structure on photocatalytic activity, ACS Catalysis 5 (3) (2015) 1700–1707. Available from: https://doi.org/10.1021/acscatal.5b00040.

[53] S. Ardo, G.J. Meyer, Photodriven heterogeneous charge transfer with transition-metal compounds anchored to TiO_2 semiconductor surfaces, Chemical Society Reviews 38 (1) (2009) 115–164. Available from: https://doi.org/10.1039/b804321n.

[54] H. Ozawa, S. Honda, D. Katano, T. Sugiura, H. Arakawa, Novel ruthenium sensitizers with a dianionic tridentate ligand for dye-sensitized solar cells: the relationship between the solar cell performances and the electron-withdrawing ability of substituents on the ligand, Dalton Transactions 43 (2014) 8026–8036. Available from: https://doi.org/10.1039/c3dt52873a.

[55] S.N. Baker, G.A. Baker, Luminescent carbon nanodots: emergent nanolights, Angewandte Chemie International Edition 49 (38) (2009) 6726–6744. Available from: https://doi.org/10.1002/anie.200906623.

[56] R. Wang, K.-Q. Lu, Z.-R. Tang, Y.-J. Xu, Recent progress in carbon quantum dots: synthesis{,} properties and applications in photocatalysis, J. Mater. Chem. A 5 (8) (2017) 3717–3734. Available from: https://doi.org/10.1039/C6TA08660H.

[57] X. Wang, L. Cao, F. Lu, M.J. Meziani, H. Li, G. Qi, et al., Photoinduced electron transfers with carbon dots, Chemical Communications 25 (2009) 3774–3776. Available from: https://doi.org/10.1039/b906252a.

[58] X. Zhang, H. Huang, J. Liu, Y. Liu, Z. Kang, Carbon quantum dots serving as spectral converters through broadband upconversion of near-infrared photons for photoelectrochemical hydrogen generation, Journal of Materials Chemistry A 1 (38) (2013) 11529–11533. Available from: https://doi.org/10.1039/C3TA12568H.

[59] Q. Jin, A. Gubu, X. Chen, X. Tang, A photochemical avenue to photoluminescent N-dots and their upconversion cell imaging, Scientific Reports 7 (1) (2017) 1–7. Available from: https://doi.org/10.1038/s41598-017-01663-x.

[60] H. Yu, H. Zhang, H. Huang, Y. Liu, H. Li, H. Ming, et al., ZnO/carbon quantum dots nanocomposites: one-step fabrication and superior photocatalytic ability for toxic gas degradation under visible light at room temperature, New Journal of Chemistry 36 (4) (2012) 1031–1035. Available from: https://doi.org/10.1039/C2NJ20959D.

[61] P. Chen, F. Wang, Z.-F. Chen, Q. Zhang, Y. Su, L. Shen, et al., Study on the photocatalytic mechanism and detoxicity of gemfibrozil by a sunlight-driven TiO_2/carbon dots photocatalyst: the significant roles of reactive oxygen species, Applied Catalysis B: Environmental 204 (2017) 250−259. Available from: https://doi.org/10.1016/j.apcatb.2016.11.040.

[62] C.N.V. McCormick, H.M. Winter, A.M. Goforth, R.M. Mackiewicz, T.M. McCormick, Photocatalytic water reduction using a polymer coated carbon quantum dot sensitizer and a nickel nanoparticle catalyst, Nanotechnology 28 (19) (2017) 195402. Available from: http://stacks.iop.org/0957-4484/28/i = 19/a = 195402.

[63] K.-H. Ye, Z. Wang, J. Gu, S. Xiao, Y. Yuan, Y. Zhu, et al., Correction: carbon quantum dots as a visible light sensitizer to significantly increase the solar water splitting performance of bismuth vanadate photoanodes, Energy & Environmental Science 10 (2) (2017) 642. Available from: https://doi.org/10.1039/C7EE90006F.

[64] Z. Ren, X. Liu, H. Chu, H. Yu, Y. Xu, W. Zheng, et al., Journal of colloid and interface science carbon quantum dots decorated MoSe 2 photocatalyst for Cr (VI) reduction in the UV − vis-NIR photon energy range, Journal of Colloid And Interface Science 488 (2017) 190−195. Available from: https://doi.org/10.1016/j.jcis.2016.10.077.

[65] Y. Wang, F. Wang, Y. Feng, Z. Xie, Q. Zhang, X. Jin, et al., Facile synthesis of carbon quantum dots loaded with mesoporous g-C3N4 for synergistic absorption and visible light photodegradation of fluoroquinolone antibiotics, Dalton Transactions 47 (4) (2018) 1284−1293. Available from: https://doi.org/10.1039/C7DT04360K.

[66] S.S. Boxi, S. Paria, Visible light induced enhanced photocatalytic degradation of organic pollutants in aqueous media using Ag doped hollow TiO2 nanospheres, RSC Advances 5 (47) (2015) 37657−37668. Available from: https://doi.org/10.1039/C5RA03421C.

[67] X. Xiong, H. Chen, Y. Xu, Improved photocatalytic activity of TiO_2 on the addition of CuWO4, The Journal of Physical Chemistry C 119 (11) (2015) 5946−5953. Available from: https://doi.org/10.1021/jp510974f.

[68] M. Wang, S. Shen, L. Li, Z. Tang, J. Yang, Effects of sacrificial reagents on photocatalytic hydrogen evolution over different photocatalysts, Journal of Materials Science 52 (9) (2017) 5155−5164. Available from: https://doi.org/10.1007/s10853-017-0752-z.

[69] S. Wonyong, As featured in: energy & environmental science photocatalysis based on modified TiO_2, Energy & Environmental Science 9 (2016) 411−433. Available from: https://doi.org/10.1039/c5ee02575c.

[70] M. Sun, X. Ma, X. Chen, Y. Sun, X. Cui, Y. Lin, A nanocomposite of carbon quantum dots and TiO_2 nanotube arrays: enhancing photoelectrochemical and photocatalytic properties, RSC Advances 4 (3) (2014) 1120−1127. Available from: https://doi.org/10.1039/c3ra45474f.

[71] C. Han, M.Q. Yang, B. Weng, Y.J. Xu, Improving the photocatalytic activity and anti-photocorrosion of semiconductor ZnO by coupling with versatile carbon, Physical Chemistry Chemical Physics 16 (32) (2014) 16891−16903. Available from: https://doi.org/10.1039/c4cp02189d.

[72] A. Makama, A. Salmiaton, E.B. Saion, T.S.Y. Choong, N. Abdullah, Microwave-assisted synthesis of porous ZnO/SnS2 heterojunction and its enhanced photoactivity for water purification, Journal of Nanomaterials 2015 (2015). Available from: https://doi.org/10.1155/2015/108297.

[73] H. Li, Z. Kang, Y. Liu, S.-T. Lee, Carbon nanodots: synthesis{,} properties and applications, Journal of Materials Chemistry A 22 (46) (2012) 24230−24253. Available from: https://doi.org/10.1039/C2JM34690G.

[74] Y. Dong, R. Wang, H. Li, J. Shao, Y. Chi, X. Lin, et al., Polyamine-functionalized carbon quantum dots for chemical sensing, Carbon 50 (8) (2012) 2810−2815. Available from: https://doi.org/10.1016/j.carbon.2012.02.046.

[75] A.B. Bourlinos, A. Stassinopoulos, D. Anglos, R. Zboril, M. Karakassides, E.P. Giannelis, Surface functionalized carbogenic quantum dots, Small 4 (4) (2007) 455−458. Available from: https://doi.org/10.1002/smll.200700578.

[76] A.M. Alam, B.Y. Park, Z.K. Ghouri, M. Park, H.Y. Kim, Synthesis of carbon quantum dots from cabbage with down- and up-conversion photoluminescence properties: excellent imaging agent for biomedical applications, Green Chemistry 17 (7) (2015) 3791−3797. Available from: https://doi.org/10.1039/c5gc00686d.

[77] V.N. Mehta, S. Jha, H. Basu, R.K. Singhal, S.K. Kailasa, One-step hydrothermal approach to fabricate carbon dots from apple juice for imaging of mycobacterium and fungal cells, Sensors and Actuators, B: Chemical 213 (July 2015) (2015) 434−443. Available from: https://doi.org/10.1016/j.snb.2015.02.104.

[78] Y. Dong, N. Zhou, X. Lin, J. Lin, Y. Chi, G. Chen, Extraction of electrochemiluminescent oxidized carbon quantum dots from activated carbon, Chemistry of Materials 22 (21) (2010) 5895−5899. Available from: https://doi.org/10.1021/cm1018844.

[79] H. Peng, J. Travas-Sejdic, Simple aqueous solution route to luminescent carbogenic dots from carbohydrates, Chemistry of Materials 21 (23) (2009) 5563−5565. Available from: https://doi.org/10.1021/cm901593y.

[80] J. Tian, R. Liu, Y. Zhao, Q. Xu, S. Zhao, Controllable synthesis and cell-imaging studies on CdTe quantum dots together capped by glutathione and thioglycolic acid, Journal of Colloid and Interface Science 336 (2) (2009) 504−509. Available from: https://doi.org/10.1016/j.jcis.2009.04.064.

[81] M. Ming, Z. Ma, Y. Liu, K. Pan, H. Yu, F. Wang, et al., Large scale electrochemical synthesis of high quality carbon nanodots and their photocatalytic property, Dalton Transactions 41 (31) (2012) 9526−9531. Available from: https://doi.org/10.1039/c2dt30985h.

[82] W. Hu, Y.C. Shin, G. King, Modeling of multi-burst mode pico-second laser ablation for improved material removal rate, Applied Physics A: Materials Science and Processing 98 (2) (2010) 407−415. Available from: https://doi.org/10.1007/s00339-009-5405-x.

[83] N. Gong, H. Wang, S. Li, Y. Deng, X. Chen, L. Ye, et al., Microwave-assisted polyol synthesis of gadolinium-doped green luminescent carbon dots as a bimodal nanoprobe, Langmuir 30 (36) (2014) 10933−10939. Available from: https://doi.org/10.1021/la502705g.

[84] A. Jaiswal, S. Sankar Ghosh, A. Chattopadhyay, One step synthesis of C-dots by microwave mediated caramelization of poly(ethylene glycol, Chemical Communications 48 (3) (2012) 407−409. Available from: https://doi.org/10.1039/c1cc15988g.

[85] C. Zhai, N. Teng, B. Pan, J. Chen, F. Liu, J. Zhu, et al., Revealing the importance of non-thermal effect to strengthen hydrolysis of cellulose by synchronous cooling assisted microwave driving, Carbohydrate Polymers 197 (March) (2018) 414−421. Available from: https://doi.org/10.1016/j.carbpol.2018.06.031.

[86] C. Hu, M. He, B. Chen, B. Hu, A sol-gel polydimethylsiloxane/polythiophene coated stir bar sorptive extraction combined with gas chromatography-flame photometric detection for the determination of organophosphorus pesticides in environmental water samples, Journal of Chromatography A 1275 (2013) 25−31. Available from: https://doi.org/10.1016/j.chroma.2012.12.036.

[87] Z.A. Qiao, Y. Wang, Y. Gao, H. Li, T. Dai, Y. Liu, et al., Commercially activated carbon as the source for producing multicolor photoluminescent carbon dots by chemical oxidation, Chemical Communications 46 (46) (2010) 8812−8814. Available from: https://doi.org/10.1039/c0cc02724c.

[88] S. Wang, L. Zhao, J. Ran, Z. Shu, G. Dai, P. Zhai, Effects of calcination temperatures on photocatalytic activity of ordered titanate nanoribbon/SnO_2 films fabricated during an EPD process, International Journal of Photoenergy 2012 (2012) 472958. Available from: https://doi.org/10.1155/2012/472958.

[89] H. Sun, Q.F. Zhang, J.L. Wu, Electroluminescence from ZnO nanorods with an n-ZnO/p-Si heterojunction structure, Nanotechnology 17 (9) (2006) 2271−2274. Available from: https://doi.org/10.1088/0957-4484/17/9/033.

[90] S. Yang, W. Cai, H. Zhang, X. Xu, H. Zeng, Size and structure control of Si nanoparticles by laser ablation in different liquid media and further centrifugation classification, Journal of Physical Chemistry C 113 (44) (2009) 19091−19095. Available from: https://doi.org/10.1021/jp907285f.

[91] Y. Li, Q. Du, T. Liu, J. Sun, Y. Wang, S. Wu, et al., Methylene blue adsorption on graphene oxide/calcium alginate composites, Carbohydrate Polymers 95 (1) (2013) 501−507. Available from: https://doi.org/10.1016/j.carbpol.2013.01.094.

[92] S. Zhuo, M. Shao, S. Lee, upconversion GQD_tio2_ACSnano 2012.pdf 2 (2012) 1059−1064.

[93] D. Ma, X. Chen, G. Huang, J. Chen, H. Zhou, L. Fang, Temperature stability, structural evolution and dielectric properties of BaTiO3-Bi(Mg2/3Ta1/3)O3 perovskite ceramics, Ceramics International 41 (5) (2015) 7157−7161. Available from: https://doi.org/10.1016/j.ceramint.2015.02.036.

[94] S. Sahu, B. Behera, T.K. Maiti, S. Mohapatra, Simple one-step synthesis of highly luminescent carbon dots from orange juice: application as excellent bio-imaging agents, Chemical Communications 48 (70) (2012) 8835−8837. Available from: https://doi.org/10.1039/c2cc33796g.

[95] A. Yuliansyah, T. Hirajima, S. Kumagai, K. Sasaki, Production of solid biofuel from agricultural wastes of the palm oil industry by hydrothermal treatment, Waste and Biomass Valorization 1 (2010) 395−405.

[96] A.N. Bugrov, O.V. Almjasheva, Effect of hydrothermal synthesis conditions on the morphology Of Zro_2 nanoparticles, Nanosystems: Physics, Chemistry, Mathematics 4 (6) (2013) 810−815.

[97] Z.A. Zulkifli, K.A. Razak, W.N.W.A. Rahman, The effect of reaction temperature on the particle size of bismuth oxide nanoparticles synthesized via hydrothermal method, AIP Conference Proceedings 1958 (2018) 020007. Available from: https://doi.org/10.1063/1.5034538.

[98] G.C. Collazzo, S.L. Jahn, E.L. Foletto, Temperature and reaction time effects on the structural properties of titanium dioxide nanopowders obtained via the hydrothermal method, Brazilian Journal of Chemical Engineering 28 (02) (2011) 265−272.

[99] A. Emanuele, S. Cailotto, C. Campalani, L. Branzi, C. Raviola, D. Ravelli, et al., Biomass-derived carbon dots and their applications, Energy & Environmental Materials 2 (3) (2019) 172−192. Available from: https://doi.org/10.3390/nano9030387.

[100] J. Shen, S. Shang, X. Chen, D. Wang, Y. Cai, Facile synthesis of fluorescence carbon dots from sweet potato for Fe^{3+} sensing and cell imaging, Materials Science and Engineering C 76 (2017) 856−864. Available from: https://doi.org/10.1016/j.msec.2017.03.178.

[101] C. Zhu, J. Zhai, S. Dong, Bifunctional fluorescent carbon nanodots: green synthesis via soy milk and application as metal-free electrocatalysts for oxygen reduction, Chemical Communications 48 (75) (2012) 9367−9369. Available from: https://doi.org/10.1039/c2cc33844k.

[102] C. Yu, T. Xuan, Y. Chen, Z. Zhao, Z. Sun, H. Li, A facile, green synthesis of highly fluorescent carbon nanoparticles from oatmeal for cell imaging, Journal of Materials Chemistry C 3 (37) (2015) 9514−9518. Available from: https://doi.org/10.1039/c5tc02057c.

[103] B.S.B. Kasibabu, S.L. D'souza, S. Jha, R.K. Singhal, H. Basu, S.K. Kailasa, One-step synthesis of fluorescent carbon dots for imaging bacterial and fungal cells, Analytical Methods 7 (6) (2015) 2373−2378. Available from: https://doi.org/10.1039/c4ay02737j.

[104] A. Sachdev, P. Gopinath, Green synthesis of multifunctional carbon dots from coriander leaves and their potential application as antioxidants, sensors and bioimaging agents, Analyst 140 (12) (2015) 4260−4269. Available from: https://doi.org/10.1039/c5an00454c.

[105] W. Lu, X. Qin, S. Liu, G. Chang, Y. Zhang, Y. Luo, et al., Sun, Economical, green synthesis of fluorescent carbon nanoparticles and their use as probes for sensitive and selective detection of mercury(II) ions, Analytical Chemistry 84 (12) (2012) 5351−5357. Available from: https://doi.org/10.1021/ac3007939.

[106] U.R.R.P. Remli, A.A. Aziz, Photocatalytic degradation of methyl orange using Carbon Quantum Dots (CQDs) derived from watermelon rinds, IOP Conference Series: Materials Science and Engineering 736 (4) (2020) 91−100. Available from: https://doi.org/10.1088/1757-899X/736/4/042038.

[107] F. Ajayi, E. Ndor, N. State, Growth and yield of water melon (Citrullus lanatus) as affected by poultry manure application, Journal of Agriculture and Social Sciences 4 (2008) 121−124.

[108] G. Gladvin, G. Sudhaakr, V. Swathi, K.V. Santhisri, Mineral and vitamin compositions contents in watermelon peel (Rind), International Journal of Current Microbiology and Applied Sciences 5 (5) (2017) 129−133.

[109] M. Mushtaq, B. Sultana, RSM based optimized enzyme-assisted extraction of antioxidant phenolics from underutilized watermelon (*Citrullus lanatus* Thunb.) rind, J Food Sci Technol. 52 (August) (2015) 5048−5056. Available from: https://doi.org/10.1007/s13197-014-1562-9.

[110] U.K. Ibrahim, N. Kamarrudin, M.U.H. Suzihaque, S. Abd Hashib, Local fruit wastes as a potential source of natural antioxidant: an overview, IOP Conference Series: Materials Science and Engineering 206 (1) (2017) 012040. Available from: https://doi.org/10.1088/1757-899X/206/1/012040.

[111] A.H. Jawad, Y.S. Ngoh, K.A. Radzun, Utilization of watermelon (*Citrullus lanatus*) rinds as a natural low-cost biosorbent for adsorption of methylene blue: kinetic, equilibrium and thermodynamic studies, Journal of Taibah University for Science 12 (4) (2018) 371−381. Available from: https://doi.org/10.1080/16583655.2018.1476206.

[112] A. Ibrahim, L. Yusof, N.S. Beddu, N. Galasin, P.Y. Lee, R.N.S. Lee, et al., Adsorption study of ammonia nitrogen by watermelon rind, IOP Conference Series: Earth and Environmental Science 36 (1) (2016). Available from: https://doi.org/10.1088/1755-1315/36/1/012020.

[113] C.S.C. Kumar, R. Mythily, S. Chandraju, B. Nagar, Studies on sugars extracted from water melon (*Citrullus lanatus*) rind, A remedy for related waste and its management, International Journal of Chemical and Analytical Science 3 (8) (2012) 1527−1529.

[114] P.L. Kiew, J.F. Toong, Akademia Baru Progress in Energy and Environment Screening of Significant Parameters Affecting Zn (II) Adsorption by Chemically Treated Watermelon Rind, 6, Akademia Baru, 2018, pp. 19−32.

[115] O.A. Oseni, V.I. Okoye, Ournal of pharmaceutical and biomedical sciences, Journal of Pharmaceutical and Biomedical Sciences 27 (14) (2013) 508−514.

[116] J. Treml, K. Šmejkal, Flavonoids as potent scavengers of hydroxyl radicals, Comprehensive Reviews in Food Science and Food Safety 15 (4) (2016) 720−738. Available from: https://doi.org/10.1111/1541-4337.12204.

[117] L.Y. Jun, R.R. Karri, L.S. Yon, N.M. Mubarak, C.H. Bing, K. Mohammad, et al., Modeling and optimization by particle swarm embedded neural network for adsorption of methylene blue by jicama peroxidase immobilized on buckypaper/polyvinyl alcohol membrane, Environmental Research 183 (January) (2020) 109158. Available from: https://doi.org/10.1016/j.envres.2020.109158.

Current prospects of carbon-based nanodots in photocatalytic CO_2 conversion

14

Sushant P. Sahu[1], *Christabel Adjah-Tetteh*[2,3],
Nagapradeep Nidamanuri[4], *Sumit K. Sonkar*[5], *Erin U. Antia*[2,3],
Tam Tran[2,3], *Guanguang Xia*[2,3], *Yudong Wang*[2,3], *Ryan Simon*[1],
Manas Ranjan Gartia[6], *Supratik Mukhopadhyay*[7], *Yu Wang*[1,2] *and*
Xiao-Dong Zhou[2,3]
[1]Department of Chemistry, University of Louisiana at Lafayette, Lafayette, LA, United States, [2]Institute for Materials Research and Innovation, University of Louisiana at Lafayette, Lafayette, LA, United States, [3]Department of Chemical Engineering, University of Louisiana at Lafayette, Lafayette, LA, United States, [4]Department of Chemistry, Middle East Technological University, Ankara, Turkey, [5]Department of Chemistry, Malaviya National Institute of Technology, Jaipur, Rajasthan, India, [6]Department of Mechanical and Industrial Engineering, Louisiana State University, Baton Rouge, LA, United States, [7]Department of Environmental Sciences, Louisiana State University, Baton Rouge, LA, United States

14.1 Introduction

Photocatalysis has been a domain of intensive research due to its vivid potential and promise in solar-driven energy conversion through sustainable pathways [1–5]. Solar energy received from the Sun is estimated to be about 120,000 TW (terawatt) annually, thus providing a clean and renewable energy source [5,6]. However, many technical limitations arise in effective utilization of this tremendous amount of solar energy in terms of efficiently harvesting and converting it into other forms of energy and storing it to fulfill global energy needs. Currently, fossil fuels such as coal, oil, and natural gas contribute 85% of the total energy consumption worldwide with total power requirement estimated to be around 16 TW globally. With ever-growing population and ever-rising demand of power, the estimated global average power requirement will almost double and reach to 30 TW by 2050 [5,6]. Therefore, in order to fulfill such an extravagant energy demand, futuristic materials and technologies that are capable of harvesting, converting, and storing energy should be invented and scaled up, thereby attaining a sustainable future.

Ever-growing crave for clean energy technologies has led to extensive search for nanostructures, which can effectively harvest solar energy. For instance, solar-driven conversion of CO_2 into value-added commodities/solar fuels and splitting of

Carbon Quantum Dots for Sustainable Energy and Optoelectronics. DOI: https://doi.org/10.1016/B978-0-323-90895-5.00020-5
© 2023 Elsevier Ltd. All rights reserved.

water for generating carbon-free fuel such as hydrogen (H_2) were both considered as emerging technologies for energy-related applications [7–17]. These investigations are aimed at finding novel material compositions and related systems that show more than 10% conversion efficiency, a minimum limit set by the US Department of Energy for a commercial photocatalyst [18–20]. Additionally, the renewed interest towards renewable energy sources requires the design and advancement of cost-effective, nontoxic, highly durable nanocatalysts with a potential for recovery and long-last functioning with no significant loss of catalytic performance for effective solar light-harvesting nanomaterials. Fueling the world with inexhaustible solar energy is an alluring substitute; further, this pathway will mitigate the problems arising from climate change and global warming, which are, in turn, caused by nauseous carbon emissions. Moreover, transforming solar energy into chemical energy in chemical bonds and generation of photocurrent will enable generation of, for example, domestic, off-the-grid power (Fig. 14.1) [20].

Photocatalytic processes on a catalytic surface like TiO_2 are perceived as a favorable conventional strategy for tackling air and water purification issues, and designing and developing self-cleaning surfaces for construction coatings or composites [21–25]. Though, the major issue is the scarcity of highly active, inexpensive, and long-lasting functional catalysts that can effectively absorb a vast amount of solar energy from the Sun while promoting efficient photoinduced charge separation at the interface, producing clean hydrogen gas during water photolysis, and activating CO_2 to enable hydrogen-coupled electron transfer to manufacture worthy hydrocarbon fuels [9,13].

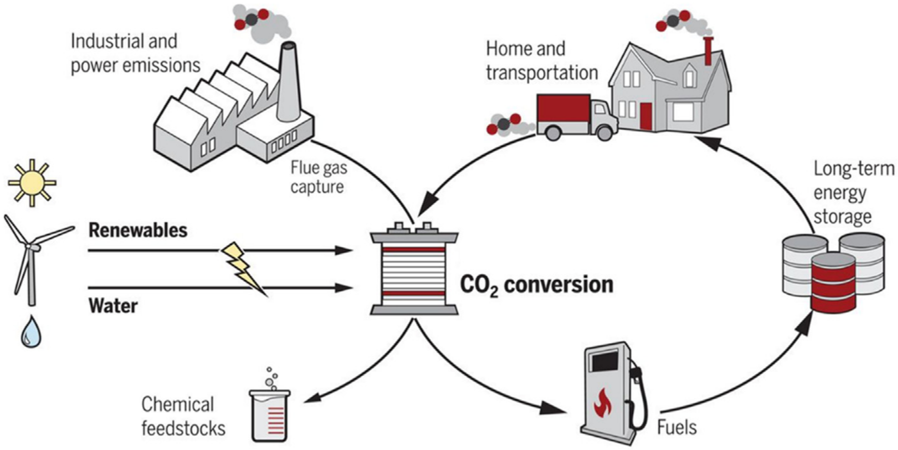

Figure 14.1 Photo- and/or electrochemical CO_2 conversion approaches to the generation of value-added commodity chemicals or solar chemical fuels while also mitigating waste CO_2 emission release from industrial processes.
Source: Adapted from P. De luna, C. Hahn, D. Higgins, S. A. Jaffer, T. F. Jaramillo, E. H. Sargent. Science 2019, 364, eaav3506.

It is well known that the solar energy received by the earth in just 1 hour exceeds the annual global energy expenditure [6]. But, effective capturing of this abundant renewable energy faces numerous challenges from different perspectives, for example, those related to synthesis. The design of nanostructured catalysts that efficiently harvest sunlight and convert its energy into prolonged charge-separated states, enable subsequent electron transfers, and promote consequent photo-induced redox reactions is critically important. Currently, solar photo-driven processes are primarily focused on splitting water to generate hydrogen as a clean fuel and the photocatalytic conversion of greenhouse CO_2 gas into hydrocarbon fuels. Ideally, the process would include both the photoreduction of CO_2 and water to generate hydrocarbon fuels and the generation of carbon-neutral clean hydrogen energy.

Nanostructured optically active semiconductors composed of metal oxides and quantum dots (QDs) are usually employed during photo-based energy conversion. Their inherent low-energy gap between valence and conduction bands enables them to serve as catalysts. For a photocatalytic reaction, the semiconductor should absorb energy that is more than or equal to their band gap, which causes the migration of an electron (e^-) from a low-energy valence band to a high-energy conduction band. This results in an electron vacancy in the valence band, which is termed as a positive hole (h^+). This pair of charge carriers (e^-/h^+) get separated and migrate favorably to react with appropriate electron donors/acceptors adsorbed close to the catalytic surface. Apart from this, these photo-generated charge carriers could also take other routes. They can recombine radiatively, which results in light emission or becoming nonradiative by generating phonons or heat dissipation, respectively. In addition, in some scenarios, these charge carriers get trapped into shallow traps due to the presence of defects and also via back electron transfer to the semiconducting photocatalytic surface from the surrounding adsorbed molecule of interest (Fig. 14.2) [3].

In order for a specific photocatalytic reaction to take place, the photocatalyst must have a suitable band-edge positions, band gap, and physicochemical characteristics. The band-edge positions (i.e., structural alignment of bands) signify the thermodynamic limitations of the redox reactions between charge carriers and the ability for light harvesting. A catalyst's physiochemical properties like particle size, shape, surface area, and crystallinity play a pivotal role in determining its catalytic performance via influencing its adsorption ability, reactivity, separation of charge carriers, and efficiency of electron transfer during photocatalytic reaction [9,13].

Nonagglomerated nano-sized particles having high surface-to-volume ratios are preferred as catalysts due to their large specific surface areas and a huge number of reactive sites on the surface denoted by a percentage of surface atoms (Fig. 14.3) [26]. These two critical features minimize the unfavorable charge carrier recombination and allow them to reach the interface coupled with a high activity of catalysts. However, quantization effects are seen in nanoscale semiconductors as the nanometer-size regime is approached where the electronic particles or excitons (e^- and h^+) of the nanostructures of semiconductors are bounded to very small sizes that are usually below the Bohr exciton radius [27,28]. Such quantum phenomena lead to the development of potential size-dependent optical and electronic

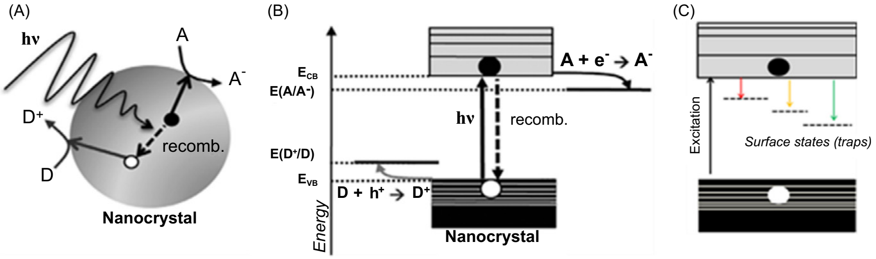

Figure 14.2 (A) Schematic illustration of a photoinduced charge transfer process in a semiconducting nanocrystal. Upon photoexcitation with light of appropriate frequency, photogenerated electrons and holes migrate to the nanoparticle surface to carry out redox reactions in which the surrounding electron acceptor (A) molecules are reduced, whereas electron donor (D) is oxidized by photogenrated holes. This competes with recombination routes for electron−hole pairs. (B) Energy states of a semiconductor for a given photoredox reaction, showing required energetics for valence and conduction band edges (E_{VB} and E_{CB}) in reference to reduction potentials of the donor and acceptor (E (D^+/D) and E (A/A^-)). (C) Schematic representation of surface trap sites with their electronic energy levels localized within the semiconductor band gap energy level.
Source: Adapted From M. B. Wilker, K. J. Schnitzenbaumer, and G. Dukovic. Israel Journal of Chemistry 2012, 52, 1002.

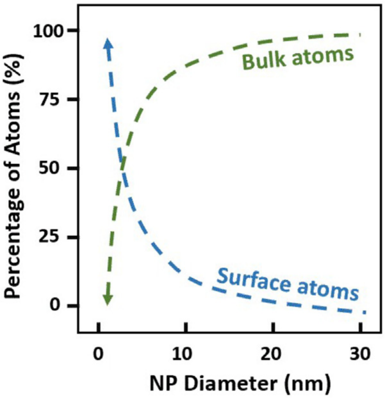

Figure 14.3 The relationship between nanoparticle size and the percentage of atoms on the surface or within the bulk of the nanoparticle.
Source: Adapted from M. Muzzio, J. Li, Z. Yin, I. M. Delahunty, J. Xie, and S. Sun. Nanoscale, 2019, 11, 18946.

properties of catalytic nanoparticles with utility in solar energy harvesting and conversion into useful chemicals via photocatalysis.

Single-crystalline one- and two-dimensional nanostructures like wires, rods, tubes, and sheets have been observed to possess high specific surface areas and low recombination rates of charge carriers than spheres due to the extended mobility of electrons. Nanostructures of these materials with high crystallinity are also beneficial in reducing the number of surface defects caused by grain boundaries, which are usual hotspots for the recombination of charge carriers [2,9,13].

Selective trapping of one of the photogenerated charges is an effective strategy to enhance the overall photochemical quantum efficiency or quantum yield (QY). Such trapping can be done in a reaction medium through deliberate introduction of sacrificial agents. Adding noble metals as co-catalysts and blending with other semiconductors so as to design a Z-scheme photosystem will prolong the lifetime of photogenerated charges to carry out redox reactions [9,13]. Nanoparticle-based metal dopants (e.g., Cu, Ag, Au, Pt) usually produce a significant amount of products since they act as electron traps/sinks due to electron affinitive nature of these metals, thereby hindering electron−hole recombination, and, hence, facilitating interfacial electron transfer. Aliphatic alcohols or amines are frequently used in the form of sacrificial substances for donating electrons by scavenging photogenerated holes, which improve overall reaction kinetics and quantum yields, resulting in yielding the desired product in higher quantities in photoreduction reactions [9,13]. Another often-used effective strategy is the combination of two nanostructured semiconductors possessing matchable band edge potentials but with different band gaps for a desired photochemical reaction. This will create a flourishing interfacial heterojunction, which will improve the light absorption range and favorable photoinduced charge carrier separation; hence, interfacial charge-transfer efficiency will be greatly enhanced, which would result in superior catalytic performance [9,13,16,17].

Carbon-based nanostructures have made a steady progress in the recent past in terms of conducting light-induced chemical reactions. They have been proven to play an important role in photochemical energy conversion with their unique broad-range visible-light absorption and rich redox chemistry. Moreover, with intrinsic features like nontoxicity, good stability, high chemical inertness, versatility, and cost-effectiveness, they have outperformed their closest competitors like metals [16,17,29−31]. The state-of-the-art and the futuristic progress of these carbon-based nanostructures from the photocatalytic research perspective are discussed in this book chapter with a prime focus on carbon-based QDs in CO_2 photoconversion. This chapter starts with the discussion of the optical and photophysical properties of carbon quantum dots (CQDs) and graphene quantum dots (GQDs) followed by their role in solar energy conversion, in particular, photocatalytic CO_2 transformation.

14.2 Synthetic approaches and optical properties of carbon quantum dots

14.2.1 Carbon dots and graphene quantum dots: an overview

In accordance with varying carbon cores, carbon QDs or simply carbon dots (CDs) have been mainly categorized into three types, namely GQDs, carbon nanodots (CNDs) or CQDs, and polymer dots (PDs) with a variety of precursors and synthetic approaches. CDs and GQDs have inspired extensive research in the domain of carbon-based luminescent nanoparticles. With the accidental discovery of luminescent carbon nanoparticles during electrophoretic purification of carbon nanotube (CNT) fragments [32], later dubbed "carbon dots" in an original report in 2006 [33], CDs have emerged as superior and universal fluorophores owing to a unique combination of numerous key merits [29–47]. CDs are quasi-spherical nanostructures without a well-defined crystal lattice and exhibited either a solid or a hollow inner core with amorphous or nanocrystalline sp^2/sp^3 carbon clusters or amorphous carbon along with sp^2-hybridized nanocrystalline domains. CDs also contain some amount of sp^3 carbons termed defects, which is attributed to the presence of various oxygenous functional groups and defective graphitic planes [46]. GQDs as a kind of CDs were initially reported by Pan et al. in 2010 as circular or elliptical, entirely crystalline structure of single or a multi-layered graphene of size as small as only several nanometers [47]. In comparison to CDs, GQDs exhibited higher crystallinity and strong quantum confinement and edge effects than CDs. CDs and GQDs are composed of sp^2 carbons with almost similar surface functionalities resulting in similar photoluminescent (PL) properties. Graphitic in-plane lattice spacing ranges between 0.18 and 0.24 nm and graphitic inter-layer spacing is generally $\sim$0.3 nm or slightly higher (if surface passivated) in both CDs and GQDs, as investigated by XRD and high-resolution transmission electron microscopy (HR-TEM) analysis. According to published reports, both quantum-confinement effects and structural defects (edge effects) play a crucial role in maintaining the optical properties of carbon or graphene-based quantum dots, which, in turn, influence their light-activated catalytic activity [29–31,40,41]. In fact, studies have concluded a common origin of observed luminescence in both GQDs and CDs ascribed to molecule-like edge states signifying shared mechanistic origins of PL in these different-yet-related carbon nanomaterials [48]. Both CDs and GQDs contain various surface defects, functional groups, and heteroatoms, depending on the synthetic route, and have significant effects on their physiochemical and structural properties.

CDs are obtained via a top-down approach that includes breaking down large carbon precursor sources into small particles, for example, plasma treatment, laser ablation, arc discharge or electrochemical oxidation of graphitic sources, and electrochemical soaking of CNTs. The other synthetic route used in the preparation of CDs is a bottom-up approach where small molecular precursors are processed to obtain larger nanoclusters. More specifically, this classification into top-down and bottom-up approaches is made based on synthetic strategies, as depicted in Fig. 14.4 [31]. Bottom-up methods include preparing CDs from relatively small carbon moieties under mild reaction conditions. These methods involve (hydro/solvo) thermal, microwave, and ultrasonic techniques, thermal oxidation, pyrolysis and vapor deposition, and proton-beam irradiation of nanodiamonds [29–31,39–41]. Significant research efforts have been devoted to the fabrication of CDs with controlled dimensions and surface properties. Various synthesis methods like acidic oxidation, metal catalyzed synthesis, hydrothermal/solvothermal synthesis, electrochemical exfoliation, microwave irradiation, organic chemical synthesis, ultrasound assisted synthesis, electron beam lithography, and pyrolysis have been adopted for

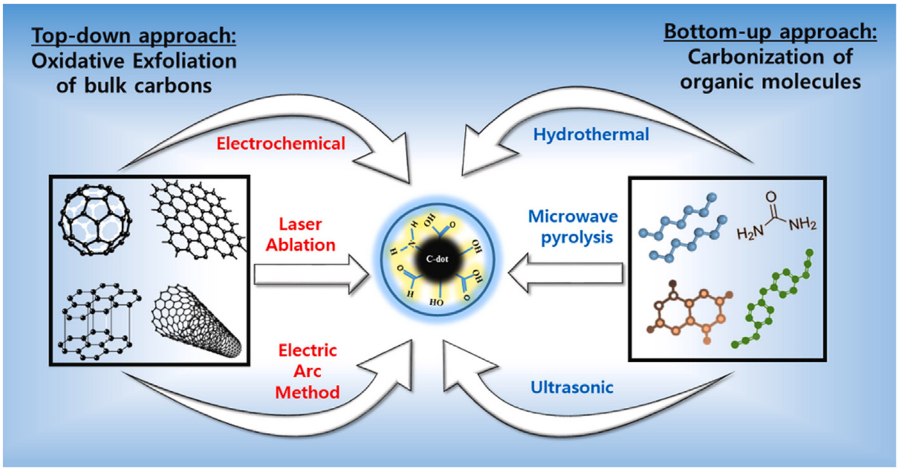

Figure 14.4 Representative synthetic routes classified into top-down and bottom-up methods in the preparation of carbon dots.
Source: Adapted from A. M. M. Hasan, M. A. Hasan, A. Reza, M. M. Islam, and M. A. B. H. Susan. Materials Today Communications 2021, 29, 102732.

the synthesis of CDs/GQDs. However, precise control of structure, size, shape, and composition of CDs and GQDs has proven to be quite challenging and has led us to a tentative relationship between structure and properties (Fig. 14.5).

In their first study, Sun and coworkers found that carbon nanoparticles (CDs) showed bright, excitation wavelength-dependent multicolor luminescence when surface functionalized with polymeric amines seen in both the solution and the solid states [33]. The resultant luminescence emissions were rather broad and observed to be dependent on the wavelength of excitation (Fig. 14.6) [33]. In previous studies, it was observed that, upon surface passivation, the surface defects or traps become more stable, which favors efficient recombination of surface-anchored holes and electrons, thus leading to stronger fluorescence emissions. Primarily, through a laser ablating graphitic precursor, these nanoparticles were synthesized and then water-soluble functional groups were introduced by oxidative acid treatment. Finally, surface passivation was carried out with an organic oligomeric polymer like PEG_{1500N} ($H_2NCH_2(CH_2CH_2O)_{35}CH_2CH_2CH_2NH_2$) or PPEI-EI (polypropionylethyleneimine-co-ethyleneimine). Both polymer-conjugated carbon nanoparticles had diameters <10 nm and exhibited good dispersion in an aqueous solution [33].

As depicted in Fig. 14.6, the luminescence emission in CDs can be explained by two separate sequential processes and corresponding efficiencies for the process: the origination of an emissive excited state (efficiency $= \Phi_1$) being the first spontaneous process and the radiative recombination of electron−hole pairs after trapping (efficiency $= \Phi_2$) being the second one. Multiplying these two efficiencies will result in observed fluorescence QY i.e., $\Phi_1\Phi_2 = \Phi_F$, which is also excitation wavelength dependent and closely follows the absorption profile of CDs; also, it was

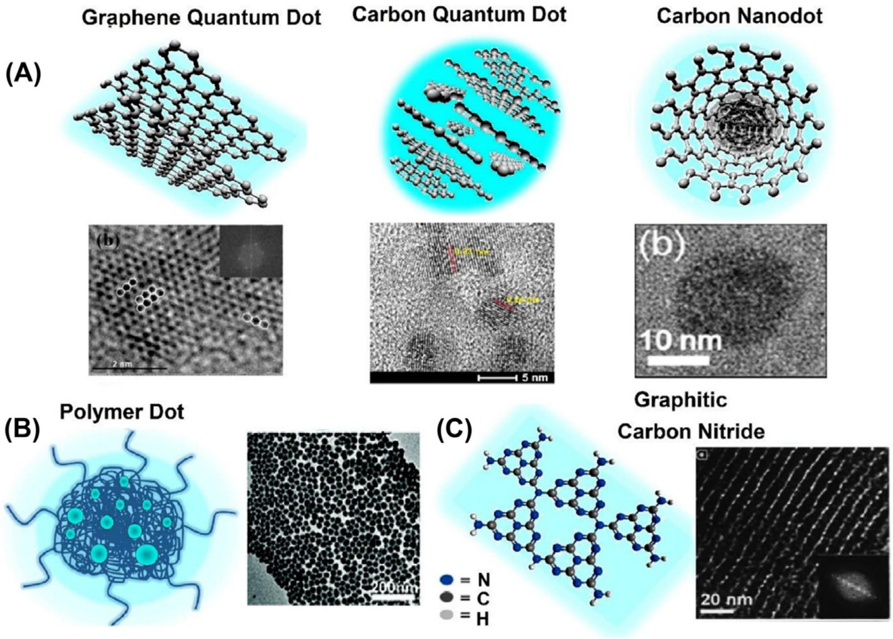

Figure 14.5 Representative structural depiction of CDs showing the passivated and possible carbon cores containing single-layered or multi-layered graphene quantum dots (GQDs), carbon quantum dots (CQDs), carbon nanodots (CNDs), and polymer dots (PDs) along with graphitic carbon nitride derived from a diverse range of carbon precursors.
Source: Adapted from S. Mandal and P. Das. Applied Materials Today, 2022, 26, 101331.

observed that fluorescence decays were quite similar at different excitation wavelengths and could be clearly decoupled from the observed emission QYs. Detailed experimental investigations revealed that the competition between radiative and nonradiative deactivations during the aforementioned second process dictates the characteristic excitation wavelength-dependent emission behavior seen in CDs [39].

In the context of semiconductor QDs, CDs display competitive optical figures of merit, which are far more superior than typical organic dye molecules as photon harvesters [49–51]. Owing to a size within the region of quantum confinement ranges, CDs exhibited a strong quantum confinement effect and ultimately lead to fascinating and unique optical properties [52]. Carbon nanoparticles possess multiple optical merits like non-blinking and photostability, multicolor emission, high molar absorptivity, and multiphoton absorptivities ($50/M_{\text{C-atom}}$/cm@450 nm, 39,000 GM) [38] and high radiative rates (1×10^8/s) and fluorescence QYs [39,40,53,54]. Moreover, when compared to organic dyes and regular semiconductor QDs, CDs exhibit excellent biocompatibility, nontoxicity, high chemical tolerance and aqueous solubility, and strong resistance to photobleaching.

Conversion of 2D graphene into 0D GQDs is gradually emerging as a potential means of facilitating the application of graphene in nanodevices since graphene

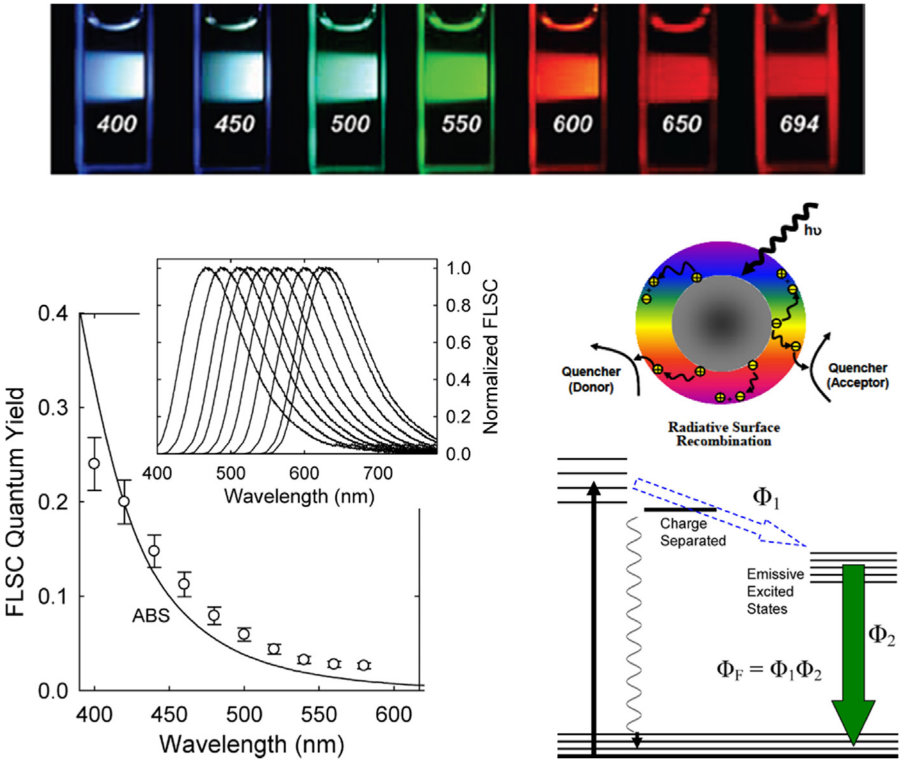

Figure 14.6 Top: Multicolor fluorescence from poly(ethylene glycol) diamine (PEG_{1500N}) passivated carbon dots excited at the specified wavelengths. Bottom (left): the optical absorption (ABS) and photoluminescence (PL) emission spectra (with progressively longer excitation wavelengths from 400 nm on the left in increments of 20 nm) of carbon dots (ethylene diamine passivated carbon dots) in their aqueous solution. Also shown are the fluorescence quantum yields at various excitation wavelengths for carbon dots (normalized to spectral peaks in the inset). Bottom (right): schematic illustration of the photoinduced redox behavior of carbon dots as both electron donor and electron acceptor and an energy-level diagram showing the mechanistic framework for fluorescence in carbon dots.
Source: Adapted from Y.-P. Sun, B. Zhou, Y. Lin, W. Wang, K. A. S. Fernando, P. Pathak, M. J. Meziani, B. A. Harruff, X. Wang, H. Wang, P. G. Luo, H. Yang M. E. Kose, B. Chen, L. M. Veca, and S.-Y. Xie. Journal of the American Chemical Society 2006, 128, 7756 and Liang W., Bunker C.E., Sun Y.-P., ACS Omega 2020, 5, 965.

offers unique characteristics such as high carrier transport mobility, excellent thermal/chemical stabilities, and superior mechanical flexibility. But, the zero band gap of graphene somehow restricts their applications in nanodevices, especially in photocatalytic structures and associated device architectures [17,55]. Over the recent past, GQDs have attracted more attention than CDs owing to excellent physicochemical properties of graphene. However, PL emissions of GQDs are mainly restricted to the dominant blue region of a visible spectrum and hence not appropriate for bio-imaging in biological window and other NIR-based PL applications [55]. In other words, similar to CDs, GQDs offer excellent water solubility, subsequent functionalization, high surface area, crystallinity, and low toxicity.

Apart from their strong and colorful luminescence, CDs are proven to be efficient visible-light photocatalysts for redox reactions involving both oxidation and reduction reactions. These photoinduced electron transfer processes are responsible for the photocatalytic processes on the dot surface [56–58]. These interesting photoinduced redox processes of CDs enable light-assisted energy conversion, developing photovoltaic device modules, and application in associated optoelectronics [56–58]. In addition, CDs also exhibited potential for use as nanoprobes for sensitive and selective detection of diverse ions [59–61].

The optical properties of CDs and GQDs enhance their application prospects. In general, they exhibit broad optical absorption across the UV–visible region (Fig. 14.7A and B) [29,30,39,61]. Upon anchoring polymeric amines onto the surface of CDs, their absorbance increases slightly in the visible region, showing a weak shoulder at around 400–450 nm [39]. Carbon nanoparticles synthesized *via* one-pot synthetic methods exhibited absorption between 200 and 320 nm largely attributed to π to π^* and n to π^* electronic transitions associated with polar surface functionalities [62–66]. Aqueous suspended smaller carbon nanoparticles exhibited strong optical absorption over the UV–Vis range (Fig. 14.7), harvesting 65% of solar radiation across the 300–800 nm range with the calculated molar absorptivity values at around 50 $\mathrm{M_{C\text{-}atom}}^{-1}$/cm (@400–450 nm) compared to 16 $\mathrm{M_{C\text{-}atom}}^{-1}$/cm for C_{60} at its first absorption band maximum [39]. Tang et al. showed that absorbance is independent of GQD size but depends on dilution with a linear relationship observed according to Beer's law (Fig. 14.7C) [62]. The GQDs were synthesized by a microwave-assisted hydrothermal method with different microwave heating times. Absorbance was found to increase in intensity with increasing microwave heating time (Fig. 14.7D and E). Precursor concentration was also found to affect the peak intensity (Fig. 14.7F–H). The optical absorption of nanoscale carbon particles is associated with the π-plasmon absorption broadly covering 65% of the solar spectrum in the UV–Vis and near-IR spectral regions from 300 to 800 nm [39] (Fig. 14.7), likely initiated by the collective excitation of π-electron density ($C = C_{\pi\rightarrow\pi^*}$) resulting from sp^2 graphitic islands (π-domains) [29,39,67–73]. Self-passivation or surface functionalization is responsible for the formation of surface states between π^* and π energy levels, leading to unique optical absorption of carbon nanoparticles. Their absorption spectrum is the superposition from diverse state transitions with strongly absorptive species lying in the blue region of the visible spectrum. Moreover, their featureless UV–Vis absorption spectrum superimposes to a great extent with the solar spectrum around the visible to near-IR region (Fig. 14.7A and B).

The PL and optical properties of CDs and GQDs are mainly behind their photocatalytic activity. Numerous reports related to the fluorescence emissions of CQDs have been published so far [29,30,39,40,74–83]. The PL emission spectra are generally broad, ranging from the UV to visible and sometimes extending to the NIR region of the spectrum (Fig. 14.8A and B) [39]. The fluorescence lifetimes measured are usually just a few nanoseconds. QY is the ratio of number of emitted photons to

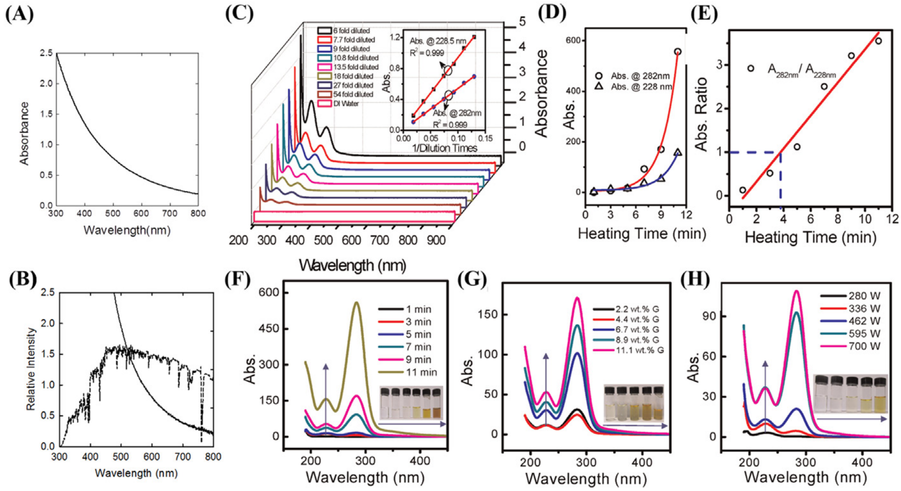

Figure 14.7 (A) A characteristic optical absorption spectrum of aqueous dispersed carbon nanodots. (B) The observed broad optical absorption feature of carbon dots (solid line) overlapping well with the solar spectrum in the visible range at sea level (dashed line) of broadly distributed carbon dots (solid line) compared with the solar spectrum around the visible spectrum at sea level (dashed line). Deep UV optical absorption spectra of the graphene quantum dots (GQDs). (C) The optical absorption spectra of the GQDs with varying dilution; the data in the inset show the observed linear behavior between optical density (at 228 and 282 nm, respectively) and 1/dilution times. (D) The observed exponential behavior between the optical density (at 228 and 282 nm) and microwave irradiation time. (E) The linear connection between the absorbance ratios at wavelengths 282 and 228 nm as a function of microwave irradiation time or heating. (F) The influence of microwave heating time on the optical density of the GQDs synthesized at 595 W. (G) The influence of source content on the optical density of the GQDs under microwave heating for 9 min at 595 W. (H) The result of microwave power on the optical density or absorbance of the GQDs heated for 7 min at 280, 336, 462, 595, and 700 W. The insets in panels (D)−(F) show respective solutions in the presence of ambient light.

Source: Adapted from Tang L., Ji R., Cao X., Lin J., Jiang H., Li X., ACS Nano **2012**, *6*, 5102.

absorbed ones. At the initial stage of their existence, unpassivated or naked CDs demonstrated a low QY (<1%) but was found to be considerably increased after surface passivation or heteroatom doping [29,39]. Such PL results from various factors like the presence of excitons, conjugated aromatic structures, oxygen-containing groups, carbene-like triplet ground state, and edge defects [29,30,39,40,74−83]. Moreover, the emission and intensity of CDs strongly depend on the excitation wavelength. Such dependence arises from quantum confinement effects resulting from different-size nanoparticles and/or surface emission traps or from yet an unknown mechanism. However, excitation-independent emissions are also reported by a few researchers (Fig. 14.8) [29,39,84−87]. PL of CDs, which could be a function of different sizes of dots, has been noted by various groups [29,39,88−90].

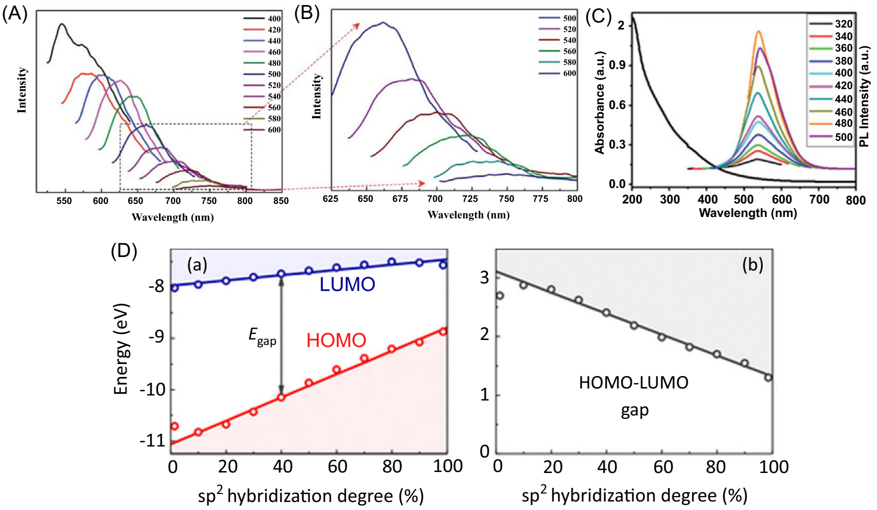

Figure 14.8 (A) Fluorescence spectra of water-soluble carbon dots (wsCDs) in the visible to near-infrared (Vis−NIR) region of the spectrum and luminescence spectrum profile of wsCDs recorded with a range of various excitation wavelengths under progressive 20 nm intervals in the range 400−600 nm. (B) Zoomed-in image of (A) representing the red and near-IR regions of visible spectrum shown up to 750 nm. Optical absorption together with emission spectra at different excitation wavelengths ranging from 320 to 500 nm with a fixed interval of 20 nm in increments of a dilute suspension of water-soluble onion-like carbon nanoparticles (wsOCNPs) prepared from camphor soot. (D) Variation in HOMO-LUMO energy gap with degree of sp^2 hybridization of carbon domains.

Source: Adapted from P. Dubey, K. M. Tripathi, and S. K. Sonkar. RSC Advances 2014, 4, 5838; Tepliakov N.V., Kundelev E.V., Khavlyuk P.D., Xiong Y., Leonov M.Y., Zhu W., et al.,*ACS Nano* **2019**, *13*, 10737.

In-depth X-ray photoelectron and infrared spectroscopic analyses suggested that the surface of CDs possess groups like C = O, C−OH, C−O−C, and C−H, which lead to various emissive traps between π and π* states of sp^2 carbon domains. Specifically, the oxygen-containing groups influence the energy gap of the trap site, thereby forming "surface states" on the dot surface. Therefore, a dissimilar distribution of emissive traps and the relative density of the functional groups on the dot surface perhaps result in varying degrees of emission intensity and different locations of peak emission wavelengths in their spectra.

Basically, when CDs are excited at a specific wavelength, a corresponding surface energy trap with an energy gap dominates the luminescence emission, which is dependent on the wavelength used. Therefore, both diverse surface defects and varying sizes of CDs control their luminescence behavior.

As per the published reports on CDs, photoactivated CDs could behave as both electron acceptors and donors depending on their photoinduced electron characteristics [29,39,56−58,91,92]. Typically, their luminescence spectra are wide with significant Stokes shifts in emission wavelength, which depends on the wavelength of excitation used, suggesting spectral heterogeneity and usually strong emission in the blue−green region of visible frequencies with luminescence QYs reported to be generally more than 10% in various batches of prepared CDs [29,39]. The fluorescence decay curves from laser-ablation-generated CDs excited at a wavelength of 407 nm displayed multi-exponential luminescence decays with average excited-state fluorescence lifetimes of 5 ns for peak emission maximum at 450 nm and 4.4 ns for peak emission maximum centered at 640 nm, indicating diverse surface emissive trap sites [33].

Surface modification, formation of nanocomposites, and heteroatom doping are usually employed to influence the PL of carbon nanoparticles. Carbon nanoparticles can be easily covalently functionalized with a wide variety of amines, polymers, biomolecules, and other functional groups, leading to strong absorption and emission in the visible region, which can be further extended into the NIR region [29,39]. Anilkumar et al. crosslinked surface functionalized CDs to obtain fluorescent probes of much enhanced optical performance in terms of their fluorescence brightness essentially proportional to the estimated probe size [93]. Sun and coworkers employed 2,2-(ethylenedioxy)bis(ethylamine) as a surface passivating agent for making CDs with diameter <5 nm, exhibiting comparable size and optical properties to that of conventional green fluorescent proteins (GFPs) [94]. Heteroatom doping in carbon nanomaterials is emerging as a potential tool for tailoring their electronic and optical properties [29,39]. A simple solution-phase photolysis method is generally used for the coating of functionalized carbon nanoparticles with gold or platinum nanoparticles, resulting in their enhanced photocatalytic reduction process, like metal coating onto semiconductor nanoparticles (e.g., Pt-coated TiO_2) [56]. Chai et al. explained the formation of a well-controlled assembly of CDs/CdS multilayers with close interfacial contact, which promotes charge separation and is advantageous for superior photoelectrochemical and/or photocatalytic performance under visible light irradiation, with built-in heterojunctions for solar energy conversion [95]. Wang et al. reported the photoreduction of aqueous silver cation into silver metal by the photoexcited carbon particles [58]. Sun's team also studied the surface passivation effects of CDs via employing an inorganic (ZnO, ZnS, and TiO_2) coating and organic functionalization together. Through a gel column fractionation, they successfully isolated CDs displaying QYs $\sim$78% attributed to improved surface passivation [39,96].

To overcome the issues of broad absorption and lack of emissions at higher excitation wavelengths in NIR, heteroatom doping provides attractive tools for the tuning of electronic energy levels and hence intrinsic emissive states of carbon nanomaterial. Synthesis of N-doped CDs was achieved by using amino acids or an N-containing precursor for simultaneous N-doping and surface passivation. Microwave and hydrothermal routes are extensively used techniques for facile synthesis under milder conditions and avoiding a multi-step synthesis process. Wang et al. microwaved a green carbonaceous source—milk, for making water-dispersible CDs in large quantities. Upon microwaving 20 mL of milk for 25 min, they produced 0.3 g of CDs with a QY of $\sim$16% [97]. Wei et al. proposed the fast synthesis of N-doped CDs using glucose as a precursor with enhanced PL characteristics [98]. Narrower size distribution of N-doped CDs was reported by using low-pressure size-exclusion chromatography following microwave synthesis to enhance QY and tune surface states [99]. In addition to single-heteroatom co-doping of heteroatoms such as N (comparable atomic size with carbon), B, S, and P also were explored to take advantage of the synergetic coupling effect between doped heteroatoms, which facilitates developing enhanced optical properties [29,39,100−103]. For instance, Kim and coworkers synthesized boron-and-nitrogen co-doped CDs (BN-CDs) *via* a microwave pyrolysis technique with increased PL properties [101]. The enhanced PL was attributed to an increased number of emitted photons per particle having graphitic core structure and tailored surface states upon doping studied by single-molecule spectroscopic analysis. S and N co-doped GQDs (S,N-GQDs) synthesized *via* a solvothermal process showed UV−Vis absorption bands (338, 467, and 557 nm), attributed to the formation of multiple emission centers. Furthermore, the nanocomposite of such synthesized S-N-GQDs with TiO_2 was explored for hydrogen production under visible light irradiation [102]. Xu et al. proposed the synthesis of semi-crystalline N,S-doped CDs with high doping efficiency and QY (55%) [103]. The synthesized CDs were reported to exhibit excitation-independent luminescence for the ultra-trace detection of Hg^{2+}.

The PL mechanism of CDs has not been elucidated conclusively yet and different theories have been proposed for the origin of PL, which are broadly categorized into three commonly acknowledged mechanisms depicted in Fig. 14.9 [104]. The first mechanism is that of typical excitation-independent fluorescence originating

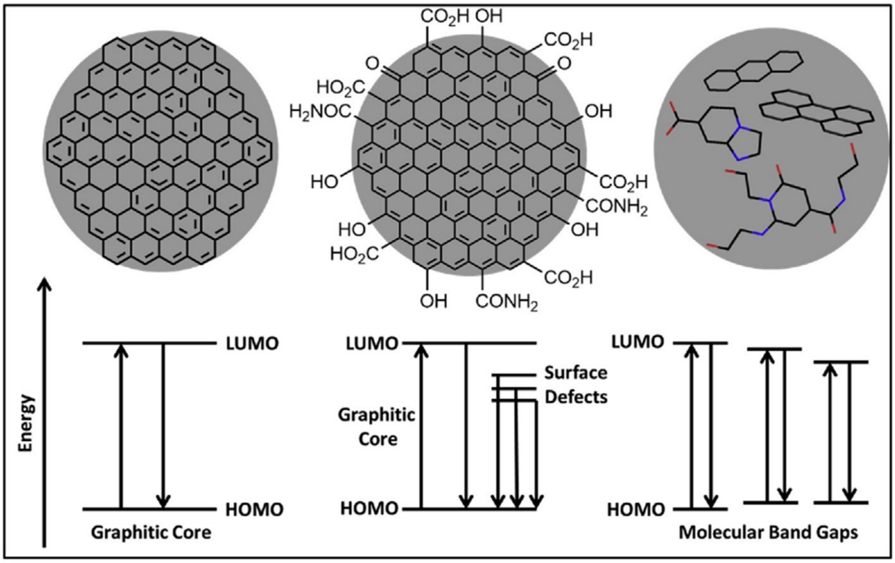

Figure 14.9 Three different chemical structures of carbon-based fluorescent nanodots depicting the control of chemical structure on the photoluminescence behavior of CDs. *Source*: Barman M.K., Patra A., Journal of Photochemistry and Photobiology C 2018, 37, 1.

from true semiconductor-like uniformity in the surface states of fluorescent CDs and degree of heterogeneity in size of CDs. The second, and the quite well-recognized, mechanism is the radiative recombination of the electron–hole pairs confined to the dot surface, phenomenologically analogous to those found in quantum-confined semiconductor quantum dots [105]. The electron–hole pair migration may occur to surface traps due to the presence of defects, leading to the formation of nonradiative relaxation channels. This unfavorable deviation quenches fluorescence, thereby causing lower PL QYs in bare carbon nanoparticles (i.e., without passivation agents) [29,30,39,40,74–83]. But, in the case of CDs with higher surface-to-volume ratios i.e., small nanoparticles with a greater fraction of surface atoms and energy traps, their in-particle interactions stabilized by passivated surface defects lead to stronger PL emissions. This type of mechanism typically shows excitation-dependent fluorescence as discussed before. The third type of fluorescence mechanism in CDs is quite analogous to that found in metal nanocrystals, where, depending on the carbon precursors in the preparation of CDs, the CD fluorescence is attributed to the superposition of various emitters such as molecular fluorophores and multi-chromophore units present in the solution of CDs [41]. Upon addition of aliphatic amines (e.g., ethyl amine) to bare CDs, surface passivation behavior was clearly seen through the luminescence quenching measurements, where at sub-mM concentrations of amines, the reverse Stern–Volmer quenching behavior was noticed with rising luminescence intensities, which is attributed to the surface passivation effect observed at low quencher concentrations [106].

Size-dependent aspects (possibly due to quantum confinement effects) for tunable PL emissions of CDs are also well established by many researchers [29,39,88–90]. Dekaliuk et al. investigated that CDs are a unique combination of surface-exposed fluorophores and behave as individual emitters [107]. Another study by Yang et al. revealed the significant contribution of surface functional groups such as carboxyl or hydroxyl groups in the origin of blue and green emissions in CDs because of the formation of intramolecular hydrogen bonds [108]. The hydrogen bonding was found to enhance the synergistic band-bending effect for the favorable charge separation and stabilization of photogenerated electron–hole pairs and offering high photocatalytic activity. Ghosh et al. suggested that CDs behave as electric dipoles, and optical properties of CDs result from a recombination of photogenerated charges at defective surfaces of CDs [109]. These defective surfaces act as charge emission centers and involve in strong coupling between the combined vibrational modes of the lattice structure and electronic transition. The optical properties of CDs and GQDs also depend on the synthetic conditions and properties of precursor sources. Core domains of sp^2-hybridized carbons embedded within a matrix comprising mainly sp^3-hybridized carbon (surface defects) are the source of main absorption features [110]. However, the actual composition and density of sp^2 core is not fully understood yet. One often-stated conjecture is that different synthetic methods or surface functionalization attributed to the variation in emissive traps or degree of quenching states are responsible for tunable emissions [111]. Presence of diverse functional groups and different conjugation lengths of core resulted in multi-chromophoric units in CDs and, consequently, led to significant heterogeneity between particles at lower energy trap sites. Das et al. investigated that oxidized CDs exhibited single chromophoric centers in contrast to reduced carbon nanoparticles, which exhibited multi-chromophoric units [111]. While some studies have argued that CDs are mainly composed of polycyclic aromatic hydrocarbon (PAHs) in their core region embedded in a large degree by sp^3-hybridized carbon [110]. Self-trapping of excitons in stacked PAH networks suggested the large Stokes shift in CDs. Selective excitation of PAHs with slightly different energy gaps and further energy transfer between larger and smaller energy gaps leads to the unique optical behavior of CDs (a tail extending far out to longer wavelengths) [110].

Carbon nanoparticles are highly absorptive across the UV–Vis range of spectrum, extending to the near-IR. Photoactivation of CDs drives the photoinduced redox reactions, which result not only in luminescence emissions but also in the formation of photogenerated electron–hole pairs, a prime feature responsible for the photocatalytic energy conversion reactions. In fact, it has been shown that aqueous-dispersed CDs can act as potent photocatalysts for H_2 evolution and CO_2 reduction through effective harvesting of visible photons [29,39–41]. In addition, quantum-confined size effect, large band gap, and strong reduction and oxidation potentials significantly contributed to excellent photocatalytic activity of CDs [29,39–41]. The lower the recombination of electron–hole pairs, the higher the photocatalytic activity, which, in turn, is generally related to PL intensity of photocatalysts tested. Considering the current status and potential of carbon nanoparticles, development of CDs in a controlled framework with tailored photophysical properties as the next step into the future is evident.

14.3 Carbon-based quantum dots in CO_2 photoconversion

14.3.1 *Photocatalytic CO_2 reduction*

In the semiconductor-driven photocatalytic CO_2 conversion, multiple sequential reactions occur where the photoinduced holes and electrons are transferred to CO_2 and H_2O. Such reactions result in diverse products ranging from hydrocarbons (e.g., CH_4) to oxygen-embedded products (e.g., HCHO, HCOOH, CO, CH_3OH) [9]:

$$CO_2 + 2H^+ + 2e^- \rightarrow HCOOH\ E^0_{Redox} = -0.61\ V$$

$$CO_2 + 2H^+ + 2e^- \rightarrow CO\ \ E^0_{Redox} = -0.53\ V$$

$$HCOOH + 2H^+ + 2e^- \rightarrow HCHO + H_2O\ \ E^0_{Redox} = -0.48V$$

$$HCHO + 2H^+ + 2e^- \rightarrow CH_3OH\ \ E^0_{Redox} = -0.38V$$

$$CH_3OH + 2H^+ + 2e^- \rightarrow CH_4 + H_2O\ \ E^0_{Redox} = -0.24V$$

$$2CO_2 + 8H^+ + 8e^- \rightarrow CH_3COOH + 2H_2O\ \ E^0_{Redox} = -0.31V$$

$$2CO_2 + 12H^+ + 12e^- \rightarrow C_2H_5OH + 3H_2O\ \ E^0_{Redox} = -0.33V$$

$$2H^+ + 2e^- \rightarrow H_2E^0_{Redox} = -0.41V$$

$$H_2O + h^+ \rightarrow OH + H^+E^0_{Redox} = +2.32V$$

$$2H_2O + 2h^+ \rightarrow H_2O_2 + 2H^+E^0_{Redox} = +1.35V$$

$$2H_2O + 4h^+ \rightarrow O_2 + 4H^+E^0_{Redox} = +0.82V$$

[Note: The potentials are in reference to a normal hydrogen electrode (NHE) at pH 7.]

Furthermore, in order to drive the conversion of CO_2 to CH_4, the electrons in the conduction band should possess a higher negative potential than the redox potential (−0.24 V vs NHE) of CO_2/CH_4 [9]. In a complex conversion like this, a plausible intermediate is presumed to be presented in multiple reaction pathways [9,112]. Fig. 14.10 illustrates the photocatalytic CO_2 reduction on the surface of a

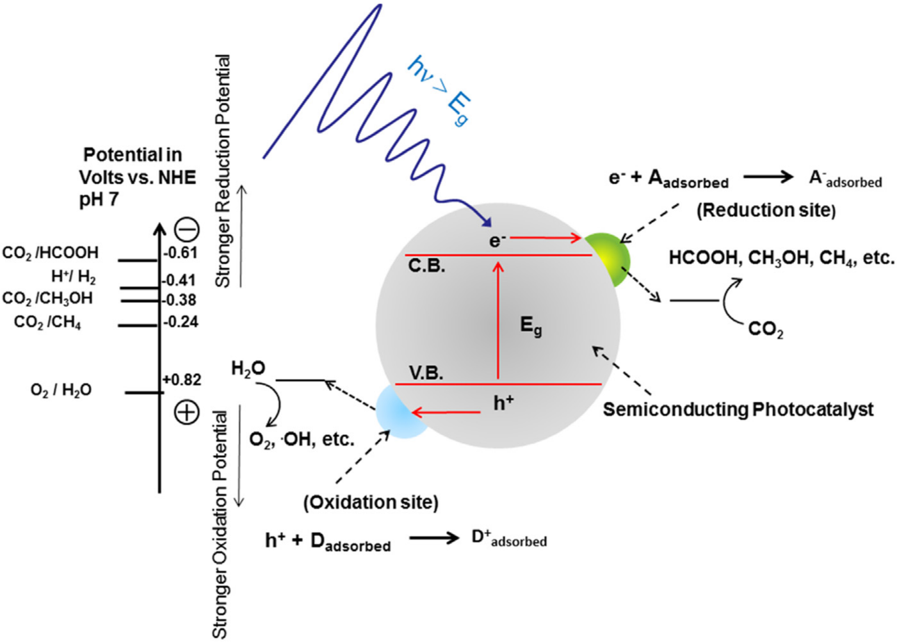
Potential in
Volts vs. NHE
pH 7
⊖
CO₂ /HCOOH
H⁺/ H₂
CO₂ /CH₃OH
CO₂ /CH₄
O₂ / H₂O
-0.61
-0.41
-0.38
-0.24
+0.82
⊕
Stronger Reduction Potential
Stronger Oxidation Potential
hν > Eg
e⁻
C.B.
Eg
V.B.
h⁺
e⁻ + A adsorbed → A⁻ adsorbed
(Reduction site)
HCOOH, CH₃OH, CH₄, etc.
CO₂
Semiconducting Photocatalyst
H₂O
O₂, ·OH, etc.
(Oxidation site)
h⁺ + D adsorbed → D⁺ adsorbed

Figure 14.10 Schematic illustration of photocatalytic CO_2 reduction on a semiconductor photocatalyst.

Source: Adapted from S. Sahu, All dissertations 1484, 2014.

semiconducting photocatalyst. The thermodynamic reaction displayed a huge positive change in Gibbs free energy.

In the case of commonly used wide band gap semiconductors, conduction and valence bands produce sufficient negative and positive redox potentials, respectively, for reducing CO_2 [9]. Such semiconductors absorb UV radiation predominantly; hence, they cannot effectively use sunlight during the photocatalytic solar energy conversion, which only consists of 4%−5% UV radiation. Hence, the use of wide band gap semiconductors remains very limited in CO_2 photoreduction [8−17]. Attaining selectivity in CO_2 reduction is a Herculean task when compared to water-splitting (outcomes: H_2 or O_2) due to the possibility of multiple final outcomes. Moreover, poor aqueous solubility of CO_2 (33 mM@25°C, 1 atm) hampers the photoconversion ability [9]. But, with increase in CO_2 pressures (Fig. 14.11) [113], the CO_2 concentration can be increased, thus enhancing photoconversion efficiency, which is expected to result in better product yields in the end.

The major problem in CO_2 photoreduction is its lower QYs. In general, the catalytic efficiency is measured in terms of production rates (μmol/h or μmol/g/h). The catalytic activity depends on the amount and active surface area of the photocatalyst, illumination time, and intensity. Photoreduction efficiency is measured in terms of apparent QYs, which are calculated through the following equation:

$$\text{Apparent Quantum Yield (AQY\%)} = \frac{\text{Number of Reacted Electrons}}{\text{Number of Absorbed Photons}} \times 100$$

The aforementioned photocatalytic efficiency of a catalyst mainly depends on the ratio of rates of surface charge carrier transfer in redox reactions to the

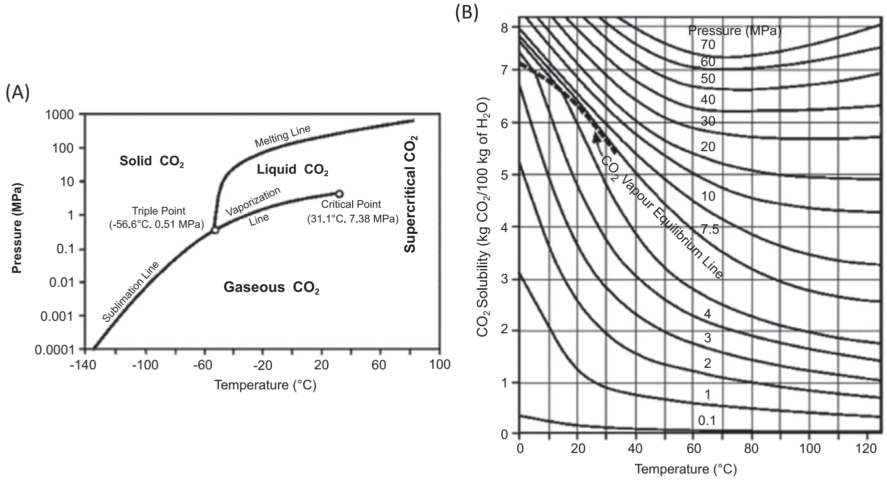

Figure 14.11 The phase diagram (A) and solubility characteristics of CO_2 as a function of CO_2 pressures in fresh water (B).

Source: Adapted from S. Bachu. Progress in Energy and Combustion Science 2008, 34, 254.

photoexcited charge carrier recombination ($k_{redox}/k_{recombination}$). Detailed time-resolved spectroscopic investigations [114,115] disclosed that almost 90% of photogenerated electron–hole pairs recombine rapidly upon photoexcitation, thereby leaving only ~5%–10% charge carriers for the required redox reactions, which are actually responsible for generating desired photoconversion products [116]. Due to this reason, most of the semiconductor-driven photocatalytic conversions end up giving very low product yields.

In spite of the aforementioned difficulties, semiconductor-based nanomaterials are widely used in solar energy conversion research due to the 1972's discovery of the Honda–Fujishima effect [117]. Among multitudinous semiconductors, titania -TiO_2, and its constitutes are the most frequently used ones as well as considered as standards in photocatalysis because of their favorable physiochemical properties and electronic structures [9]. Nevertheless, TiO_2 is a wide band gap semiconductor that absorbs UV radiation rather than visible radiation used in photocatalysis [9,12,118,119]. This can be overcome by metal doping (e.g., transition metal ions), which generally introduces newly occupied electron levels on top of the original valence band, thus enhancing the photoactivity to the visible region [9,120]. The exact cause behind this dopant-induced modification is not well understood; thus, further investigations are required for supporting the doping process during ramping up the photocatalytic activity as well as in the rational design of photocatalysts [2,9]. Apart from metallic oxide semiconductors (e.g., Ga_2O_3, Ta_2O_5, WO_3, Bi_2WO_4, etc.), non-oxide ones like sulfides, phosphides, and nitrides (e.g., ZnS, GaP, GaN, etc.) are also used for various photocatalytic applications [8–17].

Carbon-based nanomaterials are emerging at a rapid pace as nanohybrid photocatalysts due to their cost-effectiveness, unique optical properties, and reliable catalytic performance [17,56,121–131]. For instance, graphene, a conjugated 2D honeycomb-structured single-layer graphitedisplays unparalleled properties (Fig. 14.12A and B) [17] like great transparency (97.7%) and mechanical strengths, high flexibility and specific surface areas (2630 m^2/g), and high electrical and thermal conductivities (200,000 $cm^2/V/s$ and 5000 W/m/K, respectively). Further, as

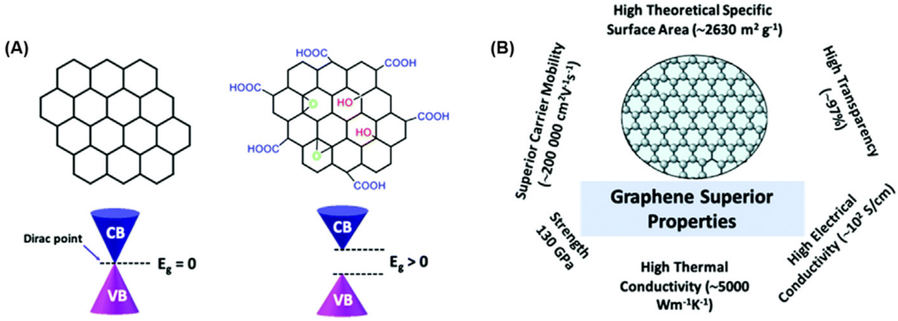
(A)
HOOC
COOH
HOOC
O
HO
COOH
HO
HOOC
O
COOH
Dirac point
CB
VB
$E_g = 0$
CB
VB
$E_g > 0$
(B)
High Theoretical Specific Surface Area (~2630 m² g⁻¹)
High Transparency (~97%)
High Electrical Conductivity (~10² S/cm)
High Thermal Conductivity (~5000 Wm⁻¹K⁻¹)
Strength 130 GPa
Superior Carrier Mobility (~200 000 cm²V⁻¹s⁻¹)
Graphene Superior Properties

Figure 14.12 Structural features and band gap characteristics of graphene and graphene oxide-based materials (A) and their superior figures of merit (B).
Source: Adapted from K. Bramhaiah and S. Bhattacharyya. Materials Advances 2022, 3, 142.

illustrated in Fig. 14.12A, at the Dirac point, the π^*-state conduction band and the π-state valence band of graphene come in contact with each other; hence, it is often referred as a zero-band gap semiconductor.

Graphene oxide (GO), an analog of graphene, have also drawn a good deal of attention from the research fraternity in the context of photocatalysis. In general, it is prepared through Hummer's method [132] in which strong oxidants are used to exfoliate graphite chemically. GO is an individual sheet of graphene possessing oxygen-imbedded groups like carbonyl, hydroxyl, and epoxy on both the basal plane and edges [133]. In composites made from graphene, it can either behave as a substrate that can facilitate the immobilization of other components or works like an active component. Besides furnishing the required mechanical strength as well as broadening the light absorption range, graphene's high specific surface area and conductivity will substantially aid charge transfer and relevant redox reactions. Hence, tying up of redox-active materials and photocatalysts onto the surface of graphene will enhance the photocatalytic performance of ensuing composites where the graphene plays a dual role of electron collector cum transporter. Moreover, it is also known that graphene hinders the recombination of electrons and holes to a great extent, by facilitating electron transport; hence, extended lifetimes are feasible for charge carriers even in the case of semiconductor nanoparticles when combined with graphene [17]. Commonly used synthetic approaches for making exfoliated graphene sheets are the chemical vapor deposition (CVD) method, mechanical cleavage of graphite crystal, and the oxidation–exfoliation–reduction of graphite powder, which results in the production of reduced graphene oxide (r-GO),yet another useful analog of graphene with better conductivity than GO [126,128,129].

14.3.2 Photophysical characteristics and CO_2 photoconversion with carbon-based catalysts

Cao et al. designed surface-modified CDs coated with platinum or gold metal for harvesting photons from visible radiation as well as to drive photocatalytic processes, similar to commonly employed semiconductor quantum dots [57]. The purpose of noble metal (Pt, Au) (Fig. 14.13) coating was to concentrate the photogenerated electrons to promote efficient interfacial electron transfer in photoreduction reactions. Formic acid was identified as a major CO_2 photoconversion product by distillation with an estimated quantum efficiency of ~0.3% [57] characterized by NMR spectroscopy, which is in agreement with past research employing semiconducting nanoparticles [9,57]. Subsequently, the group demonstrated significantly improved photoconversion yields at higher CO_2 pressures using an aqueous solution of CDs as photocatalysts with the detection of formic acid as well as acetic acid as main photoconversion products (Fig. 14.13) [134,135]. The primary objective was also to elucidate the photoinduced redox behavior, which validated photoirradiated CDs could behave as either electron donors or acceptors in the presence of quenchers, which resulted in efficient fluorescence quenching of CDs [56–58,92].

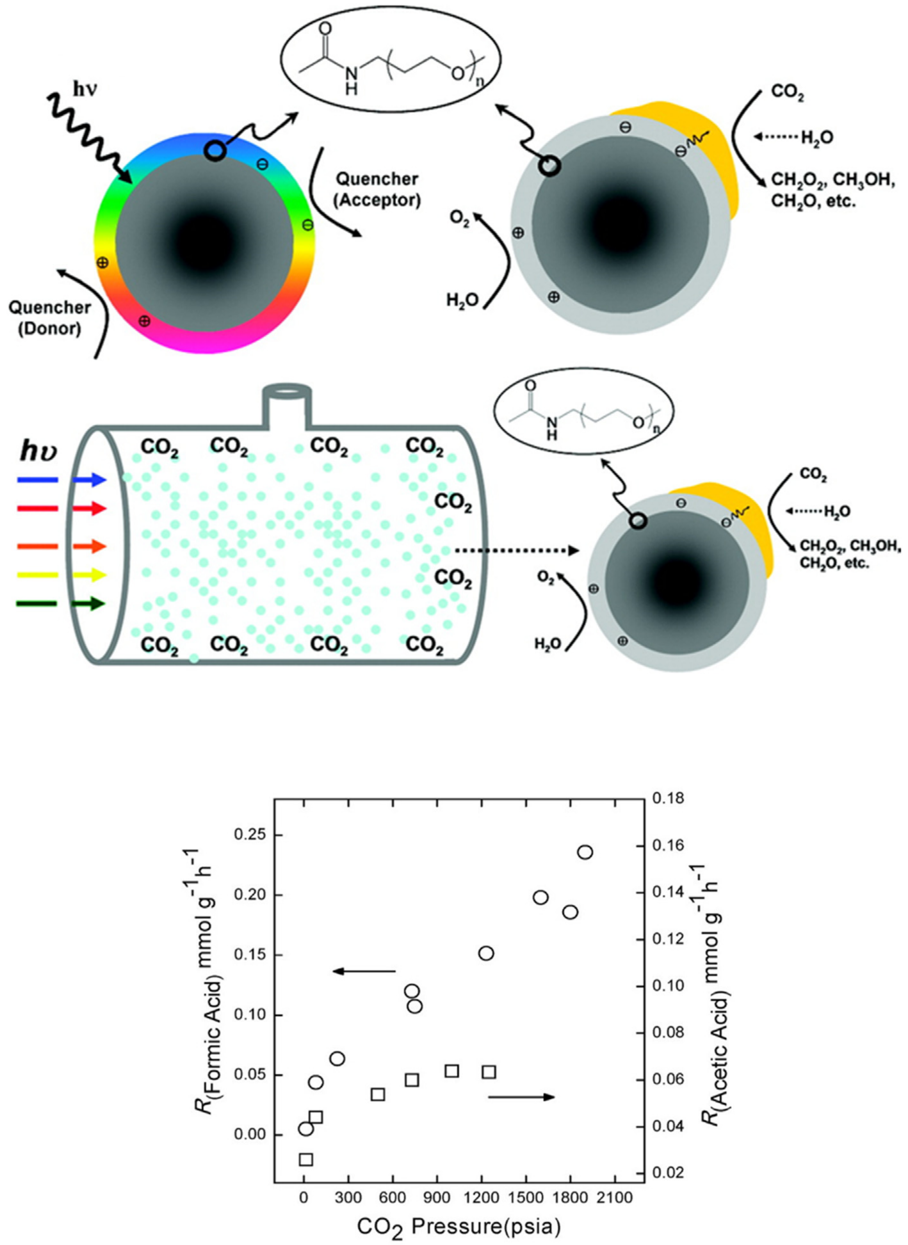
hν
Quencher (Acceptor)
Quencher (Donor)
CO2
H2O
CH2O2, CH3OH, CH2O, etc.
O2
H2O
hυ
CO2
R(Formic Acid) mmol g-1h-1
R(Acetic Acid) mmol g-1h-1
CO2 Pressure(psia)
0.00
0.05
0.10
0.15
0.20
0.25
0.02
0.04
0.06
0.08
0.10
0.12
0.14
0.16
0.18
0
300
600
900
1200
1500
1800
2100

Figure 14.13 Top: carbon nanoparticle surface functionalized with PEG diamine molecules before (left, fluorescent) and after (right, photocatalyst showing quenched fluorescence after metal coating) coating with noble metals (Au or Pt) and schematic illustration of CO_2 photoreduction using aqueous carbon dots in a CO_2 saturated glass reactor or cell with optically transparent windows. Bottom: increase in the formation rates of formic acid and acetic acid photoproducts with increasing CO_2 pressures in aqueous solutions of gold coated carbon dots. *Source*: Adapted from L. Cao, S. Sahu, P. Anilkumar, C. E. Bunker, J. Xu, K. A. S. Fernando, P. Wang, E. A. Guliants, K. N. Tackett, and Y.-P. Sun. Journal of the American Chemical Society 2011, 133, 4754; S. Sahu, Y. Liu, P. Wang, C. E. Bunker, K. A. S. Fernando, W. K. Lewis, E. A. Guliants, F. Ynag, J. Wang, and Y.-P. Sun. Langmuir 2014, 30, 8631.

It was found that CDs upon photoexcitation behaved as excellent electron donors to be able to reduce corresponding noble metal salts such as Au (III) and Pt (IV) in their aqueous solutions on the surface of dots likely at surface defect sites [92]. The presence of metals even in a very small quantity resulted in nearly complete quenching of luminescence in CDs, mainly attributed to static quenching with results essentially decoupled from luminescence decays, which, in turn, was attributed to interrupting radiative recombination of electron−hole pairs in the presence of metal, which, otherwise, would have given rise to luminescence in CDs through efficient radiative recombination of electron−hole pairs [92].

Even bare carbon nanoparticles devoid of any surface modifications are shown to absorb visible photons similar to molecular chromophores. Further, they can reduce silver and gold salts under aqueous conditions, which is evident from the increase in surface plasmon band of Au and Ag as a function of increasing irradiation times in the presence of carbon nanoparticles [51].

Using a similar photodeposition method, CD-supported Ag nanoparticles were demonstrated to enhance the performance of organic optoelectronic devices via forming Ag-decorated CDs, which play a dual role of a template as well as a reducing agent [136]. β-Cyclodextrin-made CDs with polyethylene glycol functionalization are proven to reduce Ag^+ ions to Ag nanoparticles upon irradiating with UV radiation. This was mainly due to the electron transfer from CDs to silver ions, which resulted in sub-10-nm-sized CD−Ag hybrid nanoparticles, as shown in the HR-TEM image in Fig. 14.14 [136].

Photoirradiated CDs could serve as both electron donors (e.g., N,N-diethylaniline) and acceptors (e.g., 2,4-dinitrotoluene) [58,91], as demonstrated by different groups. Considering their light-induced electron transfers, CDs are used as photocatalysts for preparing Au nanoparticles−r-GO nanocomposites. A mixture of GO and aqueous $HAuCl_4$ solution was illuminated with UV light in the presence of CDs for furnishing the required nanocomposites where the photogenerated electron transfers occurred from CDs to both GO and Au^{3+} simultaneously [137].

Li et al. described the efficient use of CQD-based CQDs/Cu_2O composites as visible-light active photocatalysts for the reduction of CO_2 into methyl alcohol with a high yield (~55.7 μmol/g/h) under visible light irradiation. These CQDs/Cu_2O composites can be used for photocatalysis purposes under visible light because of the charge separation and charge transfer capabilities of the CQDs [138]. Furthermore, Li et al. prepared CDs with a carbon thin film layer covering the Cu_2O photocatalyst, which showed improved efficiency for the photoreduction of CO_2 to CH_3OH at a production rate of ~100 μmol/g/h and a small amount of methane (~8 μmol/g/h) was also detected [138]. Methanol yield with CDs/Cu_2O covered with a thin carbon film resulted in nearly a 2-fold higher product yield than the previous report using a CQDs/Cu_2O composite photocatalyst (Figs. 14.15 and 14.16) [138].

CDs obtained from GO with a high degree of graphitic structure and nitrogen containing groups showed high selectivity for CO_2 to methane production at a formation rate of 983 μmol/g/h [138]. Yan et al. found that when GQD hybrids formed with 1,1′-bi(2-naphthylamine) labeled GQD-BNPTL composites were used as a

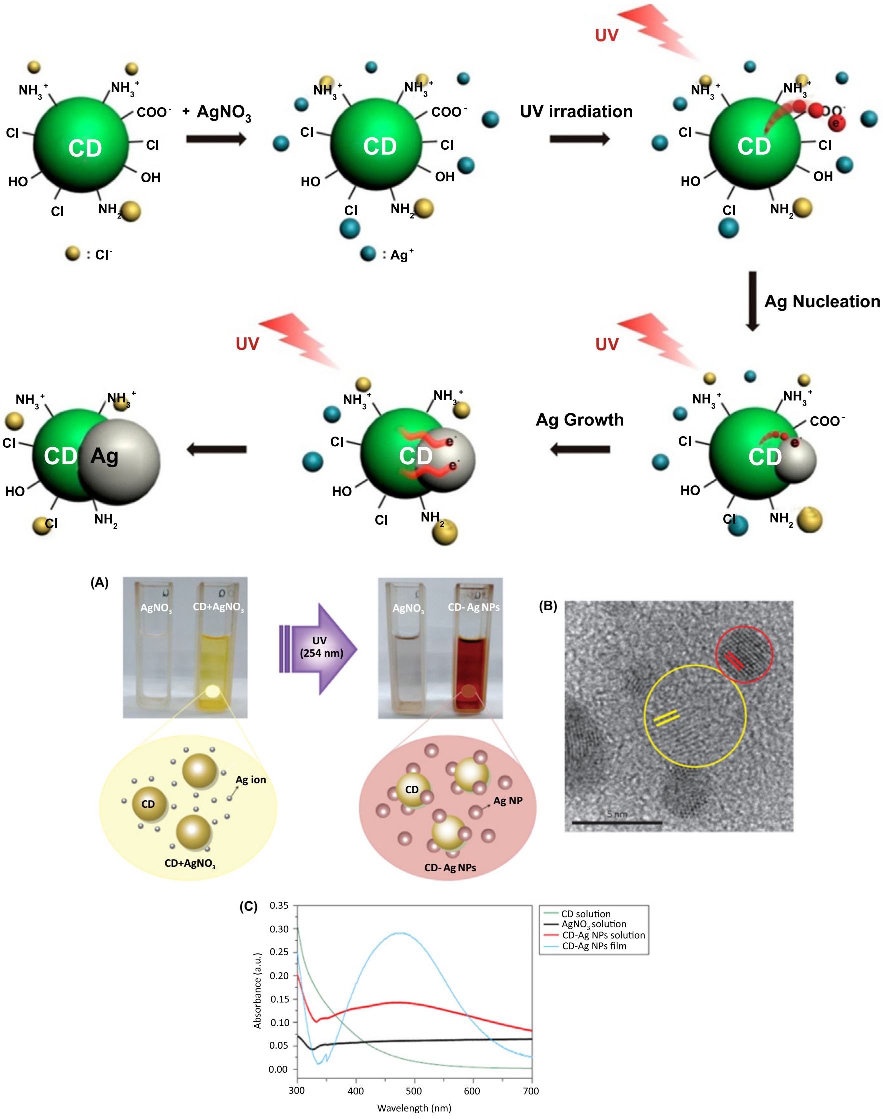
CD
NH$_3^+$
COO$^-$
Cl
HO
OH
NH$_2$
+ AgNO$_3$
: Cl$^-$
: Ag$^+$
UV irradiation
UV
e
Ag Nucleation
Ag Growth
Ag
(A)
AgNO$_3$
CD+AgNO$_3$
UV (254 nm)
CD- Ag NPs
Ag ion
CD
Ag NP
(B)
5 nm
(C)
Absorbance (a.u.)
Wavelength (nm)
0.00
0.05
0.10
0.15
0.20
0.25
0.30
0.35
300
400
500
600
700
CD solution
AgNO$_3$ solution
CD-Ag NPs solution
CD-Ag NPs film

Figure 14.14 Top: schematic representation of photoinduced electron transfer on carbon dots (CD) for the photodeposition and growth mechanism of Ag nanoparticles on the dot surface to obtain the CD–Ag nanohybrids. (A) Representative photographs and schematic diagram of AgNO$_3$ and CD + AgNO$_3$ mixed solutions before (left) and after (right) ultraviolet light exposure. (B) High-resolution transmission electron microscopy (HR-TEM) image of CD–Ag hybrid nanoparticles (NPs). Red and yellow color marked circles show the presence of CDs and Ag nanoparticles, respectively. The red- and yellow-colored parallel lines indicate the distinguishable lattice fringes (3.2 A° and 2.1 A°) of the CDs and the Ag nanoparticles, respectively. Scale bar = 5 nm. (C) Direct comparison of UV–Vis optical absorption spectra of CD–Ag composite nanoparticles in an aqueous solution and in a thin film, as well as CDs and AgNO$_3$ solutions after UV illumination.

Adapted from H. Choi, S.-J. Ko, Y. Choi, P. Joo, T. Kim, B. R. Lee, J.-W. Jung, H. J. Choi, M. Cha, J.-R. Jeong, I.-W. Hwang, M. H. Song, B.-S. Kim, and J. Y. Kim. *Nature Photonics* 2013, *7*, 732.

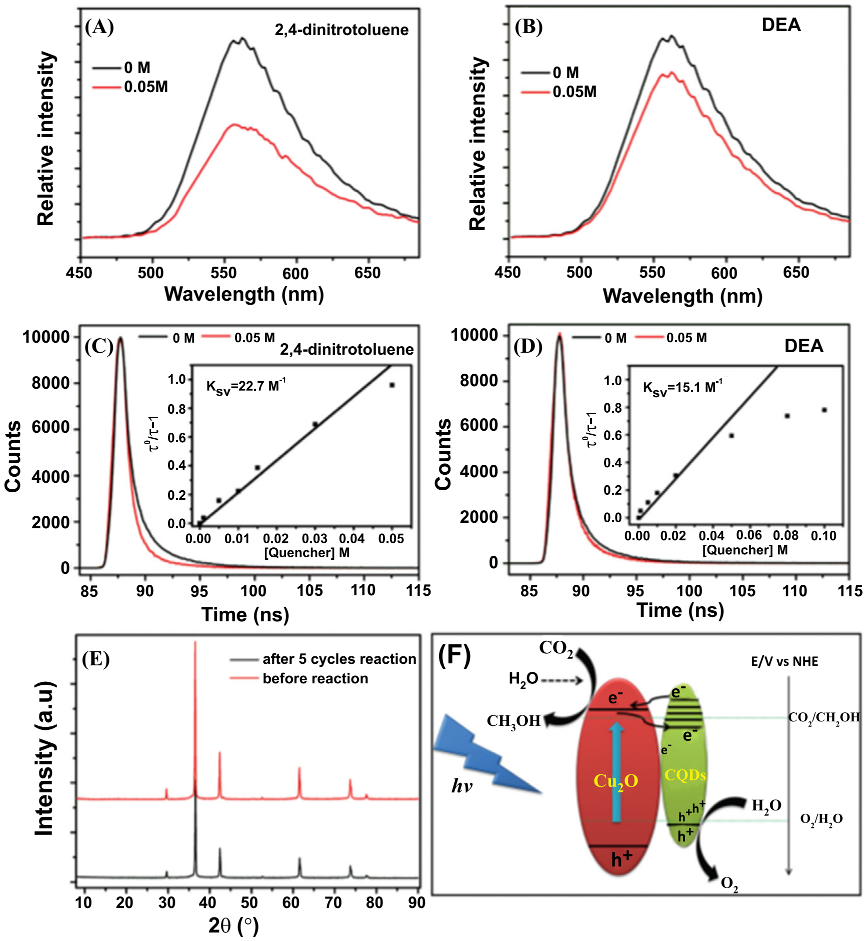

Figure 14.15 (A, B) Photoluminescence emission curves (450 nm excitation) of the carbon quantum dots (CQDs) in toluene measured with and without [2,4-dinitrotoluene and N,N-diethylaniline (DEA), both 0.05 M]. (C, D) Light-driven electron transfer characteristics of CQDs: photoluminescence decays (450 nm excitation, observed by monitoring emission at 560 nm using a narrow range bandpass filter) of the CQDs with (C) 2,4-dinitrotoluene and (D) DEA. Inset: Stern—Volmer plots for the quenching of luminescence quantum yields (450 nm excitation) of the CQDs by (C) 2,4-dinitrotoluene and (D) DEA. (E) The powder XRD phase pattern of the CQDs/Cu_2O hybrid catalyst before and after reaction. (F) A schematic illustration of the proposed photocatalytic CO_2 reduction mechanism catalyzed by a CQDs/Cu_2O composite photocatalyst. *Source*: Adapted from H. Li, X. Zhang, and D. R. MacFarlane. Advanced Energy Materials 2015, 5, 1401077.

photocatalyst, CH_3OH production rate was 0.695 μmol/h/g_{cat}, which was about three times higher than that produced by pristine GQD and much better than that of GOs as a photocatalyst [139], while no methane was detected in their study.

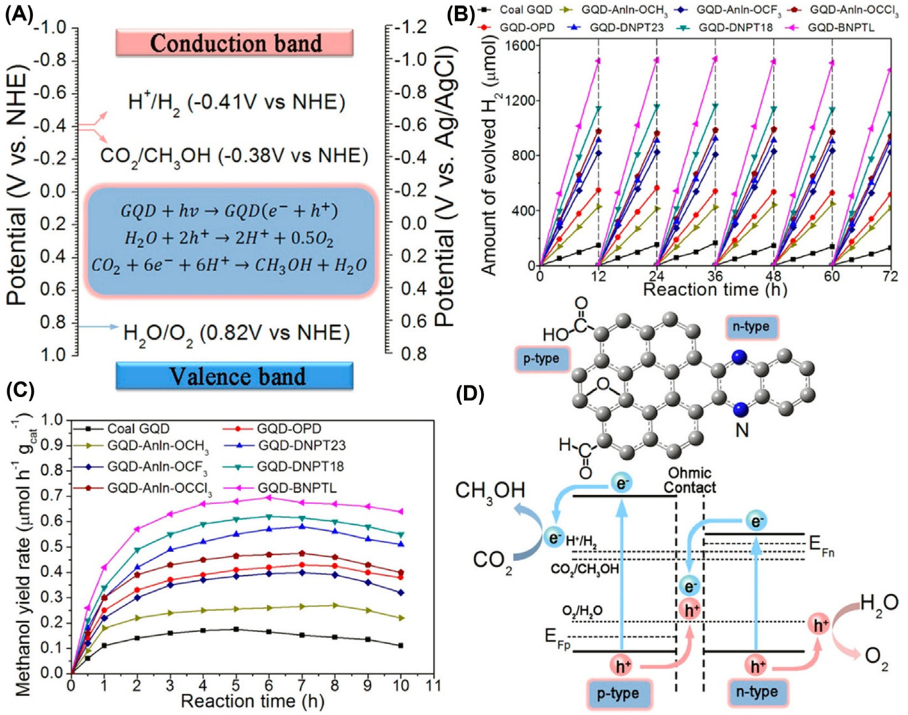

Figure 14.16 (A) Schematic depiction of standard redox potentials, conduction band minimum (CBM) and valence band maximum (VBM) of graphene quantum dots (GQDs), and redox potentials in CO_2 reduction reactions. (B and C) Time courses of H_2 evolution reaction (B) and CO_2 reduction reactions and (C) methanol production yields of all GQD types under visible light (420−800 nm) illumination. (D) Schematic representation of Z-scheme-based photocatalysis mechanism of CO_2 reduction using GQDs as a photocatalyst. *Source*: Adapted from Y. Yan, J. Chen, N. Li, J. Tian, K. Li, J. Jiang, J. Liu, Q. Tian, and P. Chen. ACS Nano 2018, 12, 3523.

Yadav et al. designed a GQD-coupled biocatalyst system through covalent functionalization of GQDs with 6-amino-2-(9,10-dioxo-6-(2-(perylen-3-yl)-4,5-di-p-tolyl-4,5-dihydro-1H-imidazol-1-yl)-9,10-dihydroanthracen-2-yl)-1H-benzo[de]isoquinoline-1,3(2 H)-dione abbreviated as ANP chromophore to enhance the light absorption and promote charge transfer characteristics. Combining the functionalized GQDs with formate dehydrogenase (FDH) enzyme resulted in selective photoconversion of CO_2 into formic acid (formation rate ~99 μmol/h) using a GQD-based photocatalyst integrated with a biocatalyst [139]. Zhong et al. reported covalent organic framework (COF)-based catalytic materials containing Ni porphyrin-based CDs prepared via in situ pyrolysis of Ni porphyrin complex and glucose in the presence of the COF for their use in selective photoreduction of CO_2 to CO at a production rate of 956 μmol/g/h under visible light illumination [139].

Nanoscaled carbons exhibited enormous potential in photocatalytic energy conversions; hence, various forms of carbons, including graphene-related ones, are widely studied for photoconverting CO_2 into solar fuels [17]. For instance, GO, a competitor of CDs, having significant $sp^2 \rightarrow sp^3$ hybridized carbons (~60%) [133] was utilized as a photocatalyst for producing methanol from CO_2 [140]. The conversion happened at a rate of 0.172 μmol/g/h upon irradiating with visible light. GO photocatalyst was made using modified Hummer's method and the CO_2 conversion yield was found to be six times higher than that of the pure TiO_2 when used under same reaction conditions (Fig. 14.17) [140].

Additionally, Shown et al. showed that when GOs were decorated with Cu nanoparticles, methanol and acetaldehyde were found to be primary reaction products observed, while H_2 was a minor product obtained [141]. Li and his coworkers

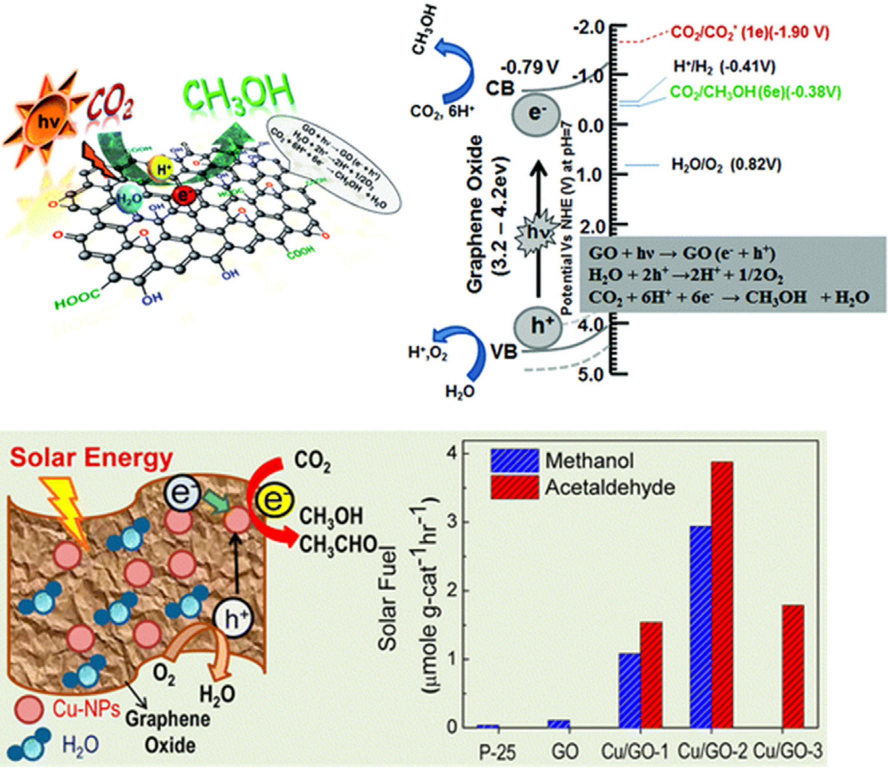
hν
CO2
CH3OH
H+
H2O
e-
COOH
OH
HOOC
CH3OH
CO2, 6H+
-0.79 V
CB
e-
Graphene Oxide
(3.2 – 4.2ev)
hν
h+
VB
H+,O2
H2O
Potential Vs NHE (V) at pH=7
-2.0
-1.0
0.0
1.0
2.0
4.0
5.0
CO2/CO2•- (1e)(-1.90 V)
H+/H2 (-0.41V)
CO2/CH3OH(6e)(-0.38V)
H2O/O2 (0.82V)
GO + hν → GO (e- + h+)
H2O + 2h+ → 2H+ + 1/2O2
CO2 + 6H+ + 6e- → CH3OH + H2O
Solar Energy
CO2
e-
e-
CH3OH
CH3CHO
h+
O2
H2O
Cu-NPs
H2O
Graphene Oxide
Solar Fuel
(μmole g-cat-1hr-1)
0
1
2
3
4
Methanol
Acetaldehyde
P-25
GO
Cu/GO-1
Cu/GO-2
Cu/GO-3

Figure 14.17 (Top) Photocatalytic CO_2 conversion into methanol is shown on graphene oxide (GO) along with their redox potentials. (Bottom) Copper-decorated GOs when used as a photocatalyst produced methanol and acetaldehyde as major reaction products.
Source: Adapted from H. C. Hsu, I. Shown, H. Y. Wei, Y. C. Chang, H. Y. Du, Y. G. Lin, C. A. Tseng, C. H. Wang, L. C. Chen, Y. C. Lin, and K. H. Chen. Nanoscale 2013, 5, 262.; I. Shown, H.-C. Hsu, Y.-C. Chang, C.-H. Lin, P. K. Roy, A. Ganguly, C.-H. Wang, J.-K. Chang, C.-I. Wu, L.-C. Chen, and K.-H. Chen. Nano Letter 2014, 14, 6097.

synthesized a novel ZnO−r-GO nanocomposite via a hydrothermal process and successfully employed it as a CO_2 reduction photocatalyst under visible light conditions for obtaining methanol at a formation rate of 4.58 μmol/g/h [142]. Similarly, Tan's team developed a TiO_2−r-GO nanohybrid via a solvothermal method [143]. Upon illuminating it with visible light, this composite reduced CO_2 into CH_4 with an effective production rate (0.135 μmol/g/h) [143]. Li et al. demonstrated that CDs enhanced the photocatalytic CO_2 reduction performance of TiO_2 by facilitating electron transfer and superior light absorption in hybrid materials. CO (0.30 μmol/h) and CH_4 (0.20 μmol/h) were major products observed in CO_2 photoconversion reactions in a CD/TiO_2 hybrid system [143].

Hersam and coworkers investigated the influence of varying degrees of defect densities on the photoreduction of CO_2 to CH_4 by synthesizing TiO_2−graphene nanocomposite thin films [144]. The corresponding investigation disclosed that nanocomposites with lower graphene defect densities showed improved performance (~7-fold) when compared to bare TiO_2. This improvement was mainly ascribed to the increased electrical mobility of the graphene, which resulted in a longer mean free path for electrons, thus promoting CO_2 reduction via enabling the rapid migration of photoexcited electrons to reactive sites. Further, the same group also showed that the dimensions of carbon nanomaterials play a pivotal role in reaction specificity through synthesizing different dimensioned carbon-TiO_2 nanosheet (TiNS) hybrid photocatalysts for the conversion of CO_2 into CH_4 [145]. SWCNT−TiNS (i.e., 1D + 2D) and graphene−TiNS (2D + 2D) nanocomposites with low carbon defect densities were made through non-covalent attachment. Under UV ($\lambda \sim 365$ nm) and visible light radiations ($\lambda > 380$ nm), these nanocomposites were explored for CO_2 reduction to CH_4 in CO_2 saturated water vapor. In-depth analyses indicated that both the nanocomposites exhibited a significant methane production rate when compared to 2D TiNS. However, under UV-light illumination, the 2D + 2D graphene−TiNS yielded stronger optoelectronic coupling than 1D + 2D SWCNT−TiNS, thereby showing enhanced photocatalytic performance for the former one. While under visible light illumination, 1D + 2D SWCNT−TiNS exhibited better performance than 2D + 2D graphene−TiNS since 1D CNTs were observed to be more efficient TiO_2 sensitizers under visible light [145].

Tu's group applied a layer-by-layer technique followed by microwave heating for fabricating graphene−titania hollow spheres composed of $Ti_{0.91}O_2$ and graphene sheets alternatively [146]. When they investigated these composites for CO_2 photoreduction, it is discovered that CO is a major product, despite traces of CH_4 detected. The respective formation rates of CO and CH_4 are 8.91 and 1.14 μmol/g/h. When referenced to the commercial standard − P25 catalyst (i.e., TiO_2), these graphene−$Ti_{0.91}O_2$ hollow spheres exhibited a 9-fold rise in photocatalytic performance. This rise in performance was attributed to the rapid electron migration from titania to graphene nanosheets, which rendered prolonged lifetimes for the light-generated charge carriers throughout the hybrid composite structure. In a following study [147], an in situ simultaneous reduction−hydrolysis was adopted for engineering sandwich-like graphene−TiO_2 nanohybrids. These 2D nanosheets were explored for CO_2 conversion in a binary solvent (ethylene diamine/H_2O) under light and water vapor [147]. Methane and ethane are produced with formation rates of 8 and 16.8 μmol/g/h, respectively, by using just 2.0 wt.% of graphene. Tan et al. [148] demonstrated that GO-supported oxygen-rich TiO_2 hybrid ($GO-O_2-TiO_2$) reduced CO_2 to CH_4 with a production rate of 0.43 μmol/gcat/h with 5 wt.% GO loading. This performance was found to be ~14-fold higher than the standard P25 catalyst.

Razzaq et al. synthesized TiO_2 nanotube arrays covered with r-GO platelets consisting of an embedded TiO_2 nanoparticle (r-GO−TNTNP) composite catalyst, which showed a CH_4 evolution rate of 5.67 ppm/cm^2/h, which was ~4.4 times greater than bare TiO_2 nanotube arrays (1.28 ppm/cm^2/h) [149].

Wang's team engineered graphene−WO_3 nanobelt composites [150] through a hydrothermal method. This novel composite generated CH_4 from CO_2 under photocatalytic conditions with an evolution rate of ~0.11 μmol/h. It is observed that this hydrocarbon fuel production would take place only in the presence of graphene in the system, which enhanced the WO_3 conduction band for enabling its superior photocatalytic features towards CO_2 reduction. Lv and coworkers [151] applied a hydrothermal technique for fabricating a novel photoactive composite $NiO_x-Ta_2O_5-rG$, where rG = reduced graphene. This composite reduced CO_2 or $CO_2/NaHCO_3$ and H_2O to methanol and hydrogen under UV-light irradiation. With 1% graphene loading, the CH_3OH production rate was raised to 3.4 times that without graphene. These findings clearly indicated that the graphene maintained the required optimum charge separation and interfacial electron transfer rates via preventing the recombination of resulting charge carriers during photolysis [151].

Kuang et al. [152] demonstrated that the photoactivation of GO enhanced the CO_2 conversion efficiency. The light illumination played several key roles in enhanced efficiency. First, irradiation of GO eliminated CO released during photochemical reactions. Second, it was observed that it further increased the density of defects and pi-conjugation of photoirradiated GO, which resulted in yielding photoelectrons and photogenerated charge carriers lifetime, as revealed by various spectroscopic techniques [152]. Kumar et al. reported r-GO coated gold nanostructures via efficient transport of hot plasmonic electrons could convert CO_2 into formic acid with a photochemical QY of 1.52% along with excellent selectivity (>90%) to formic acid under visible light illumination and was found to be superior to bimetallic nanostructure of Pt-coated Au nanoparticles (QY 1.14%). These results showed r-GO as an efficient and inexpensive charge transport material in plasmon-induced photocatalysis [153].

Jain and coworkers observed a high yield of methanol in CO_2 photoreduction using core-shell-type rGO wrapped r-GO@CuZnO@Fe_3O_4 microsphere hybrid structure under visible light irradiation, which is attributed to the synergistic effect of r-GO and CuZnO@Fe_3O_4 in the r-GO@CuZnO@Fe_3O_4 composite [154]. Similarly, the synergistic effect in $CsPbBr_3$ nanocrystals (NCs) deposited on a hierarchical branched ZnO nanowire (BZNW)/macroporous graphene scaffold ($CsPbBr_3$ NC/BZNW/MRGO) boosted the photocatalytic activity of the composite material. Therein, a high selectivity (96.7%) for CH_4 with a formation rate of 52.02 μmol/gcat/h under visible light illumination was observed, which was found to be about 4.98- and 1.65-fold higher than that of $CsPbBr_3$ NC (10.44 μmol/gcat/h) and $CsPbBr_3$ NC/MRGO (31.52 μmol/gcat/h) [155]. Kumar et al. combined GO with Ru-based coordination compounds to enhance the CO_2 photoconversion into methanol (82 μmol/gcat/h) under visible light via photoinduced electron transfer from ruthenium complex to GO conduction band [156]. Using a similar design concept, the group synthesized a cobalt phthalocyanine and ruthenium complex bearing 2-thiophenylbenzimidazole ligand immobilized GO in CO_2 photoreduction to methanol with a similar order of product formation rate for methanol at ~78.8 μmol/g/h and at 85.4 μmol/g/h, respectively [157,158].

An et al. designed Cu_2O/r-GO hybrids in photocatalytic CO_2 reduction to CO with a QY of 0.34% at 400 nm. Combining r-GO with Cu_2O increased the photoactivity of Cu_2O by 2-fold, which is attributed to enhanced charged transport at the Cu_2O/r-GO heterojunction [159]. TiO_2/nitrogen (N) doped r-GO (TiO_2/Nr-GO) showed substantial enhancement in CO_2 conversion into CO, which was ~4.4 and 2.2 times increase in CO yield over bare TiO_2 and pristine TiO_2/r-GO without N doping, respectively. It was suggested that the introduction of nitrogen dopant led to a synergistic effect of enhancing interfacial CO_2 adsorption coupled with facilitated photogenerated charge transfer accounting for superior CO_2 photoreduction rate of optimized TiO_2/Nr-GO composite catalyst [160]. In another report, grafting of CuO nanorods on r-GO significantly enhanced the CO_2 photoreduction efficiency and showed nearly a seven times increase in methanol yield (~53.41 μmol/gcat/h) compared to that of prisitine CuO nanorods (Fig. 14.18) [160].

The Z-scheme design of α-Fe_2O_3/amine–RGO/$CsPbBr_3$ hybrids exhibited highly selective photocatalytic activity for the CO_2 photoreduction to CH_4 with a formation rate of ~181.68 μmol/g (product formation rate ~12.11 μmol/g/h) after 15 h of continuous irradiation. This product yield was found to be higher than those of α-Fe_2O_3/$CsPbBr_3$ (66.64 μmol/g) and $CsPbBr_3$ nanocrystals alone (30.55 μmol/g). Methane was obtained as the main photoproduct with 93.4% selectivity along with CO and H_2 as minor photoproducts in the photocatalytic reaction [160]. Reduced graphene oxide–CdS nanorods decorated with Ag nanoparticles (Ag–r-GO–CdS) exhibited nearly 8-fold CO_2-to-CO production yield (1.61 μmol/h) than prisitine CdS (0.21 μmol/h) [161]. Various noble metal (Pt, Pd, Ag, Au) modified r-GO/TiO_2 ternary hetero-nanostructures were designed for visible-light driven photoconversion of CO_2 into methane [162]. Pt-doped r-GO/TiO_2 showed the highest photoreduction efficiency with a total CH_4 product formation yield of 0.28 μmol/g/h, which was about 2.6 and 13.2 times higher than GO/TiO_2 composite and TiO_2 (P25) alone [161].

Another predominant class of carbon-based nanostructured materials that are often explored for photocatalytic reactions is polymeric carbon nitride (g-C_3N_4), which possesses 2D graphite-like structure and significant semiconducting features [163]. Many researchers exploited this metal-free organic compound as a photocatalyst for CO_2 reduction under visible light conditions. For instance, Dong's group [164] made CO through photoreduction of CO_2 in water vapor with a formation rate of 1.9 mM/h upon irradiating the C_3N_4 catalyst with light having $\lambda > 420$ nm. Mao and coworkers [165] pyrolized urea for C_3N_4, which effectively catalyzed CO_2 photoreduction under visible light for forming methanol and ethanol with formation

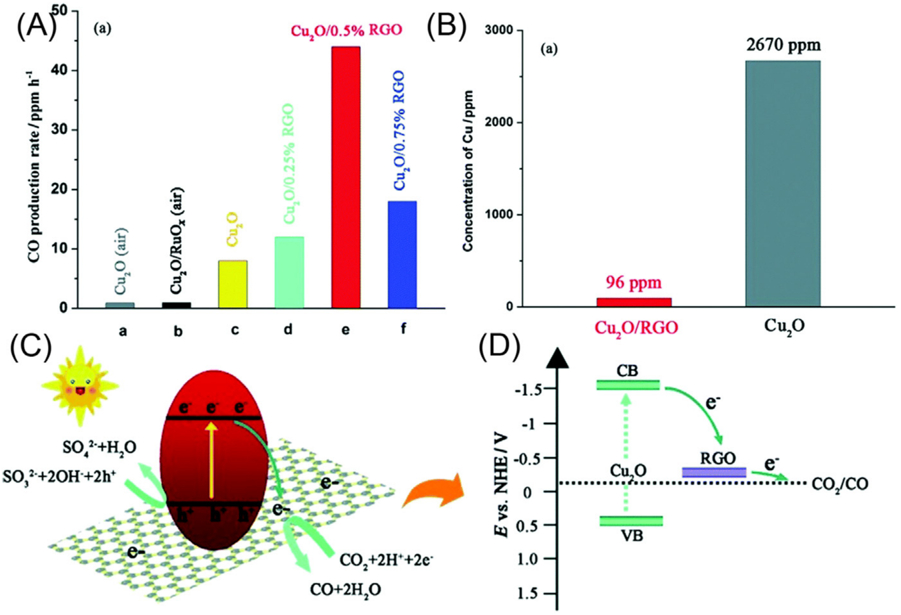

Figure 14.18 (A) CO yields over various photocatalysts, (B) plot of leaching of Cu caused by photoreduction, and (C) and (D) schematic illustrations of the CO_2 reduction mechanism and charge transfer in the r-GO−Cu_2O composite.
Source: Adapted from X. An, K. Li, and J. Tang. ChemSusChem 2014, 7, 1086.

rates of 6.28 and 4.51 μmol/g/h, respectively (overall quantum efficiency = 0.18%). While Wang's team [166] made composites of carbon nitride with mesostructured TiO_2, which reduced CO_2 and water to CH_4 and CO with gas evolution rates of 1.53 and 10.05 μmol/g/h, respectively. Maeda et al. utilized small amounts of metal complexes for making composites with C_3N_4. When ruthenium complex was used [167], a selective photoreduction of CO_2 to HCOOH was achieved with a high turnover number (triethanol amine as electron donor), with a production rate of ~431 μmol/g/h and an apparent QY of 1.5% (@400 nm). In a similar manner, C_3N_4−Co $(bpy)_3Cl_2$ hybrid catalyst was used for the selective conversion of CO_2 into CO with an evolution rate of 1.85 μmol/h [168]. Wang et al. demonstrated CDs acting as an efficient hole acceptor when decorated on carbon nitride, thus enhancing the electron lifetime of carbon nitride by six times and favoring CO_2 photoreduction to methanol at a formation rate of 13.9 μmol/g/h [168]. QY of conversion into methanol (QY ~ 6%) was further improved by nearly 300% when carbon nitride with O-containing linkers were combined with CDs [168]. Ong et al. fabricated protonated g-C_3N_4/CNDs hybrid photocatalysts to enhance charge separation in CO_2 to CH_4 and CO at formation rates of 2.9 and 5.8 μmol/g/h, respectively, under visible light. The observed product yields in a hybrid heterojunction photocatalyst were 3.6- and 2.3-fold higher than g-C_3N_4 alone [168].

CNTs,a 1D allotrope of carbon with nano-dimensionsdrew a lot of attention from photochemists in the context of energy conversion due to their apparent merits in terms of 1D structure as well as favorable physicochemical properties. Besides being chemically inert and exhibiting a high degree of stability under various catalytic conditions, CNTs possess a high surface area ($\sim 1600\ m^2/g$) and remarkable mechanical and electronic properties [130,131]. In numerous photocatalytic research reports, CNTs were used as scaffolds for tethering semiconductor nanoparticles, which boosts selectivity and efficacy. Primarily, CNTs play the following three major roles during photocatalysis. First, like graphene, CNTs are electron acceptors and promote charge transfer through obstructing charge recombination [169,170]. Second, they behave like photosensitizers, which expand the absorption range, hence increasing the light absorption efficiency of the photocatalyst [171,172]. Third, due to their wide surface area, they boost up adsorptive capacity of photocatalysts and help prevent photocorrosion [173].

Xia's group [174] synthesized multiwalled carbon nanotube- TiO_2 (MWNT−TiO_2) composites through sol−gel and hydrothermal methods, which were proven to be efficient CO_2 photoreducing catalysts with their selectivity highly dependent on the preparative technique employed. In the sol−gel method, anatase TiO_2 nanoparticles were used to decorate MWNTs, whereas in the hydrothermal method, rutile TiO_2 nanorods were utilized for uniform coating onto MWNTs. In the presence of water, ethanol was produced in the sol−gel method, whereas formic acid was achieved in the hydrothermal case. Ong et al. used co-precipitation followed by CVD for engineering CNT-Ni-doped TiO_2 nanohybrid composites (CNT@Ni/TiO_2) for reducing CO_2 [175]. Upon illuminating with visible light, methane was evolved, as shown in Fig. 14.19, with a

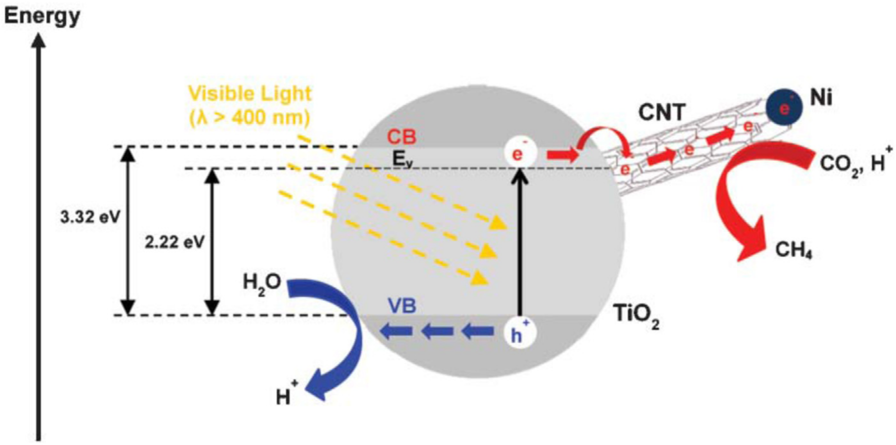

Figure 14.19 Schematic representation of the electron transfer reactions for the photocatalytic conversion of CO_2 with H_2O using CNT@Ni/TiO_2 nanohybrids in the presence of visible light illumination with the incorporation of a new energy level, Ev. *Source*: Adapted from W. J. Ong, M. M. Gui, S.-P. Chai, and A. R. Mohamed. RSC Advances 2013, 3, 4505.

formation rate of 0.145 μmol/g/h, and the CO_2 photoreduction rate followed the order $CNT@Ni/TiO_2 > Ni/TiO_2 > TiO_2$. Similarly, in an independent report by Gui's group [176], methane was prepared with almost the same evolution rate (0.1375 μmol/g/h) from CO_2 by using $MWCNT@TiO_2$ core-shell type nanocomposites (Table 14.1).

14.4 Concluding remarks

In spite of numerous documented reports in photocatalytic CO_2 conversion using carbon-based nanodots and related graphene-based hybrid photocatalysts, research on their utility for efficient CO_2 conversion into value-added products is still carried out via bench-scale experiments in academic laboratories and is far from being put into practical use. One limitation has been efficient integration of light absorption and charge carrier extraction in semiconductors to drive desired photochemical reactions with high QYs due to inherent losses within semiconductor nanostructures. Thorough investigations and analyses are paramount in dealing with these critical issues, while designing photocatalysts for CO_2 conversion that can achieve better selectivity and productivity. Usually, multiple CO_2 reduction products are detected, which demands further separation/purification processes to obtain desired pure products, especially for targeted alcohols, e.g., ethanol as a sustainable hydrocarbon fuel. In such systems (e.g., CDs), advanced probing with spectroscopic techniques like time-resolved and transient absorption is needed to understand the complex charge transfer kinetics (i.e., charge generation, separation, transport, recombination, etc.) on the catalytic surfaces. Role of structural morphology such as size, shape, crystal facets, doping strategies, and degree of defect density, including CO_2 and intermediate adsorption/desorption kinetics for targeted product selectivity, needs to be further investigated. This would involve in situ or operando experimental spectroscopic characterization along with computational models for a better understanding of structure−property relationships for rational design of photoactive carbon-based materials involving the multielectron CO_2 photoreduction processes.

Besides being cost-effective, and having rich electron transfer features and efficient light harvesting ability in a broad range of solar spectrum, CDs have proven to be propitious components for use as active components or building blocks in photocatalytic applications and associated solar energy conversion reactions. Further, the optical and photocatalytic properties of CDs can be tuned by their surface states apart from manipulating the surface defects in them. A large number of diverse physical, chemical, and electrochemical methods are available for preparing and evaluating the photochemical performance of CDs, which provides the scope for engineering both the surface and intrinsic features of CDs. By virtue of the aforementioned characteristics, they find their place in the next-generation photocatalytic systems.

Carbon-based photocatalysts were routinely employed as photo-oxidants in the context of purification, precisely degradation of organic pollutants [134]. But, they were relatively less explored for a challenging task of reducing CO_2 into value-added commodities with dependable selectivity and efficiency under light

Table 14.1 Tabular summary of the literature reports on photocatalytic CO_2 conversion employing carbon-based catalysts.

Photocatalyst	Loadings or Co-catalysts	Primary photoconversion products	Product yields μmol/g/h	Quantum efficiency (QE)	Light source and light intensity	Experimental conditions (reactants, time, T°C) comments	References
Carbon dots	Au or Pt	HCOOH	-	0.3%	450 W Xe arc lamp with 425 nm cut-off filter	CO_2 saturated aqueous solution in an optical cell under ambient conditions, 5 h irradiation, 25°C; roughly order of magnitude higher than DegussaP25 (TiO_2)	[57]
Graphene−titania nanocomposite	None	CH_4	-	-	100 W Hg vapor lamp for UV-light (~100 W/m^2) and 60 W day light bulb for visible-light (~31 W/m^2)	H_2O saturated CO_2 in 25 mL teflon reactor 3 h irradn. under ambient conditions, 25°C; 4.5 time higher CH_4 than titania under UV and 7.2 times higher than titania under visible-light	[144]
$Ti_{0.91}O_2$−graphene nanocomposite	None	CO, CH_4	8.91 1.14	-	300 W Xe lamp	CO_2 saturated water vapor in 230 mL reactor under ambient conditions, 6 h irradn.; Overall conversion ~5 times higher than pure $Ti_{0.91}O_2$ and nine times higher than commercial P25	[146]

(*Continued*)

Table 14.1 (Continued)

Photocatalyst	**Loadings or Co-catalysts**	**Primary photoconversion products**	**Product yields µmol/g/h**	**Quantum efficiency (QE)**	**Light source and light intensity**	**Experimental conditions (reactants, time, T°C) comments**	**References**
TiO_2-graphene 2D sandwich like hybrid nanosheets	None	CH_4 C_2H_6	8 16.8	-	300 W Xe lamp	CO_2 saturated water vapor in230 mL reactor under ambient conditions, 4 h irradiation	[147]
2D–2D graphene–titania nanosheet; 1D–2D carbon nanotube–titania nanosheet	None None	CH_4 CH_4	- -	- -	100 W Hg-vapor lamp for UV-light (~100 W/m^2) and 60 W day light bulb for visible light (~31 W/m^2)	H_2O saturated CO_2 in 25 mL teflon reactor 3 h irradn. under ambient conditions, 25°C; 3.5 times higher CH_4 than titania under UV and 3.7 times higher than titania under visible-light 2 times higher CH_4 than titania under UV and 5.1 times higher than titania under visible-light	[145] [145]
TiO_2–graphitic carbon composite	None	CH_4 CO	1.53 10.05	-	300 W Xe Arc lamp	CO_2 saturated water vapor in a stainless-steel reactor (1500 mL capacity) at 30° C and 110 kPa	[166]

Graphene oxide (GO) by modified Hummer's method	None	CH_3OH	0.172	-	300 W halogen lamp as simulated solar source	Continuous gas flow reactor, 0.2 g catalyst, CO_2 and water vapor under ambient conditions, 25°C; GO showed 6-fold higher activity than pure TiO_2	[140]
ZnO-reduced grapheme oxide (r-GO) nanocomposite	None	CH_3OH	4.58	-	500 W Xe lamp	CO_2 saturated glass reactor ZnO−r-GO (1 gm/L) in 100 mL of 0.0025 M $NaHCO_3$	[142]
Multiwalled carbon nanotube supported TiO_2 composites	None	HCOOH C_2H_5OH CH_4	18.67 29.87 11.74	-	15 W UV lamp 365 nm light	Stainless steel reactor, H_2O and CO_2 with mole ratio (5:1) under ambient conditions, 5 h irradiation, 25°C	[174]
CNT@Ni/TiO_2 composite	Ni	CH_4	0.145	-	75 W visible daylight lamp	Photoreactor purged with pure CO_2 flowing through a water bubbler at atmospheric pressure, 10 h irradiation	[175]
MWCNT@TiO_2 core-shell nanocomposites	None	CH_4	0.1375		15 W energy saving light bulb (Philips)	Quartz photoreactor with CO_2 saturated water under ambient conditions, 8 h irradiation	[176]

(*Continued*)

Table 14.1 (Continued)

Photocatalyst	Loadings or Co-catalysts	Primary photoconversion products	Product yields μmol/g/h	Quantum efficiency (QE)	Light source and light intensity	Experimental conditions (reactants, time, T°C) comments	References
Graphene−WO_3 nanobelt composite	None	CH_4	0.11 μmol/h	-	300 W Xe lamp 400 nm long pass filter	Glass reactor with CO_2 saturated water vapor, 0.1 g catalyst under ambient conditions (25°C, 1 atm), ~ 8 h irradiation	[150]
Graphene-modified $NiO_x-Ta_2O_5$ composite	Ni/NiO	CH_3OH H_2	1.04 μmol/h	-	400 W metal halogen lamp, UV−Vis light	10 mL quartz cuvette with 2.5 mg/mL of catalyst CO_2 saturated aqueous solution under ambient conditions; 3.4 times more CH_3OH than sample without graphene	[151]
RGO−TiO_2 nanocomposite	None	CH_4	0.135	-	15 W daylight bulb	CO_2 saturated water vapor in a continuous gas flow reactor under ambient conditions	[143]
Graphitic carbon nitride (g-C_3N_4) from melamine	None	CO	1.9 mM/h	-	300 W Xe lamp with 420 nm cut-off filter	CO_2 saturated water vapor in a glass reactor under ambient conditions	[164]
Mesoporous C_3N_4−Ru complex hybrid photocatalyst	8% Ru and triethanol amine as sacrificial donor	CO, H_2, HCOOH	431	1.5%	450 W Xe lamp with $NaNO_2$ solution filter; $\lambda >$ 400 nm	CO_2 saturated pyrex test tube reactor under ambient conditions	[167]

g-C_3N_4 from urea	None	CH_3OH C_2H_5OH O_2	6.28 4.51 21.33	0.18%	300 W Xe lamp and 267 mW/cm^2	CO_2 saturated pyrex glass reaction cell with 0.2 g catalyst in 100 mL of 1.0 M NaOH under ambient conditions, 20°C, 1 atm	[165]
$C_3N_4{-}Co(bpy)_3Cl_2$ hybrid photocatalyst	Triethanol amine as sacrificial agent	CO, H_2	1.85, 0.3 μmol/h	0.25%	300 W Xe lamp with 420 nm cut-off filter	Schlenk flask (80 mL) under an atmospheric pressure of CO_2 with 50 mg of catalyst in acetonitrile solvent under visible-light, 60°C, 1 atm	[168]
GO	None	CO	1.23	-	500 W Xe lamp	Quartz tube reactor (400 mL) with 10vol.% humidified CO_2 and 90 vol.% N_2 under ambient conditions with 50 mg of dispersed catalyst powder	[152]
Cu NP/GO hybrids	None	CH_3OH, CH_3CHO	6.84	-	300 W halogen lamp	Continuous gas flow reactor (300 mL) with humidified CO_2, initially purged with N_2 then CO_2; temperature kept at (25°C ± 0.5)	[141]
r-GO−Au NPs	None	HCOOH	3.12	1.52	Xe lamp (power 5.68 W)	Pyrex photoconversion reactor (window diameter = 11 mm), saturated with CO_2	[153]

(*Continued*)

Table 14.1 (Continued)

Photocatalyst	Loadings or Co-catalysts	Primary photoconversion products	Product yields µmol/g/h	Quantum efficiency (QE)	Light source and light intensity	Experimental conditions (reactants, time, T°C) comments	References
r-GO@CuZnO@Fe_3O_4 microspheres	None	CH_3OH	110.6	2.53	20 W white cold LED light	100 mL borosil cylindrical vessel charged with a mixture of DMF and water(45/5 mL), 100 mg catalyst, and saturated with CO_2	[154]
$CsPbBr_3$ NC/ZnO nanowire/macroporous GO	None	CH_4	52.02	-	Xe lamp (150 W)	Pyrex reaction cell saturated with CO_2 and water vapor	[155]
GO−phenanthroline ligands	None	CH_3OH	82.86	-	White cold LED flood light (20 W)	Reaction vessel of diameter 5 cm containing DMF (30 mL), triethyl amine (10 mL) and deionized water (10 mL); initially purged with nitrogen gas and saturated with CO_2	[156]
GO−heteroleptic ruthenium(II) complex	None	CH_3OH	85.42	-	White cold LED flood light(20 W)	5 cm cylindrical vessel filled with 10 mL HPLC grade water and 40 mL DMF, initially purged with nitrogen followed by CO_2 saturation	[158]
GO-doped oxygen-rich TiO_2	None	CH_4	0.43	-	Xe lamp (500 W)	A continuous gas flow reactor with humidified CO_2, operated under ambient conditions	[148]

GO−TiO_2 nanotube arrays	None	CH_4	5.67ppm cm^{-2} h^{-1}	-	Xenon solar simulator (100 W)	15.4 cm^3 stainless steel photoreactor with humidified CO_2 loaded with 2.0 x 2.0 cm^2 photocatalyst film	[149]
Cu_2O/r-GO	None	CO	46 ppm/g/h	0.34	Xenon lamp (150 W)	Septum sealed glass chamber (120 mL) with 0.5 g photocatalyst and 3 mL deionized water, operated under ambient conditions	[159]
TiO_2/Nr-GO	None	CO	50	0.0072	Xenon lamp (400 W)	Continuous flow photoreactor with 10 mg of catalyst and humidified CO_2	[160]
r-GO−CuO	None	CH_3OH	53.42	1.3	White cold LED flood light (20 W)	100 mL cylindrical borosilicate glass vessel charged with DMF (45 mL), water (5 mL) and saturated with CO_2	[160]
α-Fe_2O_3/amine−r-GO/ $CsPbBr_3$ hybrids	None	CH_4	12.11	-	Xe lamp (150 W)	56 mL sealed pyrex reaction vessel with CO_2 and saturated water vapor, operated under ambient conditions	[160]
Ag−r-GO−Cds	None	CO	1.61 µmol/h	-	Xe lamp (300 W)	80 mL Schlenk flask reactor with 5 mg catalyst, 4 mL H_2O, and 2 mL TEOA, with CO_2 introduced at a partial pressure of 1.0 atm	[161]

illumination. The prime reasons behind this are the possibility of multiple products, poor yields, selectivity, and formation rates of products, and difficulty in isotope labeling experiments. To facilitate reduction reactions, artificial electron donors are generally introduced into the reaction medium, which scavenge photogenerated holes, thereby preventing the unwanted photo-oxidations as well as photocorrosion of catalysts. But, the photocatalytic process lasts only until the sacrificial electron donor is diminished. To date, most studied systems have been largely focused on reduction half reactions of CO_2. Nevertheless, studies on full redox cycle with an emphasis on oxidation half reactions (e.g., O_2 evolution) are of great importance in the future for a better understanding of CO_2 photoreduction as well as to unravel the further possibilities like oxidation of catalytically generated products. The reduction and oxidation half reactions should be cleanly separated to avoid any reverse processes, which can be achieved via installing photoelectrochemical cells with separated compartments, which may receive further upgradations accordingly in the near future. It is not very clear from reports whether carbon-based catalysts like CDs and GOs in their hybrid nanostructures with semiconductors are active components generating charge carriers through self-excitation or they just facilitate the electron transfer process through electron conduction when combined with semiconductor photocatalysts.

Future prospects in this domain of nanostructured carbon-based photocatalysts for CO_2 conversion involve the characterization of catalysts through spectral sensitivity, and attaining control over photoactivity, product efficiency, and selectivity towards more-profitable outcomes like methane, methanol, or ethanol. Apart from these, exploring heterojunctions for driving the electronic process in the required direction, surface engineering, and doping strategies (e.g., using appropriate true metal ion, heteroatom doping) for selective excitation of localized electronic states via band gap engineering to attain better selectivity as well as develop practical photocatalytic reactor designs for continuous mode operation should receive more attention. Moreover, with the aid of advanced computational modeling techniques like Density Functional Theory (DFT) and Artificial Intelligence (AI)-based approaches, rational design of carbon nanomaterials with elevated photocatalytic characteristics may also be pursued.

Acknowledgments

SS acknowledges the Department of Chemistry at the University of Louisiana at Lafayette and Prof. Ya-Ping Sun from Clemson University for useful discussions.

References

[1] A.L. Linsebigler, G. Lu, J.T. Yates, Chemical Reviews 95 (1995) 735.
[2] B. Ohtani, Journal of Photochemistry and Photobiology C 11 (2010) 157.
[3] M.B. Wilker, K.J. Schnitzenbaumer, G. Dukovic, Israel Journal of Chemistry 52 (2012) 1002.

[4] J. Albero, Y. Peng, H. Garcia, ACS Catalysis 10 (2020) 5734.

[5] Y.H. Park, G. Murali, J.K.R. Modigunta, I. In, S.-I. In, Frontiers in Chemistry 9 (2021) 734108.

[6] N.S. Lewis, D.G. Nocera, Proceedings of the National Academy of Sciences of the United States of America 103 (2006) 15729.

[7] N. Armaroli, V. Balzani, Angewandte Chemie International Edition 46 (2007) 52.

[8] S.C. Roy, O.K. Varghese, M. Paulose, C.A. Grimes, ACS Nano 4 (2010) 1259.

[9] S.N. Habisreutinger, L. Schmidt-Mende, J.K. Stolarczyk, Angewandte Chemie International Edition 52 (2013) 7372.

[10] W. Fan, Q. Zhang, Y. Wang, Physical Chemistry Chemical Physics 15 (2013) 2632.

[11] S. Navalon, A. Dhakshinamoorthy, M. Alvaro, H. Garcia, ChemSusChem 6 (2013) 562.

[12] A. Dhakshinamoorthy, S. Navalon, A. Corma, H. Garcia, Energy & Environmental Science 5 (2012) 9217.

[13] X. Chen, S. Shen, L. Guo, S.S. Mao, Chemical Reviews 110 (2010) 6503.

[14] R. Abe, Journal of Photochemistry and Photobiology C 11 (2010) 179.

[15] K. Maeda, K. Domen, The Journal of Physical Chemistry Letters 1 (2010) 2655.

[16] G. Xie, K. Zhang, B. Guo, Q. Liu, L. Fang, J.R. Gong, Advanced Materials 25 (2013) 3820.

[17] K. Bramhaiah, S. Bhattacharyya, Materials Advances 3 (2022) 142.

[18] M.A. Green, Third Generation Photovoltaics: Advanced Solar Energy Conversion, Springer-Verlag, Berlin, 2006.

[19] A.J. Bard, M.A. Fox, Accounts of Chemical Research 28 (1995) 141.

[20] P. De luna, C. Hahn, D. Higgins, S.A. Jaffer, T.F. Jaramillo, E.H. Sargent, Science (New York, N.Y.) 364 (2019). eaav3506.

[21] M.R. Hoffmann, S.T. Martin, W. Choi, D.W. Bahnemannt, Chemical Reviews 95 (1995) 69.

[22] J.-M. Herrmann, Catalysis Today 53 (1999) 115.

[23] A. Fujishima, K. Hashimoto, T. Watanabe, Tokyo: BKC Inc (1999).

[24] N.S. Allen, M. Edge, G. Sandoval, J. Verran, J. Stratton, J. Maltby, Photochemistry and Photobiology 81 (2005) 279.

[25] M. Lu, P. Pichat, Photocatalysis and Water Purification, *Wiley-VCH*, *Weinheim*, 2013.

[26] M. Muzzio, J. Li, Z. Yin, I.M. Delahunty, J. Xie, S. Sun, Nanoscale 11 (2019) 18946.

[27] R. Rossetti, L. Brus, The Journal of Physical Chemistry 86 (1982) 4470.

[28] A.P. Alivisatos, Science 271 (1996) 933.

[29] H. Li, Z. Kang, Y. Liu, S.-T. Lee, Journal of Materials Chemistry 22 (2012) 24230.

[30] L. Li, G. Wu, G. Yang, J. Peng, J. Zhao, J.-J. Zhu, Nanoscale 5 (2013) 4015.

[31] A.M.M. Hasan, M.A. Hasan, A. Reza, M.M. Islam, M.A.B.H. Susan, Mater. Today Commun 29 (2021) 102732.

[32] X. Xu, R. Ray, Y. Gu, H.J. Ploehn, L. Gearheart, K. Raker, et al., Journal of the American Chemical Society 126 (2004) 12736.

[33] Y.-P. Sun, B. Zhou, Y. Lin, W. Wang, K.A.S. Fernando, P. Pathak, et al., Journal of the American Chemical Society 128 (2006) 7756.

[34] S. Zhu, S. Tang, J. Zhang, B. Yang, Chemical Communications 48 (2012) 4527.

[35] A.P. Demchenko, M.O. Dekaliuk, Methods and Applications in Fluorescence 1 (2013) 042001.

[36] M. Bacon, S.J. Bradley, T. Nann, Particle & Particle Systems Characterization 31 (2014) 415.

[37] L. Lin, M. Rong, F. Luo, D. Chen, Y. Wang, X. Chen, TrAC - Trends in Analytical Chemistry 54 (2014) 83.

[38] L. Cao, X. Wang, M.J. Meziani, F. Lu, H. Wang, P.G. Luo, et al., Journal of the American Chemical Society 129 (2007) 11318.

[39] W. Liang, C.E. Bunker, Y.-P. Sun, ACS Omega 5 (2) (2020) 965.

[40] S.N. Baker, G.A. Baker, Angewandte Chemie International Edition 49 (2010) 6726.

[41] S. Mandal, P. Das, Applied Materials Today 26 (2022) 101331.

[42] J. Shen, Y. Zhu, X. Yang, C. Li, Chemical Communications 48 (2012) 3686.

[43] P.G. Luo, S. Sahu, S. Yang, S.K. Sonkar, J. Wang, H. Wang, et al., Journal of Materials Chemistry B 1 (2013) 2116.

[44] J.C.G. Esteves da Silva, H.M.R. Goncalves, TrAC - Trends in Analytical Chemistry 30 (2011) 1327.

[45] C. Ding, A. Zhu, Y. Tian, Accounts of Chemical Research 47 (2014) 20.

[46] S.C. Ray, A. Saha, N.R. Jana, R. Sarkar, The Journal of Physical Chemistry C 113 (2009) 18546.

[47] D. Pan, J. Zhang, Z. Li, M. Wu, Advanced Materials 22 (2010) 734.

[48] Wang, et al., ACS Nano 8 (3) (2014) 2541.

[49] C. Xu, W.W. Webb, Journal of the Optical Society of America B 13 (1996) 481.

[50] C. Eggeling, J. Widengren, R. Rigler, C.A.M. Seidel, Analytical Chemistry 70 (1998) 2651.

[51] J. Xu, S. Sahu, L. Cao, P. Anilkumar, K.N. Tackett II, H. Quian, et al., ChemPhysChem 12 (2011) 3604.

[52] L. Deng, X. Wang, Y. Kuang, C. Wang, L. Luo, F. Wang, Nano Research 8 (2010) 2810.

[53] Y.-P. Sun, X. Wang, F. Lu, L. Cao, M.J. Meziani, P.G. Luo, et al., The Journal of Physical Chemistry C 112 (2008) 18295.

[54] X. Wang, L. Cao, S.-T. Yang, F. Lu, M.J. Meziani, L. Tian, et al., Angewandte Chemie International Edition 49 (2010) 5310.

[55] J. Shen, Y. Zhu, X. Yang, C. Li, Chemical Communications 48 (2012) 3686.

[56] K.A.S. Fernando, S. Sahu, Y. Liu, W.K. Lewis, E.A. Guliants, A. Jafariyan, ACS Applied Materials & Interfaces 7 (2015) 8363.

[57] L. Cao, S. Sahu, P. Anilkumar, C.E. Bunker, J. Xu, K.A.S. Fernando, et al., Journal of the American Chemical Society 133 (2011) 4754.

[58] X. Wang, L. Cao, F. Lu, M.J. Meziani, H. Li, G. Qi, et al., Chemical Communications (2009) 3774.

[59] L. Zhou, Y. Lin, Z. Huang, J. Ren, X. Qu, Chemical Communications 48 (2012) 1147.

[60] L. Liu, Y. Li, L. Zhan, Y. Liu, C. Huang, Science China Chemistry 54 (2011) 1342.

[61] S.Y. Lim, W. Shen, Z. Gao, Chemical Society Reviews 44 (2015) 362.

[62] L. Tang, R. Ji, X. Cao, J. Lin, H. Jiang, X. Li, et al., ACS Nano 6 (2012) 5102.

[63] V.N. Mehta, S. Jha, H. Basu, R.K. Singhal, S.K. Kailasa, Sensors and Actuators. B, Chemical 213 (2015) 434.

[64] B.-X. Zhang, G.-Y. Zhang, H. Gao, S.-H. Wu, J.-H. Chen, X.-L. Li, RSC Advances 5 (2015) 7395.

[65] Y. Yang, J. Cui, M. Zheng, C. Hu, S. Tan, Y. Xiao, et al., Chemical Communications 48 (2012) 380.

[66] X. Wang, K. Qu, B. Xu, J. Ren, X. Qu, Journal of Materials Chemistry 21 (2011) 2445.

[67] V.Y. Osipov, M.S. Shestakov, A.V. Baranov, V.A. Ermakov, A.I. Shames, K. Takai, et al., Optics and Spectroscopy 111 (2011) 220.

[68] (a) D. Dasgupta, F. Demichelis, C.F. Pirri, A. Tagliaferro, Physical Review B 43 (1991) 2131.
(b) F.L. Shyu, M.F. Lin, Physical Review B 62 (2000) 8508.

[69] R. Sen, S.M. Rickard, M.E. Itkis, R.C. Haddon, Chemistry of Materials: a Publication of the American Chemical Society 15 (2003) 4273.

[70] M.E. Itkis, D.E. Perea, R. Jung, S. Niyogi, R.C. Haddon, Journal of the American Chemical Society 127 (2005) 3439.

[71] (a) B.J. Landi, H.J. Ruf, C.M. Evans, C.D. Cress, R.P. Raffaelle, The Journal of Physical Chemistry B 109 (2005) 9952.
(b) K. Lingam, R. Podila, C. Loebick, P. Chen, P.-C. Ke, B. Powell, et al., Carbon 49 (2011) 3803.

[72] M.E. Itkis, S. Niyogi, M.E. Meng, M.A. Hamon, H. Hu, R.C. Haddon, Nano Letters 2 (2002) 155.

[73] B. Zhao, M.E. Itkis, S. Niyogi, H. Hu, J. Zhang, R.C. Haddon, The Journal of Physical Chemistry B 108 (2004) 8136.

[74] J.G. Zhou, C. Booker, R.R. Li, X.T. Zhou, T.K. Sham, X.L. Sun, et al., Journal of the American Chemical Society 129 (2007) 744.

[75] V.N. Mochalin, Y. Gogotsi, Journal of the American Chemical Society 131 (2009) 4594.

[76] S. Zhu, J. Zhang, C. Qiao, S. Tang, Y. Li, W. Yuan, et al., Chemical Communications 48 (2011) 6858.

[77] S. Sahu, B. Behera, T.K. Maiti, S. Mohapatra, Chemical Communications 48 (2012) 8835.

[78] L. Cao, M.J. Meziani, S. Sahu, Y.-P. Sun, Accounts of Chemical Research 46 (2012) 171.

[79] J. Shang, L. Ma, J. Li, W. Ai, T. Yu, G.G. Gurzadyan, Scientific Reports 2 (2012) 792.

[80] C. Galande, A.D. Mohite, A.V. Naumov, W. Gao, L. Ci, A. Ajayan, et al., Scientific Reports 1 (2011) 85.

[81] M.J. Krysmann, A. Kelarakis, P. Dallas, E.P. Giannelis, Journal of the American Chemical Society 134 (2012) 747.

[82] P. Yu, X.M. Wen, Y.R. Toh, J. Tang, The Journal of Physical Chemistry C 116 (2012) 25552.

[83] H. Li, X. He, Z. Kang, H. Huang, Y. Liu, J. Liu, et al., Angewandte Chemie International Edition 49 (2010) 4430.

[84] K.M. Tripathi, A.K. Sonker, S.K. Sonkar, S. Sarkar, RSC Advances 4 (2014) 30100.

[85] P. Dubey, K.M. Tripathi, S.K. Sonkar, RSC Advances 4 (2014) 5838.

[86] Y. Guo, Z. Wang, H. Shao, X. Jiang, Carbon 52 (2013) 583.

[87] X. Zhai, P. Zhang, C. Liu, T. Bai, W. Li, L. Dai, et al., Chemical Communications 48 (2012) 7955.

[88] N.V. Tepliakov, E.V. Kundelev, P.D. Khavlyuk, Y. Xiong, M.Y. Leonov, W. Zhu, et al., ACS Nano 13 (2019) 10737.

[89] S. Hu, J. Liu, J. Yang, Y. Wang, S. Cao, Journal of Nanoparticle Research 13 (2011) 7247.

[90] Q.-L. Zhao, Z.-L. Zhang, B.-H. Huang, J. Peng, M. Zhang, D.-W. Pang, Chemical Communications (2008) 5116.

[91] H.C. Zhang, H. Huang, H. Ming, H.T. Li, L.L. Zhang, Y. Liu, et al., Journal of Materials Chemistry 22 (2012) 10501.

[92] J. Xu, S. Sahu, L. Cao, C.E. Bunker, G. Peng, Y. Liu, et al., Langmuir 28 (2012) 16141.

[93] P. Anilkumar, L. Cao, J.-J. Yu, K.N. Tackett II, P. Wang, M.J. Meziani, et al., Small (Weinheim an der Bergstrasse, Germany) 9 (2013) 545.

[94] G.E. LeCroy, S.K. Sonkar, F. Yang, L.M. Veca, P. Wang, K.N. Tackett II, et al., ACS Nano 8 (2014) 4522.

[95] N.-N. Chai, H.-X. Wang, C.-X. Hu, Q. Wang, H.-L. Zhang, Journal of Materials Chemistry A 3 (2015) 16613.

[96] P. Anilkumar, X. Wang, L. Cao, S. Sahu, J.-H. Liu, P. Wang, et al., Nanoscale 3 (2011) 2023.

[97] J. Wang, F. Peng, Y. Lu, Y. Zhong, S. Wang, M. Xu, et al., Advanced Optical Materials 3 (2015) 103.

[98] X.-M. Wei, Y. Xu, Y.-H. Li, X.-B. Yin, X.-W. He, RSC Advances 4 (2014) 44504.

[99] F. Arcudi, L. Đorđević, M. Prato, Angewandte Chemie International Edition 55 (2016) 2107.

[100] T.-F. Yeh, C.-Y. Teng, S.-J. Chen, H. Teng, Advanced Materials 26 (2014) 3297.

[101] Y. Choi, B. Kang, J. Lee, S. Kim, G.T. Kim, H. Kang, et al., Chemistry of Materials: a Publication of the American Chemical Society 28 (2016) 6840.

[102] D. Qu, Z. Sun, M. Zheng, J. Li, Y. Zhang, G. Zhang, et al., Advanced Optical Materials 3 (2015) 360.

[103] Q. Xu, Y. Liu, C. Gao, J. Wei, H. Zhou, Y. Chen, et al., Journal of Materials Chemistry C 3 (2015) 9885.

[104] M.K. Barman, A. Patra, Journal of Photochemistry and Photobiology C 37 (2018) 1.

[105] A. Cayuela, M.L. Soriano, C. Carrillo-Carrion, M. Valcarcel, Chemical Communications 52 (2016) 1311.

[106] L. Cao, P. Anilkumar, X. Wang, J.-H. Liu, S. Sahu, M.J. Meziani, et al., Canadian Journal of Chemistry 89 (2011) 104.

[107] M.O. Dekaliuk, O. Viagin, Y.V. Malyukin, A.P. Demchenko, Physical Chemistry Chemical Physics: PCCP 16 (2014) 16075.

[108] P. Yang, J. Zhao, L. Zhang, L. Li, Z. Zhu, Chemistry—A European Journal 21 (2015) 8561.

[109] S. Ghosh, A.M. Chizhik, N. Karedla, M.O. Dekaliuk, I. Gregor, H. Schuhmann, et al., Nano Letters 14 (2014) 5656.

[110] M. Fu, F. Ehrat, Y. Wang, K.Z. Milowska, C. Reckmeier, A.L. Rogach, et al., Nano Letters 15 (2015) 6030.

[111] S.K. Das, Y. Liu, S. Yeom, D.Y. Kim, C.I. Richards, Nano Letters 14 (2014) 620.

[112] N.M. Dimitrijevic, B.K. Vijayan, O.G. Poluektov, T. Rajh, K.A. Gray, H. He, et al., Journal of the American Chemical Society 133 (2011) 3964.

[113] S. Bachu, Progress in Energy and Combustion Science 34 (2008) 254.

[114] D.E. Skinner, D.P. Colombo, J.J. Cavalieri, R.M. Bowman, The Journal of Physical Chemistry 99 (1995) 7853.

[115] D.P. Colombo, K.A. Roussel, J. Saeh, D.E. Skinner, J.J. Cavaleri, R.M. Bowman, Chemical Physics Letters 232 (1995) 207.

[116] P.V. Kamat, The Journal of Physical Chemistry C 111 (2007) 2834.

[117] A. Fujishima, K. Honda, Nature 238 (1972) 37.

[118] M.D. Hernandez-Alonso, F. Fresno, S. Suarez, J.M. Coronado, Energy & Environmental Science 2 (2009) 1231.

[119] K. Hashimoto, H. Irie, A. Fujishima, Japanese Journal of Applied Physics 44 (2005) 8269.

[120] R. Asahi, T. Morikawa, T. Ohwaki, K. Aoki, Y. Taga, Science 293 (2001) 269.

[121] Q. Xiang, J. Yu, M. Jaroniec, Chemical Society Reviews 41 (2012) 782.

[122] H. Sun, S. Wang, Energy Fuels 28 (2014) 22.

[123] C. Jianwei, S. Jianwen, W. Xu, C. Haojie, F. Minglai, Chinese Journal of Catalysis 34 (2013) 621.

[124] D. Chen, H. Zhang, Y. Liu, L. Jinghong, Energy & Environmental Science 6 (2013) 1362.

[125] L. Han, P. Wang, S. Dong, Nanoscale 4 (2012) 5814.

[126] W. Tu, Y. Zhou, Z. Zou, Advanced Functional Materials 23 (2013) 4996.

[127] Z. Zhang, J. Zhang, N. Chena, L. Qu, Energy & Environmental Science 5 (2012) 8869.

[128] S. Guo, S. Dong, Chemical Society Reviews 40 (2011) 2644.

[129] H. Chang, H. Wu, Advanced Functional Materials 23 (2013) 1984.

[130] G. Peng, S. Sahu, M.J. Meziani, L. Cao, Y. Liu, Y.-P. Sun, Carbon Nanomaterials, second ed., *CRC Press*, *Boca Raton*, 2013. Chapter 16, 463.

[131] L. Wang, H. Liu, R.M. Konik, J.A. Misewich, S.S. Wong, Chemical Society Reviews 42 (2013) 8134.

[132] W.S. Hummers, R.E. Offeman, Journal of the American Chemical Society 80 (1958) 1339.

[133] D.R. Dreyer, S. Park, C.W. Bielawski, R.S. Ruoff, Chemical Society Reviews 39 (2010) 228.

[134] S. Sahu, Development and Evaluation of Carbon-based Quantum Dots for Carbon Dioxide Photoconversion. Ph.D. Thesis, Clemson University, Clemson, SC, All dissertation 1484, December 2014.

[135] S. Sahu, Y. Liu, P. Wang, C.E. Bunker, K.A.S. Fernando, W.K. Lewis, et al., Langmuir 30 (2014) 8631.

[136] H. Choi, S.-J. Ko, Y. Choi, P. Joo, T. Kim, B.R. Lee, et al., Nature Photonics 7 (2013) 732.

[137] X. Qin, W. Lu, A.M. Asiri, A.O. Al-Youbi, X. Sun, Catalysis Science & Technology 3 (2013) 1027.

[138] a) H. Li, X. Zhang, D.R. MacFarlane, Advanced Energy Materials 5 (2015) 1401077.
b) H. Li, Y. Deng, Y. Liu, X. Zeng, D. Wiley, J. Huang, Chemical Communications 55 (2019) 4419−1404422.
c) Z. Liu, Z. Wang, S. Qing, N. Xue, S. Jia, L. Zhang, et al., Chen, Applied Catalysis B: Environmental 232 (2018) 86−92.

[139] (a) Y. Yan, J. Chen, N. Li, J. Tian, K. Li, J. Jiang, et al., ACS Nano 12 (2018) 3523.
(b) D. Yadav, R.K. Yadav, A. Kumar, N.J. Park, J.O. Baeg, ChemCatChem 8 (2016) 3389−3393.
(c) H. Zhong, R. Sa, H. Lv, S. Yang, D. Yuan, X. Wang, et al., Advanced Functional Materials 30 (2020) 2−9.

[140] H.C. Hsu, I. Shown, H.Y. Wei, Y.C. Chang, H.Y. Du, Y.G. Lin, et al., Nanoscale 5 (2013) 262.

[141] I. Shown, H.-C. Hsu, Y.-C. Chang, C.-H. Lin, P.K. Roy, A. Ganguly, et al., Nano Letters 14 (2014) 6097.

[142] X. Li, Q. Wang, Y. Zhao, W. Wu, J. Chen, H. Meng, Journal of Colloid and Interface Science 411 (2013) 69.

[143] a) L.-L. Tan, W.-J. Ong, S.-P. Chai, A.R. Mohamed, Nanoscale Research Letters 8 (2013) 465.
b) M. Li, M. Wang, L. Zhu, Y. Li, Z. Yan, Z. Shen, et al., Applied Catalysis B: Environmental 231 (2018) 269−276.

[144] Y.T. Liang, B.K. Vijayan, K.A. Gray, M.C. Hersam, Nano Letters 11 (2011) 2865.

[145] Y.T. Liang, B.K. Vijayan, O. Lyandres, K.A. Gray, M.C. Hersam, The Journal of Physical Chemistry Letters 3 (2012) 1760.

[146] W.G. Tu, Y. Zhou, Q. Liu, Z.P. Tian, J. Gao, X.Y. Chen, et al., Advanced Functional Materials 22 (2012) 1215.

[147] W.G. Tu, Y. Zhou, Q. Liu, S.C. Yan, S.S. Bao, X.Y. Wang, et al., Advanced Functional Materials 23 (2013) 1743.

[148] L.-L. Tan, W.-J. Ong, S.-P. Chai, A.R. Mohamed, Chemical Engineering Journal 308 (2017) 248.

[149] A. Razzaq, C.A. Grimes, Carbon 98 (2016) 537.

[150] P.Q. Wang, Y. Bai, P.Y. Luo, J.Y. Liu, Catalysis Communications 38 (2013) 82.

[151] X.J. Lv, W.F. Fu, C.Y. Hu, Y. Chen, W.B. Zhou, RSC Advances 3 (2013) 1753.

[152] Y. Kuang, J. Shang, T. Zhu, ACS Applied Materials & Interfaces 12 (2020) 3580.

[153] D. Kumar, A. Lee, T. Lee, M. Lim, D.-K. Lim, Nano Letters 16 (2016) 1760.

[154] P. Kumar, C. Joshi, A. Barras, B. Sieber, A. Addad, L. Boussekey, et al., Applied Catalysis B: Environmental 205 (2017) 654.

[155] Y. Jiang, J.-F. Liao, Y.-F. Xu, H.-Y. Chen, X.-D. Wang, E.-B. Kuang, Journal of Materials Chemistry A 7 (2019) 13762.

[156] P. Kumar, B. Sain, S.L. Jain, Journal of Materials Chemistry A 2 (2014) 11246.

[157] P. Kumar, A. Kumar, B. Sreedhar, B. Sain, S.S. Ray, S.L. Jain, Chemistry—A European Journal 20 (2014) 6154.

[158] P. Kumar, A. Bansiwal, N. Labhsetwar, S.L. Jain, Green Chemistry: an International Journal and Green Chemistry Resource 17 (2015) 1605.

[159] X. An, K. Li, J. Tang, ChemSusChem 7 (2014) 1086.

[160] (a) L.-Y. Lin, Y. Nie, S. Kavadiya, T. Soundappan, P. Biswas, Chemical Engineering Journal 316 (2017) 449.
  (b) R. Gusain, P. Kumar, O.P. Sharma, S.L. Jain, O.P. Khatri, Applied Catalysis B: Environmental 181 (2016) 352.
  (c) Y. Jiang, J.-F. Liao, H.-Y. Chen, H.-H. Zhang, J.-Y. Li, X.-D. Wang, et al., Chem 6 (2020) 766−780.

[161] Z. Zhu, Y. Han, C. Chen, Z. Ding, J. Long, Y. Hou, ChemCatChem 10 (2018) 1627.

[162] L.-L. Tan, W.-J. Ong, S.-P. Chai, A.R. Mohamed, Applied Catalysis B: Environmental 166−-167 (2015) 251.

[163] X. Wang, K. Maeda, A. Thomas, K. Takanabe, G. Xin, J.M. Carlsson, et al., Nature Materials 8 (2009) 76.

[164] G. Dong, L. Zhang, Journal of Materials Chemistry 22 (2012) 1160.

[165] J. Mao, T. Peng, X. Zhang, K. Li, L. Ye, L. Zan, Catalysis Science & Technology 3 (2013) 1253.

[166] Y. Wang, Y. Chen, Y. Zuo, F. Wang, J. Yao, B. Li, et al., Catalysis Science & Technology 3 (2013) 3286.

[167] K. Maeda, K. Sekizawa, O. Ishitani, Chemical Communications 49 (2013) 10127.

[168] a) J. Lin, Z. Pan, X. Wang, ACS Sustainable Chemistry & Engineering 2 (2014) 353.
  b) Y. Wang, X. Liu, X. Han, R. Godin, J. Chen, W. Zhou, et al., Nature Communications 11 (2020) 1−359.
  c) Y. Wang, R. Godin, J.R. Durrant, J. Tang, Angewandte Chemie International Edition 60 (2021) 20811−20816.
  d) W.J. Ong, L.K. Putri, Y.C. Tan, L.L. Tan, N. Li, Y.H. Ng, et al., Nano Research 10 (2017) 1673−1696.

[169] K. Woan, G. Pyrgiotakis, W. Sigmund, Advanced Materials 21 (2009) 2233.

[170] A. Kongkanand, P.V. Kamat, ACS Nano 1 (2007) 13.

[171] K. Dai, T. Peng, D. Ke, B. Wei, Nanotechnology 20 (2009) 125603.

[172] W. Wang, P. Serp, P. Kalck, J.L. Faria, Journal of Molecular Catalysis A: Chemical 235 (2005) 194.

[173] L.L. Ma, H.Z. Sun, Y.G. Zhang, Y.L. Lin, J.L. Li, E.K. Wang, et al., Nanotechnology 19 (2008) 115709.

[174] X.H. Xia, Z.H. Jia, Y. Yu, Y. Liang, Z. Wang, L.L. Ma, Carbon 45 (2007) 717.

[175] W.J. Ong, M.M. Gui, S.-P. Chai, A.R. Mohamed, RSC Advances 3 (2013) 4505.

[176] M.M. Gui, S.-P. Chai, B.-Q. Xu, A.R. Mohamed, RSC Advances 4 (2014) 24007.

Carbon quantum dots and its composites for electrochemical energy storage applications

15

S. Charis Caroline[1] *and Sudip K. Batabyal*[1,2]
[1]Department of Sciences, Amrita School of Engineering Coimbatore, Amrita Vishwa Vidyapeetham, Coimbatore, Tamil Nadu, India, [2]Amrita Centre for Industrial Research and Innovation (ACIRI), Amrita School of Engineering Coimbatore, Amrita Vishwa Vidyapeetham, Coimbatore, Tamil Nadu, India

15.1 Introduction

The growing global energy demands and the alarming increase in anthropogenic emissions call for a convenient alter in the energy storage combat. The renewable energy sector suffers mainly due to its intermittent nature. The need for a sustainable resilient energy storage system is the driving force for the development of new materials with charge storage ability. The peak energy storage in the grid could be reduced by employing supercapacitors and batteries as effective energy storage devices. The crucial parameters while considering a potential electrode material for charge storage range from the available surface area of the material to the striking electrochemical properties involved in the charge storage mechanism and later to the position in the Ragone plot. David V. Ragone's plot between the logarithmic axis of energy and power density compares two very different devices with extreme material properties [1]. A similar plot can be seen in Fig. 15.1. The present-day technology in supercapacitors and batteries is limited in energy storage and long charge-discharge cycles.

One of the finest discoveries of the 21st century is the discovery of carbon quantum dots (CQDs) while purifying single-walled carbon during electrophoresis in 2004 [2]. From then till now, the research is ever-growing in the realm of CQDs for charge storage specifically. Though standalone carbon can be tuned based on the applications, it is insoluble in water, offers weak fluorescence, and is not a good candidate for conducting electricity. However, other forms of carbon such as graphite, carbon nanotubes, fullerenes, nanodiamonds, etc. offer good conductivity. The phenomenon of the quantum confinement effect is seen in CQDs owing to their small size [3]. This causes CQDs to have a high surface area and charge storage ability while contributing to the enriched optoelectronic properties. CQDs are zero-dimensional with strong optoelectronic properties. The quantum size effect accounts for the charge storage in CQDs, allowing for surface passivation. This new class of materials is nontoxic and can dominate the metal-based quantum dots.

Carbon Quantum Dots for Sustainable Energy and Optoelectronics. DOI: https://doi.org/10.1016/B978-0-323-90895-5.00021-7
© 2023 Elsevier Ltd. All rights reserved.

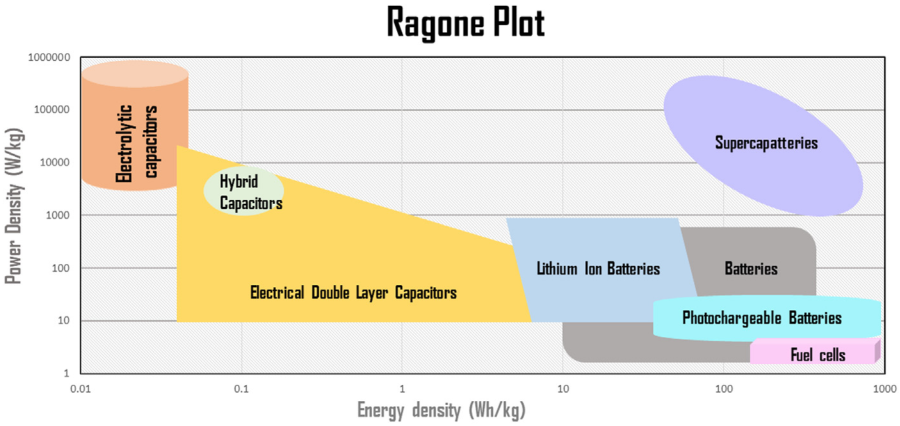

Figure 15.1 David V. Ragone plot (energy density vs power density) of various charge storage devices.

CQDs are widely used in medical imaging [4], photocatalysis [5,6], photovoltaics [7], dye degradation [8], and charge storage applications [9,10]. Quasispherical carbon nanomaterials with both amorphous and crystalline carbon base form the CQDs. The sp^3 hybridized carbon atom replaces the graphitic/carbon sp^2 sheets and exhibits fluorescence properties. In this chapter, we discuss the carbon dots (CDs), CQDs, and graphene quantum dots (GQDs), along with their respective composites in charge storage. An overview of the fundamentals of supercapacitors and batteries is elaborated. We probe into the specific properties responsible for the charge storage mechanism and expound on the role of CQDs in charge storage both individually and as a composite. An elaborate discussion is provided on the contribution of CQDs in enhancing the storage properties. The chapter is concluded with the challenges and prospects of CQDs.

15.2 Fundamentals of supercapacitors and batteries

15.2.1 Fundamentals of supercapacitors

Energy demands are rising from time to time. Energy can be stored in supercapacitors and batteries based on application. Unlike batteries, supercapacitors can release energy in large bursts in a short duration, and their kinetic energy is several orders of the scale higher than that of electrochemical batteries. Supercapacitors are a convenient alter when a large amount of peak current is required in a given instant of time. Supercapacitors work on a mechanism similar to normal capacitors with ultrahigh charge storage ability. Supercapacitors store charges by forming an electric field between two electrodes. The difference in electric potential between the two electrodes accumulates charges on one electrode, and when the charge on this electrode reaches the device's maximum capacity, it is discharged usually through a

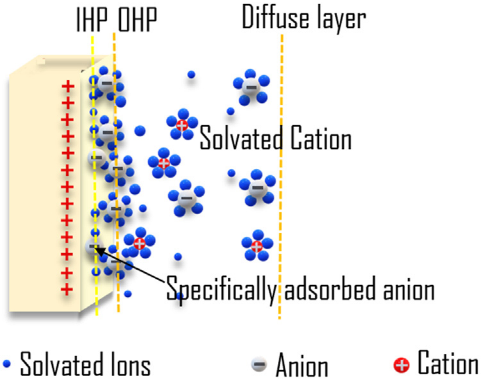

Figure 15.2 Charge storage in EDLC. *EDLC*, Electrical double-layered capacitors.

connecting wire. Supercapacitors can be broadly classified as electrical double-layered capacitors (EDLC), pseudocapacitors, and hybrid capacitors.

Charge storage in EDLC is through a non-faradaic process. It involves physical adsorption/desorption while potential is applied. When an electrode is placed in an electrochemical system, the unsolvated anions accumulate on the surface of the electrode, forming a layer called the inner Helmholtz plane. Consequently, the solvated anions arrange themselves as shown in Fig. 15.2 to form the outer Helmholtz plane. To prevent the ions from crossing the EDLC, an insulating barrier must be used. This can be achieved by using electrolytes with very low ionic conductivity or by increasing the distance between the electrodes to allow for substantial electrolyte depletion. The high surface area ensures that the stored charge is quickly discharged when applied to an electric field. The charge storage capacity is due to the high surface area of the materials. Carbon-based materials, polymers, etc. exhibit this kind of behavior. The capacitance of the EDLC is associated with the surface of the material and its porosity, while the bulk properties are neglected. The large surface area and the shortest distance between the electrode and the electrolyte can help charge storage.

The pseudocapacitive charge storage mechanism was unknown until 1980. Charge storage in pseudocapacitors is realized through the redox reaction in the active material and the electrical double layer. Pseudocapacitors work with a mechanism combining capacitors and batteries. Pseudocapacitors provide room for 10 times the charge stored using a double layer. Although the charge storage process involves double-layer capacitance, it is only a fraction of the total charge storage. Charges are stored mainly due to redox reactions, intercalation, and electrosorption.

1. Redox pseudocapacitance happens when the ions are electrochemically adsorbed into the electrode surface with all the associated faradaic reactions. When a potential is applied between electrodes, redox reactions occur fast. The redox reactions should be reversible or quasi reversible to be used as a potential candidate for supercapacitors. This can be seen in Fig. 15.3. The oxidation occurs at the anode, and reduction happens at the cathode.

2. Adsorption of the ions at the electrode–electrolyte interface can also contribute to pseudocapacitance. This condition is in cases where an adsorbed monolayer forms on the surface of a different metal at a lower negative potential compared to the equilibrium potential. The deposition of Pb ions on the surface of the gold is one common example.
3. Intercalation involves the bulk electrodes. The intercalation or the insertion of ions takes place between the electrode layers formed as a result of the faradaic process. The intercalation between layers does not alter the crystal structure or morphology, retaining the capacitance.

In hybrid supercapacitors, both faradaic and non-faradaic processes are used to the advantage. These are mainly composites. In some cases, one of the electrodes exhibits faradaic behavior, while the other shows non-faradaic behavior. The electrodes can be tailored to fit the need as shown in Fig. 15.4. In this case, at the

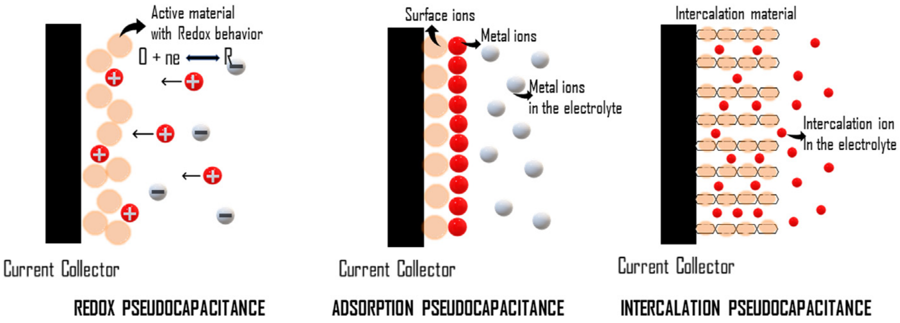
Active material
with Redox behavior
O + ne ⟷ R
Current Collector
REDOX PSEUDOCAPACITANCE
Surface ions
Metal ions
Metal ions
in the electrolyte
Current Collector
ADSORPTION PSEUDOCAPACITANCE
Intercalation material
Intercalation ion
In the electrolyte
Current Collector
INTERCALATION PSEUDOCAPACITANCE

Figure 15.3 Charge storage in pseudocapacitors.

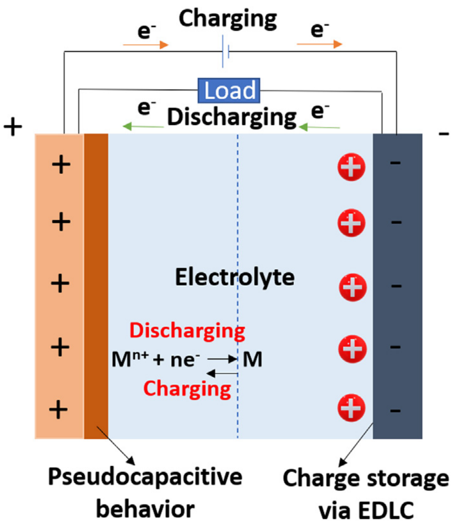
e-
Charging
e-
Load
e-
Discharging
e-
+
-
Electrolyte
Discharging
Mn+ + ne- → M
Charging
Pseudocapacitive
behavior
Charge storage
via EDLC

Figure 15.4 Charge storage in a hybrid supercapacitor.

positive electrode, a redox reaction takes place similar to the mechanism in a pseudocapacitor. While the negative electrode stores charges via the formation of double-layer like in EDLC, it also ensures the retention of the high power density and cyclic stability while increasing the energy density.

15.2.2 Fundamentals of batteries

A battery converts chemical energy into electrical energy. The existing chemical energy in the active materials of the electrode undergoes electrochemical redox reactions, and hence the energy conversion takes place. Most batteries used in present-day applications are rechargeable batteries that can restore charges once discharged through a reverse process. The electrons are transferred from one electrode to another during this time. Though the battery translates chemical energy into electrical energy, it is not limited by the second law of thermodynamics, unlike combustion engines. As compared to such systems, batteries have high energy conversion efficiency. The basic electrochemical unit is a "cell," while it is referred to as a "battery" in most cases. A battery is just a combination of two or more such cells connected in series or parallel. A cell consists of three main parts: the anode, cathode, and electrolyte. The anode is the negative electrode that gives up electrons to the external circuitry. Electrochemical oxidation occurs at the anode. While the cathode reduction occurs, the electrode accepts the electrons from the circuit. The electrolyte is chosen according to the system to facilitate ion transport mediated through it. This section discusses the principal ideas on lithium-ion batteries (LIB), sodium-ion batteries (SIB), and potassium-ion batteries (PIB) that are potential applications for CQDs.

To meet the global energy demand, energy storage in batteries, particularly LIB, has been highly favored since its first commercialization in 1990 by Sony. This is due to the high energy density, wider potential range, and long shelf life. The Li^+ ions shuttle from the positive to the negative electrodes during the charge-discharge process and vice versa. Due to this type of motion, LIB are also referred to as "rocking chair batteries." These electrodes can be studied as charge storage reservoirs. The original composition of the cell can be reconstituted by applying an electric potential between the electrodes. Such batteries are called reversible or rechargeable batteries. However, only the primary reactions in the battery are reversible. There are certain secondary reactions and mechanical processes that can take place. So, the life cycle is limited by the degradation process and not by the primary chemical reaction.

The positive electrode material is usually a metallic oxide, which must be an efficient oxidizing agent. However, the structure of the material can be layered like lithium cobalt oxide, lithium nickel cobalt aluminum oxide, and lithium nickel manganese cobalt oxide or tunneled structure as in lithium manganese oxide or even octahedra with shared O corners in lithium iron phosphate. The current collector is an aluminum foil in the case of a positive electrode. The negative electrode is a Cu foil collected with layered graphite to facilitate intercalation. During the charge-discharge process, the ions are introduced into and removed from the interlayer spacing between the active materials. The electrochemically active materials are the lithium metal oxides on the positive side and lithiated carbon on the negative side. The active materials are bound to the foil substrates by using polymer binders such as polyvinylidene difluoride, poly(3,4-ethylenedioxythiophene) polystyrene sulfonate, carboxymethyl cellulose, polyaniline (PANi), polypyrrole (Ppy) etc., along with a suitable diluent and a high surface area material like carbon black or graphite. The electrodes are electrically separated by using a separator. The separator is usually microporous and made of polyethylene or polypropylene like a film. It is used in cases wherein we use a liquid electrolyte, gel-polymer electrolyte, or solid electrolyte based on the type of batteries.

The active materials present in LIB are involved in the charge storage mechanism by incorporating lithium through intercalation. The insertion or removal of ions follows a topotactic reaction. The Li-ion insertion should not bring in any significant structural change to the host. Both the metal oxide and graphitic structure behave as hosts. The incorporation of Li ions, the guest species, occurs reversibly to form sandwich structures. During the charging process, the oxidation reaction occurs at the positive electrode while the negative electrode is reduced. In Fig. 15.5, the lithium-ion cell charge-discharge process is shown.

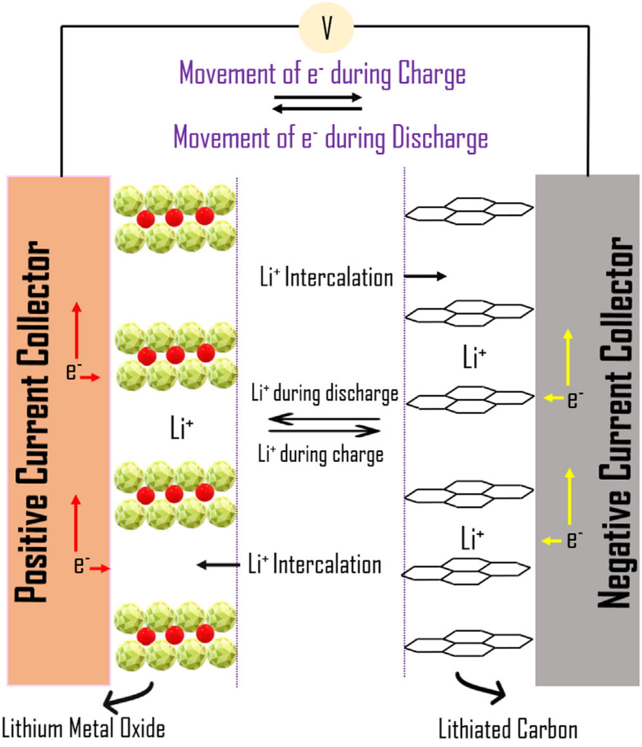
V
Movement of e⁻ during Charge
Movement of e⁻ during Discharge
Positive Current Collector
e⁻
e⁻
Li⁺
Li⁺ Intercalation
Li⁺ during discharge
Li⁺ during charge
Li⁺ Intercalation
Li⁺
Li⁺
e⁻
e⁻
Negative Current Collector
Lithium Metal Oxide
Lithiated Carbon

Figure 15.5 Charge storage mechanism of a lithium-ion battery.

The reactions that take place in the electrode in a LIB are as follows.
At the positive electrode,

$$\mathrm{LiMO_2} \underset{\text{Charge}}{\overset{\text{Discharge}}{\leftrightarrows}} \mathrm{Li_{1-x}MO_2} + \mathrm{xLi^+} + \mathrm{xe^-}$$

At the negative electrode,

$$\mathrm{C} + \mathrm{xLi^+} + \mathrm{xe^-} \underset{\text{Charge}}{\overset{\text{Discharge}}{\leftrightarrows}} \mathrm{Li_xC}$$

Overall, the reaction in the cell,

$$\mathrm{LiMO_2} + \mathrm{C} \underset{\text{Charge}}{\overset{\text{Discharge}}{\leftrightarrows}} \mathrm{Li_xC} + \mathrm{Li_{1\text{-}x}MO_2}$$

Although LIBs are prominent in the electric vehicles, there lies a quest for LIBs to conquer the rechargeable battery market. The competing chemistry in SIB calls for large-scale applications apart from consumer electronics and the vehicular market. Though the performance of SIBs is not on par with the LIBs or used in the abovesaid applications, they can still deliver about 285 Wh/kg energy density. This is half the energy density of lithium. However, the SIBs are cheaper and can find potential applications in small-scale industries or homes. The cost incurred during the production of SIBs is around 20% of that of LIBs. Sodium metal is abundantly available, significantly low cost, and is a benign material. The extraction and purification of Na are also easy.

SIBs work on a mechanism similar to that of the LIBs. The cathode is a sodium metal oxide, and the anode is carbon. SIBs are more sustainable. The SIBs are safer than LIBs and have a wider temperature range, and there is no thermal runaway. The major impediment of LIBs is the heating up of the battery, which calls for a battery management system. It adds to the production cost. Recent developments have projected that commercial SIBs can deliver 200 Wh/kg, which is close to the theoretical capacity. A comparison chart between lithium and SIB is given in Fig. 15.6.

During the charge-discharge process in SIBs, the sodium ions move between the cathode and the anode. When the battery is charged, the sodium ions from the cathode are removed and inserted into the anode. The electrons take the external circuitry route to move from cathode to anode. HC electrodes are widely used as anodes. Also, the major concern in using SIBs is the reversibility of the $\mathrm{Na^+}$ ion transport. This results in many secondary reactions at the electrode−electrolyte interface [11].

PIB works on multiple reversible reactions at the electrode interface. The cathode is a potassium-based layered metal oxide $\mathrm{KXO_2}$ where X could be any metal ion like Mn, Co, Ni, Cu, etc. The anode is graphite that facilitates charge transport.

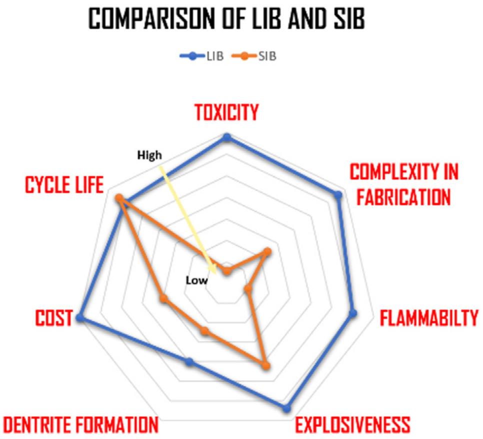

Figure 15.6 Comparison between lithium-ion and sodium-ion batteries.

The current collectors are generally metal foil like copper or aluminum [12]. During the charging process, the following reactions take place at the electrodes.

At the cathode,

$$KMO_2 \leftrightarrow K_{1-x}MO_2 + xK^+ + xe^-$$

At the anode,

$$xK^+ + xe^- + 8C \leftrightarrow K_xC_8$$

Overall reaction,

$$KMO_2 + 8C \leftrightarrow K_{1-x}MO_2 + K_xC_8$$

The most stable stoichiometric structure of the graphite intercalated compound is KC_8. It has a theoretical capacity of 279 mAh/g, which is comparable to the stable LiC_6 structure of the LIB. Just as in the LIB, a solid electrolyte interface (SEI) is formed. This protects the anode and increases the cyclic stability [13].

Lithium-sulfur batteries (LSB) are a class of LIB that has gained much research focus over the recent years. The advantage of LSB over LIB lies in the high theoretical energy density of 2600 Wh/kg. It has an open circuit potential of about 2 V. The cathode is made of lithium metal, and the anode is of elemental sulfur. During discharge at the negative electrode, the Li metal is dissolved in the electrolyte. Li^+ ions migrate to the positive electrode that has sulfur. The Li^+ ions and sulfur react to form polysulfide ions. During the charging process, the polysulfide ions are decomposed and the Li^+ ions return to the negative electrode.

The reaction mechanism in LSB is as follows:

$$S_8 + 16e^- + 16Li^+ \leftrightarrow 8Li_2S$$

The S_8 complex is converted to Li_2S_8 then as Li_2S_x, where $x = 6,4,2,0$ in the same order to result in Li_2S complex. As this reaction progresses, the solubility of the polysulfide ions is reduced. In the final stages of the electrochemical reaction, the complex Li_2S_2 and Li_2S get precipitated in solid form. This inhibits the free flow of sulfur ions from the positive electrode. On the other hand, the insoluble polysulfide ions move toward the negative electrode causing self-discharge. This leads to reduced battery life. The research focuses on development of a stable battery structure facilitating enhanced sulfur content on the positive electrode. The electrolyte should work as an aid to both sulfur and lithium [14].

Zinc-ion batteries (ZIBs) function with a mechanism similar to LIBs by reversible intercalation. During discharge, the anode, which is a zinc metal, is dissolved as Zn ions into the electrolyte. These zinc ions are absorbed in the cathode. The electrolyte acts as a transport media for the movement of the ions. The reverse process is observed during charging. Zinc has a high energy density, thus facilitating high charge storage even with a very less amount of active material. The ZIBs do not require any initial cycling for the formation of the complexes. It can be readily used. It is highly favored as it is completely safe. ZIBs use water-based electrolytes and can find a strong place in the consumer market, unlike LIBs. It is a low-cost alternative to LIBs.

15.3 Desired properties of carbon quantum dots for charge storage applications

15.3.1 Structural properties

CQDs are quasispherical 0D structures with a diameter of less than 10 nm. CQDs generally exist as mostly sp^2 hybridization states with single-bonded structures. GQDs have a higher electrical conductivity owing to the double-bonded structure. The CQDs can be amorphous or crystalline based on the synthesis conditions. Other areas of CQDs include GQDs, carbon nanodots, and polymer dots (PDs). The contrast lies in the structural properties internally and in the decorated chemical groups on the surface. A carbon frame forms the base with oxygen groups present in large numbers on the surface. Compared to traditional and metallic quantum dots, the chemical stability of CQDs is promising. Though CQDs can be synthesized by both top-down approach and bottom-up approaches, the latter approach is preferred for charge storage applications.

Based on the structural properties, CQDs are generally classified as CDs, CQDs, PDs, and GQDs. CDs are spherical structures that are nanosized. They do not exhibit the quantum confinement effect. The CDs mainly comprise sp^3 hybridization at the center and a significantly lesser amount of carbon which has sp^2 hybridization. The other properties depend on the hybridization involved in the quantum dots (QDs). This can be achieved by suitable experimental techniques. CQDs are crystalline and exhibit sp^2 hybridization. The lattice constant of CQDs is between that of graphite and graphene lattice structures. The CQDs show a quantum confinement effect. However, the size of the CDs and the CQDs are in the same range of 1–20 nm. This shows that the bandgap of the QDs is not only dependent on the size of the particle. GQDs are another class that offers high conductivity and crystallinity. CQDs show lesser crystallinity as compared to GQDs. They have a lattice constant, as in the case of graphene. In both CQDs and GQDs, the properties could be enhanced by the functional groups attached to them.

15.3.2 Electrical properties

The electrical properties can be altered based on the available mobile charge carriers. The size of the QDs plays a crucial role in the enhancement of electrical conductivity. The key to tunable electrical properties lies in the size. The much larger semiconductor structures do not offer the same properties though they may be morphologically similar to spheres. The electronic properties are collectively contributed by the surface defects, functional groups, dopant heteroatoms, and the coupling between successive atoms. It is quite clear that the crystallinity of the QDs plays a vital role in the conduction. From the structural properties, it can be understood that the GQDs offer better crystallinity. The core of the GQDs is much more crystalline, but it cannot be functionalized as it may create electron trap sites inhibiting the electron transfer. In the case of CQDs, the sp^2 hybridization mediates the electron transport while behaving as an electron acceptor/donor. The inclusion of CQDs into the material can thereby contribute to the retention of the stored charges in case of cycling. CQDs help in stopping material change or degradation over large charge-discharge cycles. The ligand length of the CQDs affects carrier mobility. The electronic structures of the CQDs can be arrived at by using molecular orbital theory.

15.3.3 Optical properties

CQDs show a good absorbance peak in the UV region and extend as a trail in the visible region. The most common transitions in the case of CQDs include n to π^* and π to π^* transitions as it requires lower energy. The π states are due to the sp^2 core. Just as the π conjugation in the organic molecules, the energy gap in the π states reduce with the increase in aromatic rings. The number of states is dependent on functional group bonding. If the functional groups have electron lone pairs, then π to π^* transition involves $C = C$ bonds. If they are attached to aromatic carbon atoms with sp^2 hybridization, then n to π^* transition with $C = O$ is favored. The excitation wavelength varies indirectly with the size of the CQDs with the obvious color change.

The excitation wavelength of the CQDs is based on the wavelength of the emission and the intensity of the peak. But the clear-cut idea of its dependence on quantum size effect and/or emission spectra is still unclear. The individual excitation wavelength peak is linked mainly to the reaction procedure. Chemiluminescence properties of the CQDs were discovered using oxidative agents. Photoluminescence

(PL) is exhibited in water-soluble CQDs along with polyvinyl alcohol. As the size decreases, the peaks are red-shifted. In the case of a smaller graphitized core, the PL peaks have higher energy. In the case of an amorphous core, an opposite trend is observed. The fluorescence properties of the CQDs depend on the functional groups attached to the surface.

15.4 Carbon quantum dots for supercapacitors

CQDs can be synthesized by various methods to increase the volumetric capacitance for supercapacitors. Bare CQDs can be prepared through acidic treatment of carbon fiber, microwave pyrolysis, purification of soot obtained during the preparation of CNTs, laser ablation, by treating a single graphene layer by laser ablation, Hummer's method by rupturing fullerenes, hydrothermal methods, etc. Although bare CQDs possess interesting properties like high surface area, enhanced optical, and electrical properties, they do not offer very high specific capacitance individually. They can be used with highly conductive materials to enhance the specific capacitance.

Quing Li and group, in 2013, worked on preparing microsupercapacitors with CDs as nanofillers on a graphene fiber [15]. The interactions between the CDs and the graphene fiber resulted in a significant increase in mechanical strength and electrical stability. The dot sheet structure shown in Fig. 15.7 bridges the CDs with the graphene sheets via the hydrogen interaction. This prevents the restacking of graphene fibers. The CDs/graphene fiber supercapacitor offers a specific capacitance of 607 mF/cm^2, with cyclic stability for over 10,000 cycles. The key idea of the work lies in the utilization of the specific surface area to up to 96%. The contribution of CDs added to the capacitance by 22.1%. The incorporation of CD aided the increase in the active sites and paved the way for more ionic channels for conduction.

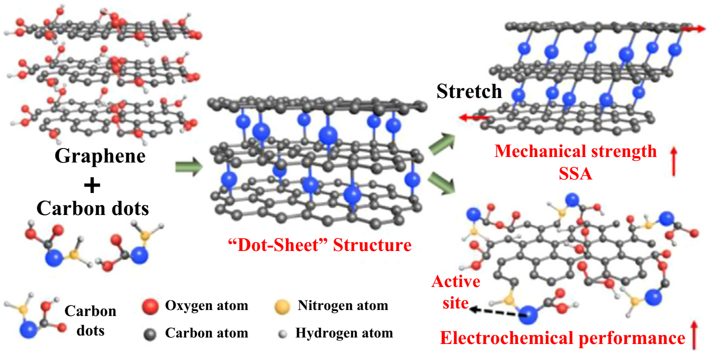

Figure 15.7 Schematic representation of carbon dot–graphene sheet structure.
Source: Reproduced from Q. Li, H. Cheng, X. Wu, C. F. Wang, G. Wu, S. Chen, Enriched carbon dots/graphene microfibers towards high-performance micro-supercapacitors, Journal of Materials Chemistry A 6 (29) (2018) 14112–14119, https://doi.org/10.1039/c8ta02124d. Copyright Royal Chemistry Society, 2018.

Another group, including Guanxiong Chen and others [16] synthesized CQDs by activation using KOH. The synthesized CQDs were freeze-dried and annealed. The ice acts as a template. The functional groups like -OH and -COOH groups assist in the stacking of CQDs due to the π-π interaction and dipole—dipole interaction between carbon layers and functional groups. The CQDs can be readily dispersed in water due to the excess oxygen groups and unstable stacking. The annealing causes the release of gas molecules creating porosity and the increase in the interlayer distancing. Symmetric supercapacitor fabricated using this material offered 106 F/g at 0.5 A/g and 84.4 F/g at 8 A/g.

The doping of CQDs using heteroatoms is a prominent method for increasing charge storage. The effect of dopants like nitrogen, phosphorus, boron, oxygen, and iodine influences the specific capacitance positively. It improves the life cycle by retaining the specific capacitance. Doping with nitrogen enhances the pseudocapacitive behavior and the insertion capacity of hydrogen ions [17]. This is due to the surface-bound groups and the ordered mesostructure. Dan Liu's group, in 2014, established that nitrogen doping could make the carbon surface short of electrons, increasing hydrogen affinity. The nitrogen functional groups also prevent recombination during desorption [18,19]. Nitrogen can be introduced after the initial synthesis procedure via heat treatment by ammonia or by immersing it in melamine [20,21].

When the phosphor is used as a dopant, the effect is seen as an increase in double-layer capacitance. The phosphor groups present in the system result in a stable porous structure which allows for system stability and high capacitance [22]. When the carbon is functionalized using phosphor, there is a wider potential window of up to 1.4 V. This increase in the potential can be attributed to the replacement of quinone groups that are electrochemically active sites for oxidation by phosphate groups. This is to eliminate the weakening of capacitance due to free oxygen atoms present on the carbon surface. The monolithic form of carbon exhibits high surface area and increased porosity [23].

The oxygen groups are contributed primarily from the C-O from the quinone species. While boron and phosphorus are used as dopants, the functional groups containing B-O, P-O, and B-P contribute to increasing the specific capacitance. The oxygen-containing groups lead to the increase in the acid content on the surface of the carbon. This, in turn, paves the way for higher absorption of ions at a high potential. The heteroatoms, whether n-type or p-type, can increase or decrease the number of charge carriers and should be tailored to gain high capacitance. Xiaochen Zhao et al reported this as early as 2011 by obtaining a homogenous distribution of B and P atoms via the hydrothermal route [24].

Van Chinh Hoang and Vincent G. Gomes propose a reduction mechanism for the functional groups [25]. The oxygen-containing functional groups are reduced by using hydrogen iodide vapor [26]. Even after the reduction reaction, the iodine remains in the system and contributes to the pseudocapacitance. The prolonged exposure to hydrogen iodide vapor reduced the aromatic iodides to enhance the pseudocapacitance by using the excess electrons to rebuild the graphene skeleton. Though the doping enhances the specific capacitance, there is a concern about the

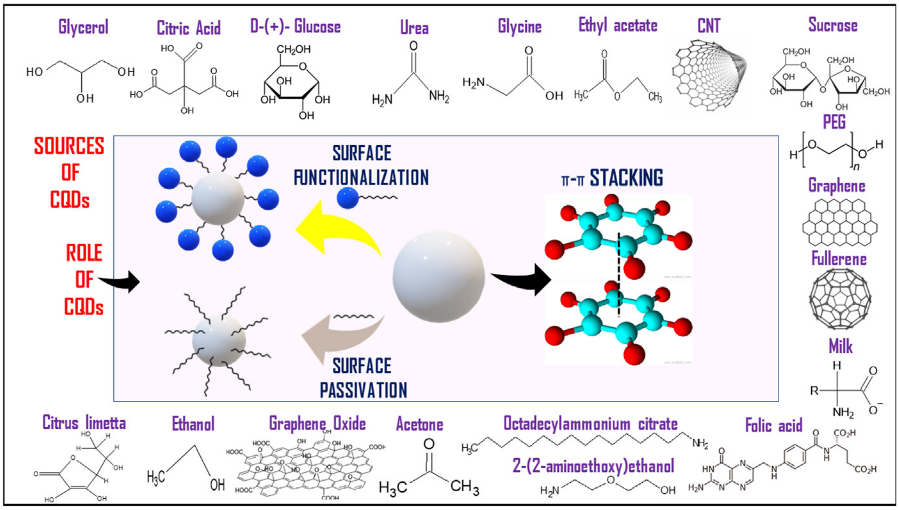
Glycerol
Citric Acid
D-(+)- Glucose
Urea
Glycine
Ethyl acetate
CNT
Sucrose
SOURCES OF CQDs
ROLE OF CQDs
SURFACE FUNCTIONALIZATION
π-π STACKING
SURFACE PASSIVATION
PEG
Graphene
Fullerene
Milk
Citrus limetta
Ethanol
Graphene Oxide
Acetone
Octadecylammonium citrate
2-(2-aminoethoxy)ethanol
Folic acid

Figure 15.8 Sources and role of CQDs in enhancing the charge storage. *CQDs*, Carbon quantum dots.

restacking of graphene. This can be a potential blocker to ion transport [25]. The aforementioned properties of doped CQDs are combined with transition metal oxides, sulfides, and organic polymers as composites to improve the specific capacitance of the supercapacitor. Fig. 15.8 shows the different sources of CQDs and their major role in the charge storage mechanism.

15.4.1 Carbon quantum dots—inorganic hybrid for supercapacitors

CQDs contain a large number of functional groups like R-OH, R-COOH, and R-COO^- groups. Due to the existence of these functional groups and their solubility in water, they have attracted numerous researchers to work on CQDs along with metals. This section offers an outline of inorganic CQDs. Transition metal oxides and transition metal sulfides have attracted much research focus. Although they possess superior properties because of their multiple oxidation states and high surface-to-charge ratio, they suffer due to the weak interactions between composites. This leads to a compromise on the retention of the capacitance over large charge storage cycles. There is noteworthy research attention on materials like MnO_2 [27,28], RuO_2 [29], $NiCo_2O_4$ [30], Ni_3S_4 [31], Ni-Al [32], Fe_3O_4 [33], NiO [34], Bi_2O_3 [35], MoS_2 [36], etc. used along with CQDs. The bond strength between the metal oxides/sulfides with conductive materials like graphene is not very strong. The weak bonding leads to poor cyclability and stability.

When CQDs are incorporated into metal composites, they can enhance the bonding between multiple materials in a system. There is a fitted bond between the metal atoms with the O-groups present on the surface of the CQDs. In such systems, CQDs, being nanosized themselves, can help in the increase in surface roughness leading to the increase in the active sites of the material. The ease of synthesis involved in the incorporation/preparation of CQDs makes it all the more viable. It acts as a stabilizer to prevent aggregation of the metal composites, enhancing stability. CQDs reduce the charge transfer resistance in the system and further increase the electronic and ionic transport in the system. The CQDs significantly reduce the series resistance and the charge transfer resistance values, which directly translates to better electrochemical behavior. While providing a good enhancement in the specific capacitance, CQDs, being good electron donors/acceptors, provide extra charges to facilitate better conduction. CQDs when used alone exhibit EDLC behavior; nevertheless, when used along with inorganic materials contributes to the pseudocapacitance. Pseudocapacitive charge storage is promoted through the improved reversible faradaic reactions due to the incorporation of the CQDs.

Haipeng Lv and group [28], in 2017, found their motivation in developing a nontoxic and low-cost material for supercapacitors compared to RuO_2. 1D nanostructures can prevent accumulation and have short diffusion paths that facilitate charge storage. The inhomogeneity in the crystal peaks increased with the incorporation of CQDs, facilitating the formation of MnO_2 nanowires. CQDs offer additional functional groups and growth in the active sites, and electrode wettability is also enhanced. This increases the electrochemical performance of the supercapacitor. Fig. 15.9 shows the experimental technique employed. It involves a simple hydrothermal route [27].

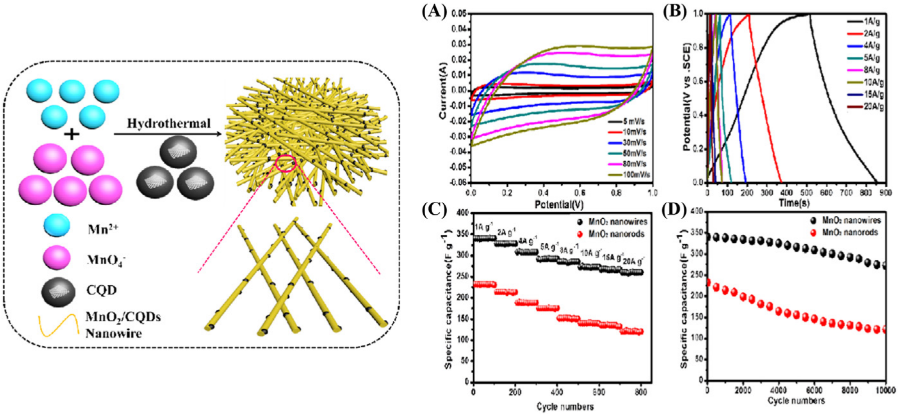

Figure 15.9 (A) CV curves, (B) GCD curves of the MnO_2/CQDs nanowires and cycling performances of MnO2/CQDs nanowires and MnO_2 nanorods, (C) corresponding specific capacitance at various current densities, (D) variation of specific capacitance for 10,000 charge – discharge cycles at 1 A g-1 [27].

Source: Reproduced with permission from H. Lv, X. Gao, Q. Xu, H. Liu, Y. G. Wang, and Y. Xia, Carbon quantum dot-induced MnO_2 nanowire formation and construction of a binder-free flexible membrane with excellent superhydrophilicity and enhanced supercapacitor performance, ACS Applied Materials and Interfaces 9 (46) (2017) 40394–40403. https://doi.org/10.1021/acsami.7b14761. Copyright 2017 American Chemical Society.

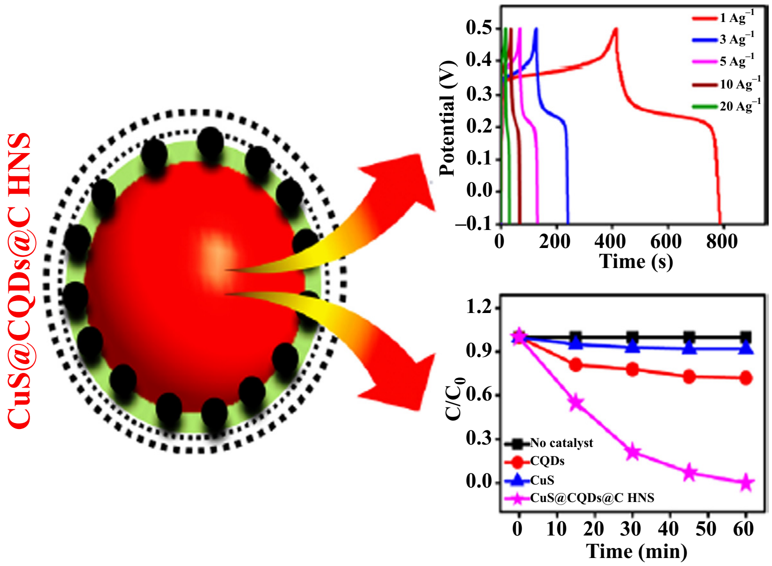

Figure 15.10 Graphical representation of core–shell CuS@CQDs@carbon hollow nanospheres.

Source: Reproduced with permission from B. De, J. Balamurugan, N.H. Kim, J.H. Lee, Enhanced electrochemical and photocatalytic performance of core-shell CuS@Carbon quantum Dots@Carbon hollow nanospheres, ACS Applied Materials and Interfaces 9 (3) (2017) pp. 2459–2468, https://doi.org/10.1021/acsami.6b13496. Copyright 2017 American Chemical Society.

Bibekananda De's group worked on metal sulfide/CQDs using the unique electronic and optoelectronic properties to their advantage. To stabilize the hollow sphere metal sulfide core–shell structure, CQDs were incorporated. Fig. 15.10 shows the graphical representation of the work. The CQDs enhance the electron transport properties while retaining the electrochemical stability in the supercapacitor [37].

Table 15.1 shows the different metal oxides/sulfide (inorganic) supercapacitors used along with CQDs.

15.4.2 Carbon quantum dots—organic hybrid supercapacitors

CQDs are enriched with optical and electronic properties. As discussed in the previous sections, CQDs as standalone materials and injunction with inorganic metals works well for charge storage. Polymers are used to encapsulate CQDs. Also, polymers exist as homopolymers, heteropolymers, and hyperbranched polymers, enabling them to act as an anchor for CQDs [38]. It can provide ionic and reactive functional groups to boost the system further. During the reaction procedure, the polymer interacts with the surface of the CQDs. The change in the original surface

Table 15.1 Comparison of CQDs-inorganic supercapacitors.

Material	Synthesis route	Morphology	Specific capacitance	Cycles/retention	Ref
MnO_2−CQDs	Hydrothermal	Nanowires	340 F/g at 1 A/g	10,000/80.1%	[3]
α-Co/Ni(OH)2−CQDs	Chemical etching	Hollow nanocage	700 C/g at 1 A/g	10,000/79.9%	[14]
CuS−CQDs	Hydrothermal	Core−shell	618 F/g at 1 A/g	4000/95%	[13]
NiO−N-doped CQDs	Chemical reaction	Shell	660 F/g at 0.5 A/g	5000/98.2 %	[15]
$NiCo_2O_4$/C@Ni − Co − S	Hydrothermal	CQDs encapsulated nanosheets	188.8 $mAhg^{-1}$ at 5 A/g	5000/79.2%	[6]
MoS_2/N-CDs	Solvothermal	Flower-like	73.92 F/g at 0.5 A/g	3500/76.9%	[12]
RCQD−RuO_2	Solgel	Hybrid network	594 F/g at 1 A/g	5000/96.9%	[5]
Bi_2O_3−CQDs	Solvothermal	Intertwined grains	345 Cg^{-1} at 0.5 A/g	2500/100%	[11]
NiS−carbon dot	Hydrothermal	Flowers	880 F/g at 2 A/g	2000/100%	[16]
N-CQDs/rGO/Fe_2O_3	Hydrothermal	Nanostructures	274.1 $mAhg^{-1}$ at 1 A/g	5000/80.4%	[9]
CuS@CQDs@C	Hydrothermal	Hollow nanosphere	618 F/g at 1 A/g	4000/95%	[37]

creates defects in the CQDs that facilitate charge storage. The CQDs are ultrasmall particles that find an application in macro-sized arenas. The properties of the CQDs should be used to the fullest as they are fused into long-chain polymers. Aerogels are also an interesting candidate to work with CQDs owing to their low density, relatively high surface area, and high porosity as they form a 3D carbon matrix [39].

Conducting polymers such as polypyrrole, polythiophene, and polyaniline have been explored widely for supercapacitors because of their electrical conductivity and ease in synthesis. The polymers suffer from poor cyclability and flexibility. Since CQDs can be well dispersed in solvents, they can be used to the advantage. Electropolymerization without the use of the electrolyte is one of the prominent methods of synthesis. The CQDs act as a supporting electrolyte. The polymeric monomers pave the way to the porous structure [40].

Xiang Zhang's group worked on a ternary composite of graphene oxide along with CDs and polypyrrole. The polypyrrole undergoes a faradaic reaction and behaves as an electron donor. The conductive graphene oxide creates a large surface area [41]. This can aid in accepting electrons and also the conductivity is enhanced. The CDs are packed between the graphene oxide and polypyrrole to channel electron transport via the active layer. CDs' specific surface area is very high and creates multiple interfacial polarization. However, the specific capacitance is enhanced [42]. The schematic representation of the stacking is shown in Fig. 15.11.

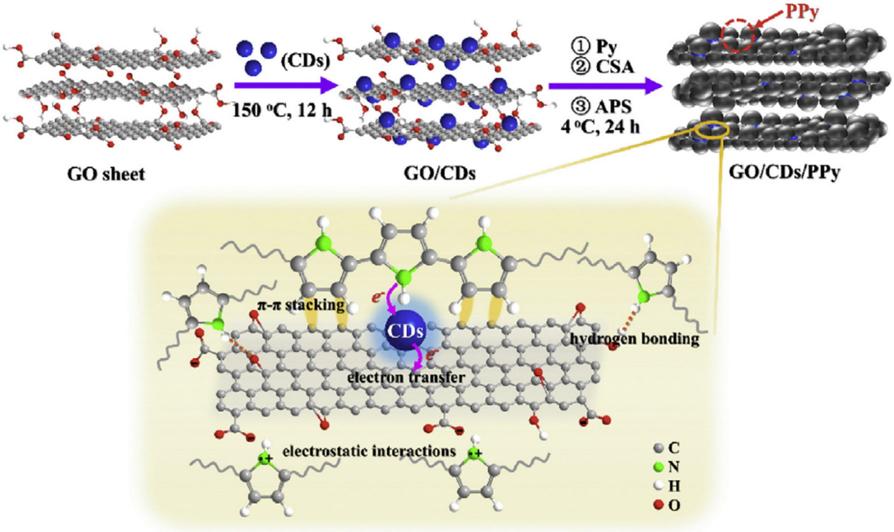

Figure 15.11 A schematic illustration of the synthesis process of GO/CDs/PPy composite. *Source*: Reproduced with permission from Zhang, X., Wang, J., Liu, J., Wu, J., Chen, H., & Bi, H. (2017). Design and preparation of a ternary composite of graphene oxide/carbon dots/polypyrrole for supercapacitor application: Importance and unique role of carbon dots. Carbon, 115, 134–146. https://doi.org/10.1016/j.carbon.2017.01.005. Elsevier.

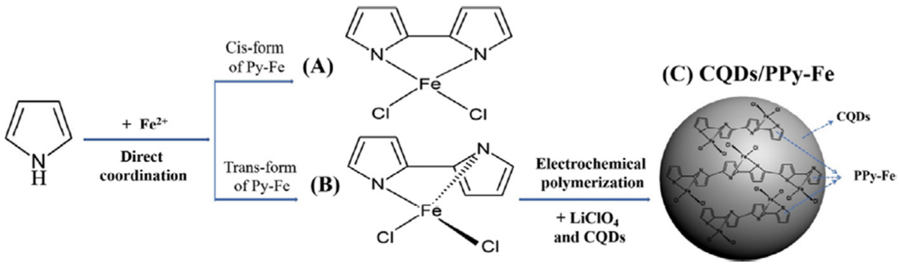

Figure 15.12 Sketches of preparation procedure for CQDs/PPy-Fe. (A) Cis-form of Py-Fe, (B) Trans-form of Py-Fe, (C) CQDs/PPy-Fe.
Source: Reproduced with permission from Y. Xie, Y. Zhou, Enhanced electrochemical stability of CuCo bimetallic-coordinated polypyrrole, Electrochimica Acta 290 (2018) 419–428, https://doi.org/10.1016/j.electacta.2018.09.037. Elsevier.

The coordination bonds in the case of the substituted polypyrrole play a vital role in surface stabilization. The metal ions have to be stabilized to improve their electrochemical properties. The coordinating ligands show steric, electronic, and conformational effects. As the central atom, the transition metal ion forms a strong coordinate bond with the nitrogen atom in the pyrrole ring. The CQDs perk up the conductivity and allow for fast electron transfer [43]. Fig. 15.12 shows the work of Yibing Xie's team in the polymerization of polypyrrole with Fe as the metal ion using CQDs.

The supercapacitor was fabricated using CQDs/PPy-Fe as the electrode offered a charge storage ability of 78/Fg at 5.0/Ag and retained the capacitance by 70.1% after 1000 cycles. Zingchao Zhao and Yibing Xie prepared a polyaniline-CQDs hybrid for the first time [44]. The photo-assisted cyclic voltammetry (CV) electrodeposition route was used to fabricate the CQDs-PANI/CFs(LI) electrode. The supercapacitor exhibits a specific capacitance of 169.2 mF/cm^2 at a current density of 1 mA/cm^2.

The introduction of CQDs reduced the charge transfer resistance and the Warburg component. This resonates with the fast diffusion process occurring during the charge-discharge process.

Rinki Malik's group prepared polypyrrole/CQD composites over a graphite sheet. They employed a controlled galvanostatic electro polymerization route. The thickness of the polymer coating is controlled using this technique. The current application affects the morphology as well as the conductivity of the film. A constant current has been applied to get a polymer film. When polymerized over a graphite electrode, the monomeric radical cation of pyrrole creates a highly porous polypyrrole film. It can enhance the charge storage ability and potential use in supercapacitors [45].

Sathish Kumar and group prepared PANi–CQDs nanocomposite using urea and glycine as the source. The fabricated device offers a capacitance of 161.3 mF/cm^2 with reasonable retention over 5000 charge-discharge cycles. The collective effect of urea and glycine enhances the charge storage ability [46]. Various organic CQDs and their charge storage capacity for supercapacitors are tabulated in Table 15.2.

Table 15.2 Organic CQDs and their charge storage capacity for supercapacitors.

Material	**Synthesis route**	**Morphology**	**Specific capacitance**	**Cycles/ retention**	**References**
PPy/CQDs	Electropolymerization	Spheres	817 F/cm^2 at 10 mA/cm^2	2000/62%	[47]
CQDs/PPy-NW	Electrostatic self assembly	Nanowire	248.5 mF/cm^2 at 0.2 mA/cm^2	5000/85.2%	[40]
GO/CDs/PPy	Insitu-electrochemical	Core−shell	576 F/g at 0.5 A/g	5000/99%	[41]
CQDs-PPy/TiO2	Electrodeposition	Nanotube	849 F/g at 0.5 A/g	2000/89.6%	[48]
rGH/CDs	Hydrothermal	3D network	264 F/g at 1 A/g	5000/89.9%	[49]
CPs-GO/CNTs	Electrochemical codeposition	Hybrid microstructure	142.2 mF/cm^2 at 1.0 mA/cm^2	5000/97.3%	[50]
FMWCNTs/CQDs/PANi	Hydrothermal	Nanostructures	534 F/g at 0.5 A/g	1000/86%	[51]
N-CQD/ PANi-3	Chemical oxidative polymerization	Flakes	498 F/g at 1 A/g	1000/70%	[52]
NiS−carbon dot	Hydrothermal	Flowers	880 F/g at 2 A/g	2000/100%	[53]
N-CQDs/rGO/Fe_2O_3	Hydrothermal	Nanostructures	274.1 mAh/g at 1 A/g	5000/80.4%	[33]

15.4.3 Graphene quantum dots

GQDs are also a class of CQDs with an ultrasmall lamellar structure less than 10 nm. The carbon framework is 0D, easing the bendability and the flexibility of the devices. Also, the optoelectronic properties are much more promising. The active edge sites and the varied functional groups enhance the electrical property of the material. The active edge sites accommodate more charges during the charge-discharge cycle, and hence better capacitance can be attained. The migration of the ions in the case of GQDs also eases the functional properties of the system, facilitating better conductivity. Materials with high fracture resistance are generally preferred for charge storage applications. Generally, 0D and 1D materials fall under this class. The major advantage lies in the crack resistance as it can withstand any rupture of the molecular structure. This in turn aids in the retention of the capacitance over large cycles. The size of the synthesized GQDs affects the $\pi - \pi$ conjugation and the number of sp^3 hybridized atoms. Based on these factors, GCQs can be used to enhance the performance of the supercapacitors.

Uniformly sized GQDs with less than 5 nm were obtained using graphene oxide as the precursor by Shuo Zhang's group. The abundant C-C bonds present in GO were oxidized and clipped using HNO_3. Specific capacitance was calculated as 296.7 F/g at 1 A/g [54]. V. Gayathri et al have prepared GQDs embedded on NiCo2S4-multiwalled CNTs. The GQDs have reportedly increased the adhesion property and increased the electrocatalytic activity of the material. The lower charge transfer resistance increases specific capacitance from 361 F/g at 2 A/g to 448 F/g. A 27% increase is seen when GQDs are incorporated [55].

Mohammad Ashourdan et al. have prepared binary CuMnO2/GQDs exhibiting a hexagonal morphology with delafossite oxides. The GQDs were used as a nucleus to form the spinel-like structure. The BET analysis done shows the adsorption/desorption of 145.5 m^2/g. The obtained structure and fine morphology are purely attributed to the GQD nucleus. The strong mechanical bond between the nickel foam and the synthesized material contributes to the specific capacitance of 520.2 C/g at 1 A/g. It also shows retention in 83.3% of the initial capacitance after 5000 cycles [56].

Mono dispersable GQDs were prepared by Sumeet Kumar's group. The authors have used ammonia as a stabilizing agent in graphene oxide to get spherical GQDs with 4–5 nm in size. Though the main focus of the work is on tunable emission, the charge storage capacity is also discussed. It shows 481 F/g at 5 mV/s. The outer surface of the GQDs contributes to the electrical double layer capacitance. However, the inner structure is unstable due to the redox reactions [57]. Further exploration can be done by using such GQDs in a core–shell structure using GQD as the shell.

Zhong et al. prepared GQDs by using sulfur and nitrogen as dopants and studied the electrochemical behavior. It shows an interesting morphology of 20 nm in a transverse direction and with 2–3 layers of graphene. The influence of the doping ratio on the system shows that the size is altered accordingly. In addition to the EDLC, nitrogen and sulfur doping has boosted the pseudocapacitive behavior due

Table 15.3 GQDs (graphene quantum dots) and their charge storage capacity.

Material	Current density	Capacity retention/ cycles	References
Amine-enriched GQDs	595 F/g at 1 A/g	90%/10,000	[60]
Bare GQDs	296 F/g at 1 A/g	97.6%/5000	[54]
CDs/graphene	91.9 F/g at 0.1 A/cm^2	96%/10,000	[15]
GH-GQD	451.7 F/g at 0.5 A/g	89%/10,000	[61]
GQDs/3DG	242 F/g at 1.17 A/g	93%/10,000	[62]
GQDs/activated carbon	388 F/g at 1 A/g	100%/10,000	[63]
GQDs/conductive porous carbon	315 F/g at 1 A/g	100%/10,000	[64]
GQDs/ultra microporous carbon	270 F/g at 1 A/g	100%/50,000	[65]
N,O-GQDs/CNT/carbon cloth	461 F/cm^3 at 0.5 mA/cm^2	87.5%/2000	[66]
N-GQDs/carbon fiber/ graphene hydrogel	93.7 F/cm^3 at 20 mA/cm^3	84.2%/10,000	[67]
ONCDs/porous hydrogels	483 F/g at 1 A/g	100%/10,000	[68]
S-GQDs	362 F/g at 5 mV/s	NP	[46]

to the increase in the charge trap sites in the material. It shows 362 F/g at 5 mV/s. Also, the material offers a tunable fluorescence range that opens the window for other potential applications [58]. The increased electrochemical behavior due to nitrogen doping is also discussed by Milon Miah's group in detail. The edge sites and the dopant sites contribute to the increase of the trap sites. The charge transport seen in the material is mainly dominated by the trap states induced [59]. Table 15.3 shows GQDs and their charge storage capacity as a supercapacitor.

15.5 Carbon quantum dots for batteries

The active materials used in the case of batteries possess certain inherent properties that have certain inherent defects. These defects can be altered by using CQDs or GQDs as a surface modification agent. The CQDs and GQDs with a graphitic morphology can be used directly as an active electrode material for LIB and SIB. It not only increases the surface area but also boosts the electron transmission rate. It increases the coulombic efficiency and retains the stability of the materials. The uniform deposition of lithium/sodium can significantly curb the formation of dendrites on the batteries [69]. The CQDs are used both as anode and cathode materials. They are mainly used as surface coatings. CQDs find their applications in LIB [35,70–74], SIB [71,75–78], PIB [69,79], ZIB [80], LSB [81–84], vanadium redox flow battery (VRFB) [85].

15.5.1 Carbon quantum dots in lithium-ion and sodium-ion batteries

Akira Yoshino in 1985 first proposed the use of CQDs in LIB. In the case of both LIB and SIB, the main research focus is on the surface modification of the active metal oxide cathode materials. GQDs are most favored in such coatings. Next to GQDs, graphitic-type CQDs are also put to use. Vanadium dioxide is one of the prominently used materials along with CQDs to enhance the charge storage process due to the low cost and large capacitance. Balogun et al. have used a 3D carbon cloth with VO_2 interwoven nanowires, further coated with CQDs. This structure is favored due to the shorter lithium-ion diffusion path and direct electron transfer path. This solves the strain concern during the charge/discharge process. For LIB, it offers 86% of the total capacity. It performs even better for SIB with an increased voltage of 2.64 V. This boosts the energy capacity offering high-rate capability [71]. Donliang Chao and others prepared VO_2 and coated GQDs onto the surface. It was tested for both LIB and SIB. A nano surface engineering technique was employed using GQDs as a surface sensitizer. The electrodes channel continuous electron and Li^+/Na^+ transfer through the network as seen in Fig. 15.13. While charging, the electrolyte can use the spacing both inside and outside the nanoarrays to allow for ion transport. The main role of the GQDs is the sensitization and protection of the surface. Sensitization opens doors for high-rate applications due to the improved ion diffusion and the charge transport kinetics. The GQDs improve the cyclic stability by inhibiting the VO_2 dissolution and agglomeration [76]. Nitrogen-doped CDs prepared from egg yolk precursors have been used for LIB. It uses egg yolk as the carbon and nitrogen source to prepare the N-doped CDs. They show a high capacity of 601 mAh/g after 300 cycles [70].

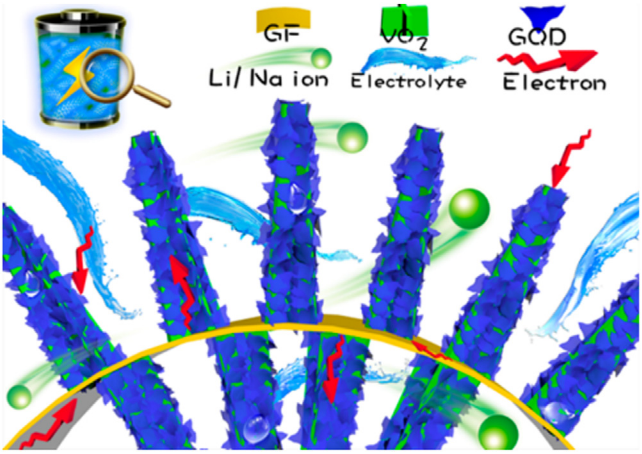

Figure 15.13 Schematic illustration of the GVG electrode with bicontinuous electron and Li/ Na ion transfer channels.

Source: Reproduced with permission from D. Chao et al., Graphene quantum dots coated VO2 arrays for highly durable electrodes for Li and Na ion batteries, Nano Letters 15(1) (2015) 565−573, https://doi.org/10.1021/nl504038s. Copyright 2014 American Chemical Society.

CQDs obtained from biomaterials are also used in batteries. CDs obtained from D-(+)- glucose were reported by Javed et al. They have used it as an anode material for LIB and SIB. The CDs show a decent capacitance of 864.9 mAh/g over 500 cycles at a capacity retention of 91.6% at a 0.5 C rate for LIB. For SIB, they show a capacity of 323.9 mAh/g with 72.4% capacity retention after 500 cycles [86]. Xuewei Zhao et al. made a hybrid structure of GQDs on a CNT electrode. The GQDs are functionalized and then put on a 3D CNT sponge through electrostatic interaction facilitating π-π stacking using a hydrothermal route. The GQDs have a good number of functional groups and defects on the edges. The incorporation of heteroatoms increases electrochemical performance. The oxygen groups present contributes to the charge storage via the redox reactions. The electrodes offer a capacity of 700 mAh/g at 100 mA/g [87]. Yingchang's group has prepared a composite containing N-doped TiO$_2$/C-dots. The as-obtained N-TiO$_2$/C-dots with increased cyclic stability of 93.6% retention after 300 cycles at 5 C. The coulombic efficiency of the material is maintained at 99.3% after cycling [88]. Various CQD-based lithium and SIB and their capacity are tabulated in Tables 15.4 and 15.5.

Table 15.4 Lithium-ion batteries and their charge storage capacity.

LIBs	Capacity	Cycle	Capacity after cyclic study	References
B-GQD	859 at 50 mA/g	500	95.7% at 200 mA/g	[89]
BGQS-30/M^{2}oS$_2$	3055 at 50 mA/g	50	1041at 0.1 A/g	[90]
C(ZIF-8)@GQDs	546.0 at 50 mA/g	200	493 at 100 mA/g	[91]
C0$_4$ O$_4$@CuO@GQDs	921 at 0.1 A/g	200	1054 at 0.1 A/g	[92]
C-GQDs/a-Fe$_i$ O$_4$-2	1091 at 5 A/g	110	1320 at 1 A/g	[60]
CQD-Bi$_1$ O$_3$	298 at 1 C	30	300 at 1 C	[93]
CQDs	341.3 at 1.0 A/g	500	415.8 at 500 mA/g	[94]
CuO + Cu + GQD	780 at 1/3 C	500	750 at 1/3 C	[95]
C-VOCQD	168 at 19.2 A/g	500	196 at 19.2 A/g	[71]
GQDs/MoS$_2$	1060 at 0.1 A/g	80	1031 at 0.1 A/g	[96]
GQDs@FFNA	161.5 at 0.2 A/g	1000	96 at 0.4 A/g	[97]
GVG	151 at 36 A/g	1500	200 at 18 A/g	[76]
LTO QDs/CFs	175 mA/g at 1 C	200	165.4 at 1 C	[98]
LTO/N, S-GQDs	126.5 at 10 C	2000	180.5 at 2 C	[99]
LTO-Al/Mn-CQDs	295.8 at 0.5 C	100	236.0 at 2 C	[100]
LTO-NGQ20	155 at 50 C	200	171 at 20 C	[101]
Mn$_3$ O$_4$/C-dots	917 at 50 mA/g	100	791 at 0.1 A/g	[102]
N-CDs-700(B1)	663.4 at 100 mA/g	300	601.0 at 500 mA/g	[70]
NiO/GQDs-COOH	980 at 0.1 A/g	250	1081 at 0.1 A/g	[103]
NiO@C0$_i$O$_4$@GQDs	1073 at 0.1 A/g	250	1158 at 0.1 A/g	[104]
N-TiOi/C-dots	116 at 100 C	1000	185 at 10 C	[88]
PF-GQD@SiNP	4066 at 50 mA/g	100	3068 at 0.1 A/g	[105]
RHAC-GQDs	431.1 at 100 mA/g	100	350 at 100 mA/g	[94]
TiOi$_{-x}$/GQDs	144.6 at 15 C	500	160.1 at 10 C	[106]
Trp-GQD@MGA-n/Si	1427 at 0.1 A/g	100	93.3% at 0.1 A/g	[107]

Table 15.5 Sodium-ion batteries and their charge storage capacity.

SIBs	Capacity	Cycles	Capacity after cyclic study	References
3D CFW	76.3 at 5 A/g	200	217.4 at 0.1 A/g	[108]
3D PCFs	290 at 0.2 A/g	10,000	99.8 at 5 A/g	[109]
B-GQD	307 at 50 mA/g	500	96 at 200 mA/g	[89]
CCD1300	302 at 30 mA/g	100	200 at 150 mA/g	[110]
CQDs	126.4 at 1.0 A/g	500	88.6 at 500 mA/g	[94]
CQDs@TiO_i	168.7 at 0.1 A/g	500	168.8 at 0.1 A/g	[111]
CTO	111.3 at 336 mA/g	2000	108.2 at 3.36 A/g	[112]
C-VOCQD	321 at 96 mA/g	100	180 at 3.2 A/g	[71]
G/P-RT^2iO_2	202.4 at 83.75 mA/g	1100	144.4 at 83.75 mA/g	[113]
GVG	127 at 18 A/g	1500	110 at 18 A/g	[76]
N-CDGB	118 at 10 A/g	10,000	125 at 10 A/g	[114]
N-TiO_2/C-dots	176 at 5 C	300	107 at 5 C	[88]
NVOPF@C	70 at 45 C	2000	57 after at 45 C	[115]
P-CNSs	328 at 0.1 A/g	5000	149 at 5 A/g	[116]
Sb@CQDs	635 at 0.1 A/g	120	510 at 0.5 A/g	[117]
SGCN	182.4 at 3.2 A/g	5000	161.8 at 5 A/g	[118]

Table 15.6 Potassium-ion batteries and their charge storage capacity.

PIBs	Capacity	Cycles	Capacity after cyclic study	References
CDs@rGO	310 at 100 mA/g	840	244 at 200 mA g1^1	[79]
HHC	186 at 0.1 A/g	150	131.7 at 0.1 A/g	[119]
p-HNCs	115 at 6.0 A/g	800	160 at 1 A/g	[120]

15.5.2 Carbon quantum dots in potassium-ion batteries

There are very few reports on PIB using CQDs. Erjin Zhang's group has prepared CDs on rGO resulting in a 3D structure. This 3D structure can improve kinetics. The electron transport distance and conduction distance have effectively been reduced. The introduction of potassium ions forms a very stable SEI layer. The battery offers a high capacity of 310 mAh/g at 100 mA/g. The graphite can form stage 1 intercalation compound as GIC, KC_8 through the intercalation of K ions [79]. Table 15.6 shows some of the PIB based on CQDs.

15.5.3 Carbon quantum dots in lithium-sulfur batteries

Lithium-sulfur cells are another class of batteries that have cathodes and anodes with sulfur and lithium. The redox reaction leads to the formation of Li_2S when sulfur takes part in the reaction. The change in volume due to the sulfur ion insertion/deinsertion is the major challenge faced in LSBs. Jungjin Park et al. have decorated

Table 15.7 Lithium-sulfur batteries and their charge storage capacity.

Li-S batteries	Capacity	Cycles	Capacity after cyclic study	References
GQDs-S/CB	800 at 1 C	100	1000 at 0.5 C	[81]
N, S CDs/rGO@S65	740.8 at 7 C	600	427.9 at 5 C	[121]
PEI-CDs@AB/S	393 at 10 mA/cm	400	3.3 mAh/cm at 8 mA/cm	[82]

GQDs on carbon cloth. The liquid phase polysulfides present in the binders can be a reason for strong sulfophilicity. The LSB shows 1454.4 mAh/g at 0.1 C and shows capacity retention of 98.2% after 300 cycles at 0.5 C [81]. Table 15.7 compares some of the LSBs based on CQDs.

15.5.4 Carbon quantum dots in zinc-ion batteries

Zhang's group has prepared CQDs decorated on V_2O_5 by a hydrothermal route. Glucose was used as the precursor to prepare CQDs without any passivation agent. The prepared CQDs/V_2O_5 electrodes were used as the cathode, and it offers a capacity of 460 mAh/g at 0.1 A/g. It also shows high-capacity retention of 85% after 1500 cycles when tested at 4 A/g. The conductivity, the zinc-ion diffusion rate, and the stability of the electrode were enhanced by the incorporation of CQDs [80].

15.5.4.1 Outlook

The recent advancements in energy storage technology have directed researchers toward the development of new materials for charge storage applications. CQDs have been employed in this arena due to their high surface area and the improved stability because of the π-π stacking. The synthesis procedure and the dopant atoms can be chosen according to the application. It can help in the tailoring of supercapacitor electrodes and battery electrode material.

The CQDs, while incorporated into the metal complexes, aid the charge storage. The CQDs can improve the volume expansion in the electrode material. They improve the reaction kinetics in an electrical double-layer capacitor. The incorporation of CQDs highly boosts the electrical conduction at the interface. Apart from using CQDs as standalone materials, it is used in junction with an introduction of a dopant or as a composite with organic and inorganic materials. The active edge sites can be increased. The edge sites can either be created or activated in the existing material. CQDs can be prepared in controllable sizes based on the precursors used.

The research findings from this book chapter can be concluded as:

- The precursors for preparing CQDs have a wide influence on the properties.
- The doping of heteroatoms increases the stability of the structure.
- The bonding between the metal oxides/polymers along with CQDs is strengthened due to the π-π stacking.
- The PL properties of the CQDs are also altered by the doping/co-doping.

- The size and morphology of the CQDs can be tuned based on the role of CQDs.
- The CQD enclosed active materials do not suffer from structural deterioration during insertion/deinsertion of ions.
- It improves the coulombic efficiency and reduces the charge transfer resistance.
- It can increase the nucleation sites available for ion interaction.
- It considerably controls the dendrite formation in batteries.

In the future, CQDs can play a vital role in designing microsupercapacitors or micro batteries that require nanosized material with uncompromised surface area. From the studies, it can be seen that the excess functional groups on the surface can be used to control the morphology. The basic mechanism involved in the electrochemical performance can be probed further to use the CQDs to the fullest in charge storage applications. Also, the quantum confinement effect seen in CQDs can be explored to look for the quantum capacitance effect. Since the quantum principles dominate the materials at a nanoscale level, it can be best used in the supercapacitor application. The electrode materials can be designed in such a manner. The increased chemical stability and photostability of the CQDs can be researched further to find a place in tomorrow's technology of photochargeable supercapacitors or batteries. The selection of CQDs should be tailored for specific applications to improve the robust nature of CQDs for energy applications.

The large-scale synthesis of the CQDs is still a concern due to their synthesis procedures. This can hinder the commercialization of CQDs shortly. To produce ecofriendly, low-cost, and zero toxic CQDs, researchers are probing into natural precursors as the source. This can open doors to a wide arena of research using cleaner technologies.

In conclusion, CQDs are promising candidates in real-life charge storage applications. The large-scale preparation, complete understanding of the electrochemical charge storage mechanism, and specific picking in case of precursors and synthesis method are necessary.

References

[1] T. Christen, M.W. Carlen, Theory of ragone plots, Journal of Power Sources 91 (2) (2000) 210−216. Available from: https://doi.org/10.1016/S0378-7753(00)00474-2.

[2] X. Xu, et al., Electrophoretic analysis and purification of fluorescent single-walled carbon nanotube fragments, Journal of the American Chemical Society 126 (40) (2004) 12736−12737. Available from: https://doi.org/10.1021/ja040082h.

[3] X. Wang, Y. Feng, P. Dong, J. Huang, A mini review on carbon quantum dots: Preparation, properties, and electrocatalytic application, Frontiers in Chemistry 7 (October) (2019) 1−9. Available from: https://doi.org/10.3389/fchem.2019.00671.

[4] S. Krishnakumar, et al., Graphene quantum dots alter proliferation and meiosis of germ cells only in genetic females of Japanese medaka during early embryonic development, ACS Applied Bio Materials 2 (2) (2019) 737−746. Available from: https://doi.org/10.1021/acsabm.8b00606.

[5] G.S. Das, J.P. Shim, A. Bhatnagar, K.M. Tripathi, T.Y. Kim, Biomass-derived carbon quantum dots for visible-light-induced photocatalysis and label-free detection of Fe(III)

and ascorbic acid, Scientific Reports 9 (1) (2019) 1−9. Available from: https://doi.org/10.1038/s41598-019-49266-y.

[6] Z. Zhang, T. Zheng, X. Li, J. Xu, H. Zeng, Progress of carbon quantum dots in photocatalysis applications, Particle and Particle Systems Characterization 33 (8) (2016) 457−472. Available from: https://doi.org/10.1002/ppsc.201500243.

[7] B. Vercelli, The role of carbon quantum dots in organic photovoltaics: a short overview, Coatings 11 (2) (2021) 1−26. Available from: https://doi.org/10.3390/coatings11020232.

[8] M.S. Kumar, K.Y. Yasoda, D. Kumaresan, N.K. Kothurkar, S.K. Batabyal, TiO2-carbon quantum dots (CQD) nanohybrid: enhanced photocatalytic activity, Materials Research Express 5 (7) (2018) 75502. Available from: https://doi.org/10.1088/2053-1591/aacbb9.

[9] D. Ghosh, K. Sarkar, P. Devi, K.H. Kim, P. Kumar, Current and future perspectives of carbon and graphene quantum dots: From synthesis to strategy for building optoelectronic and energy devices, Renewable and Sustainable Energy Reviews 135 (2021). Available from: https://doi.org/10.1016/j.rser.2020.110391.

[10] F.A. Permatasari, M.A. Irham, S.Z. Bisri, F. Iskandar, Carbon-based quantum dots for supercapacitors: Recent advances and future challenges, Nanomaterials 11 (1) (2021) 1−34. Available from: https://doi.org/10.3390/nano11010091.

[11] B.T.S. Ramanujam, A.K. Nanjundan, P.K. Annamalai, Nanocellulose-based Carbon as Electrode Materials for Sodium-ion Batteries, Elsevier Inc, 2021. Available from: http://doi.org/10.1016/b978-0-12-822350-5.00012-6.

[12] J. Zheng, Y. Wu, Y. Sun, J. Rong, H. Li, L. Niu, Advanced Anode Materials of Potassium Ion Batteries: From Zero Dimension to Three Dimensions, Springer, Singapore, 2021. Available from: http://doi.org/10.1007/s40820-020-00541-y.

[13] X. Min, J. Xiao, M. Fang, A. Wang, Y. Zhao, X. Min, Potassium-ion batteries: Outlook on present and future technologies, Energy & Environmental Science 14 (2021) 2186−2243. Available from: https://doi.org/10.1039/d0ee02917c.

[14] No author, Chapter 2 − Technologies of energy storage systems, Grid-scale energy storage systems and applications, Academic Press, 2019, pp. 17−56. Available from: 10.1016/b978-0-12-815292-8.00002-2.

[15] Q. Li, H. Cheng, X. Wu, C.F. Wang, G. Wu, S. Chen, Enriched carbon dots/graphene microfibers towards high-performance micro-supercapacitors, Journal of Materials Chemistry A 6 (29) (2018) 14112−14119. Available from: https://doi.org/10.1039/c8ta02124d.

[16] G. Chen, et al., Assembling carbon quantum dots to a layered carbon for high-density supercapacitor electrodes, Scientific Reports 6 (2016) 1−9. Available from: https://doi.org/10.1038/srep19028.

[17] D. Qu, et al., Hydrogen ion supercapacitor: A new hybrid configuration of highly dispersed MnO2 in porous carbon coupled with nitrogen-doped highly ordered mesoporous carbon with enhanced H-insertion, ACS Applied Materials and Interfaces 6 (24) (2014) 22687−22694. Available from: https://doi.org/10.1021/am506816b.

[18] D. Liu, et al., Enhancement of electrochemical hydrogen insertion in N-doped highly ordered mesoporous carbon, Journal of Physical Chemistry C 118 (5) (2014) 2370−2374. Available from: https://doi.org/10.1021/jp412099y.

[19] D. Liu, J.H. Lei, L.P. Guo, D. Qu, Y. Li, B.L. Su, One-pot aqueous route to synthesize highly ordered cubic and hexagonal mesoporous carbons from resorcinol and hexamine, Carbon 50 (2) (2012) 476−487. Available from: https://doi.org/10.1016/j.carbon.2011.09.002.

[20] J. Ludwinowicz, M. Jaroniec, Effect of activating agents on the development of microporosity in polymeric-based carbon for CO_2 adsorption, Carbon 94 (2015) 673−679. Available from: https://doi.org/10.1016/j.carbon.2015.07.052.

[21] X. Yang, C. Li, R. Fu, Nitrogen-enriched carbon with extremely high mesoporosity and tunable mesopore size for high-performance supercapacitors, Journal of Power Sources 319 (2016) 66−72. Available from: https://doi.org/10.1016/j.jpowsour.2016.04.037.

[22] H.J. Denisa, A.M. Puziy, O.I. Poddubnaya, S.G. Fabian, J.M.D. Tascón, G.Q. Lu, Highly stable performance of supercapacitors from phosphorus-enriched carbons, Journal of the American Chemical Society 131 (14) (2009) 5026−5027. Available from: https://doi.org/10.1021/ja809265m.

[23] D. Carriazo, et al., Phosphate-functionalized carbon monoliths from deep eutectic solvents and their use as monolithic electrodes in supercapacitors, ChemSusChem 5 (8) (2012) 1405−1409. Available from: https://doi.org/10.1002/cssc.201200136.

[24] X. Zhao, et al., Dual-heteroatom-modified ordered mesoporous carbon: Hydrothermal functionalization, structure, and its electrochemical performance, Journal of Materials Chemistry 22 (11) (2012) 4963−4969. Available from: https://doi.org/10.1039/c2jm15820e.

[25] V.C. Hoang, V.G. Gomes, High performance hybrid supercapacitor based on doped zucchini-derived carbon dots and graphene, Materials Today Energy 12 (2019) 198−207. Available from: https://doi.org/10.1016/j.mtener.2019.01.013.

[26] M. Konieczny, R.G. Harvey, Efficient reduction of polycyclic quinones, hydroquinones, and phenols to polycyclic aromatic hydrocarbons with hydriodic acid, Journal of Organic Chemistry 44 (26) (1979) 4813−4816. Available from: https://doi.org/10.1021/jo00394a014.

[27] H. Lv, X. Gao, Q. Xu, H. Liu, Y.G. Wang, Y. Xia, Carbon quantum dot-induced mno2 nanowire formation and construction of a binder-free flexible membrane with excellent superhydrophilicity and enhanced supercapacitor performance, ACS Applied Materials and Interfaces 9 (46) (2017) 40394−40403. Available from: https://doi.org/10.1021/acsami.7b14761.

[28] H. Lv, Y. Yuan, Q. Xu, H. Liu, Y.G. Wang, Y. Xia, Carbon quantum dots anchoring MnO2/graphene aerogel exhibits excellent performance as electrode materials for supercapacitor, Journal of Power Sources 398 (July) (2018) 167−174. Available from: https://doi.org/10.1016/j.jpowsour.2018.07.059.

[29] Y. Zhu, et al., A carbon quantum dot decorated RuO2 network: Outstanding supercapacitances under ultrafast charge and discharge, Energy and Environmental Science 6 (12) (2013) 3665−3675. Available from: https://doi.org/10.1039/c3ee41776j.

[30] Z. Xu, X. Li, S. Sun, Z. Wei, H. Li, S. Yin, Multidimensional carbon-modified NiCo2O4/Ni − Co − S nanocomposite electrode material for high-energy asymmetric supercapacitors, Energy Fuels 35 (2021) 9692−9704.

[31] J. Zheng, X. Lian, M. Wu, F. Zheng, Y. Gao, H. Niu, One-step preparation of Ni3S4 quantum dots composite graphene/carbon nanotube conductive network for asymmetric supercapacitor, Journal of Alloys and Compounds 859 (2021) 158247. Available from: https://doi.org/10.1016/j.jallcom.2020.158247.

[32] Y. Wei, X. Zhang, X. Wu, D. Tang, K. Cai, Q. Zhang, Carbon quantum dots/Ni-Al layered double hydroxide composite for high-performance supercapacitors, RSC Advances 6 (45) (2016) 39317−39322. Available from: https://doi.org/10.1039/c6ra02730j.

[33] X. Yun, et al., Porous Fe_2O_3 modified by nitrogen-doped carbon quantum dots/reduced graphene oxide composite aerogel as a high-capacity and high-rate anode material for alkaline aqueous batteries, ACS Applied Materials and Interfaces 11 (40) (2019) 36970−36984. Available from: https://doi.org/10.1021/acsami.9b12827.

[34] J. Xu, et al., Carbon quantum dots/nickel oxide (CQDs/NiO) nanorods with high capacitance for supercapacitors, RSC Advances 6 (7) (2016) 5541–5546. Available from: https://doi.org/10.1039/c5ra24192h.

[35] A. Prasath, M. Athika, E. Duraisamy, A. Selva Sharma, V. Sankar Devi, P. Elumalai, Carbon quantum dot-anchored bismuth oxide composites as potential electrode for lithium-ion battery and supercapacitor applications, ACS Omega 4 (3) (2019) 4943–4954. Available from: https://doi.org/10.1021/acsomega.8b03490.

[36] H.M. El Sharkawy, A.S. Dhmees, A.R. Tamman, S.M. El Sabagh, R.M. Aboushahba, N.K. Allam, N-doped carbon quantum dots boost the electrochemical supercapacitive performance and cyclic stability of MoS2, Journal of Energy Storage 27 (November 2019) (2020). Available from: https://doi.org/10.1016/j.est.2019.101078.

[37] B. De, J. Balamurugan, N.H. Kim, J.H. Lee, Enhanced electrochemical and photocatalytic performance of core-shell CuS@Carbon quantum Dots@Carbon hollow nanospheres, ACS Applied Materials and Interfaces 9 (3) (2017) 2459–2468. Available from: https://doi.org/10.1021/acsami.6b13496.

[38] L. Shen, Biocompatible polymer/quantum dots hybrid materials: Current status and future developments, Journal of Functional Biomaterials 2 (4) (2011) 355–372. Available from: https://doi.org/10.3390/jfb2040355.

[39] L. Lv, et al., Three-dimensional multichannel aerogel of carbon quantum dots for high-performance supercapacitors, Nanotechnology 25 (23) (2014). Available from: https://doi.org/10.1088/0957-4484/25/23/235401.

[40] X. Jian, H. min Yang, J. gang Li, E. hui Zhang, L. le Cao, Z. hai Liang, Flexible all-solid-state high-performance supercapacitor based on electrochemically synthesized carbon quantum dots/polypyrrole composite electrode, Electrochimica Acta 228 (2017) 483–493. Available from: https://doi.org/10.1016/j.electacta.2017.01.082.

[41] X. Zhang, J. Wang, J. Liu, J. Wu, H. Chen, H. Bi, Design and preparation of a ternary composite of graphene oxide/carbon dots/polypyrrole for supercapacitor application: Importance and unique role of carbon dots, Carbon 115 (2017) 134–146. Available from: https://doi.org/10.1016/j.carbon.2017.01.005.

[42] Z. Zhang, K. Chi, F. Xiao, S. Wang, Advanced solid-state asymmetric supercapacitors based on 3D graphene/MnO2 and graphene/polypyrrole hybrid architectures, Journal of Materials Chemistry A 3 (24) (2015) 12828–12835. Available from: https://doi.org/10.1039/c5ta02685g.

[43] Y. Xie, Y. Zhou, Enhanced electrochemical stability of CuCo bimetallic-coordinated polypyrrole, Electrochimica Acta 290 (2018) 419–428. Available from: https://doi.org/10.1016/j.electacta.2018.09.037.

[44] Z. Zhao, Y. Xie, Enhanced electrochemical performance of carbon quantum dots-polyaniline hybrid, Journal of Power Sources 337 (2017) 54–64. Available from: https://doi.org/10.1016/j.jpowsour.2016.10.110.

[45] R. Malik, S. Lata, U. Soni, P. Rani, R.S. Malik, et al., Carbon quantum dots intercalated in polypyrrole (PPy) thin electrodes for accelerated energy storage, Electrochimica Acta 364 (2020) 137281. Available from: https://doi.org/10.1016/j.electacta.2020.137281.

[46] S. Kumar M, Y. Yasoda K, P. Das, S. Malik, N.K. Kothurkar, S.K. Batabyal, Urea-mediated synthesized carbon quantum dots to tune the electrochemical performance of polyaniline nanorods for supercapacitor device, Journal of Science: Advanced Materials and Devices 7 (2) (2022) 100403. Available from: https://doi.org/10.1016/j.jsamd.2021.11.005.

[47] R. Malik, S. Lata, U. Soni, P. Rani, R.S. Malik, Carbon quantum dots intercalated in polypyrrole (PPy) thin electrodes for accelerated energy storage, Electrochimica

Acta 364 (2020) 137281. Available from: https://doi.org/10.1016/j.electacta.2020.137281.

[48] Y. Xie, H. Du, Electrochemical capacitance of a carbon quantum dots-polypyrrole/titania nanotube hybrid, RSC Advances 5 (109) (2015) 89689−89697. Available from: https://doi.org/10.1039/c5ra16538e.

[49] H. Feng, et al., Synthesis of three-dimensional porous reduced graphene oxide hydrogel/carbon dots for high-performance supercapacitor, Journal of Electroanalytical Chemistry 808 (December 2017) (2018) 321−328. Available from: https://doi.org/10.1016/j.jelechem.2017.12.046.

[50] H. Zhou, G. Han, Electrochimica Acta One-step fabrication of heterogeneous conducting polymers-coated graphene oxide/carbon nanotubes composite fi lms for high-performance supercapacitors, Electrochimica Acta 192 (2016) 448−455. Available from: https://doi.org/10.1016/j.electacta.2016.02.015.

[51] J. Wang, et al., Preparation and electrochemical properties of functionalized multi-Walled carbon nanotubes @ carbon quantum dots @ polyaniline ternary composite electrode materials, Applied Sciences (Switzerland) 10 (16) (2020). Available from: https://doi.org/10.3390/APP10165462.

[52] Q. Wang, H. Wang, D. Liu, P. Du, P. Liu, Synthesis of flake-shaped nitrogen-doped carbon quantum dot/polyaniline (N-CQD/PANI) nanocomposites via rapid-mixing polymerization and their application as electrode materials in supercapacitors, Synthetic Metals 231 (June) (2017) 120−126. Available from: https://doi.org/10.1016/j.synthmet.2017.06.018.

[53] S. Sahoo, A.K. Satpati, P.K. Sahoo, P.D. Naik, Incorporation of carbon quantum dots for improvement of supercapacitor performance of nickel sulfide, ACS Omega 3 (12) (2018) 17936−17946. Available from: https://doi.org/10.1021/acsomega.8b01238.

[54] S. Zhang, L. Sui, H. Dong, W. He, L. Dong, L. Yu, High-performance supercapacitor of graphene quantum dots with uniform sizes, ACS Applied Materials and Interfaces 10 (15) (2018) 12983−12991. Available from: https://doi.org/10.1021/acsami.8b00323.

[55] V. Gayathri, I. John Peter, K. Ramachandran, S. Karazhanov, C. Raja Mohan, Graphene quantum dots embedded in $NiCo_2S_4$/MWCNT nanocomposite as a promising candidate for supercapacitors and I 3 − Reduction in dye-sensitized solar cells, Energy & Fuels 35 (16) (2021) 13360−13369. Available from: https://doi.org/10.1021/acs.energyfuels.1c01471.

[56] M. Ashourdan, A. Semnani, F. Hasanpour, S.E. Moosavifard, Synthesis of $CuMnO_2$/graphene quantum dot nanocomposites as novel electrode materials for high performance supercapacitors, Journal of Energy Storage 36 (November 2020) (2021). Available from: https://doi.org/10.1016/j.est.2021.102449.

[57] S. Kumar, A.K. Ojha, B. Ahmed, A. Kumar, J. Das, A. Materny, Tunable (violet to green) emission by high-yield graphene quantum dots and exploiting its unique properties towards sun-light-driven photocatalysis and supercapacitor electrode materials, Materials Today Communications 11 (2017) 76−86. Available from: https://doi.org/10.1016/j.mtcomm.2017.02.009.

[58] Z. Ouyang, et al., Preparation and specific capacitance properties of sulfur, nitrogen co-doped graphene quantum dots, Nanoscale Research Letters 14 (1) (2019). Available from: https://doi.org/10.1186/s11671-019-3045-4.

[59] M. Miah, S. Bhattacharya, A. Gupta, S.K. Saha, Origin of high storage capacity in N-doped graphene quantum dots, Electrochimica Acta 222 (2016) 709−716. Available from: https://doi.org/10.1016/j.electacta.2016.11.027.

[60] Y. Zhang, et al., Preparation of coal-based graphene quantum dots/α-Fe2O3 nanocomposites and their lithium-ion storage properties, Fuel 241 (2019) 646−652.

[61] L. Xu, C. Cheng, C. Yao, X. Jin, Flexible supercapacitor electrode based on lignosulfonate-derived graphene quantum dots/graphene hydrogel, Organic Electronics 78 (2020) 105407. Available from: https://doi.org/10.1016/j.orgel.2019.105407.

[62] P. Luo, X. Guan, Y. Yu, X. Li, F. Yan, Hydrothermal synthesis of graphene quantum dots supported on three-dimensional graphene for supercapacitors, Nanomaterials 9 (2) (2019). Available from: https://doi.org/10.3390/nano9020201.

[63] Y. Qing, et al., Boosting the supercapacitor performance of activated carbon by constructing overall conductive networks using graphene quantum dots, Journal of Materials Chemistry A 7 (11) (2019) 6021−6027. Available from: https://doi.org/10.1039/c8ta11620b.

[64] W. Tian, et al., Micelle-induced assembly of graphene quantum dots into conductive porous carbon for high rate supercapacitor electrodes at high mass loadings, Carbon 161 (2020) 89−96. Available from: https://doi.org/10.1016/j.carbon.2020.01.044.

[65] S. Zhang, et al., Ultramicroporous carbons puzzled by graphene quantum dots: Integrated high gravimetric, volumetric, and areal capacitances for supercapacitors, Advanced Functional Materials 28 (52) (2018) 1−10. Available from: https://doi.org/10.1002/adfm.201805898.

[66] Z. Li, et al., Assembling nitrogen and oxygen co-doped graphene quantum dots onto hierarchical carbon networks for all-solid-state flexible supercapacitors, Electrochimica Acta 235 (2017) 561−569. Available from: https://doi.org/10.1016/j.electacta.2017.03.147.

[67] Z. Li, et al., Hierarchical construction of high-performance all-carbon flexible fiber supercapacitors with graphene hydrogel and nitrogen-doped graphene quantum dots, Carbon 154 (2019) 410−419. Available from: https://doi.org/10.1016/j.carbon.2019.08.040.

[68] J.S. Wei, et al., Integrating carbon dots with porous hydrogels to produce full carbon electrodes for electric double-layer capacitors, ACS Applied Energy Materials 3 (7) (2020) 6907−6914. Available from: https://doi.org/10.1021/acsaem.0c00990.

[69] R. Guo, et al., Functionalized carbon dots for advanced batteries, Energy Storage Materials 37 (November 2020) (2021) 8−39. Available from: https://doi.org/10.1016/j.ensm.2021.01.020.

[70] S. Wang, et al., Egg yolk-derived carbon: Achieving excellent fluorescent carbon dots and high performance lithium-ion batteries, Journal of Alloys and Compounds 746 (2018) 567−575. Available from: https://doi.org/10.1016/j.jallcom.2018.02.293.

[71] M.S. Balogun, et al., Carbon quantum dot surface-engineered VO2 interwoven nanowires: A flexible cathode material for lithium and sodium ion batteries, ACS Applied Materials and Interfaces 8 (15) (2016) 9733−9744. Available from: https://doi.org/10.1021/acsami.6b01305.

[72] A. Gurung, et al., Tin selenide − Multi-walled carbon nanotubes hybrid anodes for high performance lithium-ion batteries, Electrochimica Acta 211 (2016) 720−725. Available from: https://doi.org/10.1016/j.electacta.2016.06.065.

[73] J. Nai, X. Zhao, H. Yuan, X. Tao, L. Guo, Amorphous carbon-based materials as platform for advanced high-performance anodes in lithium secondary batteries, Nano Research 14 (7) (2021) 2053−2066. Available from: https://doi.org/10.1007/s12274-021-3506-9.

[74] N.S. Choi, J.G. Han, S.Y. Ha, I. Park, C.K. Back, Recent advances in the electrolytes for interfacial stability of high-voltage cathodes in lithium-ion batteries, RSC Advances 5 (2015) 2732−2748. Available from: https://doi.org/10.1039/c4ra11575a.

[75] S. Liu, et al., Carbon quantum dot modified Na3V2(PO4)2F3as a high-performance cathode material for sodium-ion batteries, Journal of Materials Chemistry A 8 (36) (2020) 18872−18879. Available from: https://doi.org/10.1039/d0ta04307a.

[76] D. Chao, et al., Graphene quantum dots coated VO2 arrays for highly durable electrodes for Li and Na ion batteries, Nano Letters 15 (1) (2015) 565−573. Available from: https://doi.org/10.1021/nl504038s.

[77] D. Kong, et al., Surface modification of Na2Ti3O7 nanofibre arrays using N-doped graphene quantum dots as advanced anodes for sodium-ion batteries with ultra-stable and high-rate capability, Journal of Materials Chemistry A 7 (20) (2019) 12751−12762. Available from: https://doi.org/10.1039/c9ta01641d.

[78] V.C. Hoang, K. Dave, V.G. Gomes, Carbon quantum dot-based composites for energy storage and electrocatalysis: Mechanism, applications and future prospects, Nano Energy 66 (June) (2019) 104093. Available from: https://doi.org/10.1016/j.nanoen.2019.104093.

[79] E. Zhang, X. Jia, B. Wang, J. Wang, X. Yu, B. Lu, Carbon dots@rGO paper as free-standing and flexible potassium-ion batteries anode, Advanced Science 7 (15) (2020) 1−8. Available from: https://doi.org/10.1002/advs.202000470.

[80] J. Zhang, et al., Carbon quantum dots promote coupled valence engineering of V2O5 nanobelts for high-performance aqueous zinc-ion batteries, ChemSusChem 14 (9) (2021) 2076−2083. Available from: https://doi.org/10.1002/cssc.202100223.

[81] J. Park, et al., Graphene quantum dots: Structural integrity and oxygen functional groups for high sulfur/sulfide utilization in lithium sulfur batteries, NPG Asia Materials 8 (5) (2016). Available from: https://doi.org/10.1038/am.2016.61.

[82] Y. Hu, et al., Carbon quantum dots−modified interfacial interactions and ion conductivity for enhanced high current density performance in lithium−sulfur batteries, Advanced Energy Materials 9 (7) (2019) 1−8. Available from: https://doi.org/10.1002/aenm.201802955.

[83] Q. Liu, et al., Layered double hydroxide quantum dots for use in a bifunctional separator of lithium-sulfur batteries, ACS Applied Materials and Interfaces 13 (15) (2021) 17978−17987. Available from: https://doi.org/10.1021/acsami.1c00974.

[84] J. Park, J. Moon, V. Ri, S. Lee, C. Kim, E.J. Cairns, Nitrogen-doped graphene quantum dots: Sulfiphilic additives for the high-performance Li-S cells, ACS Applied Energy Materials 4 (4) (2021) 3518−3525. Available from: https://doi.org/10.1021/acsaem.0c03247.

[85] M.C. Daugherty, S. Gu, D.S. Aaron, R.E. Kelly, Y. Ashraf Gandomi, C. Te Hsieh, Graphene quantum dot-decorated carbon electrodes for energy storage in vanadium redox flow batteries, Nanoscale 12 (14) (2020) 7834−7842. Available from: https://doi.org/10.1039/d0nr00188k.

[86] J. Pre-proofs, M.S. Javed, S. Shoaib, A. Shah, S. Hussain, Tuning the phase of hierarchical mesoporous manganese-selenide microflowers towards significantly enhanced electrochemical performance as a flexible symmetric 1. 8 V supercapacitor, Chemical Engineering Journal (2019) 122814. Available from: https://doi.org/10.1016/j.cej.2019.122814.

[87] X. Zhao, et al., High-performance Li-ion batteries based on graphene quantum dot wrapped carbon nanotube hybrid anodes, Nano Research 13 (4) (2020) 1044−1052. Available from: https://doi.org/10.1007/s12274-020-2741-9.

[88] Y. Yang, et al., Carbon dots supported upon N-doped TiO_2 nanorods applied into sodium and lithium ion batteries, Journal of Materials Chemistry A 3 (10) (2015) 5648−5655. Available from: https://doi.org/10.1039/c4ta05611f.

[89] A. Piriya, V. Kumar, M. Seshadhri, R. Shyiamaladevi, Applied Surface Science Facile synthesis of heteroatom doped and undoped graphene quantum dots as active materials for reversible lithium and sodium ions storage, Applied Surface Science 504 (2020) 144430.

[90] I. Riyanto, K. Sahroni, P.Y. Bindumadhavan, Chang, R.A. Doong, Boron doped graphene quantum structure and MoS2 nanohybrid as anode materials for highly reversible lithium storage, Front. Chem. 7 (MAR) (2019). Available from: https://doi.org/10.3389/fchem.2019.00116.

[91] H. Yu, et al., Porous carbon derived from metal-organic framework@graphene quantum dots as electrode materials for supercapacitors and lithium-ion batteries, RSC Advances 9 (17) (2019) 9577−9583. Available from: https://doi.org/10.1039/C9RA01488H.

[92] M. Wu, et al., Toluene degradation over Mn-TiO_2/CeO_2 composite catalyst under vacuum ultraviolet (VUV) irradiation, Chemical Engineering Science 195 (2019) 985−994. Available from: https://doi.org/10.1016/j.ces.2018.10.044.

[93] A. Prasath, M. Athika, E. Duraisamy, A.S. Sharma, P. Elumalai, Carbon-quantum-dot-derived nanostructured MnO2 and its symmetrical supercapacitor performances, Chemistry Select 3 (30) (2018) 8713−8723. Available from: https://doi.org/10.1002/slct.201801950.

[94] M. Javed, et al., Carbon quantum dots from glucose oxidation as a highly competent anode material for lithium and sodium-ion batteries, Electrochimica Acta 297 (2019) 250−257. Available from: https://doi.org/10.1016/j.electacta.2018.11.167.

[95] C. Zhu, et al., Enhanced lithium storage performance of CuO nanowires by coating of graphene quantum dots, Advanced Materials Interfaces 2 (2) (2015) 1−6. Available from: https://doi.org/10.1002/admi.201400499.

[96] F. Paquin, J. Rivnay, A. Salleo, N. Stingelin, C. Silva, Multi-phase semicrystalline microstructures drive exciton dissociation in neat plastic semiconductors, Journal of Materials Chemistry C 3 (2015) 10715−10722. Available from: https://doi.org/10.1039/b000000x.

[97] Q. Zhang, C. Sun, L. Fan, N. Zhang, K. Sun, Iron fl uoride vertical nanosheets array modi fi ed with graphene quantum dots as long-life cathode for lithium ion batteries, Chemical Engineering Journal 371 (April) (2019) 245−251.

[98] L. Li, et al., Li4Ti5O12 quantum dot decorated carbon frameworks from carbon dots for fast lithium ion storage, Materials Chemistry Frontiers 3 (9) (2019) 1761−1767. Available from: https://doi.org/10.1039/c9qm00259f.

[99] L. Ruiyi, et al., Significantly enhanced electrochemical performance of lithium titanate anode for lithium ion battery by the hybrid of nitrogen and sulfur co-doped graphene quantum dots, Electrochimica Acta 178 (2015) 303−311. Available from: https://doi.org/10.1016/j.electacta.2015.08.018.

[100] H. Nan, et al., Low-cost and environmentally friendly synthesis of an Al3 + and Mn4 + co-doped Li4Ti5O12 composite with carbon quantum dots as an anode for lithium-ion batteries, RSC Advances 9 (38) (2019) 22101−22105. Available from: https://doi.org/10.1039/c9ra03897c.

[101] F. Khan, M. Oh, J. Hyun, N-functionalized graphene quantum dots: charge transporting layer for high-rate and durable Li 4 Ti 5 O 12-based Li-ion battery, Chemical Engineering Journal 369 (February) (2019) 1024−1033.

[102] M. Jing, et al., Carbon quantum dot coated Mn3O4 with enhanced performances for lithium-ion batteries, Journal of Materials Chemistry A 3 (32) (2015) 16824−16830. Available from: https://doi.org/10.1039/C5TA03610K.

[103] X. Yin, H. Chen, C. Zhi, W. Sun, L.P. Lv, Y. Wang, Functionalized graphene quantum dot modification of Yolk−Shell NiO microspheres for superior lithium storage, Small 14 (22) (2018) 1−10. Available from: https://doi.org/10.1002/smll.201800589.

[104] X. Yin, C. Zhi, W. Sun, L.P. Lv, Y. Wang, Multilayer NiO@Co3O4@graphene quantum dots hollow spheres for high-performance lithium-ion batteries and supercapacitors, Journal of Materials Chemistry A 7 (13) (2019) 7800−7814. Available from: https://doi.org/10.1039/c8ta11982a.

[105] K. Lijuan, Y. Yongqiang, L. Ruiyi, L. Zaijun, Phenylalanine-functionalized graphene quantum dot-silicon nanoparticle composite as an anode material for lithium ion batteries with largely enhanced electrochemical performance, Electrochimica Acta 198 (2016) 144−155. Available from: https://doi.org/10.1016/j.electacta.2016.03.034.

[106] W. Zhang, T. Xu, Z. Liu, N.L. Wu, M. Wei, Hierarchical TiO_2: X imbedded with graphene quantum dots for high-performance lithium storage, Chemical Communications 54 (12) (2018) 1413−1416. Available from: https://doi.org/10.1039/c7cc09406j.

[107] K. Lijuan, L. Ruiyi, Y. Yongqiang, L. Zaijun, Multi-faceted design of a silicon anode for high performance lithium ion batteries using silicon nanoparticles encapsulated by a multiple graphene aerogel electrode material and a tryptophan-functionalized graphene quantum dot-sodium alginate binder, RSC Advances 6 (80) (2016) 76344−76354. Available from: https://doi.org/10.1039/c6ra15257k.

[108] P. Ge, et al., Multidimensional evolution of carbon structures underpinned by temperature-induced intermediate of chloride for sodium-ion batteries, Advanced Science 5 (6) (2018). Available from: https://doi.org/10.1002/advs.201800080.

[109] H. Hou, C.E. Banks, M. Jing, Y. Zhang, X. Ji, Carbon quantum dots and their derivative 3D porous carbon frameworks for sodium-ion batteries with ultralong cycle life, Advanced Materials 27 (47) (2015) 7861−7866. Available from: https://doi.org/10.1002/adma.201503816.

[110] F. Xie, et al., Unveiling the role of hydrothermal carbon dots as anodes in sodium-ion batteries with ultrahigh initial coulombic efficiency, Journal of Materials Chemistry A 7 (48) (2019) 27567−27575. Available from: https://doi.org/10.1039/c9ta11369j.

[111] M. Wu, Y. Gao, Y. Hu, B. Zhao, H. Zhang, Boosting sodium storage of mesoporous TiO2 nanostructure regulated by carbon quantum dots, Chinese Chemical Letters 31 (3) (2020) 897−902. Available from: https://doi.org/10.1016/j.cclet.2019.07.039.

[112] J. Chen, G. Zou, H. Hou, Y. Zhang, Z. Huang, X. Ji, Pinecone-like hierarchical anatase TiO_2 bonded with carbon enabling ultrahigh cycling rates for sodium storage, Journal of Materials Chemistry A 4 (32) (2016) 12591−12601. Available from: https://doi.org/10.1039/c6ta03505a.

[113] Y. Zhang, et al., Graphene-rich wrapped petal-like rutile TiO_2 tuned by carbon dots for high-performance sodium storage, Advanced Materials 28 (42) (2016) 9391−9399. Available from: https://doi.org/10.1002/adma.201601621.

[114] Z. Liu, et al., Edge-nitrogen-rich carbon dots pillared graphene blocks with ultrahigh volumetric/gravimetric capacities and ultralong life for sodium-ion storage, Advanced Energy Materials 8 (30) (2018) 1−12. Available from: https://doi.org/10.1002/aenm.201802042.

[115] G. Deng, et al., Graphene quantum dots-shielded $Na_3(VO)_2(PO_4)_2F$@C nanocuboids as robust cathode for Na-ion battery, Energy Storage Materials 5 (2016) 198−204.

[116] H. Hou, L. Shao, Y. Zhang, G. Zou, J. Chen, X. Ji, Large-area carbon nanosheets doped with phosphorus: A high-performance anode material for sodium-ion batteries, Advanced Science 4 (1) (2017). Available from: https://doi.org/10.1002/advs.201600243.

[117] F. Liu, et al., A facile carbon quantum dot-modified reduction approach towards tunable Sb@CQDs nanoparticles for high performance sodium storage, Batteries & Supercaps 3 (5) (2020) 463−469. Available from: https://doi.org/10.1002/batt.201900167.

[118] G. Zou, C. Wang, H. Hou, C. Wang, X. Qiu, X. Ji, Controllable interlayer spacing of sulfur-doped graphitic carbon nanosheets for fast sodium-ion batteries, Small 13 (31) (2017) 1−10. Available from: https://doi.org/10.1002/smll.201700762.

[119] Y. Zhang, et al., Honeycomb hard carbon derived from carbon quantum dots as anode material for K-ion batteries, Materials Chemistry and Physics 229 (March) (2019) 303−309. Available from: https://doi.org/10.1016/j.matchemphys.2019.03.021.

[120] W. Hong, et al., Carbon quantum dot micelles tailored hollow carbon anode for fast potassium and sodium storage, Nano Energy 65 (August) (2019) 104038. Available from: https://doi.org/10.1016/j.nanoen.2019.104038.

[121] J.M. Chabu, K. Zeng, G. Jin, M. Zhang, Y. Li, Y.N. Liu, Simple approach for the preparation of nitrogen and sulfur codoped carbon dots/reduced graphene oxide as host for high-rate lithium−sulfur batteries, Materials Chemistry and Physics 229 (October 2018) (2019) 226−231. Available from: https://doi.org/10.1016/j.matchemphys.2019.03.019.

Magnetic and nanophotonics applications of carbon quantum dots

16

Ravi P.N. Tripathi[1], *Vidyadhar Singh*[1], *Bharat Kumar Gupta*[2] *and*
Nikhil Kumar[2]
[1]Department of Physics, Jai Prakash University, Chapra, Bihar, India, [2]Department of Physics, Deen Dayal Upadhyay Gorakhpur University, Gorakhpur, Uttar Pradesh, India

16.1 Introduction

Luminescent carbon quantum dots (CQDs) with quantum confinement, edge effects, high edge-to-area ratio, stable fluorescence, robust chemical inertness, biocompatibility, etc. have recently emerged as potential candidates in the context of bioimaging, sensor, spintronics, photovoltaic (PV) solar cells, light-emitting diodes (LEDs), cavity-assisted nanophotonics, etc. [1−15]. Since the successful separation of CQDs from single-walled carbon nanotubes (SWCNTs) in 2004 [16], they have stimulated the subsequent studies and their engagement in a variety of applications ranging from physical/chemical sciences to biomedical engineering [1,3,5−7,17−20]. Generally, carbon is recognized as a black biocompatible material with very low fluorescence and less water solubility [16]. In contrast, CQDs are acknowledged for their strong luminescence, good water solubility, and nontoxic nature [1,3,5,6,18]. Moreover, CQDs are recognized as carbon nanolights [2,21,22] due to their strong and stable luminescence along with a wide range of tuneability, including deep ultraviolet light, green light, yellow light, and red light via chemically engineered quantum structures by surface functionalization, heteroatoms doping, quantum confinement, etc. [12,23−30]. Hence, CQDs have higher prospects for designing ultracompact magnetic, optoelectronic, and nanophotonic applications due to this wide range of optical responses.

CQDs with a single atomic layer facilitate the surface decorated with large-area active sites and oxygen-containing groups. These active sites can be further exploited for easily carrying or loading molecules to tailor electronic, optical, and magnetic responses [31−35]. In recent years, substantial efforts and associated applications have been shown in this regard [13,28,36,37]. Moreover, these efforts have also been well summarized in several excellent review articles [1,2,32,38]. However, it is worth noting that these review articles are primarily confined to the synthesis process of CQDs, biomedical imaging, and energy-related applications [35,37,39,40]. For instance, Wang et al. [32], Lim et al. [1], and Yuan et al. [38] have focused the discussion on the synthesis of CQDs, their photoelectric, and luminescent mechanism. They further extended the discussion on applications on optoelectronics, catalysis, and sensors. Chen et al. [39] discussed about preparation

Carbon Quantum Dots for Sustainable Energy and Optoelectronics. DOI: https://doi.org/10.1016/B978-0-323-90895-5.00005-9
© 2023 Elsevier Ltd. All rights reserved.

strategies of graphene quantum dots (GQDs) such as acid oxidation, hydrothermal and solvothermal reactions, etc., and their biomedical applications such as biomedical imaging, drug delivery, and biosensing. Li et al. [37] emphasized CQDs and GQDs for optoelectronic and energy storage applications such as LEDs, PV solar cell, supercapacitors, etc. Recently in 2021, Paterno et al. [41] has written an article on GQDs describing these quantum dots' synthesis route and their prospective implications on spectroscopy and photonics. This indicates a paradigm shift in CQDs' engagement for nanoscale magnetism, and nano/quantum- photonic applications.

In recent years, CQDs such as GQDs, graphene oxide quantum dots (GOQDs), etc. have been explored in the context of tailoring magnetic and optical responses at atomic limit [14,42–49]. From 2009 onwards, various research groups have theoretically argued the presence of magnetism and their electric-field modulation in carbon-based quantum structures. In 2018, Sun et al. [45] experimentally unveiled the intrinsic magnetism in 2.04 nm GQDs and proposed that the residual zigzag edges passivation via hydroxyl groups is the primarily magnetic source of GQDs. They further discussed the role of high-temperature annealing induced edge defects and reconstruction in arising edge-states magnetism in GQDs. Further, they explored the presence of intrinsic magnetism in monolayer GOQDs and found that though GOQDs are generally nonmagnetic; however, a few of GOQDs are weakly paramagnetic in nature. Recently, Hu et al. [50] were able to achieve the room-temperature magnetism and tunable energy gaps in GQDs. On the other hand, the optics/photonics communities have also shown their interest in CQDs for nanophotonics and quantum optics applications. For example, Zhao et al. [51] performed a study on the intrinsic emission properties of GQDs and further argued about its prospect as room-temperature single-photon emitters. Katzen et al. [14] embedded these CQDs inside a gold mirror cavity and investigated the optical response in a strong-coupling regime. Motivated with this, we envisage that it is virtuous to summarize the ongoing efforts of CQDs in the context of nanoscale magnetism, nanophotonics, and single-photon emission. In this chapter, an overview of the recent progress in the research of CQDs within the framework of nanoscale magnetism and nanophotonics is presented. The chapter's contents are outlined in Fig. 16.1.

16.2 Applications

16.2.1 Magnetic applications

Carbon-based nanomaterials such as CQDs and GQDs are considered to be the most promising candidates because of their characteristics, including biodegradability, lower toxicity, good electronic/magnetic features, higher solubility in various solvents, high surface areas, and plenty of edge sites for functionalization. Carbon-based quantum dots such as CQDs, GQDs, and GOQDs are very promising candidates in spintronics and have potential application in drug delivery, antioxidant, and antibacterial activity, as MRI contrasting agent, magnetic removal of heavy metal contaminants from wastewater, various types of sensors, and many more. Magnetic

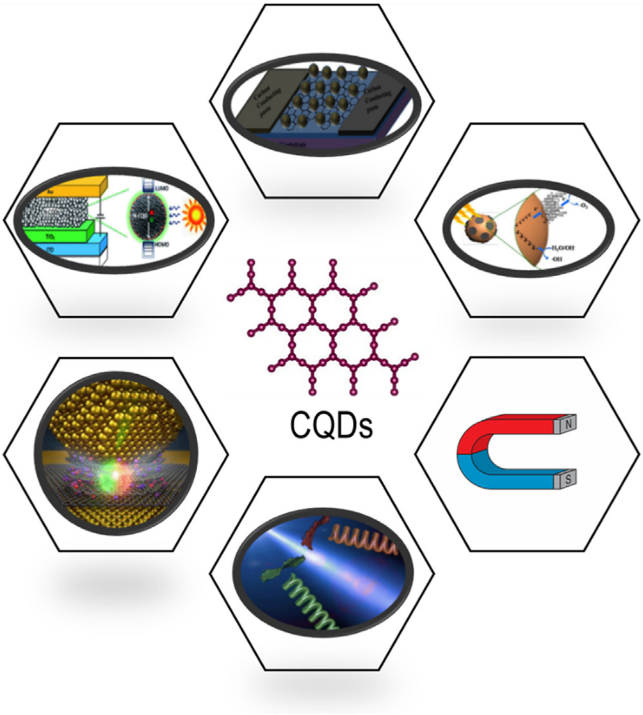

Figure 16.1 Schematic illustration of topics covered in this chapter in the context of magnetic and nanophotonics.
Source: Reproduced with permission from Refs. [14,47,52–54]. Copyright 2017 Elsevier, 2013 Springer Nature, 2016 Elsevier, 2020 & 2016 American Chemical Society.

properties of GQDs, based on magnetic nanostructure, strongly depend on the shape, size, and temperature and are characterized by spin-polarized edges, which open the door to its applications in spintronics. By using the advantage of the relaxation nature of the spin-polarized state of magnetic GQDs, Li et al. [42] proposed a facile and simple closed tube one-step strategy probe of GQDs based magnetic relaxation switches working with portable ultra-low field nuclear magnetic resonance relaxometry to detect severe acute respiratory syndrome coronavirus 2 (SARS-CoV-2). The proposed detector is rapid, safe, and sensitive in detection.

16.2.1.1 *Carbon quantum dots decorated magnetic nanoparticles*

Carbon-based nanostructures such as CQDs/GQDs decorated magnetic nanoparticles have significant potential in medical field and chemical field as active agent or nanocarriers for drug delivery. In addition, by combining optical properties of GQDs and magnetic properties of magnetic nanoparticles, GQD-based nanocomposites can be used for drug delivery dynamics and drug dose control process. GQDs decorated magnetic nanoparticles are better candidates for biomedical application in photothermal therapy, hyperthermia-based cancer therapy, biosensors, and MRI contrasting agents due to their biocompatibility, low toxicity, optical activity, and magnetic properties. Sun et al. [45] investigated nano-flakes of graphene. Interestingly, GQDs show purely paramagnetic behavior at 2 K and diamagnetism at high temperatures, as shown in Fig. 16.2. The magnetic property of GQDs is mainly because of the spin-polarized state localized at residual zigzag edges of GQDs. Sun reported that interaction of defects present in basal plane and residual zigzag edges of GQDs may enhance the overall magnetic response; magnetic correlation length plays an essential role for accounting magnetic properties of GQDs. In addition, CQDs have been hybridized with magnetic nanostructures to explore possibilities in biomedical imaging. For instance, due to optical and magnetic

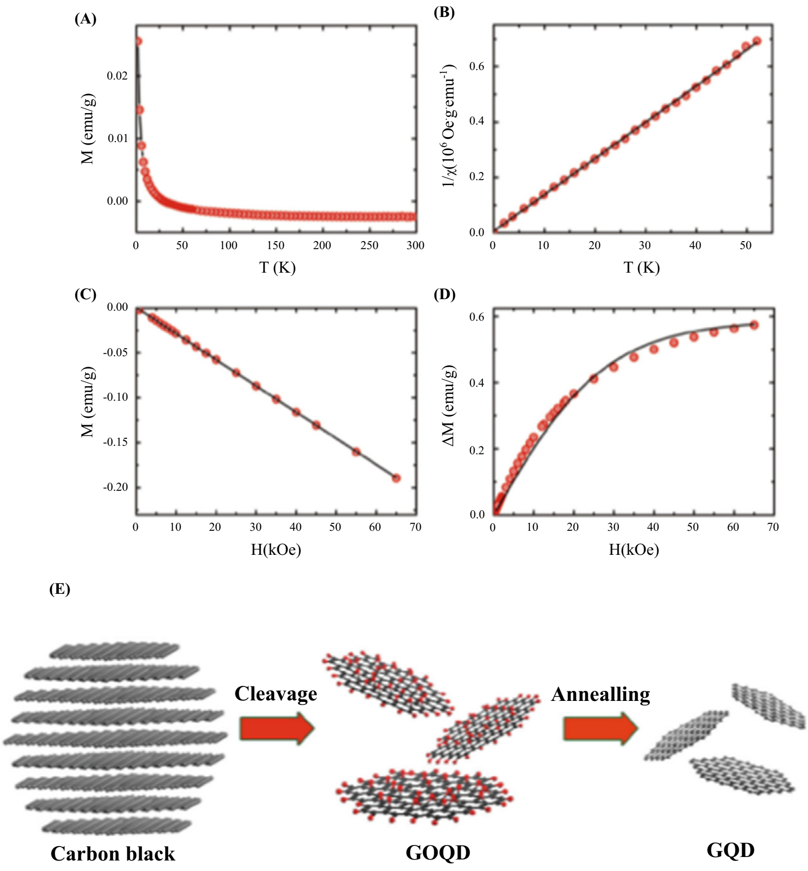

Figure 16.2 (A–D) Magnetic properties of GQDs showing Curie like paramagnetism at 2 K. (E) Fabrication scheme of GQDs. The black and red balls denoted carbon and oxygen atom, respectively. *GQDs*, Graphene quantum dots.
Source: Reproduced with permission from Y. Sun, et al., Magnetism of graphene quantum dots. NPJ Quantum Materials 2 (1) (2017) 1–7. Copyright 2017 Springer Nature.

properties of Fe_3O_4, nanoparticle decorated CQDs have been used in vivo bioimaging of tumor-bearing nude mice by combining fluorescent, magnetic resonance, and computed tomography (CT) images [55], as shown in Fig. 16.3. Fang et al. [56] developed GQDs gated hollow mesoporous carbon NPs to encapsulate an anti-cancer medicine (Doxorubicin (DOX)).

Magnetic nanoparticles (such as Fe_3O_4) decorated with GQDs are electrodeposited on glassy carbon electrode and work as a sensitive electrochemical sensor for amino acids due to their good electrocatalytic property [57]. Despite this, the presence of iron oxide (Fe_3O_4) magnetic nanoparticles with GQDs explores new possible applications. Haizhen Ding et al. [58] prepared single gadolinium (Gd) atom anchored on GQDs with dendrite-like morphology to show enhanced longitudinal relaxivity and have application as a contrast agent for high definition magnetic resonance imaging. Fe_3O_4 nanoparticles decorated CQDs, functionalized with carbon nanotubes, have also been used as new sensing platforms for electrochemical determination of LDOPA in agricultural products [59]. Apart from Fe_3O_4, other

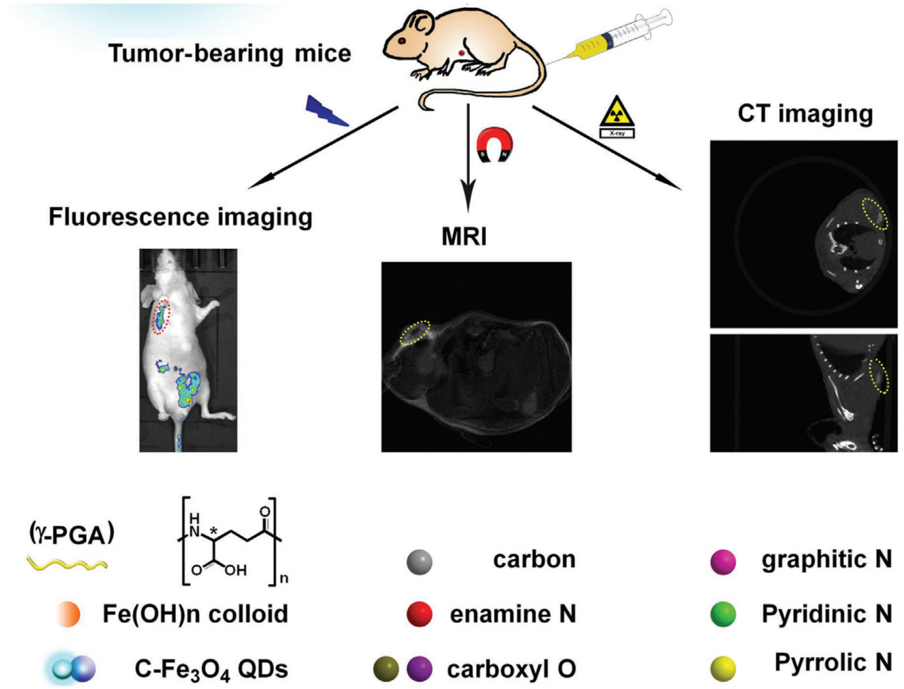

Figure 16.3 Schematic illustration of HA-HMCN(DOX) @GQDs nanoplatform targeting drug delivery and synergistic chemophotothermal therapy. *GQDs*, Graphene quantum dots. *Source*: Reproduced with permission from X. Liu, et al., Nitrogen-doped carbon quantum dot stabilized magnetic iron oxide nanoprobe for fluorescence, magnetic resonance, and computed tomography triple-modal in vivo bioimaging, Advanced Functional Materials 26 (47) (2016) 8694−8706.

magnetic nanoparticles such as manganese-doped $MnFe_2O_4$ nanoparticles decorated CQDs and GQDs have also been used for bioimaging purposes [17]. Thus CQDs and GQDs decorated magnetic nanoparticles and nanocomposites have numerous opportunities in various applications.

16.2.1.2 Carbon quantum dots encapsulated 1D magnetic nanostructures

GQDs are a kind of zero-dimensional (0D) material with characteristics of both graphene and CQDs. Study and synthesis of graphene-based one-dimensional (1D) magnetic nanostructures have great importance for understanding spin-polarized edge states, which is the key element for application in graphene-based spintronics and thus may be able to explain predicted properties related to spin, like spin confinement. Graphene nanoribbons (GNRs) are graphene-based 1D magnetic nanostructures. GNRs with zigzag edge state exhibit ferromagnetism along edges and anti-ferromagnetism between the edges [60]. Recently Sun et al. [61] reported coupled spin state (magnetic spin chain) in armchair GNRs by incorporating specifically designed monomers that explore the field of graphene-based 1D magnetic nanostructures.

16.2.2 Nanophotonic applications and single-photon emission

So far, the discussion was primarily focused on stimulating the behavior of these quantum dots under external magnetic field and their applications. Intriguingly, a similar question can be asked "how to control the light−matter interaction in these quantum structures under incident electromagnetic field?". The effective answer to this question has direct relevance not only in fundamental optical physics but also in optoelectronics, micro/nanophotonics, and quantum technologies. To address this question, light−matter interaction in several carbon-based quantum dots has been recently explored by varying shape, size, stacking arrangement, embedding these quantum structures with extended molecular structures, plasmonic structures, mirror cavities, etc. In addition, several important applications and prototypes have also been demonstrated in recent years. Herein, we summarize a few CQDs and GQDs engagement within the framework of nanophotonic applications such as LEDs, solar cells, chiral photonics, twistronics, single-photon emission, etc.

16.2.2.1 Light-emitting diodes

Owing to tunable stable fluorescence emission, inexpensive cost, and biocompatibility, CQDs emerge as a potential substitute to expensive phosphors and toxic metal-based semiconductor QDs for realizing LEDs. Interestingly, the broad-range optical response and exceptionally efficient multiphoton up-conversion in these quantum structures can be efficiently tailored as a function of shape, size, heteroatom doping, surface functionalization, etc. Therefore such efficiently controlled light emission in these carbon-based nanomaterials paves the way for their engagement in integrated nanophotonics and optoelectronics applications. In recent years, significant attention has been paid to realize the prospect of these carbon-based quantum dots in LED applications. In general, based on their excitation mechanism, LEDs can be differentiated in two different categories. Firstly, the CQDs and GQDs based dyes are optically pumped using UV-vis light source, then such type of system is labeled as phosphor-converted LEDs or pc-LEDs. In contrast, if the emission is controlled by injecting electron-hole pairs through electrical contacts and their recombination process, these are identified as electroluminescent LEDs [62]. For example, Gupta et al. [63] have demonstrated that GQDs dispersed conjugated polymers show enhanced Organic Photovoltaic (OPV) and Organic Light Emitting Diode (OLED) characteristics. Further significant performance efficiency is also registered in contrast to conventional graphene sheets because of improved morphological and optical characteristics (Fig. 16.4A). In addition, the reported LEDs have shown excellent stability and voltage-independent emission color with a maximum luminance of 136 cd/m^2. Further, Zhang et al. [64] have displayed CQDs based LEDs, in which the emission color can be tuned as per driving current

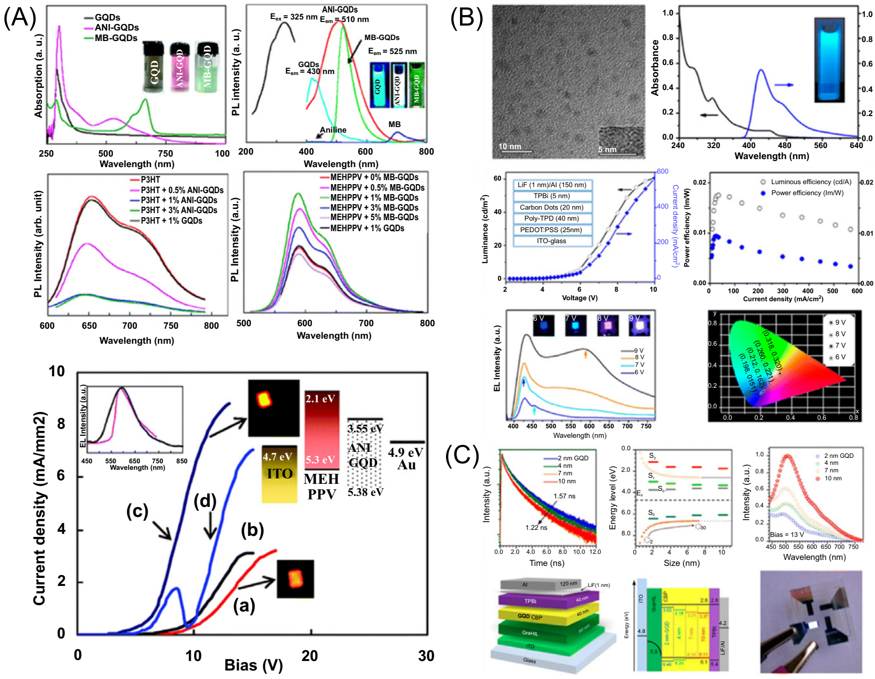

Figure 16.4 Recent development of CQDs and GQDs in the context of light-emitting diodes (LEDs). (A) Tailoring the optical photoluminescence and electroluminescence response of pristine GQDs via functionalization process with varying concentration. (B) LEDs based on carbon dots. (C) Emission properties of GQDs prepared via amidative cutting of tattered graphite by regulating amine concentration. *CQDs*, Carbon quantum dots; *GQDs*, graphene quantum dots. *Source*: Reproduced with permission from Refs. [63–65]. Copyright 2011, 2013, 2014 American Chemical Society.

voltages (Fig. 16.5B). In their devices, emissive layer of CQDs was sandwiched between an organic hole transport layer and an organic/inorganic electron transport layer. Further, they were able to tailor the multicolor emission in different wavelength regions ranging from blue to white with the same CQDs by regulating the device structure and the injected current density. Furthermore, Kwon et al. [65] have reported electroluminescence in size-controlled GQDs (Fig. 16.5C). With a controlled size of GQDs, the energy gaps have been tuned, and consequently the emission color of photoluminescence has been tailored. In addition, the group has also explored the effect of defects sites on photoluminescence, tailored emission wavelength regime, and controlled exciton lifetime. On the other hand, extensive efforts have been reported for phosphorus-converted LEDs. Tang et al. [66] have shown glucose-derived water-soluble crystalline GQDs. Interestingly, they were able to tailor the blue emission to white light by coating obtained water-soluble GQDs solution on conventional blue LEDs. In recent efforts, by constructing novel dual-fluorescence morphologies, white light emission CQDs were synthesized in organic media or polymer matrix [67,68].

16.2.2.2 Photovoltaic solar cell

Exploring the CQDs in the context of optical to electrical signal conversion is also highly desirable for their engagement in solar cell application. PV solar cells are regarded as an essential component in the context of clean and green sources of energy. Over the past two decades, substantial efforts have been devoted to meet the global energy demands. Nevertheless, several important issues such as power conversion efficiency, lower electrode conductivity, biocompatibility, chemical stability, etc., are yet to be addressed to achieve a more sustainable and efficient renewable energy source. To overcome these concerns, CQDs and GQDs have been recently explored in solar cell applications. The prime attraction of using the quantum dots is the size-dependent bandgap tuning property, which is important for tailoring solar cell applications' photoresponse. Further, by virtue of tunable energy bandgap, photon absorption efficiency, multiple exciton generation, electron acceptors, donor ability, etc., CQDs and GQDs have emerged as promising candidates for the technological improvisation of existing PV technologies. For instance, Yuanyuan et al. [69] have reported significantly improved performance efficiency of solar cells by combining CQDs with long persistence phosphors (LPPs) (Fig. 16.5A). They have observed a significant enhancement in performance efficiency and obtained monochromatic green light emission with prepared hybrid nanoarchitectures (CQDs-LPPs). The performance efficiency has been reported as high as 7.97%. Moreover, the report has underlined the usages of such hybrid architectures for generating electricity in all-weather conditions, even with dark conditions. In another effort, Chava et al. [70] have demonstrated PV solar cell based on ZnO photoanode by introducing N-CQDs as sensitizers (Fig. 16.6B). The associated studies have underlined that introducing CQDs can substantially enhance the electron-transportation, diffusion length, and charge collection efficiency. Furthermore, the absorption band spectrum and charge-transfer kinetics can be

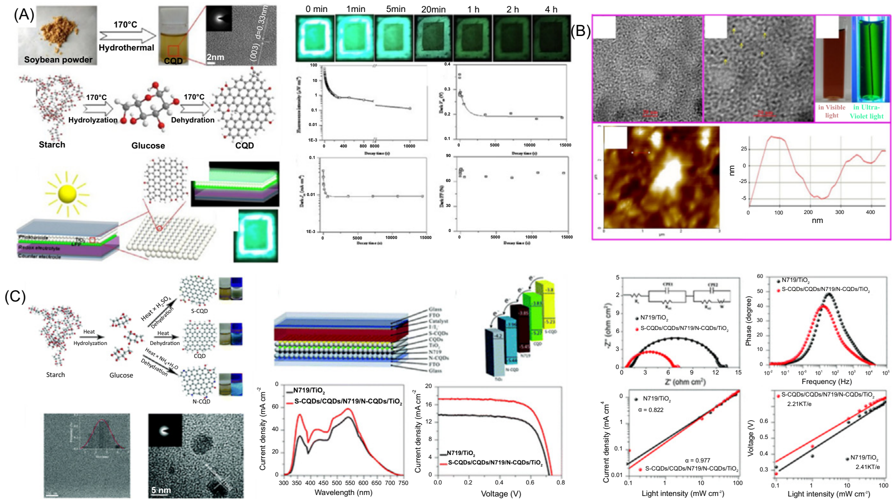

Figure 16.5 Biomass-converted CQDs for solar cells and efficiency characterization. (A) CQDs prepared using soybean starch. (B) Green luminescence emission from nitrogen-doped CQDs. (C) Solar cells via biomass-converted graded CQDs. *CQDs*, Carbon quantum dots. *Source*: Reproduced with permission from Refs. [69−71]. Copyright 2017 Elsevier and 2019 Royal Society of Chemistry.

efficiently controlled with precise control over the shape and size of CQDs for solar cell applications. The implementation of heteroatoms-doped CQDs has also been realized as a novel route to nitrogen-doped based solar cells' defects. Liu et al. [71] have prepared sulfur and nitrogen-doped CQDs and explored dye-based solar cells' performance (Fig. 16.6C). The group has reported a significant enhancement in PV solar cell performance due to enhanced electron extraction and the broad absorption spectrum of the device. Another solar cell enhanced performance efficiency approach has been reported related to engineering the photoanode with CQDs [72,73]. TiO_2 photoanode was modified with CQDs. The resultant PV efficiency enhancement of 7.32% was reported [73].

CQDs were engineered through photophysical and electronic responses for improving PV solar cell conversion efficiency in recent years. For example, Zhu et al. [74] have demonstrated the method of interfacial designing by CQDs inclusion in metal selenide-based counter electrodes, and performance efficiency of 7.01% was obtained. Recently, Ali et al. [75] showed a novel scalable and efficient catalyst by depositing nitrogen-doped CQDs over the multiwall carbon nanotubes. The studies discussed how these electron-rich surface and auxochromic nature of doped nitrogen facilitate significant improvements in these multiwall carbon nanotubes' electronic properties and surface reactivity. Consequently, higher efficiency of 9.28% was obtained compared to the pristine multiwall carbon nanotube counter electrode (6.17%).

16.2.2.3 Memory devices

In recent years, CQDs and GQDs with unique structural and photophysical properties have also emerged as versatile candidates for engagement in random access memory (RAM) applications, such as memristors, memcapacitors, etc. In recent years, several efforts have been reported in this direction. For example, Yang et al. [76] have demonstrated luminescent water-induced shape memory polymer composites with tunable shape recovery rates. Such polymer composites were developed by mixing CQDs in polyvinyl alcohol (PVA). They found that the fluorescent CQDs behave as additional physical cross-linking points in PVA. Consequently, the prepared composite shows an excellent water-induced shape memory performance at room temperature. Zhang et al. [77] demonstrated the engagement of CQDs/PVP hybrid nanolayer for performance improvement of pentacene-based organic field-effect transistor memory (OFETM) device. The researchers have found that the inclusion of CQDs in the PVP layer works as a charge trapping layer, which further improves the OFETM performance. Mihalache et al. [78] have shown CQDs and PEG1500N composite as potential candidates for stable memory effect. They demonstrated a temperature-dependent stable and reproducible resistance hysteresis, which has direct implications for in-memory applications. Interestingly, they also explored that CQDs functionalized with PEG1500N are preferably valid at higher operating temperatures as compared to bare CQD films. Nevertheless, substantial work is yet to be done for insightful understanding and tailoring the photophysical response, fast switching speed, and high-density integration for making these quantum structures compatible with CMOS.

16.2.2.4 Chiral photonics and twistronics

Chiral nanostructures are considered as an integral component of polarization-enabled optoelectronic and nanophotonic applications. Owing to the versatile nature of CQDs such as quantum confinement, edge effects, etc., understanding the manifestation of chirality in these quantum structures would be fascinating for ultracompact devices: sensing, drug delivery, optical switching, optical antenna, biomedical imaging, etc. In recent years, few initial stage efforts have been reported in this direction. For example, Suzuki and co-workers [47] have demonstrated that the covalent edge modification in GQDs and other forms of graphene sheets can lead to nanoscale chirality in these quantum structures due to intermolecular interactions of chiral surface ligands (Fig. 16.6). The group has synthesized chiral GQDs via covalent edge engineering, which leads to the nanoscale twisting of the covalent edge-modified graphene sheets. They further investigated the circular dichroism spectra of the GQDs, which exhibits signs of change for different chirality based on edge modification. In 2020, Tepliakov and co-workers [48] have theoretically studied optical activity at the atomic limit in twisted bilayer GQDs (TBG QDs). They analyzed the chiral optical response of TBG QDs by changing the vertical stacking via AA, AB, and SP in three different shapes (hexagonal, triangular, and rhomboid) of GQDs. Interestingly, they discovered that the strongest dissymmetry in the optical response in these twisted bilayer GQDs can be achieved upon out-of-plane polarized plasmons.

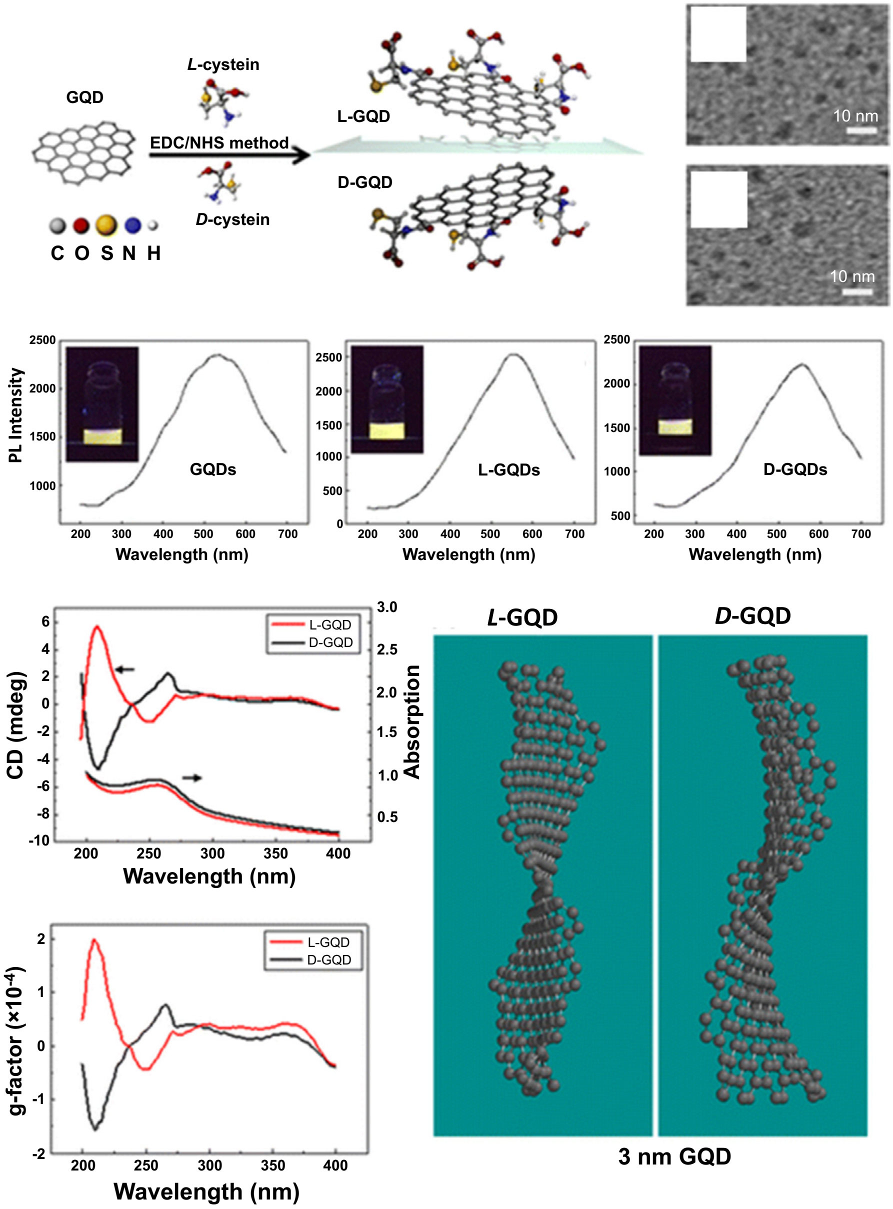

Figure 16.6 Chemical synthesis, optical responses, and circular dichroism characterization of chiral GQDs. *GQDs*, Graphene quantum dots.
Source: Reproduced with permission from N. Suzuki, et al., Chiral graphene quantum dots. ACS Nano 10 (2) (2016) 1744–1755. Copyright 2016 American Chemical Society.

Recently, photonics community has started exploring optical properties by twisting the relative angle between the vertically stacked CDQ layers, i.e., rotational symmetry breaking. Breaking of rotational symmetry in such vertical superlattice is termed twistronics. For instance, Bucko and co-workers [79] have presented a theoretical understanding of bilayer graphene moiré quantum dot structures. Also, Zarenia et al. [80] and Costa et al. [81] have theoretically discussed energy level modulation in triangular and hexagonal bilayer graphene quantum dots under magnetic and electric fields, using tight-binding approach. Further, optoelectronic properties in such twisted bilayer graphene quantum dots have been recently explored by Tiutiunnyk and co-workers [82]. They found that the dot size and geometry play an important role in determining the interband absorption threshold. In the case of armchair triangular bilayer GQDs, smaller twisting angles can moderately increase the optical gap; whereas in zigzag triangular bilayer graphene dots, the twisting originates the evolution zero-gap states associated with HOMO and LUMO states variation due to lifting of zero-energy degeneracy.

16.2.2.5 Toward single/few photons source and cavity-assisted photonics

Recently, exploring the potential of CQDs and GQDs for single/few photons emission gained significant attention from the photonics community. For example, Ghosh and co-workers [46] have explored the effect of the local chemical environment on GQDs (Fig. 16.7A). Further, a single-particle multimodal correlative study discussed how these complex interactions and their local chemical environment regulate their emission states and properties of emission centers in GQDs. Zhao et al. [51] have performed a single-emitter study that directly addresses the intrinsic emission properties of GQDs (Fig. 16.8B). GQDs were synthesized with a bottom-up approach for getting controlled shape and size. They found that the GQDs are efficient and stable single-photon emitters at room temperature. Further, they could control emission wavelength (~100 nm redshift) via functionalization of the GQD edges. Katzen and co-workers [14] have explored CQDs' optical response by embedding these quantum structures in gold plasmonic cavity (Fig. 16.8). They showed that such highly localized optical-field enable the formation of individual CQDs and empower strong coupling between localized surface plasmons and the spontaneous emission of the formed CQDs.

In the end, we would like to emphasize the fact that we could not summarize all the interestingly developments, especially in the context of optoelectronic applications for instance PV solar cells, photodetectors, and energy storage devices, due to the scope of this chapter. This chapter is intended to provide a combined overview of CQD and GQD implications in the context of magnetic and nanophotonics. Therefore the readers are also suggested to refer to the dedicated reviews on these particular topics to obtain a more rigorous overview of these applications, primarily LEDs, photodetectors, and energy storage applications [9,10,13,35,37,83].

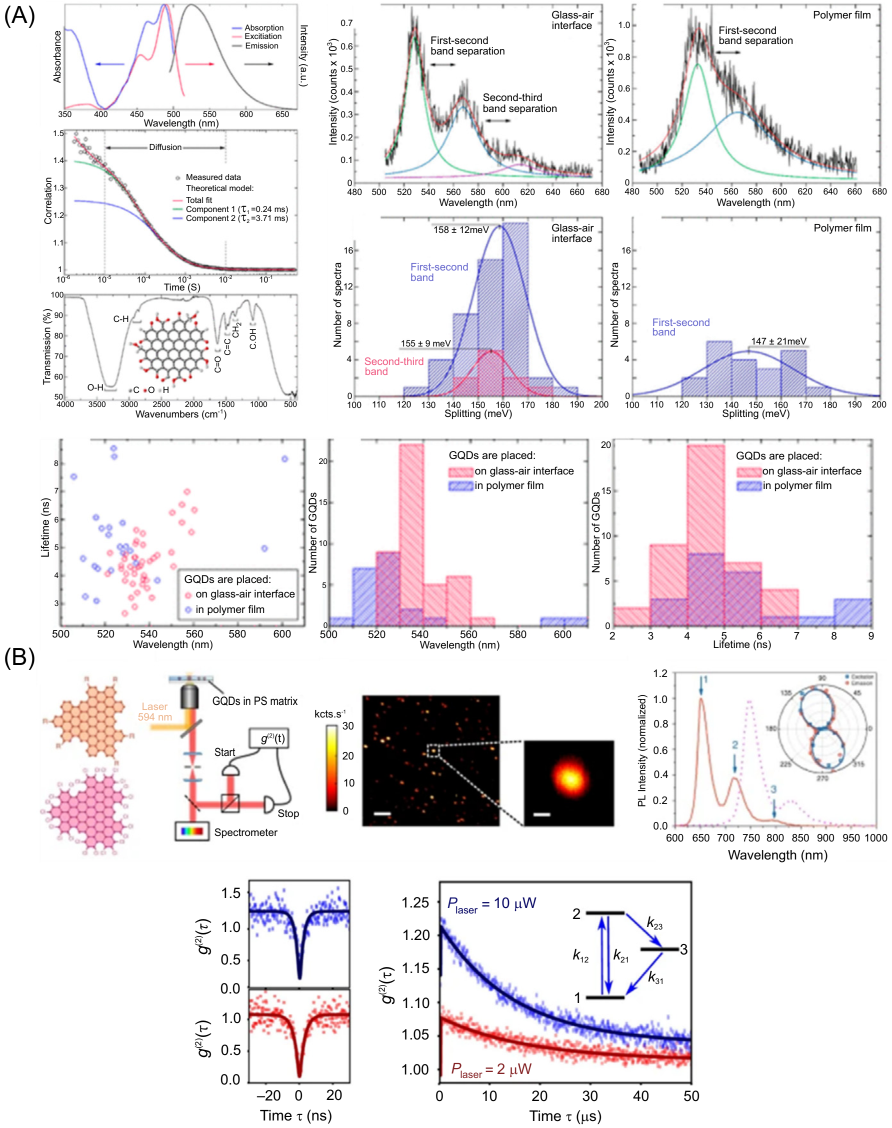

Figure 16.7 (A) Emission states variation and excited-state lifetime distributions in single GQDs. (B) Investigation on single-photon emission from graphene quantum dots at room temperature. *GQDs*, Graphene quantum dots.
Source: Reproduced with permission from S. Ghosh, et al., Emission states variation of single graphene quantum dots. The Journal of Physical Chemistry Letters 11 (17) (2020) 7356–7362; S. Zhao, et al., Single photon emission from graphene quantum dots at room temperature. Nature Communications 9 (1) (2018) 1–5. Copyright 2020 American Chemical Society and 2018 Springer Nature.

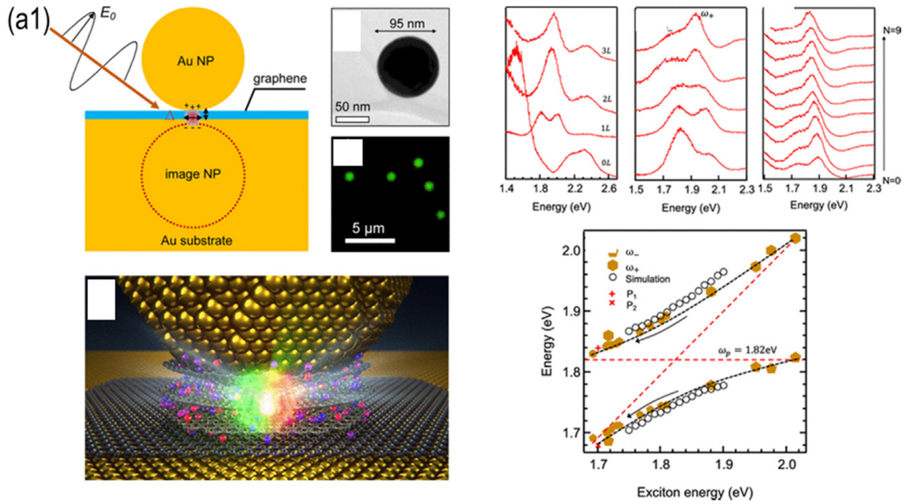

Figure 16.8 Probing the effect of CQDs inside plasmonic nanocavity facilitated hotspot and plexcitons generation. *CQDs*, Carbon quantum dots.
Source: Reproduced with permission from J.M. Katzen, et al., Strong coupling of carbon quantum dots in plasmonic nanocavities. ACS Applied Materials & Interfaces 12 (17) (2020) 19866–19873. Copyright 2020 American Chemical Society.

16.3 Summary and future perspectives

To conclude, we have discussed the recent progress in the field of CQDs with a focus on magnetic, and nanophotonics applications. Since the successful separation of CQDs from SWCNTs, substantial efforts in the context of inexpensive and straightforward synthesis have established these strong and stable luminescent CQDs as interesting nanomaterials as compared to semiconductor-based quantum dots, where strong emission and photostability are highly desirable. Hence, these developments have paved the way for merging optoelectronic, magnetic, and nanophotonic technology, resulting in many exciting applications for the years to come (Fig. 16.9). Our presented discussion on luminescent CQDs also endorses their prospects in technological improvisation for meeting the growing demand for the high performance of advanced electronic and optoelectronic devices. Nevertheless, full-fledged engagement of CQDs still demands significant attention and extensive research, especially in the context of ultracompact magneto-optic, optoelectronic, and nanophotonic applications. Moreover, several unaddressed issues, from both fundamental and application viewpoints, are still waiting to be resolved.

CQDs' photophysical/chemical properties are certainly awe-inspiring in contrast to conventional quantum dots because the optical and electrical response can be efficiently tailored by adjusting their shape, surface functionalization, doping, etc. However, the conclusive evidence and substantial explanation of the photoluminescence emission mechanism is still an unsettled issue among the scientific community.

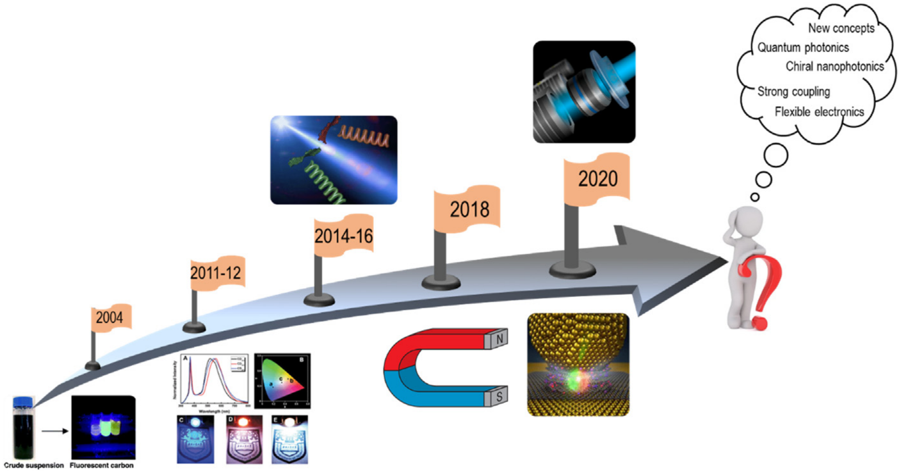

Figure 16.9 Reviewing the timeline of significant achievement of CQDs based in the context of magnetic and nanophotonic applications. *CQDs*, Carbon quantum dots. *Source*: Reproduced with permission from Refs. [10,11,14,16,46,47,84]. Copyright 2012 Royal Society of Chemistry, 2016 MDPI, 2004, 2014, 2016, and 2020 American Chemical Society.

Furthermore, the dependency of this strong and stable luminescence in CQDs on the presence of defects, crystallinity, heteroatoms doping, surface functionalization, etc. is not well understood. Therefore techniques for in-situ CQDs growth are highly desirable for the insightful understanding of these aspects. Additionally, extensive research efforts are imperative to efficiently control CQDs' shape, size, composition, and resultant quantum yield for tunable optical and electronic response at a deep subwavelength scale. In addition, it is worth noting that mostly blue and green light emitted CQDs have been reported, while very few findings associated with highly efficient white light emission have been reported so far.

CQDs and GQDs provide an emerging platform for biomedical applications such as fluorescence bioimaging, drug delivery, and disease diagnosis due to their biodegradability, outstanding luminescence, low toxicity, and excellent electronic and magnetic properties. We have already discussed various applications of CQD decorated nanoparticles and 1D structures in this review. Iron oxide decorated CQDs or GQDs have widely been explored because of their biodegradability. Calcium or magnesium doped iron oxide nanoparticle decorated CQDs and GQDs can also be investigated. The biomedical imaging applications of CQDs and GQDs have not been fully explored, despite the significant advances in recent times. The size, shape, and narrow distribution of GQDs decide the better optical, electronic, and magnetic properties. Thus getting high-quality single layer GQDs is an ideal task that is still challenging, and its large-scale industrial production is desirable. Further research is needed for the industrial and practical applications of CQDs, especially GQDs.

As discussed, CQD electronic and optical responses can be controlled via rational and controlled synthesis of CQD geometries. It would be interesting to explore further the CQDs consisting of core-shell structures and peripheral functionalization. Such efficiently controlled responses have relevance in fundamental optical physics, such as electrical conductivity, widely tunable bandgap, exciton-photon coupling, quantum electrodynamics, etc., and for sensitive photodetectors, low threshold broadband laser sources, ultrafast switching, single-photon emission, super-resolution bioimaging, etc. Such widely tunable bandgap and electrical conductivity can overcome the drawback of graphene in fabricating optoelectronic devices. Furthermore, such well-defined and controlled geometries may facilitate a better understanding of CQDs' photoluminescence emission properties, emission rates, radiative and nonradiative lifetime under complex local chemical environments. Such insightful knowledge would be imperative for conceptualizing efficient single/few photons nanoscale sources with controlled emission properties. Significantly, chiral CQDs and other related architectures would facilitate a novel way to tailor light–matter interaction at the approximately atomic limit. Moreover, controlled synthesis of chiral CQDs and other associated quantum structures can be harnessed as a testbed to realize helical/chiral nanophotonic structures. Owing to good water solubility, CQDs structures can be used to fabricate large-scale robust, flexible photonic structures with ultrasharp bending edges and disorder. Furthermore, chirality in CQDs with the twisted electronic states has opened a new avenue for polarization-sensitive optoelectronic and nanophotonic applications such as encrypted signal processing, complex nanophotonic circuits, quantum information processing, secured data transmission, optical communications, etc. In recent years, the photonic community has also started exploring the optical and electronic responses in vertically stacked CQDs by relative twisting. This could be another interesting direction to explore for spintronics, magneto-optics, valley-selective photonics, etc.

Acknowledgments

BKG acknowledges the funding support from IUAC, New Delhi, for the project fellow position. NK acknowledges DST Inspire Faculty Project grant IFA-216. VS acknowledges Science and Engineering Research Board, New Delhi for providing the Grant under Core Research Grant Scheme (CRG/2020/002826).

References

[1] S.Y. Lim, W. Shen, Z. Gao, Carbon quantum dots and their applications, Chemical Society Reviews 44 (1) (2015) 362–381.

[2] Y. Wang, A. Hu, Carbon quantum dots: synthesis, properties and applications, Journal of Materials Chemistry C 2 (34) (2014) 6921–6939.

[3] R. Jelinek, Carbon quantum dots, Springer International Publishing, Cham, 2017, pp. 29–46.

[4] R. Das, R. Bandyopadhyay, P. Pramanik, Carbon quantum dots from natural resource: a review, Materials today chemistry 8 (2018) 96−109.

[5] P.G. Luo, et al., Carbon "quantum" dots for optical bioimaging, Journal of Materials Chemistry B 1 (16) (2013) 2116−2127.

[6] P. Devi, S. Saini, K.-H. Kim, The advanced role of carbon quantum dots in nanomedical applications, Biosensors and Bioelectronics 141 (2019) 111158.

[7] Y. Dong, et al., Polyamine-functionalized carbon quantum dots for chemical sensing, Carbon 50 (8) (2012) 2810−2815.

[8] M.J. Molaei, Principles, mechanisms, and application of carbon quantum dots in sensors: a review, Analytical Methods 12 (10) (2020) 1266−1287.

[9] M. Droth, G. Burkard, Spintronics with graphene quantum dots, Physica Status Solidi Rapid Research Letters 10 (1) (2016) 75−90.

[10] S. Paulo, E. Palomares, E. Martinez-Ferrero, Graphene and carbon quantum dot-based materials in photovoltaic devices: From synthesis to applications, Nanomaterials 6 (9) (2016) 157.

[11] C. Xie, et al., Core−shell heterojunction of silicon nanowire arrays and carbon quantum dots for photovoltaic devices and self-driven photodetectors, ACS Nano 8 (4) (2014) 4015−4022.

[12] F. Yuan, et al., Bright multicolor bandgap fluorescent carbon quantum dots for electroluminescent light-emitting diodes, Advanced Materials 29 (3) (2017) 1604436.

[13] P. He, et al., Recent advances in white light-emitting diodes of carbon quantum dots, Nanoscale 12 (8) (2020) 4826−4832.

[14] J.M. Katzen, et al., Strong coupling of carbon quantum dots in plasmonic nanocavities, ACS Applied Materials & Interfaces 12 (17) (2020) 19866−19873.

[15] S. Liu, et al., Two-photon saturable absorption properties and laser Q-switch application of carbon quantum dots, Optics Letters 42 (19) (2017) 3972−3975.

[16] X. Xu, et al., Electrophoretic analysis and purification of fluorescent single-walled carbon nanotube fragments, Journal of the American Chemical Society 126 (40) (2004) 12736−12737.

[17] L. Ansari, et al., Doped-carbon dots: recent advances in their biosensing, bioimaging and therapy applications, Colloids and Surfaces B: Biointerfaces (2021) 111743.

[18] Ł. Janus, et al., Chitosan-based carbon quantum dots for biomedical applications: synthesis and characterization, Nanomaterials 9 (2) (2019) 274.

[19] M. Pan, et al., Fluorescent carbon quantum dots—Synthesis, functionalization and sensing application in food analysis, Nanomaterials 10 (5) (2020) 930.

[20] Y. Yan, et al., Recent advances on graphene quantum dots: from chemistry and physics to applications, Advanced Materials 31 (21) (2019) 1808283.

[21] S.N. Baker, G.A. Baker, Luminescent carbon nanodots: emergent nanolights, Angewandte Chemie International Edition 49 (38) (2010) 6726−6744.

[22] A. Begum, et al., Nanocomposites of carbon quantum dots−nickel (ii) dithiolene as nanolights, Journal of Materials Chemistry 21 (48) (2011) 19210−19213.

[23] L. Wang, et al., Full-color fluorescent carbon quantum dots, Science Advances 6 (40) (2020) eabb6772.

[24] Z. Qian, et al., Highly luminescent N-doped carbon quantum dots as an effective multifunctional fluorescence sensing platform, Chemistry−A European Journal 20 (8) (2014) 2254−2263.

[25] X. Shan, et al., B-doped carbon quantum dots as a sensitive fluorescence probe for hydrogen peroxide and glucose detection, Analyst 139 (10) (2014) 2322−2325.

[26] R. Zhang, W. Chen, Nitrogen-doped carbon quantum dots: facile synthesis and application as a "turn-off" fluorescent probe for detection of Hg^{2+} ions, Biosensors and Bioelectronics 55 (2014) 83−90.

[27] Y. Yang, et al., N, P-doped carbon quantum dots as a fluorescent sensing platform for carbendazim detection based on fluorescence resonance energy transfer, Sensors and Actuators B: Chemical 274 (2018) 296−303.
[28] S. Chandra, et al., Tuning of photoluminescence on different surface functionalized carbon quantum dots, RSC Advances 2 (9) (2012) 3602−3606.
[29] Y. Dong, et al., Polyamine-functionalized carbon quantum dots as fluorescent probes for selective and sensitive detection of copper ions, Analytical Chemistry 84 (14) (2012) 6220−6224.
[30] S. Zhu, et al., Photoluminescence mechanism in graphene quantum dots: quantum confinement effect and surface/edge state, Nano Today 13 (2017) 10−14.
[31] L. Tian, et al., Carbon quantum dots for advanced electrocatalysis, Journal of Energy Chemistry 55 (2021) 279−294.
[32] X. Wang, et al., A mini review on carbon quantum dots: preparation, properties, and electrocatalytic application, Frontiers in Chemistry 7 (2019) 671.
[33] Z. Wang, et al., One-step and green synthesis of nitrogen-doped carbon quantum dots for multifunctional electronics, RSC Advances 7 (35) (2017) 21969−21973.
[34] Y. Hu, et al., Carbon quantum dots−modified interfacial interactions and ion conductivity for enhanced high current density performance in lithium−sulfur batteries. Advanced Energy, Materials 9 (7) (2019) 1802955.
[35] A.S. Rasal, et al., Carbon quantum dots for energy applications: a review, ACS Applied Nano Materials 4 (7) (2021) 6515−6541.
[36] F. Yuan, et al., Engineering triangular carbon quantum dots with unprecedented narrow bandwidth emission for multicolored LEDs, Nature Communications 9 (1) (2018) 1−11.
[37] X. Li, et al., Carbon and graphene quantum dots for optoelectronic and energy devices: a review, Advanced Functional Materials 25 (31) (2015) 4929−4947.
[38] T. Yuan, et al., Carbon quantum dots: an emerging material for optoelectronic applications, Journal of Materials Chemistry C 7 (23) (2019) 6820−6835.
[39] W. Chen, et al., Synthesis and applications of graphene quantum dots: a review, Nanotechnology Reviews 7 (2) (2018) 157−185.
[40] S. Chung, R.A. Revia, M. Zhang, Graphene quantum dots and their applications in bioimaging, biosensing, and therapy, Advanced Materials 33 (22) (2021) 1904362.
[41] G.M. Paternò, et al., Large polycyclic aromatic hydrocarbons as graphene quantum dots: from synthesis to spectroscopy and photonics, Advanced Optical Materials 9 (2021) 2100508.
[42] Y. Li, et al., Magnetic graphene quantum dots facilitate closed-tube one-step detection of SARS-CoV-2 with ultra-low field NMR relaxometry, Sensors and Actuators B: Chemical 337 (2021) 129786.
[43] J. Nascimento, et al., Magnetic properties of bilayer graphene quantum dots in the presence of uniaxial strain, Physical Review B 96 (11) (2017) 115428.
[44] T. Espinosa-Ortega, I. Luk'yanchuk, Y. Rubo, Magnetic properties of graphene quantum dots, Physical Review B 87 (20) (2013) 205434.
[45] Y. Sun, et al., Magnetism of graphene quantum dots, NPJ Quantum Materials 2 (1) (2017) 1−7.
[46] S. Ghosh, et al., Emission states variation of single graphene quantum dots, The Journal of Physical Chemistry Letters 11 (17) (2020) 7356−7362.
[47] N. Suzuki, et al., Chiral graphene quantum dots, ACS Nano 10 (2) (2016) 1744−1755.
[48] N.V. Tepliakov, et al., Twisted bilayer graphene quantum dots for chiral nanophotonics, The Journal of Physical Chemistry C 124 (41) (2020) 22704−22710.
[49] M. Vázquez-Nakagawa, et al., Chirality transfer from graphene quantum dots, Chemical Communications 52 (4) (2016) 665−668.

[50] W. Hu, et al., Room-temperature magnetism and tunable energy gaps in edge-passivated zigzag graphene quantum dots, NPJ 2D Materials and Applications 3 (1) (2019) 1−5.

[51] S. Zhao, et al., Single photon emission from graphene quantum dots at room temperature, Nature Communications 9 (1) (2018) 1−5.

[52] D. Carolan, et al., Environmentally friendly nitrogen-doped carbon quantum dots for next generation solar cells, Sustainable Energy & Fuels 1 (7) (2017) 1611−1619.

[53] S.-H. Cheng, et al., All carbon-based photodetectors: an eminent integration of graphite quantum dots and two dimensional graphene, Scientific Reports 3 (1) (2013) 1−7.

[54] S. Wei, et al., Graphene quantum dots prepared from chemical exfoliation of multiwall carbon nanotubes: an efficient photocatalyst promoter, Catalysis Communications 74 (2016) 104−109.

[55] X. Liu, et al., Nitrogen-doped carbon quantum dot stabilized magnetic iron oxide nanoprobe for fluorescence, magnetic resonance, and computed tomography triple-modal in vivo bioimaging, Advanced Functional Materials 26 (47) (2016) 8694−8706.

[56] J. Fang, et al., Graphene quantum dots-gated hollow mesoporous carbon nanoplatform for targeting drug delivery and synergistic chemo-photothermal therapy, International Journal of Nanomedicine 13 (2018) 5991.

[57] M. Hasanzadeh, et al., Graphene quantum dots decorated with magnetic nanoparticles: Synthesis, electrodeposition, characterization and application as an electrochemical sensor towards determination of some amino acids at physiological pH, Materials Science and Engineering: C 68 (2016) 814−830.

[58] H. Ding, et al., Single-atom gadolinium anchored on graphene quantum dots as a magnetic resonance signal amplifier, ACS Applied Bio Materials 4 (3) (2021) 2798−2809.

[59] M. Arvand, S. Abbasnejad, N. Ghodsi, Graphene quantum dots decorated with Fe_3O_4 nanoparticles/functionalized multiwalled carbon nanotubes as a new sensing platform for electrochemical determination of l-DOPA in agricultural products, Analytical Methods 8 (29) (2016) 5861−5868.

[60] P. Ruffieux, et al., On-surface synthesis of graphene nanoribbons with zigzag edge topology, Nature 531 (7595) (2016) 489−492.

[61] Q. Sun, et al., Coupled spin states in armchair graphene nanoribbons with asymmetric zigzag edge extensions, Nano Letters 20 (9) (2020) 6429−6436.

[62] Q. Dai, C.E. Duty, M.Z. Hu, Semiconductor-nanocrystals-based white light-emitting diodes, Small 6 (15) (2010) 1577−1588.

[63] V. Gupta, et al., Luminscent graphene quantum dots for organic photovoltaic devices, Journal of the American Chemical Society 133 (26) (2011) 9960−9963.

[64] X. Zhang, et al., Color-switchable electroluminescence of carbon dot light-emitting diodes, ACS Nano 7 (12) (2013) 11234−11241.

[65] W. Kwon, et al., Electroluminescence from graphene quantum dots prepared by amidative cutting of tattered graphite, Nano Letters 14 (3) (2014) 1306−1311.

[66] L. Tang, et al., Deep ultraviolet photoluminescence of water-soluble self-passivated graphene quantum dots, ACS Nano 6 (6) (2012) 5102−5110.

[67] Y. Chen, et al., A self-quenching-resistant carbon-dot powder with tunable solid-state fluorescence and construction of dual-fluorescence morphologies for white light-emission, Advanced Materials 28 (2) (2016) 312−318.

[68] Y. Wu, et al., White-light-emitting melamine-formaldehyde microspheres through polymer-mediated aggregation and encapsulation of graphene quantum dots, Advanced Science 6 (2) (2019) 1801432.

[69] Y. Meng, et al., Biomass converted carbon quantum dots for all-weather solar cells, Electrochimica Acta 257 (2017) 259−266.

[70] R.K. Chava, Y. Im, M. Kang, Nitrogen doped carbon quantum dots as a green luminescent sensitizer to functionalize ZnO nanoparticles for enhanced photovoltaic conversion devices, Materials Research Bulletin 94 (2017) 399−407.
[71] L. Liu, et al., High efficiency solar cells tailored using biomass-converted graded carbon quantum dots, Nanoscale 11 (32) (2019) 15083−15090.
[72] M.T. Efa, T. Imae, Effects of carbon dots on ZnO nanoparticle-based dye-sensitized solar cells, Electrochimica Acta 303 (2019) 204−210.
[73] B. Rezaei, et al., The impressive effect of eco-friendly carbon dots on improving the performance of dye-sensitized solar cells, Solar Energy 182 (2019) 412−419.
[74] W. Zhu, et al., Carbon quantum dot tailored counter electrode for 7.01%-rear efficiency in a bifacial dye-sensitized solar cell, Chemical Communications 53 (71) (2017) 9894−9897.
[75] M. Ali, et al., Microwave-assisted ultrafast in-situ growth of N-doped carbon quantum dots on multiwalled carbon nanotubes as an efficient electrocatalyst for photovoltaics, Journal of Colloid and Interface Science 586 (2021) 349−361.
[76] G. Yang, et al., Luminescent poly (vinyl alcohol)/carbon quantum dots composites with tunable water-induced shape memory behavior in different pH and temperature environments, ACS Applied Materials & Interfaces 8 (50) (2016) 34744−34754.
[77] W. Zhang, et al., Organic field-effect transistor memory device based on an integrated carbon quantum dots/polyvinyl pyrrolidone hybrid nanolayer, Electronics 9 (5) (2020) 753.
[78] I. Mihalache, et al., Memory effect in carbon quantum DOT−PEG1500N composites, Current Applied Physics 14 (12) (2014) 1625−1632.
[79] J. Bucko, F. Herman, Large twisting angles in bilayer graphene moiré quantum dot structures, Physical Review B 103 (7) (2021) 075116.
[80] M. Zarenia, et al., Energy levels of triangular and hexagonal graphene quantum dots: a comparative study between the tight-binding and Dirac equation approach, Physical Review B 84 (24) (2011) 245403.
[81] D. Da Costa, et al., Energy levels of bilayer graphene quantum dots, Physical Review B 92 (11) (2015) 115437.
[82] A. Tiutiunnyk, et al., Opto-electronic properties of twisted bilayer graphene quantum dots, Physica E: Low-dimensional Systems and Nanostructures 112 (2019) 36−48.
[83] T. Chen, L. Dai, Carbon nanomaterials for high-performance supercapacitors, Materials Today 16 (7-8) (2013) 272−280.
[84] X. Guo, et al., Facile access to versatile fluorescent carbon dots toward light-emitting diodes, Chemical Communications 48 (21) (2012) 2692−2694.

Carbon quantum dots: An overview and potential applications in terahertz domain

17

Suranjana Banerjee
Department of Electronics, Dum Dum Motijheel College, Dum Dum, Kolkata,
West Bengal, India

17.1 Introduction

Quantum dots (QDs) are semiconductor nanostructures whose dimensions are reduced to the level of interatomic spacing. These miniaturized structures have size restrictions in all three directions comparable to the de Broglie wavelength. In other words, the electron energy is quantized in x, y, and z directions with restricted degrees of freedom. Epitaxial growth method and fine line lithography can be used to fabricate semiconductor devices with restricted dimensions in one, two, or three directions of the order of nanometers. Slowly, research interest shifted from bulk semiconductors to low-dimensional semiconductor structures, whose one dimension is reduced to a thickness of the order of de Broglie wavelength. The reduced dimensionality in one, two, and three directions of bulk semiconductor leads to formation of quantum well, wire, and dot, respectively. The electrons are confined to one dimension in quantum well, two dimensions in quantum wire, and three dimensions in QD.

Carbon, being the basic unit of organic compounds, is one of the most indispensable components for all living organisms. Carbon-based nanostructures, particularly carbon quantum dots (CQDs), carbon nanotubes (CNTs), and graphene, have played a pivotal role from the perspective of nanotechnology during the last three decades in various fundamental and applied research across many disciplines of science due to the acclamation of fullerenes, nanotubes, and unparalleled success of graphene. Fullerenes are zero-dimensional (0D), and since their discovery in 1985, fullerenes [1] have shown notable breakthroughs in nanoscience and nanotechnology (Fig. 17.1).

The reason behind the immense interest in miniaturized carbon materials is due to their exceptional electrical, chemical, thermal, and optical properties [2,3]. Nano carbons or carbon nanostructures comprising carbon chains arranged in distinctive geometric patterns also exhibit fascinating photonic and optoelectronic properties as they can conduct electricity and absorb and emit light [4–6]. In-depth knowledge and understanding, futuristic discoveries, and voluminous data are found in the literature, along with the optical techniques in a large spectrum extending from

Carbon Quantum Dots for Sustainable Energy and Optoelectronics. DOI: https://doi.org/10.1016/B978-0-323-90895-5.00002-3
© 2023 Elsevier Ltd. All rights reserved.

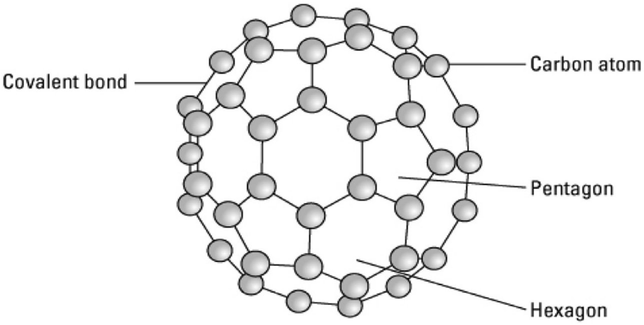

Figure 17.1 Structure of 0D fullerene.

ultraviolet (UV) to terahertz (THz) frequencies. In this chapter, several interesting topics on CQDs have been included, building the platform of current research.

Practical realization of QDs has become a reality due to modern epitaxial growth techniques like molecular beam epitaxy (MBE) and metallo organic chemical vapour deposition (MOCVD), and ultrahigh vacuum chemical vapor deposition methods coupled with very fine line lithography process technology. QD arrays over substrates can be prepared by MBE or lithographic dry etching. The application realm of CQDs extends over a vast area starting from digital, microelectronic, optoelectronic, chemical sensor, bioimaging, nanomedicine, and solar cells to various applications in THz domain.

Electrical characteristics of QDs give a clear view of the atomic picture of the QD, as they behave like artificial atoms with dimensions scaled down to interatomic spacing, or their atomic spectra replicate the energy spectra. But changing the size and shape of the 0D dot within the limit of de Broglie wavelength varies the energy spectrum of QD. For example, single-electron removal from a QD produces some important effects like coulomb blockade effect and conductance oscillation.

Some distinctive properties of CQDs are low toxicity, chemical inertness, superb biocompatibility, high crystallization, good dispersibility, photo-induced electron transfer, and good conductivity. They also exhibit superconductivity, rapid electron transfer, and good photonic and optoelectronic properties. Even quantum confinement in nano carbon dots enables modulation of light-emitting properties. Apart from having a large surface-to-volume ratio, all these interesting properties make CQDs extraordinarily acceptable for THz imaging, thus assisting medical diagnostic procedures. Carbon dots provide information about the type, size, and position of tumors in human body. They can effectively release drugs to discrete parts of human body owing to their important characteristics like good biocompatibility, feeble interaction with proteins, blocks swelling and photobleaching, and easy clearance from the body. CQD sustains cancer treatment by properly identifying the position of tumors in humans and providing information regarding their type and size and also aids in controlled delivery of drugs to various parts of the human body. Different applications of CQDs are shown in Fig. 17.2A and B.

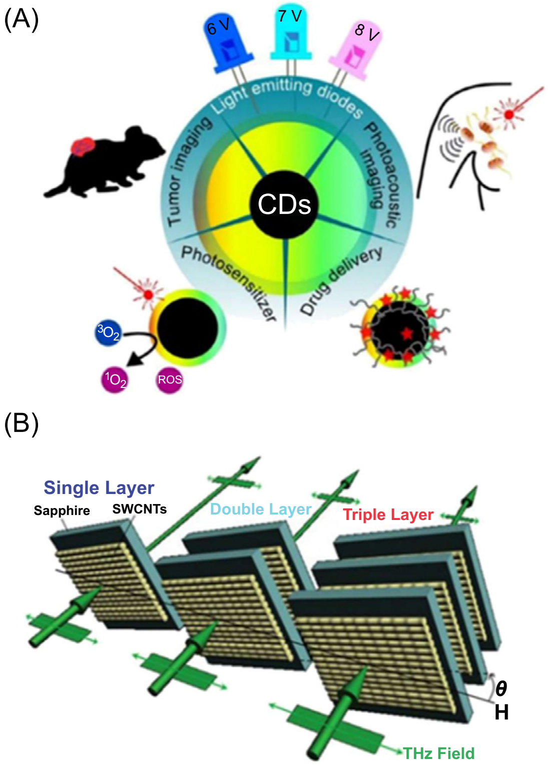
(A)
6 V
7 V
8 V
Light emitting diodes
Photoacoustic imaging
Drug delivery
Photosensitizer
Tumor imaging
CDs
$^3O_2$
$^1O_2$
ROS
(B)
Single Layer
Sapphire
SWCNTs
Double Layer
Triple Layer
θ
H
THz Field

Figure 17.2 (A) Nano carbon dots in light-emitting diode, phototransistor, and bioimaging. (B) High-yield THz polarizers.

These nanosized quantum structures also show nonlinear optical and photonic characteristics that facilitate their use as spectroscopic tools in THz frequency range and also as passive mode-locking devices for generating ultrashort laser pulses having picosecond (ps) and femtosecond (fs) pulse width [7]. Other properties favoring their proper operation are ultrafast saturation behavior and carrier energy relaxation properties [8]. Kono et al. [9] exhibited a THz polarizer manifesting broadband THz properties, 99.9% degree of polarization and extinction ratios of 30 dB in the range from 0.4 to 2.2 THz. Extensive optical and THz spectroscopic inspection reveals the performance characteristics of these carbon nanostructures for brisk optoelectronic and photonic applications.

Owing to all these interesting electronic properties, CQDs have emerged as propitious elementary units for fabricating electronic and optoelectronic solid-state devices. Integrated circuits (ICs) can be further miniaturized using nanocrystallites. Various methods used to develop CQDs are arc-discharge, microwave pyrolysis, hydrothermal, and electrochemical synthesis.

The low-dimensional or miniaturized semiconductor structures are also known as "mesoscopic devices," whose size range from some nanometers to almost 100 nm. They lie between microscopic and macroscopic objects, i.e., dimensionally larger than microscopic devices but smaller than macroscopic devices. The wave property of electrons in these nanostructured electronic and optoelectronic devices gives rise to various quantum effects, which can be explained using quantum physics instead of classical physics.

17.2 Characteristic lengths

The dimensions of the nanostructured materials in which the electron wave is propagating are of the order of or smaller than some "characteristic lengths" as described in this section.

de Broglie's theory of wave-particle duality suggests that electrons in low-dimensional structures having size in the range of 10−100 nm display wave-like properties. These structures are classified based on the number of directions in which the size of the nanostructure is confined. If the size is restricted to de Broglie wavelength or less in one dimension, the electron is free to move in the other two dimensions according to quantum mechanical theory. This gives rise to quantum well. On the other hand, electron motion is free in one direction but restricted in two directions in a quantum wire. In the same way, the structure in which electron motion is restricted to the size of de Broglie wavelength in all three dimensions is called QD. Some characteristic lengths determine the spatial dimension of the structure in one, two, or three directions. These characteristic lengths are (1) de Broglie wavelength, (2) mean free path (MFP), (3) diffusion length, (4) screening length, and (5) localization length. Various fascinating properties are manifested by the electrons embedded in such low-dimensional nanostructures, which can be explained by quantum mechanical theory.

The characteristic lengths are as follows:

1. de Broglie wavelength.

de Broglie formulated his famous theory of wave-particle duality according to which particles like electrons moving with a velocity v and having a momentum $p = mv$ exhibit wave-like behavior similar to electromagnetic waves in a waveguide.

The wave associated with the electrons of momentum p has a wavelength called de Broglie wavelength given by

$$\lambda_e = \frac{h}{p} = \frac{h}{m * v} \tag{17.1}$$

where p is the momentum, m^* is the effective mass, and v is the thermal velocity of electron.

Free electron mass is replaced by effective mass m^*, which considers the effect of periodic potential of crystal on the motion of the electron.

The thermal velocity of electrons in a semiconductor at room temperature is of the order of 10^5 m/s. The effective mass of electrons in silicon is 0.26 m_0, where m_0 is the free electron mass. Thus, de Broglie wavelength of electrons in silicon is

$$\lambda_e = \frac{h}{m * v} = \frac{6.624 \times 10^{-34}}{0.26 \times 9.11 \times 10^{-31} \times 10^5} = 2.8 \times 10^{-8} \ \text{m} = 28 \ \text{nm} \tag{17.2}$$

Quantum effect appears in those semiconductor structures where the dimension is commensurate with the de Broglie wavelength, which is inversely related to the effective mass, as clear from the earlier example; hence, nanostructures having smaller effective mass will have a noticeable quantum effect.

2. Mean free path.

Electrons moving in a perfect crystal without any imperfection like impurities, defects, lattice vibrations (phonons), etc., resemble movement in vacuum with a mass differing from the rest mass. In contrast, those moving in a real crystal with various imperfections suffer scattering with impurities, phonons, and defects. This scattering from one state to another is inelastic with the change in energy and momentum. The path or distance traveled by an electron between two successive inelastic collisions is called MFP, l_m. If the momentum or energy relaxation time between two scattering events is τ_e, then

$$l_e = v\tau_e \tag{17.3}$$

where v is the thermal velocity of electrons.

3. Diffusion length.

Electrons in a nanostructured semiconductor move either by a diffusion process or ballistic process, which depend on length L and MFP, l_e. In ballistic motion, as observed in a hot-electron transistor, the MFP, l_e, is much greater than the dimension L, and the electrons move throughout the structure without suffering any collision or scattering with impurity, phonon, defect states, etc. In this transport, "velocity overshoot" is exhibited in hot-electron transistor that indicates with increasing electric field, drift velocity overshoots to a peak value before saturation. In this case, electron energy exceeds lattice thermal energy. Ballistic transport of electrons is not controlled by Boltzmann model, contrarily diffusion process of electron transport in which $l_e \ll L$, is governed by Boltzmann transport theory.

The diffusion length is the distance the carrier travels before it makes a collision. If the diffusion coefficient be D, then

$$l_e = D\tau_e \tag{17.4}$$

where τ_e is the relaxation time for electrons.

4. Screening length

Screening length is the distance within which free electrons get scattered by nearby positively charged donor ions due to Coulomb potential within a certain distance from the ionized impurity. The Coulomb field of "hydrogenic" type of impurities is screened by other free electrons, and the potential due to the impurity instead of varying with distance as $1/r$ follows the law:

$$V(r) = -\frac{e^2}{4\pi\varepsilon r} e^{-\frac{r}{\lambda_s}} \tag{17.5}$$

where λ_s is called the screening length given by:

$$\lambda_s{}^2 = \frac{\varepsilon kT}{ne^2} \tag{17.6}$$

where ε is the dielectric constant of the semiconductor, n is the average background carrier concentration, and e is the electronic charge. The screening length in a semiconductor varies from 10 to 100 nm. In metals, λ_s is much smaller since it is inversely dependent on electron density n.

5. Localization length

In disordered semiconductors, the electrons hop from one localized state to another or a bound state. In this transport, the electron wave function is not purely a Bloch function and is given by

$$\psi = e^{-\frac{r}{\lambda_l}} \tag{17.7}$$

where λ_1 is known as localization length. Overlap between wave functions determines the conductivity of a material. The dimension of nanoscale semiconductors is of the order of screening length.

17.3 Quantum dot

In quantum wells and wires, electron movement is restricted in one and two dimensions, which leads to quantization of electron energy in 1D and 2D sub-band in wire and well, respectively. But nanostructured semiconductors having electron confinement in all three directions have been possible to cognize due to various advanced methods of growth and lithography. These 0D structures are better known as QDs in which all three degrees of freedom are restricted and whose dimensions are comparable to de Broglie wavelength. So, QDs can be thought to be artificial atoms as their dimensions are of a very small magnitude of the order of 1 Å, which is one order lower than de Broglie wavelength, and their energy spectrum bear a resemblance to that of an atom. This energy spectrum can be altered by varying the size and shape of the dot while keeping all three dimensions comparable to the de Broglie wavelength. The charging energy of the dot is analogous to the capacitor's charging energy, also called ionization energy, and is defined as the energy necessary to remove an electron from the dot or add it to the dot. In the case of a capacitor, some energy is to be spent to add a charge to it due to coulomb interaction of the charges stored in it. So, the electrical properties of the QD give a clear idea about the atomic representation of the QD. Some important phenomena like Coulomb blockade effect and conductance oscillation are observed in a QD on withdrawal of a single electron.

The energy spectrum of QD (0D system) can be obtained from the solution of time-independent Schrodinger's equation by imagining that the electrons are confined in a quantum box of all three dimensions comparable to de Broglie wavelength with a confining potential $V(x, y, z)$ that restricts electron wave propagation in all directions.

Schrodinger's equation for a quantum box can be expressed as:

$$\left[-\frac{\hbar^2}{2m_e{}^*}\left(\frac{\delta^2}{\delta x^2}+\frac{\delta^2}{\delta y^2}+\frac{\delta^2}{\delta z^2}\right)+V(x,y,z)\right]\psi_{m,n,p}(x,y,z)=E_{m,n,p}\psi_{m,n,p}(x,y,z) \tag{17.8}$$

Let us consider that the box is a parallelepiped of dimensions l_x, l_y, and l_z whose walls are impenetrable to the electrons. Thus, the potential is zero inside the box and infinite outside. The boundary conditions are as follows:

Inside the box,

$$V(x,y,z)=0 \text{ for } 0\le x\le l_x, 0\le y\le l_y, 0\le z\le l_z \tag{17.9}$$

Outside the box,

$$V(x,y,z)=+\propto \text{ for } x\le 0, x\ge l_x, y\le 0, y\ge l_y, z\le 0, z\ge l_z \tag{17.10}$$

Solution of Schrodinger's equation for a quantum box subject to the earlier boundary conditions gives rise to a stationary wave for the electron wave function as:

$$\psi_{m,n,p}=\left(\frac{8}{l_x l_y l_z}\right)^{\frac{1}{2}}\sin\left(\frac{m\pi x}{l_x}\right)\sin\left(\frac{n\pi y}{l_y}\right)\sin\left(\frac{p\pi z}{l_z}\right) \tag{17.11}$$

The energy levels of electrons are obtained as:

$$E_{m,n,p}=\frac{\hbar^2\pi^2}{2m_e{}^*}\left(\frac{m^2}{l_x{}^2}+\frac{n^2}{l_y{}^2}+\frac{p^2}{l_z{}^2}\right) \tag{17.12}$$

In Eq. (17.12), m, n, and p are positive integers.

The electron energy spectrum in a QD takes up discrete values in all three directions. This signifies that the electrons in a dot are unable to propagate freely in any direction, just like an atom. The energy levels of QD become degenerate when two or three dimensions of the box become equal.

17.3.1 Density of states of electrons in quantum dots

The energy of electrons in 0D QDs is quantized in all three directions. Electrons in these dots cannot move freely in any direction. In contrast to 2D quantum well and

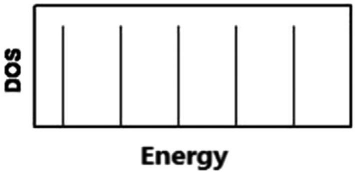

Figure 17.3 DOS of electrons in 0D QD.

1D quantum wire, the energy spectrum of electrons is discrete and designated by three quantum numbers as given in Eq. (17.12).

$$E_{m,n,p} = \frac{\hbar^2 \pi^2}{2m_e^*}\left(\frac{m^2}{l_x^2} + \frac{n^2}{l_y^2} + \frac{p^2}{l_z^2}\right) \tag{17.13}$$

The density of states (DOS) function of electrons in a QD can be therefore written in terms of delta function as:

$$\rho_{0\text{-}D}(E) = \sum_{m,n,p} \delta\left(E - E_{m,n,p}\right) \tag{17.14}$$

The contribution to the summation comes only when the total energy of the electron (E) is equal to sub-band energy corresponding to $E_{m,n,p}$, where m, n, and p take only integer values. Thus, the DOS function of electrons in an ideal 0D QD display impulse train containing impulses of infinite height and infinitesimally narrow width shown in Fig. 17.3. But in the practical case, these sharp discretized impulses get broadened with finite height and width. This happens due to electron scattering by defects, impurities, lattice defects, and phonons. Thus, it can be deduced from these facts that as the dimension reduces from 3D to 0D, DOS function of electrons get more discretized, starting from a continuous parabolic shape in 3D nanostructure to an impulse function shape in 0D structure.

17.4 Fabrication techniques of quantum dots

Different fabrication techniques of QDs are (1) physical, (2) chemical, and (3) self-assembled growth techniques. The physical method of fabrication of QDs involves fine line lithography (FLL) and advanced dry etching technique. Although this method is very much attuned to the microelectronic process technology, the size of QDs produced is not low enough to show quantum size effect. Scanning tunneling microscopy (STM) and atomic force microscopy (AFM) can be used to create QDs with size quantization.

The chemical method to grow QDs includes formation of QDs in gas phase by laser vaporization or as colloids in suspension.

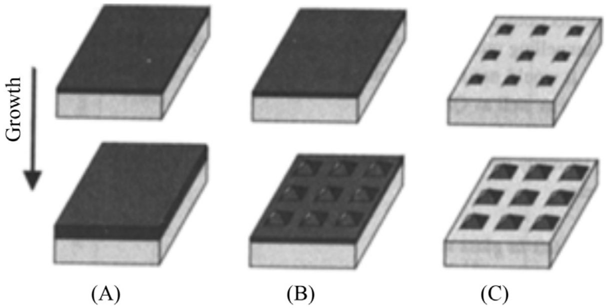

Figure 17.4 Possible growth modes: (A) monolayer by monolayer (B) S-K mode (C) V-W mode.

The self-assembled growth method of these quantum nanostructures is conformable to the fabrication technique of modern microelectronic and optoelectronic devices, which has led to heightened interest and acceptability of the particular growth technique, especially after the success of this technique in 1990. Lattice mismatch and strain energy determine the mode of operation of the self-assembled growth technique, as discussed here. Firstly, if the lattice constant of the epi layer perfectly matches with the lattice constant of substrate, then single layer-by-layer growth of epitaxial layer over the substrate takes place all over as shown in Fig. 17.4. Secondly, if there is a slight variation in lattice constants of the epitaxial layer and the substrate, then initially single layer-by-layer growth occurs, but after a certain time, the layer will start growing in island mode so that the lattice strain energy is minimized as shown in Fig. 17.4. This growth method is known as Stranski-Krastanow (S-K) mode. Thirdly, with increasing lattice mismatch, instead of single-layer growth, direct nucleation of the islands commences in the initial phase itself, known as Volmer-Weber (V-W) mode. This particular growth method is determined by the lattice mismatch, measured by the misfit factor and the lattice strain energy for the growth. Quantum size effect is clearly discernible in QDs manifesting S-K mode of self-assembled growth technique. Practical perception of self-assembled QD lasers based on heterostructures like InGaAs/GaAs, SiGe/Si, and CdSe/ZnSe is possible by S-K growth mode.

17.4.1 Quantum dots based on II–VI compound semiconductors

Nanocrystals made with semiconductors belonging to group II–VI of the periodic table like CdS and CdSe use very simple preparation methods with supersaturated viscous solutions and insert them into glass matrices. These nanocrystalline dots also enable the production of various colored filters and photochromatic glasses, which have numerous applications in various industries and technology. Additionally, doped glasses can be made by fusion of glasses using these group II–VI compound semiconductors as dopants. However, altering the bandgap absorption edge and glass color alters the size of the dots.

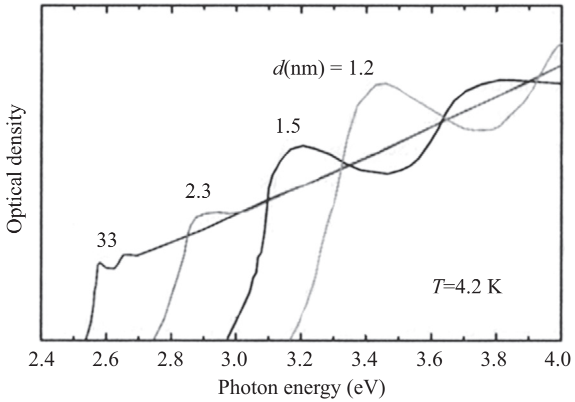

Figure 17.5 Absorption spectra of CdS nanocrystals of different sizes in a glass matrix.

Fig. 17.5 displays the absorption spectra of CdS nanocrystals of varying sizes inserted inside the glass matrices.

When optical density is varied with respect to photon energy (Fig. 17.5), a shift of the peak of the graphs is observed toward high energy values with the decrease in size of the dot due to quantum size effect, and the energy spectrum of the dots shows the same result. If the nanocrystal is made from a combination of CdS and CdSe having bandgaps of 2.6 and 1.75 eV, respectively, then full coverage of the visible optical spectrum can be obtained. Empedocles and his research group studied the absorption spectra of CdSe using single dot spectroscopy. The absorption spectra of CdSe dot nanocrystal (top) with a mean size 3.9 nm and that of a large ensemble of nanocrystals (bottom) are shown in Fig. 17.6, which shows a striking difference between the two spectra.

17.4.2 Self-assembled quantum dots

In self-assembled growth technique of dots, a slight discord of the lattice constant of the substrate and epi layer results in strain energy which is minimized by the growth of the epi layer in 3D island mode called S-K mode. This growth in 3D island mode can be discerned by transmission electron microscopy of high resolution. QD growth on InAs or GaAs substrate is an example. Research inspiration in the photonic properties of QDs increased abundantly due to success in the development of self-assembled dots since 1994. This enabled the accomplishment of practical QD lasers with InGaAs/GaAs material using MOCVD technique. Spectral representation of photoluminescence (PL) and electroluminescence (EL) properties of InGaAs/GaAs QD laser is shown in Fig. 17.7.

PL spectrum of the dots shows a vast distribution as compared to their EL spectrum due to the wide distribution of dot size. Contrasting the absorption spectra of QDs with superlattice shows that PL peaks of QDs appear at lower energies than that of superlattice, which occurs as the size of QDs is larger compared to the period of SL.

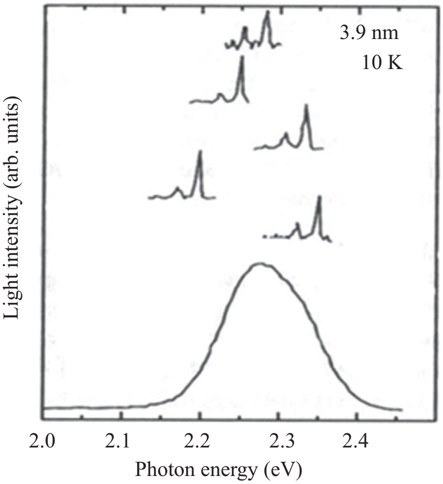

Figure 17.6 CdSe single nanocrystal absorption spectra with an average size of 3.9 nm (top) and that of a large ensemble (bottom).

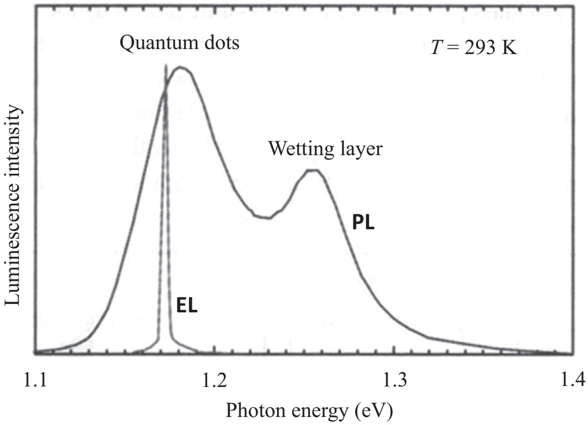

Figure 17.7 PL and El spectra of InAs/GaAs quantum dots grown by MOCVD.

17.5 Optical properties of quantum dots

The electrons in carbon nanostructures, specifically CQDs, have dimensions comparable to the de Broglie wavelength and they are quantized in all three directions. Even the energy levels of QDs are distinct and confined in three dimensions, hence appearing as discrete bound states just like isolated atoms. This complete caging of the dots in three dimensions give rise to some important optical properties discussed in the following section.

1. **Widening of bandgap**

   Bandgap widening is a phenomenon in QDs where the effective bandgap for optical absorption and emission increases due to photonic transition between the conduction and valence band energy levels. Size of the QD greatly influences the photonic properties of the dot.

   Let us consider a spherical dot of nanodimensional radius R. The different regions referring to the optical properties of QDs depend on the relative magnitudes of dot size R, and the exciton size defined by its Bohr radius R_B is given by:

   $$R_B = \frac{\hbar^2}{4\pi\varepsilon_0\varepsilon}\frac{1}{m_{er}e^2} \tag{17.15}$$

   where m_{er} is the reduced mass of the exciton given by:

   $$\frac{1}{m_{er}} = \frac{1}{m_e^*} + \frac{1}{m_h^*} \tag{17.16}$$

   The exciton, which is a bound electron-hole pair, is immersed in a semiconductor medium with permittivity, $\varepsilon_r\varepsilon_0$ where ε_r is the high-frequency relative permittivity of the semiconductor and ε_0 is the permittivity of vacuum.

   The electrons' strong and weak enclosure regions are elucidated as $R < = 2R_B$ and $R > = 4R_B$, respectively. The coulombic interaction energy exerted on the exciton is inversely proportional to the Bohr radius of the exciton, while the confinement energy QD is inversely proportional to the square of the QD size. So, the excitonic effect is not conspicuous compared to carrier confinement. In other words, in the strong confinement mode, the confinement energy shows a marked effect compared to the coulombic interaction energy. CdS dots with a size less than 50A^0 manifest these optical effects better as their excitonic Bohr radius is nearly 29A^0. Weak confinement region is defined in the region where $R > = 4R_B$. The Bohr radius of dots made with copper halides like CuCl and CuBr is of the order of 1 nm, which is appreciably small and hence is used in the weak confinement region. The transitional region from weak to strong confinement is not well defined, so theoretical analysis of this region is quite difficult.

2. **Increase of oscillator strength for phototransition**

   The oscillator strength for photonic transition is highest for 0D, while lowest for 2D QD as this depends inversely on the dimension of the nanostructure. As the dimension gradually decreases from 3D to 0D, energy concentration increases for the allowed energy states. This happens due to strong dependence of energy of DOS function. With respect to sharpness of energy levels, the behavior of QDs resembles that of atoms. So, the oscillator strength is highest for 0D structure, which plays a pivotal role in optoelectronic devices based on 0D structure. This finds application in QD laser, which provides very large optical gain due to highly concentrated energy level, and in 0D electro-optic modulator with quantum well structure.

3. **Phototransition in QDs**

   Quantum well nanostructure shows polarization of incident light in the direction in which the electron energy is quantized, i.e., in the z-direction if the incident light propagates in the x-y plane. This gives rise to another important effect of interband photonic transition in these nanostructures. Now for QDs, electron energy is quantized in all three dimensions. So, incident light can be polarized in any of three dimensions leading to phototransition in QDs.

4. **Broadening of spectral line width in QDs**

For QDs, electron energy is quantized in all three dimensions, so electron states are not continuous for optical transition to occur, which is not the case for 1D and 2D nanostructures as there the energy states are continuous in one and two directions, respectively. This nonobtainability of continuous states in dots makes their spectral line width independent of temperature. These spectral line widths of dots are quite narrow, having energy concentrated in a very small yet finite width of 0.01 eV approximately due to the nonuniform dot size in various dimensions. Spectral line width of dots cannot come much below 0.01 eV, even though they are more or less homogeneous. But for dots with wide distribution in size in different dimensions, line width increases to 0.01 eV, which is called broadening of spectral line width in QDs. Variation in dot composition also affects the spectral line width. A slight variation in dot composition causes the bandgap of QDs to change, resulting in spectral broadening. Spectral line broadening is also caused by interface surface and defect states. Single dot spectroscopy technique enables the study of the intrinsic properties of QDs without taking into account the effect of spectral line broadening. The following subsections will provide a review study of the optical properties of some QD systems.

17.5.1 Optical properties of indirect gap nanocrystal

The domain of Si photonics was in the latent stage until 1990, when notable PL properties were observed from Si nanocrystal by Canham. Fig. 17.8 shows enhanced phototransition from a Si nanocrystal. Prior to that Si, being an indirect bandgap semiconductor, was considered to be incompetent as an optoelectronic material as indirect photonic transition reduces the light-emitting efficiency of Si LED or Laser. But the use of Si QD changes the scenario as optical bandgap and various photonic properties of Si QD get amended due to the quantum size effect on the dot. Decrease of dot size results in a blue shift of emission wavelength and increases the magnitude of quantized energy of QDs as visible from the experimental reports. Single-crystal Si when dipped into an electrolyte of HF and ethanol mixture using proper electrodes results in porous Si, which shows PL in the visible

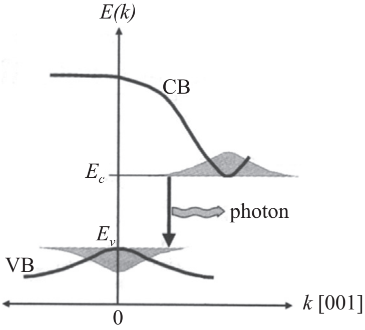

Figure 17.8 Enhanced phototransition in a silicon nanocrystal.

region. This porous Si contains 0D and 1D structured nanocrystals. Quantum size effect in porous Si causes PL and the emission spectrum is widely distributed representing Gaussian distribution. This quantum size effect is also observed in superlattices made with Si/Ge heterojunction. This heterojunction is also used to fabricate heterojunction bipolar transistor (HBT) having a high current gain. Strained Si/Ge heterojunction finds many applications in various devices that can be fabricated by suitably utilizing the difference of lattice constant and bandgap of Si and Ge.

17.6 Applications of carbon quantum dot in the biomedical field

CQDs have become an excellent choice for biomedical applications due to their important properties like slight toxicity, high hydrophilicity, water-solubility, chemical stability, and excitation wavelength-guided PL emission. Among them, the most important characteristics of CQDs like small size and biocompatibility have made them suitable as drug delivery vehicles that can be efficiently scanned inside the body owing to their PL characteristics. Thereafter, the important biomedical applications will be focused upon.

17.6.1 Optical imaging

Nanoparticles can effectively detect cancer cells in combination with peptides, antibodies, and other molecules. These include iron oxides and nanoparticles for drug delivery, QDs for bioimaging, and various molecular diagnosis. Continuous tracking of dynamic processes in a particular system for its statistical characterization can be done by single-particle tracking (SPT) technique which enables tracking of the functional behavior of a single molecule. Dots have immense applications in bioimaging field as fluorophores due to their significant photonic characteristics like broad absorption and narrow emission spectra, and high quantum yield (QY). QDs with uniform chemical composition but varying sizes exhibit fluorescence emission at different wavelengths. This occurs due to quantum confinement in dots, which restrains the number of possible energy states of an electron. Diminishing the size below the exciton Bohr radius, which is a characteristic distance of the electron-hole pair, distinct energy levels are observed in dots which results in enhancement of bandgap, hence the fluorescence emission. QDs have vast applications in bioimaging, biodiagnostics, and imaging probes in vitro/in vivo studies. Molecular and cellular mapping of human cancer samples can be done by multiplexed conjugates of QD antibodies. Single-particle tracking based on QDs can be used for the cell membrane or different intracellular parts [10], and those based on CdS, CdSe, CdTe, PbS, and MoS_2 [11−15] can be used for optical bioimaging. Nanoparticles based on semiconductor materials have a core size in the range 4−10 nm. But to make the QDs stable and biocompatible, they must have a coating or shell covering over them that increases their size to 10−30 nm, which becomes a challenging task. This reduction of size and different bioconjugation approaches have enlightened different dimensions of research in this domain [10]. Moreover, nanodots based on semiconductor material face the limitation of blinking [16], which causes fluctuation in the emission of fluorophores that hinders biological applications of fluorophores at the single-molecule level. But carbon nanodots surpass all the materials for cell and tissue imaging due to their various advantages along with being non-blinking. Unfamiliar approaches can be used for the coalescence of carbon nanodots with fluorescence in the red and near-infrared regions of the electromagnetic spectrum, which is significant with respect to decreased interference with background fluorescence and in penetration of tissues [17].

In vitro imaging: Carbon dots are successfully used for in vitro imaging, as inferred by several researchers [18–30]. Various interesting properties of dots like increased brightness, imaging sensitivity, photostability, and better resistance to metabolic degradation have increased their acceptability compared to organic dyes and fluorescent proteins. Semiconductor dots like CdSe with the core-shell structure containing CdSe/ZnS have been used for in vivo or in vitro bioimaging. But, QDs containing carbon are biocompatible and competitively ranked higher than CdSe/ZnS QDs, mainly owing to the toxicity of cadmium-based QDs. Furthermore, CQDs are smaller in size, less than 10 nm, whereas commercial QDs are larger in size, more than 20 nm. This small size of CQDs is advantageous as they can probe small biological structures and a minimal volume of in vivo injections [31]. Cao et al. amalgamated carbon dots with strong luminescence with two-photon excitation in the near-infrared (NIR) region and used poly(propionyl ethylenimine-*co*-ethylenimine) for their surface passivation. It was seen that two-photon absorption cross-sections of the synthesized and passivated CQDs were comparable with those of semiconductor QDs. Carbon dots with a size of less than 5 nm were soluble in water. It is also apparent from the two-photon excitation that the power of the pulsed infrared laser used as the excitation laser controls the luminescence intensities in CQDs. Optical characteristics of CQDs get modulated due to surface passivation [32,33,1,22]. Maltose was treated under microwave environment, and thereafter, passivation with dilute NaOH solution built CQDs. NaOH treatment adjuncted −OH groups on the sp^2 hybridized carbons amounting to increased QY. Observation shows entry of carbon dots into the cells with green emission of fluorescence but unchanged cell viability even after 24 hours of incubation with the dots [32]. Other experimental observations reveal modulation of both fluorescence intensity and emission wavelength by surface passivation.

Bioimaging applications of carbon nanodots are not restricted to smaller size less than 10 nm. Reports [34] reveal that carbon nanoparticles with a mean particle size of 70 nm can also emit fluorescence and find application in bioimaging. After breeding human cervical cancer cells or HeLa cells with carbon nanoparticles, intracellular fluorescence was seen. Fluorescence was also observed from perinuclear regions of the cytosol with confocal laser microscopy, which affirms excellent cell permeability of the carbon nanoparticles into the cells. Uniform distribution of fluorescence intensity in the tissue verifies tissue permeability for carbon nanodots which can be effectively and safely used for tissue imaging of human tumor tissues

(MCF-7). Carbon nanoparticles have photostability with low bleaching and no blinking [34], useful for bioimaging applications. They have low cytotoxicity even if they are produced from toxic ingredients. For example, nanodots obtained from halophenols (a group of industrial pollutant) residual were used as fluorescent labeling agents. Plants, fruits, and food products such as orange juice [35], apple juice [36,37], cabbage [38], *Carica papaya* juice [39], banana juice [40], unripe peach [41], waste frying oil [42], milk [43], soy milk [44], honey [45], egg [46], flour [47], coffee grounds [48], sugarcane bagasse pulp [49], etc. have also been used as the carbon source in the production of carbon dots. Using natural sources and food products results in lower toxicity of the amalgamated nanodots for biomedical applications.

Photoluminescence characteristics of carbon nanodots can be strengthened by N-doping and low oxidation levels, which have even extended the application domain of CQDs. Improved resolution of the images resulted in higher PL efficiency and even higher QY (approx. 36.3%). Fluorescence images of human HeLa cells using an excitation wavelength of 355 nm and labeled with N-doped carbon dots were brighter as compared to the dots breeded with only the cells. Furthermore, N-doped carbon dots could do the labeling at a lower dosage and had better resistance to photobleaching [50]. Experimental reports [34] show that imaging of HeLa cells bred with N-doped carbon nanodots could be done with N-doped carbon nanostructures made from hydrothermal treatment of cocoon silk in water. The applied nanodots for bioimaging have outstanding photostability along with low bleaching and no blinking. Fluorescence property of CQDs is pertinent in the NIR region (wavelength of 700−900 nm) imaging which has the merit of an ideal tissue transparency window for bioimaging in vivo. As we go to higher wavelength side of the electromagnetic (em) spectrum, fluorescence emission of carbon nanodots becomes feeble, but the signal-to-noise ratio would be improved due to decrease in the tissue autofluorescence by excitation at the red and near-infrared regions of the em spectrum. Higher wavelengths also enable better photon-tissue penetration in bioimaging which is another cause for choosing this NIR region of the spectrum for imaging [51].

In vivo imaging: CQDs are used extensively for in vivo imaging too [52−57]. Slight toxicity of CQDs makes them worthier for in vivo imaging as compared to other heavy metal-based QDs, and they are also probable of emission when energized in UV or NIR portions of the em spectrum. Higher wavelengths are favored for in vivo optical imaging due to increased photon-tissue penetration and decreased of autofluorescence, and hence, enhanced signal-to-noise ratio, although emission becomes frail at higher wavelength. CQDs have enhanced absorptivity which places them at a higher place in the competition with respect to other commercial QDs as regards bioimaging but QY gets compensated. Small size of CQDs is beneficial for tracing small molecules, proteins, and fine biological structures [31]. Surface passivation has a clear effect on the fluorescence properties of the CQDs. As an example, NIR emission of CQDs passivated with hyperbranched polymer enhanced with respect to CQDs coated with linear polymer. Fluorescence characteristics of CQDs can be further improved by doping the dots with inorganic salts like ZnS for in vivo bioimaging.

17.6.2 Photoacoustic imaging

Carbon nanodots act as NIR light excited photoacoustic (PA) imaging in vivo. PA imaging unifies photonic excitation with ultrasonic detection resulting in imaging beyond photonic imaging diffusion limits. Hence, the unification of fluorescence and PA imaging in a single probe gives rise to deeper tissue penetration with high imaging sensitivity [58].

17.6.3 Drug delivery

Drug delivery systems (DDSs) carry a drug to a certain target in the body with the aid of designing systems and proper association of the drug with the target. Nanoparticles coupled with the drug can upgrade the overall system regarding absorption, distribution, and elimination of the drugs [59]. Improved dispatch of drugs with low water-solubility, delivery of two or more drugs or therapeutic modality for different therapy simultaneously, transferring of large macromolecule drugs, and monitoring of the drug site using imaging agents on the drug carrier is made possible by the employment of nanotechnology to DDSs that resulted in drug targeting to a specific cell or tissue [60]. Various appealing properties of carbon nanodots like fluorescence emission, small size, cell membrane permeability, less toxicity, chemical inertness, solubility in water, ease of production, potential functionalization, and drug loading have captivated recognition in DDSs and the attention of several researchers in current times [61–64]. Nanodots in DDSs can exhibit magnetic properties explored in magnetic resonance imaging (MRI), thus assisting drug delivery and fluorescence imaging and MRI along with fluorescence imaging will aid superior tissue penetration and spatial resolution of MRI and easy microscopic tissue examination of fluorescent imaging.

17.6.4 Crossing blood–brain barrier

Size of the nanoparticle becomes a prime issue while using any nanostructure in living biomedical applications. Smallest human capillary being less than 4 mm, it is crucial to maintain the size of the nanoparticle below this in a living body. Small-sized nanoparticles would avert blockage in blood vessels and their elimination by the reticuloendothelial system [28]. Imaging probes delivery to brain tumors is rather complicated due to blood–brain barrier (BBB). In fact, size of the probes and their surface characteristics determine crossing the BBB [65]. But drug delivery to the brain is rather tough due to various BBB properties, which hinder the crossing of drugs like foreign proteins, chemicals, and peptides [59]. CQDs can be used for this purpose. Polymer-coated nitrogen-doped carbon nanodots with sizes ranging from 5 to 15 nm produced by solvothermal reaction could enter glioma cells in vitro and for in vivo glioma fluorescence imaging. Blood–tumor barrier (BTB) of malignant glioma microvasculature has a physiological pore size higher limit of nearly 11 nm, which suggests that carbon nanodots can cross the barrier. Moreover, nanodots with hydrophilic polymer coating have extended blood circulation time and enhanced probability of proper targeting at the tumor site [66].

17.6.5 Gene delivery

Gene therapy has captivated recognition in medical and biotechnological realm and is placed on the source of diseases using delivery and expression of extrogenous DNA encoding for missing or defective gene products. The prime factor for gene therapy is the application of proper gene vectors [67]. Various nanoparticles [68–75] and QDs [76–80] are used for gene delivery. Carbon nanodots can act as a station for gene delivery owing to their attractive properties like biocompatibility, low toxicity, strong fluorescence emission, and broad emission spectra-steady PL.

17.7 Carbon nanostructures in terahertz domain

Generation and detection of THz radiation in the technologically relevant range of the so-called THz gap (0.1–10 THz) are challenging and in their budding stage because of lack of efficient sources and detectors. CQDs have shown immense prospective for building sensitive THz detectors via photon-assisted electron tunneling. The operating region has a vast expanse, extending from a high-resolution gate-tunable THz sensor to a broadband THz detector.

17.7.1 Terahertz time-domain spectroscopy for generation of coherent radiation

Coherent THz radiation can be generated and detected using time-domain THz spectroscopy where laser pulses with a duration of the order of femtosecond are used. Conductivity and dielectric responses can be derived simultaneously in the frequency domain using THz pulses, which is of immense importance. Another advantage of using this method is highly sensitive charge carrier response, phonon resonances, and intraband transitions [81]. Optical pulse can also be used for the above purpose with the changes caused to be recorded in the THz frequency range and then analyzed in a time-resolved way (Fig. 17.9).

These time-based measurements of 2D spectroscopy in the THz pulse is quite time-consuming. The modification brought in the peak of the electric field of the THz pulse either during reflection or during transmission is the average of the total spectral weight of the probe pulse, which gives a clear view of the temporal evolution of the THz response of the pulse sample due to optical pumping. It is observed that the change in peak amplitude of the pulse with respect to the optical pump pulse is related to the change in the conductivity of the pulse within the complete bandwidth of the spectrometer, which enables the experimenter to bring out the free carrier kinetics of the system as a whole. The time range of these measurements is of the order of a few nanoseconds with subpicosecond time resolution, the

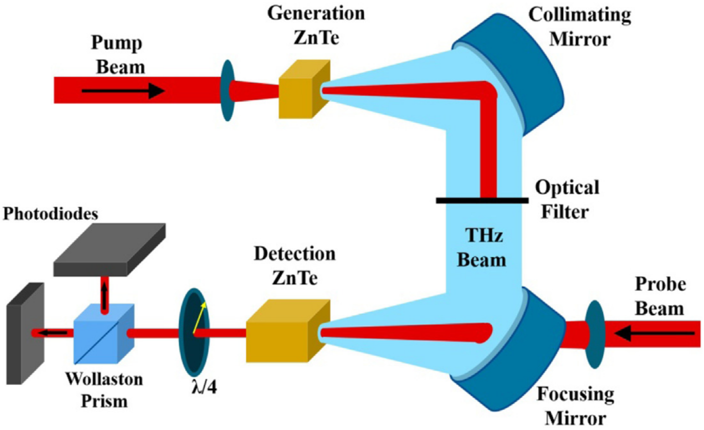

Figure 17.9 Experimental setup for THz time-domain spectroscopy with optical pumping.

limitation brought by the pumping delay for the pulse. Due to charge injection, free carriers are generated which decreases the broadband transmission. Thus, THz waveforms can be measured in the time domain by keeping the pump pulse at a particular time delay after optical excitation. Dielectric effect of the bound charges and conductivity at a higher frequency range of the free electrons or holes are the two primary effects that confer the input wave interaction at higher THz frequencies [82,83].

High signal-to-noise ratio and large spectral bandwidth of a time-domain spectrometer in the THz domain are very essential for determining various important physical events taking place during the above experiments, which are realized by the different generation and detection techniques of THz radiation like the very common optical rectification and electro-optical sampling. Most suitable materials for the above purpose are ZnTe and GaP: ZnTe has a relatively large nonlinear coefficient and phase matching at 800 nm, and GaP has a large effective bandwidth greater than 7 THz [82,84]. Another acceptable material for the above purpose is $LiNbO_3$ (LNB) which can be appropriately used to produce THz pulses at high electric field, which permits measurement of nonlinear phenomena in the THz domain or as an effective pumping source. But there are certain limitations of LNB like tilted front geometry of the pulse necessary for phase matching and comparatively narrow bandwidth of about 0.1−2 THz [82]. Air-based systems provide ultra-broadband spectroscopy yielding a large bandwidth range of 0.3 THz to more than 30 THz [85]. These air-based systems employ air plasma generation, which is very economical, and air-biased coherent detection, which requires very high voltages and is challenging with respect to construction. Generation and detection of THz radiation can also be achieved by photoconductive antennas. An external bias voltage is given to the emitter photoconductive switch, and the laser-excited ultrafast current emits THz radiation. Another alike photoconductive switch can be used for the detection of the THz radiation. In recent times, rigorous research is being carried out to establish even newer generation-detection methods; generation of high power and wide bandwidth THz radiation being our main concern.

17.7.2 Time-resolved spectroscopy and terahertz conductivity in carbon nanostructures

Mobility and charge transport in a material system are restricted by electron-phonon interactions. These interactions have a crucial effect on static conductivity in the THz region of operation, which arises from the fact that phonon modes at room temperature and a very high frequency of operation becomes thermally populated. Time-domain spectroscopy in the THz regime helps scrutinize the dielectric response of carbon nanostructures to divulge various important characteristics of low energy electrons, excitons, and phonons. Optical phonons, after interaction with the electrons, contribute to the energy and various phase relaxation phenomena occurring in solids. These dynamical processes occur in picosecond or subpicosecond time scale. Saturation responses in electron transport result from the strong coupling between optical phonons and electrons; even lifetime and dephasing time are the prime factors that control these processes. Femtosecond time-resolved pump-probe spectroscopy enables real-time capture of these lifetimes and obtains the strength of coupling between the electrons and the optical phonons. Pump pulse of large strength is firstly required to start lattice vibrations; thereafter, a delayed spectrally broad pulse actuates further lattice vibrations by stimulated Raman scattering. Spectrally resolved and time-resolved ultrafast spectroscopic inspections are reported [86–88].

17.8 Conclusion and future prospect

A tremendous momentum is seen in the nanocarbon domain due to insurgency in different techniques adopted for optical measurement and synthetic strategies used to explore this domain. Researchers and investigators will remain indebted to the pioneering development of time-resolved methodologies, particularly pump-probe spectroscopy and THz time-domain spectroscopy, which they are restyling and remodeling to unearth various hidden aspects and create some utmost experimental conditions of temperature and pressure. But a complete realization of the suitability of carbon as a material for QDs over other semiconductors and their immense application regime can only be satisfied through consistent studies, research, and modernization of the techniques and instruments. Few studies highlighted in this chapter suggest remarkable merit of CQDs in ultrafast and THz devices like sources, detectors, and modulators.

CQDs emerge as a propitious candidate for various biomedical applications like bioimaging, drug delivery, and cancer therapy which have been discussed in this chapter. It has also been accentuated that carbon nanodots have the propensity to cross the blood–brain barrier and gene delivery. Apprehension is there about the potentiality of heavy metal-based QDs in the biomedical domain as they suffer from toxicity while carbon nanodots having less toxicity in the human body are safer. On the other hand, CQDs have attractive characteristics like tunable optical features and fluorescence emission in the NIR region of the electromagnetic spectrum. Effortless synthesis and capacity to functionalize carbon dots make them superior to semiconductor dots. Research is being carried on to evaluate further blood circulation, toxicity, and coupling them in versatile and general-purpose platforms for implementing bioimaging and drug or gene delivery at the same time. But inspection and research must be continued on the consequence of doping and synthesis parameters to achieve higher QY along with biocompatibility. So, it can be concluded that CQDs have more potential and are more acceptable in the biomedical field as compared to semiconductor QDs.

References

[1] H.W. Kroto, J.R. Heath, S.C. O'Brien, R.F. Curl, R.E. Smalley, C 60: Buckminsterfullerene, Nature 318 (1985) 162−163.

[2] P. Avouris, M. Freitag, V. Perebeinos, Carbon-nanotube photonics and optoelectronics, Nature Photonics 2 (2008) 341−350.

[3] F. Bonaccorso, Z. Sun, T. Hasan, A.C. Ferrari, Graphene photonics and optoelectronics, Nature Photonics 4 (2010) 611−622.

[4] A.A. Balandin, S. Ghosh, W. Bao, I. Calizo, D. Teweldebrhan, F. Miao, et al., Superior thermal conductivity of single-layer graphene, Nano Letters 8 (2008) 902−907.

[5] K.S. Novoselov, A.K. Geim, S.V. Morozov, D. Jiang, Y. Zhang, S.V. Dubonos, et al., Electric field effect in atomically thin carbon films, Science (New York, N.Y.) 306 (2004) 666.

[6] G.-H. Lee, R.C. Cooper, S.J. An, S. Lee, A. van der Zande, N. Petrone, et al., High-strength chemical-vapor−deposited graphene and grain boundaries, Science (New York, N.Y.) 340 (2013) 1073.

[7] Q. Bao, H. Zhang, Y. Wang, Z. Ni, Y. Yan, Z.X. Shen, et al., Atomic-layer graphene as a saturable absorber for ultrafast pulsed lasers, Advanced Functional Materials 19 (2009) 3077−3083.

[8] B.A. Ruzicka, S. Wang, J. Liu, K.-P. Loh, J.Z. Wu, H. Zhao, Spatially resolved pump-probe study of single-layer graphene produced by chemical vapor deposition, Optical Materials Express 2 (2012) 708−716.

[9] L. Ren, C.L. Pint, T. Arikawa, K. Takeya, I. Kawayama, M. Tonouchi, et al., Broadband terahertz polarizers with ideal performance based on aligned carbon nanotube stacks, Nano Letters 12 (2012) 787−790.

[10] C. Manzo, M.F. Garcia-Parajo, A review of progress in single particle tracking: from methods to biophysical insights, Reports on Progress in Physics 78 (12) (2015) 124601.

[11] S. Xu, D. Li, P. Wu, One-pot, facile, and versatile synthesis of monolayer MoS_2/WS_2 quantum dots as bioimaging probes and efficient electrocatalysts for hydrogen evolution reaction, Advanced Functional Materials 25 (7) (2015) 1127−1136.

[12] J. Wang, et al., MoS_2 quantum dot@polyaniline inorganic−organic nanohybrids for in vivo dual-modal imaging guided synergistic photothermal/radiation therapy, ACS Applied Material Interfaces 8 (37) (2016) 24331−24338.

[13] W. Dai, et al., Tunable fabrication of molybdenum disulfide quantum dots for intracellular microRNA detection and multiphoton bioimaging, Small (Weinheim an der Bergstrasse, Germany) 11 (33) (2015) 4158−4164.

[14] H. Lin, et al., Colloidal synthesis of MoS_2 quantum dots: size-dependent tunable photoluminescence and bioimaging, New Journal of Chemistry 39 (11) (2015) 8492−8497.

[15] K. Zhou, et al., As-prepared MoS_2 quantum dot as a facile fluorescent probe for long-term tracing of live cells, Nanotechnology 27 (27) (2016) 275101.

[16] B. Mahler, et al., Towards non-blinking colloidal quantum dots, Nature Materials 7 (8) (2008) 659−664.

[17] P.G. Luo, et al., Carbon-based quantum dots for fluorescence imaging of cells and tissues, RSC Advance 4 (21) (2014) 10791−10807.

[18] A. Dehghani, et al., Collagen derived carbon quantum dots for cell imaging in 3D scaffolds via two-photon spectroscopy, Carbon 131 (2018) 238−245.

[19] S.-H. Chiu, et al., Rapid fabrication of carbon quantum dots as multifunctional nanovehicles for dual-modal targeted imaging and chemotherapy, Acta Biomaterialia 46 (2016) 151−164.

[20] N. Vasimalai, et al., Green synthesis of fluorescent carbon dots from spices for in vitro imaging and tumour cell growth inhibition, Beilstein Journal of Nanotechnology 9 (2018) 530.

[21] V. Ramanan, et al., Outright green synthesis of fluorescent carbon dots from eutrophic algal blooms for in vitroimaging, ACS Sustainable Chemistry & Engineering 4 (9) (2016) 4724−4731.

[22] J. Yang, et al., Ultrasmall and photostable nanotheranostic agents based on carbon quantum dots passivated with polyamine-containing organosilane molecules, Nanoscale 9 (40) (2017) 15441−15452.

[23] G. Gao, et al., On-off-on fluorescent nanosensor for Fe^{3+} detection and cancer/normal cell differentiation via silicon-doped carbon quantum dots, Carbon 134 (2018) 232−243.

[24] S. Aiyer, et al., Fluorescent carbon nanodots for targeted in vitro cancer cell imaging, Applied Materials Today 4 (2016) 71−77.

[25] L.-P. Guo, Y. Zhang, W.-C. Li, Sustainable microalgae for the simultaneous synthesis of carbon quantum dots for cellular imaging and porous carbon for CO_2 capture, Journal of Colloid and Interface Science 493 (2017) 257−264.

[26] A.K. Samantara, et al., Good's buffer derived highly emissive carbon quantum dots: excellent biocompatible anticancer drug carrier, Journal of Materials Chemistry B 4 (14) (2016) 2412−2420.

[27] Z. Liu, et al., Carbon-quantum-dots-loaded mesoporous silica nanocarriers with pH-switchable zwitterionic surface and enzyme-responsive pore-cap for targeted imaging and drug delivery to tumor, Advanced Healthcare Materials 5 (12) (2016) 1401−1407.

[28] M. Zhang, et al., Near-infrared light triggered photo- therapy, in combination with chemotherapy using magnetofluorescent carbon quantum dots for effective cancer treating, Carbon 118 (2017) 752−764.

[29] A. Kundu, et al., Facile and green approach to prepare fluorescent carbon dots: emergent nanomaterial for cell imaging and detection of vitamin B2, Journal of Colloid and Interface Science 468 (2016) 276−283.

[30] X. Chen, et al., Highly cysteine-selective fluorescent nanoprobes based on ultrabright and directly synthesized carbon quantum dots, Analytical and Bioanalytical Chemistry 410 (12) (2018) 2961−2970.

[31] S.-T. Yang, et al., Carbon dots as nontoxic and high- performance fluorescence imaging agents, The Journal of Physical Chemistry C 113 (42) (2009) 18110−18114.

[32] R.M. Shereema, et al., One step green synthesis of carbon quantum dots and its application towards the bioelectroanalytical and biolabeling studies, Electrochimica Acta 182 (2015) 588−595.

[33] Y.-Y. Zhang, et al., A new hydrothermal refluxing route to strong fluorescent carbon dots and its application as fluorescent imaging agent, Talanta 117 (2013) 196−202.

[34] W. Li, et al., Simple and Green Synthesis of Nitrogen-Doped Photoluminescent Carbonaceous Nanospheres for Bioimaging, Angewandte Chemie International Edition 52 (31) (2013) 8151−8155.

[35] D. Kumar, et al., Synthesis and characterization of carbon quantum dots from orange juice, Journal of Bionanoscience 8 (4) (2014) 274−279.

[36] V.N. Mehta, et al., One-step hydrothermal approach to fabricate carbon dots from apple juice for imaging of mycobacterium and fungal cells, Sensors and Actuators B 213 (2015) 434−443.

[37] Y. Xu, et al., Green synthesis of fluorescent carbon quantum dots for detection of Hg^{2+}, Chinese Journal of Analytical Chemistry 42 (9) (2014) 1252−1258.

[38] A.-M. Alam, et al., Synthesis of carbon quantum dots from cabbage with down-and up-conversion photoluminescence properties: excellent imaging agent for biomedical applications, Green Chemistry: An International Journal and Green Chemistry Resource: GC 17 (7) (2015) 3791−3797.

[39] B.S.B. Kasibabu, et al., Imaging of bacterial and fungal cells using fluorescent carbon dots prepared from carica papaya juice, Journal of Fluorescence 25 (4) (2015) 803−810.

[40] B. De, N. Karak, A green and facile approach for the synthesis of water soluble fluorescent carbon dots from banana juice, RSC Advance 3 (22) (2013) 8286−8290.

[41] R. Atchudan, T.N.J.I. Edison, Y.R. Lee, Nitrogen-doped carbon dots originating from unripe peach for fluorescent bioimaging and electrocatalytic oxygen reduction reaction, Journal of Colloid and Interface Science 482 (2016) 8−18.

[42] Y. Hu, et al., Waste frying oil as a precursor for one-step synthesis of sulfur-doped carbon dots with pH-sensitive photoluminescence, Carbon 77 (2014) 775−782.

[43] L. Wang, H.S. Zhou, Green synthesis of luminescent nitrogen-doped carbon dots from milk and its imaging application, Analytical Chemistry 86 (18) (2014) 8902−8905.

[44] C. Zhu, J. Zhai, S. Dong, Bifunctional fluorescent carbon nanodots: green synthesis via soy milk and application as metal-free electrocatalysts for oxygen reduction, Chemical Communications 48 (75) (2012) 9367−9369.

[45] X. Yang, et al., Novel and green synthesis of high-fluorescent carbon dots originated from honey for sensing and imaging, Biosensors & Bioelectronics 60 (2014) 292−298.

[46] J. Wang, C.F. Wang, S. Chen, Amphiphilic egg-derived carbon dots: rapid plasma fabrication, pyrolysis process, and multicolor printing patterns, Angewandte Chemie International Edition 51 (37) (2012) 9297−9301.

[47] X. Qin, et al., Microwave-assisted rapid green synthesis of photoluminescent carbon nanodots from flour and their applications for sensitive and selective detection of mercury(II) ions, Sensors and Actuators B 184 (2013) 156−162.

[48] P.-C. Hsu, et al., Synthesis and analytical applications of photoluminescent carbon nanodots, Green Chemistry: An International Journal and Green Chemistry Resource 14 (4) (2012) 917−920.

[49] S. Thambiraj, R. Shankaran, Green synthesis of highly fluorescent carbon quantum dots from sugarcane bagasse pulp, Applied Surface Science 390 (2016) 435−443.

[50] Z. Qian, et al., Highly luminescent N-doped carbon quantum dots as an effective multifunctional fluorescence sensing platform, Chemistry—A European Journal 20 (8) (2014) 2254−2263.

[51] H. Tao, et al., In vivo NIR fluorescence imaging, biodistribution, and toxicology of photoluminescent carbon dots produced from carbon nanotubes and graphite, Small (Weinheim an der Bergstrasse, Germany) 8 (2) (2012) 281−290.

[52] J.H. Zhang, et al., In vivo characterization of hair and skin derived carbon quantum dots with high quantum yield as long-term bioprobes in zebrafish, Scientific Reports 6 (August) (2016) 1−12.

[53] N. Parvin, T.K. Mandal, Synthesis of a highly fluorescence nitrogen-doped carbon quantum dots bioimaging probe and its in vivo clearance and printing applications, RSC Advance 6 (22) (2016) 18134−18140.

[54] J. Wang, et al., Synthesis, characterization and cells and tissues imaging of carbon quantum dots, Optical Materials 72 (2017) 15−19.

[55] C.T. Matea, et al., Quantum dots in imaging, drug delivery and sensor applications, International Journal of Nanomedicine 12 (2017) 5421.

[56] J. Jana, et al., One pot synthesis of intriguing fluorescent carbon dots for sensing and live cell imaging, Talanta 150 (2016) 253−264.

[57] G.E. Gu, et al., Fluorescent polydopamine nanoparticles as a probe for zebrafish sensory hair cells targeted in vivo imaging, Scientific Reports 8 (1) (2018) 4393.

[58] J. Ge, et al., Red-emissive carbon dots for fluorescent, photoacoustic, and thermal theranostics in living mice, Advanced Materials 27 (28) (2015) 4169−4177.

[59] M.S. Khan, et al., Controlled delivery of dopamine hydrochloride using surface modified carbon dots for neuro diseases, Colloids and Surfaces B 134 (2015) 140−146.

[60] O.C. Farokhzad, R. Langer, Impact of nanotechnology on drug delivery, ACS Nano 3 (1) (2009) 16−20.

[61] Z. Liu, et al., Targeted drug delivery: carbon-quantum-dots-loaded mesoporous silica nanocarriers with pH-switchable zwitterionic surface and enzyme-responsive pore-cap for targeted imaging and drug delivery to tumor, Advanced Healthcare Materials 5 (12) (2016) 1380.

[62] T. Feng, et al., Dual-responsive carbon dots for tumor extracellular microenvironment triggered targeting and enhanced anticancer drug delivery, ACS Applied Materials & Interfaces 8 (29) (2016) 18732−18740.

[63] A.R. Chowdhuri, et al., Carbon dots embedded magnetic nanoparticles@chitosan@metal organic framework as a nanoprobe for pH sensitive targeted anticancer drug delivery, ACS Applied Materials & Interfaces 8 (26) (2016) 16573−16583.

[64] Z. Peng, et al., Carbon dots: promising biomaterials for bone-specific imaging and drug delivery, Nanoscale 9 (44) (2017) 17533−17543.

[65] C. Wu, D.T. Chiu, Highly fluorescent semiconducting polymer dots for biology and medicine, Angewandte Chemie International Edition 52 (11) (2013) 3086−3109.

[66] Y. Wang, et al., Direct solvent-derived polymer-coated nitrogen-doped carbon nanodots with high water solubility for targeted fluorescence imaging of glioma, Small (Weinheim an der Bergstrasse, Germany) 11 (29) (2015) 3575−3581.

[67] X. Cao, et al., Photoluminescent cationic carbon dots as efficient non-viral delivery of plasmid SOX9 and chondrogenesis of fibroblasts, Scientific Reports 8 (1) (2018) 7057.

[68] M.S. Huh, et al., Polysaccharide-based nanoparticles for gene delivery, Topics in Current Chemistry 375 (2) (2017) 31.

[69] J. Kim, et al., Gene delivery nanoparticles to modulate angiogenesis, Advanced Drug Delivery Reviews 119 (2017) 20−43.

[70] I.M. El-Sherbiny, et al., Magnetic nanoparticles-based drug and gene delivery systems for the treatment of pulmonary diseases, Nanomedicine: Nanotechnology, Biology, and Medicine 12 (4) (2017) 387−402.

[71] I. Fernandez-Piñeiro, et al., Development and characterisation of chondroitin sulfate- and hyaluronic acid-incorporated sorbitan ester nanoparticles as gene delivery systems, European Journal of Pharmaceutics and Biopharmaceutics 125 (2018) 85–94.

[72] X. Huang, et al., Characterization of calcium phosphate nanoparticles based on a PEGylated chelator for gene delivery, ACS Applied Materials & Interfaces 9 (12) (2017) 10435–10445.

[73] B. Du, et al., Lipid-coated gold nanoparticles functionalized by folic acid as gene vectors for targeted gene delivery in vitro and in vivo, ChemMedChem 12 (21) (2017) 1768–1775.

[74] M.C. Kim, et al., Polyethyleneimine-associated polycaprolactone—Superparamagnetic iron oxide nanoparticles as a gene delivery vector, Journal of Biomedical Materials Research Part B 105 (1) (2017) 145–154.

[75] P. Zhang, et al., Regulation the morphology of cationized gold nanoparticles for effective gene delivery, Colloids and Surfaces B , 157 (2017) 18–25.

[76] M.V. Yezhelyev, et al., Proton-sponge coated quantum dots for siRNA delivery and intracellular imaging, Journal of the American Chemical Society 130 (28) (2008) 9006–9012.

[77] S.M. Ghafary, et al., Simultaneous gene delivery and tracking through preparation of photo-luminescent nanoparticles based on graphene quantum dots and chimeric peptides, Scientific Reports 7 (1) (2017) 9552.

[78] G. Lin, et al., Quantum dots-siRNA nanoplexes for gene silencing in central nervous system tumor cells, Frontiers in Pharmacology 8 (2017) 182.

[79] F. Yin, et al., Black phosphorus quantum dot based novel siRNA delivery systems in human pluripotent teratoma PA-1 cells, Journal of Materials Chemistry B 5 (27) (2017) 5433–5440.

[80] X. Yang, et al., One-step synthesis of photoluminescent carbon dots with excitation-independent emission for selective bioimaging and gene delivery, Journal of Colloid and Interface Science 492 (2017) 1–7.

[81] J.A. Spies, J. Neu, U.T. Tayvah, M.D. Capobianco, B. Pattengale, S. Ostresh, et al., Terahertz Spectroscopy of Emerging Materials, The Journal of Physical Chemistry C 124 (2020) 22335–22346.

[82] J. Neu, C.A. Schmuttenmaer, Tutorial: an introduction to terahertz time domain spectroscopy (THz-TDS), Journal of Applied Physics 124 (2018) 231101.

[83] J. Neu, E.A. Stone, J.A. Spies, G. Storch, A.S. Hatano, B.Q. Mercado, et al., Terahertz Spectroscopy of Tetrameric Peptides, The Journal of Physical Chemistry Letters 10 (2019) 2624–2628.

[84] K. Aoki, J. Savolainen, M. Havenith, Broadband terahertz pulse generation by optical rectification in GaP crystals, Applied Physics Letters 110 (2017) 201103.

[85] X. Lu, X.C. Zhang, Balanced terahertz wave air-biased-coherent-detection, Applied Physics Letters 98 (2011) 151111.

[86] J.H. Kim, K.J. Yee, Y.S. Lim, L.G. Booshehri, E.H. Hároz, J. Kono, Dephasing of G-band phonons in single-wall carbon nanotubes probed via impulsive stimulated Raman scattering, Physical Review B 86 (2012) 161415.

[87] Y.-S. Lim, K.-J. Yee, J.-H. Kim, E.H. Hároz, J. Shaver, J. Kono, et al., Coherent lattice vibrations in single-walled carbon nanotubes, Nano Letters 6 (2006) 2696–2700.

[88] J.H. Kim, K.J. Han, N.J. Kim, K.J. Yee, Y.S. Lim, G.D. Sanders, et al., Chirality-selective excitation of coherent phonons in carbon nanotubes by femtosecond optical pulses, Physical Review Letters 102 (2009) 037402.

Nanocarbon-based single-electron transistors as electrometer

18

Sourav Mitra
Institute for Functional Intelligent Materials, National University of Singapore, Singapore, Singapore

18.1 Theory

18.1.1 Introduction to single-electron transistor

The single-electron transistor (SET) is usually a submicrometer-sized tunneling device whose voltage-current characteristic is governed by the Coulomb blockade effect. It consists of a small metal island (quantum dot [QD]) connected to a metal source and a drain led by two narrow tunnel junctions. The magnitude of current that tunnels through the junctions, for a given source-drain bias, is determined by the island's electrostatic potential, which in turn is determined by the surrounding potential landscape, and this makes it very useful as a sensitive electrometer probe.

At a low temperature and proper voltage bias, the current flowing through a SET fluctuates periodically as the electrostatic potential changes. In fact, the current passes through a full period each time the electric field lines terminating on the island induce a charge of exactly one additional electron. Hence, monitoring the current through the SET as it is scanned over the sample provides a means of mapping the electric field emanating from the sample surface.

18.1.2 Origin of coulomb blockade oscillation

Let us consider a QD connected to source (s) and drain (d) electrodes via tunneling contacts, where the junctions are modeled by resistances R_s, R_d and capacitances C_s, C_d. In addition, the QD is capacitively coupled to a gate voltage, V_g, by the capacitance C_g. Fig. 18.1 shows a schematic of the equivalent circuit.

To understand Coulomb blockade, we need to look at the quantum mechanical picture shown in Fig. 18.2. The QD has discrete energy levels in a 1D potential and a consequence of charge quantization. The states in the source and drain electrodes are filled up to the electrochemical potential energies μ_s and μ_d, which are connected via the externally applied source-drain bias voltage, $V_{sd} = (\mu_s - \mu_d)/e$.

At absolute zero (and neglecting co-tunneling), transport occurs according to the following rule—current is (non) zero when the number of available states on the QD in the energy window between μ_s and μ_d is (non) zero. If an electron tunnels to

Carbon Quantum Dots for Sustainable Energy and Optoelectronics. DOI: https://doi.org/10.1016/B978-0-323-90895-5.00003-5
© 2023 Elsevier Ltd. All rights reserved.

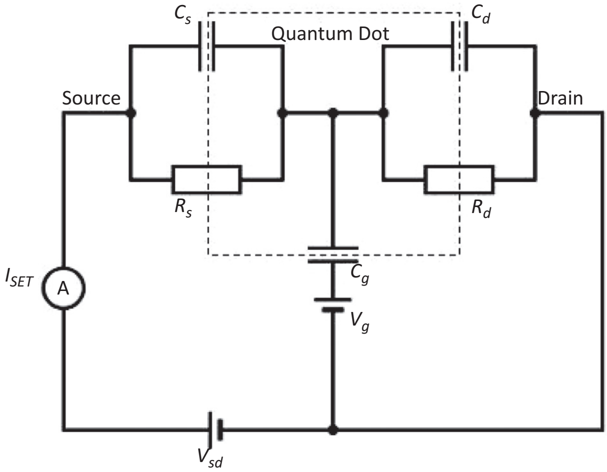

Figure 18.1 Schematic diagram for a SET showing the equivalent electrical circuit. Each tunnel junction is described by an effective resistance and capacitance in parallel. The dotted region denotes the quantum dot, whose energy levels can be manipulated using the gate voltage V_g. *SET*, Single-electron transistor.

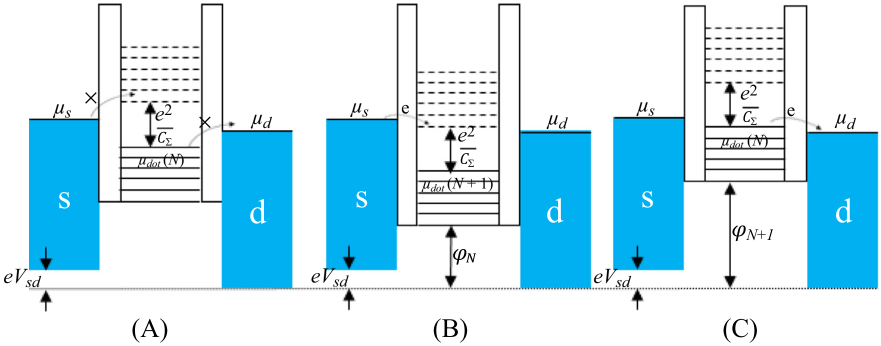

Figure 18.2 Illustration of the potential landscape across a QD. The source and drain leads have chemical potentials μ_s and μ_d, respectively, with $eV_{sd} = (\mu_s - \mu_d)$. (A) Describes the situation where both eV_{sd} and k_BT are smaller than the energy gap $2E_c = e^2/C_\Sigma$, thus preventing any electron to get in or out of the dot. At constant bias V_{sd}, sequential tunneling can take place with an electron hopping on the QD in (B) and hopping out in (C), if the gate voltage can align the lowest empty level $\mu_{dot}(N+1)$ to be in between μ_s and μ_d.

the dot, the charge of the dot will increase by e. We can express the stored electrostatic energy as $E_c = e^2/2C_\Sigma$, where $C_\Sigma = C = C_g + C_s + C_d$ is the total capacitance of the SET. We assume that C_Σ is independent of the number of electrons on the dot, i.e., we ignore self-capacitance. This is a reasonable assumption as long as the dot is much larger than the electron-electron screening length, resulting in no electric fields in the interior of the dot.

The specific mechanism can be understood as follows. In Fig. 18.2, the dashed lines represent empty single-particle states on the QD, with the solid lines representing states filled with electron population, N. The energy gap between the lowest empty state and the highest filled state, commonly known as the charging energy, is given by $E_c+E_c=2E_c=e^2/C_\Sigma$. Here, the first E_c accounts for the Coulomb repulsion between source and the QD, while the second corresponds to the repulsion between QD and the drain. We have assumed, at $T=0$, E_c is much larger than the bias eV_{sd} and the gap between two successive states. In Fig. 18.2A, the lowest available energy level is higher than μ_s, preventing tunneling from the source electrode to the dot, thus maintaining the fixed electronic number N. This is referred to as Coulomb blockade. The external gate is used to align the chemical potential in the dot with that of the source and drain. This enables an electron to tunnel from the source to the dot (Fig. 18.2B), increasing the potential to $\mu_{dot}(N+1)$ and then off the dot to the drain (Fig. 18.2C), causing the potential to drop back to $\mu_{dot}(N)$. The electrostatic potential increase $\varphi_{(N+1)}-\varphi_N=e^2/C_\Sigma$ is depicted as a change in the conduction band bottom. The tunneling of an electron from the source to the QD, and then off it to the drain, causes the electron population to go through the cycle $N\rightarrow N+1\rightarrow N$. This quantum mechanical process, whereby current is carried via successive discrete charging and discharging of the dot, is known as single-electron tunneling, and the device is called SET. It is important to note if the thermal kinetic energy exceeds the electrostatic energy, i.e., $E_c\ll k_BT$ (k_B: Boltzmann constant, T: temperature), tunneling will be suppressed.

SET is a direct consequence of charge quantization. Generalizing for an arbitrary charge distribution Q, the QD energy $E(Q)=(Q-Q_0)^2/2C_\Sigma$ is a parabolic distribution with a minima at Q_0. If the charge were not quantized by varying V_g, we could tune itto any arbitrary value of Q_0 to minimize the energy. However, charge quantization constraints $E(Q)$ to only have discrete values. Let us consider a situation where the QD has been charged with ΔN electrons. If $E(Q)$ is minimized by an integer no. of electrons, i.e., $Q_0=-\Delta Ne$, charge quantization forces ΔN to increase or decrease only by 1 (Fig. 18.3A). It can be shown that the gap corresponding to the charging energy vanishes only when $Q_0=-(\Delta N+1/2)e$ [1]. At this minima condition, the states with $Q=-\Delta Ne$ and $Q=-(\Delta N-1)e$ are degenerate, i.e., an additional electron can occupy either of them, thus causing charge fluctuation, which results in current flow (Fig. 18.3B). Therefore, with sweeping V_g, we will observe a peak in the source-drain current whenever the stored charge results in $Q_0=-(\Delta N+1/2)e$, thereby facilitating successive states to fluctuate energetically. This periodic fluctuation is called Coulomb blockade oscillation (CBO). A schematic for CBO is illustrated in Fig. 18.3C, showing the occurrence of peaks as successive states are filled up.

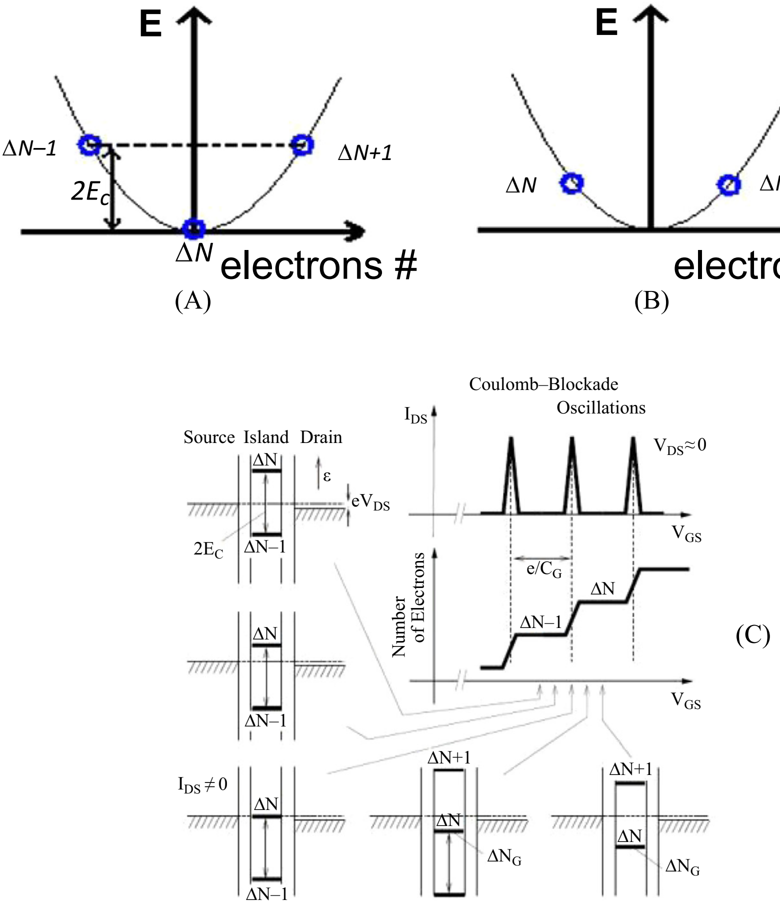
E
ΔN–1
ΔN+1
2E_C
ΔN
electrons #
(A)
E
ΔN
ΔN–1
electrons #
(B)
Coulomb–Blockade Oscillations
I_DS
V_DS≈0
V_GS
Source Island Drain
ΔN
ε
eV_DS
2E_C
ΔN–1
Number of Electrons
e/C_G
ΔN
ΔN–1
V_GS
(C)
ΔN
ΔN–1
I_DS≠0
ΔN
ΔN–1
ΔN+1
ΔN
ΔN_G
ΔN+1
ΔN
ΔN_G

Figure 18.3 (A) The energy for the states $\Delta N + 1$ or $\Delta N - 1$ being larger than ΔN, an electron cannot enter or leave the dot, resulting in zero current. (B) Shows the situation where the states ΔN and $\Delta N - 1$ are degenerate, allowing current to flow. (C) Schematic of Coulomb blockade oscillations as observed in the SET current, I_{DS}, as a function of gate voltage, V_{GS}. Only, Figure (C) has been taken from the copyright reference.
Source: From J. Weis, Single-Electron Devices, Springer Berlin Heidelberg, 2005, pp. 87–121. https://doi.org/10.1007/978-3-540-31533-9_5 Energy distribution schematic of a QD as a function of its electron population.

18.2 Application: single-electron transistor as an electrometer

18.2.1 Measuring inverse compressibility

An electronic compressibility measurement is a thermodynamic measurement and can provide information not obtained in the more conventional electrical or magnetic transport measurements. Compressibility is related to the total energy E_{total}, the chemical potential μ, and the charge carrier density n. It is usually denoted by κ and defined as [2],

$$\kappa^{-1} = n^2 \frac{\delta^2 E_{total}}{\delta n^2} = n^2 \frac{\delta \mu}{\delta n} \tag{18.1}$$

Here, $\delta\mu$ denotes the change in chemical potential introduced by the change in carrier density δn. It is worthwhile pointing out that the absence of interaction κ^{-1} is basically the inverse of the single-particle density of states at the Fermi level. Qualitatively, one can define inverse compressibility as the energy cost to add an additional electron to the sample in the presence of other electrons. A local measurement of $\delta\mu/\delta n$ can thus reveal underlying exotic physics of localized electronic states, which otherwise cannot be directly observed in a macroscopic experiment.

One key advantage of a scanning SET to a scanning tunneling microscope (STM) is that, unlike STM, SET does not require the sample to be electrically conducting. This is particularly advantageous when probing two-dimensional gases (2DEG) or, more generally speaking, two-dimensional electronic systems (2DES) such as gallium arsenide (GaAs), graphene, and transition metal dichalcogenides, where it is a common practice to use a dielectric top gate as an additional degree of freedom to tune electronic properties. The basic idea of a scanning SET is to test the screening property of the sample by introducing a density change with a backgate and recording the resulting shift in the SET current. Changing the backgate voltage by δV_g changes the electric fields by δE_0 between the backgate and the 2DES, and by δE_p between the 2DES and the SET probe. δE_p is the field penetrating the sample and directly related to the intrinsic compressibility. For example, if the sample is highly metallic, i.e., with infinite compressibility, then the sample screens the backgate completely and δE_p vanishes. While for an insulator, δE_p is very high, resulting in the SET being directly gated by the sample.

Let us try to understand how inverse compressibility is mathematically related to the SET current. The compressibility measurement scheme described below was originally developed by Jim Eisenstein [2,3].

Fig. 18.4 shows the potential landscape across the backgate-2DES-SET structure. The overall electrochemical potential energy, E (dashed line), comprises the electrostatic (φ_{2D}) and electrochemical (μ_{2D}) components as shown below,

$$E = \varphi_{2D} + \mu_{2D} \tag{18.2}$$

Here, the subscript 2D denotes potential energies intrinsic to the sample.

At thermodynamic equilibrium, E remains constant. Therefore, a change $e\delta V_g$ in the potential energy across the backgate translates into the following change in the 2DES,

$$\delta\mu_{2D} = -\,\delta\varphi_{2D} \tag{18.3}$$

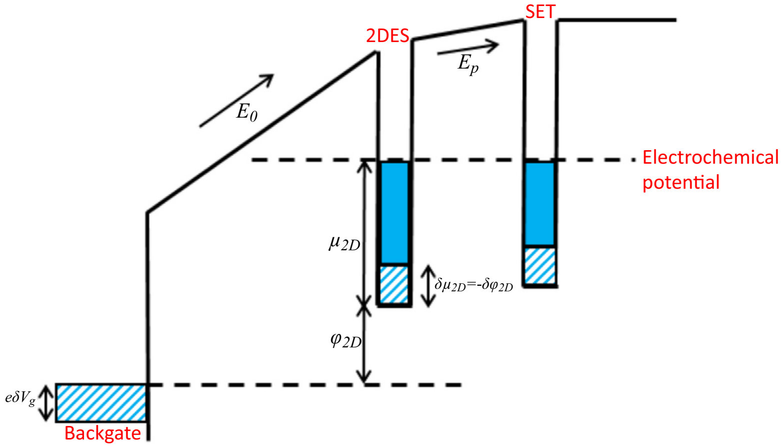
SET
2DES
E_p
E_0
Electrochemical potential
μ_{2D}
$\delta\mu_{2D}$=-$\delta\varphi_{2D}$
φ_{2D}
$e\delta V_g$
Backgate

Figure 18.4 Potential landscape for compressibility measurement using a SET scanning probe. At thermodynamic equilibrium, the electrochemical potential is constant, as indicated by the dashed line. Imposing $e\delta V_g$ on the backgate changes the electric field by δE_0, and translates into a electrochemical (electrostatic) potential change in the 2DES by $\delta\mu_{2D}(=-\delta\varphi_{2D})$. This $\delta\varphi_{2D}$ changes the field penetrating the SET by δE_p, which induces the current flow δI_{SET}.
Source: Modified from J.P. Eisenstein, L.N. Pfeiffer, K.W. West. Compressibility of the two-dimensional electron gas: Measurements of the zero-field exchange energy and fractional quantum-Hall gap. Physical Review B 50(3) (1994) 1760–1778. https://doi.org/10.1103/PhysRevB.50.1760.

Applying δV_g introduces the charge density δn_{BG} at the backgate, which induces charge densities with the opposite signs, $-\delta n_{2D}$ and $-\delta n_{SET}$ in the 2DES and SET, respectively, as shown below,

$$\delta n_{BG} = -\delta n_{2D} - \delta n_{SET} \Rightarrow \delta n_{2D} = -\delta n_{BG} - \delta n_{SET} \tag{18.4}$$

For a parallel plate capacitor, charge density per unit volume is equal to the product of the electrostatic potential difference and capacitance. Using this, we get,

$$\delta n_{BG} = \left(\delta\varphi_g - \delta\varphi_{2D}\right)C_{g-2D} = \left(e\delta V_g - \delta\varphi_{2D}\right)C_{g-2D} \tag{18.5}$$

and,

$$\delta n_{SET} = \left(\delta\varphi_{2D} - \delta\varphi_{SET}\right)C_{2D-SET} = \delta\varphi_{2D}C_{2D-SET} \tag{18.6}$$

where C_{g-2D} and C_{2D-SET} are the geometric capacitances across the backgate-sample and sample-SET, respectively. In Formula (18.6), we have used the fact that, at thermodynamic equilibrium, $\delta\varphi_{SET} = 0$ and the potential change at the SET is only determined by the 2DES.

Substituting Formulae (18.5 and 18.6) in Formula (18.4), together with the assumption that a metallic backgate gives $\delta n_{BG} \gg \delta n_{SET}$, we get,

$$\delta n_{2D} = -\left(e\delta V_g - \delta\varphi_{2D}\right)C_{g-2D} \Rightarrow \delta n_{2D} \approx -e\delta V_g C_{g-2D} \tag{18.7}$$

Here, we further approximate $\delta V_g > \delta\varphi_{2D}$.

The change in the SET current as induced by $\delta\varphi_{2D}$ can be written as $\delta I_{SET} = \alpha\delta\varphi_{2D}$. Here, α is a geometrical factor, which can be extracted by applying a bias $\delta V'_{2D}$ directly to the 2DES sample and measuring the corresponding $\delta I'_{SET}$. Assuming, $\delta\mu'_{2D} < < \delta V'_{2D}$, Formula (18.2) gives $\delta\varphi'_{2D} = e\delta V'_{2D}$. Therefore, we can write, $\delta I'_{SET} = \alpha\delta\varphi'_{2D} = \alpha e\delta V'_{2D}$, which gives, $\alpha = \delta I'_{SET}/e\delta V'_{2D}$.

Finally, we substitute Formulae (18.3 and 18.7) in Formula (18.1) to get the following expression for inverse compressibility of the 2DES,

$$\kappa^{-1} \propto \frac{\delta\mu_{2D}}{\delta n_{2D}} = \frac{\delta\varphi_{2D}}{e\delta V_g C_{g-2D}} = \frac{\delta I_{SET}}{e\delta V_g C_{g-2D}} \cdot \frac{1}{\alpha} = \frac{\delta I_{SET}}{\delta V_g C_{g-2D}} \cdot \frac{\delta V'_{2D}}{\delta I'_{SET}} \tag{18.8}$$

All the parameters on the RHS of Formula (18.8) can be measured experimentally, yielding a direct method to measure inverse electronic compressibility.

18.2.2 Experimental realization of a single-electron transistor electrometer: comparing aluminum single-electron transistor to carbon nanotube single-electron transistor

This section briefly discusses SET fabrication and the compressibility measurement principle. Fig. 18.5 illustrates the schematic of a three-layer compressibility setup comprising a 2DES sample sandwiched between a backgate layer from the bottom and a SET probe layer from the top.

The preliminary SETs used for compressibility measurement employed Al/AlO$_x$/Al structure as the tunneling junction because the oxidation condition could be easily tuned to control the characteristic of the tunneling barrier, thus giving greater control over the signal-to-noise ratio. Fig. 18.6A shows an SEM image of such an Al-based SET fabricated at the National University of Singapore by our group, on a tapered quartz fiber, using a technique described elsewhere [4]. Briefly, the technique involves thermal evaporator facilitated deposition of equally thick Al electrodes on opposite sides of the fiber to fabricate the source and drain contacts, followed by oxidation to create the AlO$_x$ tunneling junctions. Finally, Al is deposited on the flat end of the quartz to create the island, i.e., the QD. The tip diameter $\sim 111nm$ determines the spatial resolution of the SET.

In order to map the changing surface potential landscape, the position of the SET relative to the sample needs to be adjusted in the *xyz* plane. Usually, this is achieved by mounting the SET tip on an STM scanner head, with gold contacts providing an electrical connection. For preliminary approach and finding the sample

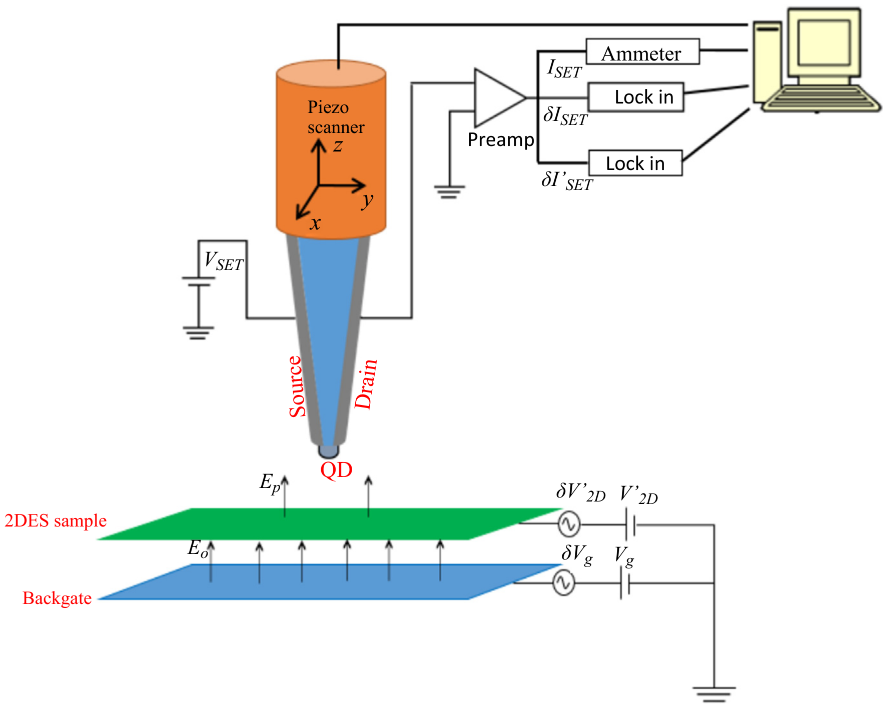

Figure 18.5 A typical experimental setup showing compressibility measurement of a 2DES sample using a scanning SET probe modulated by a backgate. The SET is fabricated on a tapered tip and mounted on the piezo scanner, which facilitates *xyz* scanning with nm resolution.

(usually a flake), the coarse motor on the scanner is used, while the piezo-based fine motors are utilized for mapping the potential distribution. A DC source-drain bias V_{SET} is applied to generate the periodic CBO current I_{SET} (usually $\sim nA$) when gated by a DC backgate V_g, which is amplified using a current preamplifier to be detected by a DC multimeter. In order to extract δI_{SET} (use Eq. 18.8), and to detect it using a lock-in amplifier, a constant AC excitation δV_g is added to the backgate. Similarly, the sample is subjected to a DC component V'_{2D} superimposed with a small AC modulation $\delta V'_{2D}$.

Fig. 18.6B shows an overlapped graph, illustrating CBO in both I_{SET} (green) and δI_{SET} (blue) as a function of the modulating V_g obtained using the tip shown in Fig. 18.6A. The AC excitation on the backgate is $0.5mV$; around 1000x smaller than CBO periodicity $\sim 0.5V$ is seen in both $I_{SET}(V_g)$ and $\delta I_{SET}(V_g)$. A lock-in time constant of 1 second was used to detect the signal. From the δI_{SET} curve, the ratio between the peak-peak amplitude and the noise amplitude is observed to be ~ 2. The SNR for this SET tip is calculated to be $0.5mV/0.5V \times 2 \approx 2000/\sqrt{Hz}$, which translates to a voltage sensitivity (smallest measurable voltage fluctuation) of $0.5V/2000 \approx 250\mu V/\sqrt{Hz}$. It should be pointed out that bringing the tip closer to

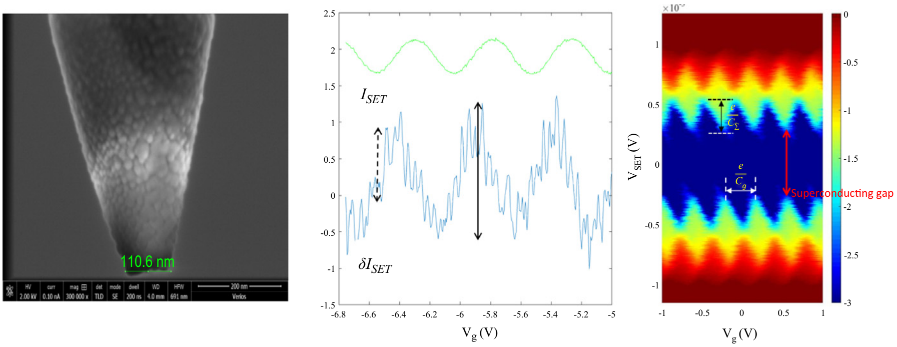

(A) (B) (C)

Figure 18.6 (A) SEM image of a SET using Al/AlOx/Al structure, showing the Al-quantum dot with diameter $\sim 111n\ m$. (B) The DC SET current I_{SET} (green curve) exhibits CBO as a function of the modulating DC backgate V_g. The AC component δI_{SET} (blue curve) has been superimposed on the same graph for comparison. The solid and dashed double-headed arrows represent the peak-peak amplitude and noise amplitude, respectively. (C) Differential conductance map of the SET measured at $170m\ K$, as a function of V_{SET} and V_g. The superconducting gap arises due to the fact that Al is superconducting below $\sim 1.2K$.

the sample will further reduce the oscillation periodicity (due to increased gate capacitance), which helps achieve lower voltage sensitivity. The charging energy, $2E_c$, oscillation periodicity, ΔV_g, and capacitance values for this tip have been extracted from the Coulomb diamond as shown in Fig. 18.6C. A Coulomb diamond is a 2D projection map where differential conductance dI_{SET}/dV_{SET} is plotted as a function of the V_{SET} and V_g [5]. The map was obtained at $T = 170mK$ using a dilution refrigerator, with the Al-SET probing a SiO_2 substrate, modulated by a Si backgate.

A recent breakthrough in realizing pristine 1D electron systems in ultraclean carbon nanotubes (CNT) and the using scanning probe microscopy to deterministically nanoassemble them at predefined positions in electronic circuits have paved the way for the fabrication of SETs using CNT QDs [6]. As shown in Fig. 18.7, the process involved growing long, parallel NT suspended over wide trenches on one chip (Fig. 18.7B), while a second independent chip supports the prefabricated electrical circuit on a narrow cantilever (Fig. 18.7C). The circuit shown here is an array of parallel electrodes having a series of shorter gate electrodes (blue) flanked on two ends by the taller electrical contacts (yellow). The scanning probe microscope was then used to insert the cantilever into a trench and “mate” it with an NT (Fig. 18.7D). The NT touches the taller electrical contacts and remains suspended over the gates (Fig. 18.7E). For each mated NT, in situ gate-dependent transport was performed at low temperature until the one with desired electronic properties was found. Finally, as shown in the inset of Fig. 18.7E, a high current was injected through adjacent pairs of contacts at the sides of the device to surgically clip the NT at well-defined locations. Fig. 18.7A shows the schematic of such a completed

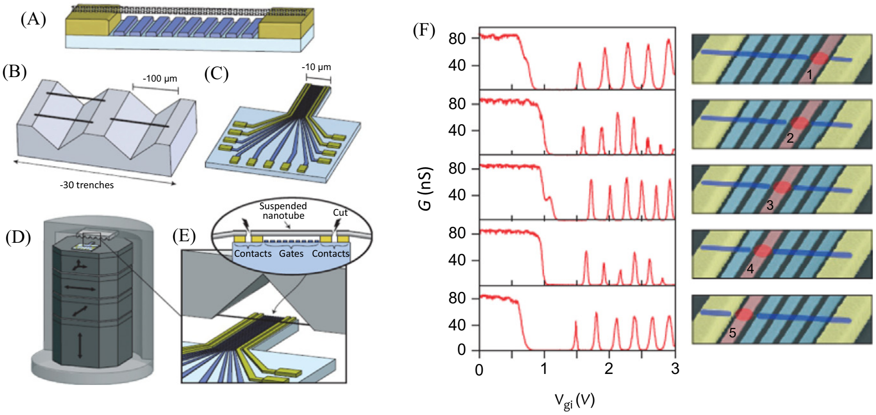

Figure 18.7 (A) A nanoassembled SET device with the CNT (black) touching the source and drain electrodes (yellow) and suspended over multiple gates (blue). The assembly process involves (B) fabricating multiple CNT on trenches and (C) the required electrical circuit on a cantilever on two independent chips. Then, (D) scanning microscopy is used to mate the cantilever to the desired NT, (E) following which the extra length of the CNT is electrically cut. (F) Realization of a CNT-based SET: Left column shows CBO in conductance as a function of a single backgate introducing electron doping, with the corresponding device SEM image being shown in the right column. The gates introducing electron (holes) are shown in red (blue). The shifting red dot in successive images represents the localized QD created in the suspended section of the CNT (dark blue) due to electron doping from successive gates.
Source: From J. Waissman, M. Honig, S. Pecker, A. Benyamini, A. Hamo, S. Ilani, Realization of pristine and locally tunable one-dimensional electron systems in carbon nanotubes. Nature Nanotechnology 8(8) (2013) 569–574. https://doi.org/10.1038/nnano.2013.143.

device, where the NT is touching the source and drain electrodes, and hanging over an arbitrary number of gates.

In order to characterize the formation of localized QDs and study the nature of Coulomb blockade behavior, the suspended segment of the NT was electron-doped locally using a single gate $V_{gi}(i{:}index)$, with the remaining length being hole-doped using the other gates, which maintain a fixed hole-doping voltage, $V_{gj} = -0.8V (j \neq i)$. Similarly, the two extreme ends of the NT are hole-doped using a pair of identical gold contacts acting as the source and drain electrodes. The left column of Fig. 18.7F presents a series of images showing CBO in the conductance $G = I/V$ as a function of V_{gi}, measured at $T = 4K$. Each image corresponds to electron doping using a single gate, forming a single localized QD above the same gate as shown in the corresponding image in the right column. As explained in the supplementary information of the chapter, at low V_{gi}, the barriers between the NT and the gold contacts are highly transparent, effectively creating a continuous NT wire populated with holes, giving the plateau-like feature. While for higher V_{gi}, p-n junctions form, spatially confining the electrons above a single gate to a localized QD with their depletion regions behaving like tunneling junctions to the source and drain electrodes. For each image, all peaks have the same periodicity, indicating clean QD's, although the difference in peak heights points to position dependence of NT electronic properties.

The parameters (charging energy, oscillation periodicity, and capacitance) obtained from the Coulomb diamond for the Al-based SET (Fig. 18.6) have been compared against the corresponding parameters for the CNT-based SET (Fig. 18.7) in Table 18.1. For the latter, charging energy and oscillation periodicity have been taken from the main text, while capacitance has been taken from the supplementary section [6]. Due to the nonavailability of the voltage sensitivity value in this chapter, we have compared the voltage sensitivity for a CNT-based SET demonstrated in a different work [7]. The sensitivity for the same is ~125 times lower than the Al-based SET, suggesting that the former would be suitable to discern voltage fluctuations on a much finer scale. Notwithstanding the superior voltage resolution, one key observation needs to be made here. With the charging energy of the CNT QD being ~240 times higher than that of the Al QD, one might be inclined to think that the former can be realized at room temperatures. It should be noted that the relevant energy scale for the CNT-based probe depends on the relative strengths of the geometrical capacitance $C_s^{geometrical}$ of the NT section physically touching the source (drain) electrodes, compared to the quantum capacitance $C_s^{quantum}$ between source (drain) and the NT segment suspended above the gates. Due to the shorter distance, $C_s^{geometrical}$ dominates over $C_s^{quantum}$, increasing the overall capacitances

Table 18.1 Comparing parameters between SETs using Al QD and CNT QD.

SET	Al-based SET: parameters calculated from Fig. 18.6	CNT-based SET: parameters taken from references
Charging energy	$2E_c = \frac{e^2}{C_\Sigma} \approx 0.25\ meV$	$59 \pm 8\ meV$
Oscillation periodicity	$\Delta V_g = \frac{e}{C_g} \approx 400\ mV$	$280 \pm 10\ mV$
Capacitance	• $C_g = \frac{e}{\Delta V_g} \approx 0.4\ aF$ • $C_\Sigma = \frac{e^2}{2E_c} \approx 644\ aF$ $C_s = C_d = (C_\Sigma - C_g)/2 \approx 320\ aF$ (since we deposit source and drain electrodes of same thickness)	• $C_s = C_d \approx 100\ aF$
Voltage sensitivity	$250\ \mu V/\sqrt{Hz}$	$2\ \mu V/\sqrt{Hz}$

Source: From 1. J. Waissman, M. Honig, S. Pecker, A. Benyamini, A. Hamo, S. Ilani, Realization of pristine and locally tunable one-dimensional electron systems in carbon nanotubes. Nature Nanotechnology 8(8) (2013) 569–574. https://doi.org/10.1038/nnano.2013.143; 2. L. Ella, A. Rozen, J. Birkbeck, M. Ben-Shalom, D. Perello, J. Zultak, T. Taniguchi, K. Watanabe, A.K. Geim, S. Ilani, J.A. Sulpizio, Simultaneous voltage and current density imaging of flowing electrons in two dimensions. Nature Nanotechnology 14(5) (2018) 480–487. https://doi.org/10.1038/s41565-019-0398-x.

$C_s = C_d = [C_s^{geometrical} - 1 + C_s^{quantum} - 1]^{-1}$, thereby suppressing the charging energy $U = e^2/(C_s + C_d + \Sigma C_{gates})$ below the value shown in Table 18.1. Correspondingly, the experimental temperature required to observe CBO is reduced, with the data in Fig. 18.7F being actually obtained at $T = 4K$.

18.3 Reviewing published work

In this section, we shall present some key publications that have utilized SET scanning probes, based on both Al and CNT QDs, to explore a wide array of novel underlying properties in 2DES.

18.3.1 *Application of Al-based single-electron transistor*

18.3.1.1 Electrical imaging of the quantum hall state

In the semiclassical picture, the quantum Hall effect (QHE) involves a 2DES being subjected to a strong perpendicular magnetic field at ultralow temperatures, which quantizes the energy spectrum into discreet Landau levels, and results in electrons executing quantized cyclotron motion in the bulk and nondissipative skipping motion along the edge [8]. Energy of each level is given by $E_n = \left(n + \frac{1}{2}\right)\hbar\omega_c[n = 0, 1, 2..]$, where $\hbar = h/2\pi$ is the reduced Plank's constant and $\omega_c = \frac{eB}{m^*}$ is the cyclotron frequency experienced by a charge e with effective mass m^* under the influence of a field B.

For a four-terminal 2DES device, the B -dependence of the Hall resistance exhibits steps (Fig. 18.8D) due to Hall quantization and can be written as $R_{xy} = h/e^2\upsilon$. Here, υ is the filling factor determining population of each level and defined as,

$$\upsilon = hn/eB \tag{18.9}$$

The earlier discovered integer quantum Hall effect (IQHE) [9,10] takes place when υ assumes exact integer values such as $\upsilon = 1, 2, 3\ldots$, whereas $\upsilon = \frac{1}{3}, \frac{2}{5}, \frac{3}{7}\ldots$ results in the more experimentally elusive fractional quantum Hall effect (FQHE) [11]. In IQHE, as a consequence of sample inhomogeneity, exact integer values of υ only occur in separate, narrow regions along the contour lines of density, the edge-state contours, given by

$$n = NB/(h/e), where\ N = 1, 2, 3... \tag{18.10}$$

Edges play a crucial role in the transport properties of quantum Hall systems. As shown in Fig. 18.8A, the edge of the 2D sample can be represented as a confining potential, causing the energies of the quantized Landau levels to increase as X approaches the edge. This implies that even if the bulk states are below the Fermi level E_F, electronic transport can still take place provided the edge states cross E_F. In the semiclassical theory, transport along the edge channels takes place via

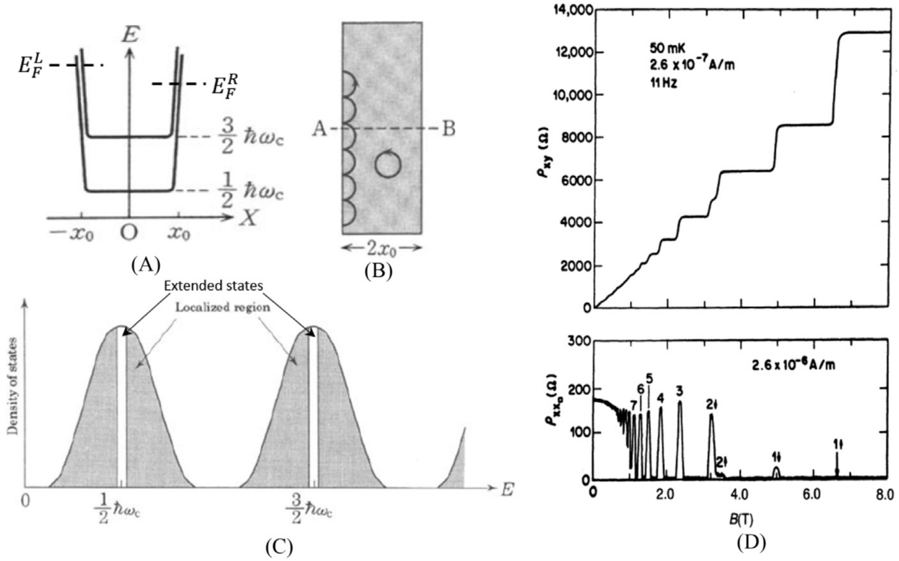

Figure 18.8 (A) Energy spectrum of a clean IQHE system as a function of guiding center position X, showing the bending of the Landau levels at the edge. Application of a Hall voltage fills these edge states to different Fermi energies E_F^L and E_F^R, resulting in a net current flow which yields the quantized Hall resistance. (B) The bulk electrons under a perpendicular magnetic field move in cyclotronic localized orbits and are incapable of carrying current. Whereas at the edges, specular reflection induces unidirectional current-carrying motion. (C) Disorder potential broadens the Landau levels into regions of localized states (black shaded regions) and extended states (central white strips) (D) IQHE in GaAs-AlGaAs heterojunction.

Source: Figures have been reproduced from the copyright Reference, with modifications in (A) and (C). Modified from "Discovery of the quantum hall effect", "Two-dimensional electrons in a magnetic field", in: D. Yoshioka (Ed.), The Quantum Hall Effect, Springer Berlin Heidelberg, 2002, pp. 1−35.

skipping trajectories involving specular reflection of the electrons, while the electrons in bulk are forced to move in closed orbits of constant disorder potential (Fig. 18.8B).

The role of disorder potential in IQHE is to create summits (local maxima) and basins (local minima) in the 2D plane. The localized states in bulk originate from the closed equipotential lines around the summits and basins, with extended states lying between them (Fig. 18.8C). As charge density is varied by sweeping the perpendicular field, the onset of the quantized Hall plateaus is observed when E_F enters the extended states, while the transition between the steps takes place when E_F traverses the localized region. Sweeping E_F across the localized states causes the trapped electrons to contribute to transport, as manifested in the longitudinal resistivity ρ_{xx} showing sharp peaks, which coincide with the step-step transitions in ρ_{xy} (Fig. 18.8D).

It has been theoretically proposed that the electrostatic energy density profile should have a smooth variation with regions of constant density at the edge states, i.e., subjected to an external potential, a 2DES in the IQHE regime largely remains compressible, marked by intermittent incompressible strips [12,13]. These incompressible strips are a direct consequence of Landau levels at the edge being fully occupied (having crossed E_F), while the compressible regions can be attributed to bulk Landau levels remaining either empty or partially filled. One of the earliest applications of a SET electrometer was by Yacoby et al., who used the scanning probe to map the distribution of the compressible and incompressible states in the quantum Hall state and successfully validated this theory [14].

The sample probed was the 2DES formed on the GaAs side of a GaAs/AlGaAs heterojunction, where the authors investigated "transparency" to a modulating backgate. Since incompressible regions cannot screen potential, electric field lines from the backgate can leak through these transparent strips and be picked by a scanning SET probe. Transparency measures the change in surface potential δV_{surf} as a function of the penetrating backgate δV_g, which is nothing but inverse compressibility κ^{-1} in thermodynamic equilibrium.

Fig. 18.9 shows a side-by-side comparison of the theoretical proposition (Fig. 18.9I) and experimental data (Fig. 18.9 II). The upper row (panels A–E) in Fig. 18.9II shows a series of transparency data at constant $B = 5.2T$, measured as a function of decreasing electronic density. The brightly colored spots correspond to transparent regions through which δV_g can penetrate the sample and reach the SET. The density reduction in steps of $\sim 2.5\%$ was achieved by applying a negative gate bias, which causes more incompressible strips to pass under the SET probe, thereby increasing the regions of bright spots. The darker zones are indicative of the compressible regions that screen the potential.

Fig. 18.9 II.G shows a potential step $\sim 4.5mV$ in the incompressible strip, which is slightly lower than characteristic energy gap $\hbar\omega_c = 1.7meV/T$ between two successive Landau levels realized in GaAs/AlGaAs heterostructures [15]. This is expected, because the incompressible strips mark the energy gap between two successive localized states, whereas $\hbar\omega_c$ corresponds to the wider energy spacing between the extended states. Fig. 18.9 II.H is a color-scale image of 50 such transparency scans, covering a finite range of field. The filling factor υ was independently extracted from the linear slope of these transparency peaks, fitted to the relation $n/B = 2/(h/e)$ (from Formula 18.10), and was found to be, $\upsilon = 2$. Thus, from mapping the electronic compressibility, albeit with a relatively poor resolution, a scanning SET electrometer provided some of the first direct images of edge states in the QH systems. Crucially, this work paved the way for SET application in studying more complex 2DES, with a keen focus on improving the voltage sensitivity and spatial resolution.

Subsequently, the SET technique has also been employed to study the interplay between localized and extended states in giving rise to QHE. Unlike extended electrons whose charge can spread over the entire sample volume, the wave function for a localized electron spreads over a limited length scale called the localization length, usually determined by the disorder potential. A single electronic charge

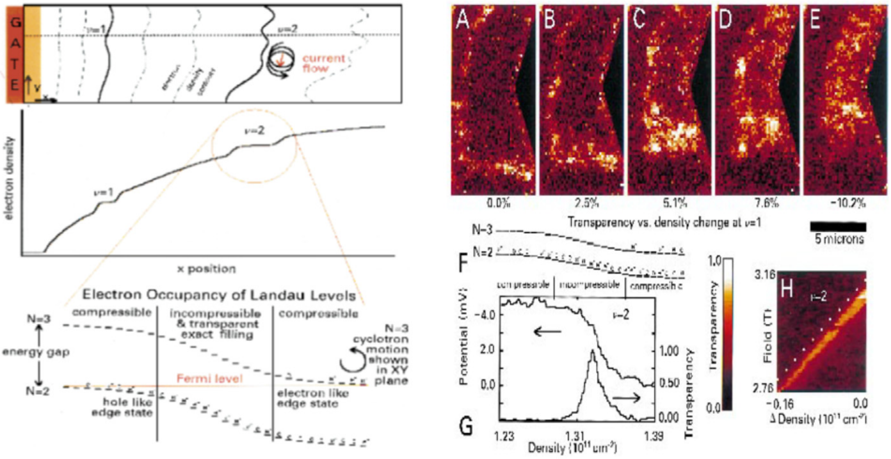

(I) (II)

Figure 18.9 (I) Top figure shows a schematic of edge modified Landau level contours, indicating the positions of $v = 1$ and $v = 2$. The edge is created by a biased gate, which induces an adjacent depleted region (orange). The bottom two figures show corresponding electron density profile and Landau level occupancy, respectively, highlighting a transition from the compressible region with partial filling to incompressible strips which are fully occupied and transparent to potential variation. (II) (A–E) Transparency sequence at $B = 5.2\ T$, showing an increase in the density of brightly colored spots as a function of decreasing electron density, which indicates increasing transparency due to enhanced movement of incompressible strips. These passing strips are detected by a SET (held at a fixed point). Comparison of (F) expected Landau level occupancy from panel (I), with (G) density-dependent data of electrostatic potential and transparency. (H) Color -scale plot showing the transparency signal as a function of the density change and the magnetic field, measured at a fixed spatial point, for $v = 2$. This shows the locus of magnetic field vs electron density for which the transparency strip does not shift.
Source: From A. Yacoby, H.F. Hess, T.A. Fulton, L.N. Pfeiffer, K.W. West, Electrical imaging of the quantum Hall state. Solid State Communications 111(1) (1999) 1–13. https://doi.org/10.1016/S0038-1098(99)00139-8.

introduced in these localized states using a backgate causes the local electrochemical potential μ to fluctuate, resulting in a spike in the derivative, $\delta\mu/\delta V_g$, i.e., in inverse compressibility. Using a scanning SET to map out $\delta\mu/\delta V_g$ in the individual localized states [16], it has been experimentally shown that the nature of localization does not strictly conform to the single-particle framework, which predicts these states to be characterized solely by the single-particle drift of noninteracting electrons along disorder-induced closed equipotential contours [17].

Fig. 18.10A shows inverse compressibility over a wide range of magnetic field (B) and carrier density (n), measured using an Al-based SET with spatial resolution $\sim 100nm$ and voltage sensitivity $\sim 1\mu V/\sqrt{Hz}$ [16]. The bright strips indicative of transparent incompressible behavior appear along with both integer and fractional

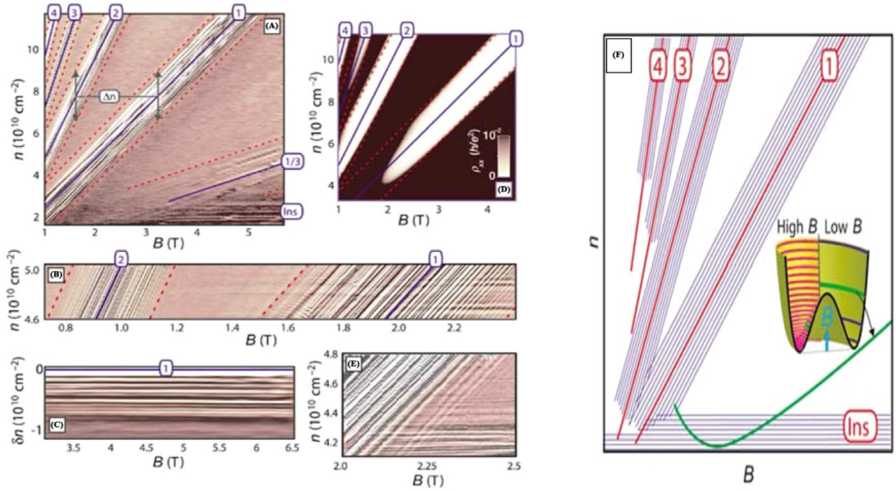

Figure 18.10 (A) Inverse compressibility, $\delta\mu/\delta V_g$, measured over a broad range in $B(T)$ and $n(\times 10^{10} cm^{-2})$ demonstrates the alternating pattern of incompressible (bright) and compressible (dark) regions. The bright regions correspond to the QH phases of the system, with the corresponding υ labeled in purple. (B) Zoomed in data for $\upsilon = 1$ and $\upsilon = 2$ incompressible regions reveal each region to have a group of parallel (black) lines, each representing the charging line of an individual localized state. All charging lines within a certain group have the same slope. (C) The charging lines around $\upsilon = 1$ plotted as a function of B and the density deviation from the filled Landau level, δn. (D) ρ_{xx}, measured on the same sample as a function of B and$n$. Red lines have been copied from (a), and mark the boundaries of the localized phases. (E) An overlap region of the $\upsilon = 1$ and $\upsilon = 0$ groups shows the coexistence of the localized states of these different groups with their original slopes intact. (F) Comparison of the measured charging lines (groups of blue) shown in (A) to a theoretically calculated single-particle charging line (green), under a model Mexican hat disorder potential (inset), illustrates the poor agreement to the single-particle picture. The energy-profile of the state (in green) giving rise to this charging line varies nonmonotonically, approaching the top of the potential hill only in the limit of high-B. This implies that as the field is swept any typical disorder potential can change the slope of charging lines to arbitrary nonquantized values in between $\upsilon = 0$ and $\upsilon = 1$, giving rise to the nonmonotonic green charging line.

Source: From S. Ilani, J. Martin, E. Teitelbaum, J.H. Smet, D. Mahalu, V. Umansky, A. Yacoby, The microscopic nature of localization in the quantum Hall effect. Nature 427(6972) (2004) 328−332. https://doi.org/10.1038/nature02230.

values of the filling factor υ, corresponding to integer and fractional QH phases, respectively. A detailed measurement of $d\mu/dV_g$ around the states $\upsilon = 1$ and $\upsilon = 2$ (Fig. 18.10B) revealed a fine structure of parallel black lines in each phase. Each line in a specific group corresponds to the charging of a single incompressible localized state. Fig. 18.10C shows the B -dependence of δn − density deviation of the lines around $\upsilon = 1$ from the fully occupied Landau level. The following observations were made from Fig. 18.10A−C: (1) the number of lines and the spacing between successive lines in each group is independent of B, implying, field-induced degeneracy does not play a significant role, (2) the width Δn of each group is constant for different QH phases, and (3) charging lines from the same group evolve in the $n-B$ plane with the same slope, which was determined from the extracted value of quantized slope $dn/dB = e\upsilon/h$ (from Formula 18.9) of the underlying QH phase. Furthermore, the slope was found to remain intact even when localized states of two different QH phases overlap as shown in Fig. 18.10E. Additionally, the authors showed in Fig. 18.10D that longitudinal resistivity ρ_{xx} is zero within each group, thereby conclusively identifying these groups to be distinct QH phases.

In order to model the experimental data to the single-particle framework, the authors considered a model disorder potential in the form of a Mexican hat (inset of Fig. 18.10F). The concentric circles on the potential landscape represent the single-particle equipotential orbits, each circle corresponding to one localized state. As B increases, the enhanced Landau level degeneracy is expected to reduce the spacing between successive states and in turn increase the number of states per unit area as shown by the transition from the blue (low- B) to the magenta (high- B) lines. However, this behavior did not agree with the compressibility data, which showed the number of charging lines to remain constant at all B values. The authors theoretically calculated the energy of a typical state and its corresponding charging line (both in green) as a function of B, which were found to have a nonmonotonic nature—initially going down for low B before climbing up. The slope of the green charging line thus asymptotically approaches nonquantized values in the $n-B$ plane. This trend is in sharp contrast to the constant quantized slopes as observed in $\delta\mu/\delta V_g$ data, highlighted in Fig. 18.10F by replotting the measured QH phases next to the green charging line.

The authors justified that the discrepancy between their experimental finding and the theoretical model arises primarily because the single-particle picture ignores Coulomb screening, which can modify the overall potential landscape by opposing the disorder potential in order to minimize the total electrostatic energy. The screening strength depends on the relative magnitude of the maximum density per Landau level, $n_{max} = B/\phi_0$ (ϕ_0: the flux quantum) and the density fluctuation amplitude $\Delta n_{disorder}$ of the disorder potential. The spatial distribution of these density profiles and the corresponding electrostatic potential for filling in the range $\upsilon = 0 \rightarrow \upsilon = 1$ have been presented to support their experimental findings (supplementary information of Ref. [16]). Since it is beyond the scope of this chapter to delve into the calculated electronic structure, we briefly present the qualitative explanation below.

It was shown that, when $\Delta n_{disorder} \gg n_{max}$, i.e., when disorder is strong or field strength is weak, all the localized states are compressible, screening the disorder completely and conforming to the single-particle phenomenology. As per their calculation, this is to be expected around half-filling. On the other hand, for the fully filled (empty) limit, with density $n = n_{max} (n = 0)$, the disorder potential is screened only in compressible pockets, surrounded by incompressible regions of QH phases $\upsilon = 1 (\upsilon = 0)$. These compressible islands surrounded by the incompressible regions behave akin to a QD, with Coulomb blockade physics expected to govern their charging phenomenon. The authors further argued that the incompressible zones should appear as strips of constant width $\Delta n_{disorder}$ centered around the integer QH filling, which agrees well with the groups of parallel lines with constant width, Δn, shown in Fig. 18.10A.

To summarize, SET compressibility measurement has shown that, for a typical QH system with disorder, the single-particle picture of localized states is only valid in low fields, while for high fields, localization is dominated by Coulomb interaction, with the localized states only appearing in isolated pockets.

18.3.1.2 Mapping graphene using a scanning single-electron transistor

The linear dispersion of the band structure in monolayer graphene arising from the two-dimensional honeycomb lattice causes its charge carriers to behave like Dirac relativistic particles. In a perfectly uniform and clean graphene sheet, free from impurities and disorder, the conduction and valence bands touch each other at a single "Dirac point," where the density of electronic states vanishes. As explained in Section 18.2.1, inverse compressibility measures the inverse of the density of states, and should therefore diverge at the Dirac point. However, for measuring real samples using a scanning SET, the disorder can affect the singular Dirac point in two possible ways: (1) for disorder on a spatial scale smaller than the SET spatial resolution, the sharp divergence is expected to be rounded off, while (2) disorder on longer length scales can introduce nonzero local charge density, thereby spatially shifting the Dirac point. In work highlighted below, the authors used an Al-based SET to investigate the nature of the disorder in monolayer graphene grown on a Si/SiO_2 wafer [18].

The blue curve in Fig. 18.11A shows the backgate dependence of inverse compressibility, $\partial\mu/\partial n_{2D}$, at zero magnetic field, with the tip held at a fixed position, at a constant height $\sim 50nm$ from the sample surface. In order to convert to units of n_{2D}, the authors performed magneto-transport measurements (not shown here), which yields a density change of $7 \times 10cm^{-2}$ corresponding to a backgate voltage difference of $1V$. For any typical correlated electron system, the chemical potential is given by $\mu = E_K + E_{ex} + E_c$, i.e., summation of the kinetic, exchange and correlation interactions, respectively [3,19]. The kinetic energy contribution to the inverse compressibility is expected to exhibit a density dependence given by $\hbar v_F \sqrt{\pi/|n|g}$, with a singularity at the charge neutrality point (CNP) [20]. Here, v_F is the Fermi velocity associated with linear dispersion, $|n|$ is the density of electrons/holes measured relative to the CNP, and g is the band degeneracy. At zero field, $g = 4$ is the product of the spin ($g_s = 2$) and valley ($g_V = 2$) degeneracies. For a perfectly clean, ungated, and undoped sample, the CNP should coincide with the Dirac point. Using only Fermi velocity as the fitting parameter, the red curve in Fig. 18.11A is best fit to the kinetic dependence, and yields an effective Fermi velocity, $v_F^{eff} = 1.1 \times 10^6 \pm 0.1 \times 10^6 ms^{-1}$. This value is similar to that reported in infrared spectroscopy studies [21]. The experimental data fit the equation reasonably well, with the key difference being the absence of the singularity point at zero backgate,

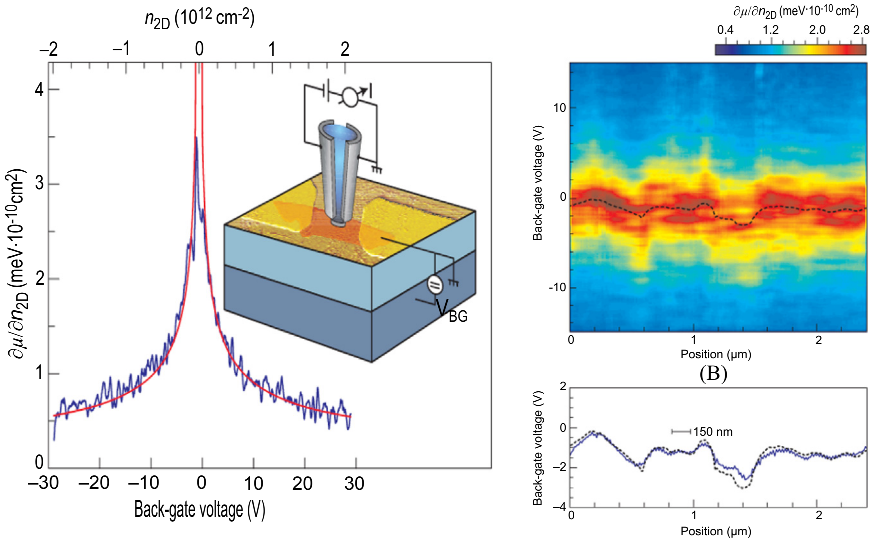

(A) (B) (C)

Figure 18.11 (A) Inverse compressibility, $\partial\mu/\partial n_{2D}(meV.10^{-10}cm^2)$ (blue curve), of monolayer graphene measured at a fixed spatial coordinate, as a function of a sweeping backgate (V) and carrier density ($\times 10^{12}cm^{-2}$). The red line is a best fit to the data using an effective Fermi velocity as a single fit parameter in the kinetic energy contribution predicted from the graphene band structure. Inset shows the SET measurement schematic. (B) Color map showing backgate dependence of $\partial\mu/\partial n_{2D}$, measured along an arbitrary linear path. The black dotted curve traces the trajectory of Dirac points, obtained from the fit of the kinetic energy term at each location. (C) Comparison of spatial fluctuation of the Dirac point from $\partial\mu/\partial n_{2D}$ measurement (black dotted curve from (B)) to that obtained by subtracting surface potential scans between zero average carrier density and high carrier density (blue solid curve).

Source: From J. Martin, N. Akerman, G. Ulbricht, T. Lohmann, J.H. Smet, K. von Klitzing, A. Yacoby, Observation of electron-hole puddles in graphene using a scanning single-electron transistor. Nature Physics 4(2) (2007) 144−148. https://doi.org/10.1038/nphys781.

which was attributed to disorder-induced broadening. This suggests that compressibility in monolayer graphene has weak contribution from the exchange and correlation terms, which is again in agreement with theoretical approximation [19,22,23].

In order to track the spatial evolution of the Dirac point, the position dependence of inverse compressibility along an arbitrary line across the sample was measured, as shown in Fig. 18.11B. This evolution as a function of position (black dotted line) originates from the different values of the backgate, which are required to compensate for the spatially varying potential landscape in order to zero the average carrier density and reach the Dirac point. Each black dot was extracted by fitting $\partial\mu/\partial n_{2D}$ measured at each location to the kinetic energy term, similar to the method used in Fig. 18.11A. As expected, the Dirac points lie within the red colored band with high values of $\partial\mu/\partial n_{2D}$, i.e., with reduced density of states.

To support these data, the authors also used an alternative approach to extract the spatial fluctuation of carrier density independently. In addition to the fluctuating local potential intrinsic to the sample, the SET tip will also pick up field lines emanating from impurity charges above the graphene layer and their image charges buried within the layer. As the modulating backgate increases the carrier density, the enhanced carrier concentration can strongly screen the local density, which implies that at a sufficiently high carrier density, the SET should only be affected by the potential from the impurity charges above. Using this rationale, surface potential scan at zero average density was subtracted from that at high carrier density to obtain the spatial fluctuation of only the local density component, i.e., the contribution due to the intrinsic chemical potential. Fig. 18.11C shows the good agreement between the density variations after subtraction (blue solid curve) with the spatial fluctuation of Dirac point (black dotted line) from Fig. 18.11B, both measured along the same straight line. The smallest length scale $\sim 150nm$ over which density fluctuation was observed was attributed to the limited spatial resolution of the QD on the SET tip.

The authors further extended the scheme to extract local density fluctuations at zero average density to a μm^2 area in the XY plane to obtain a color-rendered 2D map, as shown in Fig. 18.12. The red regions correspond to electrons, while the blue zones are due to holes, as evidenced by the sign of n_{2D}. This is one of the first direct images supporting the puddle model. This model postulates that if the density fluctuation from inhomogeneities exceeds the average density of intrinsic carriers, graphene can break down into a random network of 2D electron and hole puddles [19,22,23]. Crucially, this coexistence of oppositely charged carriers despite a vanishing average density can offer a logical explanation for the finite conductivity of graphene around the CNP, as observed in transport measurements [24,25].

18.3.2 Application of carbon nanotube-based single-electron transistor

Finally, let us discuss applications of SETs that have used carbon nanotube QDs as the sensing element. As discussed in Section 18.2.2, CNT-based SETs have been realized only recently. Contrary to Al-based SETs that have been primarily employed to explore equilibrium properties such as electronic compressibility, the CNT-based probes have been used to image dynamic voltage and current flow patterns, simultaneously in high-mobility graphene/hexagonal boron nitride (hBN) devices [7]. They have also been employed to map the electrostatic landscape and local mechanical response in the $LaAlO_3/SrTiO_3$ (lanthanum aluminate-strontium titanate) system, usually abbreviated as LAO/STO [26]. The key findings from both these papers have been discussed below.

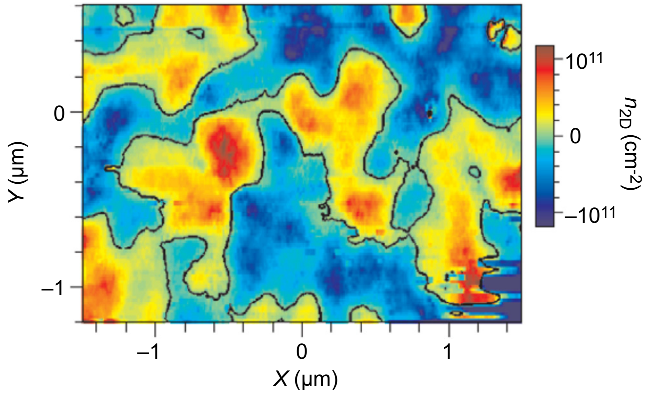

Figure 18.12 Color map of the spatial density variations in a graphene flake showing electron (red) and hole (blue) puddles. Data have been extracted from the surface potential measurements using a scanning SET. The black contour marks the zero density contour. *Source*: From J. Martin, N. Akerman, G. Ulbricht, T. Lohmann, J.H. Smet, K. von Klitzing, A. Yacoby, Observation of electron-hole puddles in graphene using a scanning single-electron transistor. Nature Physics 4(2) (2008) 144−148. https://doi.org/10.1038/nphys781.

18.3.2.1 Studying the origin of anomalous piezoelectricity in LAO/STO

Bulk of the research effort on LAO/STO has concentrated on studying the nature of the 2DES, while the effect of the STO substrate on the oxide interface remains largely unexplored. It has even been suggested that at temperatures lower than $10K$, STO could have a diverging piezoelectric response, much larger than that of conventional piezoelectrics [27]. This had motivated the authors to develop their CNT-based SET and study the effect of ferroelastic domains on the electromechanical properties of the buried conducting interface in pulse laser deposited LAO/STO, at $T = 4K$. Fig. 18.13A shows a schematic of their SET, mounted on a scanning cantilever, where the QD (shown in red) forms within a short CNT, with $p - n$ junction barriers facilitating single-electron tunneling to the source (drain) electrodes. The main structural difference between this schematic and the one shown in Fig. 18.7 is that here the CNT was suspended on a single backgate.

The measurement principle is as follows, any change in the sample-CNT capacitance C and the electrostatic potential ϕ will modulate the charge $Q = C\phi$ induced in the QD as $\delta Q = C\delta\phi + \phi\delta C$. As shown in Fig. 18.13C, fluctuation in the potential, $\Delta\phi$, shall induce a change in the SET current (refer to Section 18.2.2), thus allowing position-dependent measurement of the local surface potential. Next, to study electromechanical response, an oscillating backgate voltage, δV_{BG}, can be applied. If the domain under study is laterally piezoelectric, its local potential $\Delta\phi$ shall oscillate laterally as well (Fig. 18.13D). To visualize the lateral movement of domain walls, the authors measured the corresponding lateral electromechanical response, $d\phi/dV_{BG}$. Fig. 18.13E shows how the local piezoelectric coefficient can

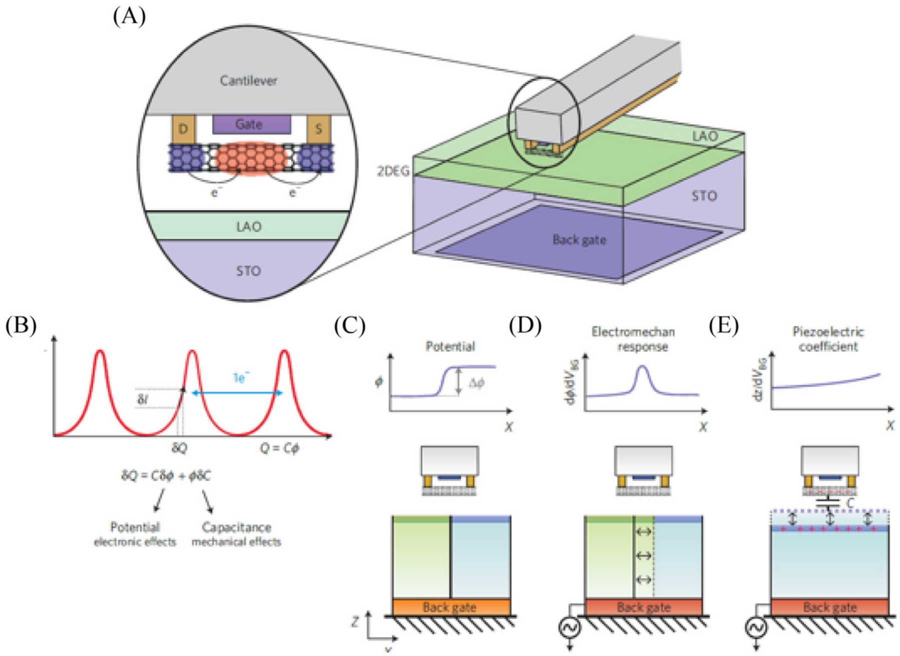
(A)
Cantilever
D
Gate
S
e⁻
e⁻
LAO
STO
2DEG
LAO
STO
Back gate
(B)
δI
1e⁻
δQ
Q = Cϕ
δQ = Cδϕ + ϕδC
Potential electronic effects
Capacitance mechanical effects
(C)
Potential
ϕ
Δϕ
x
Back gate
z
y
(D)
Electromechan response
dϕ/dV_BG
x
Back gate
(E)
Piezoelectric coefficient
dz/dV_BG
x
C
Back gate

Figure 18.13 (A) Schematic showing a cantilever-mounted SET scanning over a backgated LAO/STO sample. Inset shows single-electron tunneling between the source and drain electrodes (in purple) via the QD (in red) formed within the suspended CNT. (B) CBO in the SET current observed as a function of the charge $Q = C\phi$ induced on the dot. Fluctuation in the electrostatic potential ϕ and/or the capacitance C lead to separable contributions to this induced charge, allowing independent measurement of electronic and mechanical perturbations. The measurement principle is highlighted in (C)–(E), with the description presented in the main text.
Source: From M. Honig, J.A. Sulpizio, J. Drori, A. Joshua, E. Zeldov, S. Ilani, Local electrostatic imaging of striped domain order in LaAlO3/SrTiO3. Nature Materials 12(12) (2013) 1112–1118. https://doi.org/10.1038/nmat3810.

be extracted from vertical electromechanical response, dz/dV_{BG}. This involves measuring the local vertical displacement in response to δV_{BG} through the corresponding change in the local capacitance, dC/dV_{BG}. Finally, dz/dV_{BG} was extracted by normalizing this capacitance change with the capacitance change obtained by oscillating the SET-sample separation with a given amplitude.

Fig. 18.14A shows backgate dependence of dz/dV_{BG}, measured with the SET held at a fixed location. The two dashed lines indicate the gate voltages around which the piezoelectric coefficient exhibits a sudden transition accompanied by a change in sign. Fig. 18.14B–D show spatial scans performed over identical areas $(30\mu m \times 30\mu m)$ at three fixed values of V_{BG}, around the first transition boundary. The piezoelectric response was quite homogeneous around this transition, as shown in Fig. 18.14B and D. But dz/dV_{BG} map obtained at the exact boundary value of

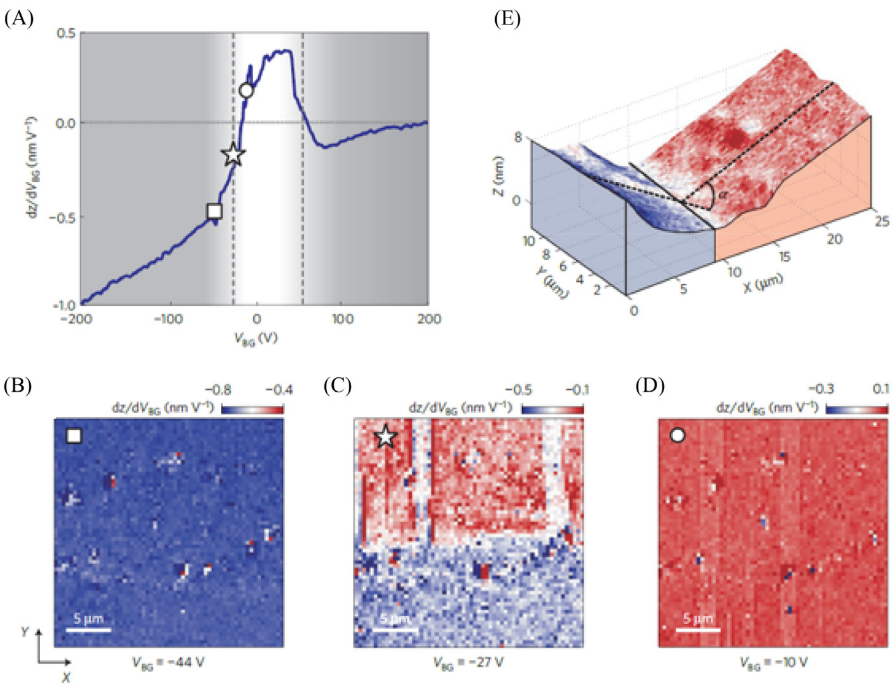

Figure 18.14 (A) The piezoelectric response, dz/dV_{BG}, in LAO/STO measured using a fixed SET as a function of backgate, reveals two sharp transitions, as indicated by the dashed lines. The 1st transition $\sim 1nmV^{-1}$ is anomalously large. (B) and (D) show spatial maps of dz/dV_{BG} at two fixed gate voltages just below and above the first transition, respectively. The maps are largely homogenous with the exception of a few scattered features that are attributed to localized disorder. (C) dz/dV_{BG} measured at the transition value of $27V$ reveals a mixed phase with two distinct piezoelectric responses in the lower and upper half of the map. The value of the response from the lower half seeps into the upper half as narrow vertical channels. (E) The surface topography measured in the mixed regime exhibits a kink. The color coding is meant to correlate this physical kink to the boundary separating the upper and lower phases in (C).
Source: From M. Honig, J.A. Sulpizio, J. Drori, A. Joshua, E. Zeldov, S. Ilani, Local electrostatic imaging of striped domain order in LaAlO3/SrTiO3. Nature Materials 12(12) (2013) 1112–1118. https://doi.org/10.1038/nmat3810.

$V_{BG} = -27V$ showed a mixing of two distinct piezoelectric regions, marked by the different colors for the upper and lower half in Fig. 18.14C. Further, on measuring the three-dimensional surface topography, it was found that the physical surface was kinked with a small angle corresponding to the boundary separating these two regions, as shown in Fig. 18.14E. The angle across the kink was estimated to be $\tan(\alpha) = \left(\frac{c}{a}\right) - 1 \approx 1/1000$, using the available values of the crystallographic axes c and a, at $T = 4K$ [28].

Next, the authors performed gate-dependent measurement of $d\phi/dV_{BG}$ around the transition region highlighted in Fig. 18.14C to extract the lateral electromechanical response. These data shown in Fig. 18.15A revealed an intricate pattern of stripes, most of which appear in pairs of positive (red) and negative (blue) signs, which were oriented either horizontally or vertically. Bulk of these stripes appeared in the upper half of the map, with the lower half remaining largely homogenous. This behavior nicely aligned with the piezoelectric response observed in Fig. 18.14C. Importantly, the magnitude of the response was identical within each pair of stripes, showing that they correspond to upward and downward potential steps of equal magnitude displaced laterally by equal amounts by the AC gate voltage.

The authors used optical imaging experiments (not shown in this chapter) to observe the onset of distinctive stripes below $105K$, around which STO undergoes a ferroelastic transition from cubic to tetragonal symmetry [29], thereby suggesting that these stripes serve as domain walls between domains with different tetragonal orientations. Fig. 18.15A shows a series of maps for the lateral electromechanical response, $d\phi/dV_{BG}$, taken at increasingly negative gate voltages through the transition at $V_{BG} = -27V$. The upper half of the image is populated by a network of stripes, each stripe representing the motion of either the rising (red) or falling (blue)

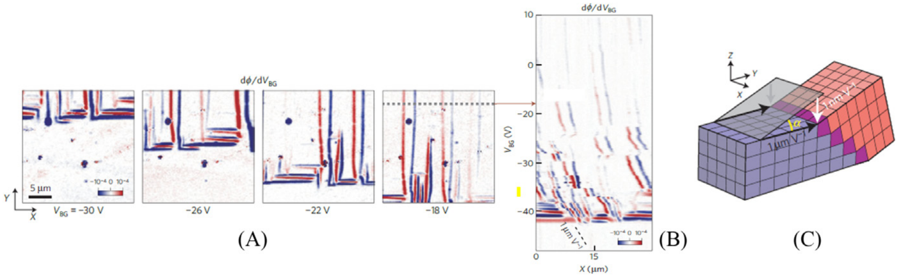

Figure 18.15 (A) Gate-dependent motion of domains, elucidated from the motion of stripes which represent domain walls. Red and blue represent peaks of alternate electromechanical response to the constant gate voltage V_{BG}. With increasing negative bias on the gate, the horizontal boundary separating the homogenous and the striped zones moves toward the upper edge of the sample with speed $\sim 1\mu mV^{-1}$. (B) $d\phi/dV_{BG}$ along a horizontal line [gray dotted line in the rightmost frame in (A)], measured as a function of continuously changing V_{BG}, demonstrating gate-induced motion of the domains within the striped phase with similar speeds. (C) Schematic illustration explaining the origin of anomalous piezoelectric response in STO. The surface is angled between the Y (blue) and Z (red) domains. Sweeping the gate voltage initiates domain wall motion (purple) with characteristic speeds $\sim 1\mu mV^{-1}$, which translates through the kink angle, inducing vertical displacement. Due to minimized dislocation and low thermal loss, the vertical motion of the Z domains takes place at similar speeds $\sim 1\mu mV^{-1}$.

Source: From M. Honig, J.A. Sulpizio, J. Drori, A. Joshua, E. Zeldov, S. Ilani, Local electrostatic imaging of striped domain order in LaAlO3/SrTiO3. Nature Materials 12(12) (2013) 1112–1118. https://doi.org/10.1038/nmat3810.

edge of a potential step at the surface. The lower half is largely homogenous, indicating a negligible lateral electromechanical response. As the successive maps in Fig. 18.15A illustrate, the boundary between the striped and the homogenous zones was found to move along the positive $y-direction$ with a typical speed $\sim 1\mu m V^{-1}$, till $d\phi/dV_{BG}$ becomes homogenous over the entire scan area at sufficiently negative gate voltages. Additionally, decreasing gate voltage caused the domains within the striped phase to laterally slide toward the positive x -direction at similar speeds, as shown in Fig. 18.15B. Considering the kink in the surface (as seen in Fig. 18.14E), it became evident that this in-plane motion of the tetragonal domain walls translates to the motion of the surface perpendicular to the plane, with a similar speed $\sim 1\mu m V^{-1}$. This has schematically been illustrated in Fig. 18.15C. Thus, it was concluded that this gate-induced vertical displacement of tetragonal domains is responsible for the piezoelectric jump observed around $V_{BG} = -27V$ in Fig. 18.14A, and should explain similar anomalously large jumps reported elsewhere.

18.3.2.2 Imaging the spatial distribution of voltage drop and current density in graphene/hexagonal boron nitride

Conventional transport measurements based on the Vander Pauw method induce carrier transport and use fixed voltage (current) probes to sample the electrochemical potential at discreet points in a device. As such, they cannot provide a complete picture of the voltage and current distribution. More importantly, for samples that show ballistic transport, the electron mean free path can be longer than the device and probe geometry. Additionally, the probe electrodes can introduce thermalized electrons randomizing the flow of the intrinsic carriers. In such situations, the fixed probes can cause a local drop-inthe electrochemical potential, hindering the natural electronic movement and necessitating the requirement for a noninvasive probe [30]. Ella et al. deemed scanning SET to be a suitable candidate and applied the technique to image the voltage drops and current density of flowing electrons in high-mobility graphene/hBN devices [7]. They used a CNT-based SET with spatial resolution $\sim 100nm$ and voltage sensitivity $\sim 2\mu\mathrm{V}/\sqrt{Hz}$, fabricated using the procedure [6] described in Section 18.2.2.

Fig. 18.16 schematically compares the conventional transport measurement (Fig. 18.16A) to the SET mapping technique (Fig. 18.16B) in a standard Hall bar device. In conventional transport, the electrochemical potential drop induced by the injected current is measured by measuring the electrochemical potential difference between predefined fixed electrodes. This is then used to extract both longitudinal (ρ_{xx}) and Hall (ρ_{xy}) resistivities. For the noninvasive SET probe, the authors measured the resistance at different spatial positions (x, y) by extracting the electrostatic potential $\delta\phi(x, y)$, and dividing it by the applied alternating current, δI. In order to achieve this experimentally, they simultaneously applied an excitation $V_s = V_{ex}cos(\omega_s t)$, on the source electrode at one frequency, ω_s, and an excitation $V_d = V_{ex}cos(\omega_d t)$ on the drain at a different frequency. This is a key difference from

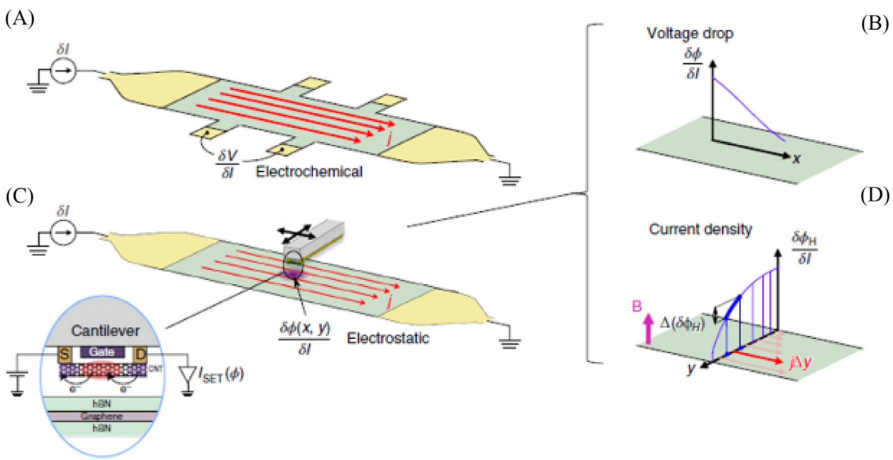

Figure 18.16 (A) In a conventional scheme to measure resistivity, alternating current, δI (in red arrows) is injected in a Hall bar device (in green), and the corresponding electrochemical potential difference (δV) is measured across lithographically printed electrodes. (B) In the proposed scheme to use a noninvasive SET probe, a CNT-based SET mounted on a scanning probe cantilever is rastered (black arrows) in the xy-plane to measure the drop in the local electrostatic potential ($\delta\phi$) at every spatial position, induced by the electron flow. Inset shows a cross-section of the SET, held at a fixed height above a dual-gated graphene device. The CNT (in purple) is flanked by the source and drain electrodes (in yellow) at the two extreme ends, with the QD (in red) forming within the suspended segment. (C) To extract information on longitudinal (x-direction) resistance, $\delta\phi$ can be normalized by the applied current δI. (D) The current density can be measured by applying a perpendicular magnetic field B, to induce a Hall current along y-direction and using the equation, $j\Delta y = \frac{ne}{B}\Delta\left(\delta\phi_H\right)$. Please refer to the main text for a detailed explanation.
Source: From L. Ella, A. Rozen, J. Birkbeck, M. Ben-Shalom, D. Perello, J. Zultak, T. Taniguchi, K. Watanabe, A.K. Geim, S. Ilani, J.A. Sulpizio, Simultaneous voltage and current density imaging of flowing electrons in two dimensions. Nature Nanotechnology 14 (5) (2019) 480–487. https://doi.org/10.1038/s41565-019-0398-x.

the inverse compressibility experiments using Al-based SETs described earlier in this chapter.

Instead of measuring the response to a single bias as described in Section 18.2.2, the CNT-based scanning SET was used to simultaneously measure the two local responses to these excitations at a given position, $H_i(x,y) = \frac{\partial I_{SET}}{\partial V_i}(i = s,d)$ by extracting the SET current I_{SET} at ω_s and ω_d. Finally, the electrostatic potential was obtained using the relation: $\phi(x,y) = \frac{V_{ex}}{2}\cdot\left[\frac{H_s - H_d}{H_s + H_d} + 1\right]$ (for a more qualitative explanation, the reader can refer to the supplementary section of Ref. [7]).

As shown in Fig. 18.16C, the longitudinal voltage drop associated with varying ρ_{xx} can be obtained by measuring $\delta\phi/\delta I$ at zero magnetic field. On the application of a finite field, $\pm B$, the electron flow bends due to the addition of the Hall voltage to the longitudinal drop. Since the longitudinal component is symmetric in B, the Hall voltage associated with ρ_{xy} can be extracted using the following relation, which cancels out the longitudinal voltage drop,

$$\delta\phi_H\Big(x, y)/\delta I \equiv \big(\delta\phi_{+B}(x, y) - \delta\phi_{-B}(x, y)\big)/2\delta I \tag{18.11}$$

This has schematically been shown in Fig. 18.16D. Next, $\delta\phi_H(x, y)$ can be used to extract the electron flow streamline function using the following expression [31],

$$\delta\psi(x, y) = \frac{ne}{B}\delta\phi_H(x, y) \tag{18.12}$$

where n and e are the local carrier density and electronic charge, respectively. Finally, the local current density j can be calculated using the standard definition, $j = \hat{z} \times \nabla\delta\psi(x, y)$, with $\hat{z}$ being perpendicular to the plane of the sample.

An optical image of the BN/graphene/BN device used is shown in Fig. 18.17A. The device was etched with two gold electrodes serving as the source/drain contacts, with the conducting channel (green) having dimensions of $11 \times 25\mu m^2$. Modulating the carrier density using a backgate exhibited typical two-probe resistance, with a sharp-peaked charge neutrality point (red dot) appearing at zero-carrier density (Fig. 18.17B). Fig. 18.17C and D show the spatial maps of the local potential drop measured at the CNP and a high hole density of $n = 1 \times 10^{12} cm^{-2}$ (blue dot in Fig. 18.17B), respectively. While the former broadly exhibits a diffusive linear drop along the channel, marred with disorder-induced resistive fluctuations, for the latter, the potential is nearly flat in bulk, with step-like resistive drops only appearing at the gold contacts indicative of ballistic behavior. The small drop in the bulk seen in Fig. 18.17D is due to the finite mean free path.

Finally, Fig. 18.18 illustrates how the CNT-based SET can be used to visualize the nature of Hall transport. In order to demonstrate this ability, the authors used a graphene device with a bent geometry as shown in Fig. 18.18A. The conducting channel is confined within etched walls (in blue), with the source/drain electrodes oriented such that they can detect curved electron flow under the influence of a finite perpendicular magnetic field. As shown in Fig. 18.18B and C, on the application of oppositely directed fields, $B = \mp 20mT$, the induced Hall voltage results in the equipotential contours (colored lines) to bend in opposite directions with respect to the channel direction. It is fascinating that this method allows for direct visual estimation of the local Hall angle. Next, they subtract these two graphs to extract the pure Hall voltage $\delta\phi_H(x, y)/\delta I$ and current electron flow streamline functions, using Formulae (18.11 and 18.12), respectively. Fig. 18.18D shows the resulting current trajectories (black lines) superimposed on the independently measured zero-field equipotential contours, clearly illustrating how the current streamlines snake around the bend in the device.

The bunching of the equipotential contours near the entrance to the bend points to an increase in resistance, providing further evidence of the ballistic nature of

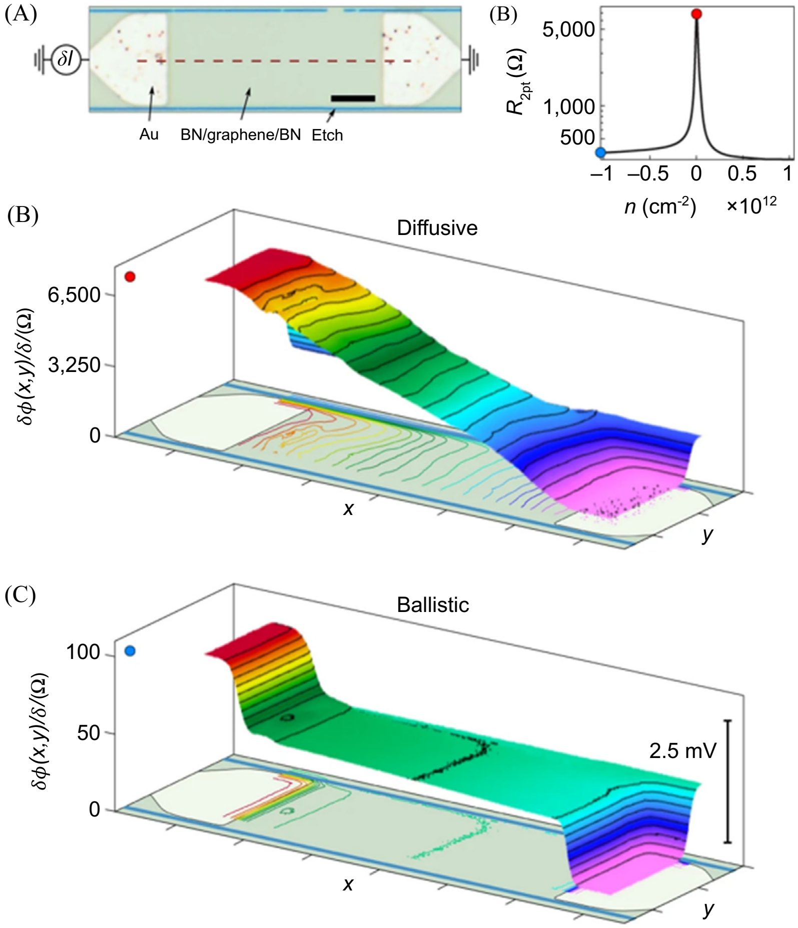

Figure 18.17 (A) An optical micrograph of the device, showing the conducting channel defined in a single-layer graphene/hBN sandwich (green), marked by chemically etched boundaries (blue), with a pair of lithographically deposited gold contacts (yellow). δI denotes the injected current. (B) Two-probe resistance, R_{2pt},measured at $4K$, as a function of backgate-modulated carrier density. (C) Map of SET-imaged electrostatic potential, normalized by the injected current, $\delta\phi(x,y)/\delta I$ (units of resistance), measured around the CNP (red dot in (B)), illustrates diffusive transport along the channel. The bottom plane shows the equipotential contours superimposed on the schematic of the device, indicating that the voltage drops gradually between the contacts, with intermittent disorder-induced deviations. (d) On the contrary, $\delta\phi(x,y)/\delta I$ measured at a high hole concentration of $n = 1 \times 10^{12} cm^{-2}$ (blue dot in (B)) shows strong signs of ballistic transport, marked by a flat potential profile in bulk, with step-like voltage drops appearing only at the contacts. *Source*: From L. Ella, A. Rozen, J. Birkbeck, M. Ben-Shalom, D. Perello, J. Zultak, T. Taniguchi, K. Watanabe, A.K. Geim, S. Ilani, J.A. Sulpizio, Simultaneous voltage and current density imaging of flowing electrons in two dimensions. Nature Nanotechnology 14 (5) (2019) 480–487. https://doi.org/10.1038/s41565-019-0398-x.

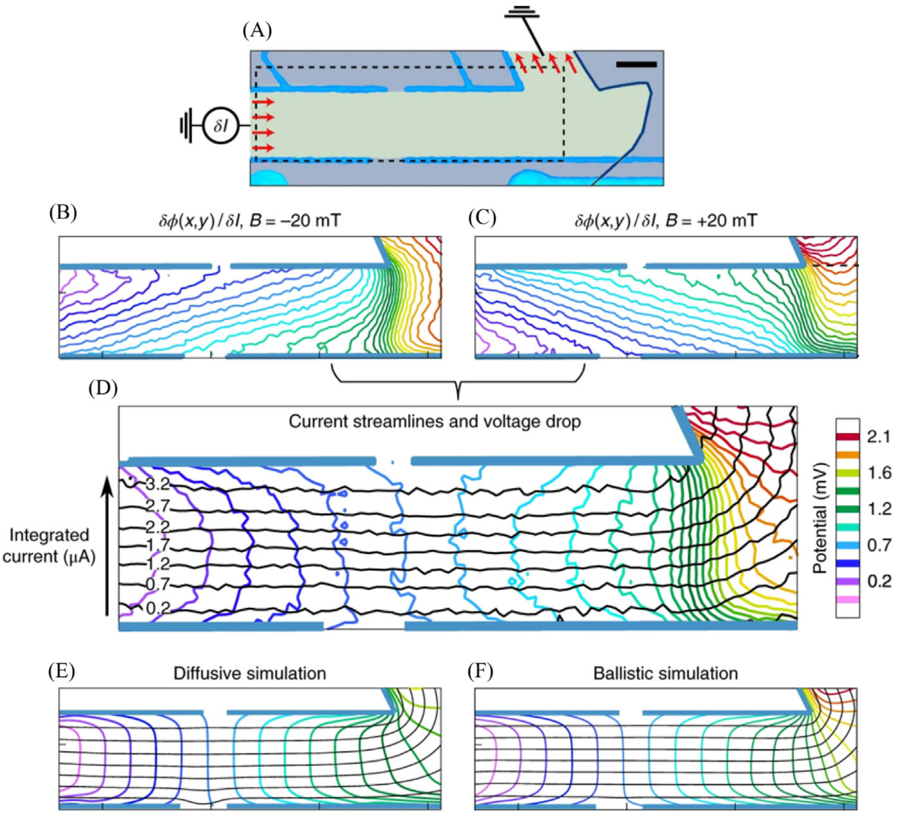

Figure 18.18 (A) Optical image of the graphene device with a bent channel (in green), with the red arrows indicating the direction of the injected alternating current, δI. (B) and (C) illustrate visualization of Hall effect: spatial profiles of the electrostatic potential, $\delta\phi(x,y)/\delta I$, in the Hall regime, on the application of perpendicular fields, $B = -20mT$ and $B = +20mT$, respectively, taken at the constant hole density of $n = 8.3 \times 10^{10}cm^{-2}$. Oppositely directed Hall electric fields induce opposite curvatures in the equipotential contours. (D) Imaged current streamlines ψ (black isocontours) superimposed on the zero-field voltage contours (color). Each streamline is defined by $\delta\psi(x,y) \equiv \frac{\delta\phi_{+B}(x,y) - \delta\phi_{-B}(x,y)}{2\left(\frac{B}{ne}\right)}$, where the numerator was obtained from the difference in the maps shown in (B) and (C). The current magnitude against each streamline has been extracted from the product of the sample area and the local current density $\boldsymbol{j} = \hat{z} \times \nabla\delta\psi(x,y)$.

Source: From L. Ella, A. Rozen, J. Birkbeck, M. Ben-Shalom, D. Perello, J. Zultak, T. Taniguchi, K. Watanabe, A.K. Geim, S. Ilani, J.A. Sulpizio, Simultaneous voltage and current density imaging of flowing electrons in two dimensions. Nature Nanotechnology 14 (5) (2019) 480−487. https://doi.org/10.1038/s41565-019-0398-x.

electron transport. As predicted by a simulation of diffusive flow for this exact device geometry (Fig. 18.18E), an increase in channel width for samples with homogenous bulk conductivity should show a resistance decrease at the bend. On the other hand, for ballistic transport, an electron billiards simulation of ballistic flow with diffusive boundaries for this device geometry (Fig. 18.18F) shows a clear bunching of the equipotential contours around the bend as in the experiment. Physically, this can be interpreted by considering that a change in channel width acts analogous to a reflecting barrier to the electron flow, increasing the resistance. The reduced increase in resistance seen in the ballistic simulation, relative to the experimental data, has been attributed to additional disorder and mechanical stress near the etched boundaries and strong electric fields near the etched corners. The ability of the SET technique to obtain such detailed maps of both the voltage and current trajectories in nonstandard sample geometries highlights one of the most potent applications, providing researchers a powerful tool to visualize certain underlying electronic interactions, which can otherwise be challenging to obtain via conventional mapping and transport techniques.

18.4 Conclusion

Single-electron transistors using carbon nanotube QDs have proved to be a significant evolution over their aluminum counterparts, both in terms of fabrication and a potential application. As explained in Section 18.2.2, the flexibility to select the best nanotube from multiple CNTs is a clear advantage over fabricating traditional Al-based SETs, which involves a tedious and usually trial-and-error-based approach. Additionally, the advancement in nanofabrication tools reduces the diameter of individual nanotubes significantly, thereby shrinking the QD, resulting in enhanced voltage sensitivity. But the true novelty of the technique has been demonstrated on the application front. Hitherto, Al-based SETs have been limited to mapping electronic compressibility at thermodynamic equilibrium, such as imaging quantum Hall states and localized charging phenomena in two-dimensional systems. While for CNT-based SETs, within the short period since the technique was implemented, they have been applied in distinctive studies, two of which have been presented here—on the one hand, they have been used as noninvasive scanning probes to map the dynamic nature of electronic transport and visualize Hall effect in graphene; on the other hand, they have provided strong evidence that anomalously large piezoelectric response in LAO/STO originates from domain wall motion. Moving forward, this imaging technique holds promise for imaging an array of phenomena presently under intense focus, such as hydrodynamic electron flow, Dirac electron optics, and Andreev reflections in the magnetic field. In a more practical direction, the technique is well suited for fully characterizing transport effects due to disorder and other scattering mechanisms in a broad class of novel materials and devices, where imaging the local electronic flow patterns can provide crucial otherwise inaccessible information via conventional methods.

References

[1] M.H. Devoret, H. Grabert, Introduction to Single Charge Tunneling, Springer, US, 1992, pp. 1−19. Available from: https://doi.org/10.1007/978-1-4757-2166-9_1.

[2] J.P. Eisenstein, L.N. Pfeiffer, K.W. West, Negative compressibility of interacting two-dimensional electron and quasiparticle gases, Physical Review Letters 68 (5) (1992) 674−677. Available from: https://doi.org/10.1103/PhysRevLett.68.674.

[3] J.P. Eisenstein, L.N. Pfeiffer, K.W. West, Compressibility of the two-dimensional electron gas: measurements of the zero-field exchange energy and fractional quantum Hall gap, Physical Review B 50 (3) (1994) 1760−1778. Available from: https://doi.org/10.1103/PhysRevB.50.1760.

[4] M.J. Yoo, T.A. Fulton, H.F. Hess, R.L. Willett, L.N. Dunkleberger, R.J. Chichester, L. N. Pfeiffer, K.W. West, Scanning single-electron transistor microscopy: imaging individual charges, Science 276 (5312) (1997) 579. Available from: https://doi.org/10.1126/science.276.5312.579.

[5] J. Weis, Single-Electron Devices, Springer, Berlin Heidelberg, 2005, pp. 87−121. Available from: https://doi.org/10.1007/978-3-540-31533-9_5.

[6] J. Waissman, M. Honig, S. Pecker, A. Benyamini, A. Hamo, S. Ilani, Realization of pristine and locally tunable one-dimensional electron systems in carbon nanotubes, Nature Nanotechnology 8 (8) (2013) 569−574. Available from: https://doi.org/10.1038/nnano.2013.143.

[7] L. Ella, A. Rozen, J. Birkbeck, M. Ben-Shalom, D. Perello, J. Zultak, T. Taniguchi, K. Watanabe, A.K. Geim, S. Ilani, J.A. Sulpizio, Simultaneous voltage and current density imaging of flowing electrons in two dimensions, Nature Nanotechnology 14 (5) (2019) 480−487. Available from: https://doi.org/10.1038/s41565-019-0398-x.

[8] D.R. Yennie, Integral quantum Hall effect for nonspecialists, Reviews of Modern Physics 59 (3) (1987) 781−824. Available from: https://doi.org/10.1103/RevModPhys.59.781.

[9] K.v Klitzing, G. Dorda, M. Pepper, New method for high-accuracy determination of the fine-structure constant based on quantized hall resistance, Physical Review Letters 45 (6) (1980) 494−497. Available from: https://doi.org/10.1103/PhysRevLett.45.494.

[10] J. Wakabayashi, S. Kawaji, Hall effect in silicon MOS inversion layers under strong magnetic fields, Journal of the Physical Society of Japan 44 (6) (1978) 1839−1849. Available from: https://doi.org/10.1143/JPSJ.44.1839.

[11] D.C. Tsui, H.L. Stormer, A.C. Gossard, Two-dimensional magnetotransport in the extreme quantum limit, Physical Review Letters 48 (22) (1982) 1559−1562. Available from: https://doi.org/10.1103/PhysRevLett.48.1559.

[12] C.W.J. Beenakker, Edge channels for the fractional quantum Hall effect, Physical Review Letters 64 (2) (1990) 216−219. Available from: https://doi.org/10.1103/PhysRevLett.64.216.

[13] A.M. Chang, A unified transport theory for the integral and fractional quantum hall effects: phase boundaries, edge currents, and transmission/reflection probabilities, Solid State Communications 74 (9) (1990) 871−876. Available from: https://doi.org/10.1016/0038-1098(90)90447-J.

[14] A. Yacoby, H.F. Hess, T.A. Fulton, L.N. Pfeiffer, K.W. West, Electrical imaging of the quantum Hall state, Solid State Communications 111 (1) (1999) 1−13. Available from: https://doi.org/10.1016/S0038-1098(99)00139-8.

[15] V.J. Goldman, J. Liu, A. Zaslavsky, Electron tunneling spectroscopy of a quantum antidot in the integer quantum Hall regime, Physical Review B 77 (11) (2007) 115328. Available from: https://doi.org/10.1103/PhysRevB.77.115328.

[16] S. Ilani, J. Martin, E. Teitelbaum, J.H. Smet, D. Mahalu, V. Umansky, A. Yacoby, The microscopic nature of localization in the quantum Hall effect, Nature 427 (6972) (2004) 328−332. Available from: https://doi.org/10.1038/nature02230.

[17] B. Huckestein, Scaling theory of the integer quantum Hall effect, Reviews of Modern Physics 67 (2) (1995) 357−396. Available from: https://doi.org/10.1103/RevModPhys.67.357.

[18] J. Martin, N. Akerman, G. Ulbricht, T. Lohmann, J.H. Smet, K. von Klitzing, A. Yacoby, Observation of electron−hole puddles in graphene using a scanning single-electron transistor, Nature Physics 4 (2) (2008) 144−148. Available from: https://doi.org/10.1038/nphys781.

[19] N.M.R. Peres, F. Guinea, A.H. Castro Neto, Coulomb interactions and ferromagnetism in pure and doped graphene, Physical Review B 72 (17) (2005) 174406. Available from: https://doi.org/10.1103/PhysRevB.72.174406.

[20] E. McCann, Electronic Properties of Monolayer and Bilayer Graphene, Springer, Berlin Heidelberg, 2012, pp. 237−275. Available from: https://doi.org/10.1007/978-3-642-22984-8_8.

[21] Z. Jiang, E.A. Henriksen, L.C. Tung, Y.-J. Wang, M.E. Schwartz, M.Y. Han, P. Kim, H.L. Stormer, Infrared spectroscopy of landau levels of graphene, Physical Review Letters 98 (19) (2007) 197403. Available from: https://doi.org/10.1103/PhysRevLett.98.197403.

[22] E.H. Hwang, S. Adam, S.D. Sarma, Carrier transport in two-dimensional graphene layers, Physical Review Letters 98 (18) (2007) 186806. Available from: https://doi.org/10.1103/PhysRevLett.98.186806.

[23] E.H. Hwang, B.Y.-K. Hu, S. Das Sarma, Density dependent exchange contribution to $\partial\mu/\partial n$ and compressibility in graphene, Physical Review Letters 99 (22) (2007) 226801. Available from: https://doi.org/10.1103/PhysRevLett.99.226801.

[24] S. Cho, M.S. Fuhrer, Charge transport and inhomogeneity near the minimum conductivity point in graphene, Physical Review B 77 (8) (2008) 081402. Available from: https://doi.org/10.1103/PhysRevB.77.081402.

[25] A.K. Geim, K.S. Novoselov, The rise of graphene, Nature Materials 6 (3) (2007) 183−191. Available from: https://doi.org/10.1038/nmat1849.

[26] M. Honig, J.A. Sulpizio, J. Drori, A. Joshua, E. Zeldov, S. Ilani, Local electrostatic imaging of striped domain order in LaAlO3/$SrTiO_3$, Nature Materials 12 (12) (2013) 1112−1118. Available from: https://doi.org/10.1038/nmat3810.

[27] D.E. Grupp, A.M. Goldman, Giant piezoelectric effect in strontium titanate at cryogenic temperatures, Science 276 (5311) (1997) 392. Available from: https://doi.org/10.1126/science.276.5311.392.

[28] M. Liu, T.R. Finlayson, T.F. Smith, High-resolution dilatometry measurements of $SrTiO_3$ along cubic and tetragonal axes, Physical Review B 55 (6) (1997) 3480−3484. Available from: https://doi.org/10.1103/PhysRevB.55.3480.

[29] P.A. Fleury, J.F. Scott, J.M. Worlock, Soft phonon modes and the 110°K Phase Transition in $SrTiO_3$, Physical Review Letters 21 (1) (1968) 16−19. Available from: https://doi.org/10.1103/PhysRevLett.21.16.

[30] M.J. McLennan, Y. Lee, S. Datta, Voltage drop in mesoscopic systems: a numerical study using a quantum kinetic equation, Physical Review B 43 (17) (1991) 13846−13884. Available from: https://doi.org/10.1103/PhysRevB.43.13846.

[31] G. Falkovich, L. Levitov, Linking spatial distributions of potential and current in viscous electronics, Physical Review Letters 119 (6) (2016) 066601. Available from: https://doi.org/10.1103/PhysRevLett.119.066601.

Nanodiamonds for advanced photonic and biomedical applications

19

Daksh Agarwal[1,2], *Nikhil Dole*[3], *Aditya Banerjee*[4] *and Amit Banerjee*[5]
[1]Department of Materials Science and Engineering, University of Pennsylvania, Philadelphia, PA, United States, [2]Lam Research Corporation, Fremont, CA, United States, [3]Department of Electrical and Computer Engineering, University of Houston, Houston, TX, United States, [4]Amity Institute of Applied Science, Amity University, Noida, Uttar Pradesh, India, [5]Physics Department, Bidhan Chandra College, Asansol, West Bengal, India

19.1 Introduction to nanodiamond photonics

Nanodiamond (ND) photonics have attracted significant attention because of their ability to act as single photon sources (SPS) at ambient temperatures and have applications in nanoscale magnetometry, biological markers, detectors, quantum optics, and quantum information processing [1–6]. Diamond has an indirect bandgap of 5.47 eV but its rich emission spectra (especially around the visible region) originate from a variety of defects and impurities in its lattice. The most commonly used defect is the negatively charged nitrogen-vacancy (NV) complex having broadband emission in near IR wavelengh range, centered around 680 nm [7]. However, since only 4% of the photons from the NV complex are emitted in the zero phonon line (ZPL), its use in nanophotonic applications is limited [8]. Some of the other defects explored for emissions are germanium vacancy (GeV) center with emission at 602 nm, Tin-vacancy (Sn-V) center with emission at 619 nm, silicon-vacancy (SiV) centers with emission at 736 nm, chromium based centers with emission at 756 nm, near infrared (NIR) single emitters with emission at 780 nm, and nickel-nitrogen complex centers with emission at 800 nm [9–14]. In the following sections, examples of two representative optical emission sources in ND are discussed followed by key applications.

19.1.1 Optical emission from diamond

As explained above, emission in ND comes from various lattice defects. SiV defect is one of the commonly used color centers consisting of an interstitial Si atom adjacent to two vacancies along the [111] crystallographic direction of the diamond structure and offers pathway to a potential SPS [15,16]. Fig. 19.1A shows schematic

Carbon Quantum Dots for Sustainable Energy and Optoelectronics. DOI: https://doi.org/10.1016/B978-0-323-90895-5.00009-6
© 2023 Elsevier Ltd. All rights reserved.

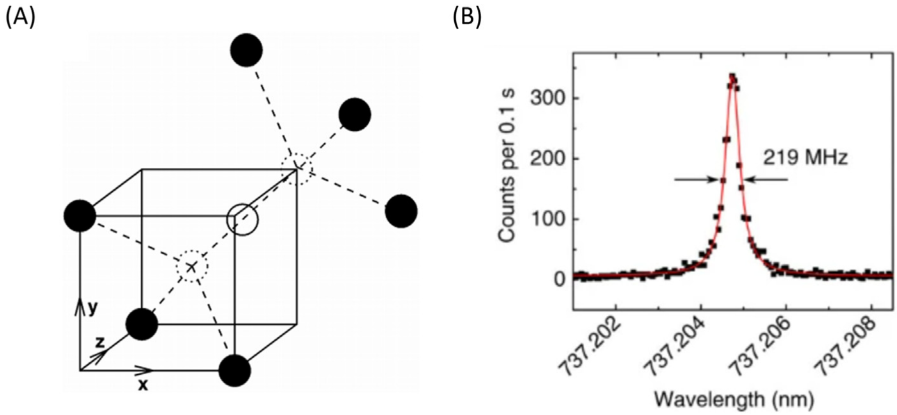

Figure 19.1 (A) Schematic representation of the SiV defect. The solid circles represent C atoms, the empty circle the relaxed Si site, and the dashed circles the vacant diamond lattice sites (vacancy) showing the Si atom neighboring two vacancies. (B) Resonant measurement of linewidth of SiV defect (C transition) at saturation power; black squares represent raw data and red curve represents the Lorentzian fit.
For (A) reproduced with permission from Goss, J. P., Jones, R., Breuer, S. J., Briddon, P. R. & Oberg, S., The twelve-line 1.682eV luminescence center in diamond and the vacancy-silicon complex. Physical Review Letters 77, 3041 (1996); reproduced with permission Y. Zhou, A. Rasmita, K. Li, Q. Xiong, I. Aharonovich & W.-B. Gao. Coherent control of a strongly driven silicon vacancy optical transition in diamond. Nature Communications 8 (2017) 14451.

of a SiV defect [15]. Emission from SiV has various advantages such as ~70% of the emission in the ZPL, similar emission from different SiV defects, and lifetime limited linewidths [15,16,18–20]. Zhou et al. showed (Fig. 19.1B) coherent control of optical transition in SiV center using resonant excitation with a peak at 737.2 nm and a linewidth of 219 MHz [17]. The linewidth without power broadening was shown to be 154 MHz which was similar to the lifetime limited bandwidth of 86 MHz.

Tran et al. showed that NDs fabricated via chemical vapor deposition have bright, highly-polarized near-infrared single photon emitters with narrow sub-GHz linewidth at a temperature of 10 K [21]. At room temperature, the emitters had a linewidth of ~2 THz and a range of ZPLs in the near IR range. At 10 K, there was narrowing of linewidth and measurement was limited by the spectrometer resolution, which makes this emission very promising for a variety for quantum photonic applications. On average, 4%–7% of the diamonds showed the NIR emission. Fig. 19.2A shows the representative emission spectra from NDs with SiV peak at 738 nm and NIR peaks in the range 756–786 nm at room temperature [21]. Fig. 19.1B shows high-resolution scans carried out at 10 K for one of the NDs with an emission at 780 nm and has a full width at half maximum (FWHM) of 79 GHz, corresponding to the spectrometer resolution [21]. The Debye-Waller factor was calculated to be 0.87, which is higher than the value for NV color center (0.04) and comparable with that of SiV and GeV defects.

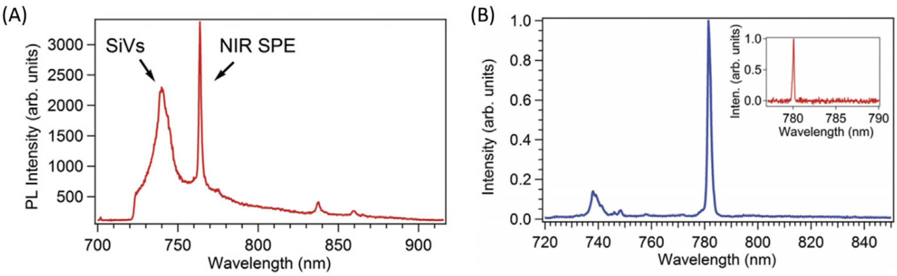

Figure 19.2 (A) A typical nanodiamond emission spectrum showing SiV as well as NIR emission at room temperature. (B) Normalized NIR emission from a color center at 10 K. Inset shows the high-resolution scan from the same emitter.
Reproduced with permission T. T. Tran, M. Kianinia, K. Bray, S. Kim, Z. Q. Xu, A. Gentle, et al., Nanodiamonds with photostable, sub-gigahertz linewidth quantum emitters. APL Photonics 2 (2017) 116103.

19.1.2 ND photonic applications

NDs have various applications because of their rich photoluminescence spectrum and their ability to act as SPS [2−6]. Han et al. showed that charged NV centers are great candidates for far-field fluorescence nanoscopy by stimulated emission depletion (STED) microscopy [22]. They worked with CW and pulsed excitation of wavelength >700 nm and were able to image the single NV centers in three dimensions, which were >6 μm inside the diamond crystal. A 5−6-fold improvement in resolution over conventional confocal recordings with a spot size extension of 110−135 nm was observed. Fig. 19.3A shows the comparison of x-z profile of diamond NV centers taken by STED and by confocal microscopy. While the individual color centers are sharply resolved with STED, they look blurry with confocal microscopy.

An alternate way to employ NDs for various applications is to couple them to photonic platforms such as GaP and SiO_2 to control and enhance their emission. GaP has high refractive index, high second-order optical coefficient, and optical transparency at the relevant wavelengths, which makes it an attractive candidate for photonic platforms [24]. One way to couple the two is to have GaP nanostructures on top of bulk diamond crystal. This allows for the NV emission to first be resonantly enhanced due to Purcell effect and efficiently waveguided because of efficient coupling in between the NV center and the GaP nanophotonic device [25]. An alternate methodology is to build the device bottom-up by using the pick and place method. This provides the ability to select the desired color center in diamond as well as the desired nanocavity for efficient coupling. This also gives the ability to place the color center at the location in cavity where the electric field is maximized for the highest possible enhancement in emission [26,27]. Diamond nanocrystals have also been coupled to a variety of SiO_2 cavities such as microresonators, fiber taper waveguides, as well as microdisc-integrated silicon photonic circuits [28−30]. High-purity, brightness, and pure SPS have been fabricated by employing color centers such as SiV and NV in a fiber-based spectroscopic technique called

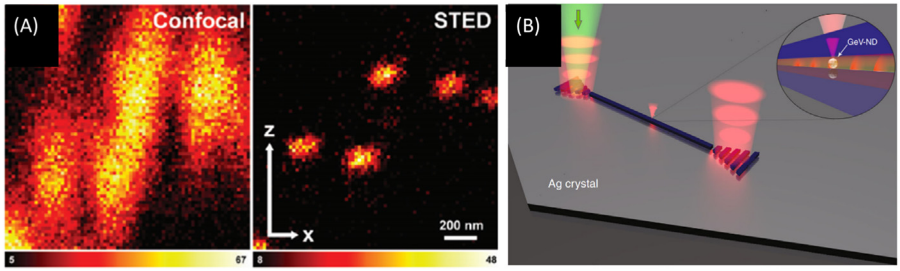

Figure 19.3 (A) xz-profile of individual NV color center in bulk diamond using confocal microscopy (left) showing blurred image and using STED microscopy showing individually resolved color centers (reproduced with permission 22). (B) Device layout schematic and working principle for on-chip excitation of a GeV color center in a ND embedded in a DLSPP waveguide.
Reproduced with permission H. Siampour, S. Kumar, V. A. Davydov, L. F. Kulikova, V. N. Agafonov and S. I. Bozhevolnyi. On-chip excitation of single germanium vacancies in nanodiamonds embedded in plasmonic waveguides. Light: Science & Applications 7 (2018) 61.

scanning cavity microscopy [31]. In one such technique, a Purcell factor of 9.2 was obtained [32].

NDs have also been coupled to plasmonic cavities for applications in nanoscale functional quantum devices. A single emitting dipole such as a ND color center when placed in the vicinity of a metal has a transformed spectral distribution as well as a different emission lifetime which is similar to Purcell enhancement effect in a cavity. Therefore, this can enhance the emission rate and improve its directionality leading to enhanced SPS [33]. Plasmonic waveguides have been used to demonstrate remote excitation of on-chip GeV color center in NDs [23]. Fig. 19.3B shows the schematic of one such experimental set up. NDs with a single GeV color center were fabricated. Dielectric-loaded surface plasmon polariton waveguides (DLSPPWs) were fabricated on single crystalline silver plates containing ND with the appropriate color defect. GeV color center was remotely excited using a 532 nm laser, and the single photons were coupled to the DLSPPW. Compared to other systems, this GeV-DLSPPW system had an excellent figure of merit value of 180 with a Purcell enhancement factor of 6 and has the potential for monolithic integration.

Coherent photons can also be generated from diamond using stimulated Raman scattering with applications in microelectronics industry, which has been an active area of research for making faster, smaller and more energy efficient devices [34–36]. Diamond Raman lasers have the advantage of availability of otherwise inaccessible wavelength due to its large Raman shift, good thermal properties, and large transparency window and have been developed in the telecom range as well as in the visible range [37,38].

Extraordinary progress has been made in developing ND-based SPS and their integration into multiple photonic platforms for on-chip integration for building quantum devices. This would enable applications in fields such as quantum information processing, communication, computation, as well as detectors including applications in medical imaging.

19.2 NDs for biomedical applications

Nanomaterial drug delivery in medical applications has garnered attention and contributed to recent advancements in nanotechnology. Nanomaterials typically have a large surface area which can increase the loading amount, improve the release kinetics of the drug delivery, and, due to their small size, can penetrate endothelial cells directly therby improving overall drug absorption [39,40]. Arvizo et al. reported that gold nanospheres can reduce tumor metastasis by blocking MAPK signaling [41]. Zhou et al. found that graphene can inhibit cancer cell migration via mitochondrial respiratory impairment [42]. Barnard et al. show that detonation NDs (DNDs) with unique faceted surfaces improve drug delivery for tumor therapy [43]. Guo et al have investigated the inhibition of tumor cell migration by carboxylate nanodiamonds (cND) [44].

For the last few years, NDs are gaining popularity in both industry and research work due to their dual properties of diamonds and nanoparticles. In comparison with other carbon-based materials such as graphene and carbon nanotube (CNT), the preparation for NDs is simple and well established. While growth of scientific ND articles has faced a steady growth since the beginning of 2000s, a search in Scopus combining “nanodiamond” with “bio” as wildcard reveals growth in the papers published considering ND for biorelevant applications took after 2008 (Fig. 19.4) [45].

NDs are, as the name suggests, nanoscopic particles of diamond generally fabricated by chemical vapor deposition (CVD), detonation ND (DND) or high-temperature high-pressure (HTHP), with new fabrication methods coming up with emerging technology [45]. Few of the remarkable properties of NDs, such as extraordinary mechanical hardness and unique optical properties, are caused by impurities or defects in diamond lattice. Additionally, NDs are relatively inexpensive, biocompatible and optically stable with easy-to-modify surface functionality. These physical properties are ideally suited for biological, biomedical applications such as medical imaging, cancer treatment, intra and extracellular drug delivery, and detection of bioactive molecules.

Concurrently, the growth and evolution of novel bioimaging methods has created a synergism of these two fields. The optical and physical properties of NDs can be tuned, rendering them highly intriguing as versatile biomedical imaging probes. In this section, the emerging applications of ND in biomedical imaging and cancer treatment is discussed and reviewed in detail, exposing current challenges in their implementation and proposing future development opportunities in this field.

19.2.1 Cancer therapy applications

Over the past several decades, substantial progress has been made toward improving cancer treatment because of the advances in prescreening, prognosis, treatment,

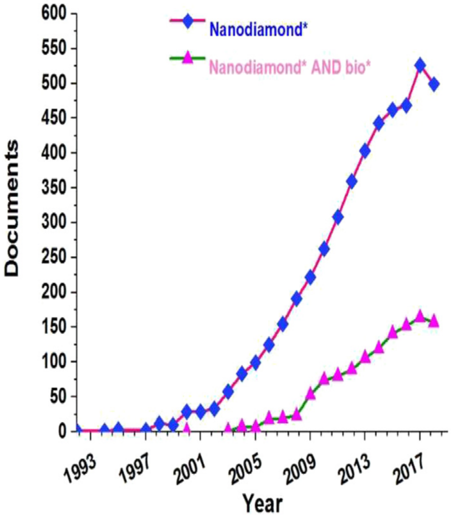

Figure 19.4 Scopus search on Nanodiamond and bio since early 1990s till late 2010s. Interest in ND-related articles took off from mid-2000s and continue to gain attention of researchers.
Reproduced with permission N. Prabhakar and J. M. Rosenholm, Nanodiamonds for advanced optical bioimaging and beyond, *Current Opinion in Colloid and Interfacial Science* 39 (2019) 220–231.

and safety of administered drugs. As new drug development and manufacturing is quite costly, engineering an efficient and safe way (with minimal side effects) for drug delivery is increasingly important [46].

The use of nanomaterials in preclinical and clinical medicine studies has created an excitement for fundamental breakthrough research in the field of cancer treatment. Many of the current obstacles in diagnosis, treatment, and follow-up medical procedures are successfully being addressed by emerging nanomaterials and their compounds. The commonly seen barriers are toxicity of the material, delivery efficiency, and drug resistance, risking other side effects. The first clinical nanomedicine advances were achieved by using single drug therapy, wherein small-molecule and nucleic acid delivery showed substantial improvements over unmodified drug administration [46]. In recent years, clinical studies have demonstrated that multiple class of nanomaterials coupled with therapeutic agents can image and treat tumors more effectively rather than a single drug therapy.

A few candidate nanomaterials are used for clinical therapeutic treatments among which carbon-based materials have received increasing attention for being used as biomedical imaging agents and efficient drug delivery. Carbon-based nanomaterials for biomedical applications include CNTs, graphene, fullerenes, and carbon dots among others. ND have received increasing attention because of their chemical-physical properties, typically their unique faceted surfaces which was observed by Barnard and colleagues [47,48]. The facet driven electrostatics play a key role in how water molecules coordinate the ND surface, thereby remarkably increasing the relaxivity values after conjugation of gadolinium (III) to ND particles. Historically, gadolinium, used for improving image contrast while scanning for tumors, inflammations, and internal organs, has a risk of side effects to the body. Combining it with ND holistically improves the image contrast along with a significant decrease in gadolinium dosing needed for the imaging.

Barnard et al. have shown that DNDs with truncated octahedral shape influence facet-specific surface electrostatic potentials and anisotropic distribution of functional groups (Fig. 19.5) [49].

The unique faceted surfaces of NDs can be treated with various functional groups to modulate interaction with water molecules, contrast agents, and other organic compounds. Barnard and team have further shown that (100) and (100)/(111) edges exhibit strong positive potential, whereas graphitized (111) surfaces exhibit either negative or neutral potential due to asymmetry of the truncated octahedral DNDs. These electrostatic properties result in favorable ND sizes through the interaction of negatively charged (111) facets with neutral (111) or (110), and

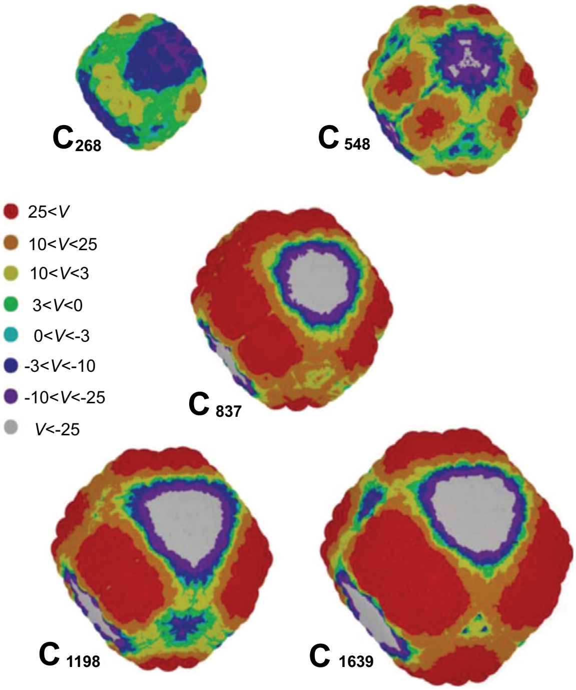

Figure 19.5 Unique electrostatic properties of octahedral DNDs demonstrate a strong relation between shape of facet and its electrostatic potential.
Reproduced with permission A. S. Barnard and M. Sternberg, Crystallinity and surface electrostatics of diamond nanocrystals. *Journal of Materials Chemistry* 17 (2007) 4811–4819.

have demonstrated critical importance of improved tumor therapy [49−51]. Chow et al. have shown that DND clusters resulted in a 10-fold increase in circulatory half-life and markedly improved intratumoral drug retention [52,53]. Hence, suitable DND sizes, with their high adsorption capacity, are effective in drug loading using suitable ND-drug complex for targeted therapy. Overall, Chow et al have demonstrated a efficient and safe approach for ND-based cancer therapy [52,53].

In another example, Guo et al investigated the inhibition of tumor metastasis by cND [44]. The surface of NDs was modified by annealing and treating with oxidizing acid ($H2SO_4$:HNO_3), followed by centrifugation and resuspension in NaOH and HCl solutions [54]. The precipitate was dried at room temperature and cND particles were obtained, which were put through ultrasound treatment every time before use. All experiments to study in vitro tumor metastasis were performed on mice by injecting them with B16 mouse melanoma cells in PBS. Later, these mice were divided in two groups: control group injected with phosphate-buffered saline (PBS) and other with colloid formed by 30 nm cNDs dissolved in PBS. The in vitro experiments show reduced migration of B16 cells using cNDs [55,56]. Guo et al. investigated the biological safety of cNDs in vivo by examining the difference in weight change between control and the cND group, which was less than 20% [44,57]. The H&E stained lung samples of the control group showed a large area of tumor cell mass that invaded the lung parenchyma as shown in Fig. 19.6A (yellow arrow) [44]. Additionally, the surrounding cavity was suppressed and narrowed with small amount of scattered tumor cells on the edges of the tissues in Fig. 19.6A (green arrow) [44].

The tumor cells have high nucleus to cytoplasm ratio with division of tumor cells with hemorrhage in Fig. 19.6A (black arrow) [44]. Conversely, few metastatic tumors were detected in mice injected with cNDs as shown in Fig. 19.6B. These results suggest that cNDs significantly reduced the activity of the lung metastasis.

19.2.2 Biomedical imaging applications

The biocompatibility of NDs, their unique physical and chemical properties, and their easy surface modifiability have made it possible for them to be used in a variety of biomedical imaging applications. In this section, applications of NDs in magnetic resonance imaging (MRI), STED microscopy, and photoacoustic imaging are discussed by illustrating some examples.

19.2.2.1 NDs as contrast agents in MRI

MRI is a noninvasive imaging method primarily used for clinical investigation to improve diagnosis for patient care. Contrary to optical methods, MRI does not have depth limitations and usually has high resolution but has low image sensitivity [45]. To enhance the contrast between healthy and unhealthy tissues, MRI usually relies on external contrast agents and hence, the development of these agents is of paramount importance to improve standards of diagnostic imaging.

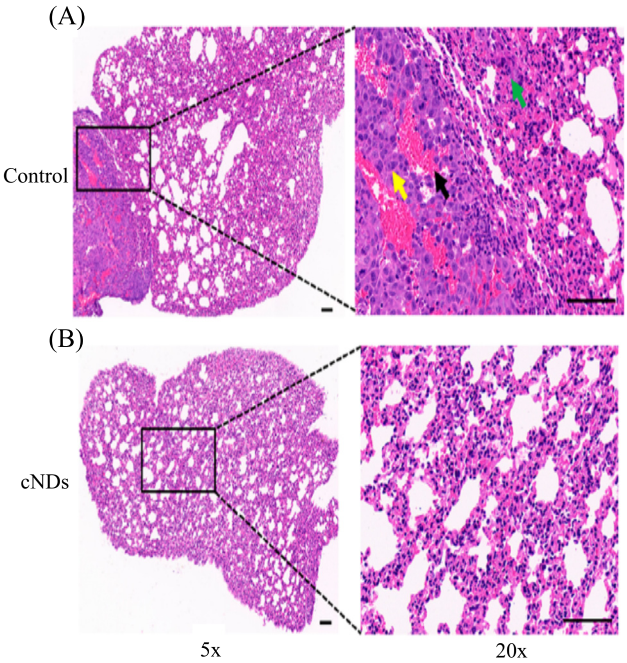

Figure 19.6 Tumor metastasis inhibited by cNDs. (A) Analysis of lung sections of mice treated with PBS (control group) and (B) lung sections of mice treated with cNDs. Reproduced with permission from Q. Guo, L. Li, G. Gao, R. Liu, Y. Einaga and J. Zhi, Nanodiamonds inhibit cancer cell migration by strengthening cell adhesion: implications for cancer treatment, ACS Applied Materials & Interfaces 13 (2021) 9620−9629.

Manus et al. have discussed approach of achieving MRI contrast using ND to attach a magnetic species such as Gd (III) [58]. With the presence of paramagnetic metal, the longitudinal spin relaxation time (T1) of water protons in the surrounding tissue is shortened and leads to contrast in T1-weighted imaging as observed by Caravan et al [59]. This technique was demonstrated to enhance MRI contrast through covalent modification of the ND surface to allow conjugation of GD(III) complexes by Manus et al [58]. In a separate illustration, Waddington et al. have applied a novel approach by using ND as contrast agents to provide high-contrast MRI images by using Overhauser effects [60]. These effects are described by the transfer of spin polarization from one population of spin-active material to another via cross relaxation and are largely used for analysis in nuclear magnetic resonance spectroscopy. NDs can have paramagnetic surface impurities that can be used to transfer spin polarization to ^{1}H spins in nearby water solution [45,61] as shown in Fig. 19.7. Due to low toxicity of NDs even at higher concentration and survivability to in vivo degradation, Waddington et al. proposed potential solution of using NDs for in vivo imaging applications [60,62,63].

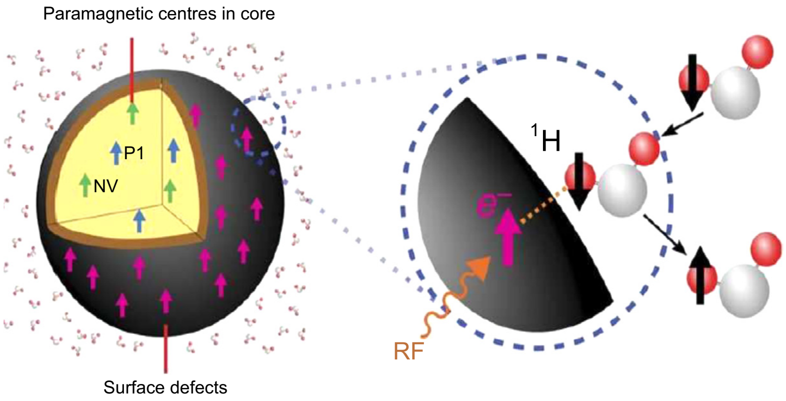

Figure 19.7 Paramagnetic impurities on ND surface to illustrate Overhauser effect, using ultralow magnetic field effectively transferring spin polarization.
Reproduced with permission from P. Caravan, J. J. Ellison, T.J. McMurry and R. B. Lauffer, Gadolinium (III) chelates as MRI contrast agents: structure, dynamics and applications, *Chemical Reviews* 99 (1999) 2293–2352.

19.2.2.2 NDs as photostable markers in STED

Additionally, NDs work well with multimodal microscopy imaging methods such as live cell and small-animal imaging and super resolution STED imaging [61,64–68]. Advantage of STED microscopy technique is its superior lateral resolution but there is a risk of photobleaching due to STED laser and is a limitation for sample observation time [69,70]. NDs have shown to be photostable markers for STED imaging as shown by a novel application of green NDs (Fig. 19.8) as compared to red NDs. This dual color STED microscopy could widen the possibilities of combining different fluorophores for detailed time-lapse imaging at superresolution [71,72]. However, there are some critical challenges to implement NDs in STED microscopy due to the phototoxicity induced by the high laser power for excitation of ND and STED depletion laser. If unresolved, these issues could gate the further implementation of NDs into STED microscopy applications.

19.2.2.3 NDs as contrast agents for photoacoustic imaging

Photoacoustic (PA) imaging is an upcoming and newly evolving noninvasive imaging technique that provides increased screening depth and spatial resolution for small animal in vivo imaging and clinical imaging [72–74]. A desirable contrast can be provided by using contrast agents such as gold nanorods, CNTs, gold nanoshells, etc. [75,76]. Chang et al. investigated NDs as a contrast agent for PA imaging due to their high optical absorbance and demonstrated improved PA imaging sensitivity and specificity [77]. Zhang et al. demonstrated a 71 times and 64 times higher PA signal using DNDs as compared to similar size gold nanorods and single

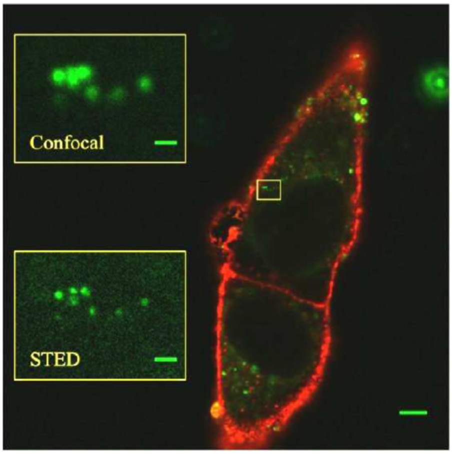

Figure 19.8 STED microscopy of green NDs internalized with membrane stained with a red dye in the HeLa cell (WGA, Alexa Fluor 680, Life Technologies). The two insets show confocal and enhanced resolution with STED microscopy resolving details about the green NDs. Reproduced with permission from G. Laporte and D. Psaltis, STED imaging of green fluorescent nanodiamonds containing nitrogen-vacancy-nitrogen centers, Biomedical Optics Express 7 (2015) 34−44.

wall nanotubes for in vivo small animal imaging [78]. The improved PA contrast in DNDs, compared to other materials, could be mainly arising due to higher optical absorbance and high thermal conductivity of the DNDs. The DNDs used for this experiment had their surface modified with carboxylic groups by strong oxidative acid treatment. Carboxylic groups are strong hydrogen bond acceptors in water which could explain the reported higher thermal conductivity of the DNDs. Chen et al. also found that hydrogen bonding on the ND surface could also play a role in improved PA signal amplitude [79] (Fig. 19.9).

In another illustration, Zhang et al have investigated irradiated NDs (IND) as a molecularly targeted contrast agent to yield sub-mm resolution which could be used for potential low-cost technology to monitor cancer progression [80]. IND surfaces were functionalized with polyethylene glycol (PEG) to improve stability and conjugated with affinity ligand, anti-HER2 peptide, to target HER2 breast cancer cells. Immunocompetent mice bearing orthotopic HER2 positive or negative tumors were administered the INDs, and PA imaging was done using a near-infrared 820 mm laser. PA imaging demonstrated that INDs are localized in tumors and HER2 targeting by INDs (PEG-anti-HER2 peptide) as external contrast agent significantly enhanced PA imaging of HER-2 positive tumors [80]. On further examining the INDs, it was termed as nontoxic. Overall, PA imaging technology can adopt this low cost, new contrast agent using INDs to achieve high resolution and closely monitor and track cancer growth.

NDs, with their extreme properties, have numerous attractive applications, ranging from wear-resistant coating, mechanical lubrication, heat sinks, IR and

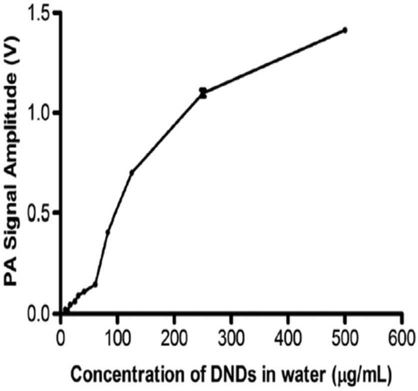

Figure 19.9 PA signal amplitude improves with increasing concentration of DNDs (with surface modified by carboxylic group) in water.

Reproduced with permission from Y. S. Chen, W. Frey, S. Kim, P. Kruizinga, K. Homan and S. Emelianov, Silica-coated gold nanorods as photoacoustic signal nanoamplifiers, *Nano Letters* 11(2) (2011) 348–354.

high-power laser lenses, window coatings ultra-fast switches, field emission devices, flat panel displays, high power devices, and other high-power, high-temperature applications. However, synthesis of ND in large quantities, commercially viable, and at low temperatures is very difficult even today. This is mainly because of the challenges involved in the nucleation and growth steps and overall slower kinetics in lower growth temperatures. There are different methods for synthesis of artificial NDs; however, three main techniques viz., DND, CVD, and HPHT are commercially most viable. However, plasma enhanced chemical vapor deposition (PECVD) is very promising field for the low temperature synthesis of NDs. The authors have previously reported the development of NDs at low temperatures with high-density plasma of microwave PECVD (MW-PECVD), utilizing halogenated precursors with critical process control and compared with other techniques and related material (e.g., diamond-like-carbon) with targeted application in devices [81–88]. Comprehensive study and understanding of the synthesis techniques are available widely in literature and are not the current focus of this chapter.

19.3 Conclusions

In this chapter, special attention has been given on application of NDs in advanced photonics, and the idea of optical emission from NDs, ND-based SPS, and its integration in photonic platforms possible on-chip integration in quantum devices have been elaborated with comprehensive literature survey. These ideas lead to application of NDs in detectors, quantum information processing, communication, computation, and medical imaging. The medical imaging e.g., contrast agents in MRI and photoacoustic imaging, photostable markers in STED, and other biomedical application of NDs are exciting and have been elaborated further, including drug delivery and specific application in cancer therapy. It is evident that the applications of NDs in photonics and biomedical fields have enormous potential and are emerging in an unprecedented speed due the advancements of synthesis techniques, materials engineering, advanced design modules, and microfabrication technologies.

Acknowledgments

This work is partially supported by DST/TDT/DDP-38/2021, Device Development Programme (DDP), by the Department of Science & Technology (DST), Ministry of Science and Technology, Government of India.

References

[1] A.D. Greentree, B.A. Fairchild, F.M. Hossain, S. Prawer, Diamond integrated quantum photonics, Materials Today 11 (2008) 22.

[2] J.M. Taylor, P. Cappellaro, L. Childress, L. Jiang, D. Budker, P.R. Hemmer, et al., High-sensitivity diamond magnetometer with nanoscale resolution, Nature Physics 4 (2008) 810−816.

[3] C.C. Fu, H.Y. Lee, K. Chen, T.S. Lim, H.Y. Wu, P.K. Lin, et al., Characterization and application of single fluorescent nanodiamonds as cellular biomarkers, Proceedings of the National Academy of Sciences of the United States of America 104 (2007) 727.

[4] V. Jacques, E. Wu, F. Grosshans, F. Treussart, P. Grangier, A. Aspect, et al., Experimental realization of Wheeler's delayed-choice gedanken experiment, Science (New York, N.Y.) 315 (2007) 966−968.

[5] L. Childress, M.V. Gurudev Dutt, J.M. Taylor, A.S. Zibrov, F. Jelezko, J. Wrachtrup, et al., Coherent dynamics of coupled electron and nuclear spin qubits in diamond, Science (New York, N.Y.) 314 (2006) 281.

[6] M.V. Gurudev Dutt, L. Childress, L. Jiang, E. Togan, J. Maze, F. Jelezko, et al., Quantum register based on individual electronic and nuclear spin qubits in diamond, Science (New York, N.Y.) 316 (2006) 1312.

[7] B.J.M. Hausmann, B. Shields, Q.M. Quan, P. Maletinsky, M. McCutcheon, J.T. Choy, et al., Integrated diamond networks for quantum nanophotonics, Nano Letters 12 (2012) 1578−1582.

[8] F. Jelezko, J. Wrachtrup, Single defect centres in diamond: a review, Physica Status Solidi (A) 203 (2006) 3207−3225.

[9] P. Siyushev, M.H. Metsch, A. Ijaz, J.M. Binder, M.K. Bhaskar, D.D. Sukachev, et al., Optical and microwave control of germanium-vacancy center spins in diamond, Physical Review B 96 (2017) 081201.

[10] T. Iwasaki, Y. Miyamoto, T. Taniguchi, P. Siyushev, M.H. Metsch, F. Jelezko, et al., Tin-vacancy quantum emitters in diamond, Physical Review Letters 119 (2017) 253601.

[11] U. Jantzen, A.B. Kurz, D.S. Rudnicki, C. Schäfermeier, K.D. Jahnke, U.L. Andersen, et al., Nanodiamonds carrying silicon-vacancy quantum emitters with almost lifetime-limited linewidths, New Journal of Physics 18 (2016) 073036.

[12] I. Aharonovich, S. Castelletto, D.A. Simpson, A. Stacey, J. McCallum, A.D. Greentree, et al., Two-level ultrabright single photon emission from diamond nanocrystals, Nano Letters 9 (2009) 3191−3195.

[13] D.G. Monticone, P. Traina, E. Moreva, J. Forneris, P. Olivero, I.P. Degiovanni, et al., Native NIR-emitting single colour centres in CVD diamond, New Journal of Physics 16 (2014) 053005.

[14] T. Gaebel, I. Popa, A. Gruber, M. Domhan, F. Jelezko, J. Wrachtrup, Stable single-photon source in the near infrared, New Journal of Physics 6 (2004) 98.

[15] J.P. Goss, R. Jones, S.J. Breuer, P.R. Briddon, S. Oberg, The twelve-line 1.682eV luminescence center in diamond and the vacancy-silicon complex, Physical Review Letters 77 (1996) 3041.

[16] L.J. Rogers, et al., Electronic structure of the negatively charged silicon-vacancy center in diamond, Physical Review B 89 (2014) 235101.

[17] Y. Zhou, A. Rasmita, K. Li, Q. Xiong, I. Aharonovich, W.-B. Gao, Coherent control of a strongly driven silicon vacancy optical transition in diamond, Nature Communications 8 (2017) 14451.

[18] E. Neu, et al., Single photon emission from silicon-vacancy colour centres in chemical vapour deposition nano-diamonds on iridium, New Journal of Physics 13 (2011) 025012.

[19] R.E. Evans, A. Sipahigil, D.D. Sukachev, A.S. Zibrov, M.D. Lukin, Narrow-linewidth homogeneous optical emitters in diamond nanostructures via silicon ion implantation, Physical Review Applied 5 (2016) 044010.

[20] K. Li, Y. Zhou, A. Rasmita, I. Aharonovich, W.B. Gao, Nonblinking emitters with nearly lifetime-limited linewidths in CVD nanodiamonds, Physical Review Applied 6 (2016) 024010.

[21] T.T. Tran, M. Kianinia, K. Bray, S. Kim, Z.Q. Xu, A. Gentle, et al., APL Photonics 2 (2017) 116103.

[22] K.Y. Han, et al., Three-dimensional stimulated emission depletion microscopy of nitrogen-vacancy centers in diamond using continuous-wave light, Nano Letters 9 (2009) 3323−3329.

[23] H. Siampour, S. Kumar, V.A. Davydov, L.F. Kulikova, V.N. Agafonov, S.I. Bozhevolnyi, On-chip excitation of single germanium vacancies in nanodiamonds embedded in plasmonic waveguides, Light: Science & Applications 7 (2018) 61.

[24] K. Rivoire, Z. Lin, F. Hatami, W.T. Masselink, J. Vučković, Second harmonic generation in gallium phosphide photonic crystal nanocavities with ultralow continuous wave pump power, Optics Express 17 (2009) 22609−22615.

[25] N. Thomas, R.J. Barbour, Y. Song, M.L. Lee, K.-M.C. Fu, Waveguide-integrated single-crystalline GaP resonators on diamond, Optics Express 22 (2014) 13556.

[26] J.C. Lee, I. Aharonovich, A.P. Magyar, F. Rol, E.L. Hu, Coupling of silicon-vacancy centers to a single crystal diamond cavity, Optics Express 20 (2012) 8891.

[27] J. Wolters, G. Kewes, A.W. Schell, N. Nüsse, M. Schoengen, B. Löchel, et al., Coupling of single nitrogen-vacancy defect centers in diamond nanocrystals to optical antennas and photonic crystal cavities, Physica Status Solidi B 249 (2012) 918−924.

[28] C. Santori, P.E. Barclay, K.-M.C. Fu, R.G. Beausoleil, S. Spillane, M. Fisch, Nanophotonics for quantum optics using nitrogen-vacancy centers in diamond, Nanotechnology 21 (2010) 274008.

[29] P.E. Barclay, C. Santori, K.-M. Fu, R.G. Beausoleil, O. Painter, Coherent interference effects in a nano-assembled diamond NV center cavity-QED system, Optics Express 17 (2009) 8081.

[30] L. Wu, H. Wang, Q. Yang, Q.-X. Ji, B. Shen, C. Bao, et al., Greater than one billion Q factor for on-chip microresonators, Optics Letters 45 (2020) 5129−5131.

[31] H. Kaupp, T. Hümmer, M. Mader, B. Schlederer, J. Benedikter, P. Haeusser, et al., Purcell-enhanced single-photon emission from nitrogen-vacancy centers coupled to a tunable microcavity, Physical Review Applied 6 (2016) 054010.

[32] H. J. Benedikter, T. Kaupp, Y. Hümmer, A. Liang, C. Bommer, A. Becher, et al., Cavity-enhanced single-photon source based on the silicon-vacancy center in diamond, Physical Review Applied 7 (2017) 024031.

[33] S. Schietinger, M. Barth, T. Alchele, O. Benson, Plasmon-enhanced single photon emission from a nanoassembled metal-diamond hybrid structure at room temperature, Nano Letters 9 (2009) 1694−1698.

[34] R. Won, Integrating silicon photonics, Nature Photonics 4 (2010) 498−499.

[35] D. Agarwal, et al., Nanocavity-enhanced giant stimulated raman scattering in Si nanowires in the visible light region, Nano Letters 19 (2019) 1204−1209.

[36] D. Agarwal, J. Yoo, A. Pan, R. Agarwal, Cavity engineering of photon − phonon interactions in Si nanocavities, Nano Letters 19 (2019) 7950−7956.

[37] P. Latawiec, et al., On-chip diamond Raman laser, Optica 2 (2015) 924−928.

[38] S. Reilly, V.G. Savitski, H. Liu, E. Gu, M.D. Dawson, A.J. Kemp, Monolithic diamond Raman laser, Optics Letters 40 (2015) 930−933.

[39] S. Sindhwani, A.M. Syed, J. Ngai, B.R. Kingston, L. Maiorino, J. Rothschild, et al., The entry of nanoparticles into solid tumours, Nature Materials 19 (5) (2020) 566−575.

[40] M.R. Ali, H.R. Ali, C.R. Rankin, M.A. El-Sayed, Targeting heat shock protein 70 using gold nanorods enhances cancer cell apoptosis in low dowse plasmonic photothermal therapy, Biomaterials 102 (2016) 1−8.

[41] R.R. Arvizo, S. Saha, E. Wang, J.D. Robertson, R. Bhattacharya, P. Mukherjee, Inhibition of tumor growth and metastasis by a self-therapeutic nanoparticle, Proceedings of the National Academy of Sciences of the United States of America 110 (17) (2013) 6700−6705.

[42] H.J. Zhou, B. Zhang, J.J. Zheng, M.F. Yu, T. Zhou, K. Zhao, et al., The inhibition of migration and invasion of cancer cells by graphene via the impairment of mitochondrial respiration, Biomaterials 35 (5) (2014) 1597−1607.

[43] L.-Y. Chang, E. Osawa, A.S. Barnard, Confirmation of the electrostatic self-assembly of nanodiamonds, Nanoscale 3 (2011) 958−962.

[44] Q. Guo, L. Li, G. Gao, R. Liu, Y. Einaga, J. Zhi, Nanodiamonds inhibit cancer cell migration by strengthening cell adhesion: implications for cancer treatment, ACS Applied Materials & Interfaces 13 (2021) 9620−9629.

[45] N. Prabhakar, J.M. Rosenholm, Nanodiamonds for advanced optical bioimaging and beyond, Current Opinion in Colloid and Interfacial Science 39 (2019) 220−231.

[46] D. Ho, C.-H.K. Wang, E.K.-H. Chow, Nanodiamonds: the intersection of nanotechnology, drug development and personalized medicine, Science Advances 1 (2015) e1500439.

[47] A.S. Barnard, Self-assemblying nanodiamond agglutinates, Journal of Materials Chemistry 18 (2008) 4038−4041.

[48] A.S. Barnard, Diamond standard in diagnostics: nanodiamond biolabels make their mark, Analyst 134 (2009) 1751−1764.

[49] A.S. Barnard, M. Sternberg, Crystallinity and surface electrostatics of diamond nanocrystals, Journal of Materials Chemistry 17 (2007) 4811−4819.

[50] L. Lai, A.S. Barnard, Anisotropic adsorption, and distribution of immobilize carboxyl on nanodiamond, Nanoscale 6 (2014) 14185−14189.

[51] A.S. Barnard, M.C. Pier, Size and shape dependent deprotonation potential and proton affinity of nanodiamond, Nanotechnology 25 (2014) 445702.

[52] E.K. Chow, X.-Q. Zhang, M. Chen, R. Lam, E. Robinson, H. Huang, et al., Nanodiamond therapeutic delivery agents mediate enhanced chemoresistant tumor treatment, Science Translational Medicine 3 (2011) 73ra21.

[53] E.K. Chow, D. Ho, Cancer nanomedicine: from drug delivery to imaging, Science Translational Medicine 5 (2013) 216rv4.

[54] J.M. Say, C. van Vreden, D.J. Reilly, L.J. Brown, J.R. Rabeau, N.J.C. King, Luminescent nanodiamonds for biomedical applications, Biophysics Reviews 3 (2011) 171−184.

[55] N. Lee, S.R. Barthel, T. Schatton, Melanoma stem cells and metastasis: mimicking hematopoietic cell trafficking? Laboratory Investigation; A Journal of Technical Methods and Pathology 94 (1) (2014) 13−30.

[56] B. Behera, K.S.P. Devi, D. Mishra, S. Maiti, T.K. Maiti, Biochemical analysis and anti-tumour effect of Abrus precatorius agglutinin derived peptides in Ehrlich's ascites and B16 melanoma mice tumor model, Environmental Toxicology and Pharmacology 38 (1) (2014) 288−296.

[57] S.A. Gerber, E.W. Sorensen, A.L. Sedlacek, J.Y.H. Lim, D. Skrombolas, J.G. Frelinger, et al., Local expression of interleukin-2 by B16 melanoma cells results in decreased tumour growth and long-term tumour dormancy, Immunology 138 (3) (2013) 280−292.

[58] L.M. Manus, D.J. Mastarone, E.A. Waters, X.-Q. Zhang, E.A. Schultz-Sikma, K.W. MacRenaris, et al., Gd (III)-nanodiamond conjugates for MRI contrast enhancement, Nano Letters 10 (2010) 484−489.

[59] P. Caravan, J.J. Ellison, T.J. McMurry, R.B. Lauffer, Gadolinium (III) chelates as MRI contrast agents: structure, dynamics and applications, Chemical Reviews 99 (1999) 2293−2352.

[60] D.E.J. Waddington, M. Sarracanie, H. Zhang, N. Salameh, D.R. Glenn, E. Rej, et al., Nanodiamond-enhanced MRI via in situ hyperpolarization, Nature Communications 8 (2017) 15118.

[61] K. Ichikawa, K. Yasukawa, Imaging in vivo redox status in high spatial resolution with OMRI, Free Radical Research 46 (2012) 1004−1010.

[62] N. Koonjoo, E. Parzy, P. Massot, M. Lepetit-Coiffe, S.R.A. Marque, J.-M. Franconi, et al., In vivo Overhauser-enhanced MRI of proteolytic activity, Contrast Media & Molecular Imaging 9 (2014) 363−371.

[63] K. Golman, I. Leunbach, J.S. Petersson, D. Holz, J. Overweg, Overhauser-enhanced MRI, Academic Radiology 9 (2002) 104−108.

[64] N. Mohan, C.-S. Chen, H.-H. Hsieh, Y.-C. Wu, H.-C. Chang, In vivo imaging, and toxicity assessments of fluorescent nanodiamonds in Caenorhabditis elegans, Nano Letters 9 (2010) 3692−3699.

[65] N. Nunn, M. d'Amora, N. Prabhakar, A.M. Panich, N. Froumin, M.D. Torelli, et al., Fluorescent single-digit detonation nanodiamond for biomedical applications, Methods and Applications in Fluorescence 6 (2018) 035010.

[66] N. Prabhakar, M. Peurla, S. Koho, T. Deguchi, T. Nareoja, H.-C. Chang, et al., STED-TEM Correlative microscopy leveraging nanodiamonds as intracellular dual-contrast markers, Small (Weinheim an der Bergstrasse, Germany) 14 (5) (2017).

[67] J.A. Gerstenhaber, F.C. Barone, C. Marcinkiewicz, J. Li, A.O. Shiloh, M. Sternberg, et al., Vascular thrombus imaging in vivo via near-infrared fluorescent nanodiamond particles bioengineered with the disintegrin bitisatin (Part II), International Journal of Nanomedicine 12 (2017) 8471−8482.

[68] Y.-C. Lin, K.-T. Wu, Z.-R. Lin, E. Perevedentseva, A. Karmenyan, M.-D. Lin, Nanodiamond for biolabeling and toxicity evaluation in the zebrafish embryo in vivo, Journal of Biophotonics 9 (2016) 827−836.

[69] G. Laporte, D. Psaltis, STED imaging of green fluorescent nanodiamonds containing nitrogen-vacancy-nitrogen centers, Biomed Opt Express 7 (2015) 34−44.

[70] S. Arroyo-Camejo, M.-P. Adam, M. Besbes, J.-P. Hugonin, V. Jacques, J.-J. Greffet, et al., Stimulated emission depletion microscopy resolves individual nitrogen vacancy centers in diamond nanocrystals, ACS Nano 7 (2013) 10912−10919.

[71] T.-L. Wee, Y.-K. Tzeng, C.-C. Han, H.-C. Chang, W. Fann, J.-H. Hsu, et al., Two-photon excited fluorescence of nitrogen-vacancy centers in proton-irradiated type lb diamond, The Journal of Physical Chemistry 111 (38) (2007) 9379−9386.

[72] J.A. Yang, H.T. Phan, S. Vaidya, C.J. Murphy, Nanovacuum: nanoparticle uptake and differential cellular migration on a carpet of nanoparticles, Nano Letters 13 (5) (2013) 2295−2302.

[73] W. Choi, E.-Y. Park, S. Jeon, C. Kim, Clinical photoacoustic imaging platforms, Biomedical Engineering Letters 8 (2018) 139−155.

[74] K.S. Valluru, J.K. Willmann, Clinical photoacoustic imaging of cancer, Ultrasonography 35 (2016) 267−280.

[75] D. Wu, L. Huang, M.S. Jiang, H. Jiang, Contrast agents for photoacoustic and thermoacoustic imaging: a review, International Journal of Molecular Sciences 15 (12) (2014) 23616−23639.

[76] K. Pu, A.J. Shuhendler, J.V. Jokerst, J. Mei, S.S. Gambhir, Z. Bao, et al., Semiconducting polymer nanoparticles as photoacoustic molecular imaging probes in living mice, Nature Nanotechnology 9 (2014) 233−239.

[77] C.-Y. Fang, C.-C. Chang, C.-Y. Mou, H.-C. Chang, Preparation, and characterization of Ion-Irradiated Nanodiamonds as Photoacoustic Contrast Agents, Journal of Nanoscience and Nanotechnology 15 (2015) 1037−1044.

[78] T. Zhang, H. Cui, C.-Y. Fang, L.-J. Su, S. Ren, H.-C. Chang, et al., Photoacoustic contrast imaging of biological tissues with nanodiamonds fabricated for high near-infrared absorbance, Journal of Biomedical Optics 18 (2) (2013) 0260181−0260186.

[79] Y.S. Chen, W. Frey, S. Kim, P. Kruizinga, K. Homan, S. Emelianov, Silica-coated gold nanorods as photoacoustic signal nanoamplifiers, Nano Letters 11 (2) (2011) 348−354.

[80] T. Zhang, H. Cui, C.-Y. Fang, K. Cheng, X. Yang, H.-C. Chang, Targeted nanodiamonds as phenotype-specific photoacoustic contrast agents for breast cancer, Nanomedicine (Lond) 10 (2015) 573−587.

[81] A. Banerjee, D. Das, Realizing a variety of carbon nanostructures at low temperature using MW-PECVD of (CH_4 + H_2) plasma, Applied Surface Science 273 (2013) 806−815.

[82] A. Banerjee, D. Das, Low temperature synthesis of spherical Nano-diamond, Amit Banerjee and Debajyoti Das, Journal of Experimental Nanoscience 9 (2014) 818−824.

[83] A. Banerjee, D. Das, Fabrication of highly transparent diamond-like carbon anti-reflecting coating for si solar cell application, American Institute of Physics Conference Proceedings 1591 (2014) 856−857.

[84] D. Das, A. Banerjee, Anti-reflection coatings for silicon solar cells from hydrogenated diamond like carbon, Applied Surface Science 345 (2015) 204−215.

[85] D. Das, A. Banerjee, Further improvements of nano-diamond structures on unheated substrates by optimization of parameters with secondary plasma in MW-PECVD, Surface and Coating Technology 272 (2015) 357–365.

[86] A. Banerjee, D. Das, Synthesis of thin film nano-diamonds on unheated substrates by secondary plasma in MW-PECVD, American Institute of Physics Conference Proceedings 1665 (2015) 050077.

[87] A. Banerjee, D. Das, R.R. Sahoo, Anti-friction diamond-like carbon nanocoatings for advanced tribological applications, Santosh Singh, American Institute of Physics Conference Proceedings 1832 (2017) 080036.

[88] A. Banerjee, D. Das, Nano-diamond and Diamond-like Carbon Thin Films for Anti-Reflecting Coating Application on Silicon Solar Cells, Materials Today: Proceedings 5 (2018) 23316–23320.

Future perspectives of carbon quantum dots

20

Amit Banerjee[1], *Sudip K. Batabyal*[2], *Basudev Pradhan*[3,4], *Kallol Mohanta*[5] *and Rama Ranjan Bhattacharjee*[6]
[1]Physics Department, Bidhan Chandra College, Asansol, West Bengal, India, [2]Department of Sciences, Amrita School of Engineering Coimbatore, Amrita Vishwa Vidyapeetham, Coimbatore, Tamil Nadu, India, [3]Department of Energy Engineering, Central University of Jharkhand, Ranchi, Jharkhand, India, [4]Centre of Excellence (CoE) in Green and Efficient Energy Technology (GEET), Central University of Jharkhand, Ranchi, Jharkhand, India, [5]PSG Institute of Advanced Studies, Coimbatore, Tamil Nadu, India, [6]Department of Chemistry, Sister Nivedita University, Kolkata, West Bengal, India

20.1 Introduction

The confinement effect in semiconductor quantum dots with tunable properties helps design new materials tailored to the specific application requirements. While there have been enormous advances in synthesis, functionalization, and fabrication processes along with materials engineering, leading to newer applications of semiconductor quantum dots, promising for commercialization, it is evident that we are still scratching the surface of the potential engagement of quantum dots in daily lives.

The carbon quantum dots (CQDs), part of the carbon nanomaterials family, fascinated researchers due to theirs ultracompact size, excellent photoluminescence, favorable biocompatibility, versatile surface and superior electron transfer ability, and superior physicochemical properties, thus leading to high photoluminescence quantum yields, advancement in sensing, bioimaging, nanomedicine, and catalysis among others [1]. CQDs are promising and nontoxic alternatives to the heavy metals containing semiconductor QDs in various in vivo and in vitro bioimaging, drug delivery, photosensors, and chemiluminescence applications [2]. CQDs have many interesting possibilities with enormous current and future application perspectives (Fig. 20.1). It is interesting to review the future perspectives in terms of scalable synthesis, strategies involved in the building development of the optoelectronic, energy devices, chemical sensing, and biosensing with CQDs. CQDs, with the combination of properties like edge effects and zero-dimensional quantum-confined, lead to development of new generation emitters for light emitting diodes, photoelectric devices (e.g., photodetectors and solar cells), further application in water splitting, and various other optoelectronic devices. However, with all that said and done in the area of CQDs, there are significant underlying challenges in application of these materials in devices, in terms of performance, sustainability, durability, and scalability with standard industrial fabrication processes [3].

Carbon Quantum Dots for Sustainable Energy and Optoelectronics. DOI: https://doi.org/10.1016/B978-0-323-90895-5.00019-9
© 2023 Elsevier Ltd. All rights reserved.

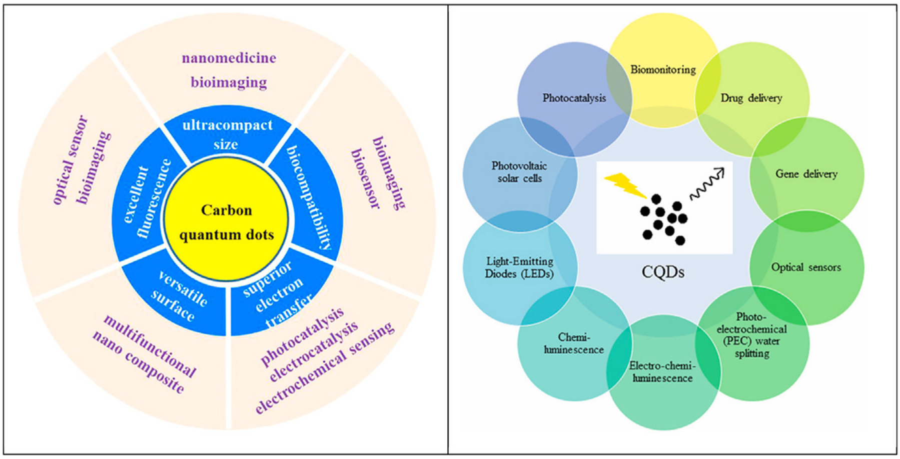
nanomedicine
bioimaging
optical sensor
bioimaging
bioimaging
biosensor
ultracompact size
excellent fluorescence
biocompatibility
Carbon quantum dots
versatile surface
superior electron transfer
multifunctional nano composite
photocatalysis
electrocatalysis
electrochemical sensing
Biomonitoring
Photocatalysis
Drug delivery
Photovoltaic solar cells
Gene delivery
CQDs
Light-Emitting Diodes (LEDs)
Optical sensors
Chemi-luminescence
Photo-electrochemical (PEC) water splitting
Electro-chemi-luminescence

Figure 20.1 Schematics on (A) new development in carbon quantum dots technical applications, mainly sensing, bioimaging, and catalysis [1]. (B) The wide range of interesting applications of CQDs.
Reproduced with permission from *Talanta*, 156–157 (2016) 245–256; *Talanta*, 196 (2019) 456–478.

20.2 Future perspectives of CQDs

Among various interesting emerging QDs which could be designed due to the tunability of these nanomaterials, few stand out with potential to build futuristic technologies.

20.2.1 Luminescent doped/co-doped CQDs for optical sensing

Optical sensing strategies based on luminescent CQDs are well established in sensing, bioimaging, biomedicine, and drug delivery and are expected to progress many folds in years [4,5]. Another interesting area would be fluorescent nanodiamonds (NDs) as a multipurpose tool for various applications such as long-term cell tracking, super-resolution imaging, and nanoscale temperature sensing, due to their robust, photostable, and biocompatible properties [6]. NDs contain high-density ensemble of negatively charged nitrogen-vacancy centers acting as fluorophores [N-V-N ∼green fluorescence; N-V∼ red fluorescence], which have applications in fluorescent bioimaging, cathodoluminescent imaging, stimulated emission depletion imaging, and other multicolor imaging. NDs have several other striking applications such as wear-resistant coating, lubrication, heat sinks, IR and high-power laser lenses, window coatings ultra-fast switches, field emission devices, flat panel displays, high power devices, and other high-power, high-temperature applications. Plasma enhanced chemical vapor deposition (PECVD) is a very promising technique for low-temperature synthesis of NDs with targeted application in fluorescent devices [7–14] (Fig. 20.2).

- **Natural and Biogreen CQDs for Biotechnology and Nanomedicine Applications**: Another interesting emerging area could be synthesis of CQDs from natural resources (nanocrystalline diamond (NCDs)) aiming biotechnology, nanomedicine, and drug delivery applications (Fig. 20.3) [15,16].
- **CQDs as Contrast Agent in Imaging:** CQDs coupled with rhodium have been used as hybrid multimodal contrast agents enabling different imaging modalities in noninvasive biodiagnostics combining optical and X-ray fluorescence [17]. There are also other emerging reports on fabrication and application of a new bimodal imaging nanoprobe (Gd-CQDs@N-Fe_3O_4) integrating the fluorescence ability of CQDs and contrast-enhancing functionality of gadolinium (Gd(III)) ions and Fe_3O_4 nanoparticles into a single hybrid nanostructure for both fluorescence and magnetic resonance imaging [18,19]. CQDs are emerging as a new class of diamagnetic chemical exchange saturation transfer MRI contrast agent [20] (Fig. 20.4).
- **Colloidal CQDs for Green Optoelectronics:** Recently there has been enormous development in different electronics fields (e.g., luminescent, optoelectronic, memory devices) with solution based and colloidal processed semiconductors QDs due to their tunable spectral response [21,22], which extends their applications in the areas of energy, optoelectronic, bioimaging, and CQD-based photodiodes (PDs), etc. [23].

  Considering a future goal for heavy metal-free QDs [23], the commonly available and environment-friendly colloidal QDs used in PDs include graphene, carbon, and silicon (Si) nanocrystals. Graphene QDs (GQDs) and CQDs are promising contenders for green optoelectronic and PD applications due to nontoxicity, biocompatibility, and excellent optoelectrectronic properties (tunable bandgap, absorptivity, etc.) [24–28] and can be used to light near UV sensing [29–31] (Fig. 20.5).

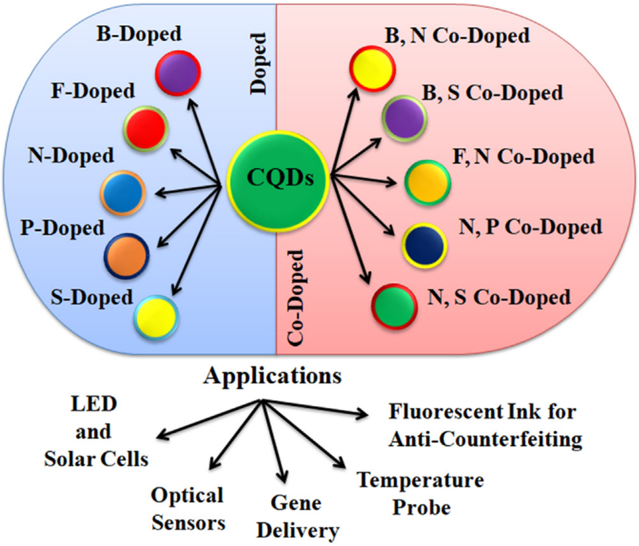
B-Doped
F-Doped
N-Doped
P-Doped
S-Doped
Doped
CQDs
Co-Doped
B, N Co-Doped
B, S Co-Doped
F, N Co-Doped
N, P Co-Doped
N, S Co-Doped
Applications
LED and Solar Cells
Optical Sensors
Gene Delivery
Temperature Probe
Fluorescent Ink for Anti-Counterfeiting

Figure 20.2 Multipotential applications of doped/co-doped CQDs [4].

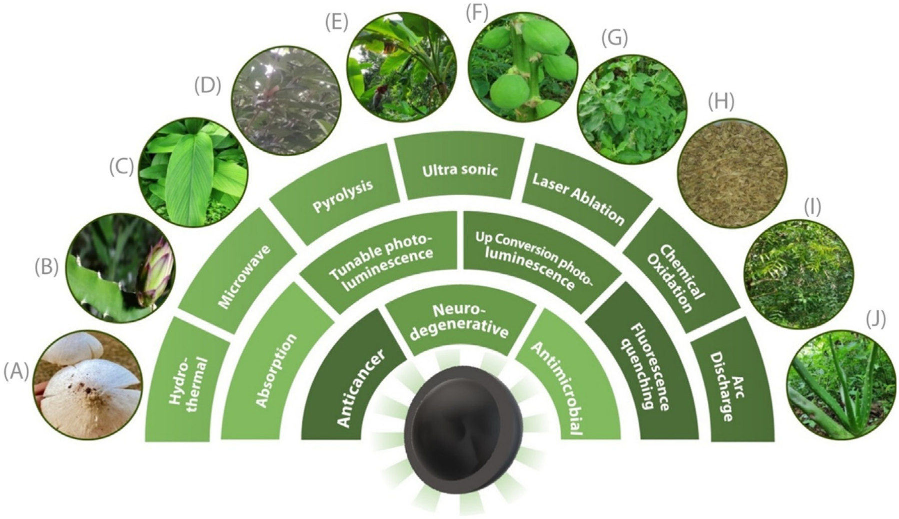
(A)
(B)
(C)
(D)
(E)
(F)
(G)
(H)
(I)
(J)
Hydro-thermal
Microwave
Pyrolysis
Ultra sonic
Laser Ablation
Chemical Oxidation
Arc Discharge
Absorption
Tunable photo-luminescence
Up Conversion photo-luminescence
Fluorescence quenching
Anticancer
Neuro-degenerative
Antimicrobial

Figure 20.3 Various NCDs with potential drug delivery applications: (A) *Pleurotus* species, (B) *Hylocereus undatus*, (C) *Curcuma longa* L., (D) *Manilkara zapota* (L.) P. Royen, (E) Banana leaf, (F) *Carica papaya*, (G) *Ocimum sanctum*, (H) *Foeniculum vulgare* Mill seeds, (I) *Azadirachta indica*, (J) *Aloe vera* (L.) Burm.f.
Reproduced with permission from *Biomedicine & Pharmacotherapy* 132 (2020) 110834.

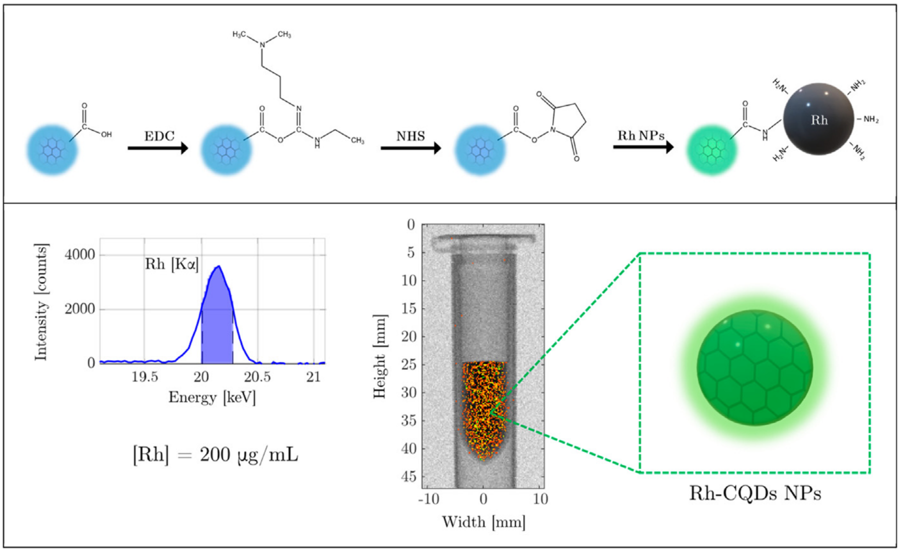
EDC
NHS
Rh NPs
Rh
NH2
Intensity [counts]
4000
2000
0
Rh [Kα]
19.5
20
20.5
21
Energy [keV]
[Rh] = 200 μg/mL
Height [mm]
0
5
10
15
20
25
30
35
40
45
-10
0
10
Width [mm]
Rh-CQDs NPs

Figure 20.4 (A) Coupling of Rh nanoparticles (NPs) with CQDs, leading to the green-emitting hybrid Rh-CQDs NPs. (B) X-ray fluorescence (XRF) experiment on Rh-CQDs NPs at 200 μg/mL with XRF spectrum recorded for 3 min at the central position of the vial: projection image of the vial with absorption and XRF signals; schematic representation of Rh-QDs NPs.
Reproduced under the Creative Commons Attribution License from *Nanomaterials* 11(9) (2021) 2165.

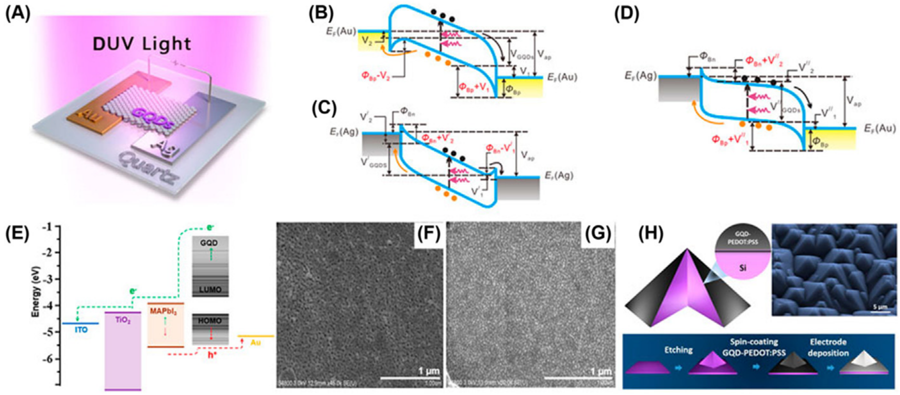

Figure 20.5 (A) Graphene QD-based PDs (B—D) with its energy band diagram: (B) Au/Au, (C) Ag/Ag, and (D) Ag/Au electrodes. (E) Schematic of energy diagram and carrier transportation mechanism of the GQD/$MAPbI_3$ PD. SEM images of (F) $MAPbI_3$ film and (G) GQD/$MAPbI_3$ film. (H) The structure, SEM image, and the fabrication procedure of the device. Reproduced under the Creative Commons Attribution License from *Frontiers in Energy Research*, 16 June 2021, https://doi.org/10.3389/fenrg.2021.666534.

20.3 Conclusion

There are enormous future possibilities for CQDs in sustainable energy and optoelectronics, with the potential to develop various emerging technologies. It is interesting to review and conduct comprehensive study of CQDs for photophysical, physical, and chemical properties, along with their synthesis, characterization, surface engineering, etc. Further, their applications in photodetectors, photovoltaic and light emitting diodes, nanoelectronics, single electron transistors, sensing, biomedical and bioimaging, photocatalytic and CO_2 conversion, electrochemical energy storage, magnetic, nanophotonics, including applications in optical to terahertz (THz) domain, are fascinating. While most of these applications have been discussed widely in the current book, this chapter highlights very specific future perspectives and applications like luminescent CQDs for optical sensing, biogreen CQDs for biotechnology and nanomedicines, CQDs as contrast agent in medical imaging, e.g., MRI, along with application of colloidal CQDs for green optoelectronics. Current discussion is not limited to these few emerging areas of research, but has crossover applications, overlapping other fields, discussed in the current book and beyond.

Acknowledgments

This work is partially supported by DST/TDT/DDP-38/2021, Device Development Programme (DDP), by the Department of Science & Technology (DST), Ministry of Science and Technology, Government of India.

References

[1] L.-M. Shen, J. Liu, New development in carbon quantum dots technical applications, Talanta 156−157 (2016) 245−256.

[2] M.J. Molaei, A review on nanostructured carbon quantum dots and their applications in biotechnology, sensors, and chemiluminescence, Talanta 196 (2019) 456−478.

[3] D. Ghosh, K. Sarkar, P. Devi, K.-H. Kim, P. Kumar, Current and future perspectives of carbon and graphene quantum dots: from synthesis to strategy for building optoelectronic and energy devices, Renewable and Sustainable Energy Reviews 135 (2021) 110391. January.

[4] G. Kandasamy, Recent advancements in doped/co-doped carbon quantum dots for multi-potential applications, Journal of Carbon Research 5 (2019) 24. Available from: https://doi.org/10.3390/c5020024.

[5] N.A. Ahmad Nazri, N.H. Azeman, Y. Luo, A.A.A. Bakar, Carbon quantum dots for optical sensor applications: a review, Optics & Laser Technology 139 (2021) 106928. July.

[6] W.W.-W. Hsiao, Y.Y. Hui, P.-C. Tsai, H.-C. Chang, Fluorescent nanodiamond: a versatile tool for long-term cell tracking, super-resolution imaging, and nanoscale temperature sensing, Accounts of Chemical Research 49 (2016) 400−407. 3.

[7] A. Banerjee, D. Das, Realizing a variety of carbon nanostructures at low temperature using MW-PECVD of (CH4 + H2) plasma, Applied Surface Science 273 (2013) 806−815.

[8] A. Banerjee, D. Das, Low temperature synthesis of spherical nano-diamond, Journal of Experimental Nanoscience 9 (2014) 818−824.

[9] A. Banerjee, D. Das, Fabrication of highly transparent diamond-like carbon antireflecting coating for Si solar cell application, American Institute of Physics Conference Proceedings 1591 (2014) 856−857.

[10] A. Banerjee, D. Das, Anti-reflection coatings for silicon solar cells from hydrogenated diamond like carbon, Applied Surface Science 345 (2015) 204−215.

[11] A. Banerjee, D. Das, Further improvements of nano-diamond structures on unheated substrates by optimization of parameters with secondary plasma in MW-PECVD, Surface and Coating Technology 272 (2015) 357−365.

[12] A. Banerjee, D. Das, Synthesis of thin film nano-diamonds on unheated substrates by secondary plasma in MW-PECVD, American Institute of Physics Conference Proceedings 1665 (2015) 050077.

[13] S. Singh, A. Banerjee, D. Das, R. Sahoo, Anti-friction diamond-like carbon nanocoatings for advanced tribological applications, American Institute of Physics Conference Proceedings 1832 (2017) 080036.

[14] A. Banerjee, D. Das, Nano-diamond and diamond-like carbon thin films for antireflecting coating application on silicon solar cells, Materials Today: Proceedings 5 (2018) 23316−23320.

[15] A. Nair, J.T. Haponiuk, S. Thomas, S. Gopi, Natural carbon-based quantum dots and their applications in drug delivery: a review, Biomedicine & Pharmacotherapy 132 (December 2020) 110834.

[16] K.K. Chan, S.H. Kit Yap, K.-T. Yong, Biogreen synthesis of carbon dots for biotechnology and nanomedicine applications, Nano-Micro Letters 10 (2018). Article number: 72.

[17] G.M. Saladino, N.I. Kilic, B. Brodin, B. Hamawandi, I. Yazgan, H.M. Hertz, et al., Carbon quantum dots conjugated rhodium nanoparticles as hybrid multimodal contrast agents, Nanomaterials 11 (9) (2021) 2165.

[18] Y. Huang, L. Li, D. Zhang, L. Gan, P. Zhao, Y. Zhang, et al., Gadolinium-doped carbon quantum dots loaded magnetite nanoparticles as a bimodal nanoprobe for both fluorescence and magnetic resonance imaging, Magnetic Resonance Imaging 68 (2020) 113−120. May.

[19] Y. Xu, X.-H. Jia, X.-B. Yin, X.-W. He, Y.-K. Zhang, Carbon quantum dot stabilized gadolinium nanoprobe prepared via a one-pot hydrothermal approach for magnetic resonance and fluorescence dual-modality bioimaging, Analytical Chemistry 86 (24) (2014) 12122−12129.

[20] A.J. Zhang, Y. Yuan, M. Gao, Z. Han, C. Chu, Y. Li, et al., Carbon dots as a new class of diamagnetic chemical exchange saturation transfer (diaCEST) MRI contrast, Angewandte Chemie 58 (29) (2019) 9871−9875. Available from: https://doi.org/10.1002/anie.201904722.

[21] M. Liu, N. Yazdani, M. Yarema, M. Jansen, V. Wood, E.H. Sargent, Colloidal quantum dot electronics, Nature Electronics 4 (2021) 548−558.

[22] C.R. Kagan, E. Lifshitz, E.H. Sargent, D.V. Talapin, Building devices from colloidal quantum dots, Science 353 (6302) (2016). Available from: https://doi.org/10.1126/science.aac5523.

[23] S. Miao, Y. Cho, Toward green optoelectronics: environmental-friendly colloidal quantum dots photodetectors, Frontiers in Energy Research (2021). Available from: https://doi.org/10.3389/fenrg.2021.666534. June.

[24] Y.-P. Sun, et al., Quantum-sized carbon dots for bright and colorful photoluminescence, Journal of the American Chemical Society 128 (24) (2006) 7756−7757. Available from: https://doi.org/10.1021/ja062677d.

[25] D. Pan, J. Zhang, Z. Li, M. Wu, Hydrothermal route for cutting graphene sheets into blue-luminescent graphene quantum dots, Advanced Materials 22 (6) (2010) 734−738. Available from: https://doi.org/10.1002/adma.200902825.

[26] Q. Zhang, et al., Solution-processed graphene quantum dot deep-UV photodetectors, ACS Nano 9 (2) (2015) 1561−1570. Available from: https://doi.org/10.1021/acsnano.5b00437.

[27] S. Tajik, et al., Carbon and graphene quantum dots: a review on syntheses, characterization, biological and sensing applications for neurotransmitter determination, RSC Advances 10 (26) (2020) 15406−15429. Available from: https://doi.org/10.1039/D0RA00799D.

[28] D. Ghosh, K. Sarkar, P. Devi, K.-H. Kim, P. Kumar, Current and future perspectives of carbon and graphene quantum dots: From synthesis to strategy for building optoelectronic and energy devices, Renewable and Sustainable Energy Reviews 135 (2021) 110391. Available from: https://doi.org/10.1016/j.rser.2020.110391.

[29] X. Hai, J. Feng, X. Chen, J. Wang, Tuning the optical properties of graphene quantum dots for biosensing and bioimaging, Journal of Materials Chemistry B 6 (2018) 3219−3234. Available from: https://doi.org/10.1039/C8TB00428E.

[30] J. Jia, et al., Facile and efficient fabrication of bandgap tunable carbon quantum dots derived from anthracite and their photoluminescence properties, Frontiers in Chemistry 8 (2020) 123. Available from: https://doi.org/10.3389/fchem.2020.00123.

[31] L. Wang, et al., Full-color fluorescent carbon quantum dots, Science Advances 6 (40) (2020) eabb6772. Available from: https://doi.org/10.1126/sciadv.abb6772.

Index

Note: Page numbers followed by "*f*" and "*t*" refer to figures and tables, respectively.

A

Advanced oxidation process and photocatalysis
  AOP classifications for wastewater treatment, 265*f*
  existing water treatment technology, 264*t*
  for water and wastewater treatment, 265*t*
Application of carbon quantum dots in photocatalysis
  for wastewater purification, 284*t*
  in water purification, 283–285
Applications of magnetic and nanophotonics
  magnetic, 378–382
    carbon quantum dots decorated, 379–382
    Curie like paramagnetism at 2K, 380*f*
    drug delivery and synergistic chemophotothermal therapy, 383*f*
    encapsulated 1D magnetic nanostructures, 382
    HA-HMCN(DOX) @GQDs nanoplatform targeting drug delivery, 381*f*
  nanophotonic applications and single-photon emission, 382–389
    chemical synthesis, optical responses, and circular dichroism characterization, 389*f*
    chiral photonics and twistronics, 386–388
    emission states variation and excited-state lifetime distributions, 390*f*
    and GQDs in the context of light-emitting diodes, 385*f*
    hotspot and plexcitons generation, 391*f*
    light-emitting diodes, 382–384
    memory devices, 386
    photovoltaic solar cell, 384–385
    single/few photons source and cavity-assisted photonics, 388–389
    for solar cells and efficiency characterization, 387*f*

B

Bioimaging applications of carbon dots
  optical property, 227
Bioimaging modalities, development of, 240–241
Biomedical applications of carbon dots
  of C-dots, 228*f*
  crossing blood-brain barrier, 229–230
  drug delivery, 227–229
  gene delivery, 230
Biosensing applications using carbon dots
  therapeutics, diagnostics, and theranostics of C, 231*f*

C

Carbon-based nanodots in photocatalytic CO_2 conversion
  nanoparticle size and percentage of atoms, 298*f*
  photo- and/or electrochemical, 296*f*
  photoconversion, 310–326
  photoinduced charge transfer process, 298*f*
  synthetic approaches and optical properties of, 299–310
Carbon-based quantum dots in CO_2 photoconversion
  with carbon-based catalysts, 314–326
    CO yields over various photocatalysts, 324*f*
    electron transfer reactions for the photocatalytic conversion, 325*f*

Carbon-based quantum dots in CO_2 photoconversion (*Continued*)
    nanoparticle surface functionalized with PEG diamine molecules, 315*f*
    photocatalytic CO_2
      conversion employing carbon-based catalysts, 327*t*
    photocatalytic CO_2 conversion into methanol, 320*f*
    photoinduced electron transfer on, 317*f*
    photoluminescence emission curves, 318*f*
    standard redox potentials, 319*f*
  photocatalytic reduction, 310–314
    graphene and graphene oxide-based materials, 313*f*
    on semiconductor photocatalyst, 311*f*
    solubility characteristics of, 312*f*
  photophysical characteristics, 314–326
Carbon dots:biomedical applications
  bioimaging applications, 226–227
  biomedical applications, 227–230
  biosensing applications, 230–231
  biosynthesis of C-dots, 226
  scope and challenges, 232–233
  structure and functionalization, 225
Carbon dots types, 30*f*
Carbon nanolights, 243
Carbon nanostructures in terahertz domain
  spectroscopy for, 414–416, 415*f*
  time-resolved spectroscopy and conductivity, 416
Carbon quantum dots
  applications of, 410–414
  carbon nanostructures in, 414–416
  characteristic lengths, 400–402
  distinctive properties of, 398
  fabrication techniques of quantum dots, 404–406
  nano carbon dots in light-emitting diode, phototransistor, 399*f*
  optical properties of quantum dots, 407–410
  quantum dot, 402–404
  structure of 0D fullerene, 398*f*
Carbon quantum dot-based nanosensors
  chemical sensing, 206–223
  introduction to, 205–206
Carbon quantum dot in the biomedical field
  applications of, 410–414
  crossing blood-brain barrier, 413–414
  drug delivery, 413
  gene delivery, 414
  optical imaging, 410–412
  photoacoustic imaging, 413
Carbon quantum dots, 243
  in all-weather solar cells, 154
  approaches for synthesis of, 244*f*
  Arc Discharge method, 245
  based bioimaging
    carbon quantum dots, 243
    cDot in bioimaging, 248–253
    development of, 240–241
    nanomaterials as imaging agents, 242–243
    properties of cDots, 247–248
    requirement of imaging agents, 241
    surface activation, 245–247
    synthesis and modifications in, 244–245
    timeline of important discovery, 240*f*
  for battery
    and charge storage capacity, 365*t*
    in lithium-ion and sodium-ion, 362–363
  for charge storage applications
    electrical, 350
    optical, 350–351
    property of, 349–351
    structural property, 349–350
  chemical ablation, 244
  as counter electrode
    bifacial DSSCs, 144*f*
    charge carrier transfer processes, 144*f*
  device applications
    EL spectra and true color photographs of multicolor, 171*f*
  doping, 247
  in dye-sensitized solar cells
    as counter electrode, 142–144
  for electrochemical energy storage applications
    for battery, 361–366
    David V. Ragone plot, 342*f*
    properties of, 349–351
    for supercapacitors, 351–361
    supercapacitors and batteries, 342–349
  electrochemical method, 244

  - EL spectra and true color photographs of multicolor
    - CDs with tethered imidazolidinones (IS-CDs), 173*f*
    - high-color-purity deep-blue (HCP-DB), 173*f*
    - quantum dot based LEDs(QD-LEDs), 174*f*
  - hydrothermal method, 245
  - laser, 200
  - laser ablation, 244–245
  - light-emitting diodes, 169–174
  - in lithium-ion and sodium-ion
    - with bicontinuous electron and Li/Na ion transfer channels, 362*f*
    - and charge storage capacity, 363*t*
    - sodium-ion batteries, 364*t*
  - in lithium-sulfur battery, 364–365
  - microwave irradiation, 245
  - normalized green lasing emission, 175*f*
  - optical gain and lasing, 174–175
  - in organic solar cells
    - S-doped CQDs (N,S-CQDs), 147–148
    - solar device with CQDs, 146*f*
    - structure of device, 146*f*
    - tandem cell architecture, 147*f*
  - in perovskite solar cells
    - current density vs voltage, 153*f*
    - red CQDs (hydroxyl-rich) (RCQs)-doped SnO_2, 152–154
    - slow photon effect, 152–154
  - in potassium-ion battery, 364, 364*t*
  - pyrolysis method, 245
  - as sensitizer, 137–142
    - device structure of, 137*f*
    - N300-CQDs and N719 cosensitized DSSCs device, 141*f*
    - NCQDs using citric acid and ammonia via direct pyrolysis method, 140*f*
    - photovoltaic devices with, 142*t*
    - synthesis scheme of, 139*f*
  - in solid-state solar cells
    - cost-effective heterojunction photovoltaic device, 148–150
    - CQDs-coated SiNWs, 149*f*
    - solid-state solar cells, 148
  - for supercapacitors
    - Bibekananda De’s group, 355
    - charge storage capacity, 361*t*
    - core-shell CuS@CQDs@carbon hollow nanospheres, 355*f*
    - CQDs-inorganic supercapacitors, 356*t*
    - CQDs/PPy, 358*f*
    - of GO/CDs/PPy composite, 357*f*
    - graphene quantum dots, 360–361
    - graphene sheet structure, 351*f*
    - inorganic hybrid for supercapacitors, 353–355
    - MnO_2/CQDs nanowires and cycling, 354*f*
    - organic CQDs and charge storage capacity, 359*t*
    - organic hybrid supercapacitors, 355–359
    - oxygen groups, 352
    - sources and role of, 353*f*
  - surface functionalization, 246–247
  - surface passivation, 246, 246*f*
  - typical device structure of, 171*f*
  - in zinc-ion battery, 365–366
    - Outlook, 365–366
- CDot in bioimaging
  - cDots in in vivo and in vitro bioimaging, 249*f*
  - microbiota using C dots, 250*f*
  - single-molecule imaging, 251–253
  - in in vitro bioimaging, 252*t*
  - in vitro imaging, 250–251
  - in vivo bioimaging, 253*t*
  - in vivo imaging, 251
- Characteristic lengths
  - de Broglie’s theory of wave-particle duality, 400
  - de Broglie wavelength, 400–401
  - diffusion, 401
  - localization, 402
  - mean free path, 401
  - screening, 401–402
- Characterization and physical properties of carbon quantum dots
  - allotropes structures, 57*t*
  - carbon quantum dots, 56–59
    - chemical and electronic structures of, 59–60, 60*f*
    - energy structure of, 57*f*
    - generalized structure of, 59*f*
    - and its lifetime, 58*f*
    - structure of, 59–60

Characterization and physical properties of carbon quantum dots (*Continued*)
  classification as allotropes, 56*f*
  types, 60–61
    doped, 61, 62*f*
    hydrophilic, 61
    hydrophobic, 61
    undoped, 61, 62*f*
Characterization of carbon quantum dots
  photophysical analysis, 80–84
    fluorescence, 82–83, 82*f*
    Forster resonance energy transfer, 83–84
    photoluminescence, 80–82, 81*f*
    riboflavin absorption, 85*f*
  stability of, 85
  structural
    atomic force microscopy, 79, 79*f*
    Fourier-transform Infrared, 78–79, 78*f*
    Raman spectroscopy, 75–76, 76*f*
    scanning electron microscope, 74
    transmission electron microscope, 74–75
    UV-vis spectra, 79–80
    X-ray photoelectron spectroscopy, 77–78, 77*f*
    X-ray powder diffraction, 73–74
    XRD pattern of crystalline, 73*f*
Charging energy, 425
Chemical sensing
  CQDs, 208–212
    fluorescence from, 208–210
    fluorescence sensing by, 211–212
    free zigzag sites with a carbine-like triplet ground state, 210
    quenching and, 211–212, 212*f*
    radiative recombination in small nano-domains, 209–210
  fluorescence-based, 206–208
    band edge and other transitions, 207*f*
    strong emission characteristics in, 207–208
  gas sensing with conducting carbon dots, 218–221
    CQDs on the electrical properties of conducting polymers, 221
    designing of gas sensors using carbonaceous, 220–221
    gas sensors using carbonaceous nanomaterials, 220–221
    of PSS-CQDs, 220*f*
  for Gas/VOC sensing, 222–223
  pH sensor, 212–215
    doped CQDs in sensors, 216–218
    extensive fluorescence quenching of DTT/C-dots, 217*f*
    hydrothermal cutting of oxidized GSs, 213*f*
    pH-dependent UV-vis absorption and PL spectra, 214*f*
    pH sensing with, 214–215
    red emitting carbon dots for specific metal ion detection, 218
    sensing dielectric of surrounding medium, 216
    of solvent sensing, 216
    surface groups in pH sensor applications of, 213–214
    time-resolved fluorescence decay curves, 217*f*
    time-resolved fluorescence decay curves of NRCDs, 219*f*
  sensors, 208
  VOC sensor based on, 221–223
Coulomb blockade oscillation (CBO), 425
Crossing blood-brain barrier, 229–230

D
DeBroglie wavelength, 400–401
DNA intercalator, 21
Drug delivery, 227–229

E
Excitation-dependent fluorescence emission, 80
Exhibiting electroluminescence (EL), 70–71

F
Fabrication techniques of quantum dots
  absorption spectra of CdS nanocrystals, 406*f*
  based on II-VI compound semiconductors, 405–406
  CdSe single nanocrystal absorption spectra, 407*f*
  growth modes, 405*f*
  PL and El spectra of InAs/GaAs, 407*f*

- self-assembled, 406

Fundamentals of carbon quantum dots
- MB degradation by, 273*f*
- semiconductors, 273–274
- simple and facile one-pot synthesis of fluorescent, 274

Fundamentals of supercapacitors
- of batteries, 345–349
  - lithium-ion, 346*f*
  - lithium-ion and sodium-ion, 348*f*
  - reaction mechanism in LSB, 348–349
- and battery, 342–349
- charge storage
  - in EDLC, 343*f*
  - in a hybrid supercapacitor, 344*f*
  - in pseudocapacitors, 344*f*
- of supercapacitors, 342–345

Future perspectives of carbon quantum dots, 474–476
- Colloidal CQDs for Green Optoelectronics, 475–476
- coupling of Rh nanoparticles (NPs), 476*f*
- CQDs as Contrast Agent in Imaging, 475
- Graphene QD-based PDs, 477*f*
- heavy metal-free QDs, 475–476
- luminescent doped/co-doped CQDs for optical sensing, 474–476
- multipotential applications of doped, 475*f*
- Natural and Biogreen CQDs for Biotechnology and Nanomedicine Applications, 475
- new development, 474*f*
- potential drug delivery applications, 476*f*

G

Gene delivery, 230

Graphene quantum dots (GQDs), 40

H

Hotoluminescence properties of carbon quantum dots
- aggregation-induced emission in, 12–20, 13*f*
  - added metal ions effect, 18–20
  - changes in, 15*f*
  - concentration-dependent luminescence mechanism, 19*f*
  - digital photographs of, 17*f*
  - emission maxima *versus* concentration of, 18*f*
  - energy transfer process, 18*f*
  - excitation-dependent emission of, 14*f*
  - GSH-CQDs in varying ethanol-water mixtures, 16*f*
  - material concentration effect, 15*f*
  - of N-CQDs, 20*f*
  - NDI-FONPs, 15*f*
  - of OPD-CQDs, 19*f*
  - PL decay curves of, 17*f*
  - PL spectra of GSH-CQDs, 16*f*
  - solvent polarity effect, 13–16
  - THF-water solvent percentage, 15*f*
- blue-, green-, yellow-, and red-emissive, 5*f*
- confinement effect, 4
- CQDs in daylight, 5*f*
- doping nonmetallic heteroatoms, 5–8
  - nitrogen precursor effect, 7*f*
  - wavelength-dependent emission maxima, 7*f*
- electroluminescence of carbon dots, 23–25
  - CQD-LED and doped CQD-LEDs, 25*f*
- Förster resonance energy transfer, 20–22
  - coupling chemistry for FRET-CQD-DDS, 19*f*
  - CQD-EtBr based FRET pair, 22*f*
  - FRET-CQD-DDS, 19*f*
- heteroatom-mediated surface defects, 8
- influence of edge states, 8–9
- nonpolar solvents, fluorescence PL, 10*f*
- normalized PL spectra of, 6*f*
- photoinduced electron transfer, 22–23
- red edge effect, 9–11
- surface defect states, 11–12
  - passivated carbon dots with PEGs, 12*f*
- triple carbenes at zigzag sites, 9*f*

Hydrothermal carbonization, 245

Hydrothermal treatment of carbon quantum dots
- type of green precursor, 281*t*

I

Imaging agents, 241

Inner filter effect, 95

Ionization energy, 402

K

Kondo effect, 36–37

L

Light-emitting diode application of carbon quantum dots
  device applications, 169–175
  optical properties of, 163–169
  synthesis methods of functionalized, 159–163
Localization length, 402, 436–437

M

Magnetic and nanophotonics applications of carbon quantum dots
  applications, 378–389
  context of magnetic and nanophotonics, 379*f*
Mechanism of photocatalysis
  principle of photocatalytic, 267*f*
  semiconductor photocatalyst, 266
Memory devices
  classifications of, 185–186, 187*f*
    light excitation dependence of photoinduced current and persistent photoconductivity, 187*f*
  random access memory, 187–193
    artificial neuromorphic networks (ANNs), 190*f*
    cyclic multiple-valued voltage, 192*f*
    effects of UV irradiation on RS, 188*f*
    energy band diagram of the rectifying memory device, 189*f*
    RS behavior and retention characteristics, 191*f*
    WRER cycles, 192*f*
Mesoscopic devices, 400
Metal sulfides
  dye wastewater, 272*t*
Methodology of carbon quantum dots
  amino-functionalized fluorescent, 94
    amino-functionalized, 95
    branched polyethylenimine functionalized, 94–95
    by hydrothermal carbonization of chitosan, 94*f*
    spiropyran-functionalized, 95–96
  condensation reaction, 100–101
    Europium-adjusted, 101
    off-fluorescence probe of, 101*f*
  microwave-assisted pyrolysis, 96–99
    hyperbranched polyethylenimine and isobutyric amide functionalized C-dots, 96–97
    organic dye-functionalized, 98–99
    organosilane functionalized, 97–98, 98*f*
    synthesis of organic dyes, 99*f*
  oxidation-polymerization reaction, 101–102
    preparation of CD-PANI, 102*f*
  sol-gel reaction, 99–100
    synthesis of CDs@MIP, 100*f*

N

Nanocarbon-based single-electron transistors as electrometer
  reviewing published work, 434–452
  single-electron transistor as an electrometer, 426–434
  theory, 423–425
Nanodiamond photonics
  ND photonic applications, 457–459
    xz-profile of individual NV color center, 458*f*
  optical emission from diamond, 455–456
    SiV defect, 456*f*
    spectrum showing SiV, 457*f*
Nanodiamonds for advanced photonic and biomedical applications
  NDs for biomedical applications, 459–466
  photonics, 455–459
Nanoelectronic applications of carbon quantum dots
  carbon quantum dot laser, 200
  memory devices, 185–193
  sensors, 194–197
  transistors, 193–197
Nanomaterials as imaging agents, 242–243
NDs for biomedical applications
  cancer therapy, 459–462
  gain attention of researchers, 460*f*
  imaging, 462–466
    contrast agents for, 464–466
    as contrast agents in MRI, 462–463
    Overhauser effect, 464*f*
    PA signal amplitude, 466*f*
    as photostable markers in STED, 464

    - STED microscopy of green, 465*f*
  - tumor metastasis inhibited by cNDs, 463*f*
  - unique electrostatic properties of octahedral DNDs, 461*f*

O

- Optical absorption and emission
  - and electrical property, 108–111
  - GQDs with size and morphology, 111*f*
  - PL spectra of NGQDs, 112*f*
  - spectrum of SNGQDs, 110*f*
- Optical absorption properties of carbon quantum dots
  - Kasha's molecular exciton theory, 3*f*
  - UV-visible spectrum and, 3*f*
- Optical properties of carbon quantum dots
  - electroluminescence, 168–169
    - based LED device structure, 170*f*
  - optical absorption, 164
    - daylight photographs, 165*f*
    - UV excited fluorescence, 166*f*
    - UV-visible optical absorption, 165*f*
  - from ultraviolet to near-infrared regions, 164–168
    - due to quantum confinement effect, 164–165
    - multicolor fluorescent CQDs, 167*f*
    - surface passivation and functionalization effect, 166–167
    - up-conversion photoluminescence, 168
    - UV excited fluorescence images of, 168*f*
- Optical properties of carbon quantum dots
  - and graphene quantum dots, 299–310
    - multicolor fluorescence, 303*f*
    - structural depiction of CDs, 302*f*
    - top-down and bottom-up methods, 301*f*
  - optical properties of, 304
    - absorption spectrum of aqueous dispersed, 305*f*
    - chemical structure on the photoluminescence behavior, 308*f*
    - fluorescence spectra of water-soluble, 306*f*
  - synthetic approaches and, 299–310
- Optical properties of indirect gap nanocrystal
  - enhanced phototransition in a silicon nanocrystal, 409*f*
- Optical properties of quantum dots
  - oscillator strength for phototransition, 408
  - phototransition in, 408
  - widening of bandgap, 408
- Optoelectronics applications of carbon quantum dots
  - Si/GQDs heterojunction solar cell, 113*f*
  - silicon-based heterojunction solar cell, 112–113

P

- Photocatalysts material
  - semiconductors on the potential scale, 269*f*
- Photocatalytic applications for wastewater treatment
  - advanced oxidation process, 263–266
  - application of, 283–285
  - binary metal oxides, 268–270
  - fundamentals of, 271–274
  - hydrothermal treatment of, 278–282
  - mechanism of photocatalysis, 266–267
  - metal sulfides, 270–271
  - in photocatalysis, 274–277
  - photocatalysts material, 268
  - synthesis route of, 277–278
  - watermelon rinds potential as, 283
- Photodetector applications of carbon and graphene quantum dots, 113–128
  - optical absorption, emission, and electrical property, 108–111
  - optoelectronics applications of, 112–113
  - synthesis of, 106–108
- Photodetector applications of carbon quantum dots
  - FET-based photodetectors using, 114–120
    - device structure of DUV photodetector, 114*f*
    - graphene/NGQDs FET-based phototransistor, 116*f*
    - MoS_2/GQDs phototransistor, 119*f*
    - photodetector fabrication process, 115*f*
    - schematic image of monolayer (ML), 118*f*
  - and graphene quantum dots, 113–128
  - polymer nanocomposite-based photodetectors, 125–128

Photodetector applications of carbon quantum dots (*Continued*)
    based photodetectors and performances, 127*t*
    growth process of the hybrid device, 125*f*
    I-V characteristics, 126*f*
  sensitized nanomaterial-based photodetectors, 120–125
    IV characteristics of GQD/ZnO NRs photodetector, 123*f*
    sensitized ZnO NR/GaN-NT heterostructure, 124*f*
    Si nanowire/CQD device, 123*f*
    time-dependent photocurrent, 122*f*
    ZnO nanorods, 121*f*
Photophysical properties of carbon quantum dots
  classes of, 2*f*
  optical absorption of, 2–3
  photoluminescence of, 4–25
Photovoltaic application of carbon quantum dots
  in all-weather solar cells, 154
  in dye-sensitized solar cells, 136–144
  in perovskite solar cells, 150–154
  in solid-state solar cells, 148–150
Physical and chemical properties of carbon dots via computational modeling
  applications in different fields, 30*f*
  different carbon dots, 29–30
  property of, 31
  theoretical study of, 32–37
Physical property of carbon quantum dots
  biological, 72
    bioimaging of HeLa cells, 72*f*
  catalytic reactions of, 66*f*
  composite and hybrid structures of, 66*f*
  optical, 66–71
    absorption, 67–68
    electroluminescence, 70–71
    fluorescence, 69
    from glucose/NaOH, 69*f*
    of MCBF, 67*f*
    phosphorescence, 69–70, 70*f*
    photoluminescence, 68–70
    up-converted photoluminescence, 71, 71*f*
  photoinduced electron transfer, 72
  physiochemical property, 64–65, 65*f*
Properties of cDots
  fluorescence, 247–248
  quantum yield, 248
Property of carbon dots
  computational methods applied to study, 31
  system size *versus* computational cost, 31*f*
Pyrolysis, 96

Q

Quantum dot
  density of states of electrons in, 403–404, 404*f*
  Schrodinger's equation for a quantum box, 403

R

Reviewing published work
  Al-based single-electron transistor, 434–442
    clean IQHE system, 435*f*
    color map of spatial density, 443*f*
    earlier discovered integer quantum Hall effect (IQHE), 434
    electrical imaging of the quantum hall state, 434–440
    inverse compressibility, 438*f*
    Landau level contours, 437*f*
    monolayer graphene, 441*f*
    scanning single-electron transistor, 440–442
  application of carbon nanotube-based single-electron transistor, 442–452
    cantilever-mounted SET scanning, 444*f*
    CNT-based SET, 449
    gate-dependent motion of domains, 446*f*
    graphene device with a bent channel, 451*f*
    optical micrograph of the device, 450*f*
    origin of anomalous piezoelectricity in LAO/STO, 443–447
    piezoelectric response, 445*f*
    resistivity, alternating current, 448*f*
    voltage drop and current density in graphene/, 447–452
Roles of carbon quantum dots in photocatalysis

  allocate additional surface for adsorption and reaction, 277
  broaden the optical absorption range of, 274–275
  charge separation and electron transfer, 276–277
  photoexcitation of, 276*f*
  upconversion photoluminescence, 276*f*

S

Scanning cavity microscopy, 457–458
Single-electron transistor as an electrometer
  Al/AlOx/Al structure, 431*f*
  backgate-2DES-SET structure, 427
  2DES sample, 430*f*
  experimental realization of, 429–434
  measurement using a SET scanning probe, 428*f*
  measuring inverse compressibility, 426–429
  nanoassembled SET device, 432*f*
  SETs using Al QD and CNT QD, 433*t*
Single-electron tunneling, 425
S-K mode, 406
Solar cell, 135–136
Surface engineering of carbon quantum dots
  in carbogenic allotropes, 93
  carbon nanotube *versus*, 91–92
  functionalities in, 92*f*
  methodology, 93–102
Synthesis methods of functionalized carbon quantum dots
  arc discharge, 160
    liquids for production of, 161*f*
  electrochemical synthesis, 160, 160*f*
  hydrothermal and solvothermal synthesis, 163, 163*f*
  microwave-assisted synthesis, 161–162, 162*f*
  pulsed laser ablation/passivation technique, 161, 162*f*
Synthesis of carbon quantum dots
  basic techniques for, 42–51
  carbon quantum dots, 39–42
    graphene oxide, 40*f*
    principles of synthesis, 41–42
    structure of, 40–41, 41*f*
Synthesis of carbon quantum dots and graphene quantum dots
  bottom-up synthesis process, 107–108
    AFM micrograph of NGQDs, 109*f*
    boron doped GQDs(BGQDs), 110*f*
  top-down synthesis process, 106–107
    growth of GQDs from SWCNTs, 107*f*
    treatment procedures of coal samples, 108*f*
Synthesis route of carbon quantum dots
  bottom-up method, 278
  methods to synthesize, 279*t*
  top-down method, 277–278

T

Techniques for carbon quantum dot preparation
  bottom-up approach, 48–51
    hydrothermal method, 49–51, 50*f*
    microwave-assisted method, 49, 49*f*
    PEG-functionalized FCNs, 52*f*
    ultrasound-assisted method, 51
  top-down approach, 42–48
    arc discharge method, 42–43
    chemical ablation/oxidation, 47–48
    controllable synthesis of fluorescent nanomaterials, 45*f*
    electrochemical synthesis, 46–47
    laser ablation, 43–45, 44*f*
    plasma treatment, 45–46
    from sugarcane bagasse pulp, 48*f*
Theoretical study of carbon quantum dots
  electrocatalytic, 35–36
    properties of CQDs and GQDs, 35*f*
  electronic structure, 32–33
    energy gap vs the size of the aromatic ring, 32*f*
  Kondo effect in, 36–37
  optical property, 33–34
  PL and fluorescence mechanisms, 34*f*
  transport, 36
    long-distance interaction via Klein tunneling, 37*f*
Theory
  energy for states, 426*f*
  origin of coulomb blockade oscillation, 423–425
  potential landscape across, 424*f*
  SET showing the equivalent electrical circuit, 424*f*
  to single-electron transistor, 423

The red edge effect, 11
Transistors
  basics of, 193–194
  carbon quantum dots used in, 194–197
    CQD channel, 195*f*
    current vs voltage curves, 197*f*
    fluorescence decay traces of, 198*f*
    humidity sensor fabrication and data acquisition setup, 199*f*
    phototransistor fabricated with the ZnS/carbon QDs, 196*f*

U
Unipolar device, 193

W
Watermelon rinds potential as carbon precursor, 283
Write-read-erase-read (WRER), 185